Model Selection for
Performance-Based Earthquake Engineering of Bridges

Richard Tyler Ranf

A dissertation submitted in partial fulfillment
of the requirements for the degree of

Doctor of Philosophy

University of Washington

2007

Program Authorized to Offer Degree: Department of Civil and Environmental Engineering

University of Washington
Graduate School

This is to certify that I have examined this copy of a doctoral dissertation by

Richard Tyler Ranf

and have found that it is complete and satisfactory in all respects,
and that any and all revisions required by the final
examining committee have been made.

Chair of the Supervisory Committee:

_____

Marc Eberhard

Reading Committee:

_____

Marc Eberhard

_____

John Stanton

_____

Pedro Arduino

_____

Laura Lowes

Date: _____

University of Washington

Abstract

Model Selection for
Performance-Based Earthquake Engineering of Bridges

Richard Tyler Ranf

Chair of the Supervisory Committee:
Professor Marc Eberhard
Civil and Environmental Engineering

Performance Based Earthquake Engineering (PBEE) is becoming an increasingly attractive alternative to traditional bridge design practice. The PBEE framework enables engineers to predict the seismic performance of a structure at multiple levels, including: force and deformation demands, expected level of damage, and likely repair costs. For bridges, these performance levels can be predicted with numerically intensive nonlinear models of the soil, foundation and structure. However, it is preferable in practice to use simpler methods to model a bridge system.

The objectives of this dissertation were to develop a calibrated numerical model of a reinforced concrete bridge on drilled shafts from three experiments (shake table, centrifuge, and pseudo-static component tests), and to use this model to evaluate the accuracy of a variety of simpler bridge modeling strategies within a performance-based framework. This research resulted in (1) the generation of experimental data from a series of shaking table tests, (2) the characterization of the shake-table specimen using response measurements and system identification methodologies, (3) the development of a calibrated numerical model of a reinforced concrete bridge on a drilled shaft foundation (prototype model), and (4) the evaluation (within a performance-based framework) of the accuracy and precision of simpler foundation and structural modeling strategies.

The accuracy and precision of demand and damage estimates from 12 simpler modeling

strategies were evaluated by comparing them to the prototype model using suites of 40 near-field and 30 far-field excitations. For stiff, dry sand, the two-span bridge system was accurately and precisely modeled using inelastic column elements and fixing the columns at the estimated depth of maximum moment within the pile (three column diameters for this bridge system). Furthermore, the accuracy and precision of the demand and damage estimates were insensitive to moderate changes in the depth of fixity, enabling the fixity depth to be estimated based on empirical equations rather than by using a nonlinear soil-foundation model.

TABLE OF CONTENTS

LIST OF FIGURES

LIST OF TABLES

xi

ACKNOWLEDGMENTS

Due to the size and scope of this project, there will undoubtedly be people I will have missed in my acknowledgements of their efforts, and for that I am sorry. And to the rest of you, who I remembered to acknowledge, I am equally sorry.

I would first like to acknowledge all of the help and guidance my advisor Marc Eberhard has provided me over the years. His insight and contributions have been unrivaled throughout this project. I would also like to thank all of the members of my committee: Marc Eberhard, Pedro Arduino, John Stanton, Laura Lowes and Charles Roeder. This committee helped ensure that this research was both practical and relevant to the current and future direction of structural engineering. Nathan Kutz, my Graduate Student Representative from the Applied Mathematics department at UW, ensured that the members of my committee placed a cap on how much useful information I put in this document.

Being that this was a collaborative project between schools, I have many people to thank at different universities. I worked closely with my colleague Nathan Johnson, and his advisors David Sanders and Saiid Saiidi, at UNR during construction and numerical modeling of our specimen. They also made me feel at home while living in Reno during construction and testing. Patrick Laplace made my time in the lab at UNR pleasant with his vast knowledge of control systems and data acquisition.

Matthew Dryden and his advisor Gregory Fenves, at UCB, also provided invaluable advice and support during the numerical modeling of the specimen.

Hyung-Suk Shin, with his advisors Pedro Arduino and Steven Kramer, at UW were great colleagues to conduct research with, providing the necessary geotechnical knowledge for many research collaborations.

Akira Makido, with his advisor Julio Ramirez, who tested a series of columns and bents at Purdue University similar to those in the shaking table specimen, were pillars for collaborative research. Sharon Wood, who conducted field tests for the SFSI project, was a great PI for the project, helping keep the goals of the project clear and the schedule on track.

Other members of the SFSI collaborative group, whom I did not interact directly with, nonetheless made the project an exciting and interesting experience.

Many of my colleagues and peers at UW made research much more pleasant by assisting me with conceptual and computational problems, including: Mike Berry, Nilanjan Mitra, Hyung-Suk Shin and Greg Banks. Mike Berry also travelled to Reno during testing to assist in damage inspection during the shake-table tests.

NSF provided funding for this project, and also provided my personal funding through a graduate research fellowship.

Finally, I would like to thank my wife Elizabeth, who had to tolerate all of my long trips to Reno, and all of my insufferable (to her) conversations about reinforced concrete.

Chapter 1

INTRODUCTION

1.1 Project Motivation

The primary goal of current bridge seismic design is to ensure a "low probability of collapse" (AASHTO, 2004). Although collapse prevention is important, the current design procedures do not provide decision makers with other important predictions of seismic performance of a bridge, such as expected levels of damage, likely repair costs, and the extent of disruption of function.

Performance Based Earthquake Engineering (PBEE) has emerged in recent years as a viable design alternative to traditional practice. PBEE attempts to explicitly predict performance levels of structures so that issues of serviceability and life safety can be addressed consistently. The Pacific Earthquake Engineering Research Center (PEER) was established to develop tools for implementing PBEE within a probabilistic framework. The importance of PBEE is reflected within the center's mission statement.

> This approach is aimed at improving decision-making about seismic risk by making the choice of performance goals and the tradeoffs that they entail apparent to facility owners and society at large. The approach has gained worldwide attention in the past ten years with the realization that urban earthquakes in developed countries - Loma Prieta, Northridge, and Kobe - impose substantial economic and societal risks above and beyond potential loss of life and injuries. By providing quantitative tools for characterizing and managing these risks, performance-based earthquake engineering serves to address diverse economic and safety needs.

- Pacific Earthquake Engineering Research Center

To successfully implement PBEE for bridges, it is necessary to develop modeling methodologies that are both accurate and precise. In some cases, it may be necessary to model the nonlinear, dynamic response of the entire soil-foundation-structure system. In practice, simpler modeling strategies are preferable. The consequences of making various modeling approximations on performance predictions need to be evaluated.

1.2 Experimental and Modeling Opportunities

The accuracy of models of bridge systems has been difficult to quantify because individual experiments are typically inadequate for accurately simulating the dynamic behavior of reinforced concrete soil-foundation-structure systems in the nonlinear range of response.

The National Science Foundation's George E. Brown Jr. Network for Earthquake Engineering Simulation (NEES, 2005) provided the framework necessary for overcoming the limitations of individual experiments, which has enabled the numerical modeling of entire soil-foundation-structure systems. Utilizing four NEES sites, four sets of experiments were conducted (Wood et al., 2004) that enabled the development of a calibrated numerical model simulating a reinforced concrete bridge on drilled-shaft foundations. An illustration of the four experimental specimens (shaking table, centrifuge, component, and field tests) is shown in Fig. 1.1. The advantages and limitations of the four experiment types are provided in Table 1.1 and are summarized in the following paragraphs.

Table 1.1: Advantages and limitations of various experiment types

Test Type	Scale	SFSI	Dynamic	Statistically Determinate	System	Large Structural Strains	Large Soil Strains
Shaking Table	1:4	No	Yes	No	Yes	Yes	No
Centrifuge	1:52	Yes	Yes	No	Yes	No	Yes
Component	1:4-1:2	No	No	Yes	No	Yes	No
Field	1:4	Yes	No	Yes	No	Yes	Yes

Shaking table tests were conducted at the University of Nevada, Reno (UNR) on a two-span reinforced concrete bridge with fixed-column bases. The tests modeled the geometry and material characteristics of the structure well, but neglected soil-structure interaction.
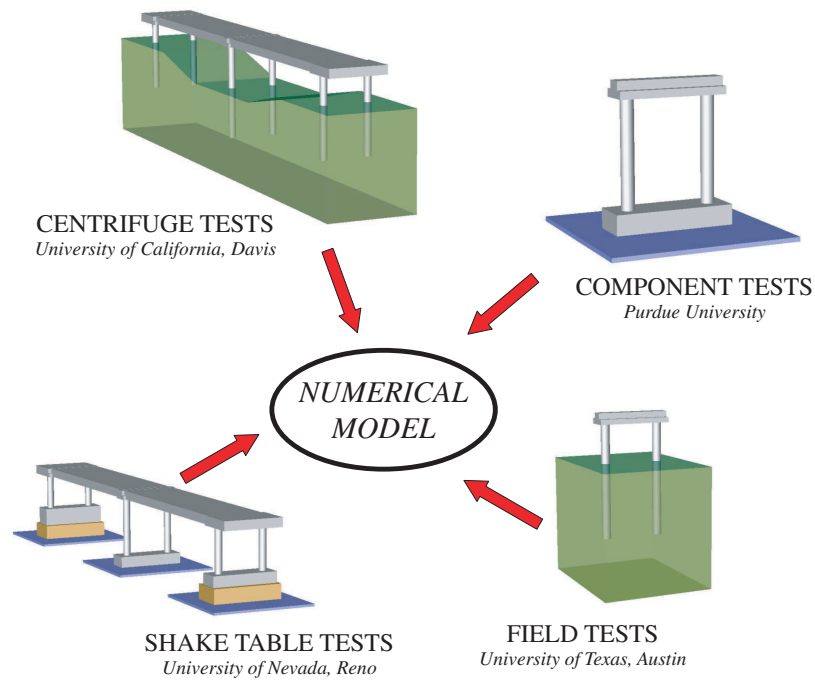
Figure 1.1: Illustration of the four experiments developed for the SFSI project

Because force-deformation data was not available for this large indeterminate system, it was difficult to characterize local effects within the structure under dynamic loading.

Centrifuge tests were conducted at the University of California, Davis (UCD) on a two-span aluminum bridge founded on drilled shafts. These tests simulated the dynamic interaction between the structure and the soil. The main limitation of this experiment was the small scales at which the specimens were tested, which made it necessary to model the reinforced concrete columns with aluminum tubes.

Pseudo-static component tests were conducted at Purdue University on fixed-base column (at 1/2 scale) and bent (at 1/4 scale) specimens with nominally identical properties as the shortest bent in the shaking table experiment. These tests provided valuable information about the cyclic force-deformation response of a column and bent, but they did not model the rate effects, the redistribution of forces from one bent to the others, or the

soil-structure interaction.

Field tests were conducted at the University of Texas, Austin (UT) on column bents supported on drilled shafts. The specimens were dynamically tested at low amplitudes, and then were subjected to static pushover tests to evaluate their nonlinear response. These tests accurately modeled the reinforced concrete structure and the static interaction between the structure and the soil in the nonlinear range. The limitations of these tests were that the low-level vibration tests did not induce significant nonlinear deformations, and pushover tests did not capture rate effects due to dynamic loading.

Individually, none of these experiments accurately simulated the soil-foundation-structure system. However, these experiments provided the opportunity to combine numerical models of the individual tests to accurately simulate a reinforced concrete bridge on drilled shafts.

1.3 Dissertation Objectives

The objectives of this dissertation were (1) to develop a calibrated model of a reinforced concrete bridge on drilled shafts from three experiments (shaking table, centrifuge and pseudo-static component tests), and (2) to use this model to evaluate the accuracy of a variety of seismic modeling strategies within a performance-based framework. In support of these objectives, this research resulted in:

1. the generation of experimental data from shaking table tests of an asymmetric, two-span, reinforced concrete bridge excited by coherent and incoherent earthquake motions;

2. an evaluation of the benefits and limitations of various system identification methodologies to characterize the dynamic properties of the shaking table specimen, and the use of these methodologies to assess the accuracy of the shaking table model;

3. the development of a numerical model of a reinforced concrete bridge on drilled shafts, calibrated using data from three experiments (shaking table, centrifuge, and component tests); and

4. the evaluation (within a performance-based framework) of the effects of foundation and material modeling approximations on the seismic response of bridges to near-field

and far-field ground motions.

1.4 Dissertation Scope and Organization

A chapter-by-chapter outline illustrating how the objectives of this research were completed is presented in Table 1.2, with a summary of each chapter provided in the following paragraphs.

Table 1.2: Dissertation Overview

Objective	Chapter	Contents
1. Experimental Testing	2	Specimen Development
	3	Motion Development and Test Schedule
2. System Characterization	4	Specimen Response and Observed Damage
	5	System Identification Algorithms
	6	System Identification Results
3. Numerical Model Development	7	Shaking Table Model Development
	8	Model Calibration and Assessment
	9	Model Refinement
	10	Prototype Model Development and Response
4. Evaluation of Seismic	11	Development of Performance-Based Framework
Modeling Strategies	12	Development and Evaluation of Modeling Strategies

A series of shaking table tests were performed by the University of Washington (UW) and the University of Nevada, Reno (UNR) researchers at the NEES facility at UNR on a quarter-scale, two-span fixed-base model of a bridge prototype. An illustration of the shaking table specimen is shown in Fig. 1.2.

Chapter 2 presents the methodology for developing the shaking table specimen, including the target geometric and material properties, test protocol, and construction procedure. All construction and erection efforts by the contractor were overseen by UNR, with help from researchers at UW. UW and UNR collaborated to design and install the instrumentation.

Chapter 3 outlines the ground-motion selection process. Geotechnical colleagues identified four ground motions likely to strongly excite the specimen. The final ground motion was selected based on the estimated nonlinear response of the shaking table specimen. The last section of Chapter 3 presents the experimental test schedule, which includes low and
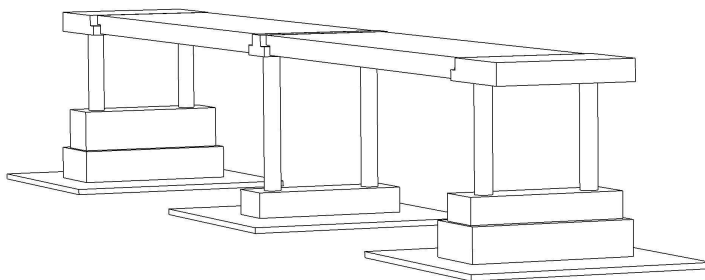
Figure 1.2: Illustration of the shaking table specimen

high-amplitude earthquake excitations, as well as the white-noise and square-wave excitations.

Chapter 4 describes the bridge response, including: material properties, achieved table accelerations, bent displacement and acceleration histories, bent displacement and acceleration maxima, displacement-strain envelopes, displacement-rotation envelopes, displacement-column elongation envelopes, and observed damage.

Chapter 5 discusses the theory of four system identification algorithms used to characterize the modal properties of the shaking table specimen. In Chapter 6, the identified modal properties of the shaking table system were compared to determine the consequences of implementing each algorithm. These comparisons include the effects of: pre-defining a structural model, including the input excitations, excitation type, and multi-directional excitation.

Chapter 7 documents the development of a nonlinear model in OpenSEES (OpenSees Development Team, 2002). This model had four main components: the distributed mass due to the self-weight of the components as well as the external masses on top of the slab, elastic elements for the slab, elastic elements for the cap beam, and inelastic elements for the columns. The columns in the OpenSEES model also had four components: the concrete and steel material properties for the column fiber section, the zero-length section at the column joints to simulate anchorage slip, the integration points for the distributed plasticity model, and the column cross-section discretization for the fiber section.

Chapter 8 documents the calibration and assessment of the OpenSEES model. The

model was calibrated using local response data (Chapter 4) and the identified modal properties (Chapter 6). The numerical model was assessed using global response characteristics, including: total system base shear, displacement response histories and maxima of the slab, and identified periods of the specimen.

Chapter 9 compares the response of the numerical model to that from pseudo-static tests on column and bent components that were conducted at Purdue University (Makido, 2007). These component tests were designed to have nominally identical geometric and material properties as the shortest bent in the shaking table tests.

Chapter 10 documents the development and assessment of the numerical model simulating a reinforced concrete bridge on drilled-shaft foundations. This model was produced by combining the calibrated structural model from the shaking table tests and component tests with a calibrated model of the soil and P-y springs from the centrifuge tests (Shin, 2006). The response characteristics of the prototype model (deformation time histories, force and deformation distributions along the columns and piles, and force and deformation maxima) were evaluated for a suite of 40 near-field and 30 far-field earthquake motions.

Chapter 11 describes the performance-based framework that was used to evaluate the accuracy of the seismic modeling strategies. This framework adopts a probabilistic approach to evaluate the various models at two levels: the estimated system force and deformation demands and the anticipated column damage.

Chapter 12 describes the seismic modeling strategies that were used to approximate the soil-foundation-structure system, including approximations of the foundation and material models. This chapter also evaluates the accuracy of these models within the performance-based framework describes in Chapter 11.

Chapter 13 summarizes the thesis, and provides conclusions from this work that fulfill the thesis objectives (Section 1.3).

Chapter 2

SPECIMEN DEVELOPMENT

The shaking table specimen was based on an idealized prototype of a typical bridge in the western United States. This chapter presents the development of the shaking table specimen, from conception of the idealized prototype bridge to completion of the specimen assembly. The development process included:

1. Selecting the geometric and material properties of the prototype bridge and shaking table specimen (Section 2.1);

2. Constructing the shaking table specimen (Section 2.2); and

3. Designing and placing the instrumentation and data acquisition system (Section 2.3).

These procedures are explained in the following sections. Johnson et al. (2006) provides a comprehensive outline of the specimen development.

2.1   Prototype and Scaled Model Properties

The conceptual design of the prototype bridge was performed by the entire SFSI project group. During this phase of the design, coarse dimensions of the prototype (column height, column diameter, span length) were designed to adhere to the proportions of the laboratory and to coincide with the experiments being conducted at the other universities involved in the SFSI project (UCD, UT, Purdue).

The prototype bridge for the shaking table specimen was a two-span section of a continuous reinforced-concrete, box-girder bridge. The superstructure was assumed to be supported by three two-column bents on drilled shafts. The length of each span was approximately 120 ft. Illustrations of the elevation and cross-section of the prototype bridge are provided in Figs. 2.1 and 2.2.
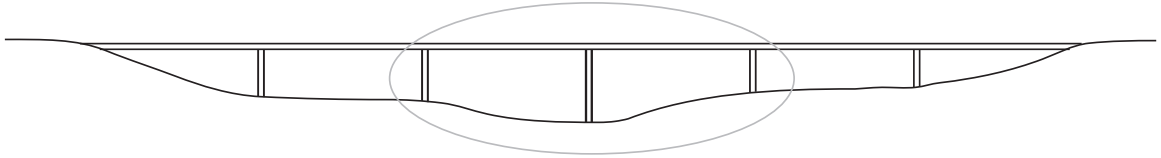
Figure 2.1: Illustration of the prototype bridge
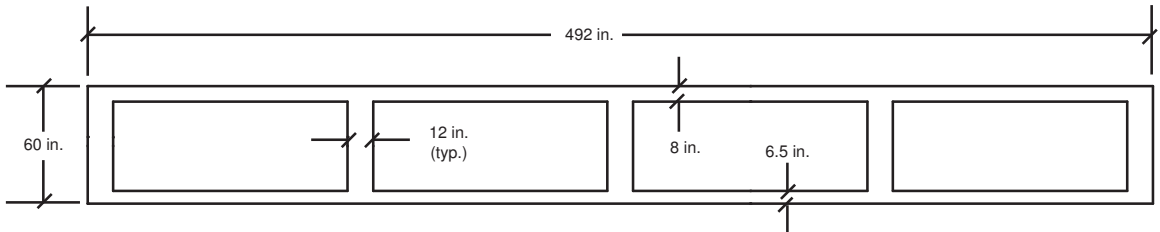
Figure 2.2: Illustration of the prototype cross-section

The shaking table specimen was a quarter-scale representation of the prototype bridge. Properties of the prototype bridge, and corresponding properties of the quarter-scale shaking table specimen, are shown in Table 2.1.

Table 2.1: Prototype and specimen properties

Property	Prototype Value	Specimen Value	Scaling Factor
Clear Column Heights (L_1,L_2,L_3) (ft)	16, 24, 12	4, 6, 3	4:1
Column Diameter (in.)	48	12	4:1
Longitudinal Reinforcement	(17) #11	(16) #3	–
Longitudinal Reinforcement Ratio	1.47%	1.56%	0.94:1
Axial Load	$0.1f'_c A_g$	$0.08f'_c A_g$	1.25:1
Span Length (ft)	120	30	4:1
Slab Width/Depth ($in. \times in.$)	492×60 (Box Girder)	90×14 (Flat Slab)	5.46:1 × 4.29:1
I_{xx} (in^4)	5.45×10^6	2.13×10^4	256:1
I_{yy} (in^4)	2.25×10^8	8.78×10^5	256:1

The span lengths of the prototype bridge (120 ft) were governed by the distance between the shaking tables at the University of Nevada, Reno (30 ft). Although the span length of the prototype was fixed by the specimen, a span length of 120 ft is typical for reinforced concrete box-girder bridges. For example, of the 726 bridges (40%) of this type in the 2000

Washington State Bridge Inventory (WSDOT, 2000) 287 (40%) had span lengths between 120 and 140 ft.

The column diameter of the specimen (12 in.) resulted from scaling the prototype column diameter (48 in.). The remaining specimen properties (actual column heights, longitudinal reinforcement ratio, axial load, and slab dimensions) deviated from direct scaling of the prototype. These deviations are explained in the following paragraphs.

Column Heights. The clear column heights of the prototype were chosen to be 16, 24 and 12 ft for bents 1, 2 and 3, respectively, to induce asymmetric behavior in the structural response during coherent motions. The shaking table specimen was designed with 6, 8 and 5 ft columns, two column diameters longer than a quarter-scale of the prototype. Two column diameters were added to the lengths of each column in the shaking table specimen to approximate the assumed depth of column fixity in a drilled-shaft foundation. This approximation was based on numerical analyses conducted by Yang and Jeremic (Yang and Jeremic, 2002).

Longitudinal Reinforcement Ratio. The longitudinal reinforcement ratio of the specimen would be closest to the prototype using (15) #3 bars ($\rho_l = 1.46\%$). However, (16) #3 bars were chosen for the specimen ($\rho_l = 1.56\%$) to make the column cross-section symmetric.

Axial Load Ratio. The axial-load ratio for the shaking table specimen was kept as close as possible to that of the prototype bridge. Because of scaling effects, external weights were added to the top of the shaking table specimen to obtain the correct axial load ratio. However, because of insufficient external weights, the axial load ratio of $0.08 f'_c A_g$ was slightly below its target value of $0.10 f'_c A_g$

Slab Dimensions. The dimensions of the solid slab on the shaking table specimen did not directly scale to the dimensions of the superstructure of the prototype bridge. Instead, the width and depth of the solid slab were chosen to reproduce the scaled moments of inertia of the box girder on the prototype bridge.

The remaining geometric properties of the shaking table specimen were designed at the specimen scale using the NCHRP Recommended LRFD Guidelines for the Seismic Design of Highway Bridges (ATC/MCEER, 2001). Therefore, prototype properties were not identified. An overview of the geometric properties of the shaking table specimen is provided in Table 2.2. The design documents for the specimen, which were developed by the UNR team (Johnson et al., 2006), are provided in Appendix B.

Table 2.2: Geometric properties for the shaking table model

Member	Property	Value
Column Dimensions	Gross Diameter ($in.$)	12
	Clear Cover ($in.$)	0.75
	Core Diameter ($in.$)	10.31
	Column Height, Bent 1 ($in.$)	72
	Column Height, Bent 2 ($in.$)	96
	Column Height, Bent 3 ($in.$)	60
	Intra-Bent Column Spacing ($in.$)	75
Longitudinal Column Reinforcement	No. of Longitudinal Bars	16
	Bar No.	3
	Longitudinal Steel Ratio (%)	1.56
Transverse Column Reinforcement	Spiral Bar	W2.9
	Spiral Spacing ($in.$)	1.25
	Spiral Bar Diameter ($in.$)	0.192
	Spiral Bar Area (in^2)	0.029
	Transverse Volumetric Steel Ratio (%)	0.90
Cap Beam Dimensions	Length ($in.$)	98
	Width ($in.$)	Variable
	Depth ($in.$)	15
Slab Dimensions	Span Length ($in.$)	360
	Width ($in.$)	90
	Depth ($in.$)	14

The nominal material properties used for the preliminary model of the shaking table specimen are listed in Table 2.3. The material properties measured before the beginning of the low-amplitude tests are reported in Chapter 4.

The modulus of elasticity of the concrete (E_c) and the tensile strength of the concrete (f_t) were calculated from the unconfined compressive strength of the concrete (f'_c), using

Table 2.3: Nominal material properties for the shaking table model

Material	Property	Value
Reinforced Concrete	ρ_m (ks^2/in^2)	2.25E-07
Unconfined Concrete	f'_c (psi)	5000
	ϵ_{co}	0.002
	E_c (ksi)	4030
	f_{to} (psi)	530
Confined Concrete	f'_{cc} (psi)	6750
	ϵ_{cc}	0.00549
Steel	f_y (ksi)	65
	f_{su} (ksi)	90
	E (ksi)	29000
	ϵ_u	0.12

the equations $E_c = 57000\sqrt{f'_c}$ and $f_t = 7.5\sqrt{f'_c}$ (ACI Committee 318, 2002). The confined concrete properties were calculated using the Mander concrete model (Mander et al., 1988).

2.2 Specimen Construction

The construction schedule for this specimen is provided in Table 2.4. The design documents were completed in June 2004, and the project was sent out to bid. UNR contracted the construction of the reinforcement cages for the footings, columns and cross-beams to Northern Nevada Rebar, and contracted the construction of the concrete components to Granite Construction. The slab was constructed at Granite Construction and delivered to UNR prior to assembly. All other components were constructed on site.

The footing and column cages were assembled (Fig. 2.3a) in September 2004. Pieces of #3 bar were welded to the tops of the column reinforcement to ensure complete stress transfer from the reinforcement to the concrete (Fig. 2.3b). Once the cages were completed, the strain gauges were placed on the longitudinal and transverse column reinforcement. The column cages were then attached to the footing cages and the concrete for the footings was poured in October 2004. The concrete for the columns were poured approximately one month after the pouring of the footings. The cap beam cages were assembled (Fig. 2.3c)

Table 2.4: Specimen construction schedule

Description	2004								2005	
	May	Jun	Jul	Aug	Sep	Oct	Nov	Dec	Jan	Feb
Design Documents	x	x								
Instrumentation Plan Developed			x	x						
Column Cage Assembly					x					
Footing Pour						x				
Column Pour							x			
Beam/Cantilever Assembly							x			
Cap Beam Pour							x			
Bridge Erection and Assembly								x	x	
Low Level Testing									x	x
High-Level Testing										x

and the concrete for the beams was poured approximately two weeks after the columns were poured.

The specimen components were assembled on the shaking tables within the laboratory in December 2004. Concrete spacer blocks below the footings on bents 1 and 3 were added to maintain a level slab with various column heights. The bents were placed on top of the spacer blocks (Fig. 2.3d) and post-tensioned to the tables using eight one-inch diameter threaded rods.

Once the bents were assembled on the tables, the slab was placed on the bents. Transverse post-tensioning was applied to provide transverse continuity across the slab beams. Longitudinal post-tensioning was then applied to provide continuity between the slab and the bents. After the slab was post-tensioned to the bents, external masses were added to the top of the slab (Fig. 2.3e). The majority of the external mass was provided by three concrete blocks placed on each span near the exterior bents. Additional crates of lead weights were added on the interior spans near the concrete blocks and on the cantilevers of the exterior bents. Steel frames were installed underneath the slab on each shaking table as a safety measure in case of specimen collapse during the high-amplitude tests.

After the assembly of the specimen, the potentiometers were attached to the columns and slab. The locations of the strain gauges and potentiometers are provided in the instru-

mentation plans, located in Appendix C. The assembled shaking table specimen before the low-amplitude testing is shown in Fig. 2.3f.

The low-amplitude testing commenced in late January. The last part of the low-amplitude testing, which included subjecting the structure to excitations measured during the centrifuge tests, was postponed for two weeks until early February. These tests were postponed to allow time to obtain and interpret preliminary results from the centrifuge tests. The high-amplitude testing lasted two days, immediately following the final day of the low-amplitude testing.

Figure 2.3: Photographs of construction sequence, including: a) column cages, b) column welds, c) beam cages, d) bent assembly, e) external slab masses, and f) final pre-test specimen

2.3   Instrumentation and Data Acquisition

Forty-four tests were conducted on the shaking table specimen: 15 low-amplitude earthquake excitations, 10 high-amplitude earthquake excitations, 12 white-noise excitations, and 7

square-wave excitations. For each test, 313 channels of data were recorded, 307 of which were relevant to the response of the system. The location of the gauges on the shaking table specimen are provided in the instrumentation plans (Appendix C). The remaining 6 channels recorded information from the data acquisition system. Table 2.5 outlines the functionality for each channel. Examples of the instrumentation are shown in Fig. 2.4, and discussed in the following paragraphs.

Table 2.5: Data acquisition channel count and description

Recorder Type	Recorded Response	# Recorders	Notes
Strain Gauges	Longitudinal Reinforcement	104	All columns
	Transverse Reinforcement	56	All columns
Potentiometers	Slab Displacements	25	Transverse, Longitudinal and Vertical
	Footing Slip	3	Slip between footing and table on bent 3
	Column Curvature	68	All bents
	Column Shear	15	Bent 3, west column
Accelerometers	Slab Accelerations	14	Transverse, Longitudinal and Vertical
	Support Frame Acceleration	1	Added after TEST3B
Miscelaneous	Long. Table Response	9	Displacement, Velocity and Acceleration
	Trans. Table Response	9	Displacement, Velocity and Acceleration
	Data Acquisition	3	one channel for each table
	Function Recording	3	one channel for each table
	Time Recording	3	one channel for each table
Total		**313**	
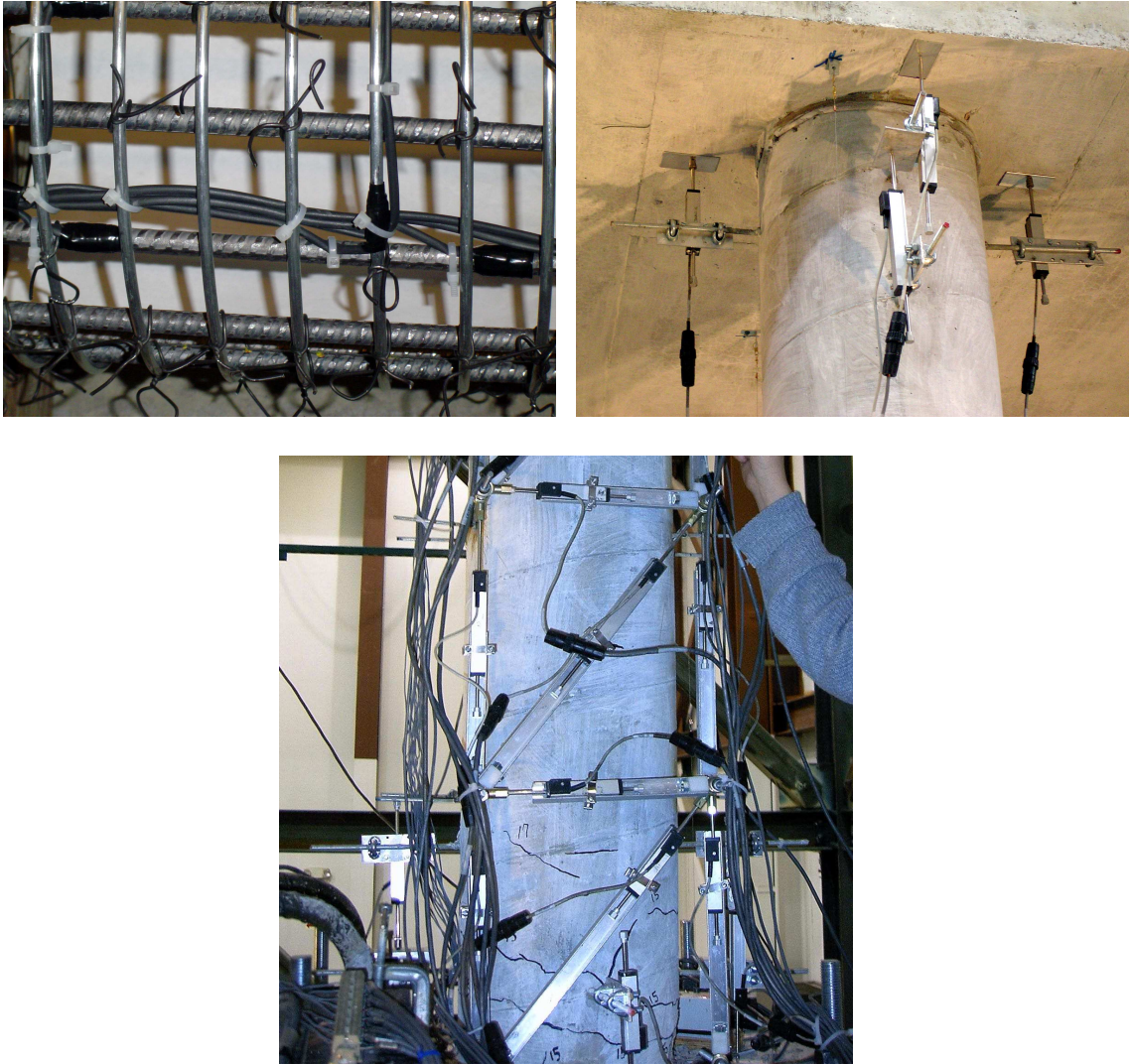
Figure 2.4: Photographs of instrumentation, including: a) longitudinal and transverse strain gauges, b) curvature potentiometers, and c) shear rig potentiometers.

2.3.1 Strain Gauges

A total of 160 strain gauges were installed on the reinforcement of the six columns, 104 on the longitudinal reinforcement and 56 on the transverse reinforcement (Fig. 2.4a). The longitudinal strain gauges were placed at six locations along the length of the column: at each column-anchorage interface, 6 inches into the column from each interface, and 6 inches into each anchorage. Before attaching the strain gauges, the reinforcement was ground smooth at the gauge location. The strain gauges were then glued to the bars and wrapped

with electrical tape. The wires of the strain gauges were strung through shrink tubing and attached to the inside of the column reinforcement.

2.3.2 Slab Displacement Potentiometers

Five potentiometers were used to measure the transverse slab displacement at each bent and at the midpoint of each span. Four potentiometers (two on each end) recorded the longitudinal slab displacement. The vertical slab displacements were captured using 16 potentiometers, four measurements on each bent and two measurements at the midpoint of each span.

Base slip at bent 3 was recorded using three potentiometers. The slip between the concrete spacer block and the shaking table was monitored with two potentiometers. The slip between the footing and the concrete spacer block was monitored with one potentiometer.

2.3.3 Column Deformation Potentiometers

There were a total of 68 potentiometers measuring column curvature (Fig. 2.4b). Average column curvatures were measured over the first 12 inches of each column fixity in the transverse direction. The column curvatures were measured over intervals of 5 and 7 inches using four potentiometers at each column fixity (for a total of 48 gauges). The column curvature in the longitudinal direction was measured over the first 5 inches using two potentiometers at each column fixity. However, longitudinal column curvatures for the west column of bent 2 were not measured.

A shear rig was assembled using 15 potentiometers on the west column of bent 3. The potentiometers in the shear rig were situated in rectangles with approximately 12-in. sides (Fig. 2.4c). Each quadrant consisted of two vertical potentiometers, two horizontal potentiometers, and one diagonal potentiometer.

2.3.4 Slab Accelerometers

A total of 15 accelerometers were used to measure accelerations of the slab and the support frame near bent 2. Ten accelerometers measured the transverse and longitudinal acceler-

ations at each bent and at the midpoint of each span. Two accelerometers measured the vertical accelerations at the midpoint of each span, and two measured the vertical accelerations at the ends of the cantilevers near bents 1 and 3.

The accelerometers on Bent 2 recorded excessive vibration during the low-amplitude tests. To determine the source of the vibration, an accelerometer was added to the support frame near bent 2 after Test 3B.

Chapter 3

GROUND MOTION DEVELOPMENT

The base motion for the shaking table specimen was chosen based on maximizing the likely structural response without exceeding the operational limits of the shake tables. This chapter describes the selection and development of the ground motions for the shaking table tests. This process included:

1. Choosing candidate outcrop motions (30) based on target peak ground acceleration and epicentral distance (Section 3.1).

2. Reducing the number of candidate outcrop motions to four by inspecting the motions in the time and frequency domains (Section 3.1).

3. Choosing the primary motion using nonlinear structural response estimates while considering shaking table limits (Section 3.2).

4. Developing an experimental test schedule from the primary test motion (Section 3.3).

3.1   Candidate Outcrop Motions

The Northridge earthquake was chosen for this research because of its broad use in previous analytical studies and its relevance to bridges on the west coast of the United States. Approximately 30 outcrop motions from the Northridge earthquake (M = 6.7) were chosen from the PEER strong motion database (PEER, 2005) based on a target peak ground acceleration (PGA) near 0.25g and an epicentral distance near 25 km (Shin, 2006).

Four candidates were chosen from the field of 30 motions (Table 3.1) through inspection of the motion records in the time and frequency domains. Specifically, the candidate motions were inspected in the time domain for earthquake duration and to ensure there were no large individual amplitude spikes. The response spectrum of the motion was inspected for narrow bandwidth or amplitude gaps below periods of one second. These attributes in both the time

and frequency domain might have led to an insufficient structural response. Time histories and elastic response spectra (5% damping) of the four unscaled candidate outcrop motions are shown in Figs. 3.1 - 3.4. Because the geometric scale of the shaking table specimen was 1/4, the time scale of the candidate motions were condensed by 2. The computed spectral accelerations are normalized by the peak ground acceleration of each motion.

Table 3.1: Northridge earthquake candidate outcrop motions

Motion No.	1	2	3	4
Location	Century City CC North (090)	Century City CC North (360)	Lake Hughes #12A	LA - University Hospital
Abbreviation	CCN090	CCN360	H12090	UNI095
PGA (g)	0.256	0.222	0.174	0.214
Dist. To Surface Rupture (km)	18.3	18.3	24.8	32.8
Duration (s)	14.38	14.12	7.75	11.85

The peak spectral acceleration (PSA) for motions 1 (Fig. 3.1) and 3 (Fig. 3.3) were approximately four times larger than their peak ground accelerations (PGA). Both motions had PSAs near a period of 0.1s. The PSA for motions 2 (Fig. 3.2) and 4 (Fig. 3.4) were approximately 2 and 3.5 times their PGAs, respectively. The bandwidths of motions 1 and 2 were the largest out of the four motions. For example, the spectral accelerations for motions 1 and 2 are larger than the PGA for periods less than 0.5 and 0.75 seconds, respectively. In contrast, the spectral accelerations for motions 3 and 4 are larger than the PGA only for periods less than 0.25 and 0.35 seconds, respectively.
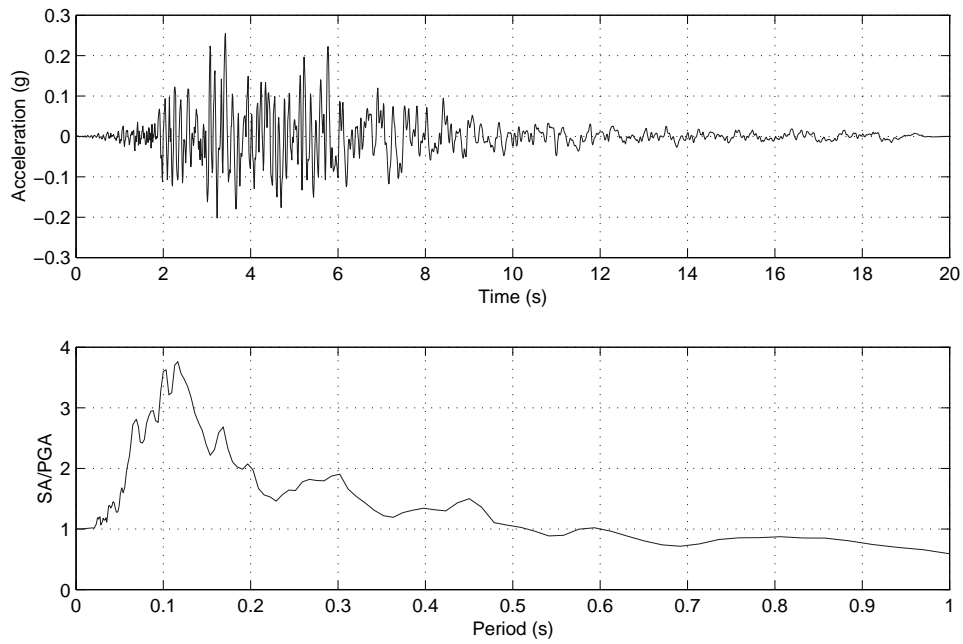
Figure 3.1: Acceleration history and spectral acceleration for Motion 1 (CCN090)
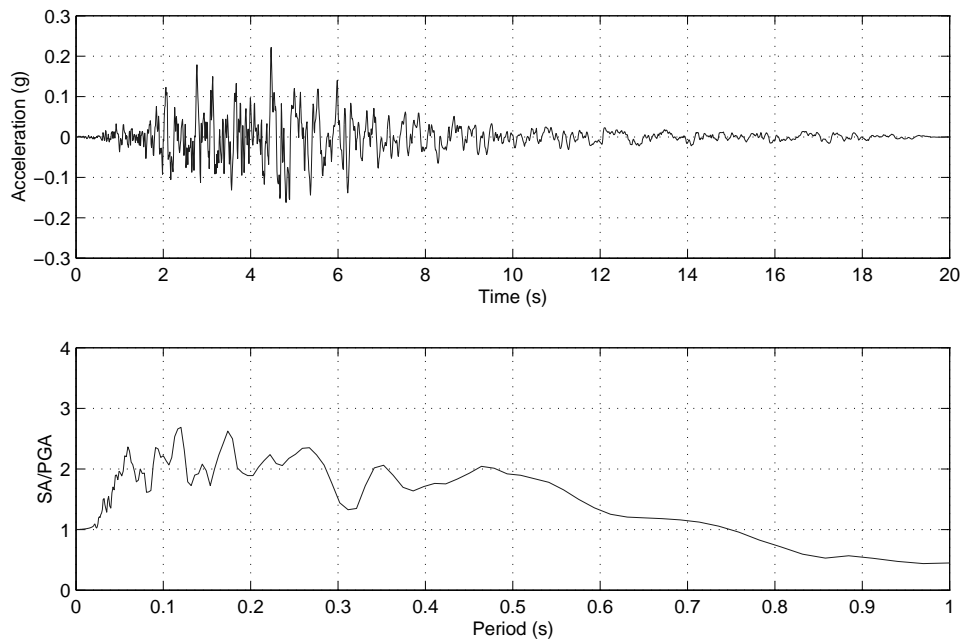
Figure 3.2: Acceleration history and spectral acceleration for Motion 2 (CCN360)
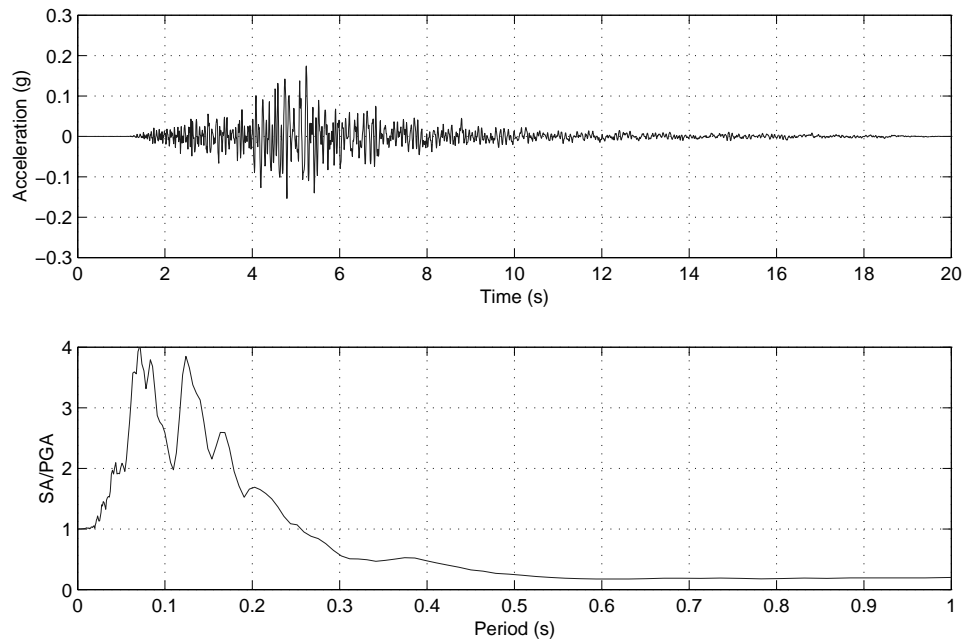
Figure 3.3: Acceleration history and spectral acceleration for Motion 3 (H12090)
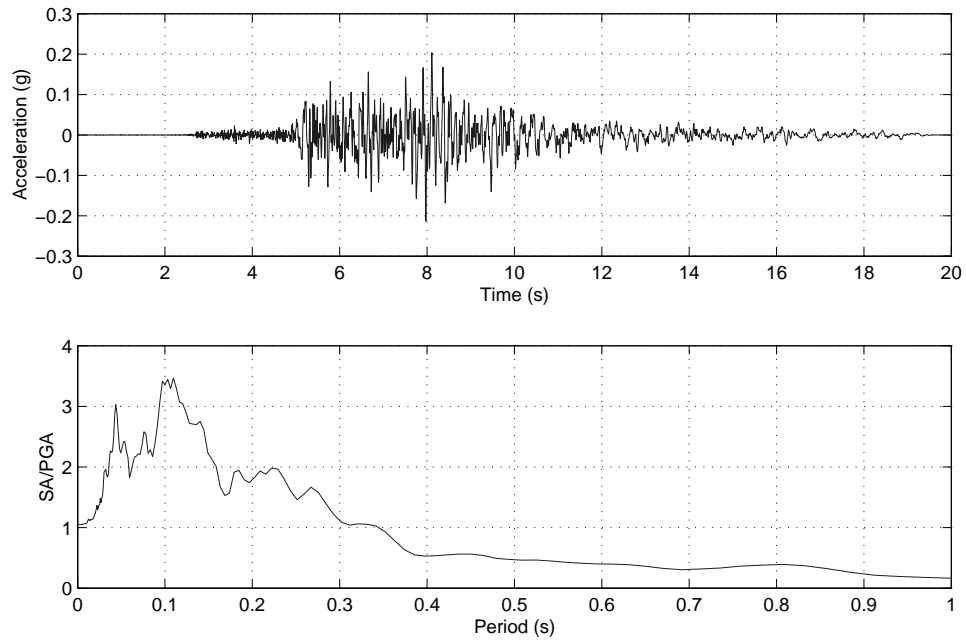
Figure 3.4: Acceleration history and spectral acceleration for Motion 4 (UNI095)

3.2 Outcrop Motion Selection

To generate bedrock motions, Shin (2006) deconvoluted the four candidate outcrop motions to the bedrock level through rock (approximately 27 m below the surface in prototype scale). For initial comparison, the unscaled motions were then convoluted through the soil to the estimated location of column fixity, approximately two column diameters below the surface. Each free-field motion (at the point of column fixity) was scaled to peak accelerations of 0.25g, 0.50g, 0.75g, 1.00g, and 1.50g. Fig. 3.5 illustrates the process of generating the free-field motions for the shaking table model.
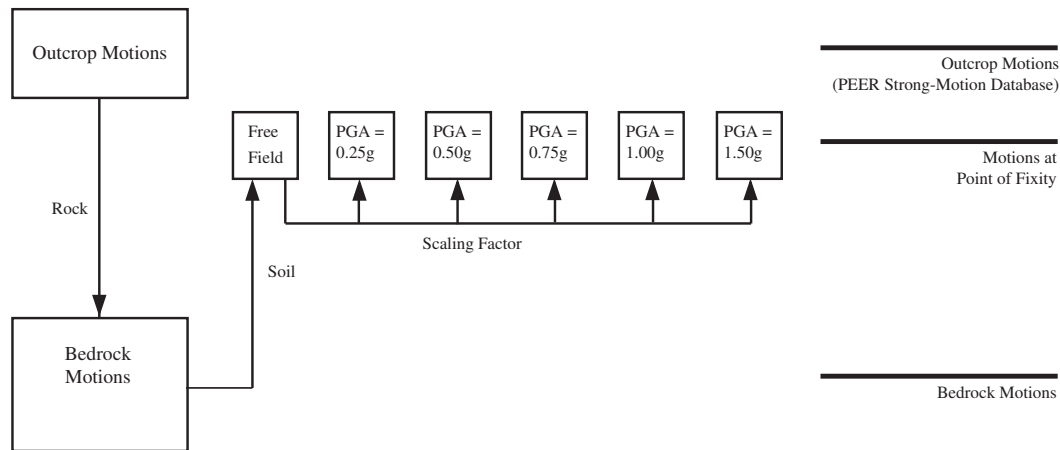
Figure 3.5: Diagram for developing the acceleration records for initial motion selection.

The motions at the point of column fixity were used to excite the preliminary numerical model (see Chapter 2). The peak displacement responses at each bent for these motions are reported in Table 3.2, and shown in Fig. 3.6. The largest bent drift ratio for each level of PGA is highlighted in Table 3.2. Taking the motions scaled to 1.0g as an example, motion 2 yields the largest drift response for bent 1 (2.55%), compared to a response of 1.92% for motion 1, and much smaller responses for motions 3 and 4 (approximately 1.0%).

For all motion intensities, the estimated drift ratios using motions 1 and 2 were larger at each bent than those calculated using motions 3 and 4 (Fig. 3.6). For the majority of the motions, the peak bent responses for motion 2 were larger than those for motion 1. For

Table 3.2: Calculated transverse bent drift ratios for the four ground motions at various levels of peak ground acceleration

Response Characteristics	Peak Ground Acceleration (g)	Ground Motions			
		Motion 1	Motion 2	Motion 3	Motion 4
Bent 1	0.25	**0.65**	0.63	0.29	0.34
Drift Ratio	0.50	1.08	*1.34*	0.53	0.53
(Δ_{max}/L) (%)	0.75	1.46	*1.99*	0.75	0.72
	1.00	1.92	*2.55*	0.94	0.96
	1.50	3.03	*3.83*	1.33	1.52
Bent 2	0.25	*0.43*	0.41	0.22	0.24
Drift Ratio	0.50	0.78	*0.79*	0.39	0.39
(Δ_{max}/L) (%)	0.75	1.08	*1.25*	0.55	0.56
	1.00	1.41	*1.68*	0.69	0.75
	1.50	2.17	*2.51*	0.98	1.10
Bent 3	0.25	*0.58*	0.52	0.33	0.41
Drift Ratio	0.50	*1.15*	0.93	0.58	0.66
(Δ_{max}/L) (%)	0.75	*1.64*	1.61	0.80	0.89
	1.00	2.13	*2.32*	1.02	1.12
	1.50	3.27	*3.63*	1.46	1.62
Peak Table	0.25	4.91	5.35	4.04	2.97
Velocity	0.50	9.81	10.69	8.09	5.93
(in./s)	0.75	14.72	16.04	12.13	8.90
$(V_{lim} = 40in./s)$	1.00	19.62	21.39	16.17	11.86
	1.50	29.43	32.08	24.26	17.79
Peak Table	0.25	0.52	0.45	0.51	0.20
Displacement	0.50	1.04	0.90	1.01	0.41
(in.)	0.75	1.56	1.35	1.52	0.61
$(\Delta_{lim} = 12in.)$	1.00	2.08	1.80	2.03	0.81
	1.50	3.12	2.69	3.04	1.22

example, at a PGA of 1.5, the drift ratios of bent 3 for motions 1 and 2 were 3.27% and 3.63%, respectively. Based on these results, motions 3 and 4 were eliminated from further consideration.

Table 3.2 also provides the peak table velocity and displacement demands for each motion. The velocity demands were calculated by integrating the acceleration record over the condensed time scale. The displacement demands were calculated by integrating the acceleration record twice. These table demands were checked to verify that the estimated table limits were not exceeded. As discussed in Appendix A, the nominal table limits were $\Delta_{lim} = 12in.$, $V_{lim} = 40in./s$, and $A_{lim} = 1.4g$. As seen in Table 3.2, none of the table
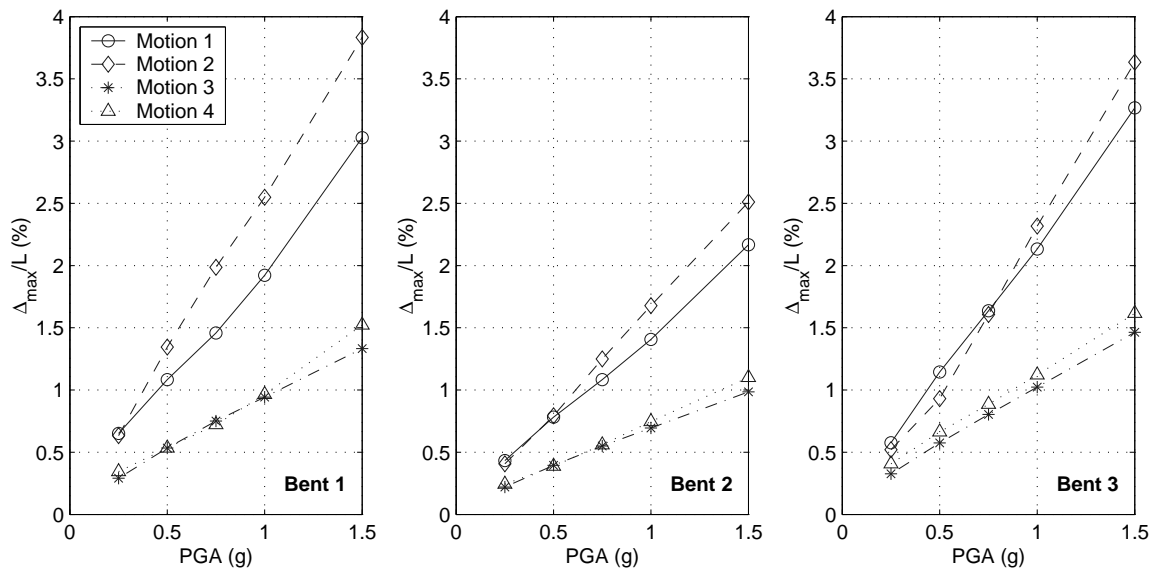
Figure 3.6: Response comparison between the four candidate ground motions for: a) bent 1, b) bent 2, and c) bent 3

velocity or displacement demands exceeded the nominal table limits.

Although the peak drift ratios for motion 2 were generally higher than those for motion 1, the final ground motion selection was based on the amount of bent cycling at high drift ratios. To help decide between outcrop motions 1 and 2, these motions were deconvoluted to the bedrock level and scaled to a peak bedrock acceleration of 0.4g. The bedrock motions at this intensity were then convoluted to the point of column fixity where free-field and pile motions were generated. These motions were then re-scaled to a peak acceleration of 1.0g. This process resulted in four motions (two free-field and two pile motions) with peak accelerations of 1.0g (see Fig. 3.7 for an illustration of this process). Table 3.3 provides the maximum drift ratio at each bent for these four motions.

The bent drift ratios resulting from free-field motion 2 were generally larger than those for motion 1. The opposite is true for the pile motions. Table 3.3 also presents two measures cumulative high-amplitude cycling, hysteretic energy and cumulative plastic displacement

The hysteretic energy dissipated by the bents was calculated by integrating the total bent base shear over the displacement history. Cumulative plastic displacement is the
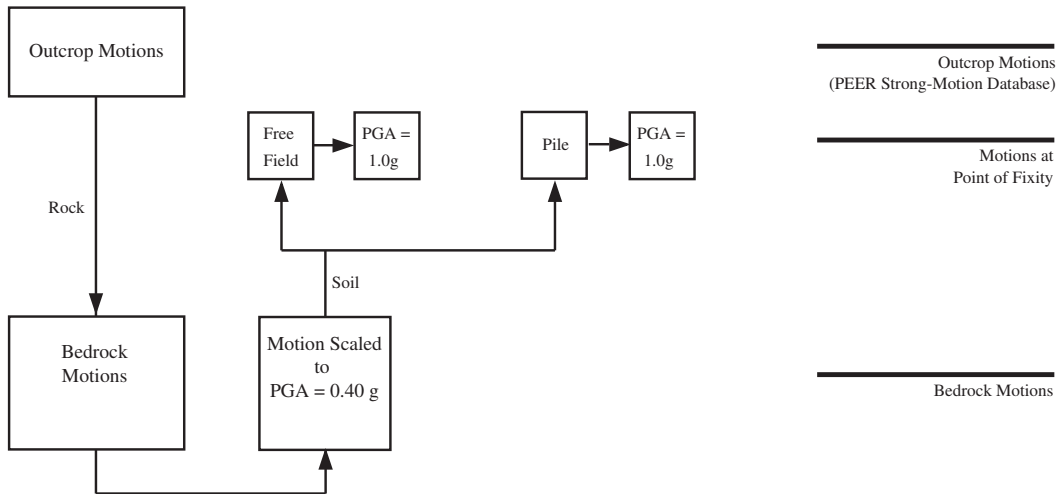
Figure 3.7: Diagram for developing the acceleration records for final motion selection.

Table 3.3: Calculated drift ratios for free-field and pile motions 1 and 2

Response Measurement	Bent	Free Field Motion		Pile Motion	
		1	2	1	2
Peak Bent Drift Ratio (%)	1	4.68	4.65	8.22	6.38
	2	3.03	3.45	5.49	4.51
	3	4.25	5.47	7.71	6.84
E_h (k-in.)	1	868	626	943	631
	2	382	291	524	273
	3	978	839	953	589
CPD (in.)	1	53.9	35.0	68.7	34.1
	2	32.9	19.9	43.7	18.7
	3	46.5	39.0	57.1	38.5

total amount of displacement beyond the yield displacement that the bent experiences. This measure of cycling does not incorporate the column forces, but has been shown to adequately characterize damage influenced by cycling (Ranf et al., 2005).

As seen in Table 3.3, both measures of cycling show the numerical model predicted more

high-level cycling when excited by motion 1 than motion 2. For example, the cumulative plastic deformation of bent 1 resulting from free-field motion 1 was 53.9 in., 54% larger than the cumulative plastic displacement of bent 1 from free-field motion 2 (35.0 in.). The displacement time histories and hysteresis curves of bent 1 resulting from free-field motions 1 and 2 are shown in Fig. 3.8. There is a large pulse in the response to free-field motion 2. However, there are many more large secondary displacements resulting from free-field motion 1.

Based on consideration of cycling, motion 1 was used as the primary motion for the shaking table tests because it caused both large maximum bent displacements and large amounts of cycling. However, because motion 2 (CCN360) was recorded at the same location as motion 1 (CCN090), except at an orthogonal orientation, motion 2 was used in combination with motion 1 for the bi-directional shaking table tests.
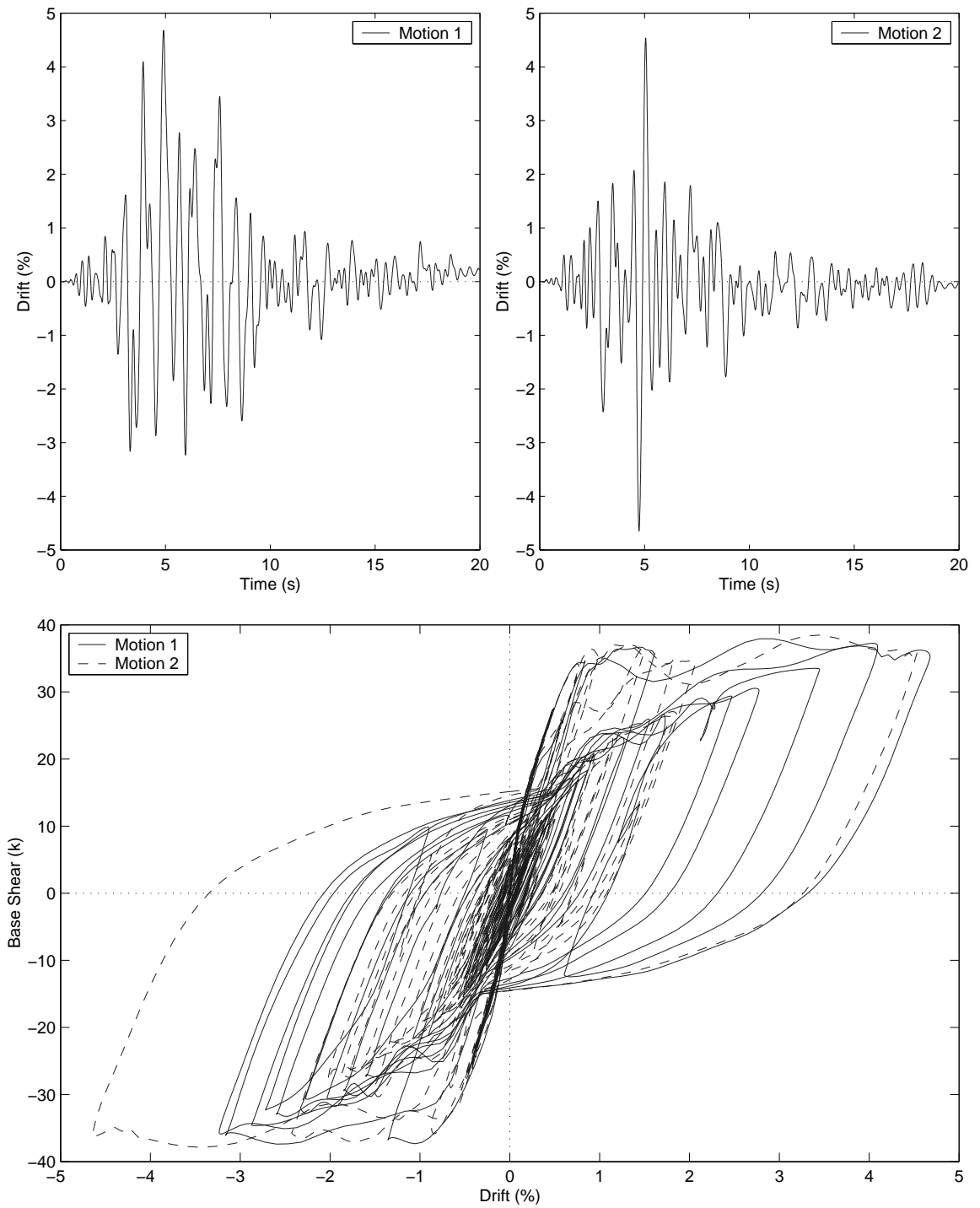
Figure 3.8: Response comparisons from free-field motions 1 and 2.

3.3 Final Test Motions at the Estimated Point of Column Fixity

The CCN090 (motion 1) acceleration history was chosen as the primary motion for the shaking table tests. This motion was deconvoluted to the bedrock level and scaled twice to create peak bedrock accelerations of 0.06g and 0.40g.

For the low-amplitude tests, the motion at the bedrock level was scaled to a peak bedrock acceleration of 0.06g. The low-amplitude motion was convoluted to the point of column fixity assuming various bedrock depths. The baseline bedrock depth (d) was assumed to be 25.4m. The various bedrock depths used during the the low-amplitude tests included: 0d (bent attached directly to the bedrock), 1/3d, 1/2d, and 2/3d. The time histories and response spectra for these four low-amplitude test motions are shown in Fig. 3.9.

The CCN360 (motion 2) acceleration history was used for the longitudinal excitation of the biaxial tests. This motion was deconvoluted to bedrock, scaled so that the peak acceleration was 0.06g, and then convoluted to the point of column fixity assuming a bedrock depth of 1/3d. The time history and response spectra for this longitudinal motion are shown in Fig. 3.10.

The shaking table excitations were expected to exceed 1.0g during the high-amplitude tests. Therefore, the high-amplitude motion was scaled to a peak bedrock acceleration of 0.4g, then convoluted to the estimated point of column fixity. The time history and the response spectrum for this motion are shown in Fig. 3.11.

The test schedule for the low and high-amplitude tests (Table 3.4) were developed using the motions presented in Figs. 3.9 - 3.11. The low-amplitude tests were composed of coherent, incoherent, biaxial and centrifuge excitations, all designed to create bent responses smaller than the estimated bent yield displacements. The high-amplitude tests were composed of coherent excitations with increasing intensity. A detailed description of the tests are provided in the following paragraphs.

- Tests 1A-1B were coherent half-scale and full-scale excitations used to create a baseline structure response to compare with the incoherent excitations. The half-scale excitation was used to ensure that the bent response from the full-scale excitation would not exceed the estimated bent yield displacements.

- Tests 2A-6 were used to investigate the effects of varying soil depth (and motion incoherency) on the response of the structure. Although the soil depth under individual bents varied in these tests, the average soil depth remained constant at d/3.

- Test 7 used the same motions as Test 1B to investigate the accumulated effects of the incoherent motion tests on the structure.

- Test 9A-9B subjected the structure to half-scale and full-scale biaxial motions. The motion in the transverse direction came from the CCN090 outcrop motion, while the motion in the longitudinal direction came from the CCN360 outcrop motion. Again, a half-scale test was first conducted to ensure the bent responses from the full-scale test would not exceed the estimated yield displacement.

- Tests 10-11 used accelerations recorded during the centrifuge tests at the University of California, Davis (UCD). The motions from Test 10 and 11 were free-field and pile accelerations, respectively, at two column diameters below the ground surface.

- Tests 12-20 were the high-amplitude excitations. These tests all used the same motion, generated from a bedrock acceleration scaled to a peak ground acceleration of 0.4g, then convoluted through 25.4 m of soil to the assumed point of column fixity. This motion was then scaled from 0.08g to 1.66g to produce a gradual progression of structural damage (the achieved table accelerations ranged from 0.07g to 2.20g). The excitations increased in intensity until Test 20, at which point excessive damage to bent 3 required the unloading of the external mass from bent 3.

- Tests 21-22 were high-amplitude excitations without the external mass above bent 3. These tests were used to induce further damage to bents 1 and 2 without risking collapse of bent 3.

Twelve white-noise and 7 square-wave excitations were dispersed throughout the low and high-amplitude excitations. During the low-amplitude tests, these were used to ensure that the large amount of testing did not significantly change the modal properties of the structure. During the high-amplitude tests, these excitations were used to identify the progression of structural damage. White-noise and square-wave tests were conducted in tandem to identify the modal properties using two types of excitation.
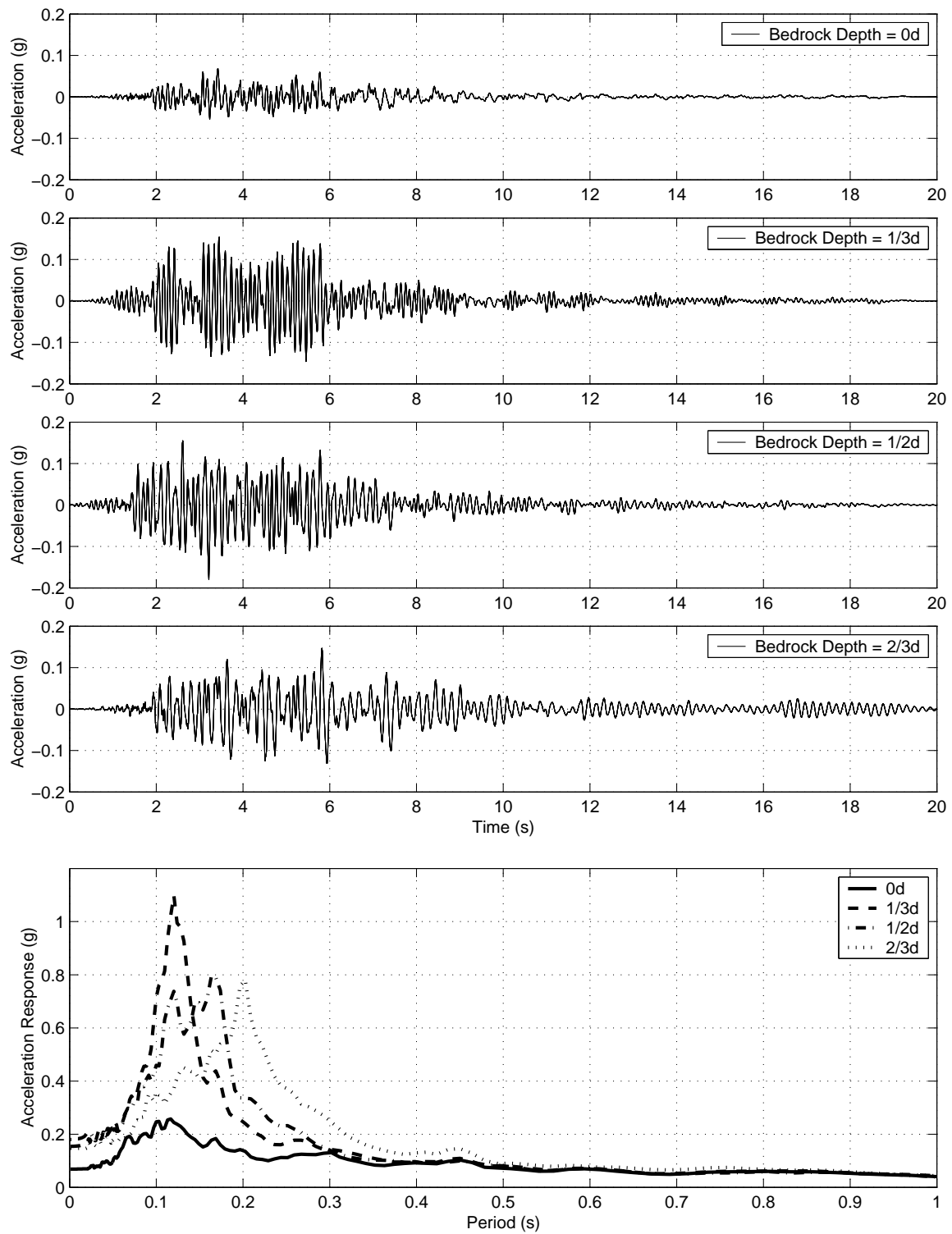
Figure 3.9: Time history and response spectrum for the low-level motions
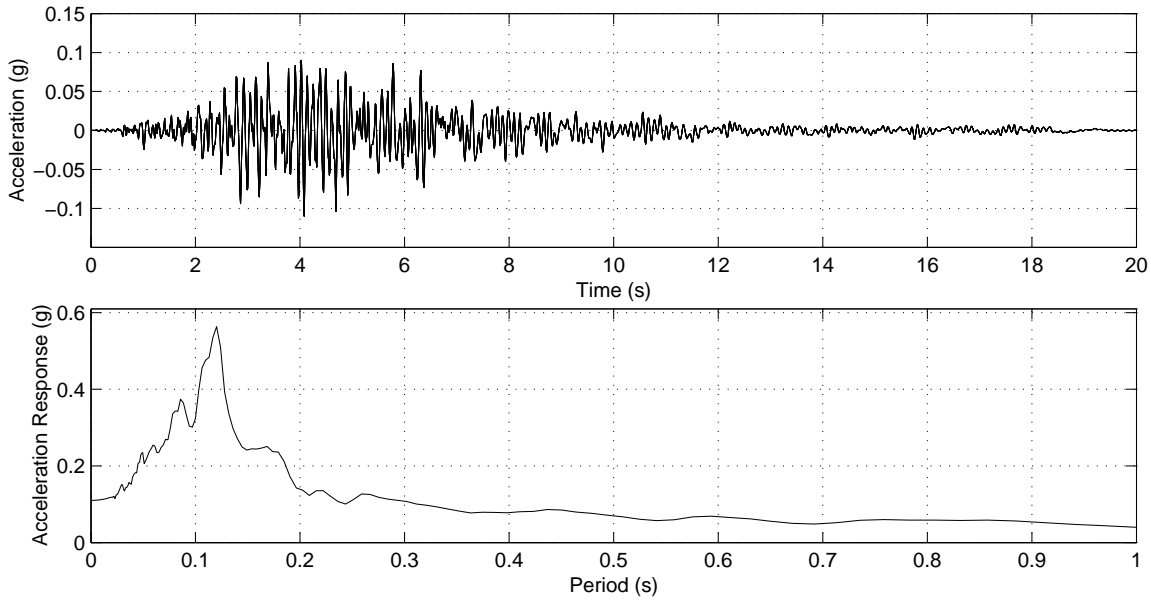
Figure 3.10: Time history and response spectrum for the low-level longitudinal motion
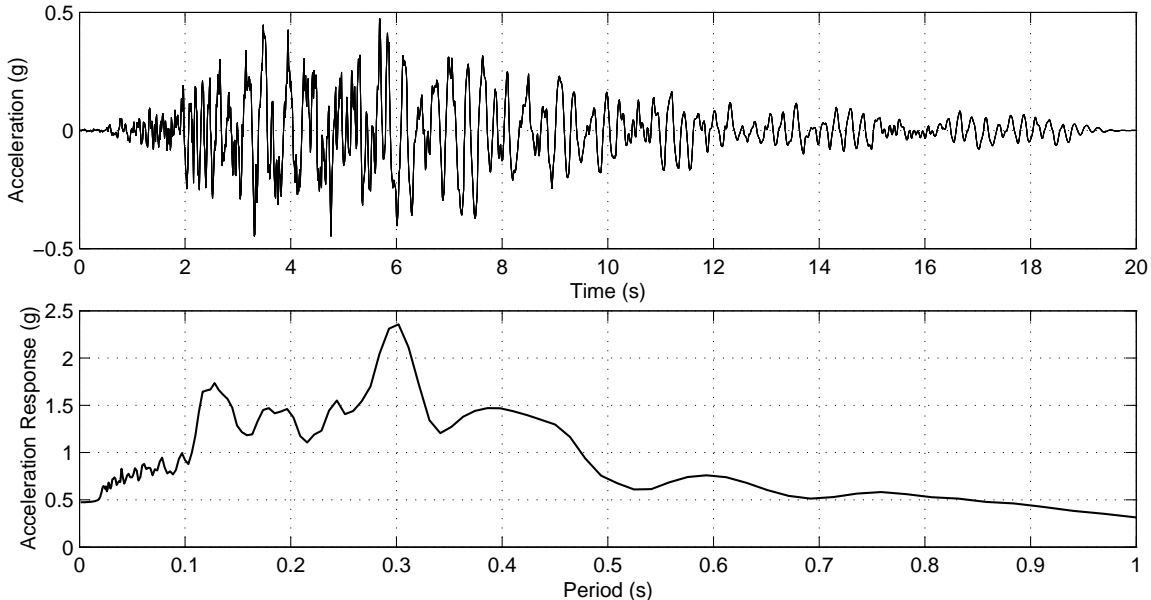
Figure 3.11: Time history and response spectrum for the high-level motion

Table 3.4: Experimental test schedule

Test		Test Date	Significance	Transverse Direction		Bent		
				Motion	PBA (g)	1	2	3
WN0001	Low Level	Jan. 27, 2005	White Noise					
1A			Coherent Motion	1	0.06	d/3	d/3	d/3
1B				1	0.06	d/3	d/3	d/3
2A			Incoherent Motion	1	0.06	0	d/3	2d/3
2B				1	0.06	0	d/3	2d/3
3A				1	0.06	2d/3	d/3	0
3B				1	0.06	2d/3	d/3	0
WN0304A			White Noise					
WN0304B			White Noise					
4			Incoherent Motion	1	0.06	0	d/2	d/2
5				1	0.06	d/2	0	d/2
6				1	0.06	d/2	d/2	0
7			Coherent Motion	1	0.06	d/3	d/3	d/3
WN0709A			White Noise					
WN0709B		Feb. 8, 2005	White Noise					
SQ0709B			Square Wave					
9A			Biaxial Motion	1	0.06	d/3	d/3	d/3
9B				1	0.06	d/3	d/3	d/3
10			Centrifuge Motion	1	0.1	d	d	d
11				1	0.1	d	d	d
WN1112A			White Noise					
SQ1112A			Square Wave					
WN1112B	High Level	Feb. 9, 2005	White Noise					
SQ1112B			Square Wave					
12			Coherent Motion	1	0.4	d	d	d
13				1	0.4	d	d	d
14				1	0.4	d	d	d
WN1415			White Noise					
SQ1415			Square Wave					
15			Coherent Motion	1	0.4	d	d	d
16				1	0.4	d	d	d
17				1	0.4	d	d	d
WN1718			White Noise					
SQ1718			Square Wave					
18			Coherent Motion	1	0.4	d	d	d
WN1819		Feb. 10, 2005	White Noise					
SQ1819			Square Wave					
19			Coherent Motion	1	0.4	d	d	d
WN1920			White Noise					
SQ1920			Square Wave					
20			Coherent Motion	1	0.4	d	d	d
WN2021			White Noise					
MASS OFF			Mass Removed From Bent 3					
21			Coherent Motion	1	0.4	d	d	d
22				1	0.4	d	d	d
Notes: d = the depth from the point of column fixity to bedrock, 25.4 m.								

Chapter 4

MEASURED RESPONSE

This chapter describes the response of the shaking table specimen. The instrumentation used to capture the response of the specimen is listed in Table 2.5. The response characteristics presented in this chapter are outlined in Table 4.1. These response characteristics were used in subsequent analyses for calibration and assessment of a three-dimensional numerical model. Uses of the specimen response characteristics are also shown in Table 4.1.

Table 4.1: Measured response characteristics

Response	Section	Use	Chapter
Material Properties	Section 4.1	Material Model Calibration	Chapter 8
Measured Table Accelerations	Section 4.2	Model Calibration	Chapter 8
		Model Assessment	Chapter 8
Displacement/Acceleration Histories	Section 4.3	System Identification	Chapter 6
Displacement/Acceleration Maxima	Section 4.4	Numerical Model Assessment	Chapter 8
Displacement-Strain Envelopes	Section 4.5	Anchorage Slip Calibration	Chapter 8
Displacement-Rotation Envelopes	Section 4.6	Numerical Model Assessment	Chapter 8
Displacement-Column Elongation Envelopes	Section 4.7	Effective Beam Width Calibration	Chapter 8

4.1   Material Properties

The measured material properties that are presented in this section were used to calibrate the material models for the OpenSEES numerical model (Chapter 8). Three batches of concrete (footings, columns, and cross-beams) and two types of steel (longitudinal and transverse reinforcement) were used in the shaking table specimen. Material tests were performed at the University of Nevada, Reno.

The concrete compressive strength was determined by testing 6in. x 12in. diameter cylinders. Three cylinders each were tested for each concrete batch at 7 (or 16) days, at 28 days, and just before the beginning of the low-amplitude tests. The average compressive stress from the three cylinders is presented in Table 4.2. Fig. 4.1 shows the progression of

the concrete strengths for the three bent components.

The measured strength for the column concrete at 28 days was 4810 psi, which was close to the design 28-day strength of 5000 psi. Because each bent component was cast at different times, the ages of the components at the beginning of the low-amplitude tests varied for the footings (133 days), columns (103 days), and cross-beams (83 days).

Table 4.2: Measured concrete strength (psi)

Component	Age (Days)					
	7	**16**	**28**	**83**	**103**	**133**
Footing	—	3430	4020	—	—	4780
Column	2600	—	4810	—	5910	—
Cap Beam	3430	—	5650	6990	—	—
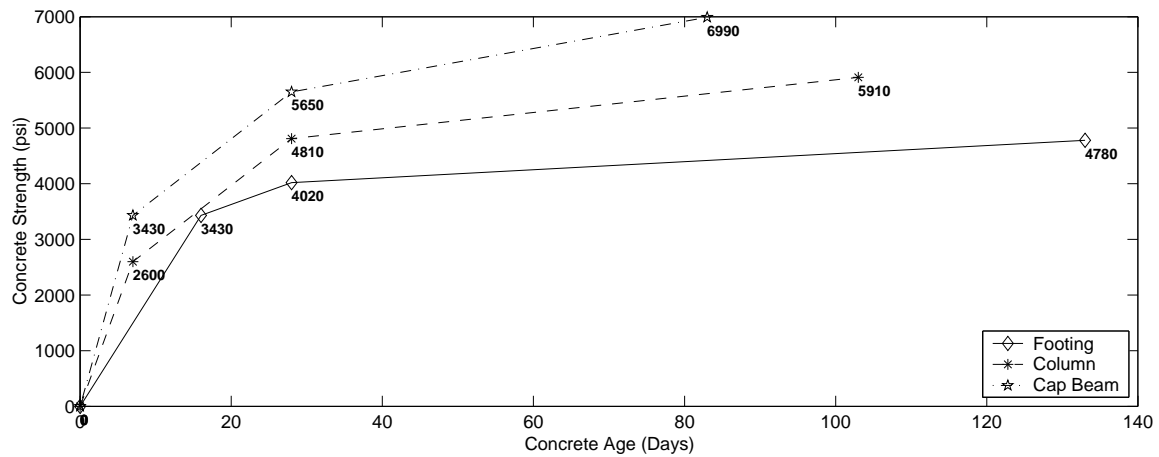
Figure 4.1: Concrete strength progression for the two-span structure

The concrete strengths used in subsequent analyses are presented in Table 4.3. The elastic modulus (E_c) and rupture modulus (f_t) of the concrete were calculated using Eq. 4.1 (ACI Committee 318, 2002).

$$E_c = 57,000\sqrt{f_c'} \tag{4.1a}$$

$$f_t = 7.5\sqrt{f_c'} \tag{4.1b}$$

Table 4.3: Concrete test properties

Component	$f'_c(psi)$	$f_t(psi)$	$E_c(ksi)$
Footing	4800	520	3900
Column	5900	580	4400
Cross-beam	7000	630	4800

The columns were longitudinally reinforced with (16) #3 bars and transversely reinforced with W2.9 wire spaced at 1.25 in. Multiple coupon tests were performed at the University of Nevada, Reno for both bar types. The measured yield stress, ultimate stress and elastic modulus for the three longitudinal steel tests and the two transverse steel tests are presented in Table 4.4. The experimental stress-strain relationships for the longitudinal and transverse reinforcement are shown in Figs. 4.2 and 4.3. The elastic modulus of the steel was calculated as the average slope of the stress-strain curve up to a bar stress of 30 ksi. The yield stress was estimated using the 0.2% strain offset method. An ultimate strain could not be measured because necking and bar failures did not occur within the gauge length.

Table 4.4: Measured steel properties

Bar	Test	E (ksi)	σ_Y (ksi)	σ_U (ksi)
#3	1	30100	74.3	97.2
	2	30800	68.0	97.9
	3	26200	66.8	96.0
	Avg.	**29000**	**69.7**	**97.0**
D12	1	28700	67.2	79.2
	2	31700	67.0	79.2
	Avg.	**30200**	**67.1**	**79.2**
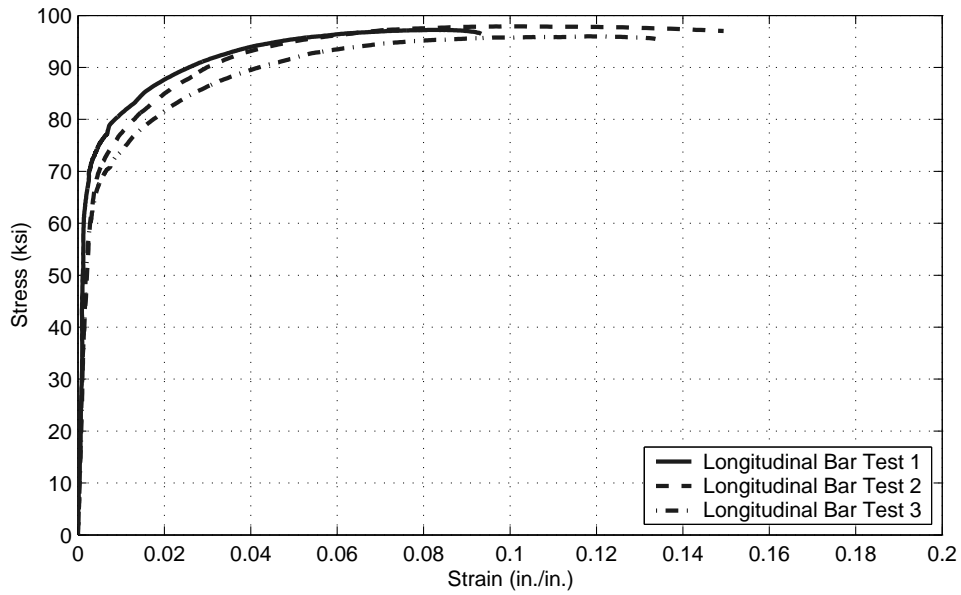
Figure 4.2: Measured stress-strain relationship for the longitudinal reinforcement
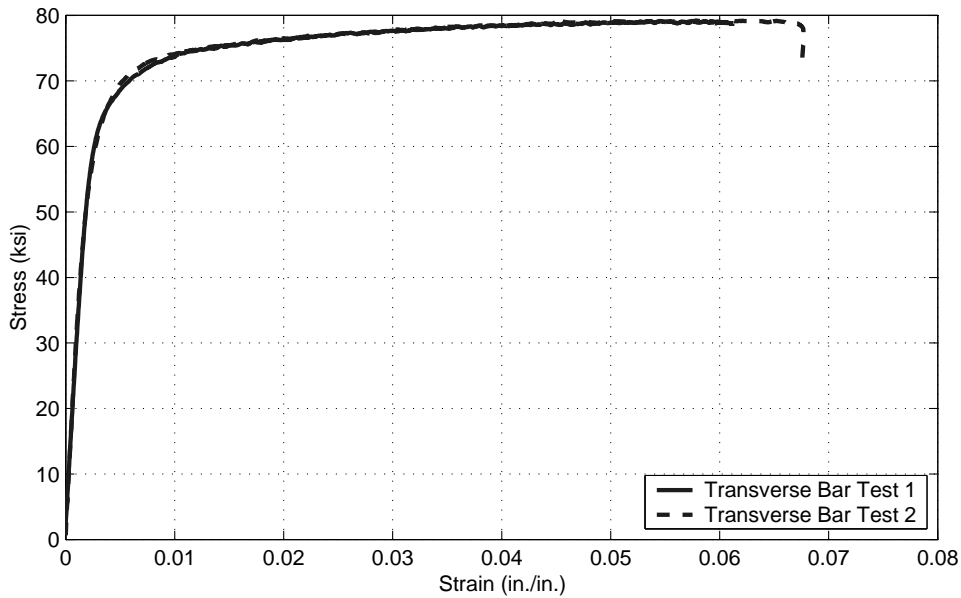
Figure 4.3: Measured stress-strain relationship for the transverse reinforcement

4.2 Target and Achieved Table Accelerations

The target table accelerations for the shaking table specimen were developed from the Century City North record of the Northridge earthquake (see Chapter 3). The various ground motions were developed by convoluting the earthquake record through soil strata of various depths. The peak target accelerations are presented in Table 4.5. Tests 1-11 represent incoherent and biaxial low-amplitude tests. Tests 12-19 represent coherent motions of increasing intensity. The damage to bent 3 was so severe following Test 19 that the intensity of Test 20 was reduced. The masses over bent 3 were removed for Tests 21 and 22 in an attempt to further damage bents 1 and 2 without causing bent 3 to collapse.

Table 4.5: Target and achieved peak table accelerations

Test	Target PGA (g)			Achieved PGA (g)			Difference (%)		
	Bent 1	Bent 2	Bent 3	Bent 1	Bent 2	Bent 3	Bent 1	Bent 2	Bent 3
1A	0.08	0.08	0.08	0.13	0.23	0.13	70	203	68
1B	0.15	0.15	0.15	0.21	0.32	0.25	34	108	62
2A	0.03	0.08	0.07	0.03	0.13	0.07	0	74	1
2B	0.07	0.15	0.15	0.07	0.34	0.16	7	120	12
3A	0.07	0.08	0.03	0.08	0.13	0.05	14	65	35
3B	0.15	0.15	0.07	0.17	0.38	0.08	13	145	19
4	0.07	0.18	0.18	0.07	0.22	0.23	4	19	30
5	0.18	0.07	0.18	0.21	0.10	0.25	15	44	36
6	0.18	0.18	0.07	0.20	0.21	0.09	12	18	32
7	0.15	0.15	0.15	0.17	0.22	0.21	7	42	38
9A	0.08	0.08	0.08	0.09	0.10	0.10	14	30	31
9B	0.15	0.15	0.15	0.17	0.33	0.21	8	114	35
10	0.06	0.06	0.08	0.08	0.10	0.10	22	61	25
11	0.06	0.05	0.09	0.07	0.09	0.10	27	70	12
12	0.08	0.08	0.08	0.07	0.10	0.08	-7	29	9
13	0.15	0.15	0.15	0.18	0.18	0.17	18	19	15
14	0.25	0.25	0.25	0.35	0.31	0.28	39	25	12
15	0.50	0.50	0.50	0.67	0.65	0.72	34	29	44
16	0.75	0.75	0.75	0.98	0.94	1.25	31	25	67
17	1.00	1.00	1.00	1.20	1.50	1.09	20	50	9
18	1.33	1.33	1.33	1.56	1.81	1.59	17	36	19
19	1.66	1.66	1.66	2.00	2.13	2.20	20	28	33
20	1.00	1.00	1.00	1.26	1.30	1.44	26	30	44
21	1.00	1.00	1.00	1.22	1.21	1.34	22	21	34
22	1.33	1.33	1.33	1.61	1.50	1.71	21	12	29

The achieved table accelerations for each test are also shown in Table 4.5. Table friction and structural feedback made it difficult to achieve table accelerations similar to the

target accelerations. Table friction had more influence during low-amplitude excitations, in which the target motions were near the friction thresholds of the tables. During the high-amplitude tests, structural feedback had more influence. The differences between the target and achieved table accelerations were minimized by creating a transfer function to adjust the input motion so that the target acceleration would be achieved. However, because the target motion changed in shape and intensity throughout the tests, and the structure changed significantly during the high-amplitude tests, finding the correct transfer function for each test was difficult.

The difference between the maximum target and achieved table accelerations was generally the greatest for the table at bent 2 (200% for Test 1A). There were also large differences in the other bents (70% at bent 1 for test 1A) during the low-amplitude tests.

For the high-amplitude tests, the differences were generally smaller. The average difference during the high-amplitude tests (Tests 13-20) was approximately 30%. Fig. 4.4 shows the achieved table accelerations versus the target accelerations. The achieved peak accelerations were almost always larger than the target peak accelerations, the one minor exception being Bent 1 during Test 12.
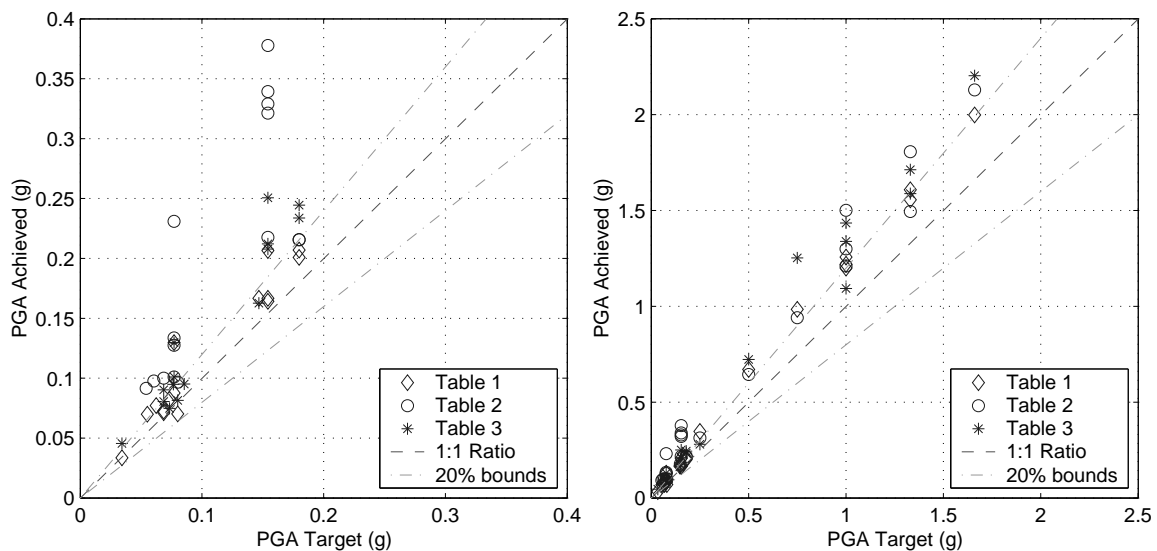
Figure 4.4: Target and achieved peak ground accelerations for the (a) low-amplitude tests and (b) high-amplitude tests

Typical response spectra (5% damping) for the low and high-amplitude tests are shown in Fig. 4.5. Fig. 4.5a shows the target and achieved response spectra for shaking table 3 during Test 12. Below a period of approximately 0.15s, the achieved spectral acceleration exceeded the target. Above this period, the target was larger. Fig. 4.5b shows the target and achieved response spectra during Test 18. The two response spectra were similar for periods between 0.22 and 0.33s. Outside of this range, the achieved response spectra was smaller than the target.
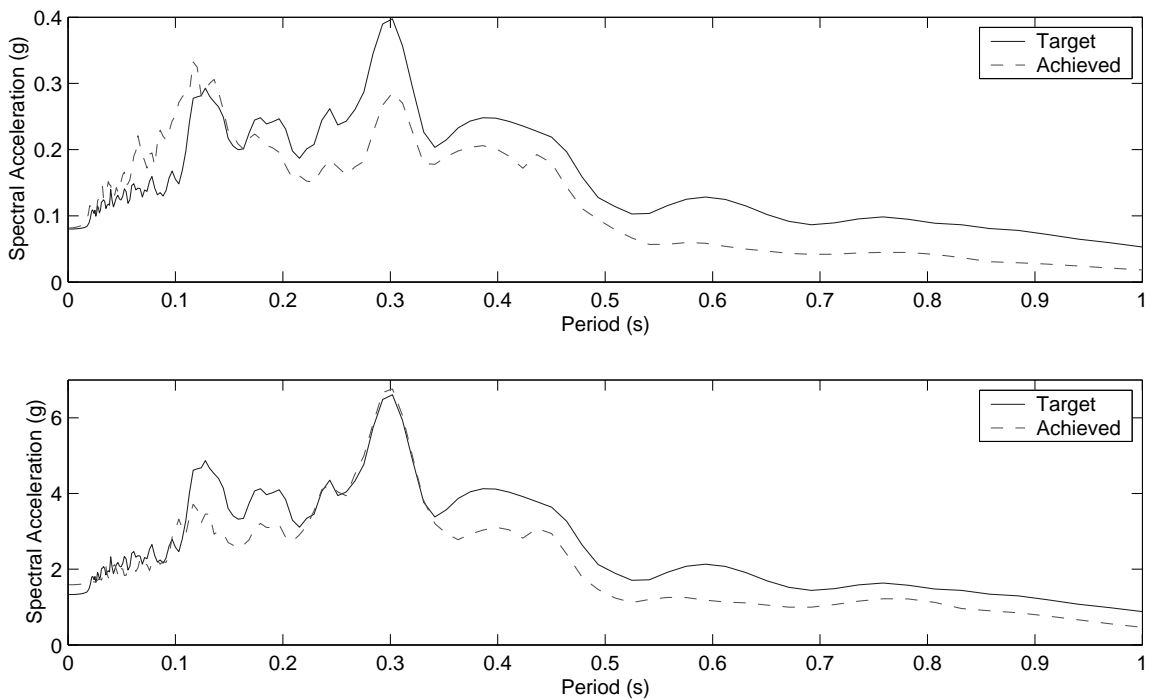
Figure 4.5: Spectral accelerations for typical (a) low-amplitude tests (Test 12) and (b) high-amplitude tests (Test 18)

The average periods of the first two transverse modes of the shaking table specimen during the low-amplitude tests were 0.33s and 0.26s (Chapter 6). The spectral accelerations at these periods are shown in Figs. 4.6 and 4.7, respectively, for all of the low and high-amplitude tests. During the low-amplitude tests, the achieved spectral accelerations at periods of 0.33s and 0.26s varied from approximately 30% to 250% of the targets spectral accelerations. During the high-amplitude tests, this range was reduced to 70% to 150%.
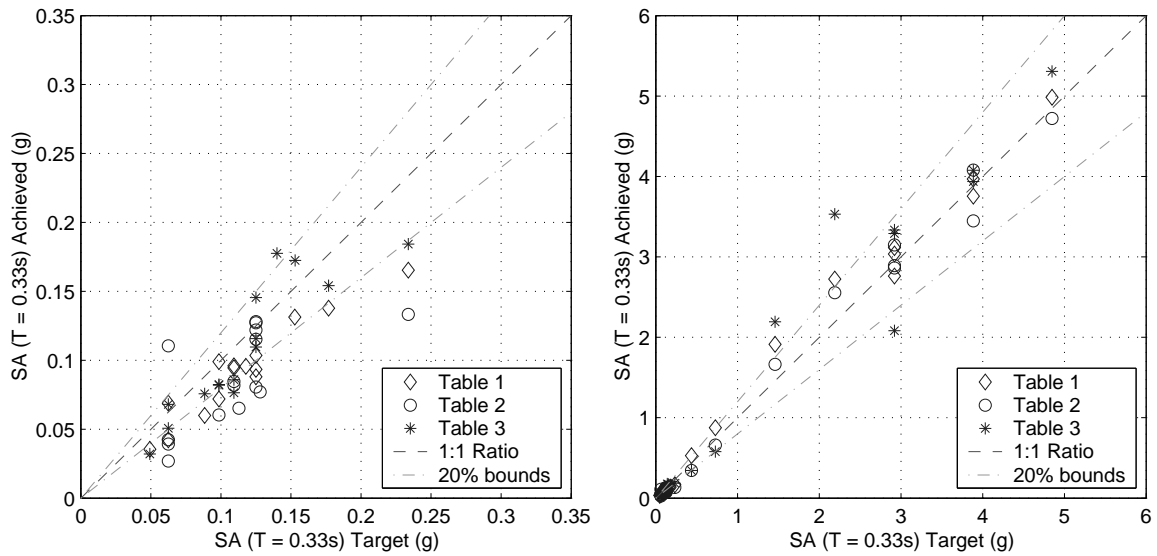
Figure 4.6: Target and achieved spectral acceleration at T = 0.33s for the (a) low-amplitude and (b) high-amplitude tests
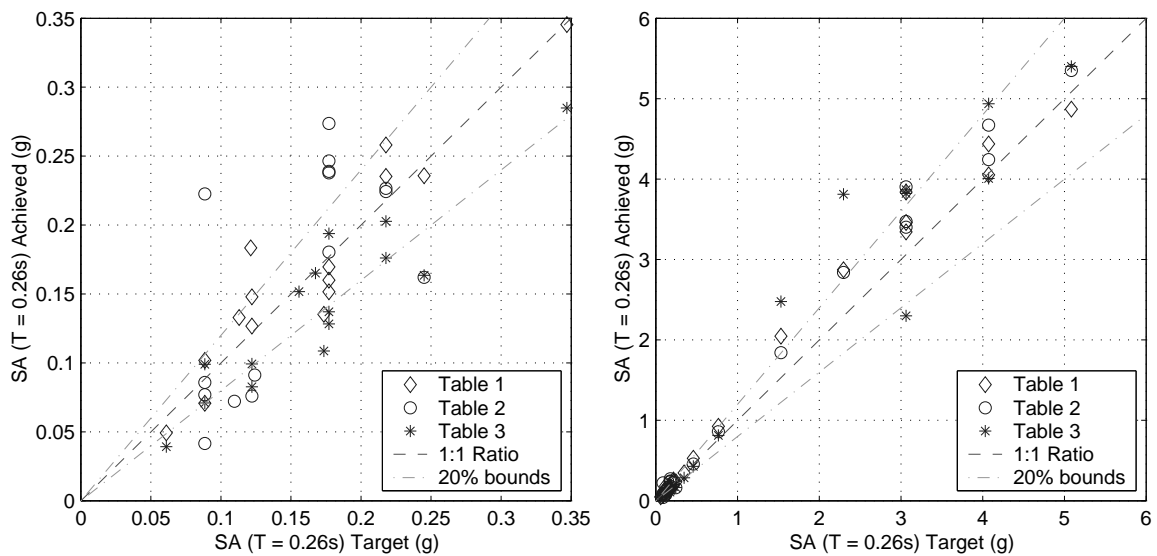
Figure 4.7: Target and achieved spectral acceleration at T = 0.26s for the (a) low-amplitude and (b) high-amplitude tests

4.3 Bent Displacement and Acceleration Response Histories

The displacement response of each bent was measured using five string potentiometers located on the west face of the bent caps and at the midpoint of each span. Accelerometers

were placed on the top of the bridge deck at the center of the bent caps and at the midpoint of each span. Displacement and acceleration histories of typical low-amplitude and high-amplitude tests are shown in Figs. 4.8 and 4.9.

Fig. 4.8 shows the displacement and acceleration response at each bent for Test 12. The response of the specimen during this test lasted approximately ten seconds. As the specimen became softer due to column damage, the transient response of the specimen extended. For example, for the same excitation time as Test 12, the bent response from Test 18 (Fig. 4.9) lasted for approximately 20 seconds.

Measurement noise was relatively large in both the displacement and the acceleration data during the low-amplitude tests. The ratios of the peak noise measurements to the peak response measurements are shown in Fig. 4.10 for both the displacement and acceleration data. The peak measurement noise was estimated as the peak signal during the first five seconds of each test, before the excitation in the input signal began.

The noise to peak displacement response ratios were largest for bent 3 during the low-amplitude tests, with a mean value of 0.3. the ratios for bents 1 and 2 were almost always below 0.05. The maximum ratio occurred during Test 9A (Fig. 4.11). The displacement response for bent 3 during this test was fully obscured by measurement noise. Near the end of the test, measurement noise was approximately 2.5 times larger than the maximum displacement response of 0.04 in. During the high-amplitude tests, as the maximum noise remained constant and the maximum response increased, this ratio decreased. The average noise-to-signal ratio for the displacement data after Test 14 was 0.01.

The noise to peak acceleration response ratios were large for bent 2 during the low-amplitude tests, with a mean ratio of 0.055. The ratios for bents 1 and 3 were almost always below 0.02. Similar to the displacement data, the noise-to-signal ratio for the acceleration data decreased during the high-amplitude tests. For example, the average noise-to-signal ratio for the acceleration data after Test 14 was approximately 0.01.

44
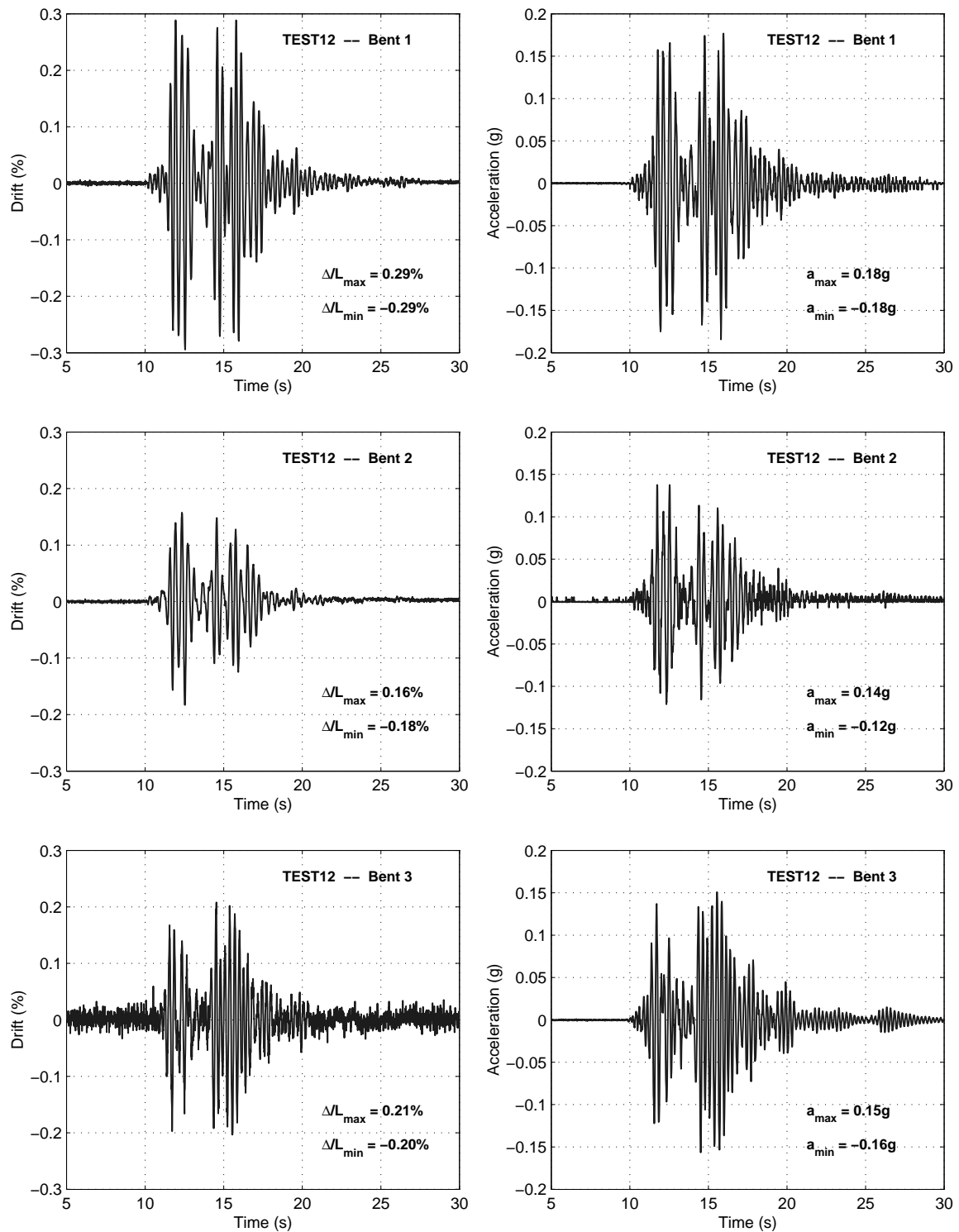
Figure 4.8: Displacement and acceleration histories for Test 12
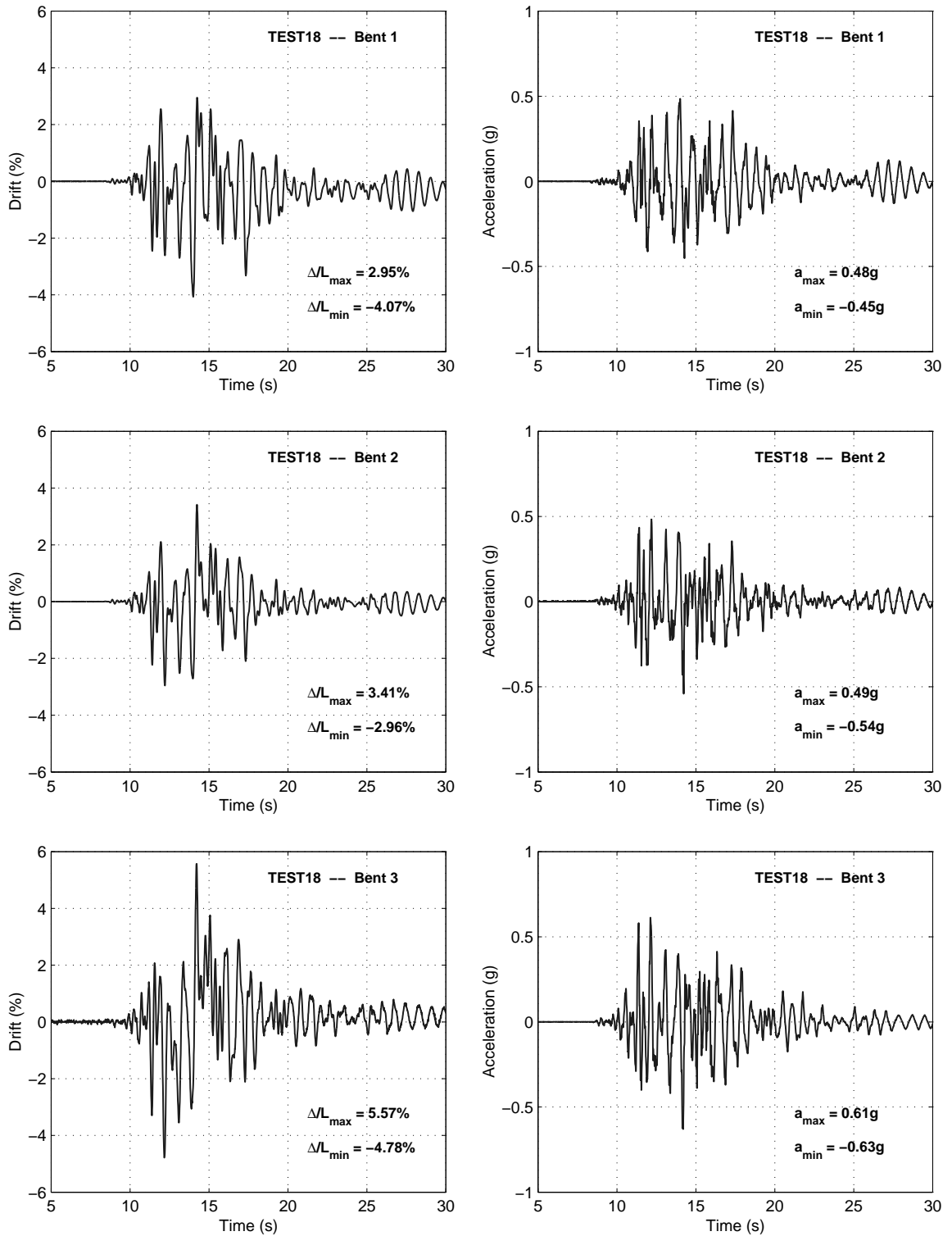
Figure 4.9: Displacement and acceleration histories for Test 18
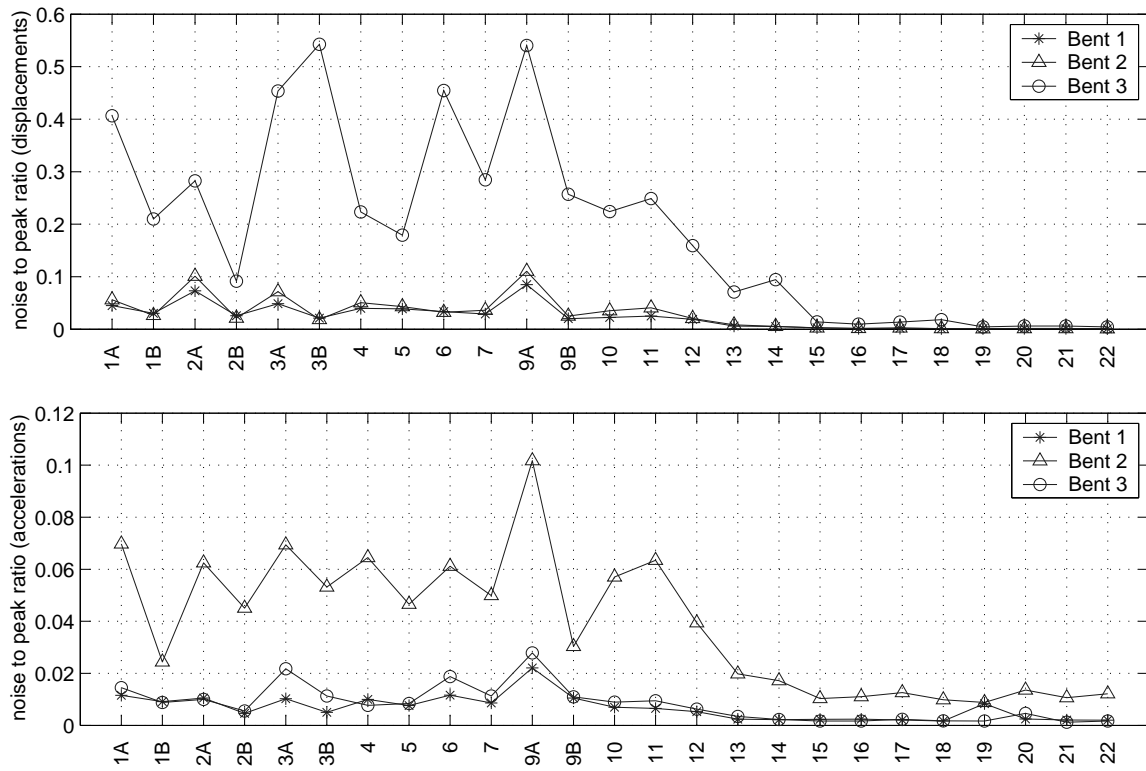
Figure 4.10: Noise to maximum response ratios for (a) acceleration data and (b) displacement data
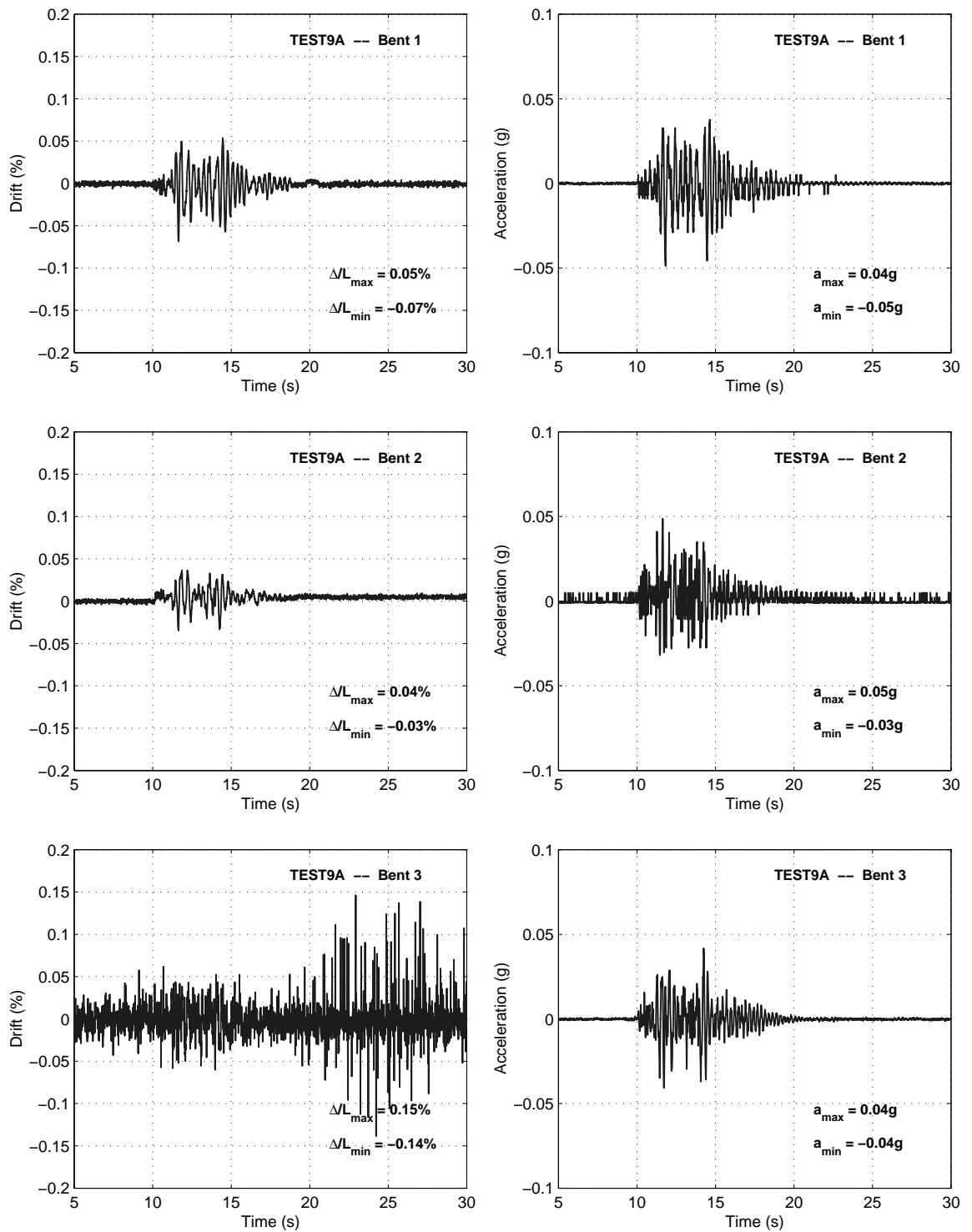
Figure 4.11: Displacement and acceleration histories for Test 9A

4.4 Bent Displacement and Acceleration Response Maxima

The maximum measured bent displacements and accelerations were used to assess the accuracy of the numerical model. For each test, the maximum bent displacements, drift ratios and accelerations are listed in Table 4.6, and plotted in Figs. 4.12 and 4.13. The maximum bent drift and bent acceleration during the low-amplitude tests were 0.32% and 0.23g, respectively (Bent 3, Test 2B). The maximum bent accelerations reach a plateau near Test 15, signifying that the force capacity of each bent was reached. Although the peak accelerations levelled off, the maximum bent displacements continued to increase. Before the mass was removed from bent 3 (Test 21), the maximum bent drift reached 8% (bent 3, Test 19).

Table 4.6: Maximum bent displacements and accelerations

Test	Max. Bent Disp. (in.)			Max. Bent Drift (%)			Max. Bent Accel. (g)		
	Bent 1	Bent 2	Bent 3	Bent 1	Bent 2	Bent 3	Bent 1	Bent 2	Bent 3
1A	0.09	0.08	0.05	0.13	0.09	0.08	0.09	0.08	0.08
1B	0.15	0.14	0.08	0.20	0.14	0.14	0.12	0.14	0.13
2A	0.06	0.04	0.07	0.08	0.04	0.11	0.08	0.07	0.11
2B	0.13	0.12	0.19	0.17	0.13	0.32	0.18	0.12	0.23
3A	0.07	0.05	0.05	0.10	0.05	0.08	0.08	0.06	0.04
3B	0.18	0.15	0.07	0.25	0.16	0.12	0.18	0.11	0.08
4	0.09	0.10	0.11	0.13	0.10	0.19	0.10	0.08	0.15
5	0.11	0.08	0.10	0.15	0.08	0.16	0.11	0.11	0.13
6	0.11	0.09	0.05	0.15	0.10	0.09	0.09	0.08	0.07
7	0.12	0.11	0.07	0.16	0.12	0.12	0.10	0.11	0.10
9A	0.05	0.03	0.04	0.07	0.04	0.06	0.05	0.05	0.04
9B	0.13	0.14	0.08	0.17	0.15	0.13	0.11	0.13	0.10
10	0.16	0.10	0.09	0.23	0.11	0.15	0.15	0.09	0.13
11	0.13	0.08	0.10	0.18	0.08	0.16	0.13	0.08	0.13
12	0.21	0.17	0.12	0.30	0.18	0.21	0.18	0.14	0.16
13	0.61	0.43	0.32	0.85	0.45	0.53	0.36	0.28	0.30
14	0.78	0.56	0.49	1.08	0.59	0.82	0.42	0.32	0.41
15	1.54	1.26	1.45	2.14	1.31	2.42	0.48	0.52	0.58
16	2.70	2.32	1.93	3.76	2.41	3.22	0.47	0.52	0.56
17	1.86	1.85	1.43	2.58	1.93	2.38	0.43	0.41	0.50
18	2.93	3.28	3.35	4.07	3.42	5.58	0.48	0.54	0.63
19	3.58	4.32	4.80	4.97	4.50	8.00	0.53	0.47	0.59
20	2.30	3.05	3.27	3.20	3.18	5.44	0.42	0.30	0.24
21	3.04	3.36	3.59	4.22	3.50	5.98	0.48	0.44	0.79
22	3.26	5.12	6.56	4.53	5.33	10.93	0.44	0.42	0.51

The maximum center-of-mass and twist displacement of the slab for all of the tests are shown in Fig. 4.14. The response at the center-of-mass of the shaking table specimen was
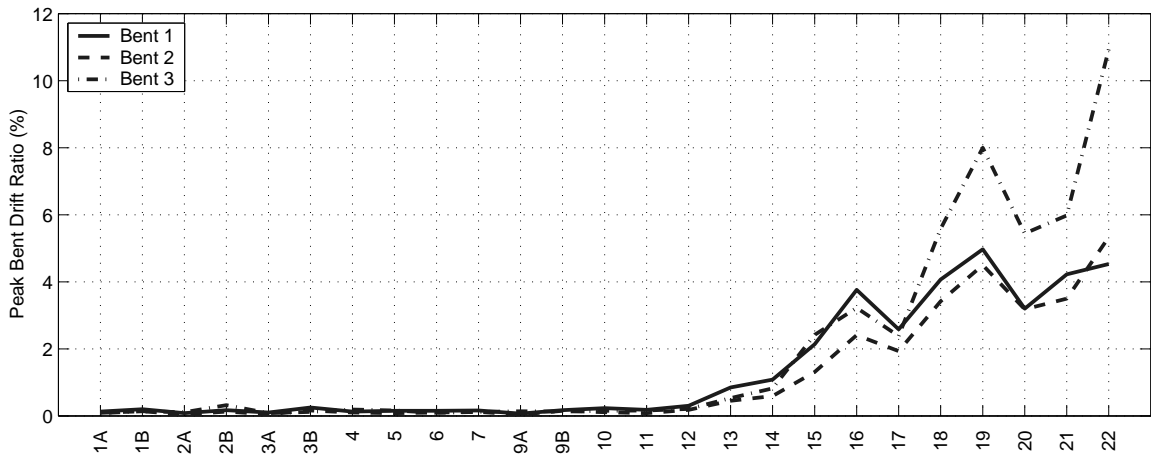
Figure 4.12: Measured displacement maxima
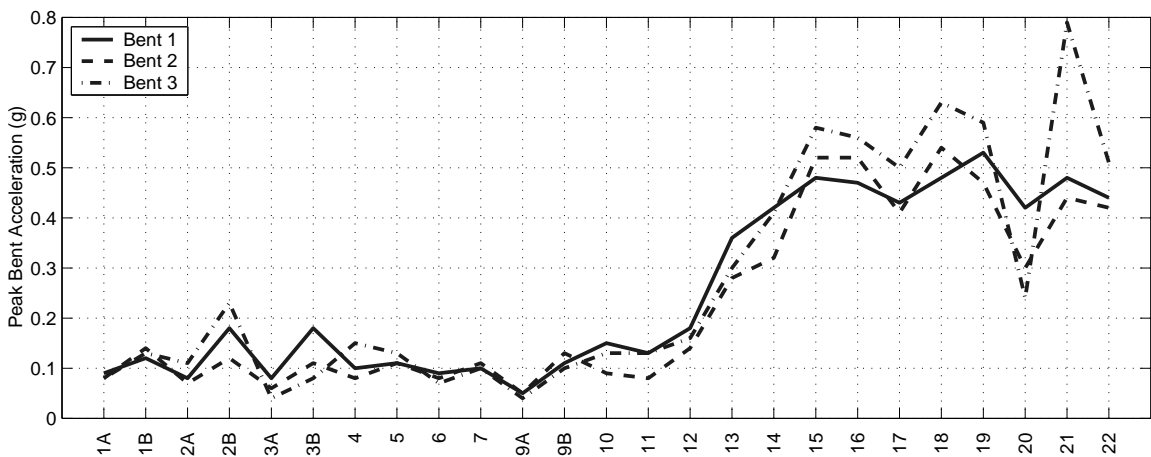
Figure 4.13: Measured acceleration maxima

calculated by averaging the response measured at the five slab locations.

$$\Delta_{cm} = \frac{1}{5} \sum_{i=1}^{5} \Delta_i \qquad (4.2)$$

The twist displacement was calculated by taking the difference in the measured displacements at Bents 1 and 3.

$$\Delta_{twist} = \Delta_1 - \Delta_5 \qquad (4.3)$$

Fig. 4.14 also shows the twist displacement at the time of the maximum center-of-mass displacement. Because of the stiffness of the slab, the center-of-mass displacement was approximately equal to the bent 2 displacement.
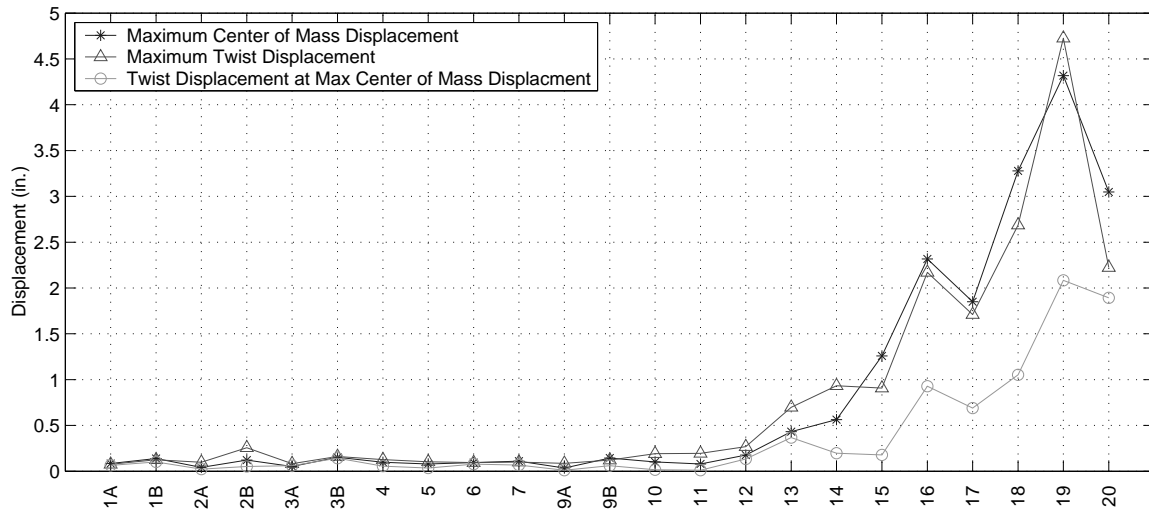
Figure 4.14: Maximum center-of-mass and twist displacements

Fig. 4.15 shows the maximum twist displacement versus the maximum center of mass displacement for the low and high-amplitude tests.
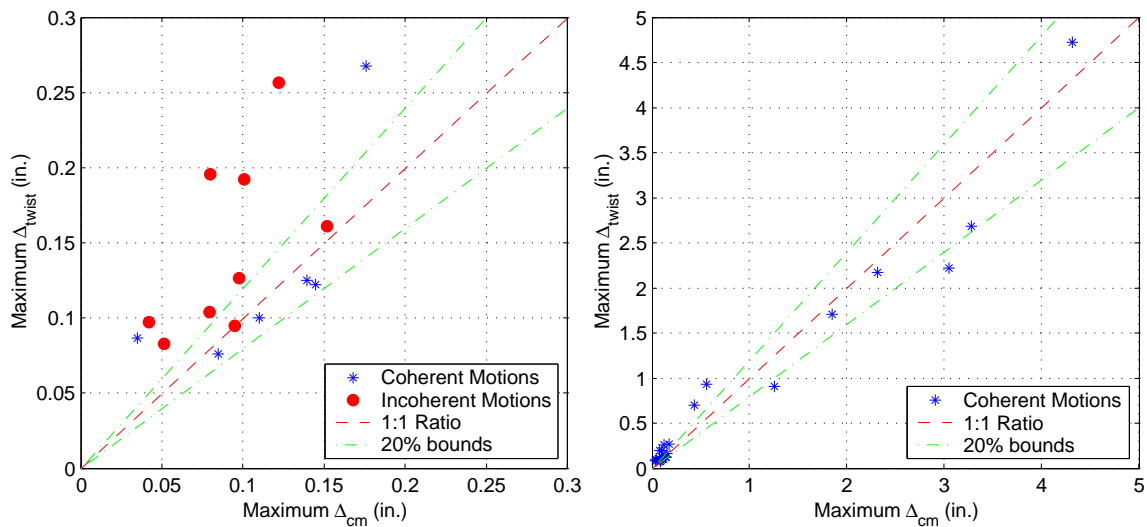
Figure 4.15: Maximum twist displacement vs. maximum center of mass displacement for (a) low-amplitude and (b) high-amplitude tests.

The circles denote tests with target incoherent motions. The asterisks denote tests with target coherent motions. During the low-amplitude tests (Fig. 4.15a), many of which had incoherent motions, the maximum twist displacements were almost always larger than the

center-of-mass displacements. During the high-amplitude tests (Fig. 4.15b), which were nominally coherent, the maximum twist displacements were similar in amplitude to the maximum center-of-mass displacements.

The effects of ground motion variation are usually expressed in terms of the unlagged coherency function (Lupoi et al., 2005), defined as

$$\psi_{ij}(\omega) = \frac{real(S_{ij}(\omega))}{\sqrt{S_{ii}(\omega)S_{jj}(\omega)}} \tag{4.4}$$

where $\psi_{ij}(\omega)$ is the unlagged coherency function, which varies between -1 and 1. The terms $S_{ii}(\omega)$ and $S_{jj}(\omega)$ are the power spectral densities of the two motions, and $S_{ij}(\omega)$ is the cross spectral density of the two motions. The unlagged coherency accounts for differences in frequency content and phase of the two motions. For example, for two identical motions, this term will have a value of one. For two motions that are identical except for opposite sign, this term will have a value of negative one. However, this formulation does not account for differences in motion amplitude that would be expected to affect the structural response.

For the purpose of comparing the effects of spatial variation on the structural response, the unlagged coherency was adjusted by a factor that accounts for the differences in motion amplitude. The weighted coherency is defined as

$$\overline{\psi}_{ij}(\omega) = \left[\frac{real(S_{ij}(\omega))}{\sqrt{S_{ii}(\omega)S_{jj}(\omega)}} \right] \left[\frac{S_{ai}(\omega)}{S_{aj}(\omega)} \right]^{0.5} \tag{4.5}$$

where $\overline{\psi}_{ij}(\omega)$ is the weighted coherency function, which also varies between -1 and 1. The terms $S_{ai}(\omega)$ and $S_{aj}(\omega)$ are the acceleration response spectra (5% damping) for the two motions. The ratio of the spectral accelerations always ranges between zero and one, which accounts for differences in motion amplitude. For two identical motions, this term will have a value of one. If one of the motions is identical to the other in frequency content, but has an amplitude that is 25% of the amplitude of the other motion, this term would be equal to 0.5.

The effects of the weighted motion incoherency on the measured center of mass and twist displacements are shown in Fig. 4.16.

As seen in this figure, the ratio between the measured center-of-mass displacement and the average spectral displacement was independent of motion coherency, with a correlation
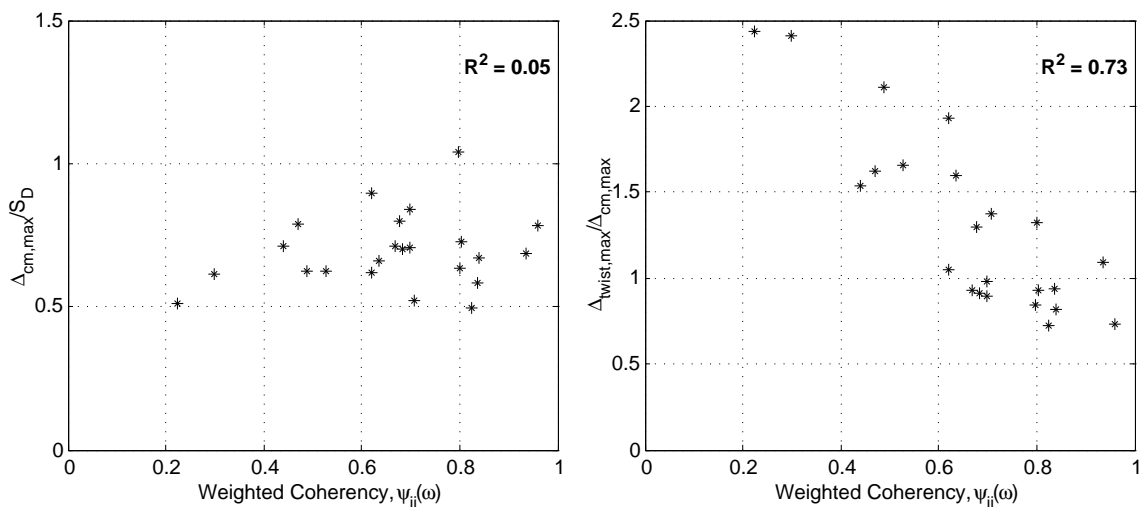
Figure 4.16: Measured center-of-mass and twist displacements as a function of the weighted motion coherency

coefficient (R^2) of 0.05. The ratios between the measured twist displacement and the center of mass displacement are plotted in Fig. 4.16b, as a function of the weighted motion coherency. This figure shows that the twist displacements were inversely correlated with the weighted coherency function ($R^2 = 0.73$).

The measured peak center-of-mass response was compared with the calculated spectral displacements (SD) and spectral accelerations (SA) at 5% damping. The spectral values were averaged over the three table excitations. Fig. 4.17 compares the measured center-of-mass displacement to the spectral displacement at a period of T =0.33s (the mean first mode period for the low-amplitude tests).

The spectral displacements at T = 0.33s were near the measured center of mass displacements for the low-amplitude tests. The mean and standard deviation of the differences between the measured center of mass displacements and the spectral displacements for the low-amplitude tests were 16% and 14%, respectively. The maximum difference was 51%. Eleven of the 15 spectral displacement estimates were within 20% of the measured center-of-mass displacements.

During the high-amplitude tests, the mean and standard deviation of the differences between the measured center of mass displacements and the spectral displacements were
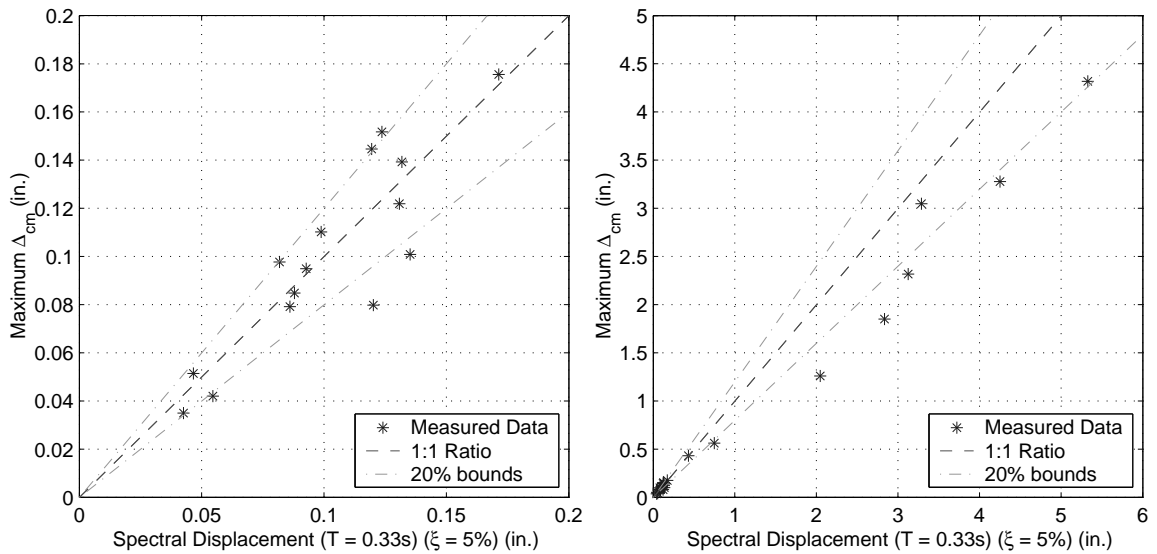
Figure 4.17: Measured peak displacement vs. SD (T = 0.33s) for (a) low-amplitude and (b) high-amplitude tests.

31% and 21%, respectively. The maximum difference was 63%. Six of the 9 spectral displacement measurements were within 20% of the measured displacement.

The same analysis was conducted for the acceleration response (Fig. 4.18). During the low-amplitude tests, the spectral acceleration at T = 0.33s provided a good estimate of the center of mass acceleration. The mean and standard deviation of the differences between the measured center of mass accelerations and the spectral accelerations were 17% and 12%, respectively. The maximum difference was 42%. Eight of the 15 tests were within 20% of the measured acceleration. As the system became more nonlinear, the spectral accelerations increasingly overestimated measured accelerations. By test 23, the spectral acceleration overestimated the measured center of mass acceleration by 950%.

The modal properties of the specimen were estimated using system identification algorithms for all of the tests (Chapter 6). Using the results from this analysis, the spectral displacement was estimated using the identified fundamental period for each test. The center-of-mass displacement is plotted vs. the spectral displacement estimates using these test specific periods in Fig. 4.19. The mean and standard deviation of the differences between the measured center of mass accelerations and the spectral displacements using the
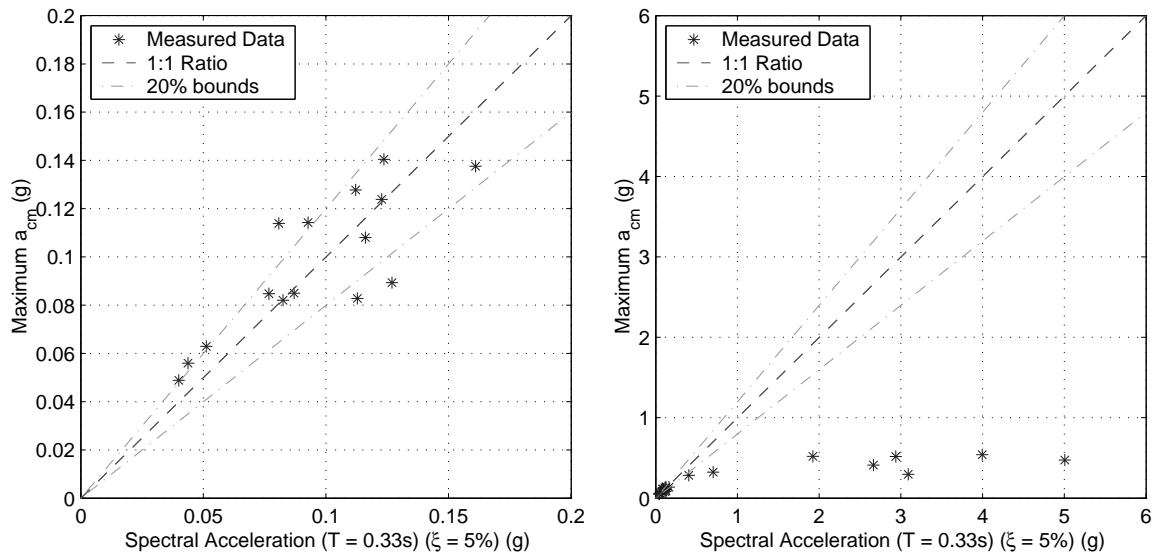
Figure 4.18: Measured peak acceleration vs. SA (T = 0.33s) for (a) low-amplitude and (b) high-amplitude tests.

identified structural periods were 13% and 10%, respectively. The maximum difference was 35%. The period T = 0.33s is the average fundamental period during the low-amplitude tests. As a result, using the actual fundamental period for the low-amplitude tests (which ranged from 0.31s - 0.35s) improved the results, but not significantly.

During the high-amplitude tests, using the identified period of the structure while also using a set damping of 5% caused the spectral displacement estimates to overestimate the measured center-of-mass displacements. By Test 20, the spectral displacement overestimated the center of mass displacement by 120%.
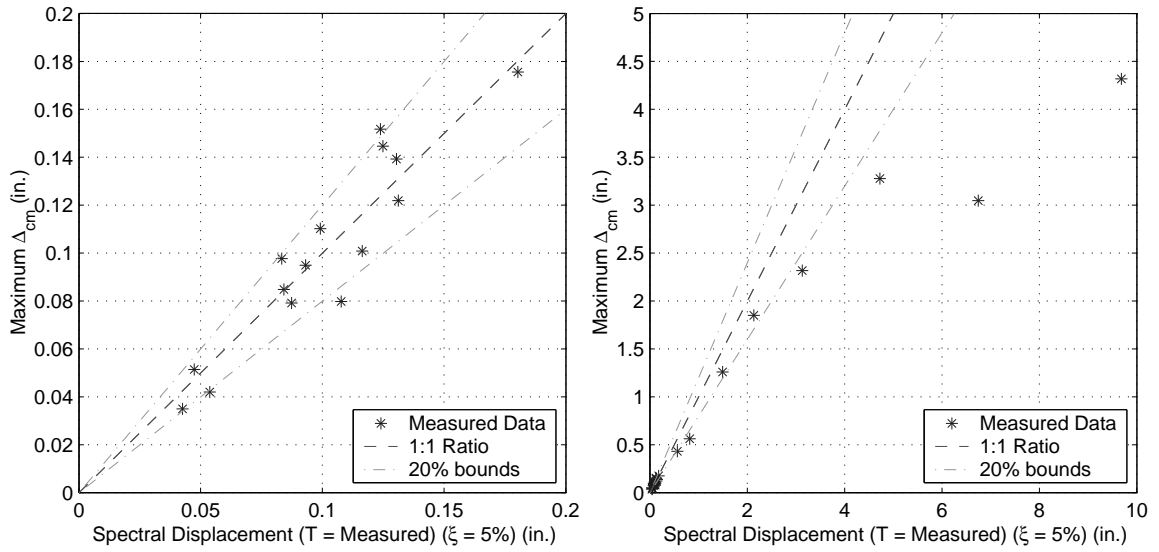
Figure 4.19: Measured peak displacement vs. SD (test specific identified periods) for (a) low-amplitude and (b) high-amplitude tests.

4.5 Displacement-Strain Envelopes

A total of 160 strain gauges were placed on the longitudinal and transverse reinforcement within each of the columns. The location of each of the strain gauges is documented in Appendix C. Fig. 4.20 illustrates the strain-gauge nomenclature.
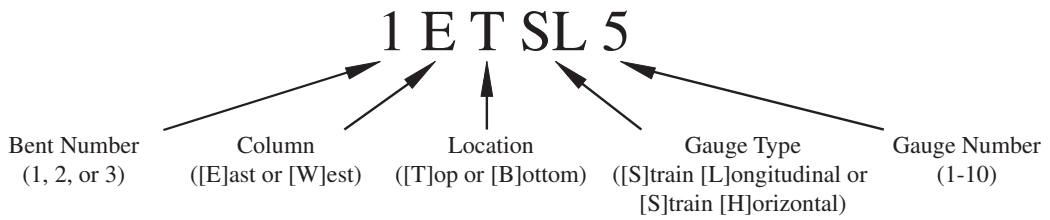
Figure 4.20: Strain gauge nomenclature

Displacement-strain envelopes were developed at three locations along the longitudinal reinforcement and one location on the transverse reinforcement near the column-anchorage interface. These four locations, which are shown in Fig. 4.21, are as follows.

- **Anchorage Gauges:** Strain gauges (4 per column) on the longitudinal reinforcement

within the anchorage zone, 6 in. from the column-anchorage interface.

- **Interface Gauges:** Strain gauges (4 per column) on the longitudinal reinforcement at the column-anchorage interface.

- **Column Gauges:** Strain gauges (4 per column) on the longitudinal reinforcement within the column, 6 in. from the column-anchorage interface.

- **Transverse Gauges:** Strain gauges (4 per column) on the transverse reinforcement within the column, 4 in. from the column-anchorage interface.
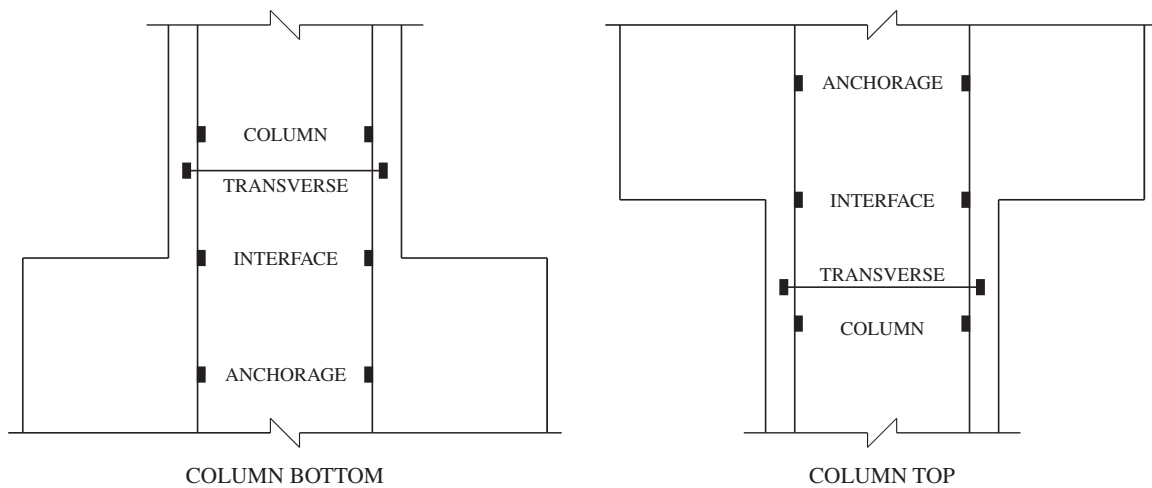
Figure 4.21: Illustration of the strain gauge locations used in developing the displacement-strain envelopes.

The combination of 4 strain gauges per column for each of the 4 locations, 2 columns per bent, and 3 bents for the structure created 96 displacement-strain envelopes throughout the structure. The envelopes for these 96 gauges are presented in Appendix D. Some strain gauges showed zero strain or very large strains for all displacement levels, presumably because they were damaged during construction. For example, gauge 1ETSL5 (Fig. D.1b) shows zero strain for all displacements.

The average displacement-strain envelopes across all similar longitudinal gauge locations (anchorage, interface, or column) are shown in Fig. 4.22 for each bent. Despite the difference in aspect ratio, all three bents were similar. For each bent, the interface gauges recorded

larger strains than either the column gauges or the anchorage gauges. The anchorage strains were always the smallest. On average, the anchorage gauges recorded approximately 10% of the strain of the other two gauge locations.

The longitudinal strain gauges were further divided into four groups, illustrated in Table 4.7. The displacement-strain envelopes for the groupings in Table 4.7 are shown in Figs. 4.23 - 4.25.

Table 4.7: Description of strain gauge groups

Group Number	Column Location	Column Action	Column Face
1	Bottom	Tension	Exterior
2	Bottom	Compression	Interior
3	Top	Compression	Exterior
4	Top	Tension	Interior

Fig. 4.23 shows the displacement-strain envelopes for the average east-column and west-column gauges. The averages for these two groupings are nearly identical. The largest discrepancy is in the bent 2 anchorage envelopes. This observation establishes confidence in the strain gauge measurements at all of these locations, because there is no reason to expect a significant difference between the two columns of each bent.

The average displacement-strain envelopes for the top and the bottom gauges are shown in Fig. 4.24. The averages of the top and bottom gauges for the interface and the column are similar. However, for a given displacement, the anchorage strains in the gauges at the bottom of the columns are generally larger than the anchorage strains at the top of the columns.

The tensile-side strain gauges were defined as the gauges that were in tension when the overturning force induced column tension. The compression gauges are those that are in tension when the overturning force caused compression. The compression gauges generally had larger absolute strains than the tensile gauges for a given drift ratio (Fig. 4.25). For example, the average compression and tension envelopes for the footing gauges in bent 3 show that at a drift ratio of 2%, the average compression gauges have a strain ductility of 0.7 while the average tensile gauges have a strain ductility of approximately 0.55. This trend is apparent in 5 of the 9 cases when the gauge is in tension and 7 of the 9 cases when

58
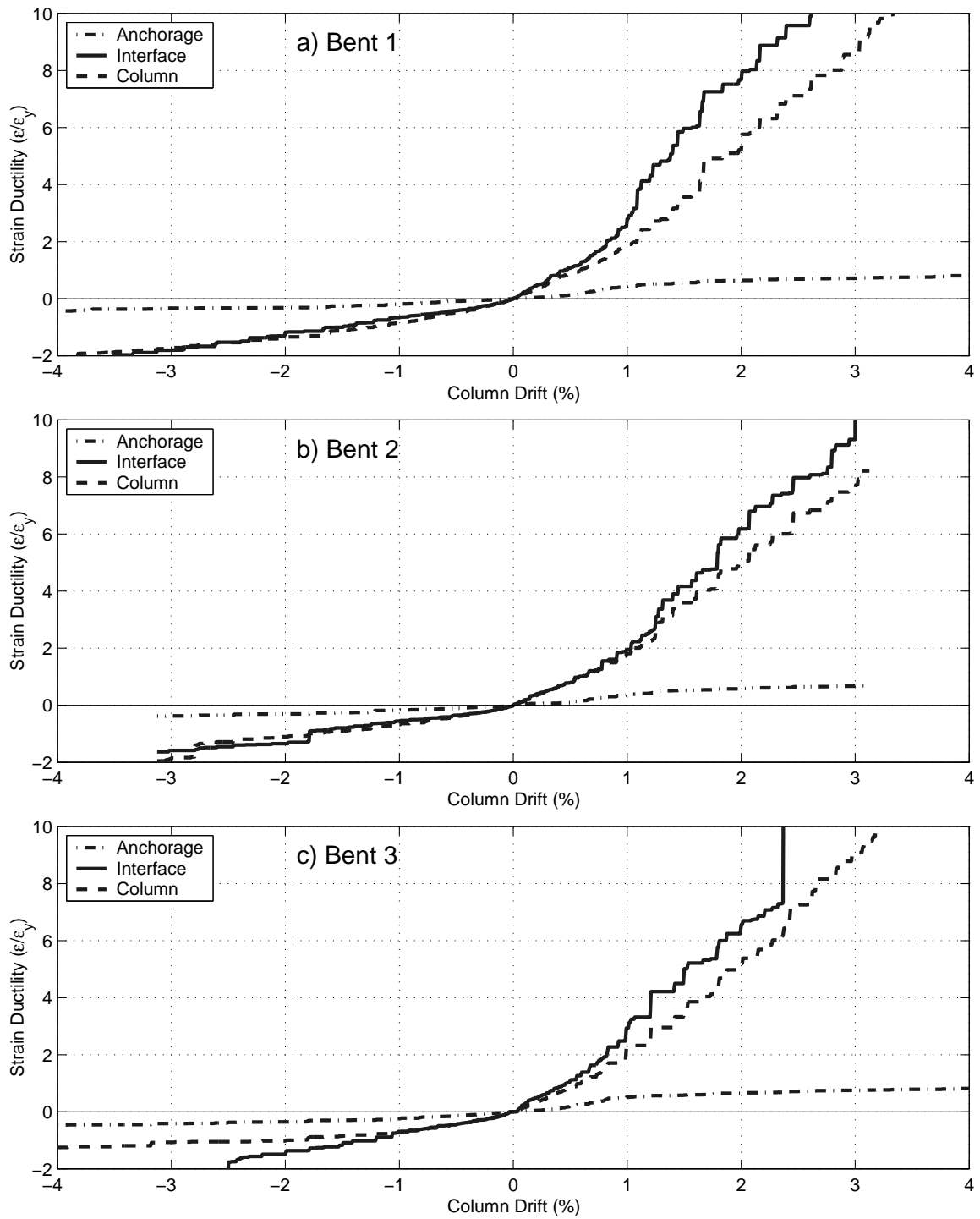
Figure 4.22: Displacement-strain envelopes for (a) bent 1, (b) bent 2, and (c) bent 3.

the gauge is in compression. For the other cases, the compression and tension gauges have approximately the same envelope. These observations are contrary to what is expected from a moment-curvature analysis.
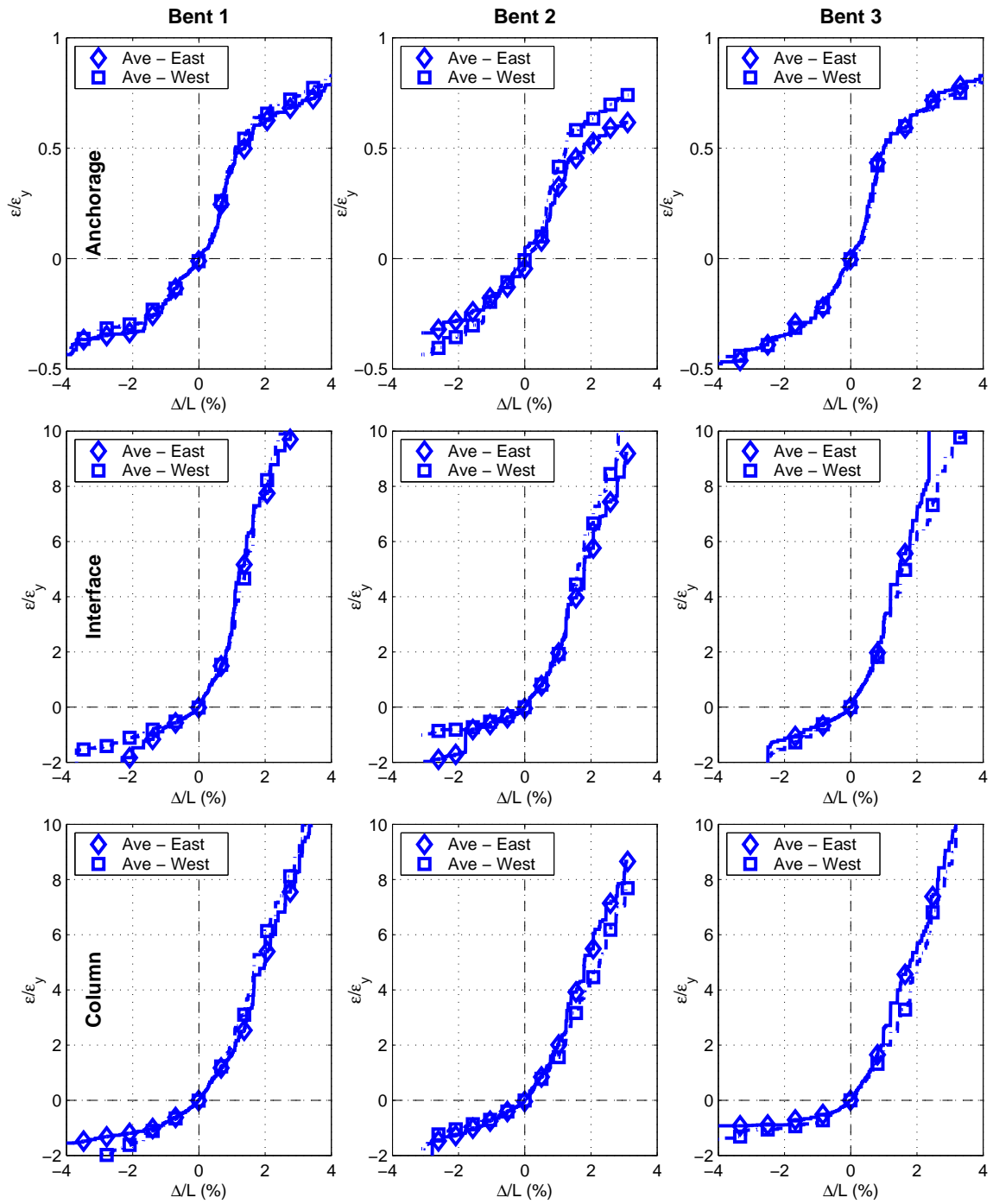
Figure 4.23: Average displacement-strain envelopes for east and west gauges
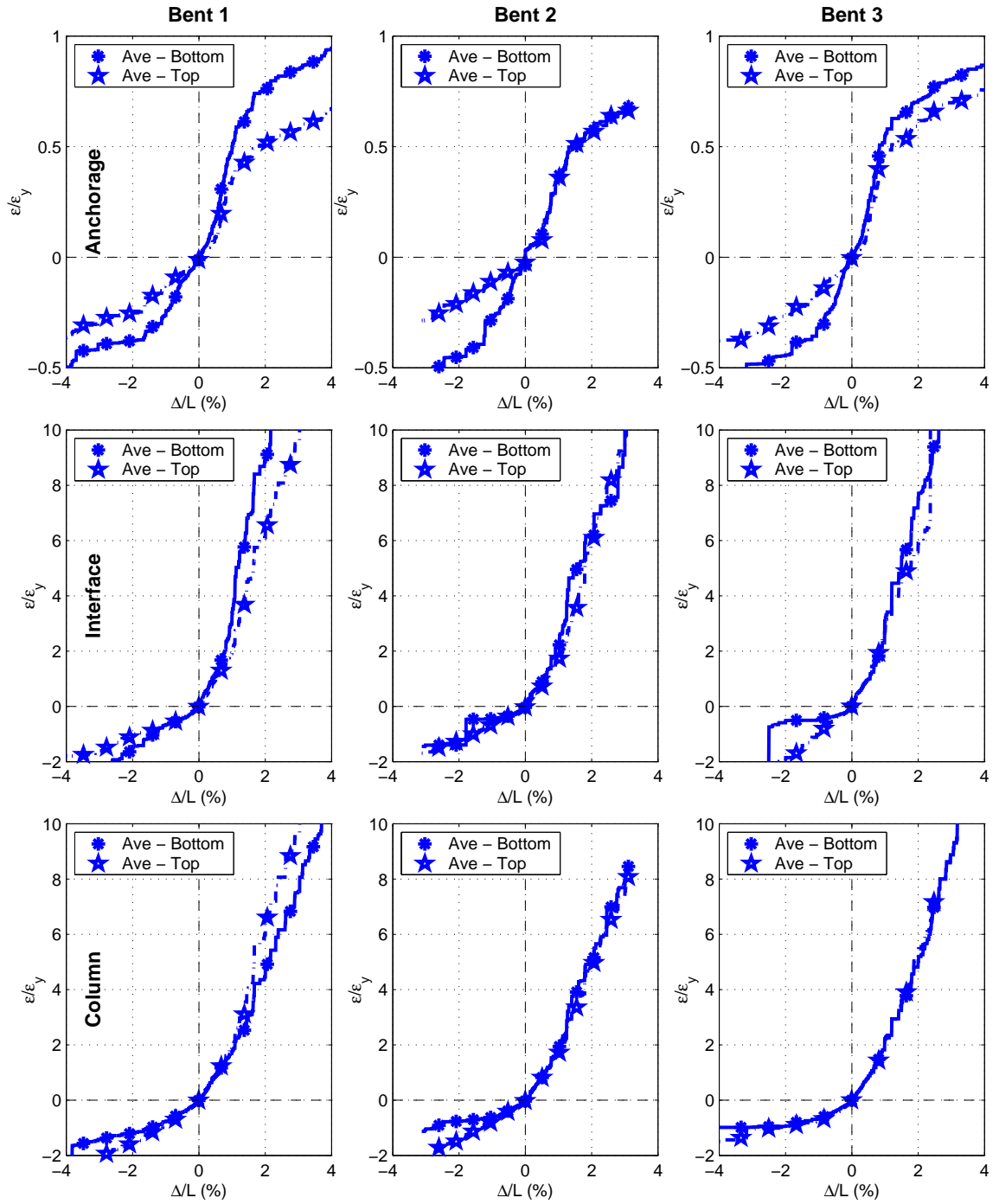
Figure 4.24: Average displacement-strain envelopes for top and bottom gauges
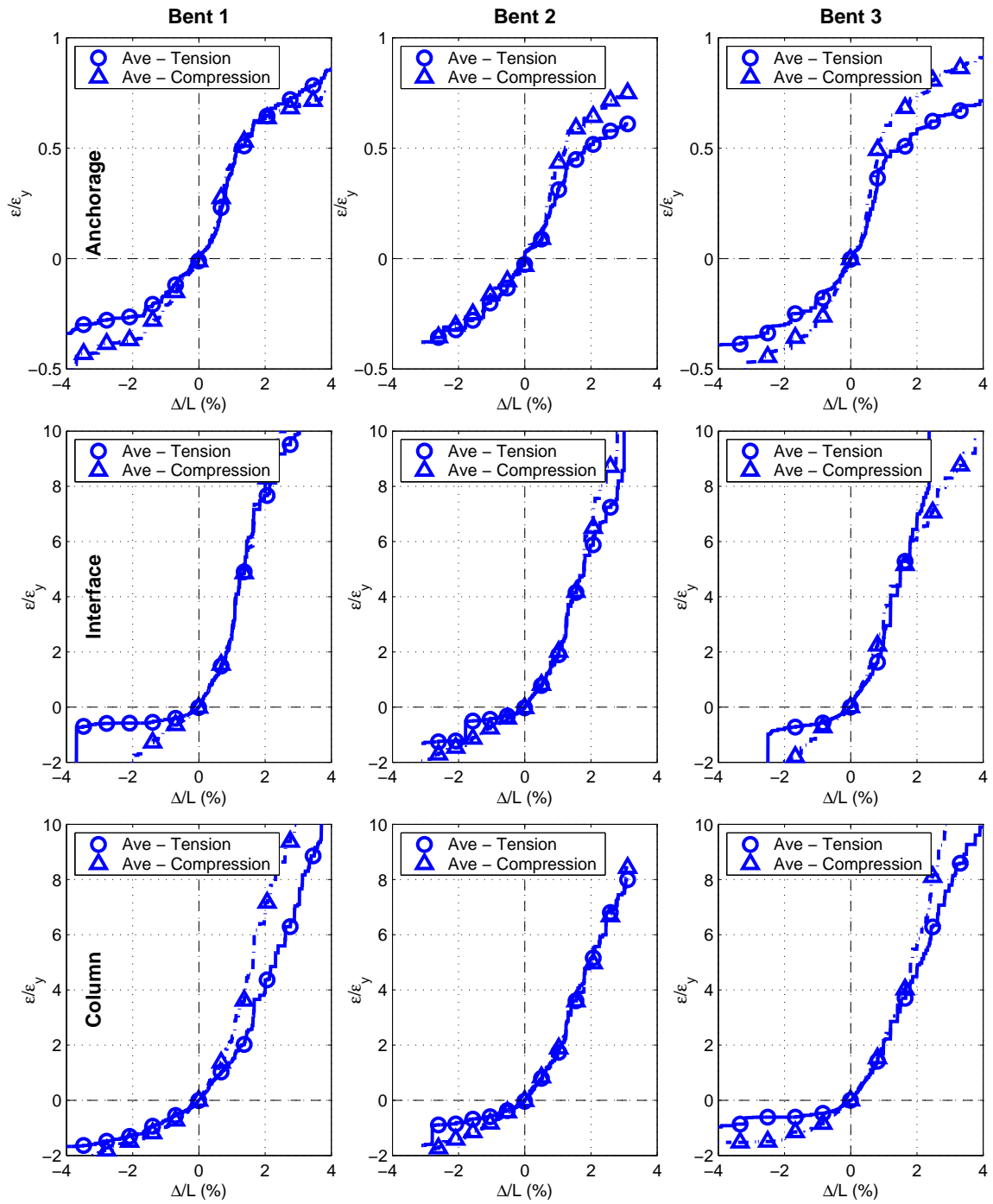
Figure 4.25: Average displacement-strain envelopes for compression and tension gauges

4.6 Displacement-Average Curvature Envelopes

Column rotations were measured with potentiometer sets at two locations within each column interface, illustrated in Fig. 4.26. For all cases, the potentiometers were located at 3.5 ± 0.125 in. from the column face. The gauge lengths for potentiometer sets T-I and B-I were 5.0 in., while the gauge lengths for potentiometer sets T-C and B-C were 7.0 in. Fig. 4.27 illustrates the nomenclature for the rotation potentiometers.

TOP-INTERFACE SET (T-I)
TOP-COLUMN SET (T-C)

BOTTOM-COLUMN SET (B-C)
BOTTOM-INTERFACE SET (B-I)
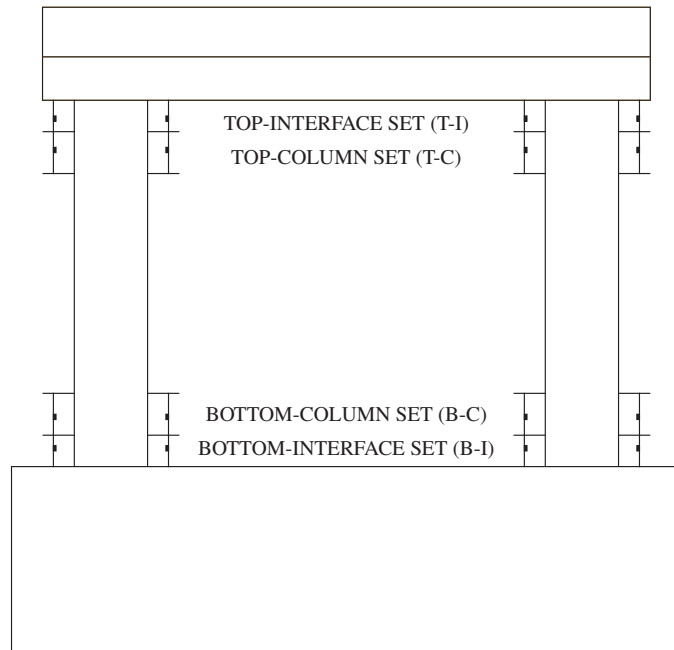
Figure 4.26: Rotation gauge layout

1 E T R 5

Bent Number (1, 2, or 3)   Column ([E]ast or [W]est)   Location ([T]op or [B]ottom)   Gauge Type ([R]otation)   Gauge Number (1-6)
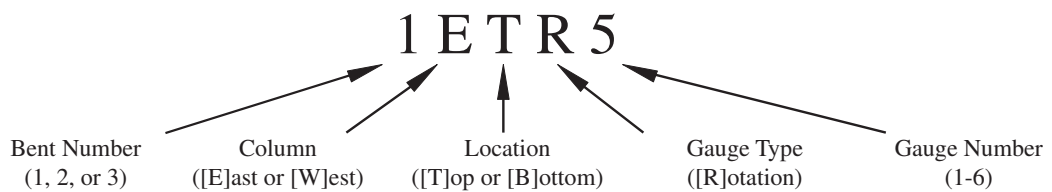
Figure 4.27: Rotation gauge nomenclature

The displacement - rotation envelopes were calculated using each set of potentiometers to bent drifts of ±4.0%. Average curvatures were computed by dividing the measured

rotations by the gauge length of each potentiometer set. The displacement-average curvature envelopes are shown in Fig. D.4.

The average curvatures calculated from the top and bottom interface sets (T-I and B-I) are greater than those from the top and bottom column sets (T-C and B-C). This is attributed to two causes. First, the column moments in sections T-I and B-I are larger than those in sections T-C and B-C. Second, the rotations from potentiometer sets T-I and B-I include the rotation due to the slip of the longitudinal reinforcement within the column-anchorage interface.

The average displacement-curvature envelopes over the 12 in. interface zone are shown in Fig. 4.28 for each bent. The average curvatures across these lengths are similar for each column. For example, at a drift of 3% the curvature of the first 12 inches of the column end ranged from 2.1×10^{-3} rad/in to 2.4×10^{-3} rad/in. The displacement-rotation envelope can be accurately characterized using a bilinear relationship. The envelope remains approximately linear for each bent to a drift of 1%. After this, a plastic hinge develops, creating a new linear relationship.

Fig. 4.29 shows the displacement-average curvature envelopes for the first 12 inches of each column end. These average curvatures were calculated by summing the measured rotations for the interface and column potentiometer sets (T-I + B-I, T-C + B-C), and dividing by the total gauge length of 12 in. For each bent, there are four column ends (top and bottom for the two columns). This figure allows two comparisons: the average curvature of the east column vs. the average curvature of the west column, and the average curvature at the top of the columns vs. the average curvature at the bottom of the columns.

The displacement-average curvature envelopes for the east and west columns are similar for each bent. For example, when bent 1 was at -4% drift, the average curvatures at the top of the east and west columns were -3.3×10^{-3} rad/in. Because there should be no difference between the two columns of each bent, this comparison shows that the curvature measurements are consistent for each bent.

The displacement-average curvature envelopes at the top and bottom of the columns are also similar for each bent. For example when bent 1 was at -4% drift, the average curvature at the top and bottom of the west column was -3.3×10^{-3} rad/in and -3.1×10^{-3} rad/in,
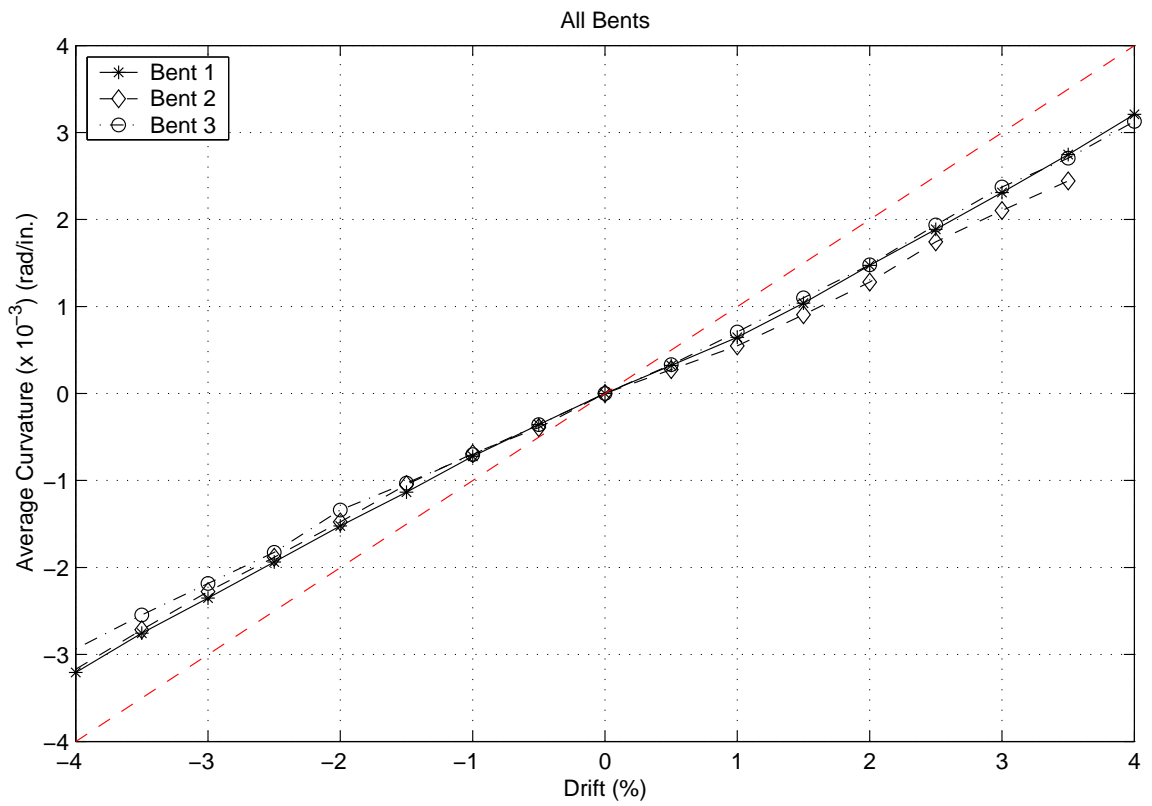
Figure 4.28: Average displacement-rotation envelopes for bents 1, 2, and 3

respectively. This similarity shows that the cross beam flexibility did not significantly affect the measured column rotation.
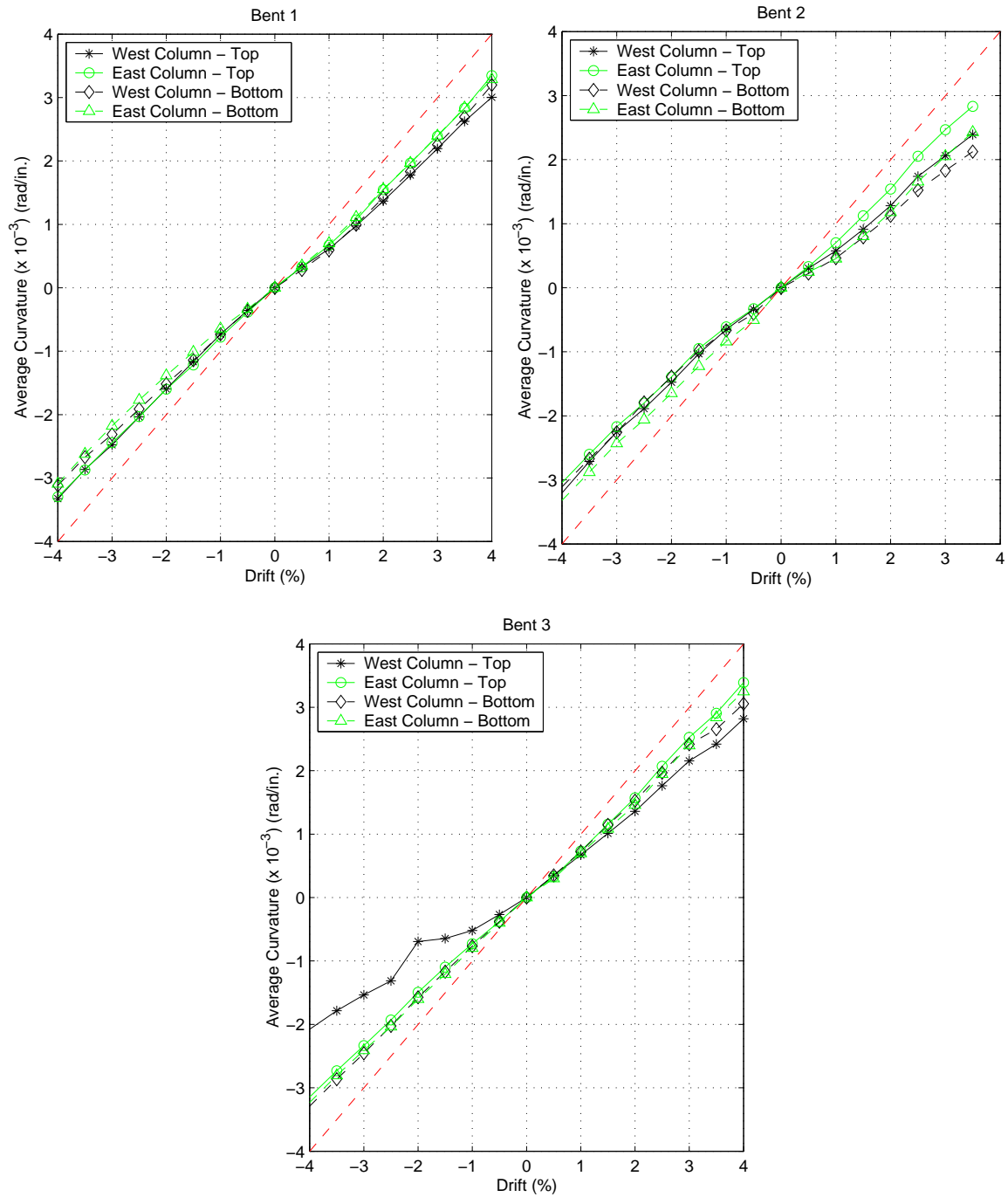
Figure 4.29: Displacement-rotation envelopes for the first 12 inches of the column for bents 1, 2, and 3

4.7 Displacement-Column Elongation Envelopes

The column-beam joint rotation and column elongation were not measured directly during the shaking table tests. Instead, these quantities were calculated using a series of four vertical displacement measurements $(D_1\text{-}D_4)$ along each bent. The locations of these four measurements are illustrated in Fig. 4.30.
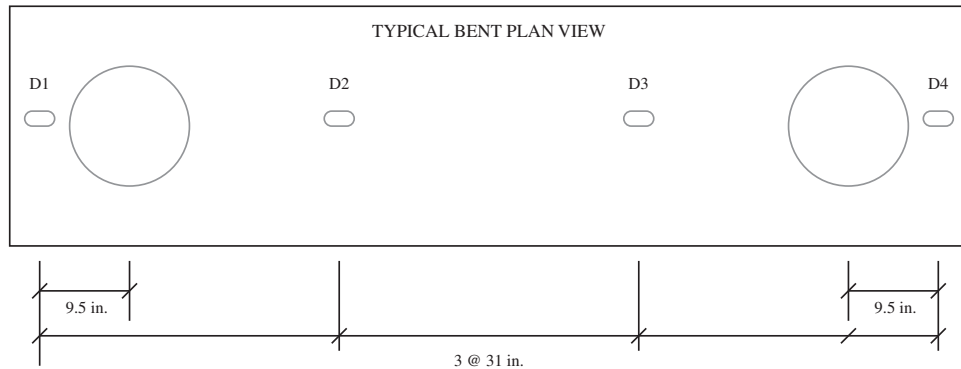
Figure 4.30: Vertical displacement measurement locations

The process of calculating the column-beam joint rotations (θ_1 and θ_2) and the column elongations (V_1 and V_2) from the vertical displacement measurements along the bent (D_1-D_4) is as follows:

1. With elastic beam theory, the displacement anywhere along the beam can be calculated if the vertical displacements and rotations at the column joints are known. Vertical displacements (D_2 and D_3) were measured at two locations between the columns, approximately 21.5 in. from each column. The vertical displacements at these two locations are calculated from the column data using Eq. 4.6, where L is the center to center spacing of the columns (75 in.).

$$\left\{ \begin{array}{c} D_2|_{x=21.5in} \\ D_3|_{x=52.5in} \end{array} \right\} = \left\{ \begin{array}{cccc} \frac{(L-x)^2(L+2x)}{L^3} & \frac{(3L-2x)x^2}{L^3} & \frac{(L-x)^2x}{L^2} & \frac{(x-L)x^2}{L^2} \\ \frac{(L-x)^2(L+2x)}{L^3} & \frac{(3L-2x)x^2}{L^3} & \frac{(L-x)^2x}{L^2} & \frac{(x-L)x^2}{L^2} \end{array} \right\} \left\{ \begin{array}{c} V_1 \\ V_2 \\ \theta_1 \\ \theta_2 \end{array} \right\} \qquad (4.6)$$

2. Vertical displacements were also measured on the exterior of the two columns (D_1 and D_4), approximately 9.5 in. from the centerline of each column. These measurements were related to the column displacements and rotations by assuming rigid displacement of the exterior of the bent cap using the equation

$$\begin{Bmatrix} D_1 \\ D_4 \end{Bmatrix} = \begin{bmatrix} 1 & 0 & -9.5 & 0 \\ 0 & 1 & 0 & 9.5 \end{bmatrix} \begin{Bmatrix} V_1 \\ V_2 \\ \theta_1 \\ \theta_2 \end{Bmatrix} \tag{4.7}$$

3. Equations 4.6 and 4.7 can be combined to estimate the vertical displacements and rotations at the tops of the columns as a function of the four vertical displacement measurements.

$$\begin{Bmatrix} V_1 \\ V_2 \\ \theta_1 \\ \theta_2 \end{Bmatrix} = \begin{bmatrix} 1 & 0 & -9.5 & 0 \\ 0.795 & 0.205 & 10.972 & -4.505 \\ 0.205 & 0.795 & 4.505 & -10.972 \\ 0 & 1 & 0 & 9.5 \end{bmatrix}^{-1} \begin{Bmatrix} D_1 \\ D_2 \\ D_3 \\ D_4 \end{Bmatrix} \tag{4.8}$$

The drift-column elongation envelopes for the three bents are presented in Fig. 4.31. The west column of each bent is under tension (or less compression than the east column) when the drift is positive (in the east direction). The east column is the tension column under negative drift. As shown in Fig. 4.31, for a given drift the tension column of each bent has approximately 25% to 50% more column elongation than the compression column.

The joint rotation envelopes are shown in Fig. 4.32. For a given drift, the joint rotation for the west column of bent 1 was slightly larger than the east column. The two joints in bent 2 had similar responses to each other. As a result of measurement noise in the bent 3 data, and the small contribution of the column joint rotations to the recorded vertical displacements measured along the bent, the bent drift-column joint rotation envelope for bent 3 contained many jumps.
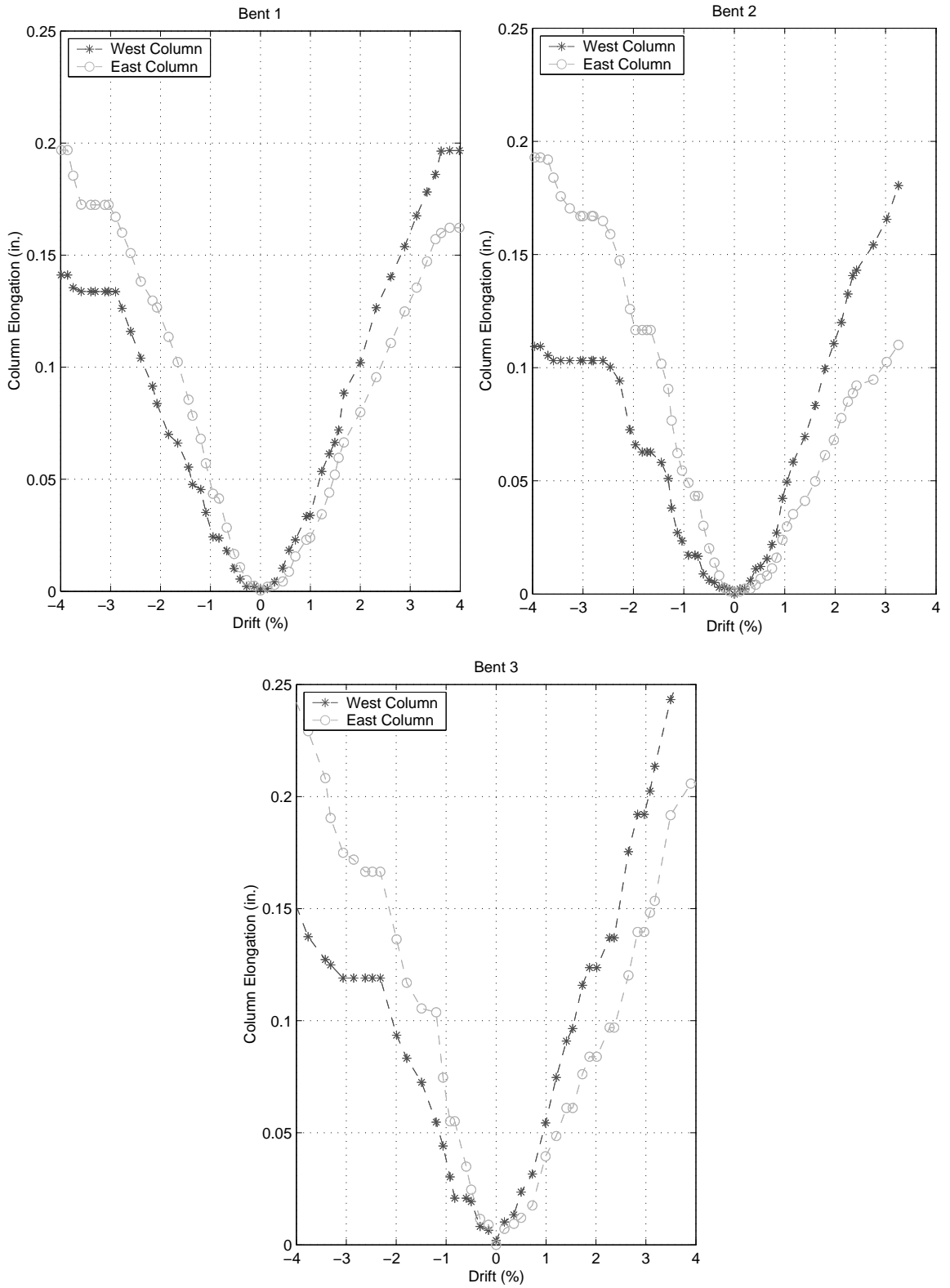
Figure 4.31: Displacement-column elongation envelopes for bents 1, 2, and 3
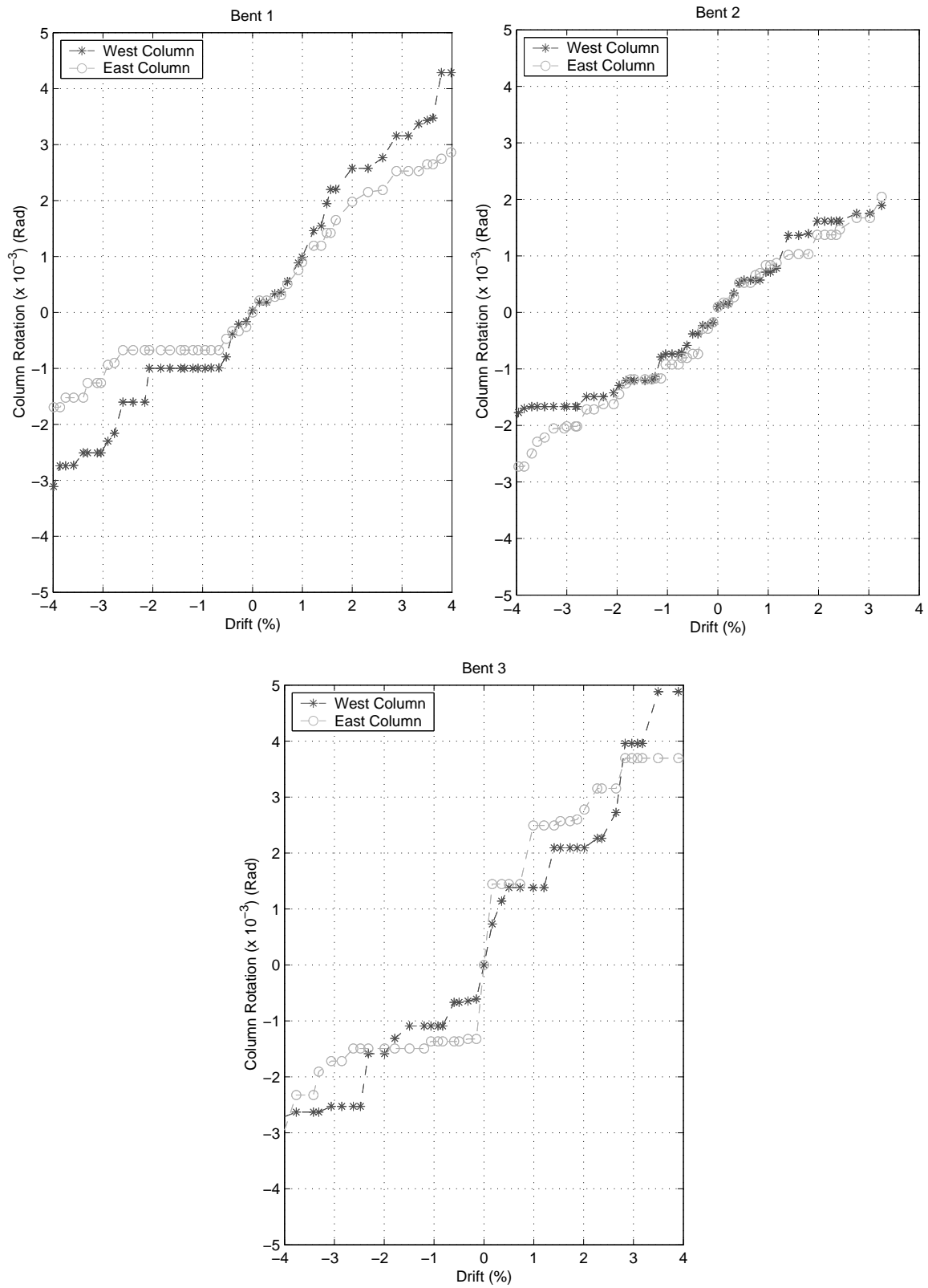
Figure 4.32: Displacement-joint rotation envelopes for bents 1, 2, and 3

4.8   Observed Damage

The three bents of the shaking table specimen were inspected for damage after every test. Aside from slight cracking around the columns in the cross beams beginning at Test 19, all damage was confined to the columns. No column damage was observed throughout the low-amplitude tests. The measures of column damage that were recorded during the tests were:

- maximum crack width,

- height of spalling,

- exposure of transverse and longitudinal reinforcement,

- the extent of bar buckling,

- the extent of bar fracture (both longitudinal and transverse), and

- core degradation

Abbreviations and descriptions of the damage states are presented in Table 4.8.

The shaking table specimen was separated into 24 damage observation locations for each test; two faces per anchorage-column interface, two interfaces per column, six columns. Table 4.9 summarizes the maximum damage of the 8 observation locations for each bent.

As seen in Table 4.9, no damage was observed in any of the columns through Test 12. Residual cracking began during Test 13. Significant spalling was first observed following Test 15. After significant spalling occurred at a particular observation location, crack width measurements at that location were stopped because the crack was almost always obscured. Bar buckling was observed in Bent 3 after Test 18, and in bents 1 (incipient) and 2 after Test 22. Fracture of the longitudinal and transverse reinforcement was first observed in bent 3 after Test 19. Fracture of the longitudinal or transverse reinforcement was not observed in bents 1 or 2.

Table 4.8: Recorded damage observation abbreviations

Damage Abbrev.	Description
CR(#, size)	Column residual cracking (the crack number refers to the nth crack from the column-anchorage interface, which may be due to the spalling of previous cracks, size = maximum crack width in mm)
FL	Flaking of cover concrete
SP(height)	Column spalling at the column-anchorage interface (height of spalling in mm)
TE(#)	Exposure of the transverse reinforcement (number of bars)
LE(#)	Exposure of the longitudinal reinforcement (number of bars)
iLB(#)	Incipient buckling of the longitudinal reinforcement (This accounts for bars that are separated from the concrete, but do not appear buckled at the end of the test. These bars may have buckled during the tests)
LB(#)	Buckling of longitudinal reinforcement (number of bars)
TF(#)	Fracture of transverse reinforcement (number of bars)
LF(#)	Fracture of longitudinal reinforcement (number of bars)
CD	Core degradation

Table 4.9: Summary of observed bent damage for the high-amplitude tests

Test	Observed Damage		
	Bent 1	Bent 2	Bent 3
12	—	—	—
13	CR(1, neg)	—	—
14	CR(1, 0.08)	CR(1, neg)	CR(1, neg)
15	CR(1, 0.25), FL	CR(1, 0.08)	CR(1, 0.25), SP(100)
16	CR(1, 0.50), SP(125)	CR(0.17), FL	CR(1, 0.33), SP(100), TE(1)
17	CR(1, 0.50), SP(150), TE(2)	CR(1, 0.25), FL	CR(1, 0.50), SP(100), TE(1)
18	CR(1, 0.50), SP(150), TE(2)	CR(1, 0.50), SP(100), TE(1)	CR(2, 2.00), SP(140), TE(3), LE(2), iLB
19	CR(2, 0.75), SP(150), TE(3)	CR(1, 2.00), SP(115), TE(1)	CR(3, 2.00), SP(150), TE(6), LE(8), LB(6), TF(2)
20	CR(2, 0.75), SP(150), TE(3), LE(1)	CR(1, 2.00), SP(125), TE(1)	CR(3, 2.00), SP(150), TE(6), LE(8), LB(8), TF(2), LF(2)
21	CR(2, 0.75), SP(150), TE(3), LE(2)	CR(1, 2.00), SP(125), TE(1)	CR(3, 2.00), SP(150), TE(6), LE(8), LB(8), TF(2), LF(5), CD
22	CR(2, 0.75), SP(150), TE(3), LE(2), iLB	CR(1, 2.00), SP(200), TE(2), LE(2), LB(1)	CR(3, 2.00), SP(150), TE(6), LE(8), LB(8), TF(2), LF(5), CD

Fig. 4.33 shows the maximum previous bent displacement as a function of the high-amplitude test number. The figure also shows the test after which each damage state was observed on the three bents.

For all bents, residual cracking and spalling occurred at a drift ratio of approximately 3.5%. Exposure and incipient buckling of the longitudinal reinforcement occurred at a drift
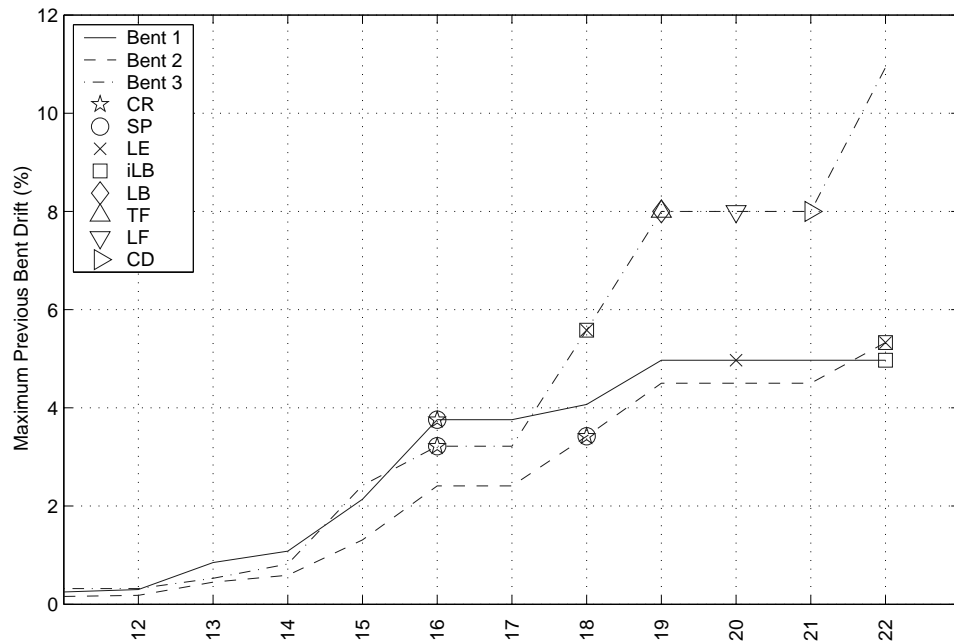
Figure 4.33: Vertical displacement measurement locations

ratio of approximately 5%. Bents 1 and 2 did not experience any more extensive damage. For bent 3, longitudinal buckling and fracture of the longitudinal reinforcement, fracture of the transverse reinforcement, and core degradation all occurred when the maximum previous bent drift was approximately 8%.

The progression of damage for the top west face of the east column of bent 3 (B3WTE) is shown in Fig. 4.34. Residual cracking was first observed on this face after Test 14. Buckling of the reinforcement began during Test 19. After Test 21, four longitudinal reinforcing bars fractured. By the end of the tests, bent 3 was badly damaged, resulting in a reduction in the height of the bent of nearly 2 in.
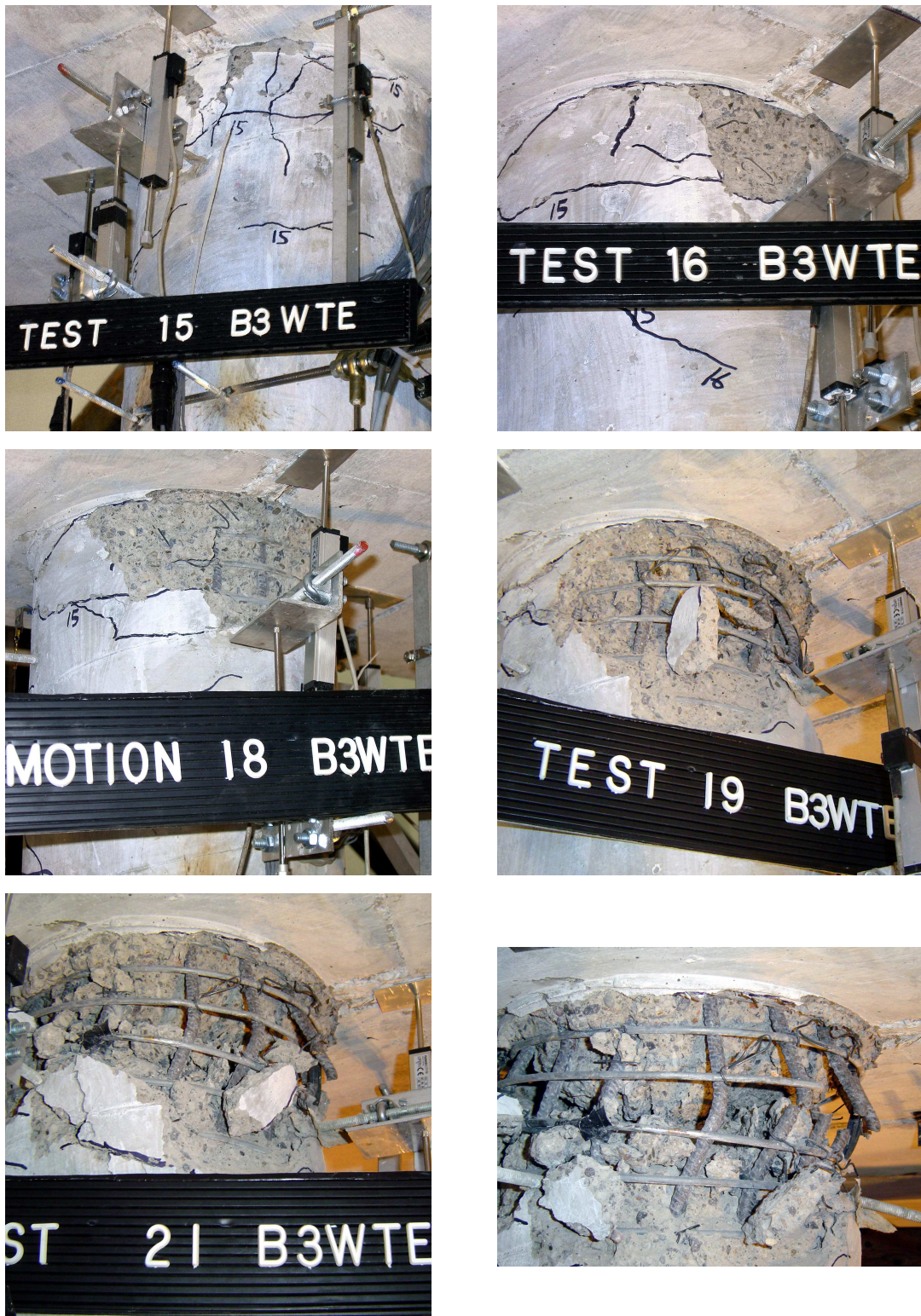
Figure 4.34: Damage progression at the east face of the top of the west column of bent 3: (a) cracking and flaking, (b) spalling, (c) exposure of longitudinal and transverse reinforcement, (d) buckling of longitudinal reinforcement and fracture of the transverse reinforcement, (e) fracture of the longitudinal reinforcement, and (f) total damage after testing.

Chapter 5

SYSTEM IDENTIFICATION ALGORITHMS

The shaking table specimen was subjected to 15 low-amplitude transverse earthquake excitations, seven transverse white-noise (ambient-vibration) excitations, three longitudinal white-noise excitations, and three transverse square-wave (free-vibration) excitations. The white-noise and square-wave excitations were applied intermittently throughout the earthquake excitations (see Fig. 3.4 for the low-amplitude test schedule). During each of the tests, three-dimensional displacement and acceleration data were measured at the bases of each of the three bents, as well as at five locations along the bridge deck.

Two types of algorithms were implemented for identifying the system, parametric algorithms and non-parametric algorithms. The successive linear programming (SLP) algorithm identifies the modal properties of the system parametrically by calibrating a linear model of the shaking table specimen, then extracting the modal data using an eigen-analysis (Section 5.2). The autoregressive with exogenous excitation (ARX) algorithm was used to identify the modal properties of the system non-parametrically. This algorithm uses the input and output response data to estimate the modal parameters with no knowledge of the structural system (Section 5.3). The modal properties identified with each of these algorithms are presented in Section 6.1.

Stochastic (output-only) identification algorithms were used to investigate the effect of not accounting for the frequency content within the input motion. An output-only version of the ARX algorithm (AR) is discussed in Section 5.4. A stochastic subspace identification (SSI) algorithm is discussed in Section 5.5.

The algorithms and data discussed in this chapter were used to compare the results of the system identification methodologies. These comparisons include:

- the abilities to identify modes in three dimensions using one-dimensional excitations;

- parametric and non-parametric identification algorithms;

- the effects of various excitation types;

- using acceleration data vs. displacement data; and

- using input/output vs. output-only algorithms.

The effects of implementing each of these methodologies on the identification of the system properties for the low-amplitude tests are presented in Chapter 6.

In addition to making comparisons between various system identification methodologies, the modal damping ratios identified in Section 6.1 were used to calibrate the damping terms of a three-dimensional numerical model (Chapter 8). Softening in the test specimen and numerical model was compared through the progression of the modal properties of the two systems (Chapter 8).

5.1 Background

System identification is an important part of monitoring the health of a system and identifying critical response frequencies. The appropriate level of complexity of the system identification approach depends on the complexity of the system, the properties that need to be identified, and the importance of the accuracy of the results. For single degree-of-freedom systems, the system can be described using a single-input/single-output (SISO) algorithm, such as a frequency response function. A more complex system will be better described using multiple-input/multiple-output (MIMO) algorithms.

Identification algorithms of varying complexities and for various systems are addressed in Ljung (1999), Allemang (1999), and Juang (1994). To help select among the numerous algorithms, researchers have compared algorithms under various conditions. Petsounis and Fassois (2001) compared time-domain methods for identifying the modal properties of structural systems subjected to noise-corrupted random excitations. They found that each of the investigated algorithms could accurately identify the characteristics of the system when noise is negligible and when the structural system is simple (lightly damped with separated modes), as is the case with the shaking table specimen. Peeters and De Roeck (2001) performed similar comparisons for frequency-domain methods.

5.1.1 Stochastic Algorithms

Stochastic (output-only) system identification methods assume that the input can be characterized as white noise. If the excitation has dominant frequencies, output-only algorithms cannot distinguish these frequencies from structural frequencies. Due to the frequent ambient excitation of bridges (e.g., traffic, wind), most research on system identification of bridges has focused on output-only methods, assuming that the input excitation is white-noise. Ren et al. (2004) conducted an output-only modal analysis on a six-span steel-girder bridge using ambient vibrations. The modal data from these tests were used to calibrate a numerical model that was then used to estimate the seismic response of the bridge. Similarly, Pridham and Wilson (2005) used ambient-vibration data to identify the modal properties of the Quincy Bayview cable-stayed bridge. Peeters and Ventura (2003) compared the abilities of various identification algorithms for a three-span bridge. They found that the estimated frequencies of the bridge were easily identifiable with all complexities of identification algorithms. However, the damping ratios and mode shapes were best modeled using the more complex identification algorithms, such as the stochastic subspace identification (SSI) algorithm.

5.1.2 Input/Output Algorithms

Research has also been conducted on bridges using input-output algorithms, which account for the frequency content of the excitation. Arici and Mosalam (2003) used Multi-input/Single-output (MISO) methods for determining the modal properties of seven California bridge systems subjected to low-amplitude earthquake excitations. They found that the autoregressive with exogenous excitation (ARX) algorithm provided an excellent fit of the recorded motions from the seven bridges. Smyth et al. (2003) used a multi-input/multi-output algorithm, along with an assumed structural model, to identify the mass, damping, and stiffness matrices of the Vincent Thomas suspension bridge during seismic excitation. From these matrices, they identified the modal properties of the bridge.

Each of these studies used a single form of excitation. Huang and Lin (2001) investigated the influence of three excitation types on the identification of the modal properties of two

types of structures. An impulse response (free-vibration) excitation was applied to a three-span bridge, while the ambient-vibration tests and seismic response tests were applied to a five-story steel frame. Using these structures, Huang and Lin were able to adequately estimate the modal properties of the structures subjected to all three types of excitations.

5.1.3 Algorithm Implementation

The tests on the shaking table specimen provide a unique opportunity to investigate the accuracy of the various algorithms for the three excitation types (earthquake excitation, ambient-vibration, and free-vibration). The modal properties using each of these excitation types were identified using stochastic (output-only) and input/output parametric and non-parametric algorithms, which were chosen based on the frequency of their use in previous research.

Four algorithms were implemented using the same data set. These algorithms are listed in Table 5.1.

Table 5.1: Identification algorithms used on shaking table data

Abbreviation	Data Use	Algorithm Type	Algorithm Name	Section
SLP	Input/Output	Parametric	Successive Linear Programming	Section 5.2
ARX	Input/Output	Non-Parametric	Autoregressive with Exogenous Excitation	Section 5.3
AR	Output-Only	Non-Parametric	Autoregressive	Section 5.4
SSI	Output-Only	Non-Parametric	Stochastic Subspace Identification	Section 5.5

The modal parameters identified with the input/output SLP and ARX algorithms are presented in Section 6.1. The modal properties identified with the AR and ERA algorithms are presented in Section 6.7 to investigate the effect of not accounting for the input excitation. These algorithms are presented in the following sections.

5.2 Successive Linear Programming Algorithm

The dynamic properties of the bridge were determined parametrically by creating a numerical model of the shaking table specimen and calibrating the parameters of that model with a successive linear programming (SLP) algorithm in the time domain. Beck and Jennings

(1980) performed a similar methodology for a 42-story steel-frame building that experienced minor damage during the 1971 San Fernando earthquake. The SLP algorithm performs a series of one-dimensional optimizations to determine the parameters of the numerical model that minimize the error between the estimated and measured output accelerations. Similar algorithms were used in the frequency domain for identifying the properties of a 10-story frame building (McVerry, 1980), and for an 8-story frame building (Zhao et al., 1995). The model for the shaking table specimen, and the SLP algorithm used to calibrate the model, are described in the following sections.

5.2.1 Numerical Model

A two-dimensional, 13-degree-of-freedom (13-DOF) linear model of the shaking table specimen was used for the SLP algorithm, and is illustrated in Fig. 5.1. Although this methodology can be applied to a three-dimensional structure, the number of modes in the optimization process greatly influences the numerical performance. Because almost all of the structural excitation was in the transverse bridge direction, only the transverse linear model was developed.
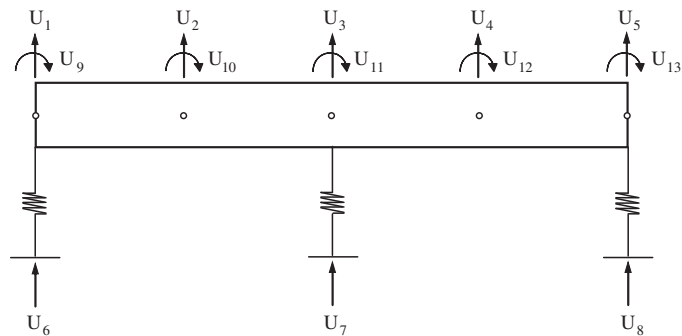
Figure 5.1: Plan view of the 13-DOF linear shaking table model.

In Fig. 5.1, the three springs represent the transverse stiffnesses of the bents, and the beam represents the transverse slab stiffness. Five translational and five rotational degrees of freedom (one at each accelerometer location) were used to model the bridge superstructure. Additionally, one translational degree of freedom was used at the base of each bent

to represent the locations of the input excitations. The system mass and damping were assumed to be lumped at degrees of freedom 1-5. The equation of motion for the numerical model is shown in Eq. 5.1. In this equation, M, C, and K are the mass, damping, and stiffness matrices for the 13-DOF system. Vector u is the displacement, with the dots above the u denoting derivatives of the displacement with respect to time.

$$M_T \ddot{u}(t) + C_T \dot{u}(t) + K_T u(t) = P(t) \tag{5.1}$$

where

$$K_T = \left[\begin{array}{ccccccccccccc}
k_b^1 + k_{s1} & -k_{s1} & 0 & 0 & 0 & -k_b^1 & 0 & 0 & -k_{s2} & -k_{s2} & 0 & 0 & 0 \\
-k_{s1} & 2k_{s1} & -k_{s1} & 0 & 0 & 0 & 0 & 0 & k_{s2} & 0 & -k_{s2} & 0 & 0 \\
0 & -k_{s1} & k_b^2 + 2k_{s1} & -k_{s1} & 0 & 0 & -k_b^2 & 0 & 0 & k_{s2} & 0 & -k_{s2} & 0 \\
0 & 0 & -k_{s1} & 2k_{s1} & -k_{s1} & 0 & 0 & 0 & 0 & 0 & k_{s2} & 0 & -k_{s2} \\
0 & 0 & 0 & -k_{s1} & k_b^3 + k_{s1} & 0 & 0 & -k_b^3 & 0 & 0 & 0 & k_{s2} & k_{s2} \\
-k_b^1 & 0 & 0 & 0 & 0 & k_b^1 & 0 & 0 & 0 & 0 & 0 & 0 & 0 \\
0 & 0 & -k_b^2 & 0 & 0 & 0 & k_b^2 & 0 & 0 & 0 & 0 & 0 & 0 \\
0 & 0 & 0 & 0 & -k_b^3 & 0 & 0 & k_b^3 & 0 & 0 & 0 & 0 & 0 \\
-k_{s2} & k_{s2} & 0 & 0 & 0 & 0 & 0 & 0 & k_{s3} & k_{s4} & 0 & 0 & 0 \\
-k_{s2} & 0 & k_{s2} & 0 & 0 & 0 & 0 & 0 & k_{s4} & 2k_{s3} & k_{s4} & 0 & 0 \\
0 & -k_{s2} & 0 & k_{s2} & 0 & 0 & 0 & 0 & 0 & k_{s4} & 2k_{s3} & k_{s4} & 0 \\
0 & 0 & -k_{s2} & 0 & k_{s2} & 0 & 0 & 0 & 0 & 0 & k_{s4} & 2k_{s3} & k_{s4} \\
0 & 0 & 0 & -k_{s2} & k_{s2} & 0 & 0 & 0 & 0 & 0 & 0 & k_{s4} & k_{s3}
\end{array} \right]$$

where k_b^α is the transverse stiffness for bent α, and $k_{s1}, k_{s2}, k_{s3}, k_{s4}$ are the various slab stiffnesses, defined as

$$k_{s1} = \frac{12E_s I_s}{(L_s)^3}, \qquad k_{s2} = \frac{6E_s I_s}{(L_s)^2}, \qquad k_{s3} = \frac{4E_s I_s}{L_s}, \qquad k_{s4} = \frac{2E_s I_s}{L_s}$$

Eq. 5.1 was partitioned into the translational degrees of freedom (subscript t) and the rotational degrees of freedom (subscript r). The partitioned equation of motion is displayed in Eq. 5.2

$$\begin{bmatrix} m_{tt} & 0 \\ 0 & 0 \end{bmatrix} \begin{Bmatrix} \ddot{u}_t \\ \ddot{u}_r \end{Bmatrix} + \begin{bmatrix} c_{tt} & 0 \\ 0 & 0 \end{bmatrix} \begin{Bmatrix} \dot{u}_t \\ \dot{u}_r \end{Bmatrix} + \begin{bmatrix} k_{tt} & k_{tr} \\ k_{rt} & k_{rr} \end{bmatrix} \begin{Bmatrix} u_t \\ u_r \end{Bmatrix} = \begin{Bmatrix} p_t(t) \\ 0 \end{Bmatrix} \tag{5.2}$$

Because mass was lumped at the translational degrees of freedom, the rotational degrees of freedom were condensed out of the system, giving the condensed 8-degree-of-freedom equation of motion and stiffness matrix in Eq. 5.3.

$$m_{tt} \ddot{u}_t + c_{tt} \dot{u}_t + \hat{k}_{tt} u_t = p_t(t) \tag{5.3a}$$

$$\hat{k}_{tt} = k_{tt} - k_{rt}^T k_{rr}^{-1} k_{rt} \tag{5.3b}$$

The 8-DOF system was further partitioned between the slab degrees of freedom and the support degrees of freedom (subscript g), shown in Eq. 5.4.

$$
\begin{bmatrix} m & m_g \\ m_g^T & m_{gg} \end{bmatrix} \begin{Bmatrix} \ddot{u}^t \\ \ddot{u}_g \end{Bmatrix} + \begin{bmatrix} c & c_g \\ c_g^T & c_{gg} \end{bmatrix} \begin{Bmatrix} \dot{u}^t \\ \dot{u}_g \end{Bmatrix} + \begin{bmatrix} \hat{k} & \hat{k}_g \\ \hat{k}_g^T & \hat{k}_{gg} \end{bmatrix} \begin{Bmatrix} u^t \\ u_g \end{Bmatrix} = \begin{Bmatrix} 0 \\ p_g(t) \end{Bmatrix} \tag{5.4}
$$

The system was further simplified to a five-degree-of-freedom system by assuming that the damping terms are very small compared to the inertial terms and that the ground degrees of freedom do not have mass. The validity of these assumptions are discussed in Chopra (1995). The equation of motion for the 5DOF system is shown in Eq. 5.5.

$$
m\ddot{u} + c\dot{u} + \hat{k}u = p_{eff}(t) \tag{5.5a}
$$

$$
p_{eff}(t) = -mi\ddot{u}_g(t) \tag{5.5b}
$$

$$
i = -\hat{k}^{-1}\hat{k}_g \tag{5.5c}
$$

$$
\hat{k} = \begin{bmatrix} k_b^1 & 0 & 0 & 0 & 0 \\ 0 & 0 & 0 & 0 & 0 \\ 0 & 0 & k_b^2 & 0 & 0 \\ 0 & 0 & 0 & 0 & 0 \\ 0 & 0 & 0 & 0 & k_b^3 \end{bmatrix} + \frac{E_s I_s}{28 L_s^3} \begin{bmatrix} 45 & -102 & 72 & -18 & 3 \\ -102 & 276 & -264 & 108 & -18 \\ 72 & -264 & 384 & -264 & 72 \\ -18 & 108 & -264 & 276 & -102 \\ 3 & -18 & 72 & -102 & 45 \end{bmatrix} \tag{5.5d}
$$

5.2.2 SLP Algorithm Implementation

The seven unknowns in the numerical model were assumed to be the three bent stiffnesses (k_b^1, k_b^2, k_b^3), the slab modulus of rigidity $(E_s I_s)$, and the three modal damping ratios (ξ_1, ξ_2, ξ_3). These parameters were optimized to minimize the following objective function.

$$
J(k_b^1, k_b^2, k_b^3, EI_s, \xi_1, \xi_2, \xi_3) = \sqrt{\sum_{i=1}^{NDOF} \left[\frac{\int_{t_i}^{t_f} (a - a_0)^2 dt}{(t_f - t_i)(\max|a_0|)^2} \right]^2} \tag{5.6}
$$

where t_i and t_f are the initial and final times over which the measured and calculated accelerations (a_0 and a) are compared. Eq. 5.6 was minimized through a series of one-dimensional optimization processes. For example, the first process involved varying k_b^1

while keeping the other six parameters constant to minimize the objective function. Once k_b^1 was found, the next process used the optimized k_b^1 as a constant, then varied k_b^2 to further reduce the objective function. After all seven parameters were optimized, this procedure was replicated five more times (for a total of six cycles) to identify all seven optimal parameters.

Because the objective function in Eq. 5.6 contains many local minima, each one-dimensional process involved a search of the entire reasonable domain of the variable in question. For example, while k_b^1 was being optimized, the search domain spanned 5% - 100% of the gross bent stiffness. To further refine the parameter estimates, the domain was reduced to $\pm 50\%$ of the optimized parameters from the previous cycle for the last two cycles.

Once the objective function was minimized and the entire stiffness matrix estimated, the modal frequencies and mode shapes were calculated using an eigenanalysis.

$$K\Phi = \Lambda M\Phi \tag{5.7}$$

where Φ is a matrix of the system mode shapes, and the system periods are related to the diagonal of the eigenvalue matrix.

$$T = \frac{2\pi}{\sqrt{diag(\Lambda)}} \tag{5.8}$$

5.3 Autoregressive with Exogenous Excitation Algorithm

The autoregressive with exogenous excitation (ARX) algorithm uses a series of polynomials to define a current output state from previous output and input states (Petsounis and Fassois, 2001). The MIMO ARX algorithm is mathematically described by the equation

$$y(t) = \sum_{i=1}^{p} A_i y(t - i\Delta t) + \sum_{j=1}^{p} B_j x(t - j\Delta t) + w(t) \tag{5.9}$$

where $y(t)$ is a vector of the m current state output signals, $y(t - i\Delta t)$ is a vector of the m output signals at previous state i, and $x(t - j\Delta t)$ is a vector of the n input signals at previous state j. The integer p in Eq. 5.9 specifies the number of previous output and input states to be related to the current output state (referred to as the model order). Increasing the model order increases the fit of the numerical model to the data. However, this also increases the number of extraneous (non-structural) modes that are identified and increases

the computational demands. An appropriate model order was estimated using Akaike's Final Prediction Error (FPE) (Akaike, 1971), defined in Eq. 5.10. In Eq. 5.10, V is the determinant of the covariance matrix of the white noise, $w(t)$.

$$FPE = V\frac{1 + p/m}{1 - p/m} \tag{5.10}$$

For an identified model order, p, matrices A_i (dimension $m \times m$) and B_j (dimension $m \times n$) are time-invariant relationships between the current and past states. The term $w(t)$ is included to account for the existence of white-noise in the system. The matrices A_i, B_j and w were estimated using a least squares algorithm and QR factorization. The matrices will be denoted as best-fit estimates using a tilde ($\tilde{A}_i$, $\tilde{B}_j$, and $\tilde{w}$). The best-fit coefficient matrix $\tilde{A}$ is defined as

$$\tilde{A}_{mp \times mp} = \begin{pmatrix} \tilde{A}_1 & \tilde{A}_2 & \cdots & \tilde{A}_{m-1} & \tilde{A}_m \\ I & 0 & \cdots & 0 & 0 \\ 0 & I & \cdots & 0 & 0 \\ 0 & 0 & \ddots & 0 & 0 \\ 0 & 0 & \cdots & I & 0 \end{pmatrix} = S\Lambda S^{-1} \tag{5.11}$$

where $\tilde{A}_{mp \times mp}$ is a square matrix that is composed of smaller matrices $\tilde{A}_{i,m \times m}$, where integer m is the number of output measurements. The terms I and 0 in Eq. 5.11 denote identity and zero square matrices of size $m \times m$. The modal parameters of the system are determined through the eigen-decomposition of state matrix ($\tilde{A}$), also shown in Eq. 5.11, into a matrix of eigenvectors $S_{mp \times mp}$ and a diagonal matrix of eigenvalues $\Lambda_{mp \times mp}$. Each eigenvector is composed of real and imaginary parts. The phase of these parts was adjusted so that the imaginary part of the eigenvector was orthogonal to the real part (Neumaier and Schneider, 2001). The mode shapes of the system, S_k, are components of the eigenvectors of the assembled coefficient matrix.

$$S_k = S_{((p-1)m+1:mp,k)} \tag{5.12}$$

The frequencies and damping ratios of the structure are obtained from the complex

eigenvalues.

$$\frac{\ln(\lambda_k)}{\Delta t}, \frac{\ln(\lambda_k^*)}{\Delta t} = -\xi_k \omega_k \pm j \omega_k \sqrt{1 - \xi_k^2} \tag{5.13}$$

where λ_k^* is the complex conjugate of eigenvalue λ_k. Solving for the frequencies and damping ratios

$$f_k = \frac{1}{2\pi\Delta t} \sqrt{\left(\frac{\ln(\lambda_k \cdot \lambda_k^*)}{2}\right)^2 + \left(\cos^{-1}\left(\frac{\lambda_k + \lambda_k^*}{2\sqrt{\lambda_k \cdot \lambda_k^*}}\right)\right)^2} \tag{5.14}$$

$$\zeta_k = \sqrt{\frac{(\ln(\lambda_k \cdot \lambda_k^*))^2}{(\ln(\lambda_k \cdot \lambda_k^*))^2 + 4\left(\cos^{-1}\left(\frac{\lambda_k + \lambda_k^*}{2\sqrt{\lambda_k \cdot \lambda_k^*}}\right)\right)^2}} \tag{5.15}$$

where dt is the time step of the recorded motion, k is the mode, and λ^* is the complex conjugate of the eigenvalue λ, which are the diagonal terms from the eigenvalue matrix Λ.

Eigendecomposition results in $m * p$ modes. Of the $m * p$ calculated modes, only a few are structurally significant. A strategy to separate the physical modes from the numerical modes was adopted from Neumaier and Schneider (2001).

The modes can be initially screened by determining those that are known to be purely numerical. The sampling time for the data acquisition system was 0.01 seconds. Therefore, the algorithm cannot identify physical modes with frequencies greater than $1/(2dt)$, or 50 Hz. All identified modes with frequencies greater than this are numerical modes.

The structural modes were determined from the remaining modes by combining two methods. Researchers in the past have identified the structural modes as those with the least amount of damping. The reasoning behind this was that if all modes are equally excited, those with the least damping will dominate the system. However, this method is problematic when there are large amounts of noise in the data. Another theory estimates the structural modes by how much each mode was excited during the tests (Neumaier and Schneider, 2001). This relationship is defined in Eq. 5.16, where $C' = S^{-1}CS^{-1T}$ and the subscript k refers to the mode in question. The matrix C is the variance of the estimated noise $\hat{w}(t)$.

$$\sigma_k = \frac{C'_{kk}}{1 - |\lambda_k|^2} \tag{5.16}$$

This method of identifying the structural modes may misidentify the modes if they were not adequately excited during the test. Therefore, this research used a combination of both methods, defining the structural modes as those with the highest ratio between the excitation (σ_k) and the damping ratio (ζ_k).

5.4 Stochastic Autoregressive Algorithm

The stochastic (output-only) autoregressive (AR) algorithm was introduced by Akaike (1969). The AR algorithm is a simplified form of the ARX algorithm that is commonly used in situations when only the output response of the structure is known. The AR model is described by Eq. 5.17.

$$y(t) = \sum_{i=1}^{p} A_i y(t - i\Delta t) + w(t) \tag{5.17}$$

The algorithm in Eq. 5.17 is derived from Eq. 5.9 without the input term. The rest of the process for determining the modal parameters from the time-invariant matrices $\hat{A}_i$ is the same as the ARX algorithm. Results from the AR algorithm are used in Section 6.7 to investigate the effects of not accounting for the frequency content within the input excitation.

5.5 Subspace Identification Algorithms

Subspace identification algorithms can be used to identify the modal properties of the shaking table specimen by transforming the equation of motion (Eq. 5.18) into a set of controllability and observability equations (Eq. 5.19).

$$M\ddot{U}(t) + C_2\dot{U}(t) + KU(t) = F(t) = B_2 u(t) \tag{5.18}$$

$$\dot{x}(t) = A_c x(t) + B_c u(t)$$
$$y(t) = Cx(t) + Du(t) \tag{5.19}$$

where M, C_2, and K are the mass, damping and stiffness matrices. The term U is a vector of the output displacements, and F is the vector of input forces. B_2 is an influence matrix on the input excitations $u(t)$. The transformation from the equation of motion to the subspace system of equations is described in the following sections.

5.5.1   Continuous Subspace Formulation

Starting with a trivial equation and rearranging the equation of motion, the set of equations becomes

$$\dot{U}(t) = \dot{U}(t)$$
$$\ddot{U}(t) = -M^{-1}KU(t) - M^{-1}C\dot{U}(t) + M^{-1}B_2 u(t)$$

$$(5.20)$$

Arranging this equation into matrix format, the system becomes

$$\begin{Bmatrix} \dot{U}(t) \\ \ddot{U}(t) \end{Bmatrix} = \begin{bmatrix} 0 & I_n \\ -M^{-1}K & -M^{-1}C_2 \end{bmatrix} \begin{Bmatrix} U(t) \\ \dot{U}(t) \end{Bmatrix} + \begin{Bmatrix} 0 \\ M^{-1}B_2 \end{Bmatrix} u(t) \qquad (5.21)$$

The final controllability system of equations is expressed as follows

$$\dot{x}(t) = A_c x(t) + B_c u(t) \qquad (5.22)$$

where

$$x(t) = \begin{Bmatrix} U(t) \\ \dot{U}(t) \end{Bmatrix} \qquad A_c = \begin{bmatrix} 0 & I_n \\ -M^{-1}K & -M^{-1}C_2 \end{bmatrix} \qquad B_c = \begin{Bmatrix} 0 \\ M^{-1}B_2 \end{Bmatrix}$$

and subscript c indicates that the system is continuous in time.

Assuming that the response of the structure was measured by m output quantities $y(t)$, one can write the observability equation as

$$y(t) = C_a \ddot{U}(t) + C_v \dot{U}(t) + C_d U(t) \qquad (5.23)$$

The state matrices C_a, C_v, and C_d are influence matrices for the recorded (observed) acceleration ($\ddot{U}$), velocity ($\dot{U}$) and displacement (U) vectors. Because these matrices tie in the three types of measurements into the measurement vector $y(t)$, they contain the necessary conversion factors between the differing units. The magnitude of these influence matrices depends on the types of observations being made. For example, if only the accelerations were measured, then C_v and C_d would be zero.

Substituting Eq. 5.20 into Eq. 5.23, the observability equation becomes

$$y(t) = C_a M^{-1} \left[B_2 u(t) - C_2 \dot{U}(t) - KU(t) \right] + C_v \dot{U}(t) + C_d U(t) \qquad (5.24)$$

Rearranging like terms, the equation can be written as

$$y(t) = \begin{bmatrix} C_d - C_a M^{-1} K & C_v - C_a M^{-1} C_2 \end{bmatrix} \begin{Bmatrix} U(t) \\ \dot{U}(t) \end{Bmatrix} + C_a M^{-1} B_2 u(t) \tag{5.25}$$

The observability equation can be written as

$$y(t) = Cx(t) + Du(t) \tag{5.26}$$

where

$$C = \begin{bmatrix} C_d - C_a M^{-1} K & C_v - C_a M^{-1} C_2 \end{bmatrix}, \qquad D = C_a M^{-1} B_2$$

The state space model is described by the controllability and observability equations

$$\begin{aligned} \dot{x}(t) &= A_c x(t) + B_c u(t) \quad (controllability) \\ y(t) &= Cx(t) + Du(t) \quad (observability) \end{aligned} \tag{5.27}$$

5.5.2 Discrete Subspace Formulation

Because measurements are made at discrete time intervals, the continuous controlability/observability state space model (defined by Eq. 5.27) needs to be transformed into a discrete state space model. By making the approximation that

$$\dot{x} = \frac{x_{k+1} - x_k}{\Delta t}$$

where k denotes the discrete step and Δt is the time step, the controllability equation of Eq. 5.27 becomes

$$\dot{x} = \frac{x_{k+1} - x_k}{\Delta t} = A_c x_k + B_c u_k \tag{5.28}$$

Solving for the state at the $k + 1$ time step

$$x_{k+1} = (I + A_c \Delta t) x_k + (I \Delta t) B_c u_k \tag{5.29}$$

This equation can be rewritten as

$$x_{k+1} = A x_k + B u_k \tag{5.30}$$

where

$$A = I + A_c\Delta t, \qquad B = (I\Delta t)B_c$$

When more terms of the Taylor series expansion of $\dot{x}$ are used, the discrete subspace matrices A and B are defined as

$$A = I + A_c\Delta t + \frac{1}{2!}(A_c\Delta t)^2 + \ldots = e^{A_c\Delta t}$$

$$B = \left[I\Delta t + \frac{1}{2!}A_c(\Delta t)^2 + \ldots\right]B_c = [A - I]\,A_c^{-1}B_c \tag{5.31}$$

Because there are no derivatives in the observability equation, the discrete form of the equation is the same as the continuous form. The discrete subspace system is

$$x_{k+1} = Ax_k + Bu_k$$

$$y_{k+1} = Cx_k + Du_k \tag{5.32}$$

Vectors w_k and v_k are added to account for measurement noise in both the controllability and observability equations

$$x_{k+1} = Ax_k + Bu_k + w_k$$

$$y_{k+1} = Cx_k + Du_k + v_k \tag{5.33}$$

5.5.3 Stochastic Subspace System

For a stochastic (output-only) system $(u_k = 0)$, the subspace system in Eq. 5.33 becomes

$$x_{k+1} = Ax_k + w_k$$

$$y_{k+1} = Cx_k + v_k \tag{5.34}$$

where w_k and v_k account for the noise in the controllability and observability equations.

5.5.4 Subspace Identification

Subspace matrices A and C were identified using the stochastic subspace identification algorithm, developed by Van Overschee and De Moor (1996). This algorithm was modified by Peeters and De Roeck (1999) to increase the stability at lower model orders and to decrease the computational demands.

The system matrices, A and C, are estimated from the block Hankel matrix, shown in Eq. 5.35.

$$H = \frac{1}{\sqrt{j}} \left[\begin{array}{cccc} Y(1:m,1) & Y(1:m,2) & \cdots & Y(1:m,j) \\ Y(1:m,2) & Y(1:m,3) & \cdots & Y(1:m,j+1) \\ \vdots & \vdots & \ddots & \vdots \\ Y(1:m,i) & Y(1:m,i+1) & \cdots & Y(1:m,j+i-1) \\ \hline Y(1:m,i+1) & Y(1:m,i+2) & \cdots & Y(1:m,j+i) \\ Y(1:m,i+2) & Y(1:m,i+3) & \cdots & Y(1:m,j+i+1) \\ \vdots & \vdots & \ddots & \vdots \\ Y(1:m,2i) & Y(1:m,2i+1) & \cdots & Y(1:m,j+2i-1) \end{array} \right] \tag{5.35}$$

where $Y \in \mathbb{R}^{m \times N}$ is the matrix of m output vectors of length N. The terms $Y(1:m,k)$ denote the output measurements for observations 1 through m at time step k. The size of the block Hankel matrix is $H \in \mathbb{R}^{2i \times j}$, where $j = N - 2i + 1$, which accounts for the shifting in the data in the matrix. Integer i is the order of the model.

The past (Y_p) and the future (Y_f) parts of the Hankel matrix are defined in Eq. 5.36 . These components are used to formulate the current step $\hat{X}_i$.

$$\left(\frac{Y_p}{Y_f} \right) = \left(\frac{H(1:m(i),:)}{H(m(i)+1:m(2i),:)} \right) \tag{5.36}$$

The Hankel matrix is then subdivided into three parts to represent the shifted past and future components, and the current state (Eq. 5.37). These divisions are used to formulate the future step $\hat{X}_{i+1}$.

$$\left(\frac{Y_{p+}}{Y_{i|i}} \over Y_{f-} \right) = \left(\frac{H(1:m(i+1),:)}{\frac{H(m(i)+1:m(i+1),:)}{H(m(i+1)+1:m(2i),:)}} \right) \tag{5.37}$$

The projection of the future outputs (Y_f) onto the reference past outputs (Y_p) is defined as

$$P_i = Y_f Y_p^t (Y_p Y_p^t)^\dagger Y_p \tag{5.38}$$

where $\dagger$ represents the pseudo-inverse of the matrix. Similar operations can be performed on the shifted matrices.

$$P_{i+1} = Y_{f-} Y_{p+}^t (Y_{p+} Y_{p+}^t)^\dagger Y_{p+} \tag{5.39}$$

The state sequence $(\hat{X}_i)$ is obtained from a singular value decomposition (SVD) of the projection matrix (P_i)

$$SVD(P_i) = U_i S_i V_i^T$$
$$O_i = U_i S_i^{1/2}$$
$$\hat{X}_i = O_i^\dagger P_i$$

(5.40)

The shifted state sequence $(\hat{X}_{i+1})$ is developed through the state sequence by the relationship

$$O_{i+1} = O_i(1:m(i-1))$$
$$\hat{X}_{i+1} = O_{i+1}^\dagger P_{i+1}$$

(5.41)

The state matrices (A and C) are then calculated from a least-squares fit of the overdetermined set of equations shown in Eq. 5.42

$$\begin{pmatrix} \hat{X}_{i+1} \\ H_{i|i} \end{pmatrix} = \begin{pmatrix} \tilde{A} \\ \tilde{C} \end{pmatrix} \hat{X}_i$$

(5.42)

where $\tilde{A}$ and $\tilde{C}$ are the best fit estimates of the state matrices A and C. The residual from the best-fit are the noise matrices w_k and v_k.

5.5.5   Modal Identification

The modal properties of the structural system are identified from state matrices $\tilde{A}$ and $\tilde{C}$ (Peeters and De Roeck, 1999). The periods and damping ratios of the discrete system are identified by an eigen-decomposition of the state matrix $\tilde{A}$. The mode shapes also use information from the estimated state matrix $\tilde{C}$ to produce physical mode shapes from the eigenvectors of $\tilde{A}$.

$$A = \Psi \Lambda \Psi^{-1}$$

(5.43)

where Λ is a diagonal matrix of the eigenvalues of the discrete system (λ) and Ψ is the matrix of eigenvectors of the discrete system. With the relationship in Eq. 5.31, the eigenvectors and eigenvalues for the continuous system are

$$\lambda_c = \frac{ln(\lambda)}{\Delta t} \qquad\qquad \Psi_c = \Psi$$

The modal frequencies, damping ratios and mode shapes are determined from the continuous eigenvalues and eigenvectors

$$\lambda_c, \lambda_c^* = -\xi_c \omega_c \pm j\omega_c \sqrt{1 - \xi_c^2} \tag{5.44}$$

$$\Phi_c = C\Psi_c \tag{5.45}$$

where λ_c^* is the complex conjugate of the continuous eigenvalue λ_c. Solving for ω_c and ξ_c in terms of the eigenvalue pairs

$$f_c = \frac{1}{2\pi\Delta t} \sqrt{\left(\frac{\ln(\lambda \cdot \lambda^*)}{2} \right)^2 + \left(\cos^{-1} \left(\frac{\lambda + \lambda^*}{2\sqrt{\lambda \cdot \lambda^*}} \right) \right)^2} \tag{5.46}$$

$$\zeta_c = \sqrt{\frac{(\ln(\lambda \cdot \lambda^*))^2}{(\ln(\lambda \cdot \lambda^*))^2 + 4 \left(\cos^{-1} \left(\frac{\lambda + \lambda^*}{2\sqrt{\lambda \cdot \lambda^*}} \right) \right)^2}} \tag{5.47}$$

Chapter 6

SYSTEM IDENTIFICATION RESULTS FOR LOW-AMPLITUDE EXCITATIONS

This chapter presents the modal properties (periods, damping ratios and mode shapes) of the shaking table specimen identified using system identification techniques. Section 6.1 presents the modal properties identified using two input/output algorithms (ARX and SLP). Because the SLP algorithm was only configured to identify the transverse modal properties of the system, this section only compares the transverse properties identified with the two algorithms. The sensitivity of the objective function used to identify the modal properties for the SLP algorithm to the parameters of the shaking table specimen is presented in Section 6.2. The three-dimensional modal properties identified with the ARX algorithm are presented in Section 6.3 using both the transverse and the longitudinal excitations. The modal properties identified using various methodologies were compared to investigate the effects of those methodologies on the property estimates. The comparisons in this chapter include:

1. A comparison of the three-dimensional modal properties identified with the ARX algorithm using excitations in both the transverse and longitudinal bridge directions (Section 6.3);

2. A comparison of the modal properties identified using a parametric input/output algorithm (SLP) and a non-parametric input/output algorithm (ARX) to determine the influence of the numerical algorithm on the identified modal properties (Sections 6.4);

3. A comparison of the modal properties identified using three types of ground excitations (earthquake, ambient vibration, and free vibration) to investigate the influence of input type on the identified parameters (Section 6.5);

4. A comparison of the modal properties identified using acceleration data with those

identified using displacement data to investigate the influence of frequency and noise content (Section 6.6); and

5. A comparison of the identified modal properties using input/output algorithms with those using stochastic (output-only) algorithms to investigate the influence of frequency content within the input motions on the identified properties (Section 6.7).

6.1 Identified Modal Properties

The modal properties (periods, damping ratios and mode shapes) of the shaking table specimen were identified using two input/output algorithms (SLP and ARX) for three types of excitations (earthquake, white-noise, and square-wave).

The identified periods of the structure are presented for the earthquake excitations (Table 6.1 and Fig. 6.1a), white-noise excitations (Table 6.2 and Fig. 6.1b), and square-wave excitations (Table 6.3 and Fig. 6.1c). All of these tables and figures show that the first three modes had periods of approximately 0.33s, 0.26s, and 0.078s.

Table 6.1 and Fig. 6.1 show that the periods of the first two modes gradually increase throughout the shaking table tests. Taking the ARX results as an example, Table 6.1 shows that at the beginning of the low-amplitude earthquake excitations (TEST 1A) the period for mode 1 was 0.317s. By the end of the low-amplitude earthquake excitations (TEST 12), the mode 1 period increased by 12% to 0.354s. The increase in the periods of the first two modes during these tests is attributed to the propagation of cracking within the columns and anchorage slip. The third mode is primarily a function of the slab stiffness. Because the slab was post-tensioned longitudinally and transversely, little damage occurred in the slab, so the mode 3 period remained approximately constant.

Theoretically, more than three modes could be identified in the structural system. However, only modes 1-3 could be identified using the ARX algorithm for any of the excitations. The SLP algorithm uses a calibrated 5-DOF numerical model to identify the modal properties of the structure. Therefore, this algorithm could identify the modal properties for modes 4 and 5 from the calibrated mass and stiffness matrices. The periods identified with the SLP algorithm for modes 4 and 5 were approximately 0.03s and 0.01s, respectively. In

comparison, the sampling rate of the data was 0.01s, and the lowest period that can be identified from the data is $2\Delta t$, or 0.02s. Based on this comparison, it is not possible to identify the mod 5 period using non-parametric algorithms. Although it is theoretically possible to identify the mode 4 properties, the participation of mode 4 in the overall structural response was small, and this mode could not be identified either.

The identified modal damping ratios using the two input/output algorithms are shown in Tables 6.4 - 6.6 and plotted in Fig. 6.2. The damping ratios identified with either algorithm ranged from 1 to 4% for nearly every test and mode. The damping ratios did not vary with the number of tests.

Table 6.1: Identified periods for earthquake excitations

Test	Mode 1			Mode 2			Mode 3		
	ARX	SLP	Ratio	ARX	SLP	Ratio	ARX	SLP	Ratio
$1A$	0.317	0.317	1.001	0.240	0.237	1.011	0.078	0.077	1.007
$1B$	0.323	0.324	0.998	0.247	0.246	1.004	0.079	0.078	1.014
$2A$	0.320	0.323	0.994	0.247	0.244	1.012	0.078	0.077	1.012
$2B$	0.329	0.327	1.007	0.260	0.261	0.994	0.079	0.078	1.013
$3A$	0.324	0.323	1.003	0.245	0.252	0.970	0.079	0.078	1.010
$3B$	0.335	0.334	1.003	0.253	0.251	1.008	0.079	0.078	1.007
4	0.334	0.330	1.013	0.258	0.262	0.984	0.079	0.079	1.006
5	0.333	0.332	1.003	0.259	0.260	0.996	0.079	0.078	1.013
6	0.335	0.332	1.011	0.253	0.253	1.000	0.079	0.078	1.007
7	0.335	0.333	1.006	0.260	0.259	1.004	0.079	0.079	1.008
$9A$	0.332	0.330	1.007	0.256	0.255	1.004	0.079	0.078	1.008
$9B$	0.345	0.340	1.014	0.267	0.265	1.007	0.080	0.078	1.014
10	0.345	0.345	1.000	0.265	0.268	0.990	0.080	0.079	1.005
11	0.345	0.347	0.996	0.269	0.268	1.003	0.080	0.079	1.008
12	0.354	0.353	1.005	0.271	0.271	1.001	0.080	0.078	1.017
μ	0.334	0.332	1.004	0.257	0.257	0.999	0.079	0.078	1.010
σ	0.010	0.010	0.006	0.009	0.010	0.011	0.001	0.001	0.004
δ	0.031	0.030	0.006	0.036	0.037	0.011	0.007	0.007	0.004

Table 6.2: Identified periods for white-noise excitations

Test	Mode 1			Mode 2			Mode 3		
	ARX	SLP	Ratio	ARX	SLP	Ratio	ARX	SLP	Ratio
$WN0001T$	0.314	0.313	1.005	0.236	0.234	1.007	0.078	0.077	1.011
$WN0304TA$	0.319	0.319	1.000	0.243	0.242	1.004	0.078	0.077	1.007
$WN0304TB$	0.332	0.332	1.001	0.254	0.252	1.009	0.079	0.078	1.010
$WN0709TA$	0.333	0.333	1.000	0.254	0.252	1.009	0.079	0.078	1.011
$WN0709TB$	0.335	0.335	1.000	0.256	0.254	1.010	0.078	0.078	1.008
$WN1112TA$	0.341	0.341	1.002	0.259	0.256	1.012	0.079	0.078	1.010
$WN1112TB$	0.342	0.341	1.002	0.260	0.258	1.009	0.079	0.078	1.011
μ	0.331	0.330	1.001	0.252	0.250	1.009	0.078	0.078	1.010
σ	0.011	0.011	0.002	0.009	0.008	0.002	0.001	0.001	0.002
δ	0.032	0.033	0.002	0.035	0.034	0.002	0.007	0.006	0.002

Table 6.3: Identified periods for square-wave excitations

Test	Mode 1			Mode 2			Mode 3		
	ARX	SLP	Ratio	ARX	SLP	Ratio	ARX	SLP	Ratio
$SQ0709$	0.329	0.332	0.992	0.256	0.255	1.005	0.078	0.077	1.010
$SQ1112A$	0.336	0.339	0.992	0.257	0.258	0.996	0.079	0.078	1.012
$SQ1112B$	0.336	0.338	0.994	0.259	0.257	1.006	0.079	0.078	1.013
μ	0.334	0.336	0.993	0.257	0.257	1.002	0.079	0.078	1.012
σ	0.004	0.004	0.001	0.001	0.002	0.006	0.001	0.001	0.002
δ	0.013	0.012	0.001	0.006	0.006	0.006	0.008	0.007	0.002
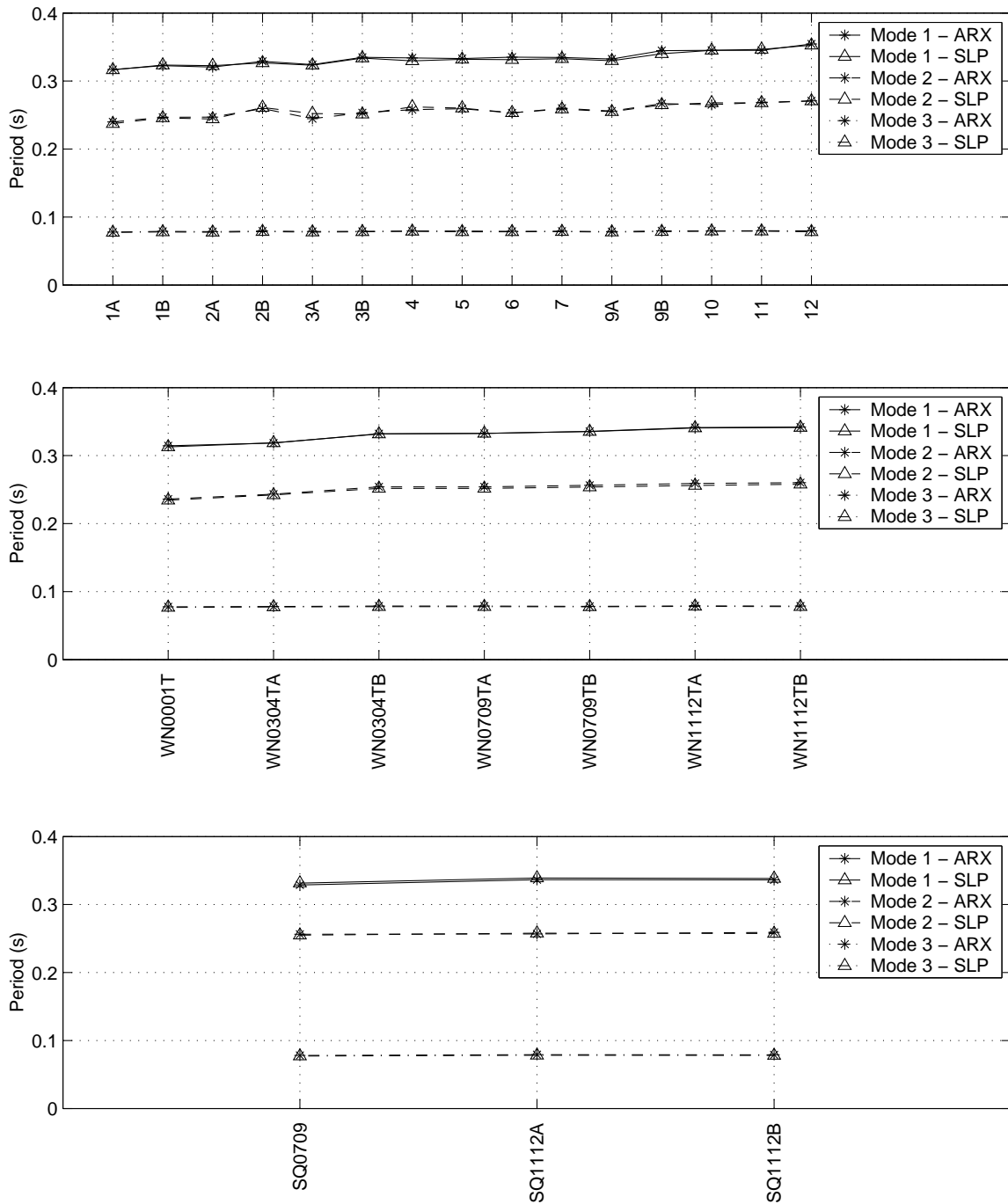
Figure 6.1: Identified periods using acceleration data for (a) low-amplitude, (b) white noise, and (c) square wave excitations

Table 6.4: Identified damping ratios for earthquake excitations

Test	Mode 1			Mode 2			Mode 3		
	ARX	SLP	Ratio	ARX	SLP	Ratio	ARX	SLP	Ratio
$1A$	1.16	1.56	0.743	3.28	2.00	1.636	1.84	1.60	1.144
$1B$	1.90	2.13	0.891	2.25	2.86	0.786	1.99	1.85	1.072
$2A$	1.49	1.95	0.765	2.96	2.43	1.217	2.17	1.95	1.116
$2B$	1.45	1.02	1.424	2.84	5.05	0.563	1.94	2.49	0.777
$3A$	1.92	2.19	0.876	3.60	7.25	0.496	1.71	1.85	0.925
$3B$	2.12	2.13	0.992	3.62	7.71	0.469	1.55	2.43	0.637
4	1.82	1.27	1.431	3.11	3.93	0.792	1.72	2.16	0.796
5	1.41	2.75	0.514	3.42	2.58	1.323	1.99	2.35	0.847
6	2.11	2.50	0.843	1.83	2.04	0.896	1.61	1.46	1.102
7	1.90	1.95	0.974	2.05	2.93	0.700	1.52	1.26	1.213
$9A$	2.10	2.04	1.029	2.97	3.51	0.846	1.70	1.44	1.178
$9B$	2.30	2.62	0.879	1.91	1.65	1.155	1.99	1.51	1.316
10	1.50	1.98	0.759	2.13	1.86	1.147	1.70	1.82	0.931
11	2.28	2.96	0.771	1.99	1.28	1.558	2.27	2.24	1.017
12	2.69	1.73	1.552	1.67	2.53	0.661	1.92	2.04	0.938
μ	1.88	2.05	0.963	2.64	3.31	0.950	1.84	1.90	1.001
σ	0.41	0.53	0.291	0.69	1.94	0.371	0.22	0.39	0.187
δ	0.22	0.26	0.302	0.26	0.59	0.391	0.12	0.20	0.187

Table 6.5: Identified damping ratios for white-noise excitations

Test	Mode 1			Mode 2			Mode 3		
	ARX	SLP	Ratio	ARX	SLP	Ratio	ARX	SLP	Ratio
$WN0001T$	2.01	1.56	1.288	3.50	2.10	1.666	2.10	2.13	0.984
$WN0304TA$	3.08	2.51	1.229	2.76	2.82	0.980	1.94	1.60	1.207
$WN0304TB$	1.90	2.22	0.852	2.62	2.16	1.209	1.75	1.95	0.899
$WN0709TA$	1.76	2.10	0.839	2.61	2.54	1.028	1.98	1.98	1.002
$WN0709TB$	1.95	1.98	0.984	2.66	3.28	0.810	1.98	1.74	1.134
$WN1112TA$	1.96	2.10	0.935	2.57	2.74	0.938	2.01	1.85	1.083
$WN1112TB$	1.93	1.98	0.978	2.52	2.82	0.893	1.94	1.92	1.010
μ	2.08	2.06	1.015	2.75	2.64	1.075	1.96	1.88	1.046
σ	0.45	0.29	0.177	0.34	0.41	0.289	0.11	0.17	0.103
δ	0.21	0.14	0.174	0.12	0.16	0.269	0.05	0.09	0.099

Table 6.6: Identified damping ratios for square-wave excitations

Test	Mode 1			Mode 2			Mode 3		
	ARX	SLP	Ratio	ARX	SLP	Ratio	ARX	SLP	Ratio
$SQ0709$	1.97	2.27	0.865	3.55	2.19	1.619	1.94	2.39	0.811
$SQ1112A$	2.28	2.01	1.134	3.47	1.23	2.813	1.68	2.39	0.703
$SQ1112B$	1.72	1.98	0.872	4.85	1.84	2.642	1.94	2.31	0.837
μ	1.99	2.09	0.957	3.96	1.75	2.358	1.85	2.36	0.784
σ	0.28	0.16	0.153	0.78	0.49	0.646	0.15	0.04	0.071
δ	0.14	0.08	0.160	0.20	0.28	0.274	0.08	0.02	0.091
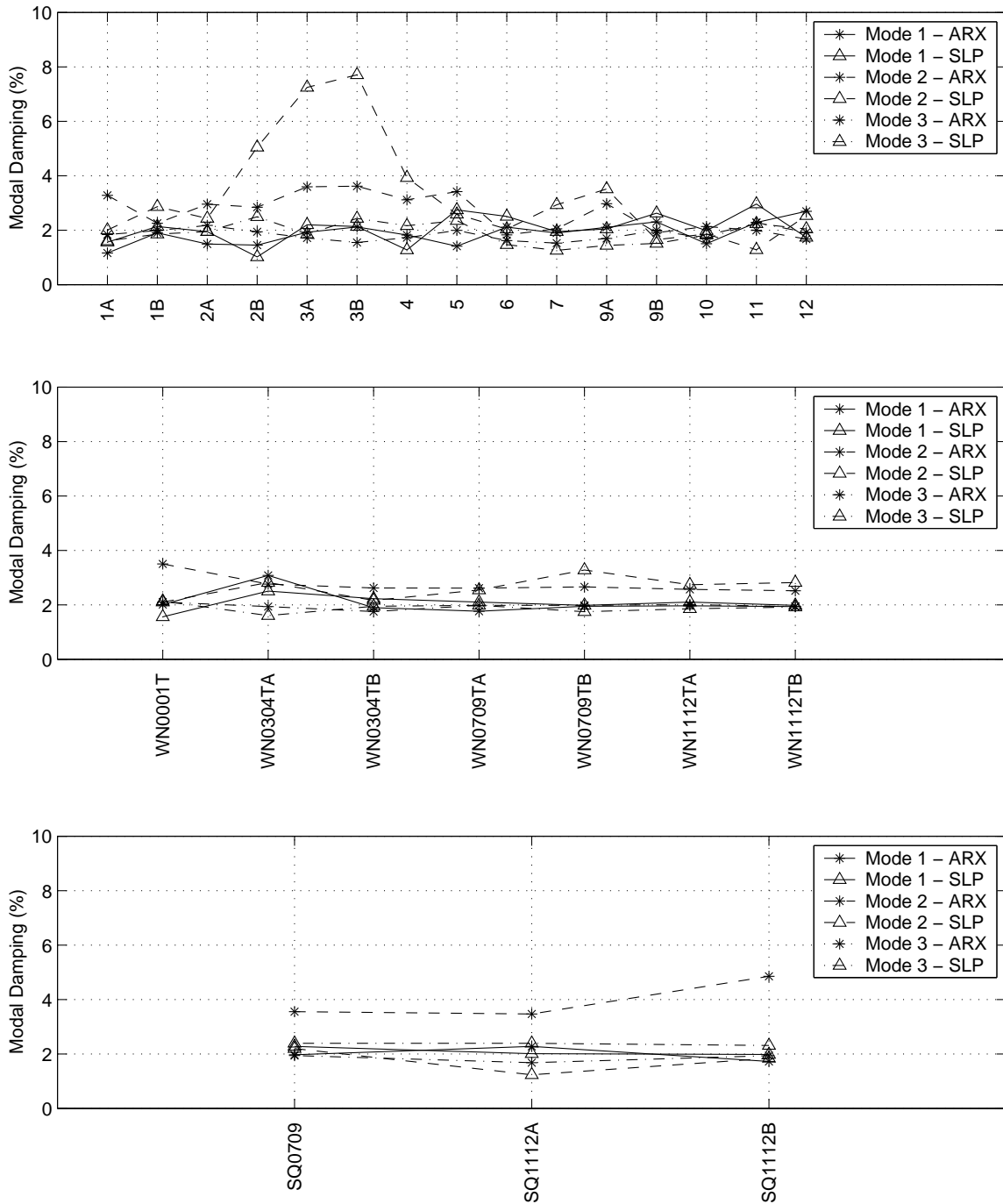
Figure 6.2: Identified damping ratios using acceleration data for (a) low-amplitude, (b) white noise, and (c) square wave excitations

The mode shapes for the first three modes of the shaking table specimen were also identified using the ARX and SLP algorithms. The mode shapes were described by orthonormal basis vectors (s_j, where integer j is the number of the basis vector), which are shown in Table 6.7 and Fig. 6.3. The first three orthonormal basis vectors represent pure translation, pure twisting, and beam bending, respectively. Basis vectors 4 and 5 represent asymmetric and double symmetric bending of the slab.

Table 6.7: Basis vector ordinates

Measurement Location	Basis Vector				
	s_1	s_2	s_3	s_4	s_5
Bent 1	0.44721	0.63246	-0.52943	-0.31623	0.14035
1 - 2	0.44721	0.31623	0.24834	0.63246	-0.48819
Bent 2	0.44721	0	0.56218	0	0.69567
2 - 3	0.44721	-0.31623	0.24834	-0.63246	-0.48819
Bent 3	0.44721	-0.63246	-0.52943	0.31623	0.14035
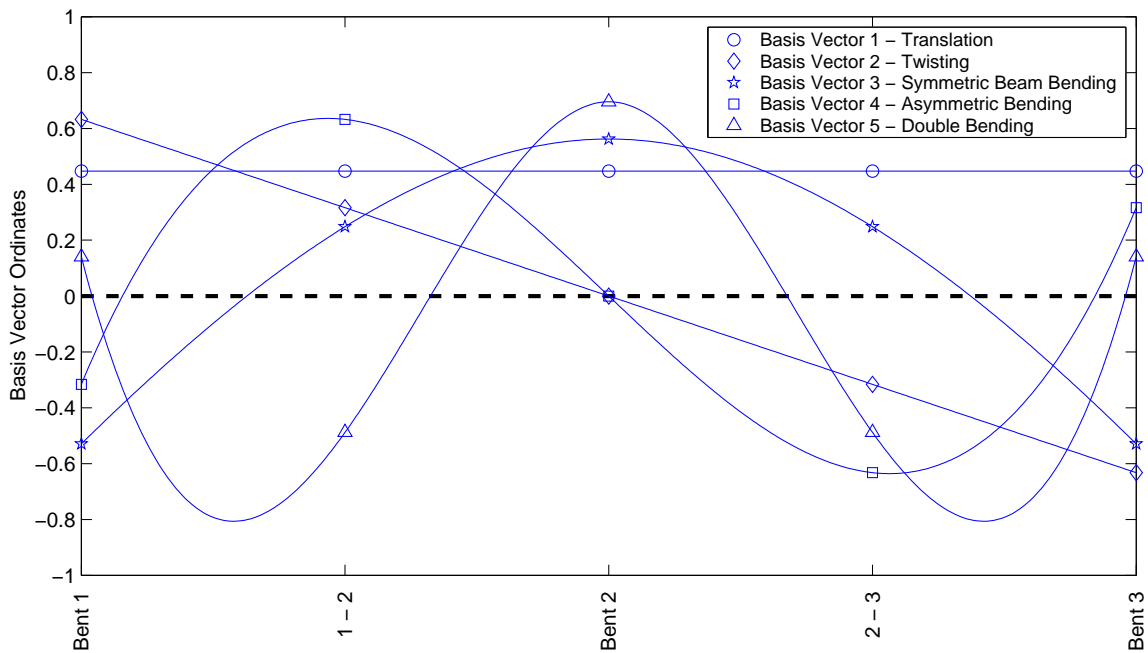
Figure 6.3: Orthonormal basis vectors for a 5-output system

Tables 6.8 - 6.10 provide the projection of mode 1 onto the three basis vectors for the three types of excitations and the two input/output identification algorithms. The tabulated values are the projection of the mode shape onto the orthonormal basis vectors ($\phi_i^T s_j$).

Because both the modes and the basis vectors are unit length, and the basis vectors are orthogonal, the square of the projection of the mode onto a basis vector, $(\phi_i^T s_j)^2$, represents the percentage of the mode that is defined by that basis vector. The percentages of each mode that is described by the first three basis vectors is tabulated for both the SLP and ARX algorithms. The projections of the modes onto basis vectors 4 and 5 were computed, but were not tabulated because of their small contribution to the first three modes.

Fig. 6.4 shows the envelopes created by the identified mode 1 shapes using all tests for each excitation type. It is apparent that both algorithms identify basis vector 1 as the predominant component of mode 1 for any of the three excitation types. For example, using the ARX algorithm for the earthquake excitations, basis vector 1 averaged 87% (0.935^2) of mode 1. Basis vector 2 averaged 12% (0.346^2) of mode 1. The first three basis vectors made up 99.9% of mode 1.

The same procedure was followed for describing the mode shapes for mode 2. The projection of mode 2 onto the first three basis vectors are presented in Tables 6.11 - 6.13 for the three excitations. The envelopes of the mode 2 mode shapes are displayed in Fig. 6.5. Mode 2 was primarily composed of basis vector 2 (slab twisting) for all types of excitations, with some contribution from basis vector 1 (slab translation). Basis vector 3 (beam bending) had small influence on mode 2. For example, using the ARX algorithm for the earthquake excitations, basis vector 2 averaged 76% (0.871^2) of mode 2, while basis vector 1 averaged 24% (-0.488^2). The first three basis vectors made up 99.9% of mode 2.

Mode 3 results are displayed in Tables 6.14 - 6.16. The envelopes of the mode shapes are shown in Fig. 6.6. Mode 3 was composed mainly of basis vector 3 (slab bending). For example, using the ARX algorithm for the earthquake excitations, basis vector 3 averaged 92% (0.960^2) of mode 3. The first three basis vectors made up 98.9% of mode 3.

Table 6.8: Mode 1 basis vector components for earthquake excitations

Test	basis vector 1			basis vector 2			basis vector 3			Total % of mode	
	ARX	SLP	Ratio	ARX	SLP	Ratio	ARX	SLP	Ratio	ARX	SLP
1A	0.932	0.895	1.041	0.361	0.446	0.811	-0.030	-0.024	1.257	99.928	99.999
1B	0.918	0.911	1.008	0.394	0.412	0.956	-0.033	-0.028	1.175	99.943	99.999
2A	0.914	0.907	1.008	0.404	0.420	0.961	-0.029	-0.027	1.091	99.917	99.999
2B	0.957	0.873	1.097	0.286	0.488	0.585	-0.031	-0.011	2.952	99.923	99.999
3A	0.916	0.905	1.012	0.400	0.425	0.941	-0.039	-0.023	1.727	99.988	99.999
3B	0.907	0.881	1.029	0.419	0.473	0.887	-0.030	-0.017	1.777	99.945	99.999
4	0.959	0.900	1.066	0.278	0.435	0.639	-0.035	-0.019	1.904	99.870	99.999
5	0.956	0.924	1.034	0.289	0.381	0.758	-0.033	-0.027	1.201	99.803	100.000
6	0.927	0.914	1.014	0.373	0.405	0.922	-0.037	-0.027	1.355	99.950	100.000
7	0.946	0.923	1.025	0.318	0.383	0.830	-0.028	-0.028	0.995	99.780	100.000
9A	0.949	0.920	1.033	0.309	0.392	0.789	-0.009	-0.028	0.336	99.709	100.000
9B	0.926	0.929	0.997	0.374	0.368	1.018	-0.018	-0.028	0.622	99.848	100.000
10	0.966	0.927	1.041	0.254	0.373	0.682	-0.026	-0.028	0.913	99.783	100.000
11	0.935	0.941	0.994	0.352	0.337	1.045	-0.038	-0.033	1.138	99.973	100.000
12	0.923	0.907	1.018	0.382	0.421	0.908	-0.029	-0.021	1.376	99.985	100.000
μ	0.935	0.910	1.028	0.346	0.411	0.849	-0.030	-0.025	1.321	99.890	100.000
σ	0.019	0.018	0.027	0.053	0.040	0.138	0.008	0.006	0.612	0.086	0.000
δ	0.020	0.020	0.026	0.153	0.098	0.162	0.260	0.232	0.463	0.001	0.000

Table 6.9: Mode 1 basis vector components for white-noise excitations

Test	basis vector 1			basis vector 2			basis vector 3			Total % of mode	
	ARX	SLP	Ratio	ARX	SLP	Ratio	ARX	SLP	Ratio	ARX	SLP
WN0001T	0.922	0.902	1.022	0.384	0.430	0.892	-0.034	-0.027	1.253	99.914	99.999
WN0304TA	0.935	0.932	1.003	0.353	0.361	0.977	-0.033	-0.037	0.896	99.941	100.000
WN0304TB	0.940	0.918	1.024	0.335	0.395	0.849	-0.035	-0.029	1.201	99.811	100.000
WN0709TA	0.925	0.920	1.006	0.377	0.391	0.964	-0.033	-0.030	1.086	99.946	100.000
WN0709TB	0.922	0.901	1.024	0.385	0.433	0.888	-0.031	-0.023	1.344	99.946	100.000
WN1112TA	0.924	0.912	1.013	0.381	0.409	0.932	-0.029	-0.027	1.052	99.945	100.000
WN1112TB	0.923	0.915	1.009	0.383	0.403	0.951	-0.030	-0.027	1.091	99.951	100.000
μ	0.927	0.914	1.014	0.371	0.403	0.922	-0.032	-0.029	1.132	99.922	100.000
σ	0.007	0.011	0.009	0.019	0.025	0.047	0.002	0.004	0.147	0.051	0.000
δ	0.008	0.012	0.009	0.052	0.061	0.051	0.077	0.147	0.130	0.001	0.000

Table 6.10: Mode 1 basis vector components for square-wave excitations

Test	basis vector 1			basis vector 2			basis vector 3			Total % of mode	
	ARX	SLP	Ratio	ARX	SLP	Ratio	ARX	SLP	Ratio	ARX	SLP
SQ0709	0.944	0.923	1.023	0.324	0.385	0.843	-0.038	-0.029	1.333	99.774	100.000
SQ1112A	0.954	0.924	1.032	0.295	0.380	0.777	-0.025	-0.030	0.821	99.755	100.000
SQ1112B	0.947	0.923	1.026	0.313	0.384	0.815	-0.059	-0.030	1.985	99.810	100.000
μ	0.948	0.923	1.027	0.311	0.383	0.812	-0.041	-0.030	1.380	99.780	100.000
σ	0.005	0.001	0.004	0.015	0.002	0.033	0.017	0.001	0.583	0.028	0.000
δ	0.005	0.001	0.004	0.047	0.006	0.041	0.419	0.029	0.423	0.000	0.000
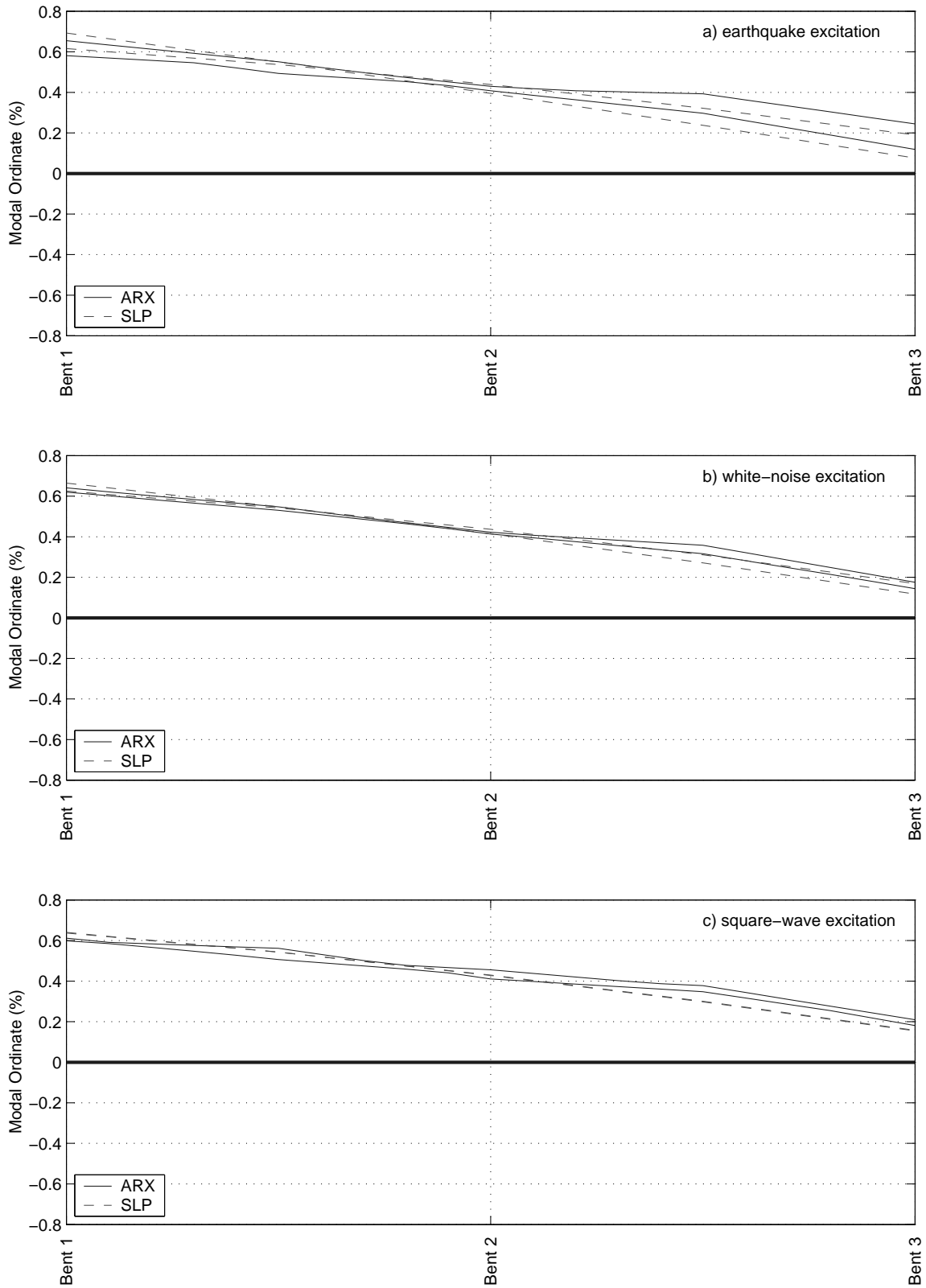
Figure 6.4: Identified mode shape envelopes using acceleration data for mode 1 using the low-amplitude (a) earthquake, (b) white noise, and (c) square wave excitations

Table 6.11: Mode 2 basis vector components for earthquake excitations

Test	basis vector 1			basis vector 2			basis vector 3			Total % of mode	
	ARX	SLP	Ratio	ARX	SLP	Ratio	ARX	SLP	Ratio	ARX	SLP
1A	-0.513	-0.533	0.963	0.856	0.845	1.014	0.056	0.044	1.288	99.993	99.995
1B	-0.488	-0.497	0.980	0.871	0.867	1.006	0.051	0.040	1.268	99.980	99.995
2A	-0.492	-0.506	0.972	0.869	0.861	1.009	0.042	0.041	1.038	99.946	99.995
2B	-0.470	-0.574	0.819	0.882	0.818	1.077	0.010	0.028	0.360	99.878	99.996
3A	-0.538	-0.509	1.056	0.841	0.860	0.978	0.044	0.035	1.277	99.894	99.996
3B	-0.552	-0.560	0.985	0.833	0.828	1.006	0.020	0.038	0.521	99.817	99.996
4	-0.461	-0.520	0.887	0.887	0.854	1.038	0.038	0.031	1.223	99.970	99.996
5	-0.488	-0.462	1.056	0.872	0.886	0.983	0.045	0.032	1.407	99.952	99.996
6	-0.508	-0.489	1.039	0.860	0.872	0.987	0.042	0.037	1.125	99.904	99.996
7	-0.450	-0.465	0.968	0.892	0.885	1.008	0.037	0.034	1.095	99.954	99.996
9A	-0.474	-0.475	0.997	0.879	0.879	0.999	0.054	0.035	1.541	99.905	99.996
9B	-0.440	-0.447	0.983	0.897	0.894	1.003	0.047	0.032	1.503	99.967	99.996
10	-0.497	-0.453	1.095	0.867	0.891	0.973	0.043	0.032	1.358	99.988	99.996
11	-0.489	-0.414	1.182	0.872	0.910	0.958	0.012	0.032	0.386	99.908	99.996
12	-0.459	-0.505	0.909	0.888	0.863	1.029	0.028	0.032	0.896	99.973	99.997
μ	-0.488	-0.494	0.993	0.871	0.867	1.005	0.038	0.035	1.086	99.935	99.996
σ	0.031	0.043	0.087	0.018	0.025	0.029	0.014	0.004	0.384	0.049	0.001
δ	0.064	0.087	0.088	0.021	0.029	0.029	0.376	0.124	0.354	0.000	0.000

Table 6.12: Mode 2 basis vector components for white-noise excitations

Test	basis vector 1			basis vector 2			basis vector 3			Total % of mode	
	ARX	SLP	Ratio	ARX	SLP	Ratio	ARX	SLP	Ratio	ARX	SLP
$WN0001T$	-0.503	-0.517	0.973	0.863	0.855	1.010	0.027	0.045	0.597	99.854	99.995
$WN0304TA$	-0.459	-0.443	1.037	0.887	0.896	0.991	0.009	0.040	0.217	99.829	99.995
$WN0304TB$	-0.492	-0.478	1.028	0.869	0.877	0.991	0.045	0.038	1.178	99.972	99.996
$WN0709TA$	-0.503	-0.474	1.059	0.863	0.879	0.982	0.023	0.038	0.612	99.873	99.996
$WN0709TB$	-0.503	-0.519	0.968	0.863	0.854	1.011	0.017	0.037	0.456	99.839	99.996
$WN1112TA$	-0.508	-0.494	1.028	0.861	0.869	0.991	0.021	0.038	0.551	99.893	99.996
$WN1112TB$	-0.504	-0.487	1.036	0.863	0.873	0.988	0.024	0.037	0.643	99.907	99.996
μ	-0.496	-0.487	1.019	0.867	0.872	0.995	0.024	0.039	0.608	99.881	99.995
σ	0.017	0.026	0.034	0.009	0.015	0.011	0.011	0.003	0.290	0.049	0.001
δ	0.034	0.054	0.034	0.011	0.017	0.011	0.470	0.068	0.477	0.000	0.000

Table 6.13: Mode 2 basis vector components for square-wave excitations

Test	basis vector 1			basis vector 2			basis vector 3			Total % of mode	
	ARX	SLP	Ratio	ARX	SLP	Ratio	ARX	SLP	Ratio	ARX	SLP
$SQ0709$	-0.471	-0.467	1.010	0.881	0.884	0.997	0.026	0.035	0.744	99.951	99.996
$SQ1112A$	-0.439	-0.462	0.949	0.896	0.886	1.011	0.055	0.036	1.529	99.758	99.996
$SQ1112B$	-0.437	-0.466	0.937	0.898	0.884	1.016	0.048	0.036	1.326	99.974	99.996
μ	-0.449	-0.465	0.966	0.892	0.885	1.008	0.043	0.036	1.200	99.894	99.996
σ	0.019	0.003	0.039	0.009	0.001	0.010	0.015	0.001	0.408	0.119	0.000
δ	0.043	0.006	0.040	0.010	0.001	0.010	0.354	0.019	0.340	0.001	0.000
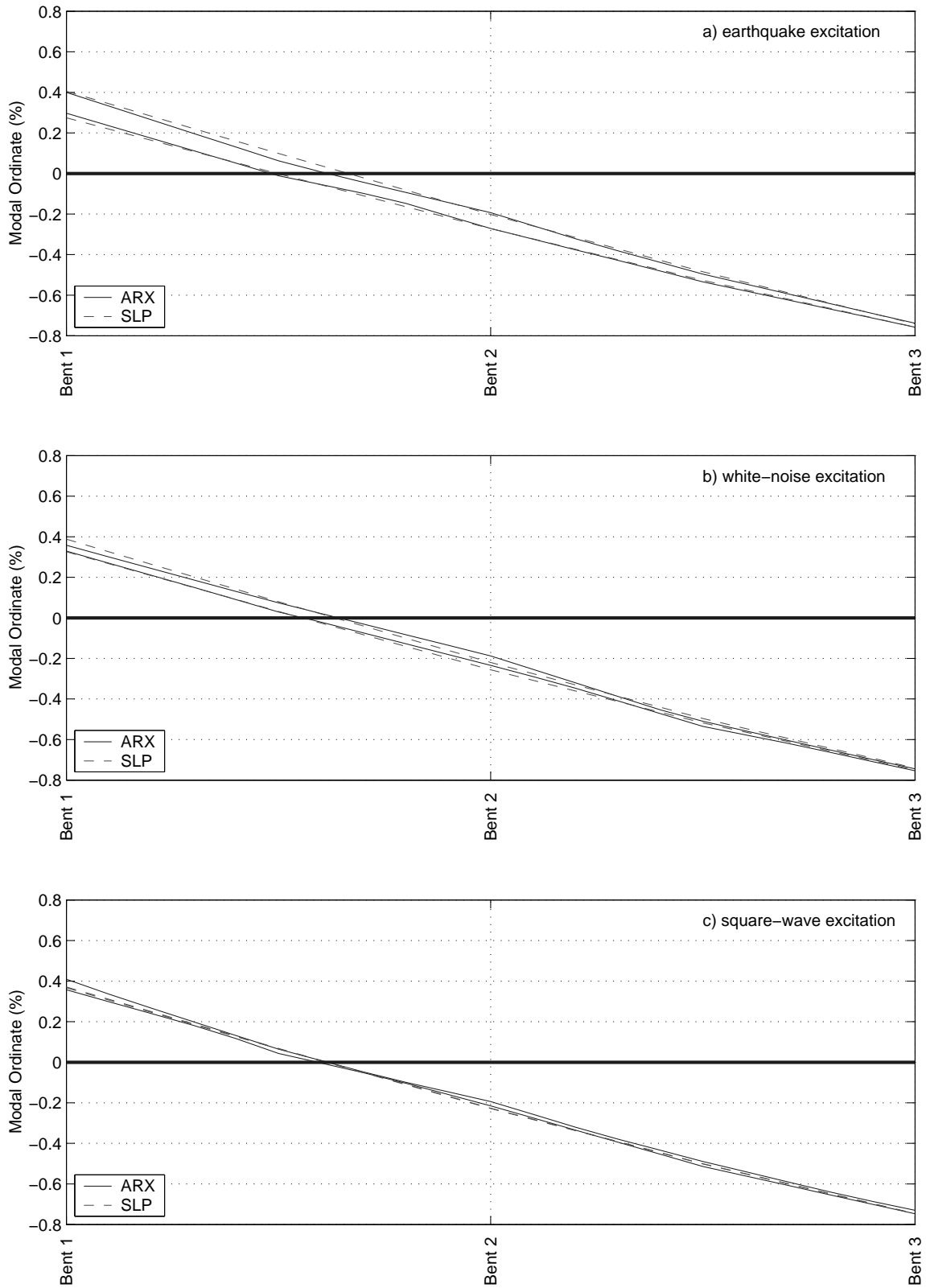
Figure 6.5: Identified mode shape envelopes using acceleration data for mode 2 using the low-amplitude (a) earthquake, (b) white noise, and (c) square wave excitations

Table 6.14: Mode 3 basis vector components for earthquake excitations

Test	basis vector 1			basis vector 2			basis vector 3			Total % of mode	
	ARX	SLP	Ratio	ARX	SLP	Ratio	ARX	SLP	Ratio	ARX	SLP
$1A$	-0.255	-0.241	1.058	0.005	-0.019	-0.247	0.964	0.970	0.994	99.522	99.998
$1B$	-0.269	-0.241	1.115	0.008	-0.016	-0.507	0.960	0.970	0.989	99.335	99.999
$2A$	-0.259	-0.241	1.073	0.006	-0.017	-0.339	0.960	0.970	0.989	98.846	99.999
$2B$	-0.272	-0.255	1.064	0.007	-0.013	-0.497	0.959	0.967	0.992	99.311	99.998
$3A$	-0.274	-0.246	1.115	-0.000	-0.014	0.019	0.957	0.969	0.988	99.146	99.998
$3B$	-0.266	-0.248	1.074	0.005	-0.017	-0.296	0.959	0.969	0.990	99.044	99.998
4	-0.238	-0.250	0.951	0.002	-0.013	-0.141	0.964	0.968	0.996	98.672	99.998
5	-0.247	-0.244	1.009	-0.005	-0.012	0.420	0.963	0.970	0.993	98.783	99.999
6	-0.256	-0.242	1.056	0.010	-0.015	-0.701	0.964	0.970	0.994	99.461	99.999
7	-0.243	-0.243	1.000	-0.005	-0.013	0.414	0.960	0.970	0.990	98.170	99.999
$9A$	-0.241	-0.243	0.993	-0.001	-0.014	0.076	0.962	0.970	0.992	98.419	99.999
$9B$	-0.239	-0.244	0.978	-0.005	-0.012	0.422	0.964	0.970	0.994	98.601	99.999
10	-0.250	-0.244	1.025	0.013	-0.012	-1.043	0.960	0.970	0.991	98.526	99.999
11	-0.288	-0.241	1.197	0.006	-0.011	-0.491	0.952	0.970	0.981	98.897	99.999
12	-0.275	-0.248	1.108	0.009	-0.013	-0.688	0.959	0.969	0.990	99.460	99.999
μ	-0.258	-0.245	1.055	0.003	-0.014	-0.240	0.960	0.969	0.991	98.946	99.999
σ	0.015	0.004	0.064	0.006	0.002	0.443	0.003	0.001	0.004	0.421	0.000
δ	0.060	0.017	0.061	1.652	0.156	1.847	0.004	0.001	0.004	0.004	0.000

Table 6.15: Mode 3 basis vector components for white-noise excitations

Test	basis vector 1			basis vector 2			basis vector 3			Total % of mode	
	ARX	SLP	Ratio	ARX	SLP	Ratio	ARX	SLP	Ratio	ARX	SLP
$WN0001T$	-0.245	-0.239	1.025	-0.010	-0.019	0.529	0.965	0.971	0.994	99.163	99.998
$WN0304TA$	-0.262	-0.235	1.113	-0.007	-0.015	0.481	0.962	0.972	0.989	99.326	99.999
$WN0304TB$	-0.247	-0.241	1.027	-0.014	-0.015	0.966	0.962	0.970	0.991	98.626	99.999
$WN0709TA$	-0.256	-0.240	1.067	-0.009	-0.015	0.591	0.962	0.971	0.992	99.193	99.999
$WN0709TB$	-0.252	-0.245	1.028	-0.008	-0.015	0.547	0.964	0.969	0.994	99.229	99.999
$WN1112TA$	-0.252	-0.242	1.041	-0.008	-0.015	0.526	0.964	0.970	0.994	99.281	99.999
$WN1112TB$	-0.254	-0.243	1.047	-0.005	-0.014	0.315	0.963	0.970	0.993	99.218	99.999
μ	-0.253	-0.241	1.050	-0.009	-0.016	0.565	0.963	0.970	0.992	99.148	99.999
σ	0.006	0.003	0.032	0.003	0.001	0.198	0.001	0.001	0.002	0.237	0.000
δ	0.022	0.013	0.030	0.342	0.089	0.350	0.001	0.001	0.002	0.002	0.000

Table 6.16: Mode 3 basis vector components for square-wave excitations

Test	basis vector 1			basis vector 2			basis vector 3			Total % of mode	
	ARX	SLP	Ratio	ARX	SLP	Ratio	ARX	SLP	Ratio	ARX	SLP
$SQ0709$	-0.251	-0.243	1.035	-0.070	-0.013	5.211	0.960	0.970	0.990	98.986	99.999
$SQ1112A$	-0.253	-0.241	1.049	-0.030	-0.014	2.194	0.961	0.970	0.991	98.900	99.999
$SQ1112B$	-0.275	-0.242	1.139	-0.018	-0.014	1.280	0.959	0.970	0.988	99.507	99.999
μ	-0.260	-0.242	1.074	-0.039	-0.014	2.895	0.960	0.970	0.990	99.131	99.999
σ	0.013	0.001	0.056	0.027	0.000	2.057	0.001	0.000	0.001	0.329	0.000
δ	0.052	0.003	0.052	0.693	0.018	0.710	0.001	0.000	0.001	0.003	0.000
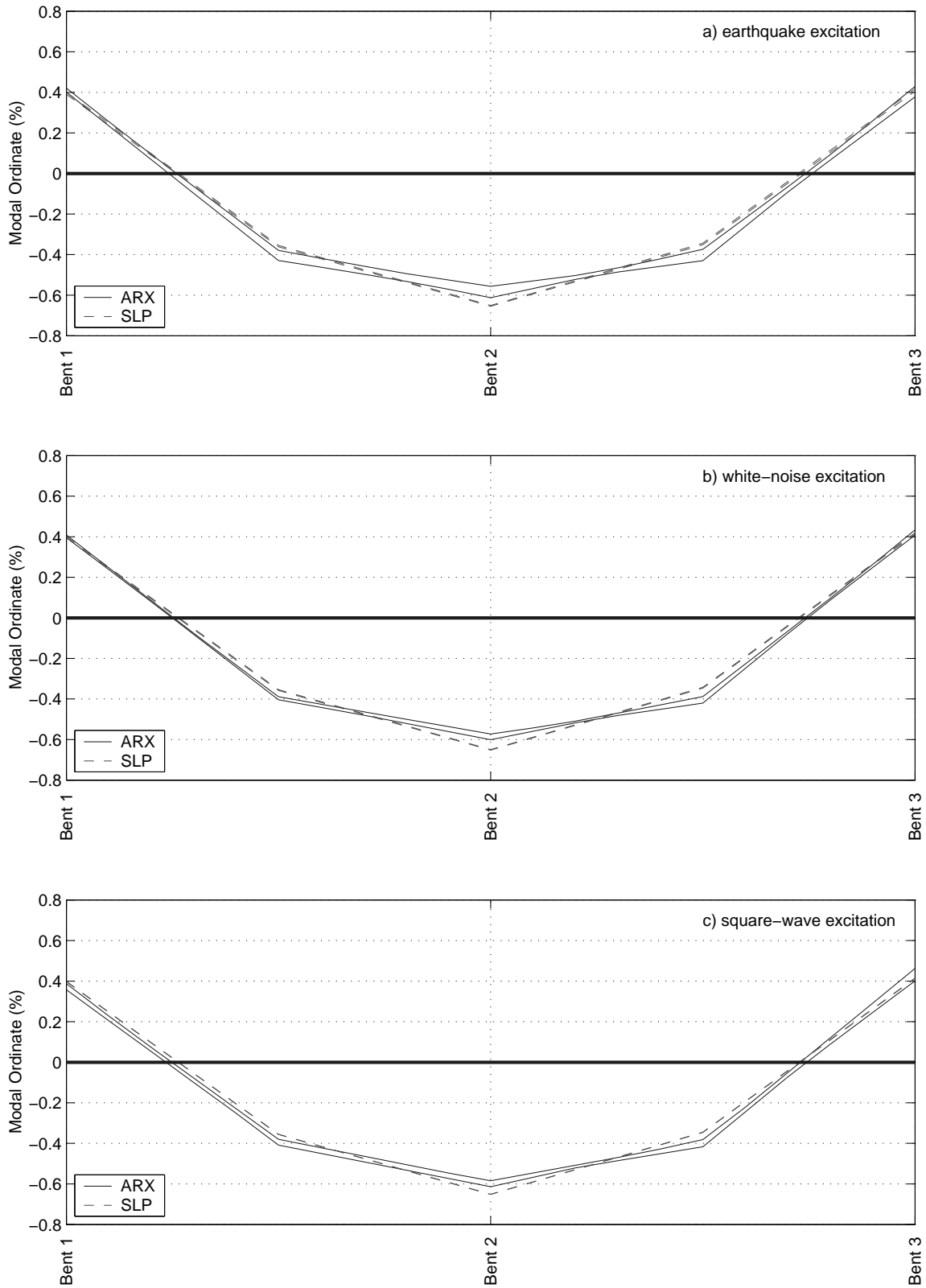
Figure 6.6: Identified mode shape envelopes using acceleration data for mode 3 using the low-amplitude (a) earthquake, (b) white noise, and (c) square wave excitations

6.2 Parameter Sensitivity Study using SLP Algorithm

The successive linear programming (SLP) algorithm was used to investigate the sensitivity of the objective function (Eq. 5.6) to the seven calibration parameters of the numerical model. The sensitivity of the objective function was evaluated for incremental changes in each parameter in both the negative and positive directions. The sensitivity of the objective function to the specimen properties was quantified by computing the increase from the value of the optimal objective function and the value of the objective function using non-optimal parameters, given by the equation

$$\%Increase = \frac{J - J_{min}}{J_{min}} \times 100 \tag{6.1}$$

where J is the value of the objective function for any combination of parameters, and J_min is the minimum value of the objective function for the optimal parameters.

The results of this study are presented in Fig. 6.7. In this figure, the effect of each parameter on the objective function was averaged for all of the tests within each excitation type. For example, the effect of the bent 1 stiffness on the objective function during the earthquake excitations (Fig. 6.7a) was quantified as the mean for all 15 tests. Tables 6.17 - 6.19 show the percent change of the objective function due to a $\pm5\%$ change in each parameter.

The objective function is the most sensitive to changes in the bent 1 and 3 stiffness parameters (k_b^1 and k_b^2), while still sensitive to the bent 2 and slab stiffnesses (k_b^3 and EI_s). The objective function was much less sensitive to the damping ratios (ξ_1, ξ_2, and ξ_3) for all excitation types. Because mode 3 had the smallest influence on the structural response, varying the damping ratio for this mode had small effects on the response. For example, during the earthquake excitations, a positive change of 5% in the stiffness of bents 1 or 3 caused an average increase of the objective function by approximately 101% and 264%. In contrast, a positive change of 5% of any of the damping ratios caused an average increase of the objective function by no more than 0.5%. The small influence of the damping ratios on the objective function could account for the large amount of scatter in the identified damping ratios in Section 6.1. Fig. 6.7 also shows that the objective function is more sensitive to negative deviations in each of the three modal damping ratios than positive deviations.

Table 6.17: Sensitivity Study for earthquake excitations

Test	k_b^1		k_b^2		k_b^3		ξ_1		ξ_2		ξ_3		EI_s	
	-5%	+5%	-5%	+5%	-5%	+5%	-5%	+5%	-5%	+5%	-5%	+5%	-5%	+5%
1A	268.1	93.3	7.7	4.9	294.5	197.4	0.0	0.1	0.2	0.1	0.1	0.1	77.4	30.7
1B	152.6	64.6	3.0	3.2	116.4	152.2	0.1	0.1	0.3	0.5	0.1	0.1	31.9	17.5
2A	78.5	25.3	3.9	1.9	895.7	1421.5	0.0	0.0	1.2	1.4	0.1	0.0	34.3	15.4
2B	5.5	13.8	1.9	2.0	125.7	337.9	0.0	0.0	1.2	1.2	0.0	0.0	0.7	4.8
3A	185.6	158.7	6.7	11.9	5.3	2.4	0.3	0.2	0.1	0.0	0.1	0.2	110.8	64.0
3B	510.6	281.6	14.4	11.1	13.8	10.3	0.6	0.4	0.3	0.4	0.1	0.1	51.2	44.8
4	34.8	30.4	1.9	3.3	168.1	426.1	0.0	0.0	1.6	0.8	0.0	0.0	11.2	7.5
5	36.5	43.0	1.8	1.0	346.8	315.0	0.1	0.0	0.5	0.8	0.2	0.2	104.2	146.2
6	118.8	71.9	4.4	6.0	100.1	46.4	0.2	0.2	0.1	0.1	0.1	0.1	218.0	72.0
7	174.0	100.0	3.1	4.7	189.9	123.8	0.1	0.1	0.4	0.3	0.1	0.0	141.8	56.6
9A	61.3	119.7	2.3	4.3	42.0	94.3	0.1	0.1	0.3	0.2	0.1	0.1	160.1	24.9
9B	136.0	71.2	3.5	3.8	466.0	157.3	0.2	0.2	0.2	0.2	0.0	0.0	35.8	23.3
10	369.3	119.3	2.6	1.2	459.1	204.1	0.2	0.1	0.4	0.6	0.0	0.0	2.5	0.7
11	150.9	118.1	1.2	0.6	1291.7	290.4	0.1	0.1	0.5	0.3	0.0	0.0	4.1	1.2
12	255.2	198.2	3.2	2.6	141.9	175.3	0.1	0.1	0.5	0.7	0.0	0.0	6.0	2.9
μ	169.2	100.6	4.1	4.2	310.5	263.6	0.1	0.1	0.5	0.5	0.1	0.1	66.0	34.2
σ	136.5	71.3	3.4	3.4	357.1	342.6	0.2	0.1	0.4	0.4	0.1	0.1	67.3	38.8
δ	0.8	0.7	0.8	0.8	1.2	1.3	1.1	0.9	0.9	0.8	0.9	1.0	1.0	1.1

Table 6.18: Sensitivity Study for white-noise excitations

Test	k_b^1		k_b^2		k_b^3		ξ_1		ξ_2		ξ_3		EI_s	
	-5%	+5%	-5%	+5%	-5%	+5%	-5%	+5%	-5%	+5%	-5%	+5%	-5%	+5%
$WN0001T$	462.7	352.9	7.9	8.7	217.9	188.8	0.2	0.1	0.2	0.3	0.1	0.1	58.3	31.5
$WN0304TA$	155.1	87.0	3.2	2.8	38.4	30.1	0.5	0.3	0.1	0.1	0.1	0.1	85.8	42.3
$WN0304TB$	808.2	254.4	7.6	14.5	191.8	63.5	0.7	0.6	0.2	0.1	0.1	0.1	91.3	26.2
$WN0709TA$	1022.2	326.5	12.6	10.3	140.3	78.5	0.8	0.5	0.2	0.3	0.1	0.1	101.6	43.8
$WN0709TB$	1063.9	288.9	10.9	16.4	120.1	56.8	0.4	0.6	0.3	0.2	0.2	0.1	183.8	59.7
$WN1112TA$	887.3	386.7	7.5	14.1	111.7	85.5	0.5	0.5	0.3	0.1	0.2	0.1	168.4	63.0
$WN1112TB$	964.8	362.6	9.1	13.9	60.8	129.8	0.4	0.4	0.3	0.2	0.2	0.1	128.5	56.4
μ	766.3	294.1	8.4	11.5	125.9	90.4	0.5	0.4	0.2	0.2	0.1	0.1	116.8	46.1
σ	335.6	101.9	3.0	4.6	64.7	53.1	0.2	0.2	0.1	0.1	0.1	0.0	45.7	14.2
δ	0.4	0.3	0.4	0.4	0.5	0.6	0.4	0.4	0.3	0.4	0.4	0.3	0.4	0.3

Table 6.19: Sensitivity Study for square-wave excitations

Test	k_b^1		k_b^2		k_b^3		ξ_1		ξ_2		ξ_3		EI_s	
	-5%	+5%	-5%	+5%	-5%	+5%	-5%	+5%	-5%	+5%	-5%	+5%	-5%	+5%
$SQ0709$	270.7	169.1	9.5	6.0	46.4	26.7	0.6	0.3	0.0	0.0	0.1	0.1	40.1	28.9
$SQ1112A$	458.7	324.0	11.6	10.4	110.0	52.6	0.6	0.6	0.0	0.0	0.1	0.1	68.7	24.9
$SQ1112B$	380.7	269.9	7.6	16.7	58.5	50.5	0.8	0.4	0.1	0.0	0.1	0.1	61.2	35.3
μ	370.0	254.3	9.6	11.0	71.7	43.2	0.7	0.4	0.0	0.0	0.1	0.1	56.7	29.7
σ	94.5	78.6	2.0	5.4	33.8	14.4	0.1	0.1	0.0	0.0	0.0	0.0	14.8	5.2
δ	0.3	0.3	0.2	0.5	0.5	0.3	0.2	0.3	0.5	0.4	0.2	0.2	0.3	0.2
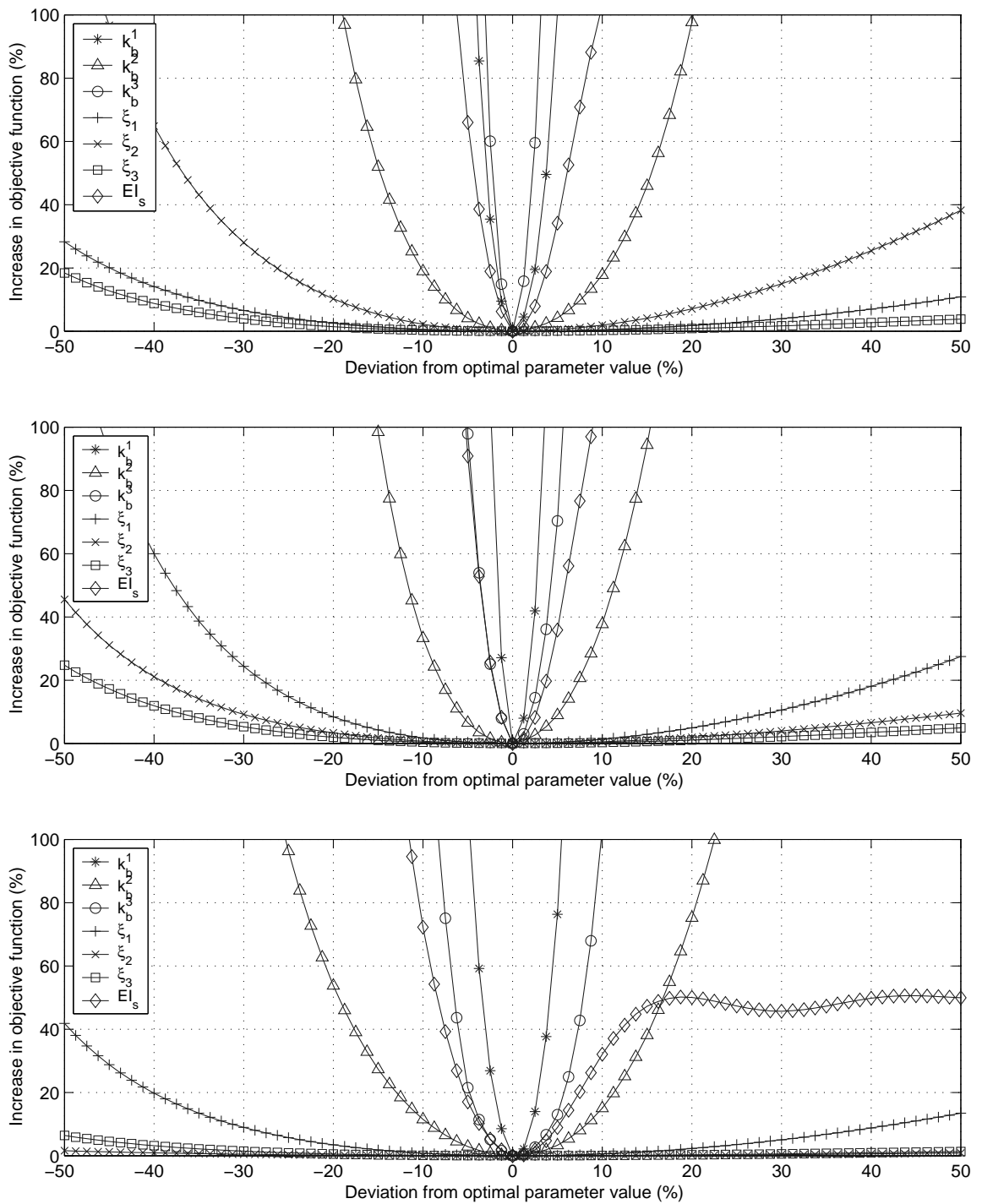
Figure 6.7: Identified objective function sensitivity to the structural parameters for low-amplitude (a) earthquake, (b) white noise, and (c) square wave excitations

6.3 Three-Dimensional System Identification using ARX Algorithm

The modal properties of the shaking table system were identified in three dimensions (transverse, vertical, and longitudinal) using the ARX algorithm. To identify the three-dimensional modal properties, both the transverse and longitudinal shaking table motions were used as the input excitations, and the slab response in all three directions was used as the output response. Transverse and longitudinal accelerations were measured at five locations along the slab: one at each bent and one at each mid-span. The vertical accelerations were measured at four locations along the slab: one at each mid-span, and one at the ends of each cantilever section.

In addition to the series of transverse excitations that were reported in Section 6.1, three longitudinal white-noise motions were used to excite the structure. Using the 14 response measurements and the six excitation measurements, a total of 6 modes were identified for the shaking table specimen: three transverse modes (reported previously in Section 6.1), two vertical modes (asymmetric and symmetric slab bending), and one longitudinal mode (rigid slab translation). The identified periods for each of the low-amplitude excitations are listed in Table 6.20.

The longitudinal mode was only identifiable for five excitations, the three longitudinal excitations and the two biaxial excitations. The longitudinal mode was never identifiable for the strictly transverse excitations. Similarly, the transverse modes were unidentifiable for the strictly longitudinal excitations.

Because of the mass and stiffness of the slab, the vertical accelerations on the slab were substantial for both the transverse and the longitudinal excitations. Therefore, the two vertical modes were easily identified for all excitations. Furthermore, the periods of the vertical modes identified with the longitudinal excitations were within 2% of the periods for the same modes identified with the transverse excitations. For example, the second vertical mode identified with the longitudinal white noise test WN1112LA was 0.157s, 1.9% lower than that same mode identified with the transverse white noise test WN1112TA (0.160s). This suggests that the identified vertical modes are independent of the type or direction of the excitation.

Table 6.20: Identified periods in three dimensions using ARX

Excitation Type	Test	Mode					
		T1	T2	T3	V1	V2	L1
EQ	1A	0.317	0.240	0.078	0.197	0.156	*
	1B	0.323	0.247	0.079	0.199	0.158	*
	2A	0.320	0.247	0.078	0.196	0.157	*
	2B	0.329	0.260	0.079	0.193	0.158	*
	3A	0.324	0.245	0.079	0.191	0.154	*
	3B	0.335	0.253	0.079	0.197	0.157	*
	4	0.334	0.258	0.079	0.192	0.156	*
	5	0.333	0.259	0.079	0.195	0.156	*
	6	0.335	0.253	0.079	0.197	0.158	*
	7	0.335	0.260	0.079	0.197	0.158	*
	9A	0.332	0.256	0.079	0.212	0.162	0.334
	9B	0.345	0.267	0.080	0.211	0.164	0.346
	10	0.345	0.265	0.080	0.186	0.157	*
	11	0.345	0.269	0.080	0.189	0.154	*
	12	0.354	0.271	0.080	0.200	0.161	*
WN, Tran	WN0001T	0.314	0.236	0.078	0.197	0.157	*
	WN0304TA	0.319	0.243	0.078	0.196	0.159	*
	WN0304TB	0.332	0.254	0.079	0.194	0.160	*
	WN0709TA	0.333	0.254	0.079	0.194	0.160	*
	WN0709TB	0.335	0.256	0.078	0.193	0.159	*
	WN1112TA	0.341	0.259	0.079	0.198	0.160	*
	WN1112TB	0.342	0.260	0.079	0.196	0.160	*
WN, Long	WN0709LB	*	*	*	0.198	0.158	0.325
	WN1112LA	*	*	*	0.199	0.157	0.329
	WN1112LB	*	*	*	0.199	0.158	0.329
SQ	SQ0709	0.329	0.256	0.078	0.201	0.158	*
	SQ1112A	0.336	0.257	0.079	0.202	0.160	*
	SQ1112B	0.336	0.259	0.079	0.202	0.160	*

6.4   Influence of Input/Output Algorithm Type

The two input/output algorithms identify the modal properties of the structure using two approaches. The ARX algorithm identifies the modes non-parametrically, using the input and output measurements without any prior knowledge of the structure. The SLP algorithm identifies the modes parametrically by first calibrating a numerical model of the structure using the input and output data. The modes are then extracted from the calibrated mass and stiffness matrices of the numerical model. The influence of the algorithm type on the identified modal parameters was investigated using the data presented in Section 6.1.

The periods for the three modes identified with the two algorithms (Tables 6.1 - 6.3) were similar for all excitation types. These tables also show the ratios between the periods

identified with the ARX algorithm to those identified with the SLP algorithm. These ratios ranged from 0.96 (Test 3A, mode 2) to 1.02 (Test 12, mode 3). The mean ratio of the identified periods for all three modes and all three excitation types was 1.00, with a standard deviation of 0.01.

The damping ratios identified with the two algorithms were less similar than the identified periods for all excitation types. For the earthquake excitations, the ratio of the mode 1 damping ratio identified with the ARX algorithm to that identified with the SLP algorithm ranged between 0.45 (Test 3A, mode 2) to 1.64 (Test 1A, mode 2). This large range was attributed to the insensitivity of the response of the shaking table specimen to small changes in the modal damping ratios (Section 6.2). Although the range of these ratios was large, the mean ratios were near 1.0. For example, the mean ratio for mode 1 using the earthquake excitations is 0.95.

The ARX algorithm more consistently identified the modal damping ratios than the SLP algorithm for the earthquake excitations. For example, the coefficients of variation of the mode 2 damping ratios during the earthquake excitations were 0.24 (ARX) and 0.59 (SLP). The high coefficient of variation using the SLP method is partially due to the large mode 2 damping estimates for Tests 2B-3B. For the other types of excitations (white-noise and square-wave), this difference was not as pronounced.

The ratio of the basis vector components using the ARX algorithm to those using the SLP algorithm are presented in Tables 6.8 - 6.10 for mode 1. These ratios for the three types of excitations ranged between 0.82 (Test 2B, basis vector 2) and 1.18 (Test 11, basis vector 2). Most of the scatter was due to the contribution of basis vector 2 to mode 1 during the earthquake excitations. For example, under earthquake excitation the coefficient of variation of the ratios for the basis vector 2 during earthquake excitations was 9%. The coefficient of variation for basis vector 1 was only 3%.

The ratios between the two input/output algorithms for basis vector 2 ranged from 0.96 to 1.08, with a mean value of 1.01. The scatter was much larger for basis vectors 1 and 3 due to their smaller influence on mode 2. For example, the ratio from basis vector 3 during the earthquake excitations ranged from -1.04 to 0.42. This range was large because the projection of mode 2 onto basis vector 3 was small. For example, during Test 10 the ARX

algorithm identified the basis vector 2 component of mode 2 as 0.867, while the basis vector 3 component was 0.013.

The estimation of the basis vector 3 component was insensitive to the algorithm type. For example, using the earthquake excitations, the ratio for basis vector 3 ranged from 0.98 to 1.00. This ratio had more scatter for basis vectors 1 and 2, which was attributed to the small contributions of basis vectors 1 and 2 on mode 3. For example, during the earthquake excitations, the mean and coefficient of variation for the basis vector 1 ratio was estimated as 1.31 and 46%, respectively.

The comparison between the identified modal properties using the two input/output algorithms show that the values of the periods were insensitive to the algorithm type. The damping ratios for modes 1 and 3 were also similar for the two algorithms, while there were larger dissimilarities for the mode 2 damping ratio. This was attributed to a few tests with large damping ratio deviations. While the primary basis vector component of each mode shape was also similar between the two algorithms, the secondary components had large variations. These variations were attributed to the small influence of the secondary basis vectors on the mode shapes.

6.5 Influence of Excitation Type

Three types of excitations (earthquake, white-noise and square-wave) were used to identify the modal properties of the structure. The influence of each of these excitation types on the identified modal properties was investigated using the data presented in Section 6.1.

Tables 6.1 - 6.3 show the influence of the excitation type on the estimation of the structural periods. Because the input/output identification algorithms account for the frequency content of the input motions, there is very little difference between the identified periods for each excitation type. For example, using the ARX algorithm, the periods for the three modes identified from the Test 7 earthquake excitation were 0.335s, 0.260s, and 0.079s. The periods from the white noise test conducted directly after Test 7 (WN0709TA) were identified as 0.333s, 0.254s, and 0.079s. The periods from the square wave test conducted directly after Test 7 (SQ0709) were identified as 0.329s, 0.256s, and 0.078s.

The identified modal damping ratios (Tables 6.4 - 6.6) were similar for the three exci-

tation types. For example, using the ARX algorithm, the mean damping ratio of mode 1 was identified as 1.85% (earthquake excitation), 2.08% (white-noise excitation), and 1.99% (square-wave excitation). Using the SLP algorithm, the mean mode 1 damping ratios were identified as 2.05%, 2.06%, and 2.09% for the three excitation types.

The influence of each basis vector on mode 1 is similar for all excitation types, showing that the identified mode shape for mode 1 is insensitive to the type of excitation. For example, using the ARX algorithm the mean value of the projection of mode 1 onto basis vector 1 was identified as 0.935 (earthquake excitation), 0.927 (white-noise excitation), and 0.948 (square-wave excitation).

The basis vector components of mode 2 were similar for all three excitation types. For example, using the ARX algorithm the projection of mode 2 onto basis vector 2 was estimated as 0.872 (earthquake excitation), 0.867 (white-noise excitation), and 0.892 (square-wave excitation). Because the contribution of basis vector 3 to mode 2 was small, the projection onto basis vector 3 was less consistent for the three excitation types.

The basis vector components of mode 3 were also similar for the three excitation types. For example, using the ARX algorithm the mean projection of mode 3 onto basis vector 3 was identified as 0.960 (earthquake excitation), 0.963 (white-noise excitation), and 0.960 (square-wave excitation).

Comparison of the modal parameters (periods, damping ratios and mode shapes) identified with the three excitation types showed that the identified periods were insensitive to the excitation type. The mode 1 and 3 damping ratios were less sensitive to the excitation type than the mode 2 damping ratio. Larger variations in the mode 2 damping ratio were attributed to the insensitivity of the structural response to slight changes in this parameter. These results are consistent with the sensitivity study in Section 6.2. This insensitivity to the damping ratios is illustrated in Figs. 6.8 - 6.10 for earthquake excitation Test 7, and the white-noise and square-wave tests immediately following Test 7 (WN0709TA and SQ0709). The identified primary basis vector component for each mode shape (e.g. basis vector 1 for mode 1, basis vector 2 for mode 2) was insensitive to the excitation type. Although the secondary basis vectors were also consistent for each excitation type, they varied more than the primary basis vector because of their small influence on the mode.
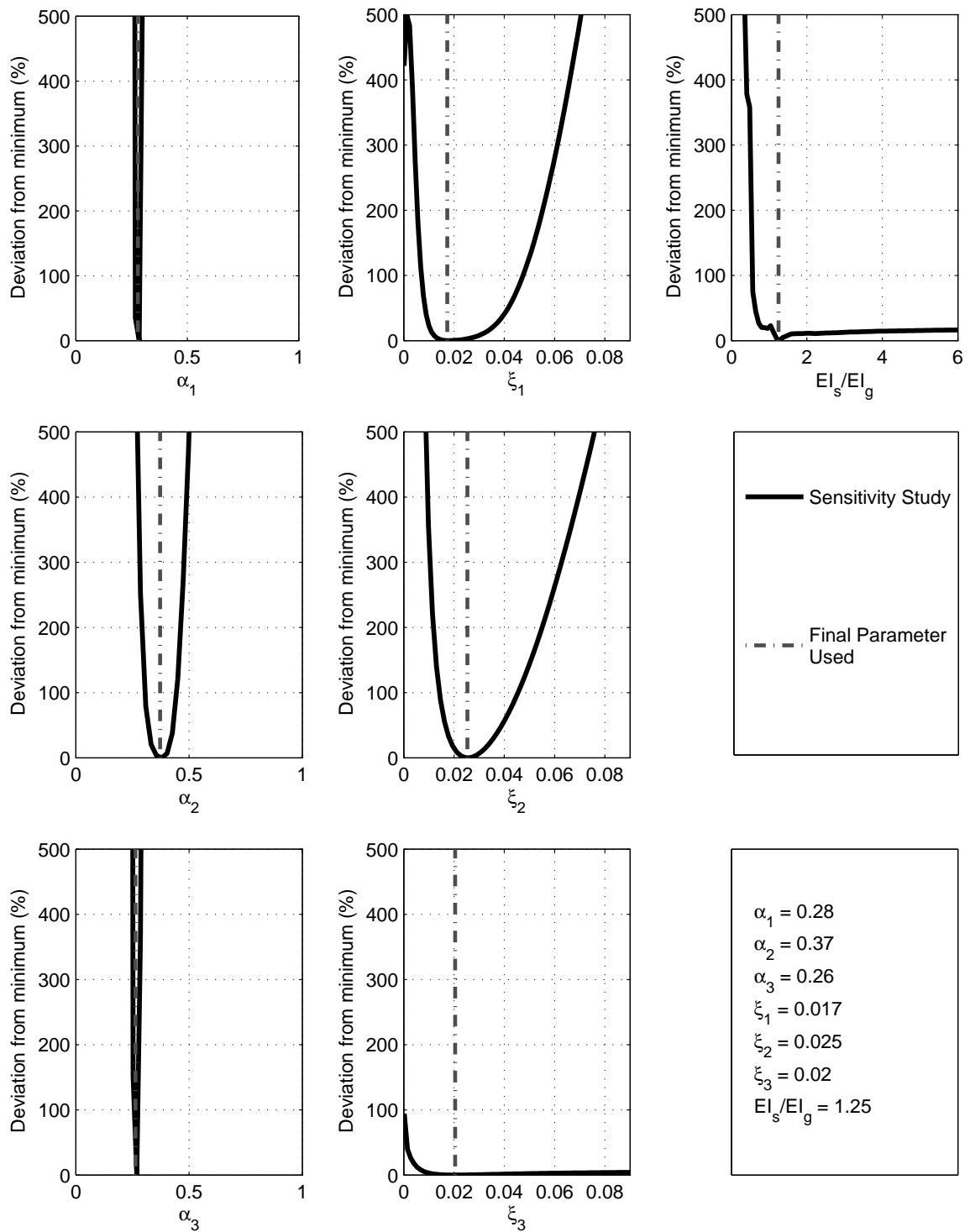
Figure 6.8: Sensitivity study for TEST12
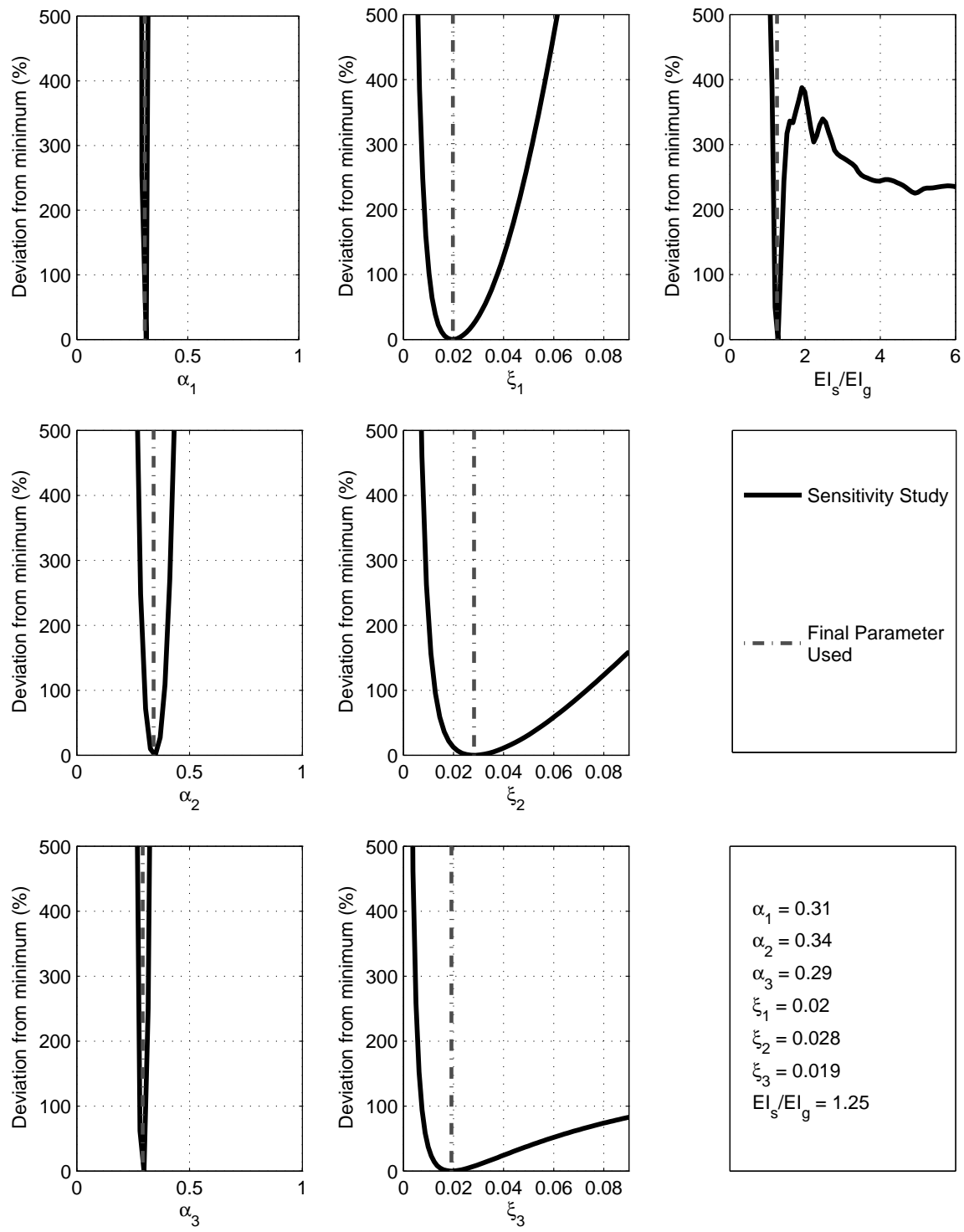
Figure 6.9: Sensitivity study for WN1112B
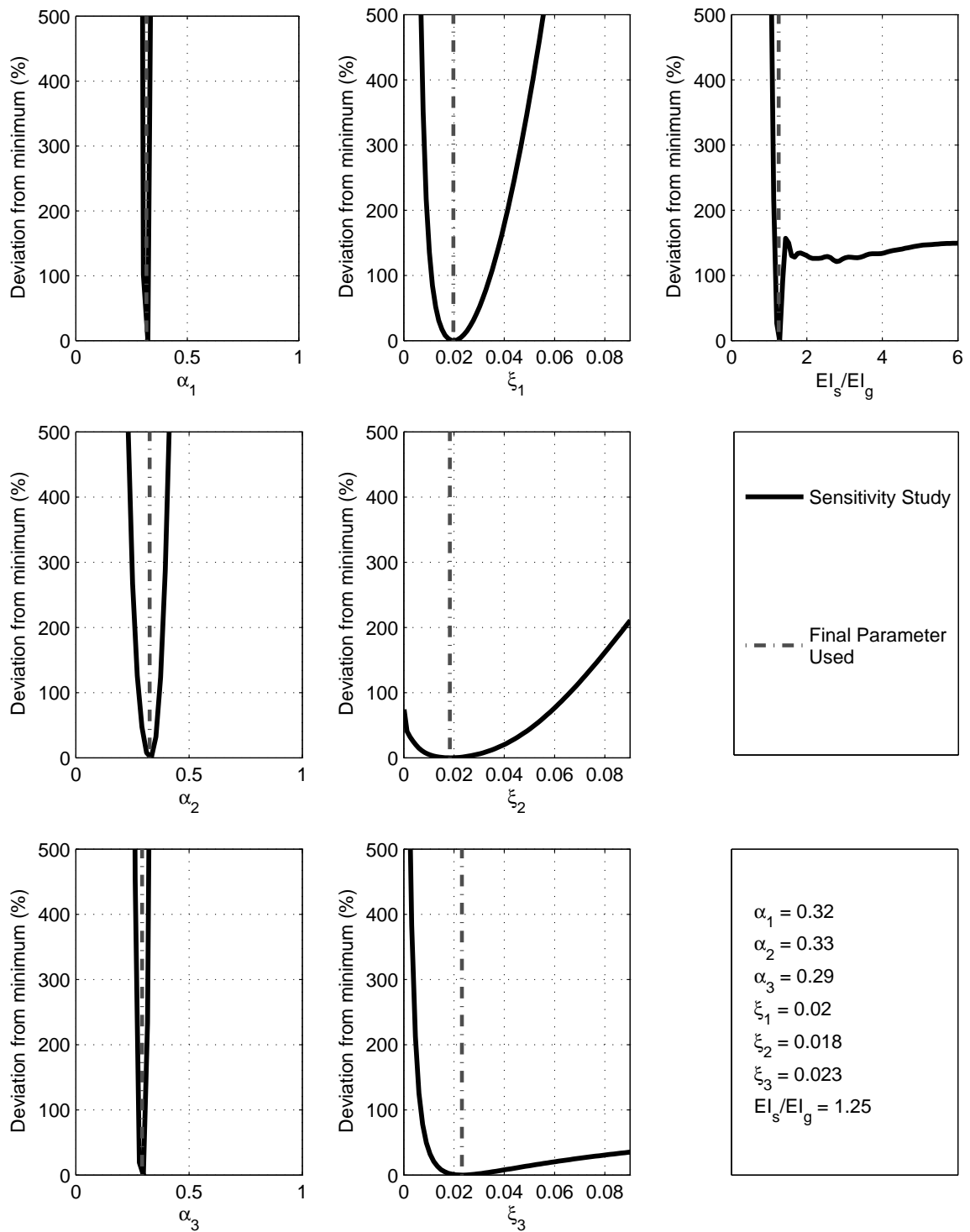
Figure 6.10: Sensitivity study for SQ1112B

6.6 Influence of using Acceleration and Displacement Data

Displacement data were recorded during the shaking table tests at the same locations as the recorded acceleration data, which provided an opportunity to compare the system identification results using the two sets of data. The identified modal properties of the shaking table specimen using displacement data are provided in Appendix F.

Fig. 6.11 shows the periods identified with the ARX algorithm using acceleration and displacement data. As seen in Fig. 6.11, the mode 1 period identified with displacement data is slightly higher than that identified with acceleration data for all excitation types. There were also small differences in the mode 2 period, most notably during the square wave tests.

The mode 3 period was the most difficult to identify using the displacement data for both the earthquake excitations and the square-wave excitations. This was attributed to the small contribution of mode 3 to the overall response of the system and the high noise to peak signal ratio in the bent 3 displacement data (see Section 4.4). For example, during the low-amplitude earthquake excitations, the average noise in the bent 3 data was approximately 30% of the peak displacement response. The maximum noise/peak ratio occurred during Tests 3B and 9A, where the ratio increased to approximately 55%. Noise in the acceleration data was much less prevalent. The maximum noise/peak ratio occurred in bent 2, with an average value of 5%.

Using displacement data the ARX and SLP algorithms overestimated the mode 2 and 3 damping ratios for all excitation types. Taking the ARX algorithm as an example, the mean damping ratio during the white-noise tests identified with acceleration data was 2.75%. Using displacement data, the average mode 2 damping ratio was estimated as 17.5%, 540% higher. As discussed in the previous paragraph, mode 3 was misidentified using the ARX algorithm, so the damping ratios are expected to be different.

The difficulty in identifying the modes of the shaking table specimen using displacement data was also evident in the identified mode shapes. The complete set of identified modal parameters (periods, damping ratios, and mode shapes) using displacement data for both the SLP algorithm and the ARX algorithm are presented in Appendix F.
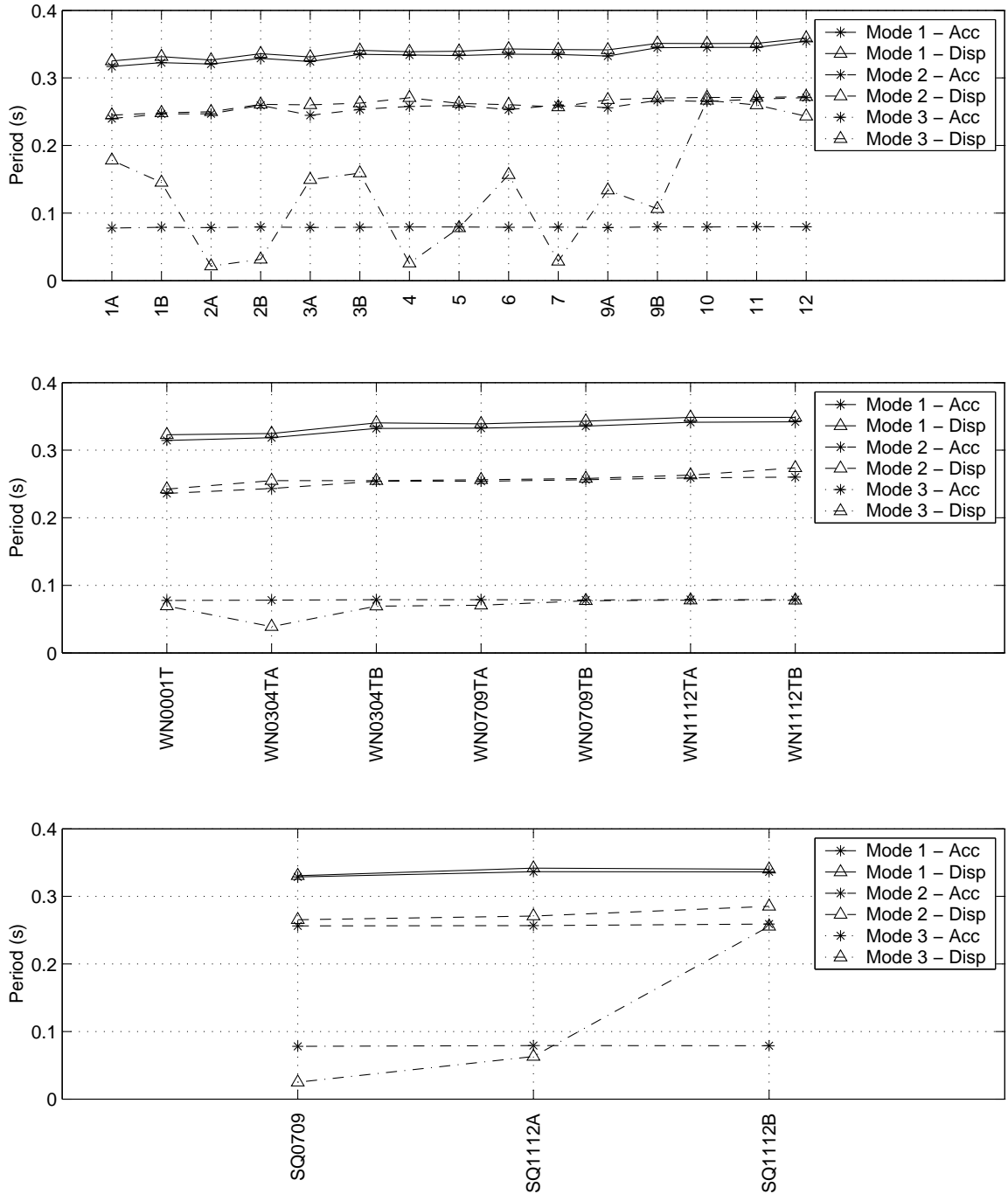
Figure 6.11: Identified periods using acceleration and displacement data for (a) low-amplitude, (b) white-noise, and (c) square-wave excitations

6.7   Influence of using Input/Output and Stochastic Algorithms

This section compares the modal periods identified with the non-parametric input/output algorithm (ARX) with those identified using two stochastic (output-only) algorithms (AR and SSI). Fig. 6.12 shows the results for these three algorithms. The mean values for the periods identified with the two stochastic algorithms was slightly larger than the mean values using the ARX algorithm. For example, the mean identified periods for mode 1 during the earthquake excitations is 0.33s (ARX), 0.37s (AR), and 0.39 (SSI). Also, the identified mode 1 period fluctuated from test to test by up to 0.04s using the AR algorithm (from Test 3A to Test 3B) and by up to 0.08s using the SSI algorithm (from Test 3A to Test 3B). The fluctuation using the ARX method is less than 0.01 seconds.

There were also large differences between the identified damping ratios using the input/output algorithm (ARX) with those using the stochastic algorithms (AR and SSI). Fig. 6.13 shows the damping ratios identified with the three algorithms for the three types of excitations. The damping ratios identified with the stochastic algorithms are closest to those identified using the ARX algorithm for the white-noise excitations. In contrast, there were large differences between the damping ratios for the earthquake and square-wave excitations. For example, using the ARX algorithm, the average mode 1 damping ratio during the earthquake excitations was 1.88%. Using the stochastic AR and SSI algorithms, the estimated damping ratios for this mode were 6.98% and 11.15%. The ranges of the estimated damping ratios were much larger while using the stochastic algorithms as well. For example, under earthquake excitation, the mode 1 damping ratio identified with the SSI algorithm varied from 5.63% to 16.78%.

Differences between the input/output algorithms and the stochastic algorithms are expected when the input excitation has non-random frequency content (such as the earthquake excitations). Nonetheless, a difference in the identified periods of the structure was also found when the target input of the system was white-noise, where there are no predominant frequencies. This is likely due to a difference in the target and achieved white-noise excitations. The frequency content of the excitations at the three bents for Test WN1112TB is shown in Fig. 6.14.

The target white noise excitation had an unbiased frequency content from 0 to 30 Hz. As seen in Fig. 6.14, the content of the input excitations was larger at multiple periods, most notably at a period near 0.4s. This peak is near the first mode of the shaking table specimen. Because the frequency of the excitation is indistinguishable from the frequency content of the structure using output-only identification algorithms, this raised the identified periods of the structure for modes 1 and 2.
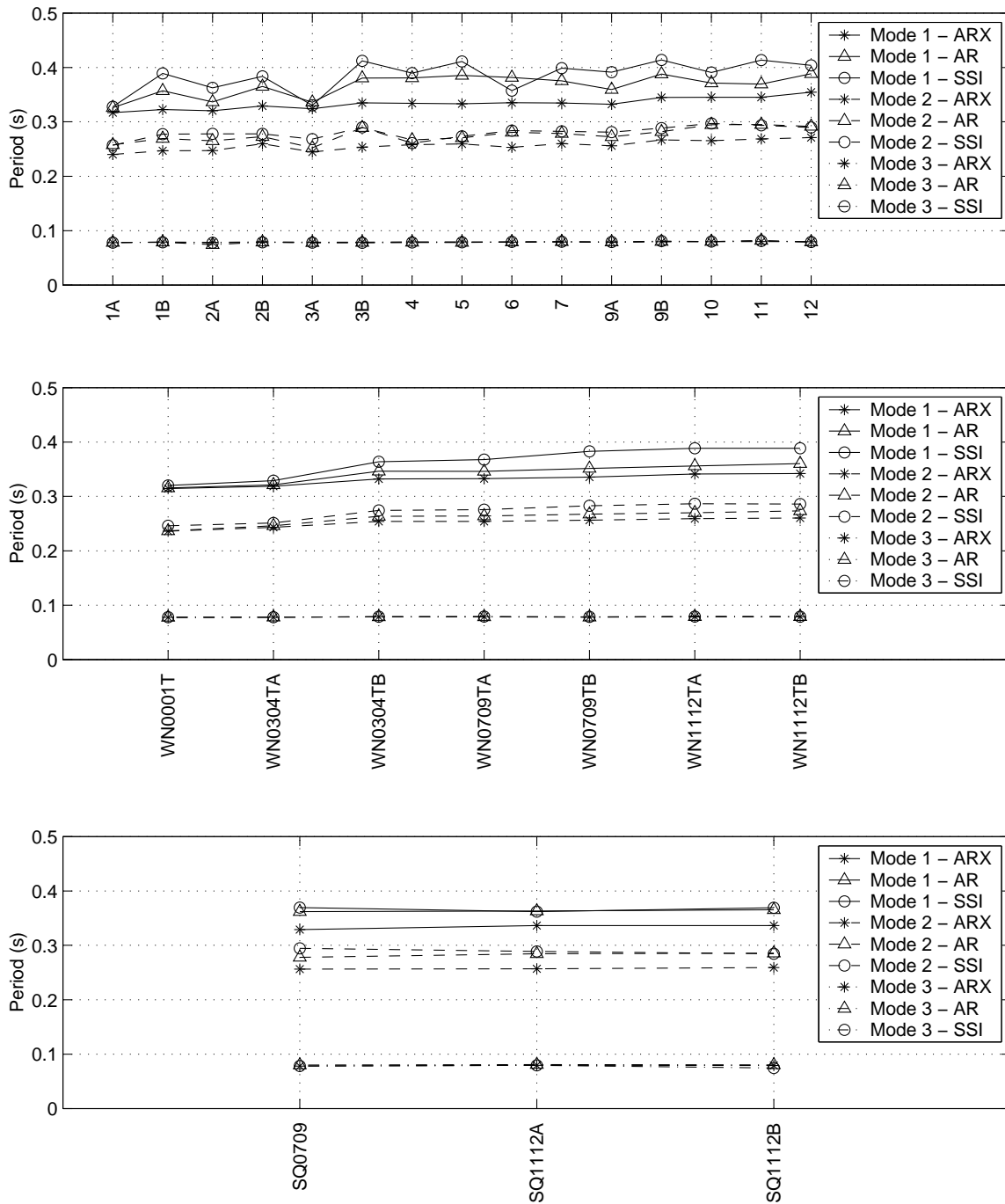
Figure 6.12: Identified periods using output-only and input/output algorithms for (a) low-amplitude, (b) white-noise, and (c) square-wave excitations

123
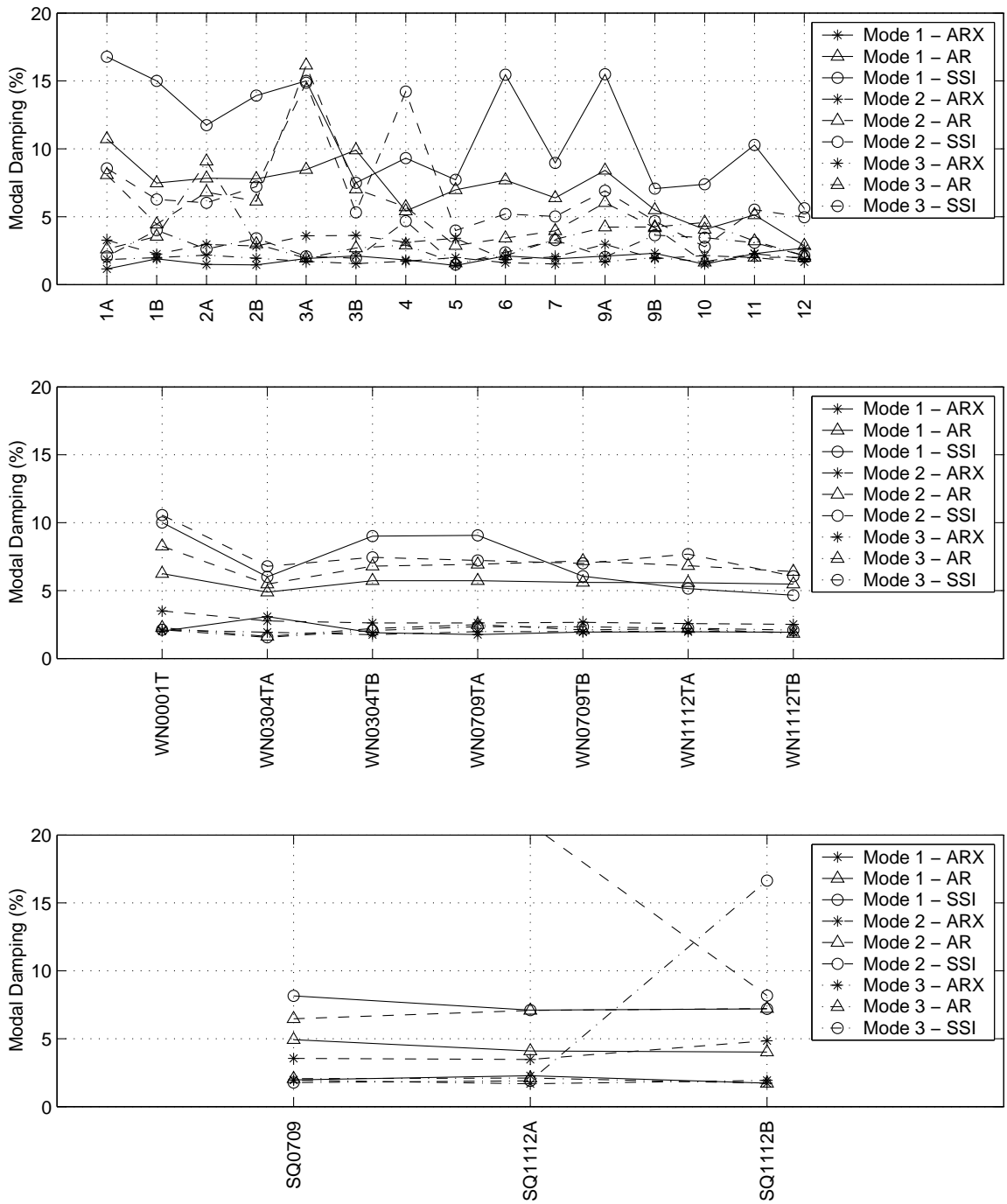
Figure 6.13: Identified damping ratios using output-only and input/output algorithms for (a) low-amplitude, (b) white-noise, and (c) square-wave excitations
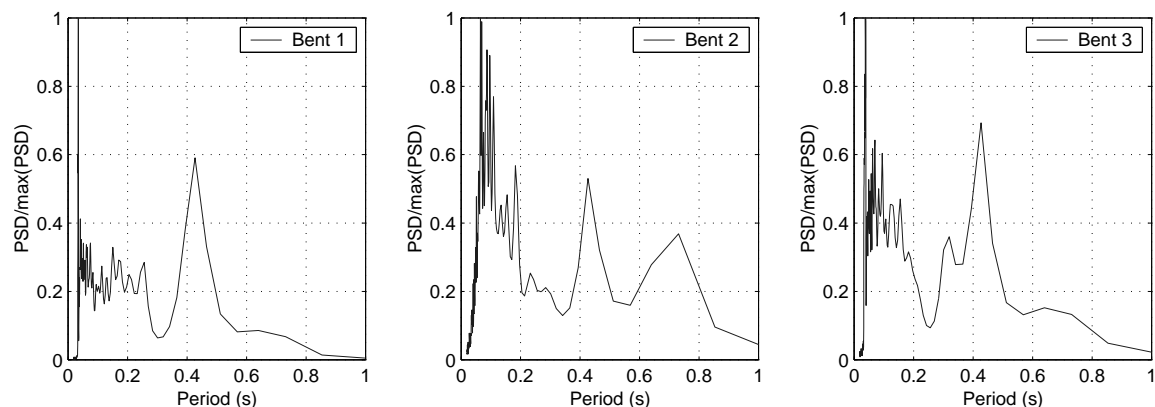
Figure 6.14: Frequency content of base accelerations for WN1112TB

6.8 Summary and Conclusions

Shaking table tests were performed in the NEES site at the University of Nevada, Reno on a two-span quarter-scale reinforced concrete bridge. Tests conducted on the bridge were separated into low-amplitude and high-amplitude tests. The low-amplitude tests included earthquake excitations (15 tests), white-noise excitations (7 tests) and square-wave excitations (3 tests). Data from these low-amplitude tests provided a unique opportunity to evaluate the ability of various algorithms and excitation types to accurately identify the modal properties of the structure. The effectiveness of each of the methodologies for identifying the system was assessed by comparing the identified modal properties. A summary of the findings of this research is listed in Table 6.21. Each of the components to this table are discussed in the following sections.

Table 6.21: Conclusions from the comparison of modal identification strategies

Algorithm	Data Use	Response	User Expertise	Comput. Demand	Ident. Consistency	Total Ident.
SLP	Input/Output	Acceleration	Low	High	High	Yes
ARX	Input/Output	Acceleration	Medium	Medium	High	Yes
SLP	Input/Output	Displacement	Low	High	Medium	No
ARX	Input/Output	Displacement	Medium	Medium	Medium	No
AR	Output-Only	Acceleration	Medium	Medium	Low	Yes
SSI	Output-Only	Acceleration	High	Low	Low	Yes

6.8.1 Modal Property Identification

Two input/output identification algorithms (ARX and SLP) were used to identify the modal properties of the shaking table specimen for three excitation types (earthquake, white-noise, and square-wave). For both algorithms and all excitation types, the average periods for the first three modes were identified as 0.33s, 0.26s, and 0.078s. Modes higher than mode three were not identified from the algorithms due to their small participation in the dynamic response of the system, measurement noise, and the sampling frequency of the data acquisition system.

The identified damping ratios of the first three modes ranged from 1% to 4% for almost all excitations using both algorithms. The few identified damping ratios that were outside of this range occurred with mode 2. The large range for the identified damping ratios was due to the small influence of deviations in the values of the damping ratios on the structural response.

The first three mode shapes of the shaking table specimen involved combinations of translation, in-plane twisting, and bending. For the earthquake excitations, mode 1 was composed of slab translation (87%) and slab twisting (12%). Mode 2 was composed of slab twisting (76%) and slab translation (24%). Mode 3 was composed of slab bending (92%) and slab translation (7%). with a smaller component of slab twisting.

6.8.2 Sensitivity Analysis

The SLP algorithm estimates the modal properties of the structure by first calibrating the structural parameters of the bridge (bent stiffnesses, deck stiffness, and modal damping ratios). This allowed a study to be conducted to investigate the sensitivity of the structure to the individual structural parameters.

The sensitivity study using the SLP algorithm found that the structure was most sensitive to deviations in the bent stiffnesses and the slab modulus of rigidity. For all excitation types, the objective function was less sensitive to the three damping ratios. The mode 3 damping ratio was the least influential parameter. This was attributed to the small influence of mode 3 on the dynamics of the system. Because the mode 3 contribution is already

small, a slight change in the mode 3 contribution would have little effect on the system. The insensitivity of the objective function to the damping ratios is responsible for the large scatter in the identified damping using both the ARX and SLP algorithms.

6.8.3   Influence of Input/Output Algorithm Type

Two input/output identification algorithms were used to estimate the modal properties of the structure. The autoregressive with exogenous excitation (ARX) algorithm was used to estimate the properties of the structure non-parametrically from the base and bent accelerations (Multi-Input/Multi-Output). This algorithm does not use any prior knowledge of the structural parameters to make the estimations (non-parametric). The successive linear programming (SLP) algorithm determined the modal parameters parametrically by performing an eigen-analysis on a calibrated model of the specimen. This model was calibrated based on a best-fit of the measured acceleration response at five locations along the bridge deck.

Both the non-parametric (ARX) and the parametric (SLP) input/output algorithms gave similar results for the estimations of the periods, damping ratios, and predominant components of the mode shapes of the first three modes of the shaking table specimen for all excitation types. For example, the ratios of the periods estimated with the ARX algorithm to those estimated with the SLP algorithm ranged from 0.96 to 1.02.

The ratios of the damping ratios estimated with the ARX algorithm to those estimated with the SLP algorithm ranged from 0.45 to 1.64. This larger range was attributed to the insensitivity of the structural response to small changes in the damping ratios.

The value of the basis vector component of each mode shape was similar for the two algorithms. Taking the average results from the earthquake excitations as an example, the ARX algorithm estimated that basis vector 1 made up 87% of mode 1. Using the SLP algorithm, this value was 83%.

6.8.4   Influence of Excitation Type

Three types of motions (earthquake, white-noise and square-wave) were used to excite the shaking table specimen during the low-amplitude tests. Because the ARX and the SLP

algorithm both account for the frequency content of the excitation, there was very little difference between the periods identified with the two algorithms. Using the ARX algorithm as an example, the mode 1 period identified during Test 7 was 0.335s. The periods identified with the white-noise and square-wave tests directly after Test 7 (WN0709TA and SQ0709) were 0.333s and 0.329s.

The mode 3 damping ratios were also similar for each excitation type. Using the ARX algorithm as an example, the mean damping ratio of mode 1 was identified as 1.85% (earthquake excitation), 2.08% (white-noise excitation), and 1.99% (square-wave excitation).

The mode shapes identified with each algorithm were also insensitive to the excitation type. For example, using the ARX algorithm the mean percentage of mode 1 described by basis vector 1 was 87.4% (earthquake excitation), 85.9% (white-noise excitation), and 89.9% (square-wave excitation).

6.8.5 Influence of Data Measurement Type

Accelerations and displacements were measured along the bridge deck at the same locations. The ARX and SLP algorithms were used to identify the modal properties of the specimen for both the displacement and the acceleration data sets. With the results, the influence of frequency content and noise content within the measured data was investigated.

Modal estimates were not as consistent using displacement data as those using acceleration data. The mode 1 and 2 periods identified using displacement data were slightly larger than those using acceleration data for all excitation types. Also, mode 3 was difficult to capture using displacement data for earthquake and square-wave excitations. This was attributed to the high level of noise in the bent 3 data, which reached 55% of the peak displacement response. Noise in the acceleration data only reached 5% of the peak acceleration response.

6.8.6 Influence of input/output and stochastic algorithms

A common practice for in-situ structural identification of bridges is to use only the output response of the structure to identify the modal properties using stochastic (output-only)

algorithms. These algorithms give the correct modal properties of the structure if the input excitation is white-noise. However, without the input data, the frequency content of the ground motion are indistinguishable from the modal properties of the bridge. This research investigates the influence of frequency content within the input motion on the identified modal properties by using both input/output and output-only algorithms.

The modal properties using the stochastic (output-only) identification algorithms (AR and SSI) deviated much more than those using the ARX algorithm. During the earthquake excitations, the identified periods for modes 1 and 2 deviated from test to test by as much as 0.04s using the AR algorithms and up to 0.08s using the SSI algorithm. The deviation of the periods using the ARX algorithm was less than 0.01s. The mean mode 1 and 2 periods estimated with the stochastic algorithms were slightly larger than those using the ARX algorithm for all excitation types. For example, the mean mode 1 period for the low-amplitude earthquake excitations was identified as 0.33s (ARX), 0.37s (AR) and 0.39s (SSI).

Chapter 7

MODEL DEVELOPMENT
(SHAKE-TABLE TESTS)

A three-dimensional numerical model was developed in OpenSees (OpenSees Development Team, 2002) to simulate the dynamic response of the 2-span, quarter-scale shaking table specimen. The initial model was developed prior to the shaking table tests to aid in developing the ground motion protocol. Fig. 7.1 illustrates the OpenSees model of the shaking table specimen. Each of the components in this illustration are discussed in the following sections. The development of the components of the numerical model (Table 7.1) is discussed within this chapter.

Table 7.1: Components of the OpenSees model

Model Component	Section
Column Modeling	7.1
Cross-Beam Modeling	7.2
Slab Modeling	7.3
Mass Distribution	7.4
Numerical Procedures	7.5
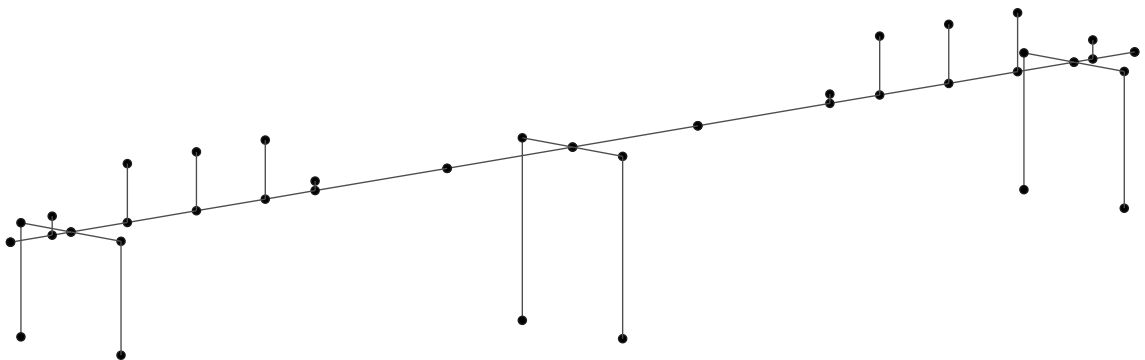
Figure 7.1: Illustration of the OpenSees model

The model calibration procedure, performed following the shaking table tests, is documented in Chapter 8. Chapter 8 also evaluates the analytical model.

7.1 Column Modeling

The columns of the shaking table specimen were modeled in OpenSees with distributed-plasticity forced-based elements (nonlinearBeamColumn). Distributed plasticity elements were used to capture the local strain response at the column-anchorage interfaces. A distributed plasticity model also provides a consistent transition between a fixed-base model (the shaking table specimen) and a model with drilled shaft foundations (the centrifuge specimen). This consistent transition was necessary for investigating the effects of soil-foundation-structure interaction.

Using a distributed plasticity model allows the flexibility due to the column and the flexibility due to the anchorage slip to be modeled separately. The components of the column elements are presented in Table 7.2 and illustrated in Fig. 7.2.

Table 7.2: Column components in the OpenSees model

Column Components	Section
Nonlinear Material Models	7.1.1
Elastic Response Components	7.1.2
Column Cross-Section Discretization Scheme	7.1.3
Integration Scheme	7.1.4
Anchorage Slip	7.1.5

As displayed in Fig. 7.2, the columns were composed of four main components. The inelastic flexural response of the columns were modeled using nonlinear elements (nonlinearBeamColumn), which required a cross-section to be defined at each of the integration points. The elastic shear and torsional flexibilities of the specimen were added to the element. Additionally, the flexibility due to anchorage slip was modeled in OpenSees with a zeroLengthSection element. Each of the column components are discussed in the following sections.

7.1.1 Nonlinear Material Models

The flexural response of the nonlinearBeamColumn elements was developed using the measured concrete and steel properties from the shaking table tests. The compressive strength
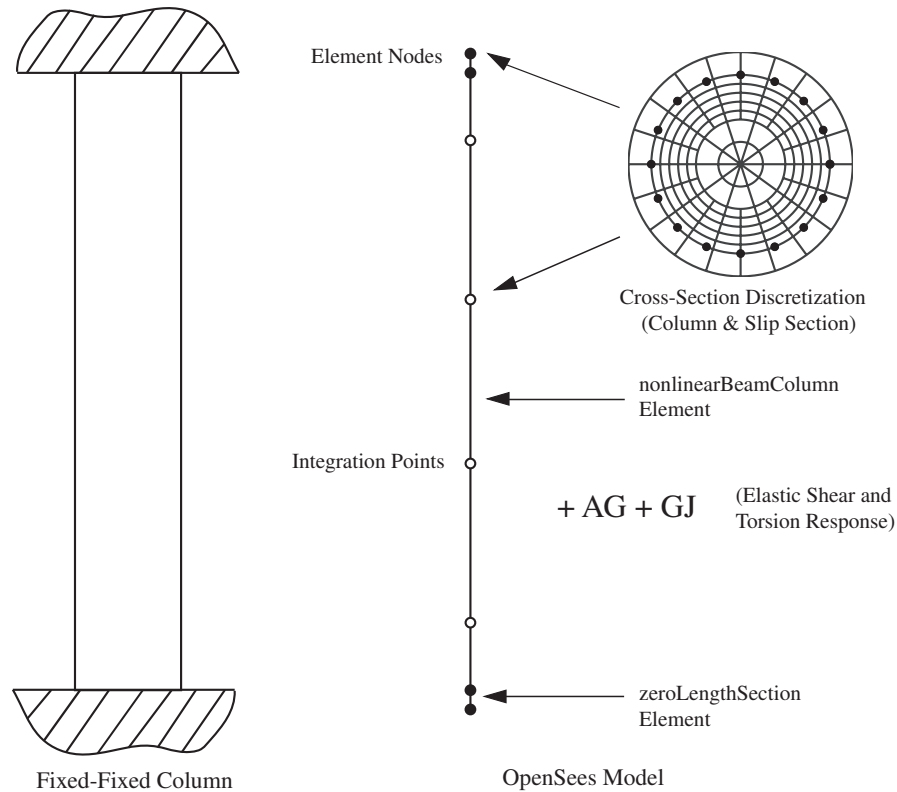
Figure 7.2: Elements of the numerical column model

of the concrete was determined from cylinder tests near the day of testing (Table 4.3). The concrete was modeled in OpenSees using the Popovics curve with parameters determined from the Mander confinement model (Mander et al., 1988). The amount of column confinement was determined from the reinforcement detailing (Appendix B). The properties of the unconfined and confined concrete parameters used in the numerical model are shown in Table 7.3. The Popovics curves for the unconfined and confined concrete are shown in Fig. 7.3. The concrete was modeled in OpenSees using the Concrete04 constitutive model.

Table 7.3: Concrete test properties

Concrete	$f'_c(psi)$	ϵ_{co}	ϵ_{cu}	$E_c(ksi)$
Cover	5900	0.002	0.004	4400
Core	7800	0.005	0.017	4400
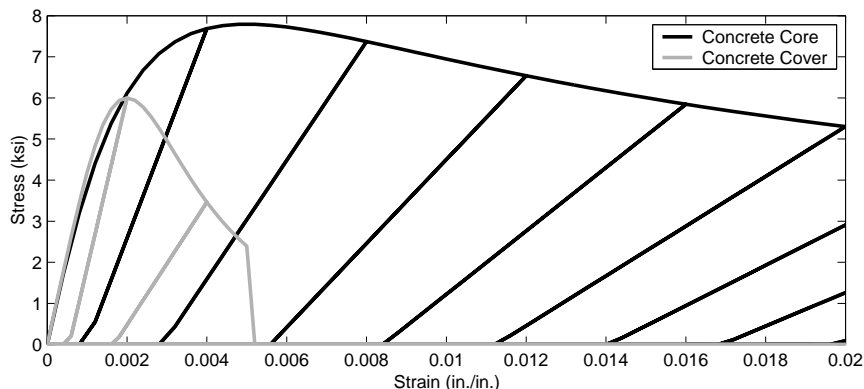
Figure 7.3: Confined and unconfined concrete models.

Three coupon tests of the longitudinal reinforcement were conducted at the University of Nevada, Reno. The measured stress-strain relationships from these three tests are shown in Fig. 7.4. The elastic modulus of the steel was estimated as the average of the three computed elastic moduli from the coupon tests (29050 ksi). The remainder of the stress-strain curve was fit using a Giuffre-Menegotto-Pinto curve (Taucer et al., 1991) up to a strain of 0.10 in/in. The parameters for the calibrated steel model are presented in Table 7.4. The estimated stress-strain response using these parameters is shown in Fig. 7.4. The steel was modeled in OpenSees using the Steel02 constitutive relationship with the parameters in Table 7.4.

Table 7.4: Estimated steel properties

Property	E_s (ksi)	E_{sh} (ksi)	R	σ_0 (ksi)
Reinforcement	29050	191	2.32	81.5

7.1.2 Elastic Response Components

The nonlinearBeamColumn element provides nonlinear flexural response. Elastic shear and torsional flexibilities were estimated based on gross-section properties of the column. These elastic components of the column response were aggregated into the inelastic flexural
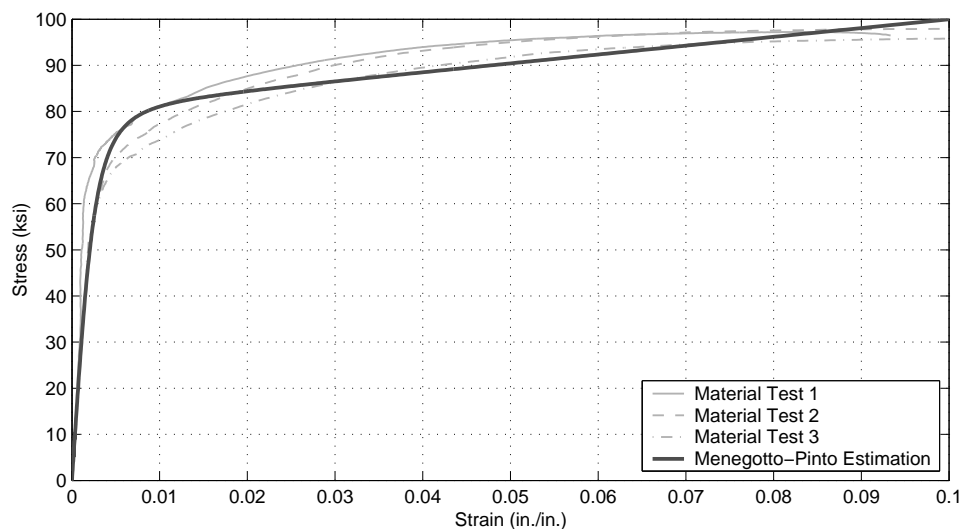
Figure 7.4: Three steel coupon tests and calibrated Giufre-Menegotto-Pinto steel model.

response of the column element. The shear modulus of the concrete (1800 ksi) was calculated using a Poisson's ratio of 0.2 and the measured concrete compressive strength reported in Chapter 8 (5900 psi).

7.1.3 Column Cross-Section Discretization Scheme

The nonlinearBeamColumn element requires a cross-section to be defined at each of the integration points. The cross-section was modeled in OpenSees with a series of fiber elements, each fiber having an independent constitutive relationship. An accurate estimation of the column behavior requires accurate modeling of the column cross-section. Increasing the discretization of the cross-section reduces mesh sensitivity but increases computational demands. A balance between convergence and computational efficiency was determined by Berry (2006).

In this study, Berry compared the moment-curvature relationships for various column discretization schemes to those from a fully discretized section for 75 circular spirally-reinforced flexure-critical concrete columns from the UW-PEER column database (Berry et al., 2004). The convergence study found that the discretization scheme presented in Ta-

ble 7.5 (Fig. 7.5), which uses a constant discretization scheme for the entire core, adequately modeled the moment-curvature behavior while maintaining computational efficiency. Because the columns had circular sections, the fibers were defined by radial and tangential discretizations.

Table 7.5: Cross-section discretization

Section	Disc. Dir.	Disc. #		Section	Disc. Dir.	Disc. #
cover	tangential	20		cover	tangential	20
	radial	1			radial	1
core	tangential	20		inner core	tangential	10
	radial	10			radial	2
				outer core	tangential	20
					radial	5
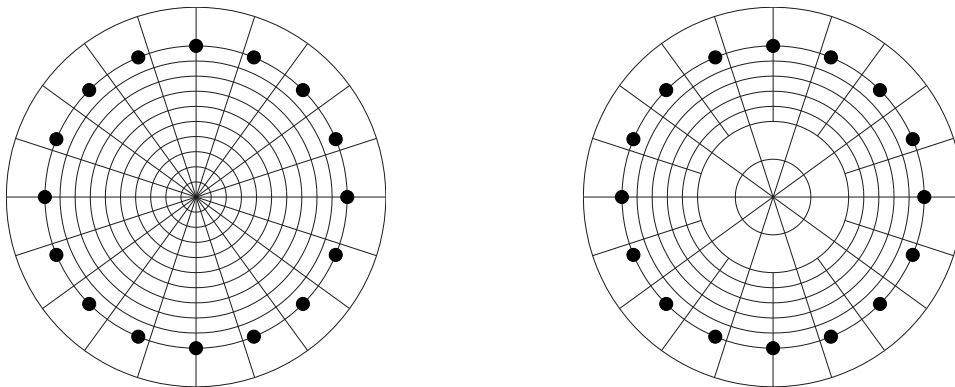
Figure 7.5: Column cross-section discretization

Berry found that computational demands could be reduced significantly without sacrificing convergence if the core was non-uniformly discretized. A moment-curvature analysis of the column section of the shaking table specimen determined that the depth of the neutral axis at first yield of the longitudinal reinforcement was approximately 29% of the column diameter. Since the inner half of the concrete core does not extend into the neutral axis, this part of the core could have less discretization without significantly affecting the results. In his convergence study, Berry found that the best balance between accuracy and efficiency

using a coarser inner core discretization scheme was obtained using the specifications shown in Table 7.5 (Fig. 7.5).

7.1.4 Integration Scheme

The nonlinearBeamColumn element in OpenSees uses the Gauss-Labotto integration scheme. This integration scheme includes integration points at the ends of the member to capture plasticity near the joints. Using this integration scheme, the location of the plasticity of these elements is largely controlled by the extent of hardening in the system and the number of integration points in the element. Berry (2006) investigated the number of integration points needed to best estimate the force-displacement relationship and measured strains for eight ductile columns under double curvature and various hardenings: hardening columns, neutral columns, and softening columns. Based on his findings, Berry suggested using six integration points.

7.1.5 Anchorage Slip

The anchorage rotation due to bond slip was modeled in OpenSees using zero-length fiber sections (zeroLengthSection). This strategy makes it possible to model three-dimensional column response. The zero-length fiber section used the same section discretization as the column elements. To obtain a moment-rotation response from a zero-length section, the fiber properties needed to be stress-displacement relationships. The stress displacement relationship of the steel was modeled as the stress-slip relationship for the anchorage zone, which was calibrated using strain gauge data, and is presented in Chapter 8. The stress-strain relationship of the anchorage concrete was assembled by using the stress-strain relationship of the column core concrete up to f_{co}. Because of the amount of confinement provided by the steel and surrounding concrete within the anchorage zone, the concrete was assumed to not degrade following the peak concrete strength. The stress-displacement relationship for the anchorage concrete was assumed to be this assembled stress-strain relationship, multiplied by an effective concrete depth over which an assumed constant stress acts.

This effective concrete depth was calibrated by Berry (2006) using eight test columns

from the UW-PEER column database (Berry et al., 2004). He found that the bond-slip rotation was adequately modeled when the effective concrete depth was estimated as the depth to the neutral axis (d) at the first yield of the longitudinal yield (ϵ_y). From a moment-curvature analysis of the shaking table columns, the neutral axis depth at first yield of the longitudinal reinforcement was determined to be approximately 29% of the column diameter (D) (Fig. 7.6). As seen in Fig. 7.6, the neutral axis depth levelled off after the initial yield of the longitudinal reinforcement. The stress-displacement relationship for the anchorage concrete is shown in Fig. 7.7.
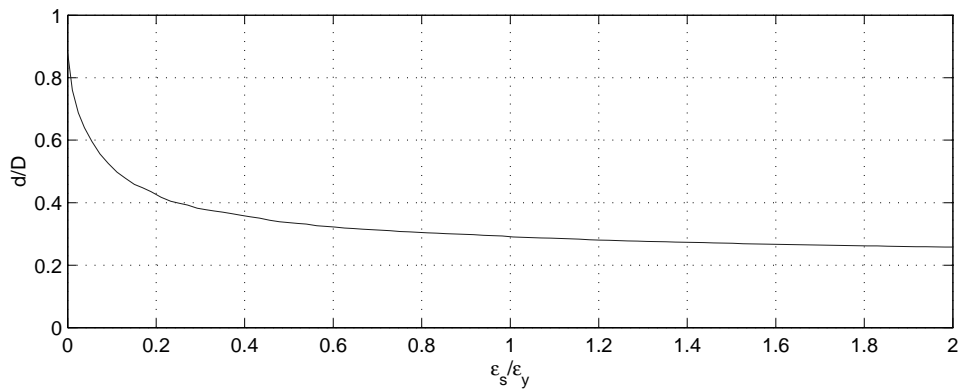
Figure 7.6: Depth of neutral axis as a function of the strain in the longitudinal reinforcement.
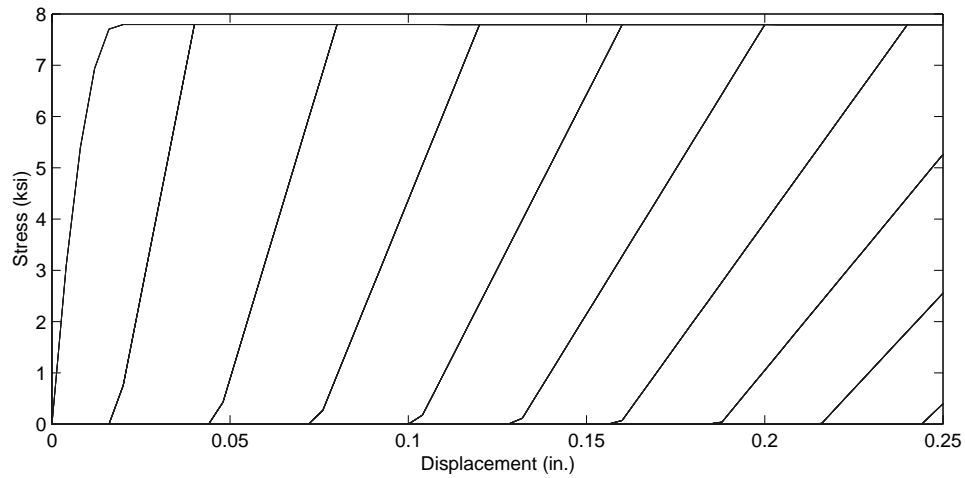
Figure 7.7: Stress-displacement relationship for the anchorage concrete

7.2 Cross-Beam Modeling

The bent cross-beams were modeled in OpenSees using elastic elements (elasticBeamColumn) to represent the cracked effective stiffness of the cross-beam and slab. The appropriateness of this elastic modeling strategy was determined by comparing the yield moment of the cross-beams with the plastic moment capacity of the columns. For example, if the effective width of the cross-beam was approximated as the diameter of the column (12 in.) plus the depth of the slab (15 in.), the yield moment for the cross-beams on bents 1 and 3 is approximately 2000 k-in. This is more than twice the calculated plastic capacity of the columns (750 k-in.). Therefore, the cross-beams in the structure would remain elastic well beyond the plastic moment capacity of the columns, allowing the cross-beam elements to be modeled elastically. The effective width of the cross-beam elements used in the OpenSees model is calibrated in Chapter 8.

7.3 Slab Modeling

The slab was modeled three ways: (1) as a rigid diaphragm directly connecting the tops of the columns, (2) as a beam element (with the same moments of inertia as the slab), connecting to the center of each bent, and (3) as a flat slab using quadrilateral shell elements

(ShellMITC4). An illustration of the three models is shown in Fig. 7.8.
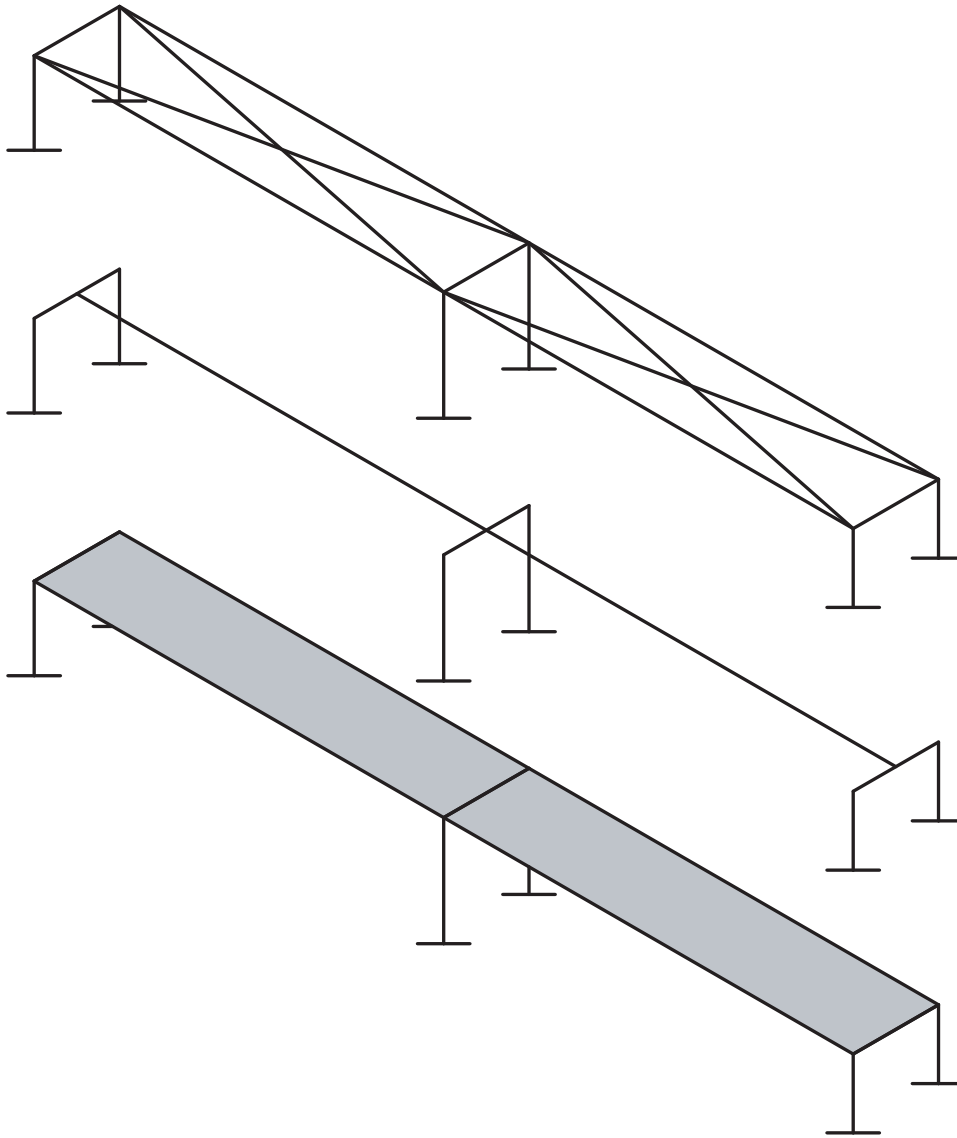
Figure 7.8: Slab types tested in analysis: (a) rigid diaphragm, (b) beam, and (c) flat slab

The rigid diaphragm (Fig. 7.8a) was created by connecting the top of the columns with elastic elements that possessed very stiff properties. "Rigid" elements were not used in OpenSees because of numerical instabilities that occurred during modeling. Because the diaphragm was essentially rigid, all masses and loads were added to the tops of the columns.

Beam elements with the same dimensions of the slab were used to approximate the slab while maintaining the same moments of inertia (Fig. 7.8b). Using this element, the slab self-weight and self-mass were distributed along the length of the beam. Additionally, the external slab weights were modeled as point loads along nodes in the beams, raised to the elevation of the center of gravity of the masses.

The flat slab (Fig. 7.8c) was modeled using quadrilateral shell elements. A slab thickness of 14 in. was used for the interior spans, while a slab thickness of 15 in. was used for the exterior cantilever spans. The masses and loads due to the weight of the slab and the external weight on top of the slab were distributed over the nodes of the slab. The loads due to the vertical curvature of the longitudinal post-tensioning were distributed along the slab. Longitudinal loads and moments were also applied to the nodes at the ends of the slab to simulate the forces at the post-tensioning anchorages.

Preliminary analyses showed that the computational demand using the quadrilateral shell elements was large compared with the other two modeling strategies. The computational demands were much smaller using the rigid diaphragm. Although the response of the rigid diaphragm system was similar to that of the shell element system, the rigid diaphragm system was only able to estimate the first two transverse modes (rigid body translation and rigid body rotation of the slab). It was unable to reproduce the third transverse mode, which was beam bending of the slab.

The computational demands decreased significantly without sacrificing the dynamic properties of the response by using beam elements to model the slab. Therefore, a beam element with the same stiffness properties as the flat slab was used in the OpenSees model.

7.4   Mass Distribution

The mass in the system came from two sources: the self weight of the components of the structure, and the external weights added to the top of the slab to achieve a column axial load ratio of approximately $0.08A_g f_c'$.

The masses due to the self-weight of the bridge components were modeled as point masses. Therefore, to distribute the masses along the slab, the slab was discretized into multiple elements, and the masses were lumped at each node based on tributary area. The

cross-beams were assumed to be massless because this mass was already accounted for in the slab calculations. The mass due to half of the column weight was lumped at the top of each column.

The masses due to the external weights on top of the slab were lumped at nodes above the slab elements at the location of the center of gravity of the external weights. These nodes were connected to slab nodes directly beneath them with rigid links.

Masses were only modeled in the transverse and longitudinal directions due to numerical problems when vertical masses were applied. The vertical loads in the system were assumed to be the system mass multiplied by the acceleration of gravity. The vertical system loads were placed at the same locations as the masses.

7.5   Numerical Procedures

The Newton-Raphson algorithm was the default method for advancing to the next time step in the OpenSees analysis. If this method failed to converge within a tolerance of 1E-8 after 1000 iterations, the algorithm was temporarily switched to the modified Newton-Raphson algorithm. To reduce computational demand, this algorithm was switched back to the Newton-Raphson algorithm once convergence was obtained.

The Newmark average acceleration method (Newmark, 1959) was used as the integration algorithm in OpenSees. The suggested values of $\gamma = 0.5$ and $\beta = 0.25$ were used to create an unconditionally stable integration algorithm and to minimize errors associated with numerical damping.

Chapter 8

MODEL CALIBRATION AND ASSESSMENT
(SHAKE-TABLE TESTS)

Following the shaking table tests, the numerical model was refined by calibrating parameters specific to the shaking table specimen (e.g., bond stress, damping ratios) through comparisons with measured data. The calibrated parameters are presented in Table 8.1. Table 8.1 also shows the measurements that were used to calibrate each parameter. The calibration procedure for each of the parameters is discussed within the first three sections of this chapter.

Table 8.1: Calibration Parameters

Parameter	Calibration Source	section
Average Bond Stress	Strain Gauge Comparisons	8.1
Effective Beam Width	Drift - Joint Rotation Envelopes	8.2
Modal damping ratios	System Identification	8.3

Each of the specimen specific parameters was independently calibrated using measured data. The last four sections in this chapter evaluate the ability of the numerical model to simulate the global response of the shaking table specimen. For this evaluation, the 23 earthquake excitations (up through Test 20) were applied to the OpenSees model in series to include the accumulation of structural damage. The response quantities that are evaluated for this model are outlined in Table 8.2.

Table 8.2: Assessment Parameters

Parameter	Assessment Source	section
Total Base Shear	Accelerometer Data	8.4
Displacement Maxima	Potentiometer Data	8.5
Modal Properties	Accelerometer Data and System I.D.	8.6
Displacement Histories	Potentiometer Data	8.7

8.1 Anchorage Slip Calibration

The stress-slip displacement relationship of the column anchorages was based on a two-component bond stress model (Lehman, 1998). The model was modified to account for development of bond stress at low bar strains. An illustration of the model is presented in Fig. 8.1.
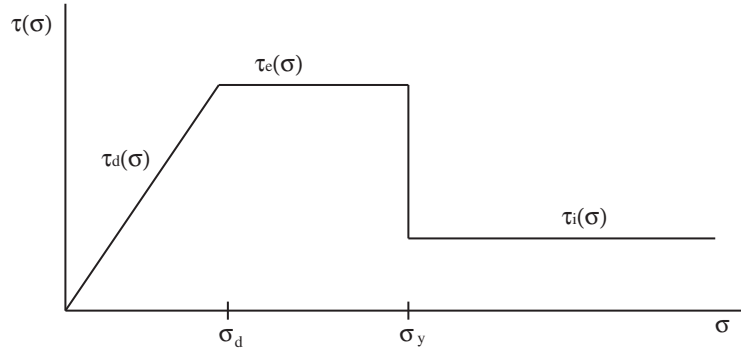
Figure 8.1: Bond model illustration

In Fig. 8.1, σ is the axial stress in the longitudinal reinforcement, σ_d is the axial stress in the reinforcements in which the bond stress is fully developed, and σ_y is the yield stress of the reinforcement. $\tau_d(\sigma)$ is the developing bond stress, linearly related to the axial stress in the reinforcement below σ_d. $\tau_e(\sigma)$ is the elastic bond stress, which is considered to be constant between σ_d and σ_y. $\tau_i(\sigma)$ is the bond stress between the concrete and the reinforcement after the bars have yielded (inelastic bond stress). The components of the model are described in Eq. 8.1,

$$\tau(\sigma) = \begin{cases} \tau_e \dfrac{\sigma}{\sigma_d} = a \dfrac{\sigma}{\sigma_d} \sqrt{f_c'} & \sigma \leq \sigma_d \\ \tau_e = a\sqrt{f_c'} & \sigma_d \leq \sigma \leq \sigma_y \\ \tau_i = b\sqrt{f_c'} & \sigma_y \leq \sigma \end{cases} \tag{8.1}$$

where a and b are the elastic and inelastic bond stress coefficients respectively. Using the bond stress defined in Eq. 8.1, the change in strain (change in stress) along the length of

the reinforcement is described by the differential equation presented in Eq. 8.2.

$$\frac{dF}{dx} = \frac{\pi d_b^2}{4}\frac{d\sigma}{dx} = \tau(\sigma)\pi d_b$$
$$\frac{d\sigma}{dx} = \frac{4\tau(\sigma)}{d_b}$$

(8.2)

The three parameters of the bond model (σ_d, a, and b) were calibrated by comparing the strains measured in the columns at the anchorage-column interface with the strains measured six inches within the anchorage at 24 locations within the shaking table structure. An illustration of the strain gauge layout for each column is shown in Fig. 8.2. Of the 24 possible strain gauge sets, measurements from both of the strain gauges were reliable up to an interface strain of 0.015 in/in for 14 sets. The envelopes of the interface gauge strains versus the anchorage gauge strains for the 14 strain gauge sets are shown in Fig. 8.3.
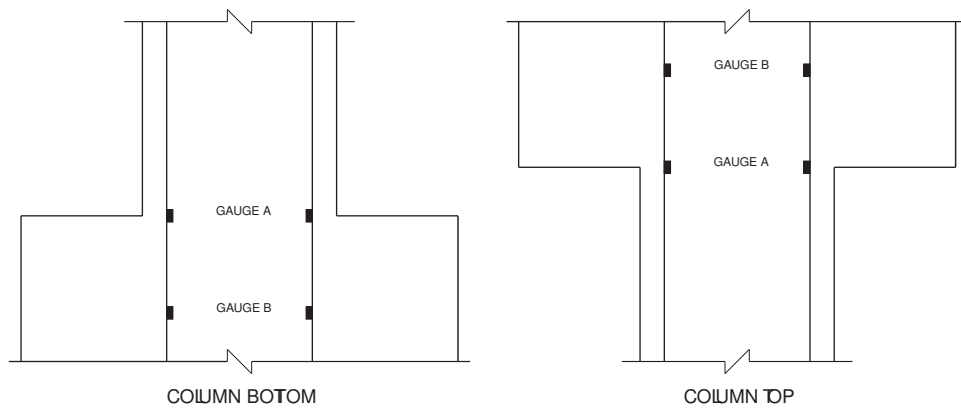
Figure 8.2: Strain gauges used for anchorage slip calibration

The best fit of the envelopes from the 14 strain gauge sets shown in Fig. 8.3 was realized using elastic and inelastic bond stress coefficients of $a = 8$ and $b = 4$, and a development stress of $\sigma_d = 0.25\sigma_y$. Using these parameters, the stress-slip relationship for the reinforcement was determined by integrating the strain across the bar for a given interface bar stress (Fig. 8.4). A bilinear hysteretic material was used in OpenSees to model this stress-slip behavior. The bilinear approximation is shown in Fig. 8.4. The parameters for the bilinear model are shown in Table 8.3.

Table 8.3: Properties for the stress-slip model in OpenSees

Property	E (ksi)	E_{sh} (ksi)	σ_0 (ksi)
Reinforcement	5000	150	81.5
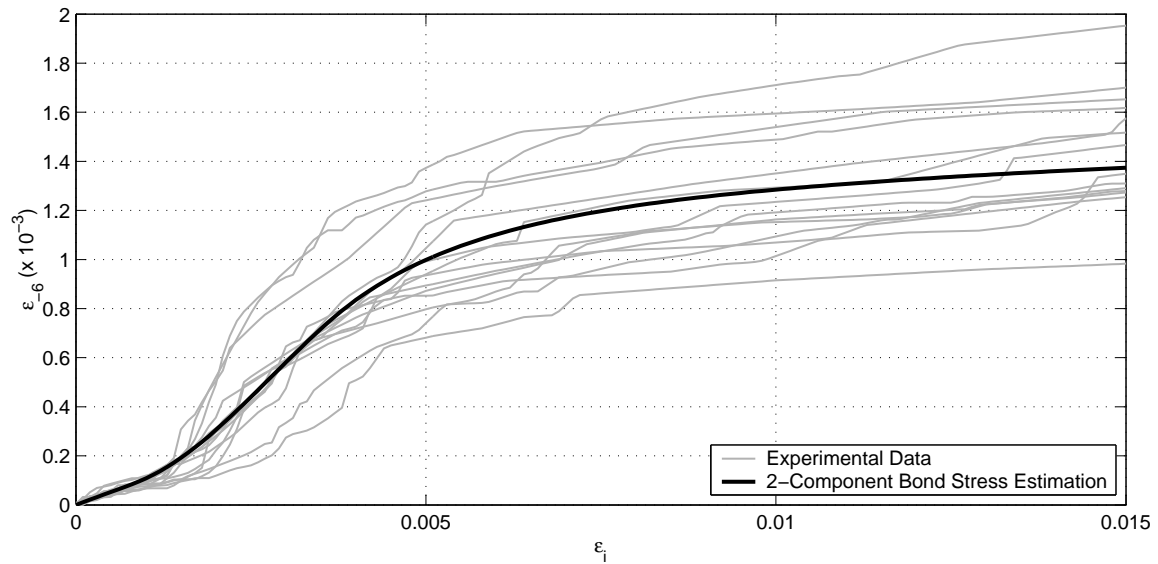
Figure 8.3: Strain gauge envelopes with best fit using the 2-component bond stress model.
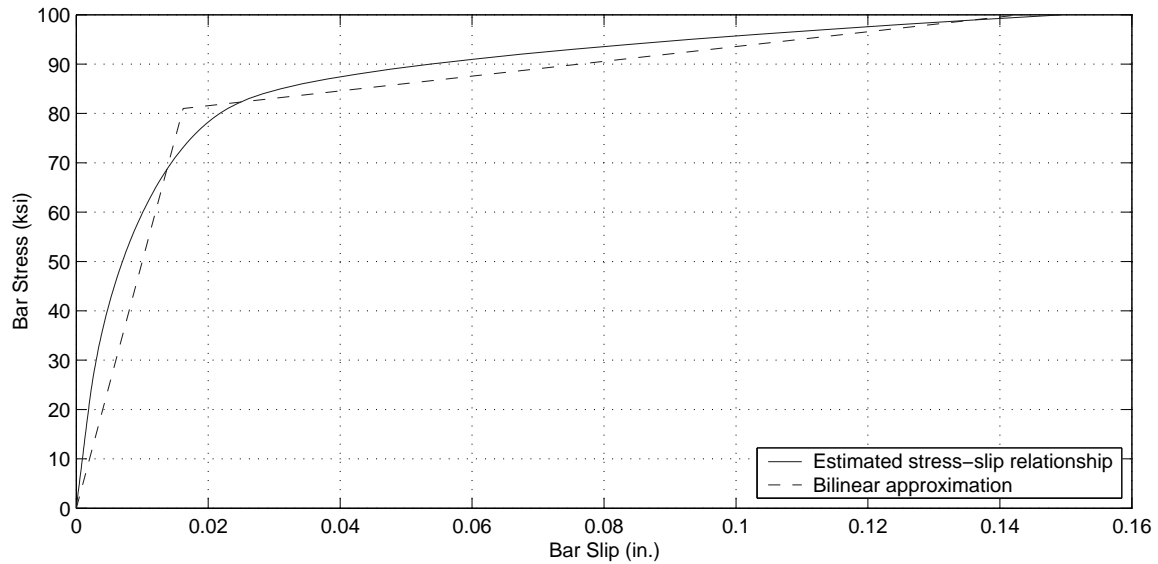
Figure 8.4: Estimated stress-slip relationship using modified 2-component bond stress model and bilinear approximation

8.2   Effective Beam Width Calibration

The effective beam width for the bent caps was calibrated by comparing the column drift-column joint rotation envelopes from a pushover analysis in OpenSees to the envelopes calculated from the measured shaking table data.

The column-beam joint rotation was not measured directly during the shaking table tests. Instead, these rotations were calculated from a series of four vertical displacement measurements along each bent. The process of calculating the column-beam joint rotations is documented in Section 4.7.

As a result of measurement noise in the bent 3 data, and the small contribution of the column joint rotations to the recorded vertical displacements measured along the bent, the bent drift-column joint rotation envelope for bent 3 could not be determined accurately. The envelopes for bents 1 and 2 are shown in Fig. 8.5. The best fit of the measured envelopes for bents 1 and 2 was obtained using a beam width of 25 in (Fig. 8.5). This width is approximately equal to the column diameter plus the slab depth.

Along with the beam-column joint rotation envelopes, the vertical displacement of the beam-column joint were also calculated. These envelopes are also shown in Fig. 8.5. In Fig. 8.5, the west column experiences more tension than the east column during positive drift. Similarly, the west column is in more compression during negative drift. Although for this level of beam width, the column elongation was insensitive to changes in beam width, the envelopes of the column elongation vs. bent drift give confidence to the calculation for the joint rotation. For example, both the simulated data and the measured data show that the west column (tension column during positive drift) elongates more than the east column during positive drift. The simulated envelopes are similar for bents 1 and 2.

Given the reinforcement detailing specified in the design documents for the cross-beams (App. B), the cracked modulus of elasticity of a 27-in. wide beam is 2100 in^4. Because the slab beams were post-tensioned transversely prior to longitudinally post-tensioning them to the cross-beams, it was assumed that the cross beams could crack. Also, the yield moment of the beams was much larger than the plastic moment capacity of the columns. Therefore, the beams would remain in a cracked elastic state throughout the tests. For computational

efficiency, the beam was modeled in OpenSees as an elastic element with the same moment of inertia as the cracked moment of inertia of the inelastic element. This translates into an effective beam width of approximately 9 in.
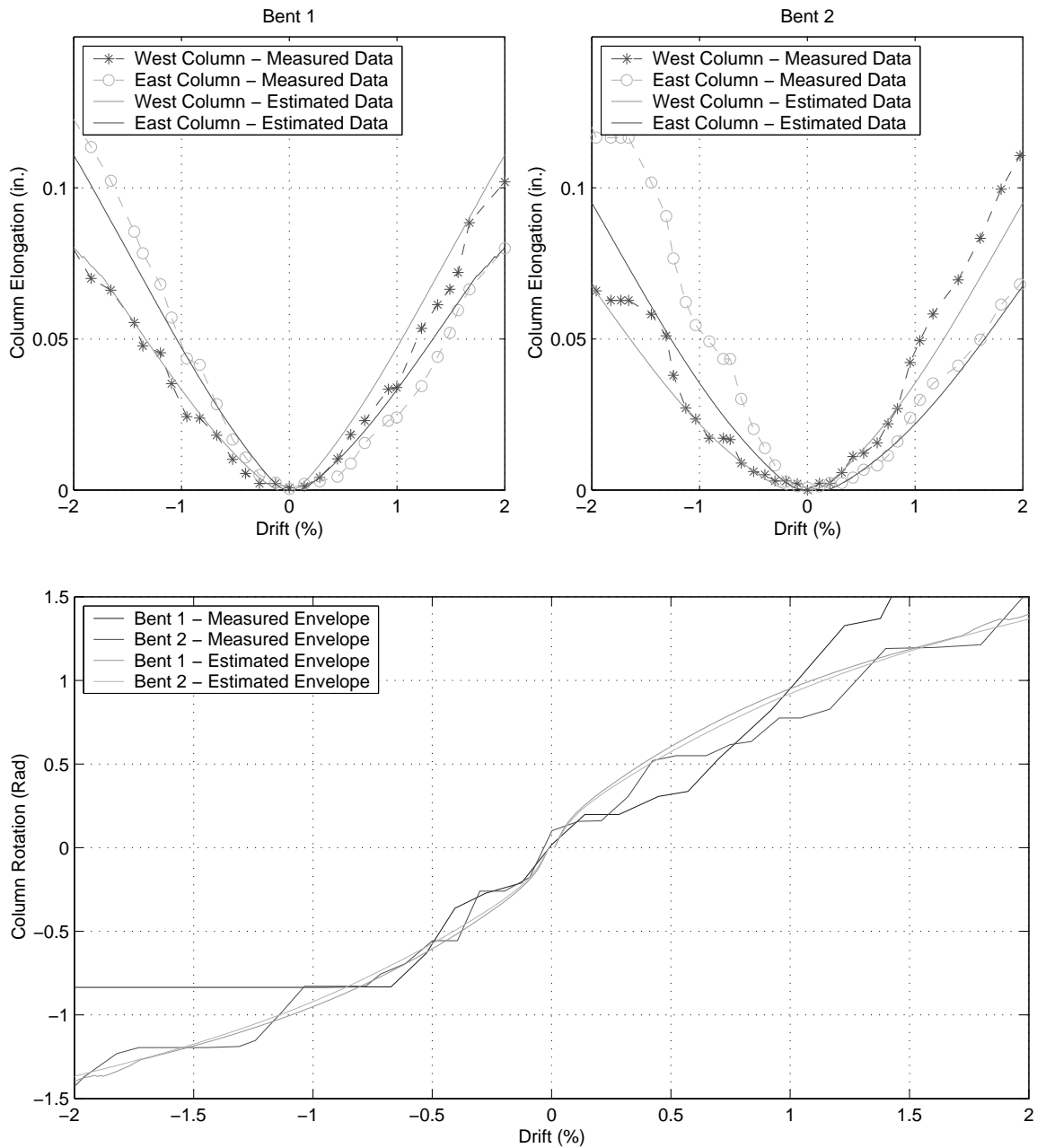
Figure 8.5: Column drift - column rotation relationship

8.3 Modal Damping Ratio Calibration

The modal damping ratios were estimated using system identification techniques and the base and bent accelerations. The results from these methods during the low-amplitude tests are documented in Chapter 5. The estimated modal damping ratios for all of the low-amplitude earthquake excitations are shown in Tables 6.4 - 6.6. Viscous damping in OpenSees is controlled using Rayleigh damping, and was approximated as the average damping for the first three transverse modes throughout the low amplitude tests ($\xi_{1,m} = 1.9\%$, $\xi_{2,m} = 2.6\%$, $\xi_{3,m} = 1.8\%$), leading to a target damping ratio of 2.1% for the numerical model.

8.4 Total Base Shear Assessment

Because of the indeterminacy of the system, the force distribution among the bents is unknown. However, the total base shear in the shaking table system can be approximated as the sum of the bent accelerations multiplied by the tributary masses. The envelope of the total base shear as a function of the center of mass displacement was developed from the 23 earthquake excitations, and is shown in Fig. 8.6.
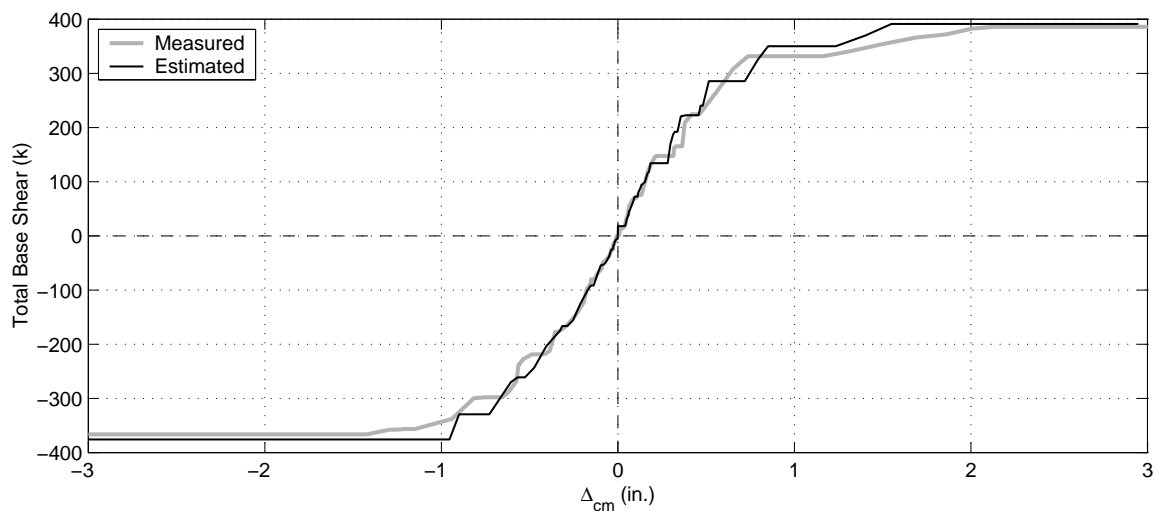
Figure 8.6: Envelope of total base shear vs. the displacement of the center of mass for the 21 earthquake excitations.

As seen in Fig. 8.6, the total base shear estimated from the OpenSees model (initial slope of 760 k/in) is similar to the measured total base shear (initial slope of 730 k/in) for center of mass displacements under 1 in. Also, the estimated ultimate base shear in the positive direction is 1.3% larger than the measured (386k measured vs. 391k estimated), while the estimated ultimate base shear in the negative direction is 2.7% larger than the measured (-366k measured vs. -376k estimated).

8.5 Peak Displacement Assessment

The transverse stiffness of the slab is large relative to that of the bents. As a result, the majority of the response of the shaking table specimen was attributed to either rigid-body translation or rigid-body rotation of the slab. The rigid-body translation of the shaking table specimen was assumed to be the displacement of the center of mass, which through mass symmetry is the displacement of bent 2. The maximum and minimum center of mass displacements for the measured and estimated responses during each of the 23 earthquake excitations is presented in Fig. 8.7. The relative displacement was also monitored (Fig. 8.8). The relative displacement was defined as the difference in the displacements between bents 1 and 3.

The estimated center of mass displacement is similar to the measured for all of the tests, particularly the low-amplitude tests. For the last five tests (Tests 16-20), the estimated peak center of mass displacement was slightly smaller than the measured for both the positive and negative directions. A similar trend is also visible with the relative displacements. As shown in Fig. 8.8, the estimated relative displacement compares well with the measured during the low-amplitude tests. However, Tests 18-20 show much larger deviations from the measured data.
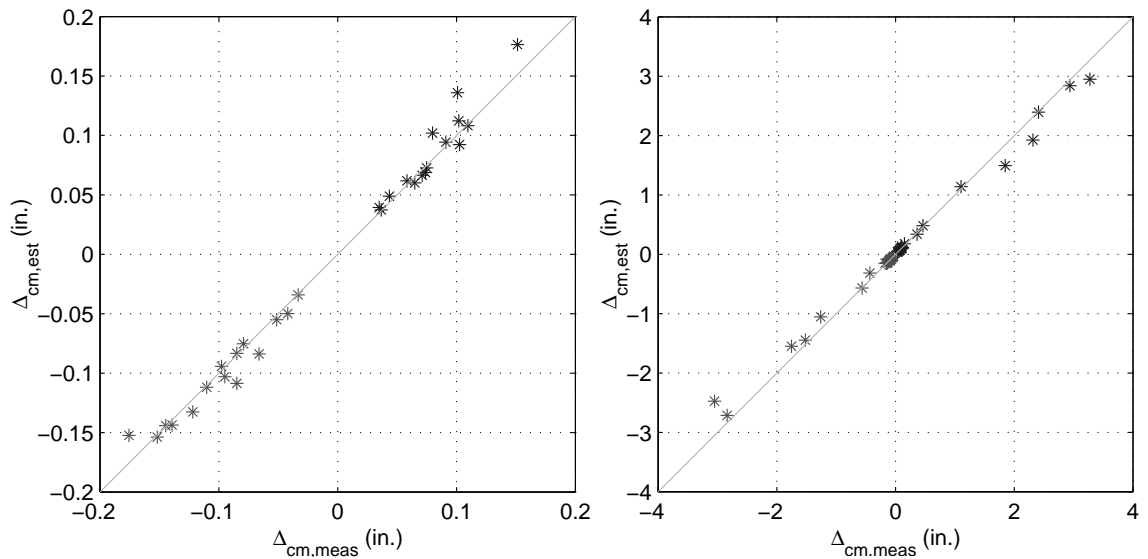
Figure 8.7: Maximum and minimum center of mass displacements for the measured and estimated responses during (a) low-amplitude tests and (b) all tests.
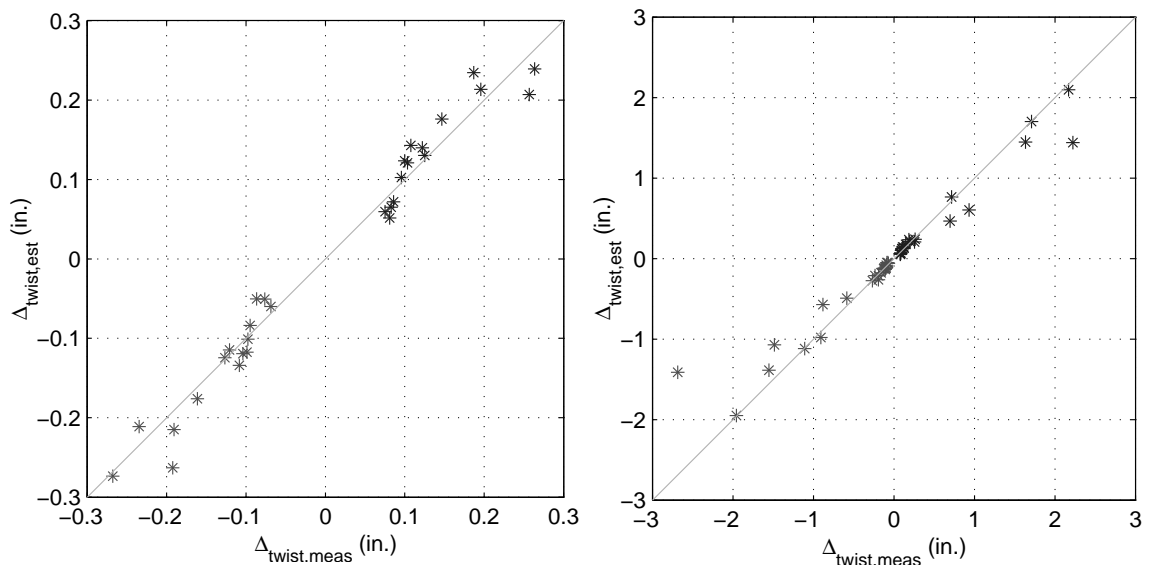
Figure 8.8: Maximum and minimum relative displacements for the measured and estimated responses during (a) low-amplitude tests and (b) all tests.

8.6 Modal Period Progression Assessment

Linear system identification techniques (Chapter 5) were employed to determine the effective modal properties for the first three modes of the structure from the measured and the

estimated response. The periods of the first three modes for each of the tests are shown in Fig. 8.9 for the estimated and measured data.
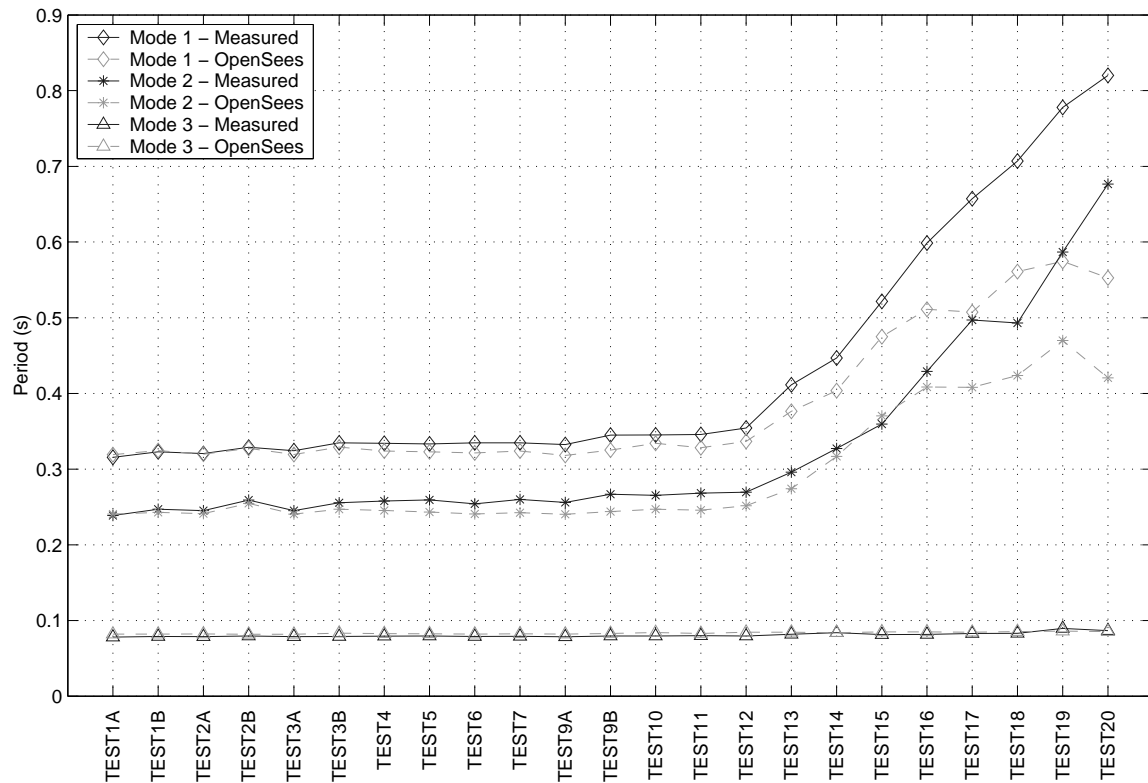
Figure 8.9: Comparison of estimated periods for the measured and simulated data.

Fig. 8.9 shows that the first three periods estimated from the OpenSees data are close to the periods estimated from the measured data at the beginning of the low-amplitude tests. The results begin to diverge slightly during the low amplitude tests. By the end of the low-amplitude tests (Test 12) the estimated mode 1 period from the OpenSees data (0.336 s) is 5% lower than the mode 1 period from the measured data (0.354 s). Because the slab is post-tensioned in both the transverse and longitudinal directions, an increase in the periods of the structure can be directly related to a decrease in the bent stiffness. Therefore, Fig. 8.9 suggests that the OpenSees model does not capture the extent of column softening during the low-amplitude tests.

The OpenSees model captures the period elongation during the high-amplitude tests,

although the extent of period elongation is not as large as the measured response. For example, the mode 1 period of the estimated model (0.561s) is 21% less than the mode 1 period of the measured data (0.707s). This trend can also be seen from the displacement histories in the time and frequency domains, which are presented in the following section.

8.7   Displacement History Assessment

A more demanding measure of the ability of the OpenSees model to accurately estimate the dynamic response is a comparison of the bent displacement histories in the time and frequency domains. The bent displacement histories for significant tests are presented in Figs. 8.10 to 8.15. The significance and key dynamic properties of these tests are shown in Table 8.4.

Table 8.4: Damage levels and properties of significant tests

Test	Test Significance	Max. Bent Drift (%)			Max. Table Acc. (g)		
		Bent 1	Bent 2	Bent 3	Bent 1	Bent 2	Bent 3
1B	First full-scale low-amplitude test	0.20	0.14	0.14	0.21	0.32	0.25
12	Last low-amplitude test	0.30	0.18	0.21	0.07	0.10	0.08
15	First observed spalling	2.14	1.31	2.42	0.67	0.65	0.72
16	First visible transverse reinforcement	3.76	2.41	3.22	0.98	0.94	1.25
18	Incipient buckling	4.07	3.42	5.58	1.56	1.81	1.59
20	Fracture of Longitudinal Reinforcement	3.20	3.18	5.44	1.26	1.30	1.44

Tests 1B and 12 were chosen to show how well the OpenSees model captures the accumulation of column damage due to long-term low-amplitude cycling. The other four tests (Tests 15, 16, 18, and 20) were chosen because of their significance in the progression of column damage.

As seen in Fig. 8.10, the OpenSees model accurately estimates both the amplitude and periodicity of the measured displacement histories for all three bents during Test 1B. As discussed previously, bent 3 had a lot of measurement noise within the system. As a result, the high-frequency component of bent 3 was not well reproduced.

Although the maximum bent displacements during Test 12 (Fig. 8.11) are similar for the three bents (maximum measured and estimated center of mass drifts of 0.16% and 0.18%, respectively) the periodicity of the estimated displacement history has already begun to

diverge from the measured data. This divergence was attributed to the accumulation of cracks within the columns of the experimental specimen throughout the experiments, which the numerical model did not simulate.

Test 15 (Fig. 8.12) marked the onset of spalling. The OpenSees model performed well in matching both the amplitude and periodicity of the measured data until the post-peak displacement response. For example, the maximum center of mass drifts for the measured and estimated data are 1.15% and 1.19%, respectively. After the peak displacement response, the OpenSees model does not match the amplitude of the subsequent cycles well. This trend is also visible for the remaining five tests.

Although the estimated peak displacements continue to be similar to the measured data for Tests 16 and 18 (Figs. 8.13 - 8.14), the periodicity and post-peak amplitudes of the response begin to diverge from the measured displacement data.

The measured and estimated peak displacements are also similar for Test 20 (Fig. 8.15). However, the OpenSees model poorly estimates the measured displacement histories at this level of damage. This was attributed to the current inability of the model to capture bar buckling and bar fracture in OpenSees.
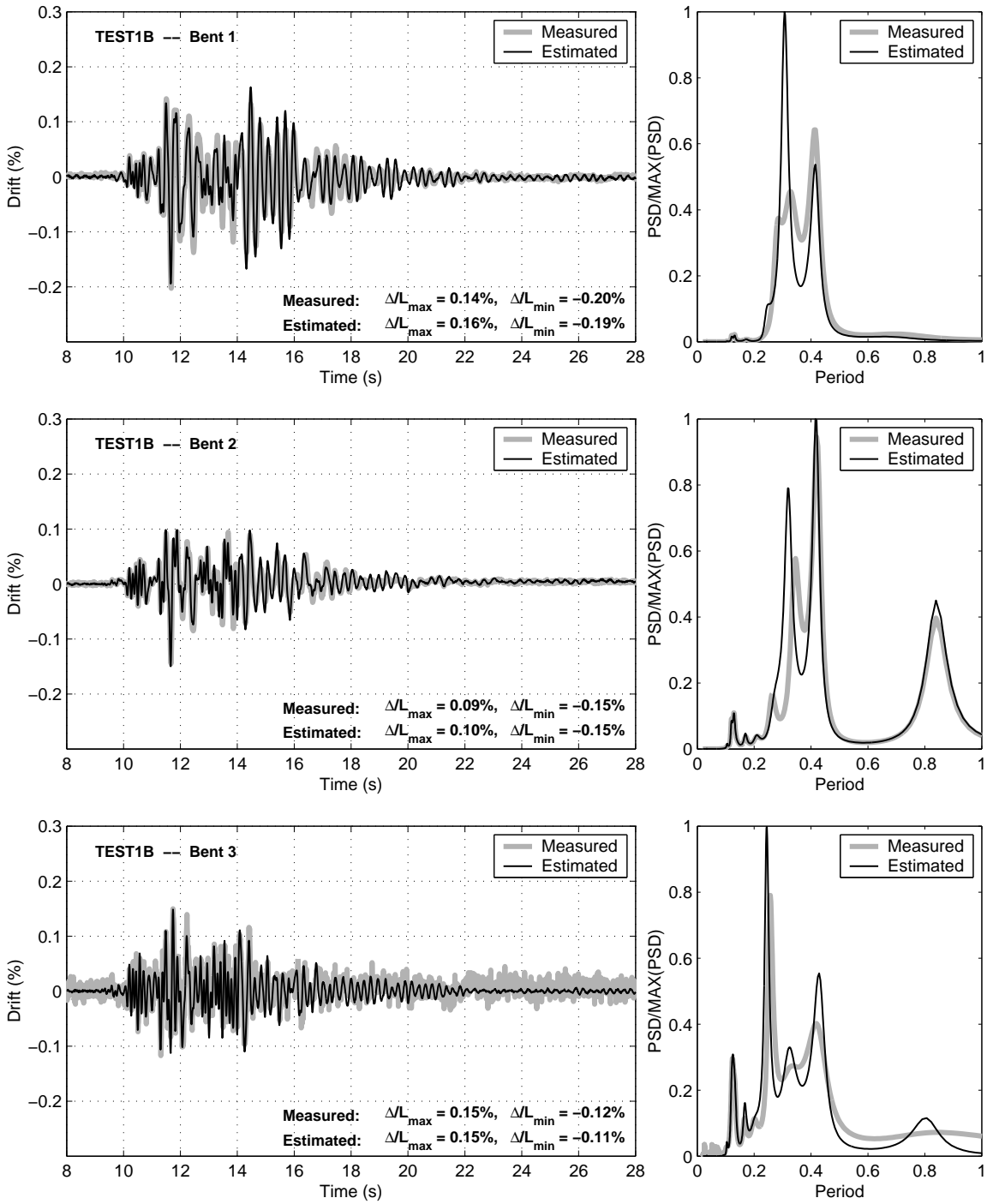
Figure 8.10: TEST1B displacement histories for the three bents in the time and frequency domain.
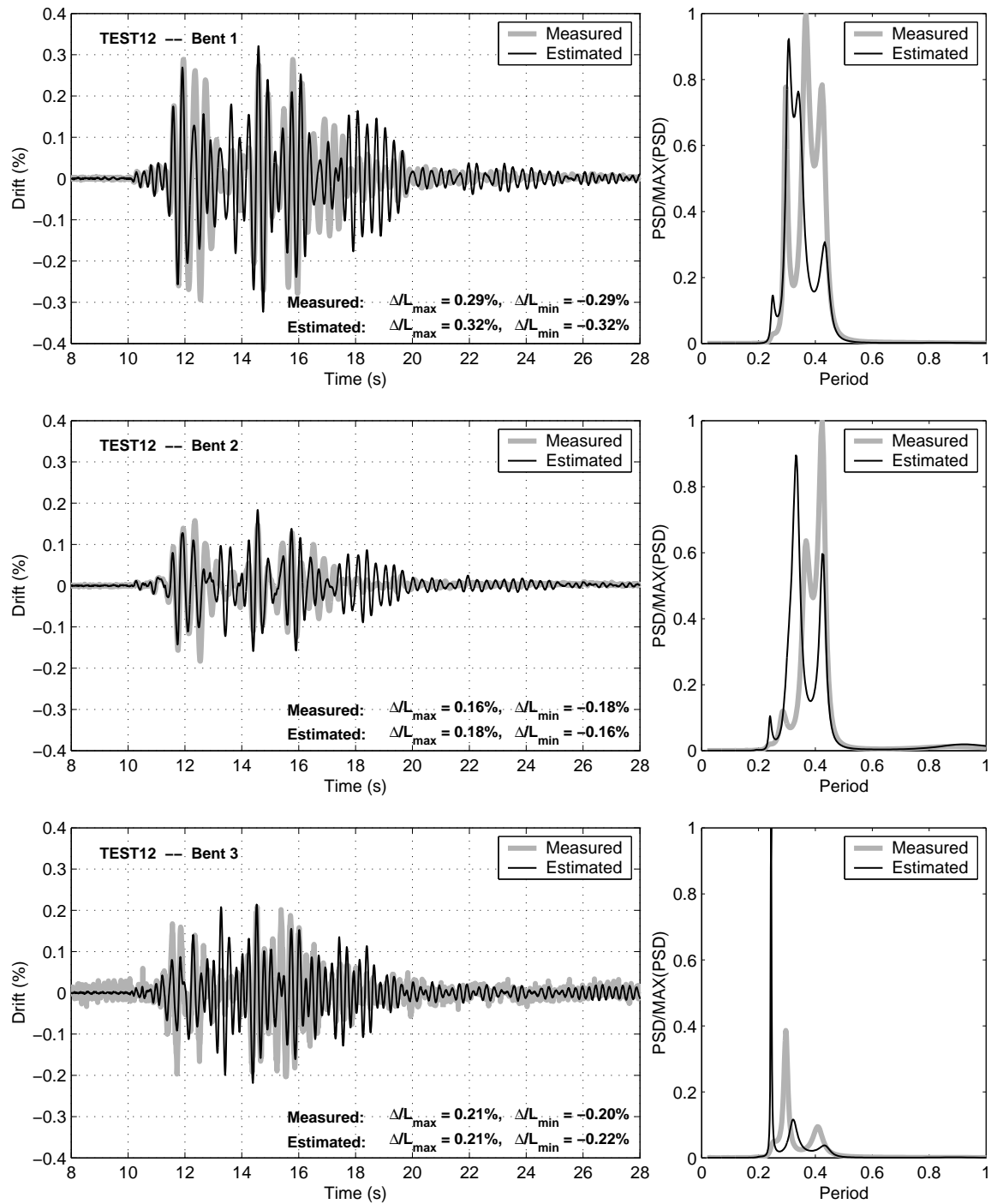
Figure 8.11: TEST12 displacement histories for the three bents in the time and frequency domain.
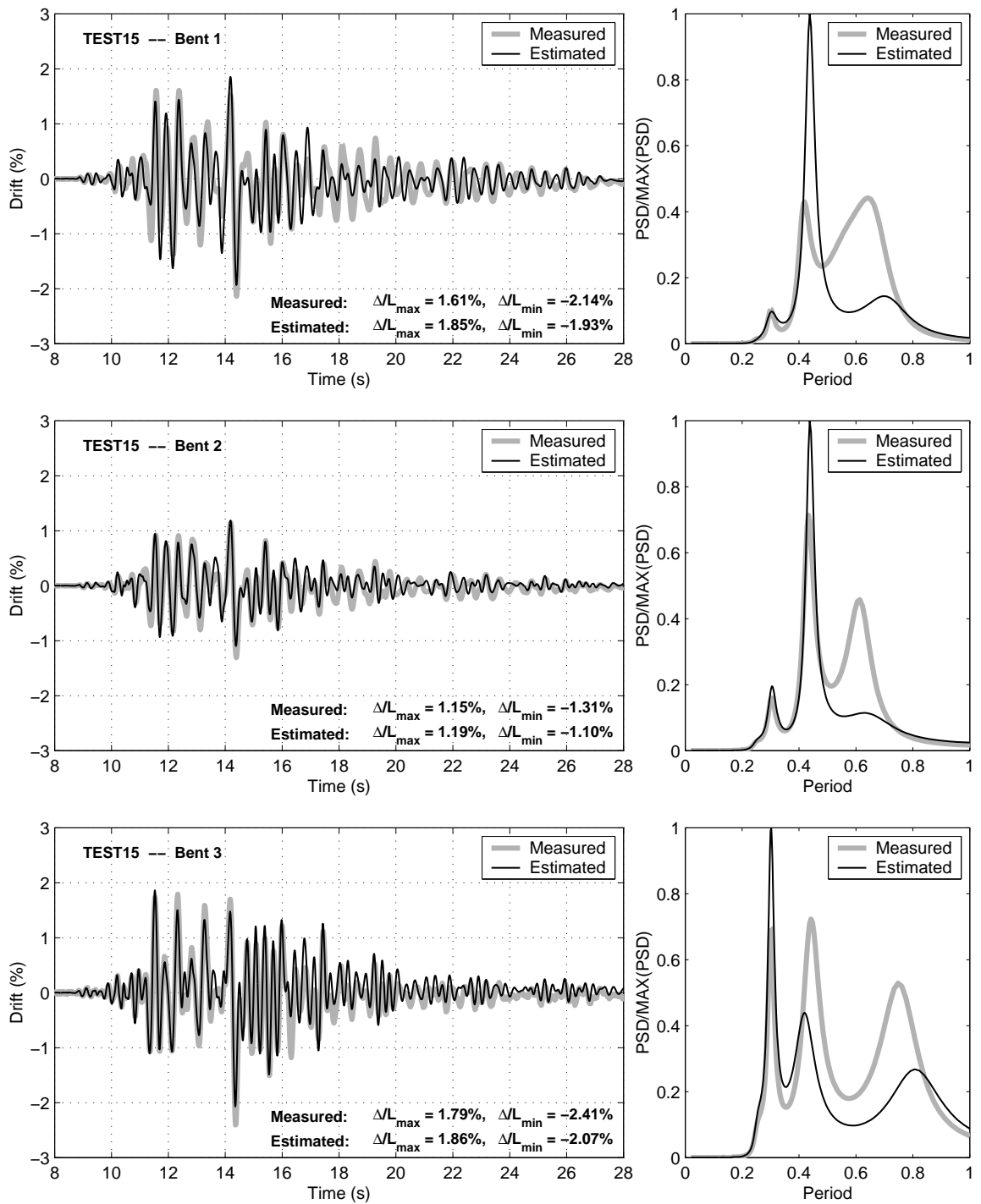
Figure 8.12: TEST15 displacement histories for the three bents in the time and frequency domain.
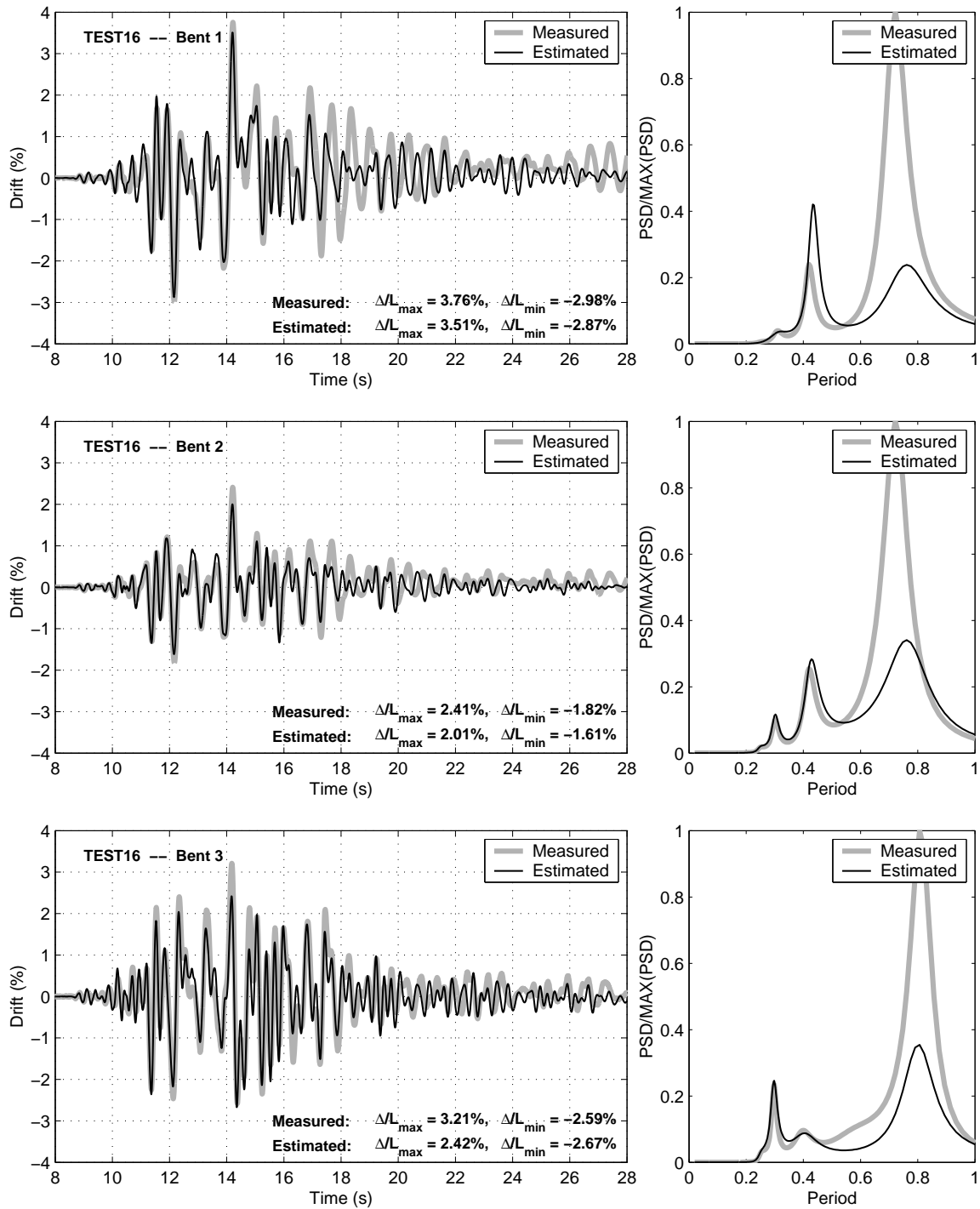
Figure 8.13: TEST16 displacement histories for the three bents in the time and frequency domain.
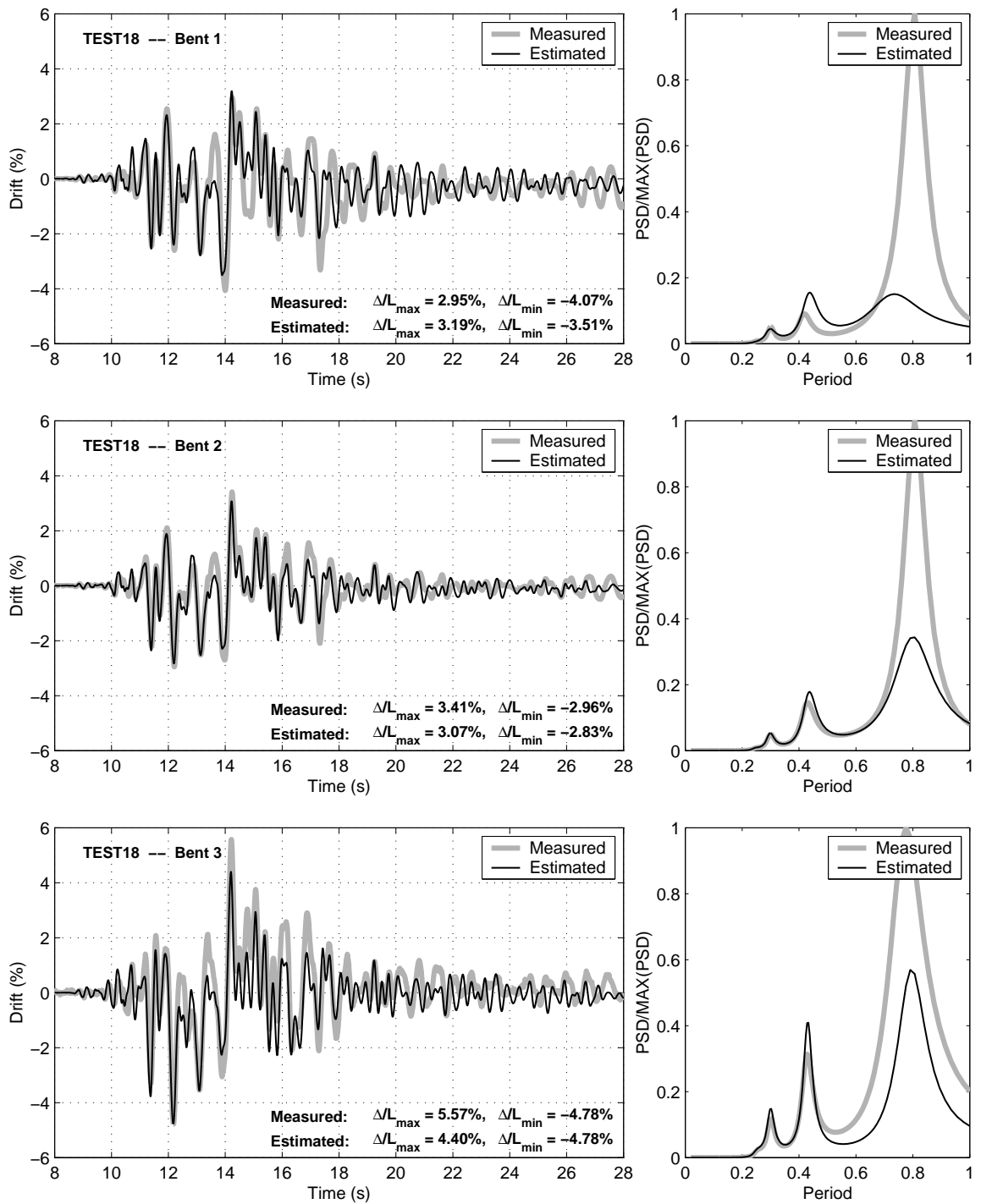
Figure 8.14: TEST18 displacement histories for the three bents in the time and frequency domain.
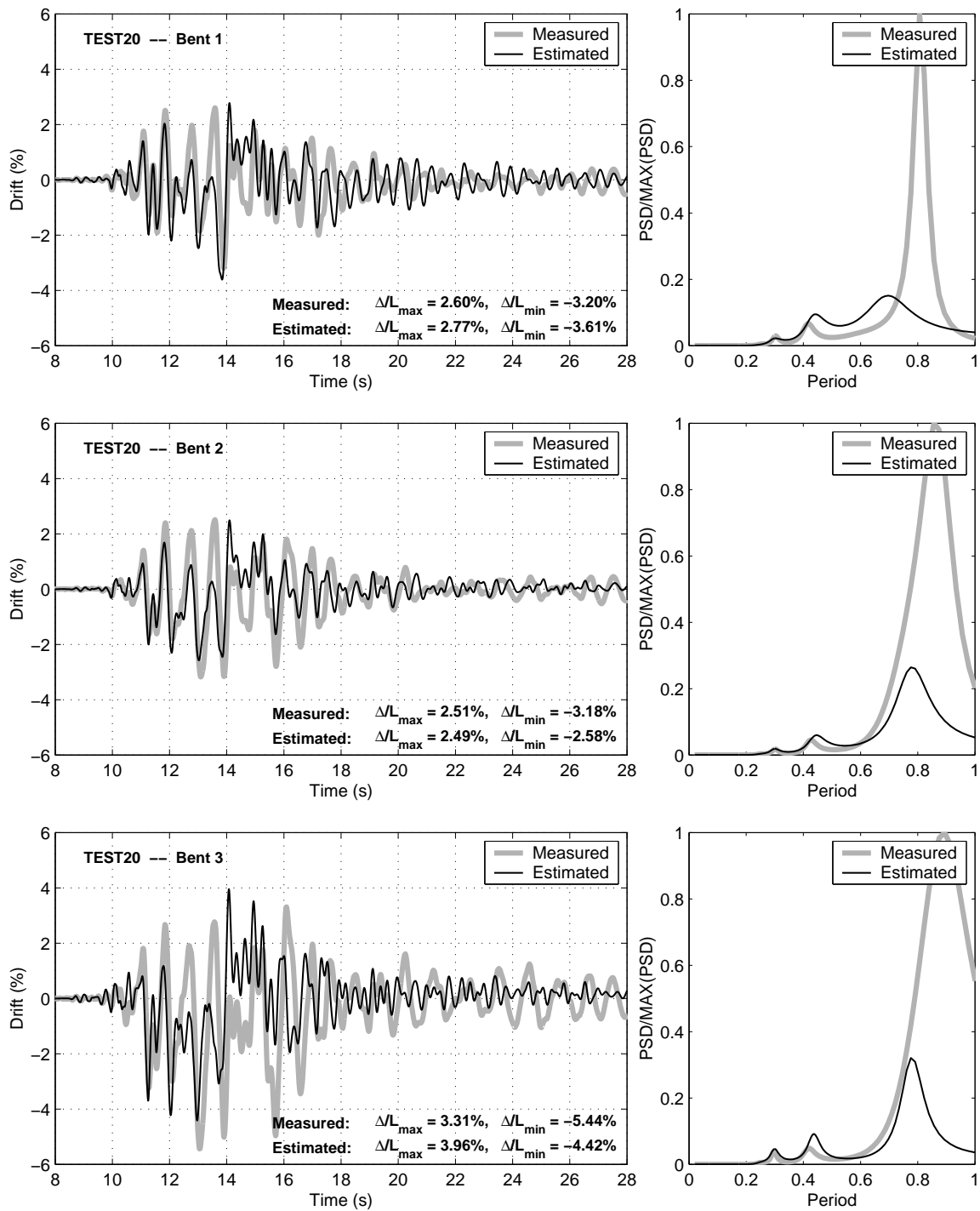
Figure 8.15: TEST20 displacement histories for the three bents in the time and frequency domain.

Chapter 9

MODELING OF STATIC COMPONENT TESTS

Pseudo-static component tests were conducted by Ramirez and Makido (2006) at Purdue University to evaluate the effects of reinforcement detailing, scale, and span-to-depth ratio on the cyclic response of columns and bents. Two of the specimens that were tested at Purdue had properties nominally identical to those of the columns in the shortest bent in the shaking table tests, which made it possible to compare the results from these tests with the calculated response from the OpenSEES model.

This chapter describes the specimens tested at Purdue University (Section 9.1), the instrumentation used during the tests (Section 9.2), and the development of the target displacement history (Section 9.3). This chapter also compares key force and deformation measurements between the numerical model simulations and the measured experimental data (Section 9.4), and compares the estimated and observed damage progression (Section 9.5).

9.1 Specimen Description

A set of five column and bent specimens were tested at Purdue University. The key features of each specimen are listed in Table 9.1.

Table 9.1: Component specimens tested at Purdue University (Makido, 2007)

Component Type	Bent Name	Scale	Height (in.)	Span-to-Depth Ratio	Transverse Reinforcement Ratio
Bent	B-1	1:4	60	5	0.93
	B-2	1:4	60	5	0.47
Column	C-1	1:2	120	5	0.85
	C-2	1:2	72	3	0.85
	C-3	1:2	72	3	0.43

Two of the five specimens tested at Purdue University had nominally identical properties

to the columns in bent 3 of the shaking table tests, including a quarter-scale bent (Specimen B-1) and a half-scale column (Specimen C-1). Because the shaking table specimen was an indeterminate system, a primary objective of these component tests was to provide insight into the force-deformation response of the shortest bent of the shaking table specimen, and to assess the accuracy of the numerical model.

The other columns tested at Purdue made it possible to observe the effects of: transverse reinforcement ratio (Specimens B-1 vs. B-2, and Specimens C-2 vs. C-3), scale (Specimens B-2 vs. C-1), and span-to-depth ratio (Specimens C-1 vs. C-2). This chapter focuses on the response of Specimens B-1 and C-1 (illustrated in Fig. 9.1) for comparison with the shaking table tests. Photographs of the two specimens are shown in Fig. 9.2.

Courtesy of Makido (2007)
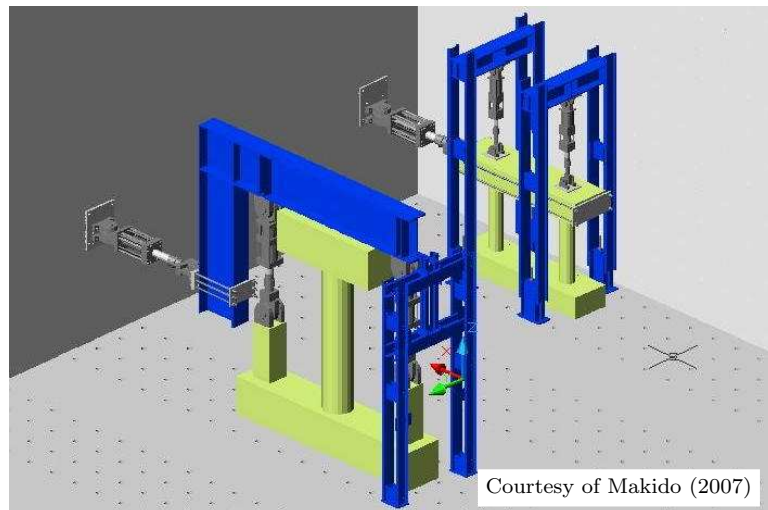
Figure 9.1: Illustration of Purdue specimens B-1 and C-1

The key geometric and material properties for the two specimens are listed in Tables 9.2 and 9.3, respectively. The target concrete strength for these specimens was 5000 psi. The measured concrete strengths for Specimens B-1 and C-1 on the day of testing was 4200 psi and 5500 psi, 16% lower and 10% higher, respectively, than the target strength. The measured concrete strength of the columns in the shaking table specimen was 5900 psi. The steel properties were obtained through three coupon tests for each specimen.

Figure 9.2: Test setup for (a) specimen B-1 and (b) specimen C-1

Table 9.2: Geometric properties of the Purdue specimens (Makido, 2007)

Member	Property	Specimen B-1	Specimen C-1	Ratio
Column Dimensions	Diameter (*in.*)	12	24	1:2
	Clear Cover (*in.*)	0.75	1.50	1:2
	Core Diameter (*in.*)	10.31	20.62	1:2
	Column Height (*in.*)	60	120	1:2
	Column Spacing (*in.*)	72	NA	NA
Column Reinforcement	No. of Longitudinal Bars	16	16	1:1
	Bar Size	#3	#6	1:2
	Longitudinal Steel Ratio (%)	1.56	1.56	1:1
	Spiral Bar	W2.9	3	NA
	Spiral Spacing (*in.*)	1.25	2.5	1:2
	Spiral Bar Diameter (*in.*)	0.192	0.375	1:1.95
	Spiral Bar Area (*in.*^{2})	0.029	0.11	1:3.79
	Transverse Volumetric Steel Ratio (%)	0.93	0.85	1:0.91
Beam Dimensions	Width (*in.*)	32	NA	NA
	Depth (*in.*)	18	NA	NA

Table 9.3: Measured material properties for the Purdue specimens (Makido, 2007)

Material	Property	Shake Table	Specimen B-1	Specimen C-1
Concrete	f'_c (ksi)	5.9	4.2	5.5
Steel	f_y (ksi)	70	68	63
	f_{su} (ksi)	97	95	93
	E (ksi)	29000	28000	27000
	ϵ_u	0.12	0.10	0.14

9.2 Instrumentation

Load cells, potentiometers, and strain gauges were used to measure the response of all of the specimens. The instrumentation for Specimens B-1 and C-1 are listed in Table 9.4.

Table 9.4: Instrumentation for Specimens B-1 and C-1 (Makido, 2007)

Instrument Type	Measurement	Instrument Quantity	
		Specimen B-1	Specimen C-1
Load Cells	Lateral Force	1	1
	Vertical Force	2	2
Potentiometers	In-Plane Column Displacement	2	2
	Out-of-Plane Column Displacement	2	2
	Vertical Column Displacement	2	2
	Column Rotation	16	16
Strain Gauges	Longitudinal Steel Strains	106	27
	Transverse Steel Strains	12	0
Totals		143	52

Displacements at the tops of the columns in the transverse, longitudinal, and vertical directions were measured using two string potentiometers each. For Specimen B-1, the vertical potentiometers were placed on the outside of each column. For Specimen C-1, the vertical potentiometers were placed on both sides of the column. Column rotations and shear deformations were measured at four locations for each specimen (illustrated in Fig. 9.3) using four sets of four gauges: vertical (2), horizontal (1), and diagonal (1).

Strains were measured on the longitudinal reinforcement for both specimens, and on the transverse reinforcement for Specimen B-1, as illustrated in Fig. 9.4. The longitudinal strain gauges were located on six bars at each cross-section, with five cross-sections at each column joint. The first cross-section was located at the column-anchorage interface. Two cross-sections were located within the anchorages and the columns. Strain gauges were placed on the transverse reinforcement at two locations within three cross-sections at each joint.
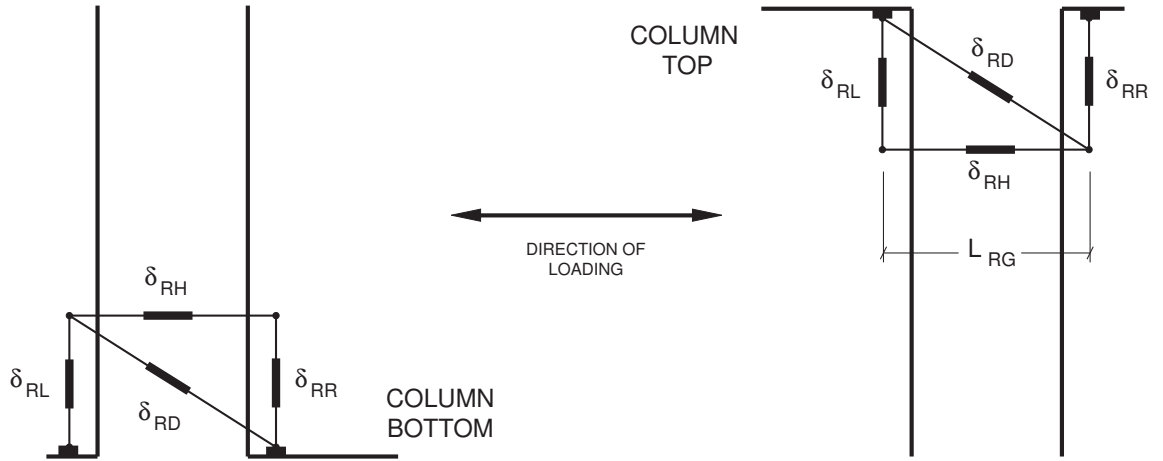
Figure 9.3: Rotation Gauge Placement
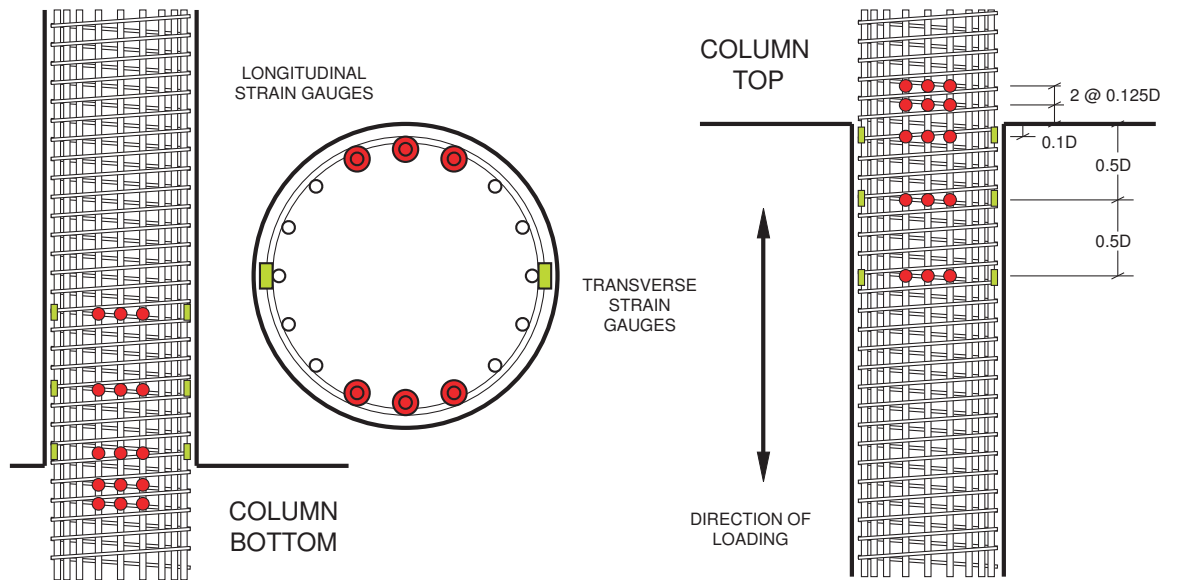
Figure 9.4: Strain Gauge Placement

9.3 Target Displacement History

Specimens B-1 and C-1 were tested to gain insight into the response of the shortest bent within the shaking table specimen. For lightly confined columns, Ranf et al. (2005) found that for some critical damage levels (bar buckling, loss of lateral load capacity, loss of axial load capacity), large amounts of plastic displacement reduced the maximum displacement before damage. To account for this effect, the target displacement history for the Purdue tests was chosen to simulate the amount of cumulative plastic displacement that bent 3 had experienced during the shaking table tests. Fig. 9.5 shows the target displacement history for the Purdue specimens. The amplitudes of each displacement cycle are listed in Table 9.5.

The target displacement history for the component tests resembles a standard cyclic test. The amplitudes of the drift at each set were determined by a rainflow analysis of the displacement history of bent 3 during the shaking table tests. To better match the cumulative plastic deformation in the shake-table tests, only two cycles were used in sets with larger displacements. Fig. 9.6 plots the maximum displacement versus the cumulative plastic deformation for the component specimens and for bent 3 of the shaking table tests. As seen in this figure, the target displacement history for Specimens B-1 and C-1 reproduces the amount of cumulative plastic deformation in the shaking table specimen throughout the test history.

Table 9.5: Target drift ratios for Specimens B-1 and C-1

Set	Cycle	Drift (%)
1	1-3	0.08
2	4-6	0.25
3	7-9	0.50
4	10-12	0.80
5	13-15	1.20
6	16-18	2.40
7	19-21	3.20
8	22-23	3.80
9	24-25	4.40
10	26-27	5.00
11	28-29	5.40
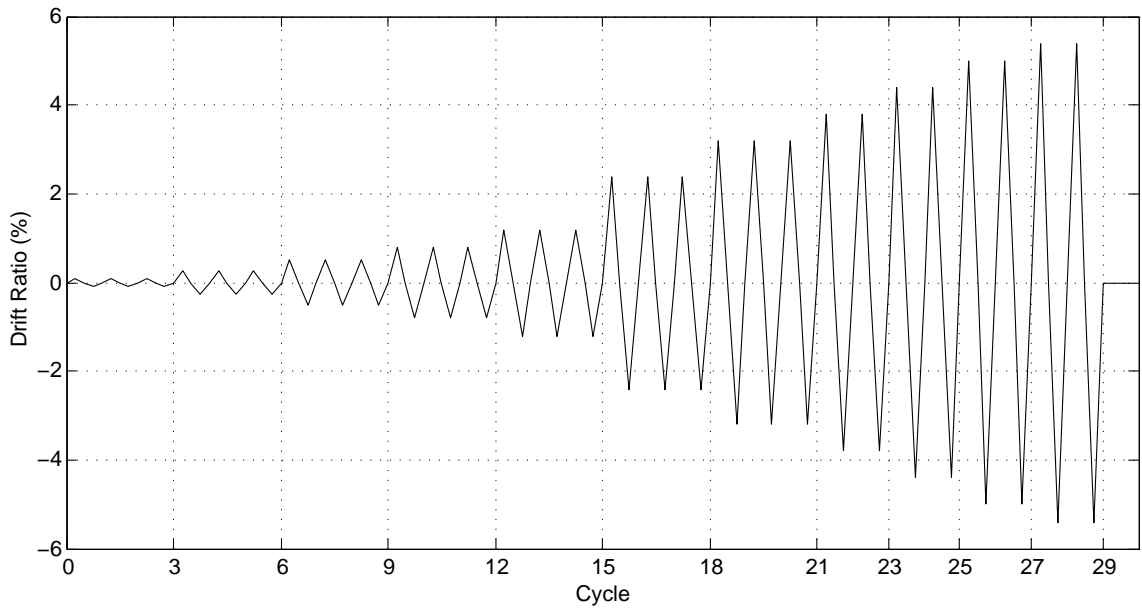
Figure 9.5: Displacement history for Specimens B-1 and C-1
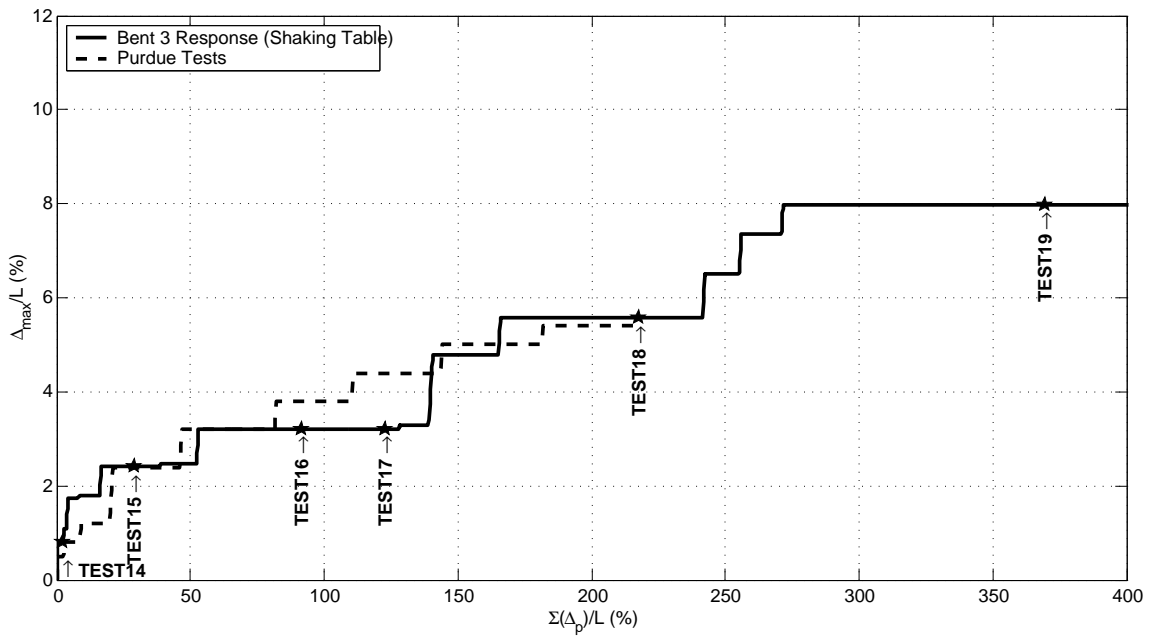
Figure 9.6: Cumulative plastic displacement comparison for shaking table and Purdue tests.

9.4 Response Comparisons

To model the column and bent tests, the numerical model of the shaking table specimen was adjusted to incorporate small differences in the material properties (measured concrete

and steel properties) and geometric properties (effective cross beam). The differences in the material properties between these specimens and the shaking table specimen are listed in Table 9.3.

The dimensions of the cross beam in Specimen B-1 (32 in. wide by 18 in. deep) also varied from the effective cross beam in the shake-table tests (9 in. wide by 14 in. deep). From an inelastic moment-curvature analysis, the ultimate moment capacity of the columns in Specimen B-1 was estimated to be 750 k-in., which was approximately 25% smaller than the cracking moment of the cross beam. Therefore, the cross beam was modeled elastically, using the gross section stiffness.

This section compares key characteristics of the measured and simulated responses of Specimens B-1 and C-1, including: force-displacement response, column elongation response, and displacement-rotation response.

9.4.1 Force-Displacement Response

The measured and simulated force-displacement responses for Specimens B-1 and C-1 are plotted in Fig. 9.7. The envelopes of these force-displacement responses are compared in Fig. 9.8. The simulated response was generated by subjecting the numerical models to the measured displacement histories. In Table 9.6, the simulated responses are compared with the measured in terms of: maximum base shear, reduction of shear capacity, and dissipation of hysteretic energy. The force response from the numerical models of the two specimens is very similar to the measured force response. For example, the maximum simulated base shear for Specimen B-1 was 48k, only 4% below the maximum measured base shear (50k). For specimen C-1, the maximum simulated base shear was 96k, the same as the maximum measured base shear.

Table 9.6: Force-displacement comparison statistics

Quantity	Dir.	Specimen B-1			Specimen C-1		
		Measured	Simulated	ratio	Measured	Simulated	ratio
Maximum Base Shear (k)	P.	50	48	0.96	96	96	1.00
	N.	-46	-48	1.04	-96	-96	1.00
Lateral Capacity Reduction (%)	P.	56	40	0.71	40	43	1.07
	N.	57	52	0.91	41	48	1.20
Hysteretic Energy (k-in.)		1700	2500	1.48	7600	10900	1.39
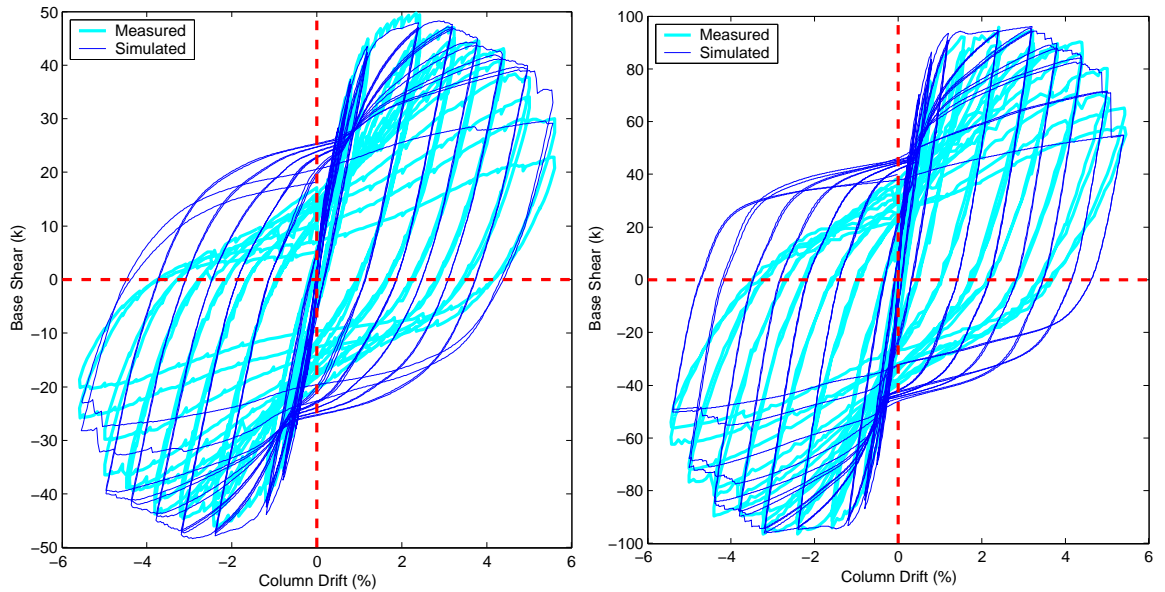
Figure 9.7: Force-displacement comparison between measured data and numerical simulation for (a) Specimen B-1 and (b) Specimen C-1.
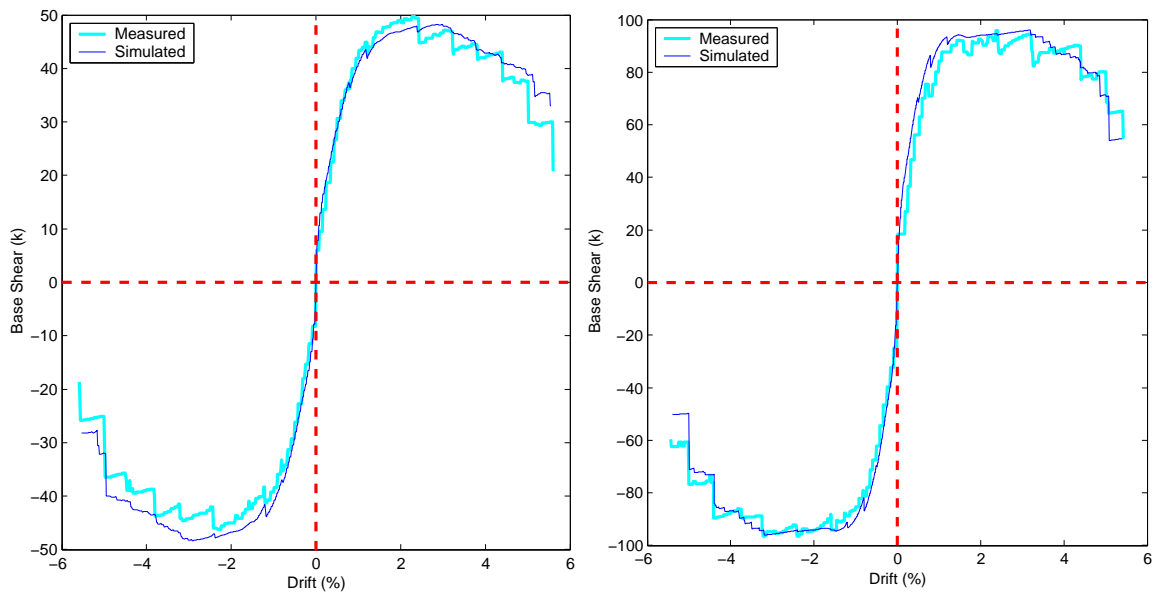
Figure 9.8: Force-displacement envelopes for the measured and numerical data for (a) Specimen B-1 and (b) Specimen C-1.

The numerical model also simulated well the force degradation within the specimens. As seen in Fig. 9.7, both the measured data and the model simulations lost between 40% and 60% of their strength by the end of the tests. In the numerical models, all of the degradation

was deformation based. However, from the measured response, it is apparent that some of the degradation also came from cycling. For example, during testing of specimen C-1, the peak strength for the first cycle at a drift of 5% was 80k. This strength was reduced to 69k during the second cycle to that same drift level.

The measured and simulated responses were also compared in terms of hysteretic energy, defined as

$$E_h = \int_{t=0}^{t=t_f} f(t)dx(t) \tag{9.1}$$

As seen in Table 9.6, the numerical model overestimated the total amount of hysteretic energy for both specimens. For example, the total hysteretic energy dissipated by the numerical model of Specimen B-1 was 2500 k-in. 48% higher than the hysteretic energy dissipated by Specimen B-1 (1700 k-in.). The majority of the differences between the measured and the computed hysteretic energies were attributed to the inability of the numerical model to adequately capture the degree of pinching that was observed in the experiments. Possible reasons for the differences in the pinching include the degree of pinching in the anchorage slip model (Section 8.1), and the inability of the numerical model to simulate buckling of the longitudinal reinforcement.

9.4.2 Column Elongation Response

Column elongation was measured on the specimens with vertical string potentiometers. For Specimen B-1, the vertical potentiometers were placed on the outside of each column, approximately 12 in. from the column face. These displacements were compared directly with vertical measurements at the same locations in the numerical model, and are shown in Fig. 9.9. A positive column drift creates tension in the left column and compression in the right column. This overturning effect is visible within the displacement measurements presented in Fig. 9.9. For example, the left column elongates more during positive drifts than during negative drifts. The opposite is true for the right column. For both columns, the main difference between the experimental and simulated column elongation is that the experimental specimen retained larger residual elongations than the numerical model predicted.
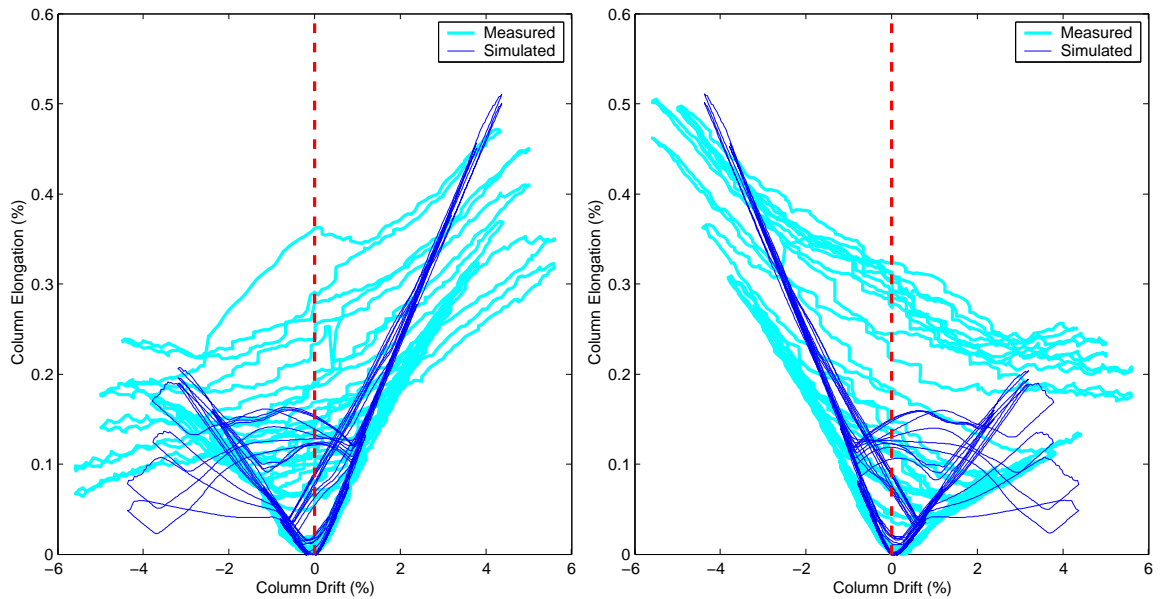
Figure 9.9: Displacement-elongation comparison between measured data and numerical simulation for Specimen B-1 for a) left column and b) right column.

For Specimen C-1, the vertical potentiometers were placed on the outer edges of the cross-beam. The column elongation was approximated as the average of these two measurements. Fig. 9.10 shows the calculated column elongation from the experiment and the numerical model.

For both the experimental specimen and the numerical model, the column elongations are approximately equal for both positive and negative drift. This symmetry was expected because there are no overturning forces on the single-column specimen. Fig. 9.10 also shows that Specimen C-1 had residual elongations (at low drifts) that were larger than the numerical model simulated, which resulted in overall elongations that were also larger than the elongation measurements from the numerical model. As the damage accumulated in the numerical model, the column stopped elongating during negative drifts. This trend was not visible in the experiments.
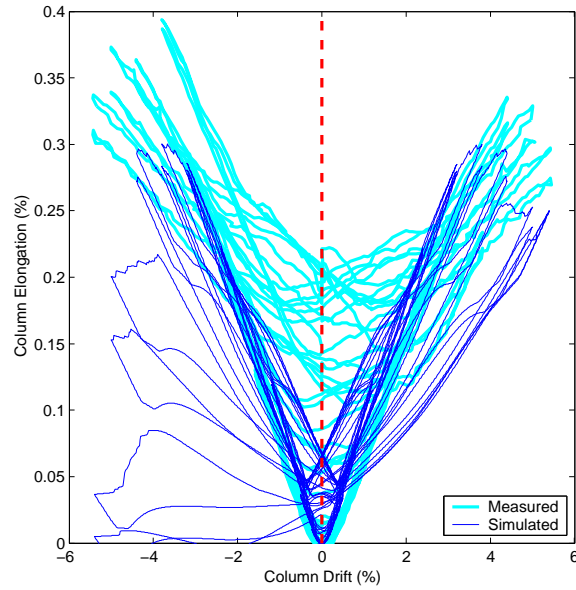
Figure 9.10: Displacement-elongation comparison between measured data and numerical simulation for Specimen C-1

9.4.3 Displacement-Rotation Response

The rotations at the ends of each column were measured over lengths of 11 in. and 21 in. for Specimens B-1 and C-1, respectively (Makido, 2007). Rotations across this same length were calculated for the numerical model using rotations from anchorage slip and column flexure, defined as

$$\theta_{tot} = \theta_{col} + \theta_{slip} \tag{9.2}$$

where θ_{tot} is the total column rotation over the measurement gauge length. The terms θ_{col} and θ_{slip} are the column rotations attributed to column flexure and anchorage slip, respectively. The column rotations due to column flexure are calculated by summing the elastic rotation ($\theta_{col,e}$) and the plastic rotation ($\theta_{col,p}$) components of the column flexure.

$$\theta_{col} = \theta_{col,e} + \theta_{col,p} \tag{9.3}$$

Distributed plasticity column elements (Section 7.1) were used for the numerical model, allowing the computation of curvature data at discrete locations along the length of the columns. Using this data and assuming the columns undergo double curvature, the elastic

component of the rotation can be calculated from the curvature at the first integration point (ϕ_1).

$$\theta_{col,e} = \phi_1 L_g \left[1 - \frac{L_g}{L_{col}}\right] \qquad\qquad \phi_1 \leq \phi_y \qquad\qquad (9.4)$$

where L_g and L_{col} are the gauge length of the measurement device and the height of the columns respectively. The rotation that comes from the plastic flexure of the column was approximated using plastic curvatures from the first two integration points within the column, defined as

$$\theta_{col,p} = \frac{\phi_{p1} w_{ip1} L_{col}^2 (1 - w_{ip1}) + \phi_{p2} w_{ip2} L_{col}^2 (1 - 2w_{ip1} - w_{ip2})}{(L_{col} - L_p)} \qquad (9.5)$$

$$\phi_{pj} = \phi_j - \phi_y \geq 0 \qquad\qquad (9.6)$$

where ϕ_{pj} and w_{ipj} are the plastic curvatures and weighting factors associated with integration point j, and L_p is the plastic hinge length of the columns, defined in Eq. 9.7 (Berry, 2006).

$$L_p = 0.05 L_{col} + 0.1 \frac{f_y d_b}{f_c'} \leq \frac{L_{col}}{4} \qquad\qquad (9.7)$$

where f_y and d_b are the yield strength and diameter of the longitudinal reinforcement, and f_c' is the compressive strength of the concrete.

The average displacement-rotation histories for both specimens are shown in Fig. 9.11. For Specimen B-1, the average displacement-rotation history was computed by averaging the displacement-rotation relationship at all four column joints within the bent. For Specimen C-1, this measurement was averaged over the two column joints. The displacement-rotation histories for the measured and numerical data are similar for both specimens, and are approximately linear. This signifies that throughout testing, the proportion of column deformation due to the measured rotation zone was constant. The force-rotation response for both specimens are shown in Fig. 9.12. Because there is approximately a linear relationship between the rotation and the displacement, the force-rotation plots resemble the force-displacement plots presented in Section 9.4.1. These rotation comparisons show that the source of the column deformation in the numerical model simulates well the source of the deformation in Specimens B-1 and C-1.
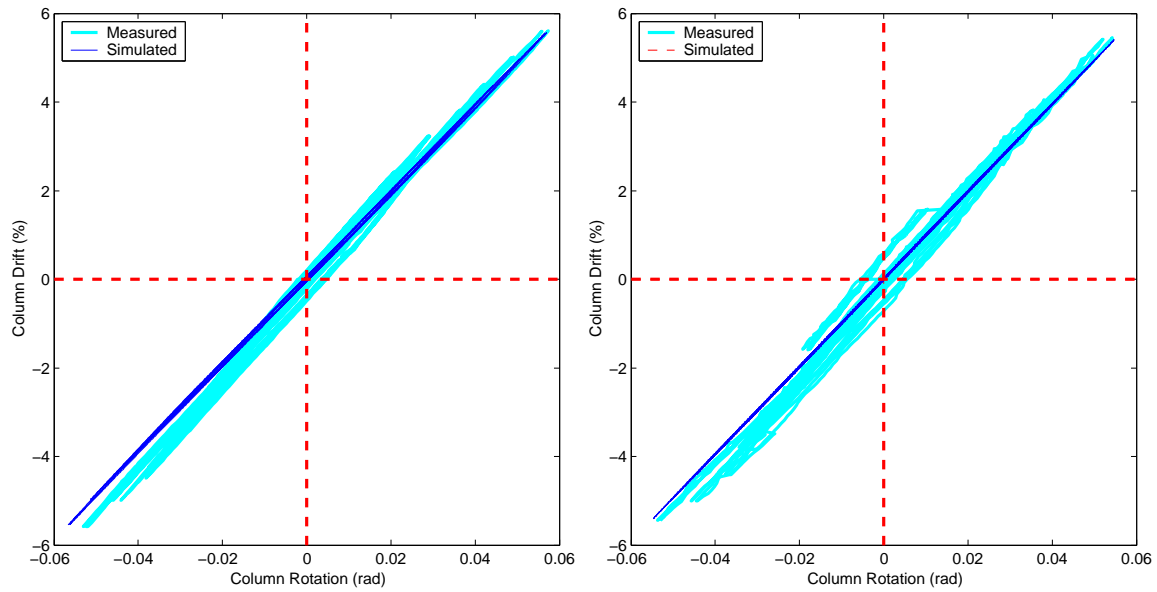
Figure 9.11: Displacement-rotation comparison between measured data and numerical simulation for (a) Specimen B-1 and (b) Specimen C-1
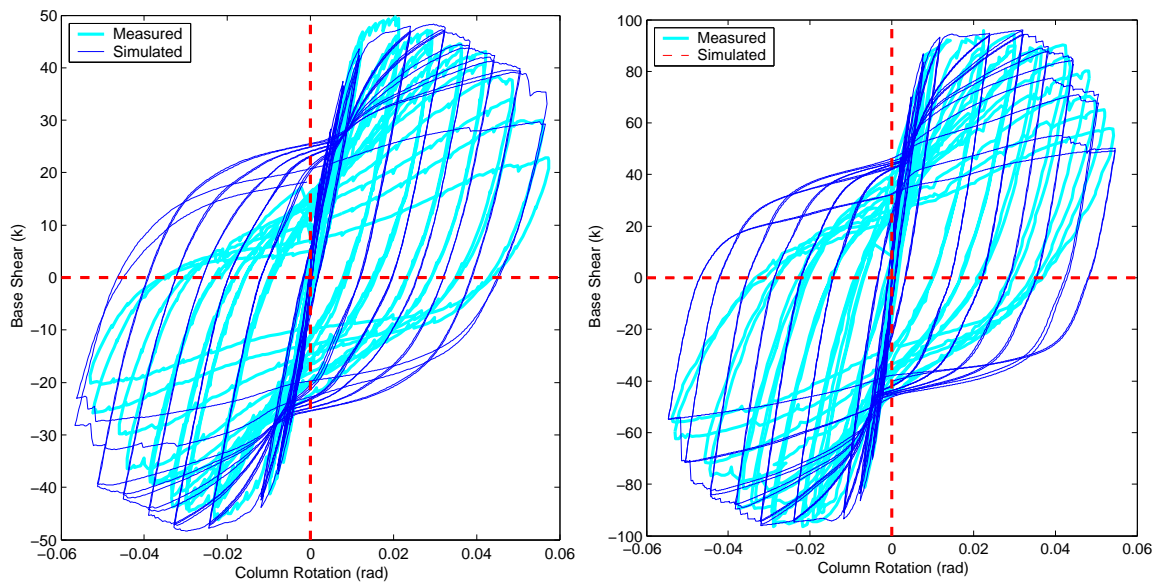
Figure 9.12: Force-rotation comparison between measured data and numerical simulation for (a) Specimen B-1 and (b) Specimen C-1

9.5 Damage Progression

Five damage states were tracked during the tests of Specimens B-1 and C-1: yielding of the longitudinal reinforcement, concrete spalling, buckling of the longitudinal reinforcement,

fracture of the transverse reinforcement, and fracture of the longitudinal reinforcement (Makido, 2007). Three of these five damage states were simulated in the numerical model: longitudinal bar yielding, concrete spalling, and longitudinal bar fracture.

The strain at bar yielding was calculated from the measured yield stress and the elastic modulus during coupon tests of the reinforcement. The strains at concrete spalling and longitudinal bar fracture are more difficult to characterize because they are dependent on the properties and loading history of the individual specimen. Therefore, these limit states were calibrated in the material models so that the column drifts at which these states occurred matched with what was observed in the experiments. The optimal strains at which this damage occurred are listed in Table 9.7.

Table 9.7: Comparison of strains at key damage states

Specimen	Bar Yielding ϵ_s	Concrete Spalling ϵ_c	Bar Fracture ϵ_s
B-1	0.0024	0.006	0.12
C-1	0.0023	0.008	0.12

The calibrated strains for concrete spalling and bar fracture are close to what has been observed in other studies. For example, Berry (2006) found that the mean concrete strain at spalling for circular, well-confined columns was 0.008, with a coefficient of variation of 49%.

The resulting column displacements at these damage states are listed in Table 9.8. The numerical models of Specimens B-1 and C-1 simulates well the drift ratios at bar yielding, concrete spalling, and bar fracture. These comparisons provide more confidence in the numerical model of the shaking table specimen.

Table 9.8: Comparison of column drift ratios at key damage states

Specimen	Damage State	Measured	Simulated
B-1	Bar Yielding	0.50	0.50
	Concrete Spalling	1.2	1.2
	Bar Fracture	5.0	5.2
C-1	Bar Yielding	0.67	0.42
	Concrete Spalling	1.2	1.2
	Bar Fracture	5.0	4.9

Chapter 10

SIMULATION OF THE PROTOTYPE

This chapter describes the assembly of the prototype model from the calibrated shaking table and centrifuge models (Section 10.1), introduces the suite of near-field and far-field ground motions that were used to excite the numerical models (Section 10.2), and documents the seismic response of the prototype model (Section 10.3). Key observations of the calculated system response are summarized in Section 10.4.

10.1   Prototype Model Development

A model was assembled to simulate the full-scale reinforced concrete bridge on drilled shafts. This model was developed by combining the structural properties from a calibrated model of the shaking table tests (Chapter 8) with the soil properties from a calibrated model of the centrifuge tests (Shin, 2006). The geometric and material properties of the piles were extrapolated from the columns from the shake-table tests. The assembly of the prototype model is illustrated in Fig. 10.1.
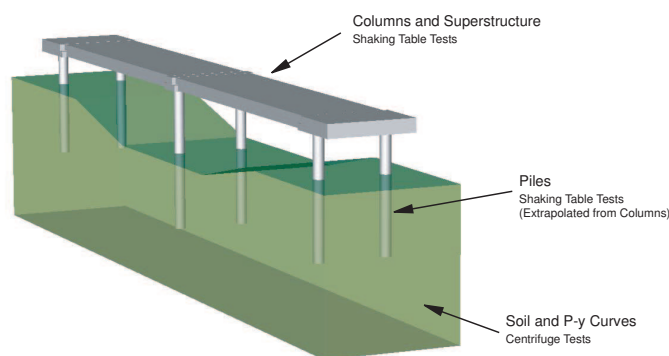
Figure 10.1: Illustration of prototype assembly

The geometric properties of the structural components of the prototype specimen re-

sulted from scaling of the shaking table model from quarter-scale to full-scale. With the exception of the concrete strength (5000 psi), all of the material properties of the structure were kept the same as the shaking table specimen. The piles were modeled with the same material and geometric properties as the columns.

The bridge superstructure was modeled as a flat slab with the same moduli of inertia as a box girder. A consequence of this approximation was that the cross-sectional area of the flat slab exceeded that of the box girder. To compensate for this effect, the concrete density of the slab in the numerical model was reduced by 49%, so that the column axial-load ratio would remain at its target value of 8%.

The geometric properties of the soil were scaled from the 1/52-scale centrifuge tests to the full-scale prototype. Because the centrifuge tests were conducted under a gravitational acceleration of 52g, the soil weight in the centrifuge tests, and therefore the stresses within the soil, did not change as a result of geometric scaling.

The mode shapes and periods of vibration of the prototype model are shown in Fig. 10.2 for the first six structural modes: three transverse modes, two vertical modes, and one longitudinal mode. The first three modes are dominated by rigid translation of the slab. The next three modes are dominated by either vertical or transverse slab bending.

| (a) $T_{1,long} = 0.705s$ | (b) $T_{1,tran} = 0.612s$ | (c) $T_{2,tran} = 0.491s$ |

| (d) $T_{1,vert} = 0.378s$ | (e) $T_{2,vert} = 0.271s$ | (f) $T_{3,tran} = 0.198s$ |
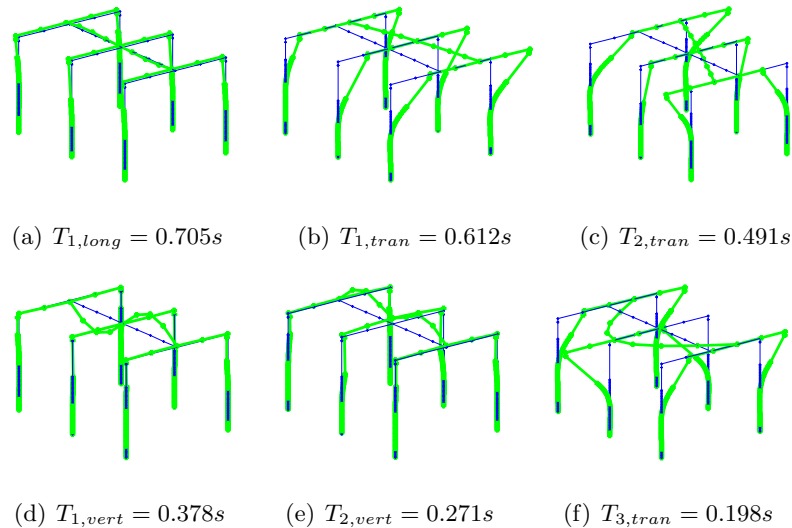
Figure 10.2: Prototype mode shapes

10.2 Ground Motion Development by Shin (2006)

To excite the prototype model, Shin (2006) developed two suites of 40 near-field and 30 far-field earthquake motions at a variety of intensity levels. The near-field suite of motions came from the PEER I-880 testbed project. The far-field suite of motions came from the PEER Van Nuys testbed project. For convenience, the prototype bridge developed in this research was located at each of these sites to make the motions relevant to this research. Both suites are described in the following sections.

10.2.1 Near-Field Excitations

Somerville and Collins (2002a) generated hazard spectra at the I-880 site for near-field outcrop motions at three hazard levels: 50%, 10% and 2% in 50 years. The peak ground accelerations at these three hazard levels are 0.45g, 0.87g, and 1.23g, respectively. Based on the deaggragation described by Somerville and Collins (2002a), the modal magnitudes of these three hazard levels were 6.6, 6.8, and 7.0. The characteristics of each hazard spectra are listed in Table 10.1.

Table 10.1: Comparison of I-880 near-field hazard spectra characteristics (Shin, 2006)

Hazard	PGA (g)	M_w	MSF	PGA/MSF (g)
50% in 50 years	0.45	6.6	1.52	0.30
10% in 50 years	0.87	6.8	1.34	0.65
2% in 50 years	1.23	7.0	1.23	1.00

Shin (2006) added a fourth hazard level, 97% in 50 years, to the suite of motions to investigate the response of the model during low-intensity excitations.

For a separate PEER project, Shin (2006) classified the hazard levels based on the ratio between the peak ground acceleration and the magnitude scaling factor (MSF), two characteristics of the ground motions that are often used in analyses involving liquefiable soils. These hazard classifications were used in this research for convenience, and do not significantly affect the results of this research because the response of the structure due to

a particular hazard level is not investigated. The MSF is defined as

$$MSF = \begin{cases} \left(\dfrac{7.5}{M_w}\right)^{2.95} & M_w \leq 7.5 \\ \left(\dfrac{7.5}{M_w}\right)^{2.56} & M_w > 7.5 \end{cases} \qquad (10.1)$$

Based on the hazard analysis conducted by Somerville and Collins (2002a), the ratios of the peak ground acceleration to the magnitude scaling factor (MSF) for the 50%, 10% and 2% in 50 year ground motions were 0.30g, 0.65g, and 1.00g.

Somerville and Collins (2002a) chose 10 near-field outcrop motions at each of these hazard levels, which are listed in Table 10.2. Shin (2006) scaled these 40 near-field motions so that the ratio of the peak ground acceleration to the magnitude scaling factor equalled the target ratios listed in Table 10.1. The scaled peak ground accelerations for each of these outcrop motions are listed in Table 10.2.

To obtain the excitations for the prototype model, Shin (2006) deconvolved the 40 scaled outcrop motions to bedrock underneath the prototype. The peak ground acceleration of the resulting bedrock motions are listed in Table 10.2. The acceleration response spectra (2% damping) for the 40 bedrock motions that were used to excite the structure are presented in Appendix G.

Table 10.2: Characteristics of the near-field earthquake ground motions

Hazard Level	ID	Earthquake	M_w	MSF	PGA_M (g)	Station	PGA bedrock (g)
97% / 50yr	D01	Coyote Lake	5.7	2.247	0.202	Coyote Lake Dam abut.	0.168
	D02					Gilroy #6	0.167
	D03	Parkfield	6.0	1.931	0.188	Temblor	0.156
	D04					Array #5	0.137
	D05					Array #8	0.119
	D06	Livermore	5.5	2.497	0.226	Fagundes Ranch	0.189
	D07					Morgan Territory Park	0.147
	D08	Morgan Hill	6.2	1.753	0.147	Coyote Lake Dam abut.	0.122
	D09					Anderson Dam DS	0.126
	D10					Halls Valley	0.124
50% / 50yr	A01	Coyote Lake	5.7	2.247	0.672	Coyote Lake Dam abut.	0.574
	A02					Gilroy #6	0.609
	A03	Parkfield	6.0	1.931	0.578	Temblor	0.469
	A04					Array #5	0.470
	A05					Array #8	0.393
	A06	Livermore	5.5	2.497	0.747	Fagundes Ranch	0.605
	A07					Morgan Territory Park	0.483
	A08	Morgan Hill	6.2	1.753	0.524	Coyote Lake Dam abut.	0.423
	A09					Anderson Dam DS	0.435
	A10					Halls Valley	0.463
10% / 50yr	B01	Loma Prieta	7.0	1.226	0.799	Los Gatos Pres. Ctr.	0.687
	B02					Saratoga Aloha Avenue	0.727
	B03					Corralitos	0.708
	B04					Gavilan College	0.699
	B05					Gilroy Historic	0.691
	B06					Lexington Dam abut.	0.758
	B07	Kobe	6.9	1.279	0.834	Kobe JMA	0.780
	B08	Tottori	6.6	1.458	0.951	Kofu	0.622
	B09					Hino	0.896
	B10	Erzincan	6.7	1.395	0.909	Erzincan	0.696
2% / 50yr	C01	Loma Prieta	7.0	1.226	1.228	Los Gatos Pres. Ctr.	1.100
	C02					Saratoga Aloha Avenue	1.141
	C03					Corralitos	1.077
	C04					Gavilan College	1.054
	C05					Gilroy Historic	1.062
	C06					Lexington Dam abut.	1.190
	C07	Kobe	6.9	1.279	1.282	Kobe JMA	1.220
	C08	Tottori	6.6	1.458	1.461	Kofu	1.091
	C09					Hino	1.397
	C10	Erzincan	6.7	1.395	1.398	Erzincan	1.106

10.2.2   Far-Field Excitations

Somerville and Collins (2002b) generated hazard spectra at the Van Nuys testbed site for far-field outcrop motions at three hazard levels: 50%, 10% and 2% in 50 years. The peak ground accelerations at these three hazard levels are 0.25g, 0.63g, and 0.99g, respectively. Based on the deaggragation described by Somerville and Collins (2002b), the modal magnitudes for all hazard levels was 6.75. The characteristic of each far-field hazard spectra are listed in Table 10.3.

Table 10.3: Comparison of Van Nuys far-field hazard spectra characteristics (Shin, 2006)

Hazard	PGA (g)	M_w	MSF	PGA/MSF (g)
50% in 50 years	0.25	6.75	1.36	0.18
10% in 50 years	0.63	6.75	1.36	0.46
2% in 50 years	0.99	6.75	1.36	0.73

Similar to the near-field excitations, Shin (2006) classified the hazard based on the ratio between the peak ground acceleration and the magnitude scaling factor (MSF). Based on the hazard analysis conducted by Somerville and Collins (2002b), the ratios of the peak ground acceleration to the magnitude scaling factor (MSF) for the 50%, 10% and 2% in 50 year ground motions were 0.18g, 0.46g, and 0.73g. These ratios are also listed in Table 10.3.

Somerville and Collins (2002b) chose 10 near-field outcrop motions at each of these hazard levels, which are listed in Table 10.4. Shin (2006) scaled these 30 near-field motions so that the ratio of the peak ground acceleration to the magnitude scaling factor equalled the target ratios listed in Table 10.3. The scaled peak ground accelerations for each of these outcrop motions are listed in Table 10.4.

To obtain the excitations for the prototype model, Shin (2006) deconvolved the 30 scaled outcrop motions to bedrock underneath the prototype. The peak ground acceleration of the resulting bedrock motions are listed in Table 10.4. The acceleration response spectra (2% damping) for the 30 far-field bedrock motions that were used to excite the structure are presented in Appendix G.

Table 10.4: Characteristics of the far-field earthquake ground motions

Hazard Level	ID	Earthquake	M_w	MSF	PGA_M (g)	Station	PGA bedrock (g)
50% / 50yr	F01	Palm Springs	6.0	1.931	0.351	Palm Springs Airport	0.237
	F02	Northridge	6.7	1.375	0.254	Ventura Blvd. #1	0.189
	F03					Ventura Blvd. #9	0.230
	F04					Lankershim Blvd. #1	0.212
	F05					V. Nuys - Sher. Circle #1	0.209
	F06					Oxnard Street #4	0.216
	F07	San Fernando	6.6	1.458	0.265	14724 Ventura Blvd.	0.226
	F08					15250 Ventura Blvd.	0.205
	F09					V. Nuys - 7-Story Hotel	0.227
	F10	Whit. Narrows	6.0	1.931	0.351	Cal Tech, Brown Ath. Bldg.	0.254
10% / 50yr	G01	Northridge	6.7	1.395	0.642	Topanga Canyon Blvd.	0.454
	G02					Sepulveda VA Hosp.	0.584
	G03					V. Nuys - Sher. Circle #1	0.533
	G04					V. Nuys - 7-Story Hotel	0.553
	G05					Oxnard Street #4	0.560
	G06	San Fernando	6.6	1.458	0.671	14724 Ventura Blvd.	0.558
	G07					15910 Ventura Blvd.	0.537
	G08					15250 Ventura Blvd.	0.612
	G09					633 E. Broadway	0.590
	G10					V. Nuys - 7-Story Hotel	0.564
2% / 50yr	H01	Northridge	6.7	1.395	1.011	Ventura Blvd. #1	0.805
	H02					Ventura Blvd. #9	0.939
	H03					Lankershim Blvd. #1	0.859
	H04					Nordhoff Fire Station	0.975
	H05					Northridge, Roscoe #1	0.884
	H06					13248 Roscoe Blvd.	0.944
	H07					Sepulveda VA Hosp.	0.926
	H08					V. Nuys, Sher. Way #1	0.971
	H09					V. Nuys - 7-Story Hotel	0.862
	H10	San Fernando	6.6	1.458	1.057	V. Nuys - 7-Story Hotel	0.961

10.2.3   Comparison of Near-Field and Far-Field Excitations

This section compares the peak ground accelerations, spectral accelerations, and earthquake duration of the near-field and far-field bedrock excitations.

The peak ground acceleration for the four near-field and the three far-field earthquake hazard levels are shown in Fig. 10.3a. The average peak ground acceleration of the motions at each hazard level are listed in Table 10.5. For each hazard level, the average peak ground acceleration was always larger for the near-field excitations. For example, at the 10% in 50

year hazard level, the mean PGA for the near-field excitations was 0.73g, 33% larger than the mean PGA for the far-field excitations (0.55g).

The spectral accelerations at the first period of the structure (T = 0.61s) and 2% damping are plotted in Fig. 10.3b for each motion. The means of these values are listed in Table 10.5. For each hazard level, the mean spectral accelerations were always larger for the near-field excitations than for the far-field excitations. However, this difference was smaller than the difference in the peak ground accelerations. For example, at the 10% in 50 year hazard level, the mean spectral acceleration for the near-field excitation was 1.65g, only 1% larger than the mean spectral acceleration for the far-field excitations (1.63g).

Fig. 10.3c plots the durations of both near-field and far-field earthquakes. The mean durations for each hazard level are listed in Table 10.5. For this comparison, duration was defined as the time between when the acceleration first and last exceeded 20% of its maximum acceleration. The durations of the near-field earthquakes were typically much shorter than those for the far-field earthquakes. For example, at the 10% in 50 year hazard level, the mean duration for the near-field excitations was 6.9s, 59% shorter than the mean duration for the far-field excitations (16.9s).

Table 10.5: Average characteristics of the near-field and far-field bedrock motions

Hazard	Field	PGA (g)	SA(T = 0.61s) (g)	Duration (s)
97% in 50 years	Near-Field	0.15	0.21	4.5
	Far-Field	*	*	*
50% in 50 years	Near-Field	0.49	0.84	4.3
	Far-Field	0.22	0.48	16.1
10% in 50 years	Near-Field	0.73	1.65	6.9
	Far-Field	0.55	1.63	16.9
2% in 50 years	Near-Field	1.14	2.55	7.4
	Far-Field	0.91	2.24	12.1
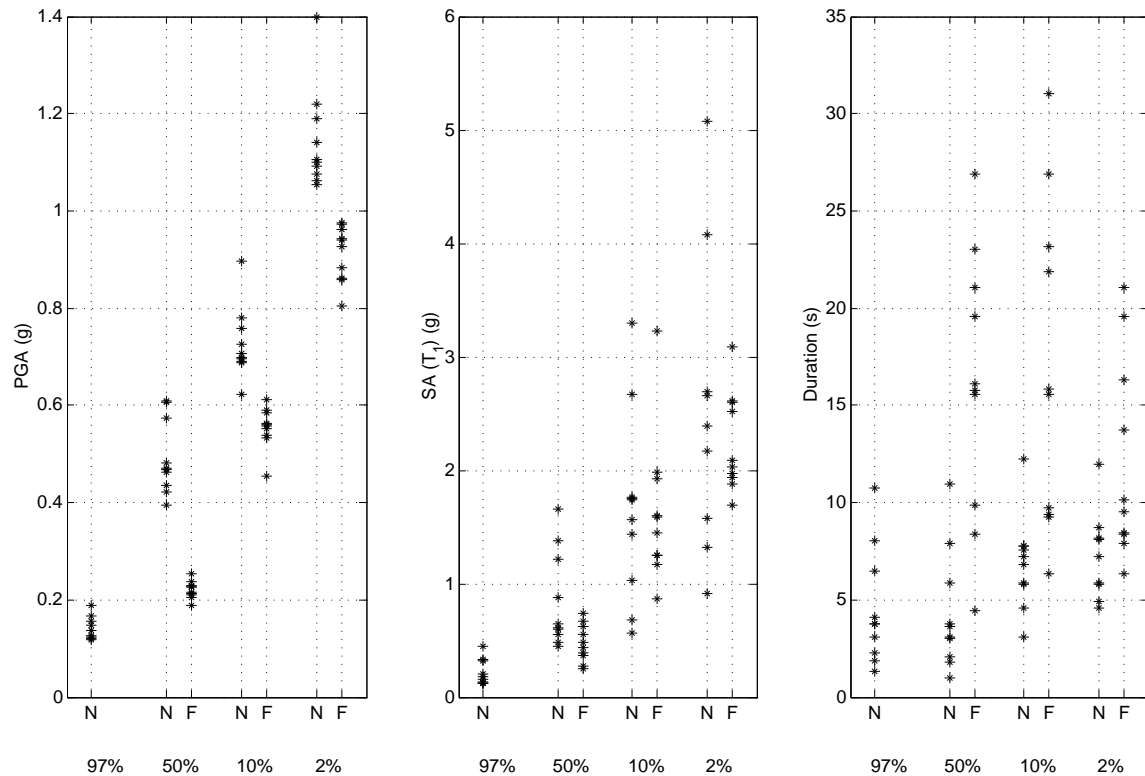
Figure 10.3: Excitation characteristics for near-field and far-field excitations, including: a) peak ground acceleration, b) spectral acceleration (T = 0.61s, $\xi = 2\%$), and c) earthquake duration.

10.3   Prototype Response

This section presents key characteristics of the prototype response to the 40 near-field and 30 far-field earthquake excitations, including: response histories and response distributions for representative far-field excitations, and response maxima for all excitations.

10.3.1   Representative Far-Field Ground Motions

This section illustrates typical response to far-field excitations by describing in detail the response for three motions, one at each hazard level. The ground motions from the 50% and 10% in 50 year hazard levels were recorded at the Van Nuys - Sherman Circle #1 station (records F05L and G03L, Table 10.4). The ground motion from the 2% in 50 year

hazard level was recorded at the Van Nuys - Sherman Way #1 station (record H08L). The acceleration time histories and acceleration response spectra (2% damping) of these three motions are shown in Fig. 10.4. The peak acceleration occurred at approximately 4s for each record, with the duration of the earthquake between 20s and 30s. For the 50% and 10% in 50 year earthquakes, the peak spectral acceleration occurred at a period of approximately 0.25s, which is nearly 60% less than the first period of vibration of the structure (0.61s). At this period, the spectral acceleration were 0.27g and 0.86g. For the 2% in 50 year earthquake, the peak spectral acceleration was near 0.15s. The spectral acceleration at the period of the structure was 1.69g.

10.3.2   Far-Field Response Histories

The drift ratio was approximated as the tangential deviation between the top of the column and the point of column inflection (δ_{infl}), divided by the length from the top of the column to the inflection point (L_{infl}), defined as ($Drift = \delta_{infl}/L_{infl}$). The length to the inflection point was computed at displacement maxima, then used to compute drift ratios for the entire displacement history. The column deformation from the top of the column to the inflection point (δ_{infl}) was defined as

$$\delta_{infl} = \delta_{infl,s} + \delta_{infl,f} \tag{10.2}$$

where $\delta_{infl,s}$ is the relative displacement to the inflection point due to anchorage slip, defined as

$$\delta_{infl,s} = \theta_s L_{infl} \tag{10.3}$$

where θ_s is the rotation of the slip element. The term $\delta_{infl,f}$ is the relative displacement to the inflection point due to column flexure, defined as

$$\delta_{infl,f} = \sum_{i=1}^{N} \phi_i w_i L_e \left(L_{infl} - \sum_{m=0}^{i-1} w_m L_e - \frac{w_i L_e}{2} \right) \tag{10.4}$$

where ϕ_i and w_i are the curvature and weight of integration point i, $w_0 = 0$, and L_e is the length of the column element. The term N is the number of integration points between the top of the column and the point of inflection.
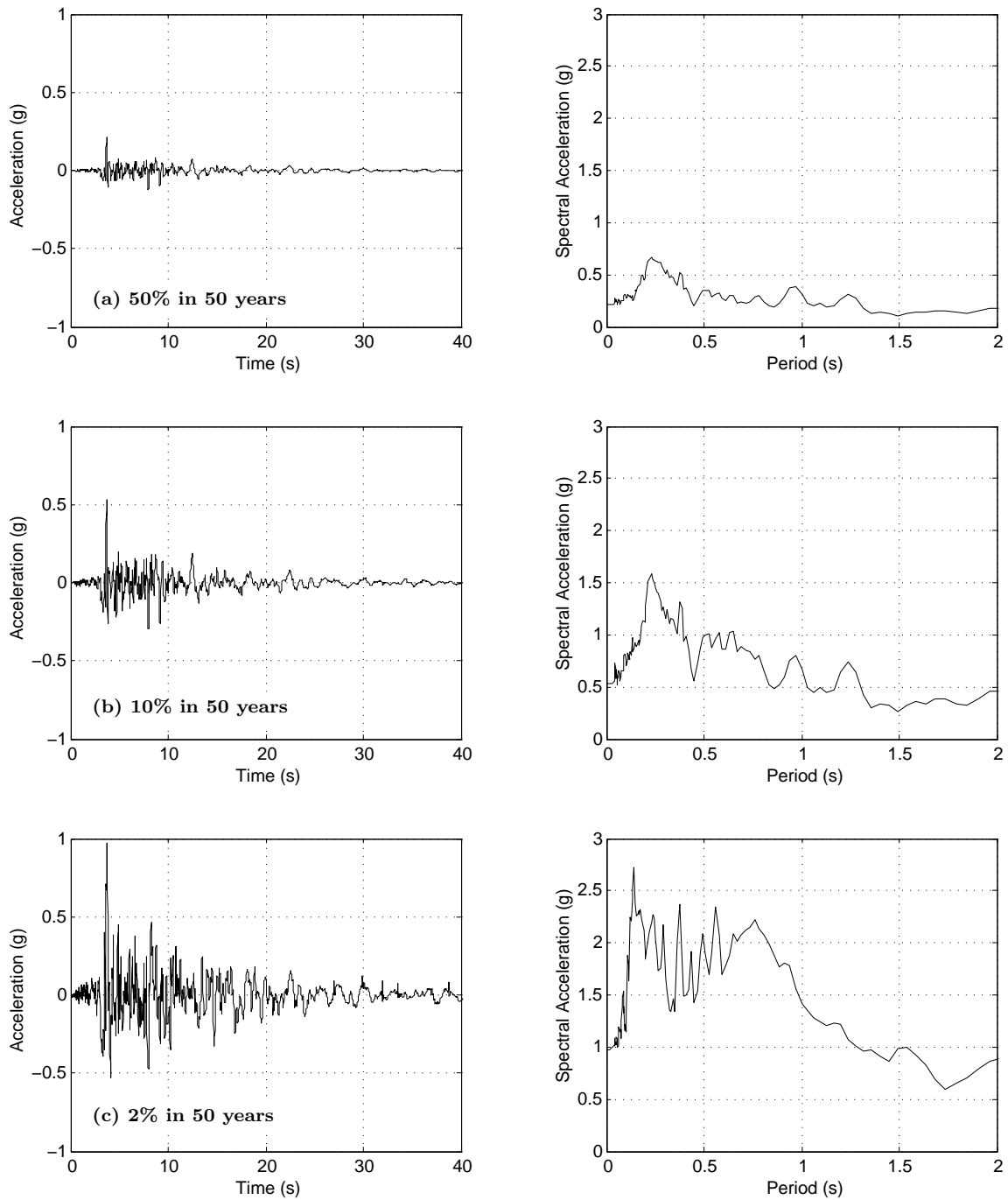
Figure 10.4: Acceleration time histories and acceleration response spectra (2% damping) for motions (a) F05L, (b) G03L, and (c) H08L.

Fig. 10.5 shows the drift ratio histories for all three bents and the three representative excitations. Bent 1 (medium height bent) had the largest response during the 50% and 10% in 50 year earthquakes at a maximum drift ratio of approximately 0.75% and 2%, respectively.

The shift of the maximum response from bent 1 to bent 3 was also visible in the shaking table experiments (Table 4.6). During Tests 12-14, bent 1 of the shaking table specimen sustained the largest maximum drift ratio of the three columns. For example, during Test 12, the maximum drift ratio of bent 1 was 0.30%, 42% larger than the maximum drift ratio of bent 3 (0.21%). After Test 14, bent 3 sustained the largest maximum drift. For example, during Test 19, bent 3 reached a drift ratio of 8%, 61% larger than the maximum drift ratio of bent 1 (5.0%). This shift in system behavior, which is evident in both the prototype model and the shaking table specimen, was attributed to the nonlinear interaction of the bents that cannot be simulated in component tests or elastic analyses.

Because residual column drift ratios affect bridge alignment rather than column damage, the residual column drift ratio was approximated as the ratio of the relative displacement between the top of the columns and the ground surface (δ_{clear}), and the clear column height (L_{clear}), defined as ($Drift_{res} = \delta_{clear}/L_{clear}$). During the larger excitation, bent 3 experienced the largest maximum drift ratio at 4.1%. Bent 3 also sustained significant residual drifts (0.4%) during the high-intensity ground motion. Bents 1 and 2 had negligible residual drift.
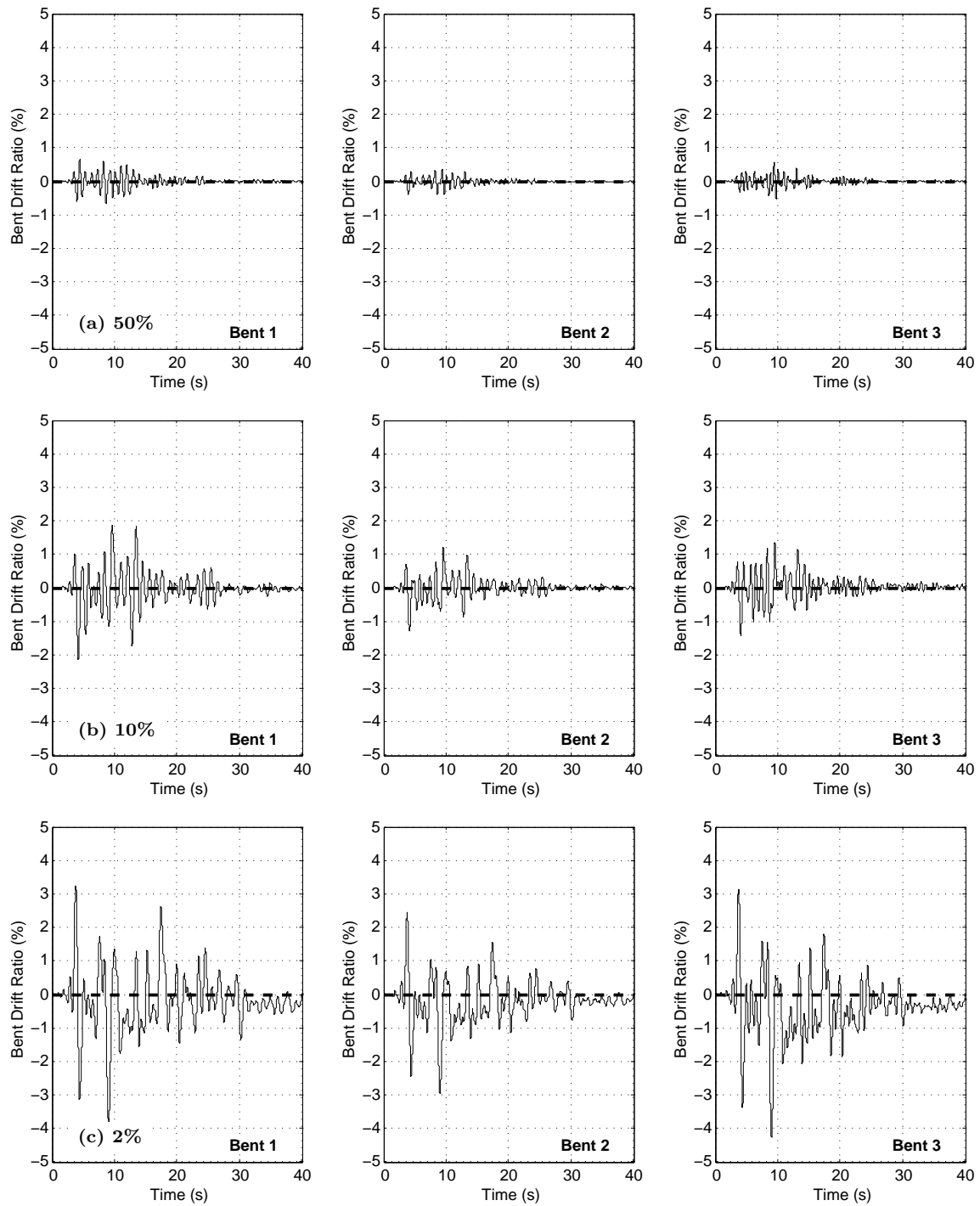
Figure 10.5: Drift histories for three far-field earthquake hazard levels: a) 50% in 50 years (F05L), b) 10% in 50 years (G03L), and c) 2% in 50 years (H08L)

10.3.3 Far-Field Response Distributions

This section presents the moment, shear, and plastic rotation distributions for the columns and piles, excited by the three representative far-field earthquake motions with hazard levels of 50%, 10% and 2% in 50 years.

Moment Distribution

The moment distributions along the columns and piles at the time of maximum moment, and at intervals of 0.4s, are shown in Fig. 10.6 for the three earthquake excitations. The moment distribution for the low-intensity earthquake (F05L) was governed by a single mode, with maximum bending moments at the top of the column. The point of maximum moment within each pile remained nearly constant at 3D throughout the excitation history, ranging between 2.5 column diameters (for the most flexible bent) to 3.5 column diameters (for the stiffest bent).

The depth of maximum moment within the piles increased slightly as the ground motions intensified. For example, the depth to maximum moment of the stiffest bent (bent 3) increased from approximately 3.5 column diameters during the low-intensity ground motion to approximately four column diameters during the high-intensity ground motion. This suggests that the ratio of pile to soil stiffness increased during the high-intensity excitations.

Shear Distribution

The distribution of shear forces within the columns and piles are shown in Fig. 10.7 for the three representative ground motions. The point of zero shear corresponds to the point of maximum moment within the piles (Fig. 10.6). It is also evident from this figure that as the column and soil underwent significant deformations, the shear distribution with the pile was governed by more than one mode.

At all levels of excitation, the shear within the columns were generally the smallest for bent 2 (tallest bent), and largest for bent 3 (shortest bent). The shear forces within the columns varied according to column height. In contrast, the shear forces within the piles were similar for each bent. For example, during the 2% in 50 year motion, the maximum

shear force within the piles of bents 1, 2 and 3 were 84%, 80% and 84% of the nominal shear capacity (ϕV_n), according to ACI Committee 318 (2002). For this same motion, the shear forces within the pile of bent 2 were approximately 1.8 times larger than those in the column.

Plastic Curvature Distribution

The plastic curvature at the tops of the columns was approximated by dividing the calculated plastic rotation by the estimated plastic hinge length. The plastic rotation at the top of the column (θ_p) was calculated by summing the rotation due to anchorage slip ($\theta_{p,s}$) and the plastic rotation due to column flexure ($\theta_{p,f}$), defined as

$$\theta_p = \theta_{p,f} + \theta_{p,s} \tag{10.5}$$

The plastic rotations within the columns were calculated from curvatures at the column integration points, and by equating displacements calculated from the distributed-plasticity model to those calculated using a plastic-hinge model. Based on plastic hinge analysis, the relative displacement between the top of the column and the inflection point ($\delta_{p,infl}$) is defined as

$$\delta_{p,infl} = \phi_p L_p \left(L_{infl} - \frac{L_p}{2} \right) \tag{10.6}$$

where L_p is the length of the plastic hinge (Eq. 9.7), L_{infl} is the length of the column from the top fixity to the inflection point, and ϕ_p is the plastic curvature across the plastic hinge zone. The plastic curvature was calculated by subtracting the yield curvature from the measured curvature values, $\phi_p = \phi - \phi_y \geq 0$. The yield curvature was estimated as the curvature at which the extreme tensile steel reached a strain of 0.002, or when the extreme compressive concrete reached a strain of 0.003, whichever came first.

The plastic displacement based on the distributed-plasticity model (modified from Eq. 10.4) is defined as.

$$\delta_{p,infl} = \sum_{i=1}^{N} \phi_{pi} w_i L_e \left(L_{infl} - \sum_{m=0}^{i-1} w_m L_e - \frac{w_i L_e}{2} \right) \tag{10.7}$$

Berry (2006) found that for steel with less than 5% strain hardening, the first two integration points accounted for all of the plastic displacement attributed to flexure within the column.

The strain hardening ratio of the steel for this system was less than 1%. Using $N = 2$, and equating Eq. 10.6 and Eq. 10.7, the plastic rotation due to flexure is

$$\theta_{p,f} = \frac{\phi_{p1} w_{ip1} L_e \left(L_{infl} - \frac{w_{ip1} L_e}{2} \right) + \phi_{p2} w_{ip2} L_e \left(L_{infl} - w_{ip1} L_e - \frac{w_{ip2} L_e}{2} \right)}{\left(L_{infl} - \frac{L_p}{2} \right)} \quad (10.8)$$

Simplifying the equation and adding the rotation due to the slip element, the plastic rotation at the top of the column is defined as

$$\theta_p = \frac{\phi_{p1} w_{ip1} L_e^2 \left(\frac{2L_{infl}}{L_e} - w_{ip1} \right) + \phi_{p2} w_{ip2} L_e^2 \left(\frac{2L_{infl}}{L_e} - 2w_{ip1} - w_{ip2} \right)}{(2L_{infl} - L_p)} + \theta_{p,s} \quad (10.9)$$

To provide an interface with the soil elements used in the numerical model, it was necessary to use pile elements with lengths approximately 1/5 of the pile diameter. Because the individual elements were short, and the moment gradient within the pile was gradual, the plastic curvature within the pile elements was approximated as

$$\phi_p = \frac{|\theta_i - \theta_j|}{L_e} - \phi_y \qquad\qquad \phi_p \geq 0 \qquad (10.10)$$

where θ_i and θ_j are the rotations at each end of the element, and L_e is the length of the pile element.

The plastic curvature distribution for the columns and piles are shown in Fig. 10.8. For all excitation levels, the plastic curvatures in the columns greatly exceeded the plastic curvatures in the piles. This effect was attributed to a more gradual moment gradient within the piles. As a result, the piles did not begin to undergo plastic curvature until the 10% in 50 year excitation. During the high-intensity ground motion, the plastic curvatures within the columns were approximately 9 times the plastic curvatures within the piles. For example, the plastic curvatures at the tops of the columns were approximately $22\phi_y$, $13\phi_y$, and $27\phi_y$ for bents 1, 2, and 3 respectively. During this same motion, the maximum curvature within the pile of bent 3 was approximately $3\phi_y$.
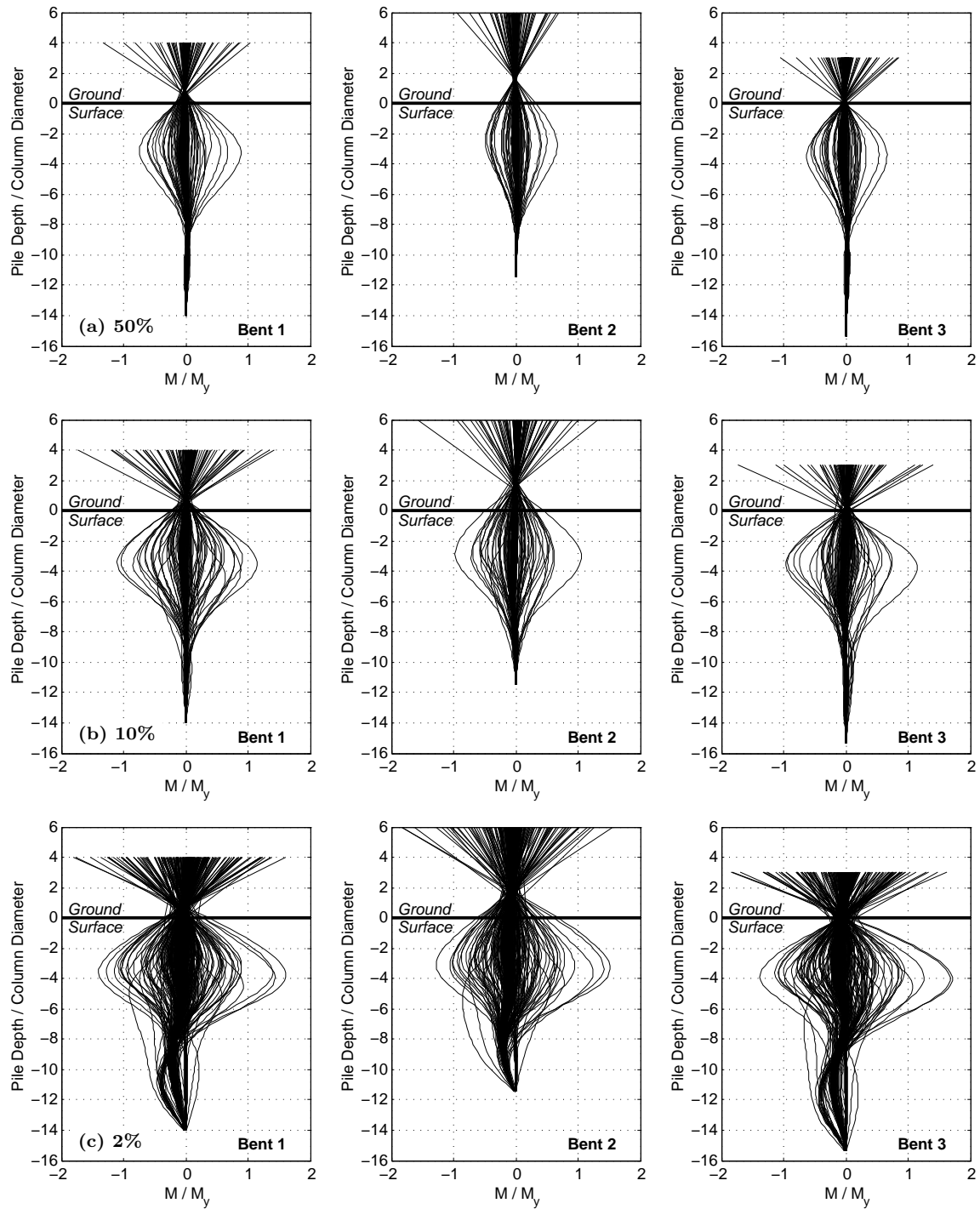
Figure 10.6: Moment distributions for three far-field earthquake hazard levels: a) 50% in 50 years (F05L), b) 10% in 50 years (G03L), and c) 2% in 50 years (H08L)
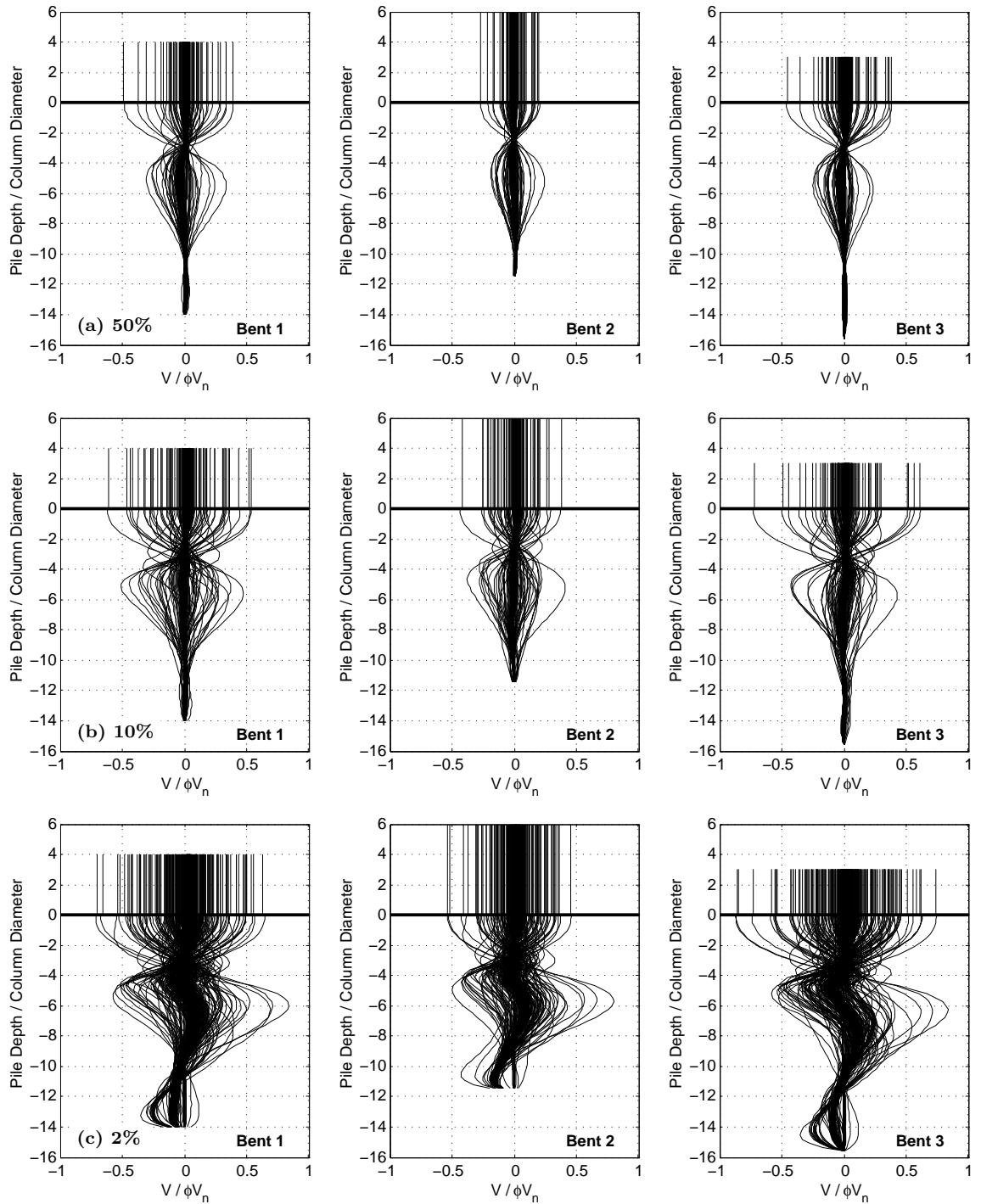
Figure 10.7: Shear distributions for three far-field earthquake hazard levels: a) 50% in 50 years (F05L), b) 10% in 50 years (G03L), and c) 2% in 50 years (H08L)

192
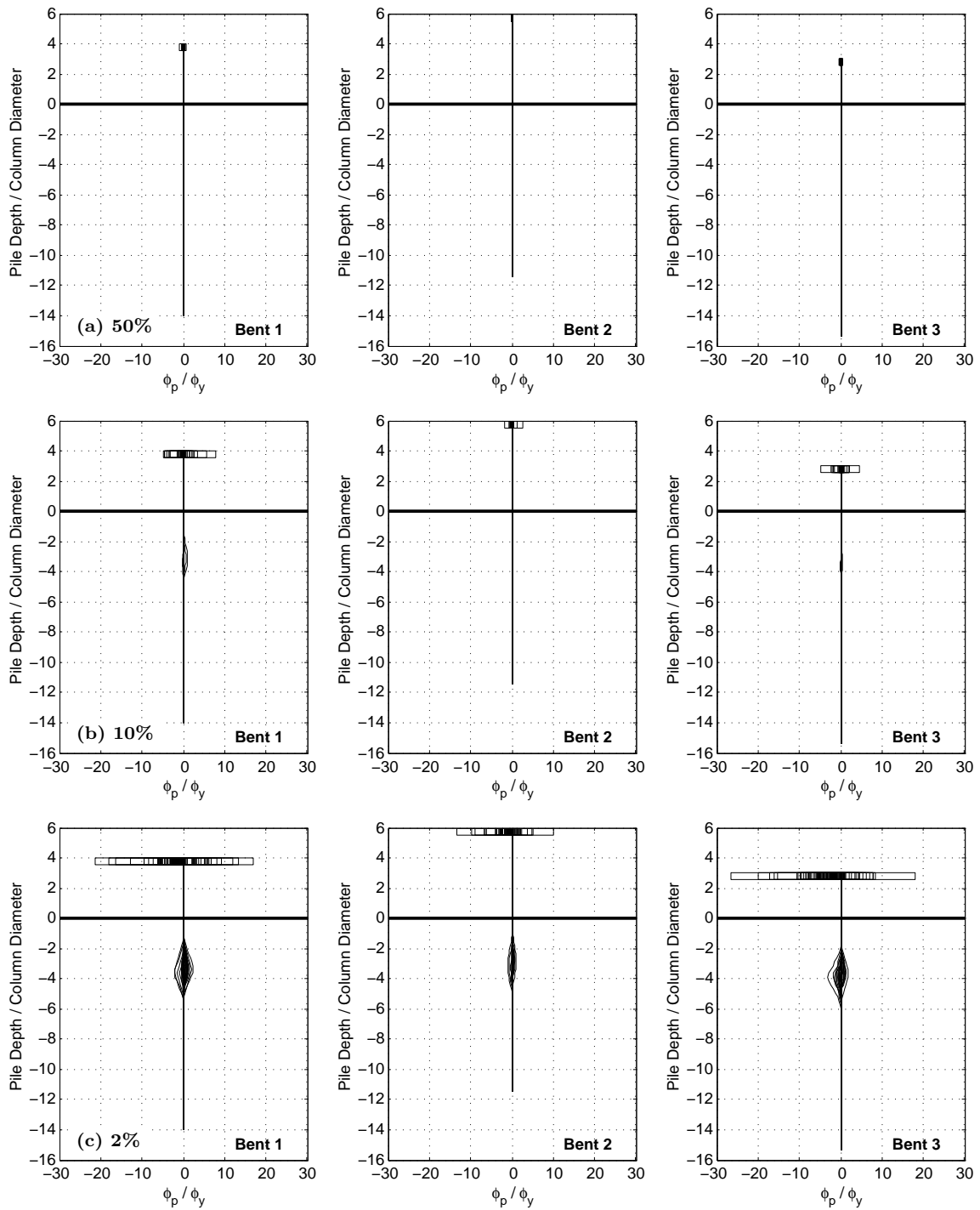
Figure 10.8: Plastic Rotation distributions for three far-field earthquake hazard levels: a) 50% in 50 years (F05L), b) 10% in 50 years (G03L), and c) 2% in 50 years (H08L)

10.3.4 Response Maxima

This section presents maxima of key response characteristics for the suite of 40 near-field and 30 far-field excitations, including: maximum bent drift ratio, residual bent drift ratio, maximum plastic rotation within the columns, total plastic rotation within the piles, maximum column shear, and maximum pile shear. The response maxima were plotted against the intensity of each ground motion, quantified using the Cordova parameter (Cordova et al., 2000). This parameter, defined in Chapter 11, accounts for system softening by using the spectral acceleration at one and two times the first period of vibration of the structure.

Maximum and Residual Drifts

The maximum bent drift ratios are plotted in Fig. 10.9 for both near-field and far-field excitations. For each bent, the average drift ratio at a Cordova of 0.3g and 3.0g is listed in Table 10.6. On average, the bent 1 drift ratios were slightly larger than the drift ratios for bent 3 during the low-intensity excitations for both near-field and far-field excitations. For example, due to the far-field excitations, the average bent 1 drift ratio at a Cordova of 0.3g was 0.88%, 13.9% higher than the average bent 3 drift ratio (0.77%). During the high-intensity excitations, the drift ratios for these two bents were similar. For example, due to the far-field excitations, the average bent 1 drift ratio at a Cordova of 3.0g was 8.71%, only 3.6% larger than the average bent 3 drift ratio (8.41%). The drift ratios for bent 2 (longest bent) were almost always smaller than the drift ratios for bents 1 or 3.

Table 10.6: Average prototype drift maxima at a Cordova of 0.3g and 3.0g for near-field and far-field excitations

Response	Bent	0.3g			3.0g		
		NF	FF	NF/FF	NF	FF	NF/FF
Maximum Drift Ratio (%)	1	1.03	0.88	1.17	7.87	8.71	0.90
	2	0.74	0.57	1.32	5.73	6.63	0.86
	3	0.98	0.77	1.28	7.84	8.41	0.93
Residual Drift Ratio (%)	1	0.032	0.010	3.20	0.90	0.81	1.12
	2	0.029	0.010	2.85	0.73	0.49	1.49
	3	0.028	0.010	2.78	0.93	0.53	1.75

The drift ratios for all three bents were generally larger during the high-intensity far-field

excitations than during the near-field excitations. For example, at a Cordova of 3.0g, the average drift ratios of bents 1, 2 and 3 for the far-field excitations were 8.71%, 6.63%, and 8.41%, respectively. These drift ratios were 11%, 16% and 7% larger than the drift ratios at this intensity for the near-field excitations.

The large drift ratios for each bent suggest that significant damage will occur at the tops of the columns. For example, according to the bar buckling equation developed by Berry (2006), at a Cordova parameter of 3.0g during the far-field excitations, bents 1, 2, and 3 had a probability of bar buckling of 90%, 55%, and 87%, respectively.

Fig. 10.10 shows the residual drift ratios for all three bents excited by the near-field and far-field excitations. The residual drift ratios for all bents were only weakly correlated with the Cordova parameter. For example, the R^2 value for the far-field excitations was 0.60, 0.49, and 0.50 for bents 1, 2, and 3, respectively.

Subjected to the near-field excitations, the average residual drift ratio of bents 1 and 3 at a Cordova of 3.0g were approximately 0.9%. Large residual drift ratios may have important consequences on the functionality of the bridge following an earthquake.

Column and Pile Plastic Rotations

Fig. 10.11 shows the maximum plastic rotation at the tops of the columns. The average plastic rotations are for a Cordova of 0.3g and 3.0g are listed in Table 10.7. On average, bents 1 and 3 experienced similar maximum plastic rotations. The plastic rotation in bent 2 (tallest bent) was almost always smaller than both of the shorter bents. For example, for the near-field earthquakes at a Cordova of 0.3g, bents 1, 2, and 3 underwent plastic rotations of 1.03%, 0.74%, and 0.98%, respectively.

The amount of plastic rotation in bents 1 and 3 was similar for the near-field and far-field excitations. For example, at a Cordova of 3.0g, the average plastic rotations in bent 1 were 10.72% (near-field) and 10.83% (far-field). In bent 2, the maximum plastic rotation was larger for near-field excitations during the low-intensity excitations, but larger for far-field excitations during the high-intensity excitations. For example the plastic rotation of bent 2 at a Cordova of 3.0g was 6.84% for the near-field excitations, 31% less than the plastic

Table 10.7: Average prototype plastic rotation maxima at a Cordova of 0.3g and 3.0g for near-field and far-field excitations

Response	Bent	0.3g			3.0g		
		NF	FF	NF/FF	NF	FF	NF/FF
Column Plastic Rotation (%)	1	0.40	0.41	0.98	10.72	10.83	0.99
	2	0.19	0.11	1.67	6.84	9.84	0.69
	3	0.40	0.35	1.14	10.61	10.66	1.00
Total Pile Plastic Rotation (%)	1	0.06	0.13	0.48	10.02	8.34	1.20
	2	0.32	0.08	4.20	2.86	4.09	0.70
	3	0.23	0.13	1.82	5.72	6.24	0.92

rotation for the far-field excitations (9.84%).

The large plastic rotations at each bent indicate that the tops of the columns would undergo significant flexural damage. For example, according to the bar buckling equation developed by Berry (2006), the mean plastic rotation at bar buckling for these columns is approximately 9.2%. The likelihood that bars would have buckled in bents 1, 2, and 3 at a Cordova of 3.0g during the far-field excitations is 79%, 66%, and 77%.

Fig. 10.12 plots the total plastic rotation within the piles. The total plastic rotation was calculated by summing all of the plastic rotations within the pile at an instant in time. For many of the low-intensity near-field and far-field excitations, there was no plastic rotation within the piles. These points do not appear on the plot.

For all levels of near-field and far-field excitations, the total pile plastic rotation was always smaller than the plastic rotation at the top of the column. For example, at a Cordova of 3.0g the total plastic rotations within the piles during the far-field excitations were 8.34%, 4.09%, and 6.24% for bents 1, 2, and 3, respectively. These values were 23%, 58%, and 41% lower than the plastic rotations within the columns, respectively. The difference between the total plastic rotation within the piles and the maximum plastic rotation within the columns is attributed to the larger distribution of deformation within the piles.

Column and Pile Shear Forces

Fig. 10.13 plots the maximum shear force within each column. The average shear forces at a Cordova of 0.3g and 3.0g are listed in Table 10.8. The scatter for this parameter was

small compared to the other demand parameters, because this quantity was limited by the flexural strength of the columns. On average, the maximum shear force within the columns was largest for bent 3 (short bent), and smallest for bent 2 (tall bent).

Table 10.8: Average prototype plastic rotation maxima at a Cordova of 0.3g and 3.0g for near-field and far-field excitations

Response	Bent	0.3g			3.0g		
		NF	FF	NF/FF	NF	FF	NF/FF
Column Shear (k)	1	242	255	0.95	395	384	1.03
	2	160	162	0.98	302	305	0.99
	3	292	301	0.97	458	451	1.02
Pile Shear (k)	1	248	243	1.02	436	459	0.95
	2	170	154	1.10	402	423	0.95
	3	295	302	0.97	473	459	1.03

The maximum shear force within the piles is shown in Fig. 10.14. The average shear forces within the piles at a Cordova of 0.3g and 3.0g are listed in Table 10.8. The maximum pile shear forces were similar to the maximum shear force within the columns for low-intensity earthquakes. For example, at a Cordova of 0.3g, the shear force within the pile of bent 2 due to the far-field excitations was 154k, 5% smaller than the shear force within the column (162k).

During the high-intensity excitations, the maximum shear force within the piles were larger than the shear forces within the piles. For example, at a Cordova of 3.0g, the shear forces within the piles due to the far-field excitations are 459k, 423k, and 459k. These shear forces are 19%, 39%, and 2% larger than the shear forces in the columns (384k, 305k, and 451k). This finding signifies that for lightly-confined columns, shear failure might occur below the ground surface rather than within the visible portion of the columns.
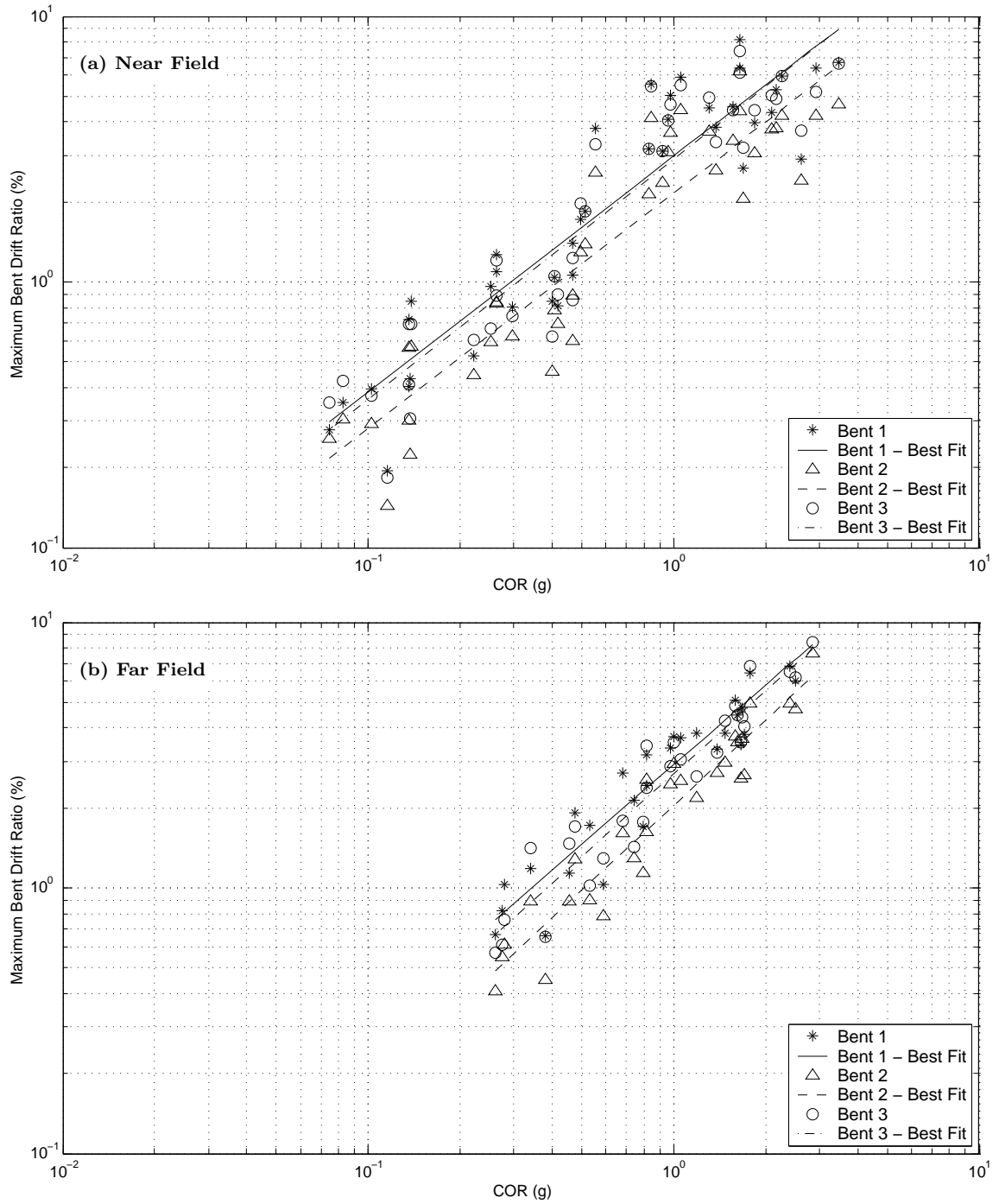
Figure 10.9: Drift ratio maxima for bents 1, 2, and 3 using (a) near-field excitations and (b) far-field excitations.
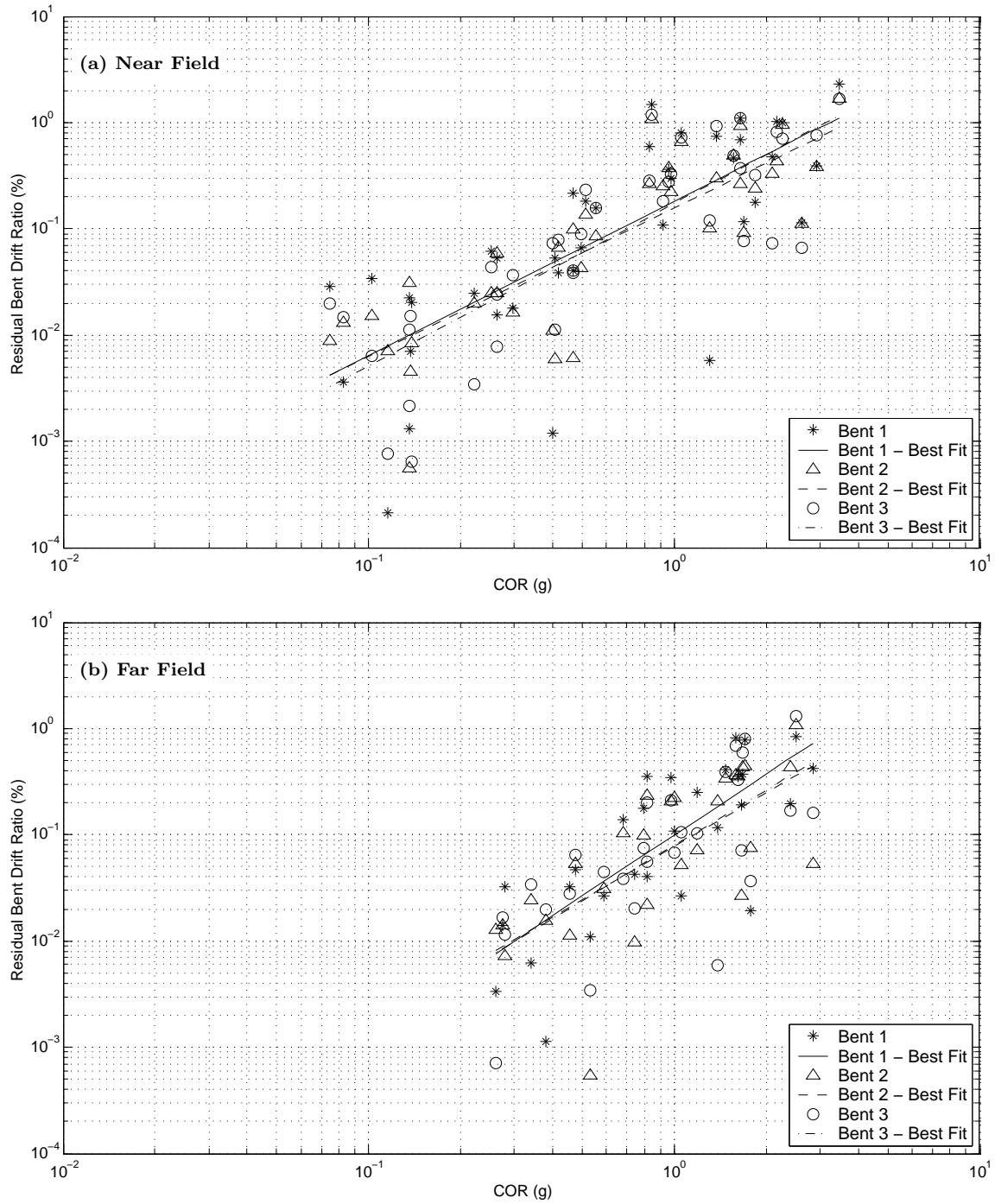
Figure 10.10: Residual drift ratios for bents 1, 2, and 3 using (a) near-field excitations and (b) far-field excitations.
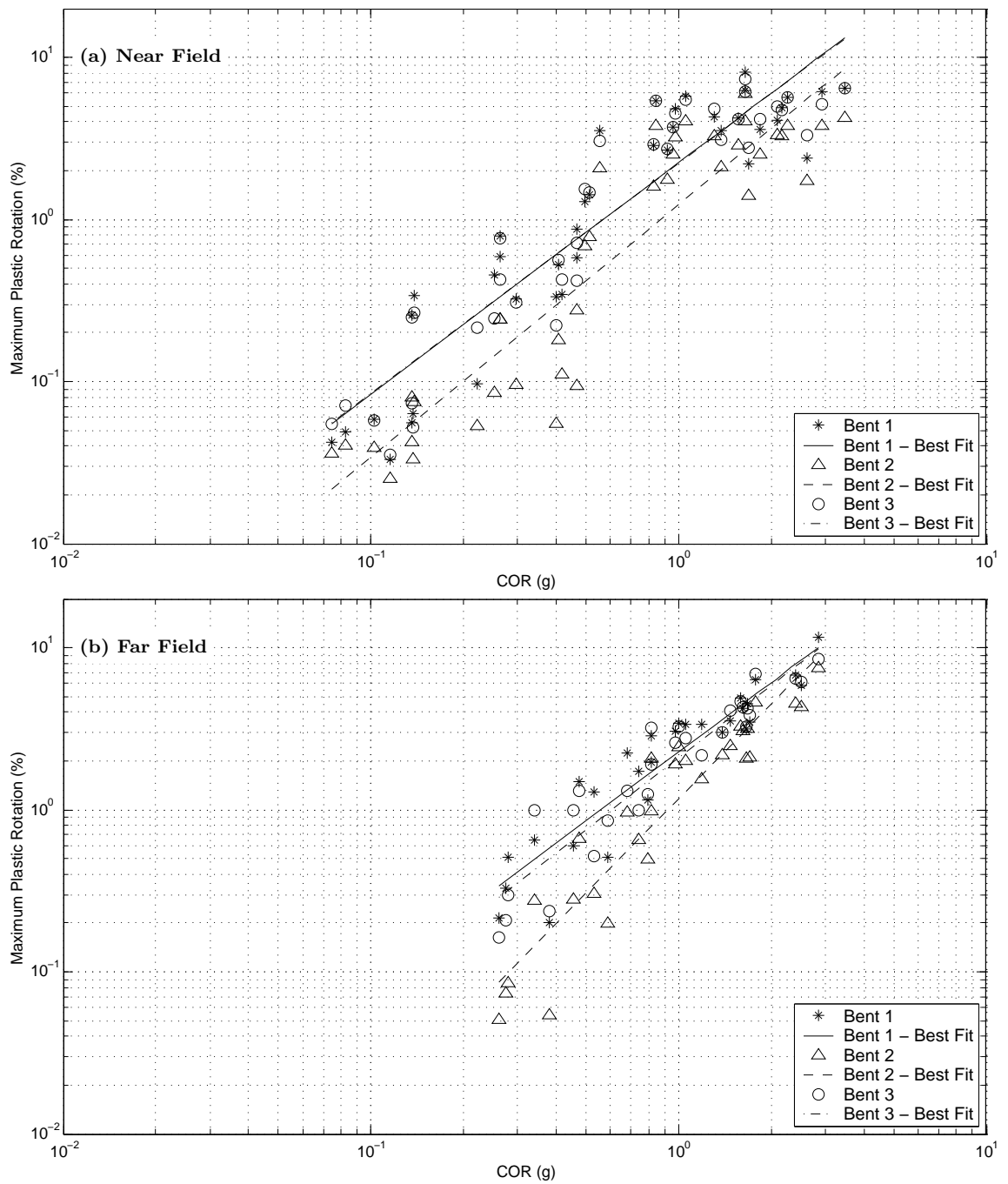
Figure 10.11: Column plastic rotation maxima for bents 1, 2, and 3 using (a) near-field excitations and (b) far-field excitations.
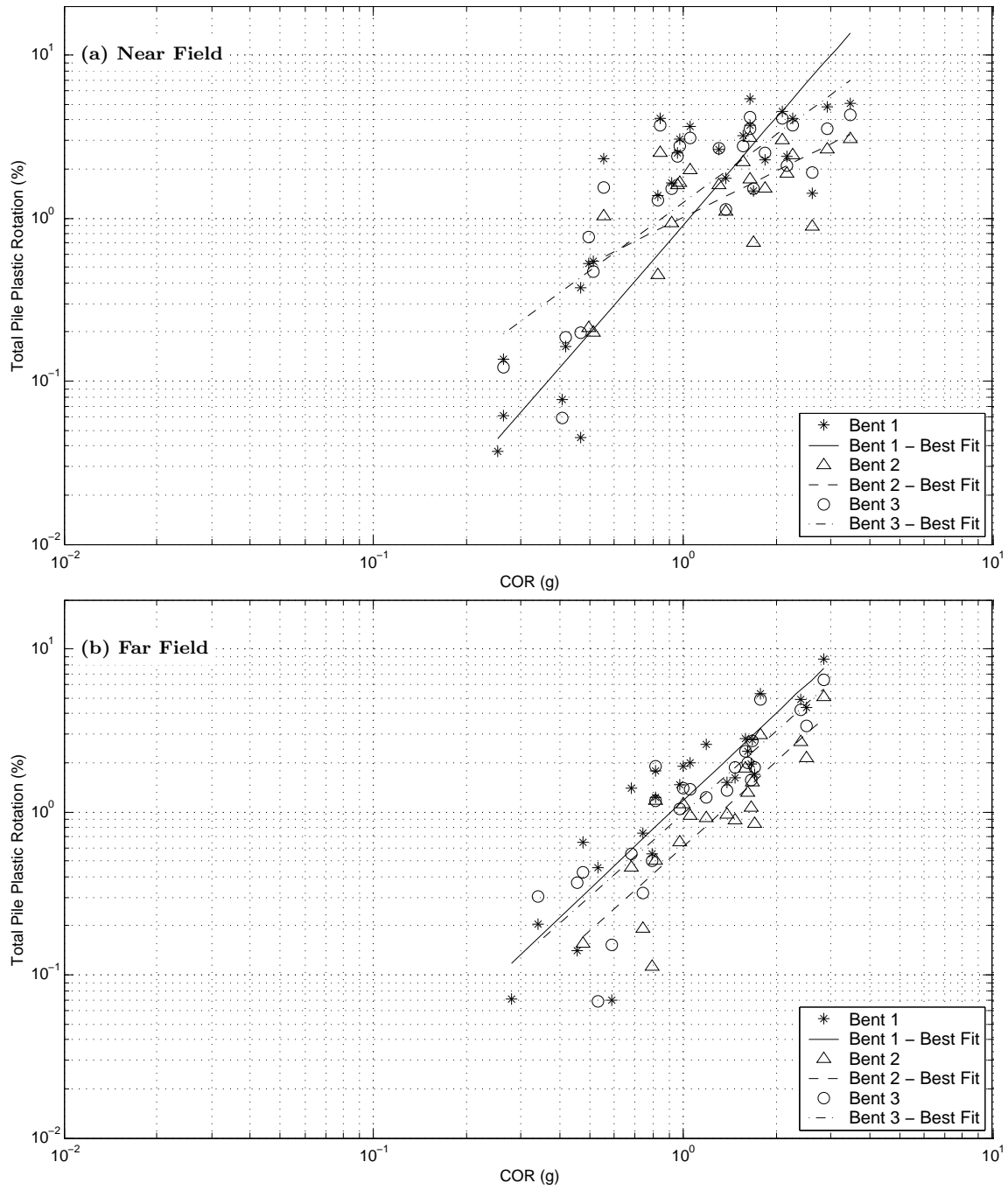
Figure 10.12: Total pile plastic rotation for bents 1, 2, and 3 using (a) near-field excitations and (b) far-field excitations.
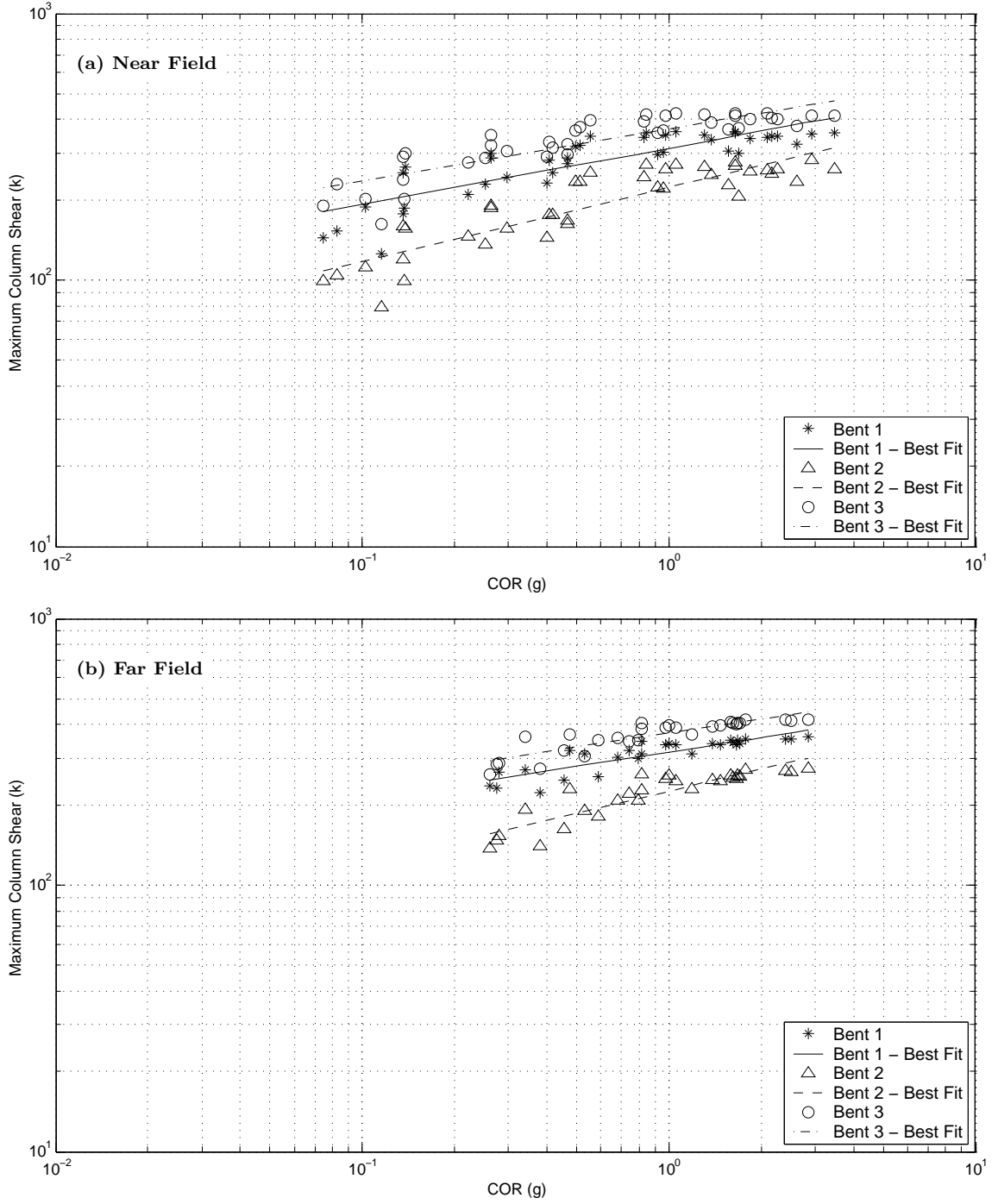
Figure 10.13: Maximum column shear for bents 1, 2, and 3 using (a) near-field excitations and (b) far-field excitations.
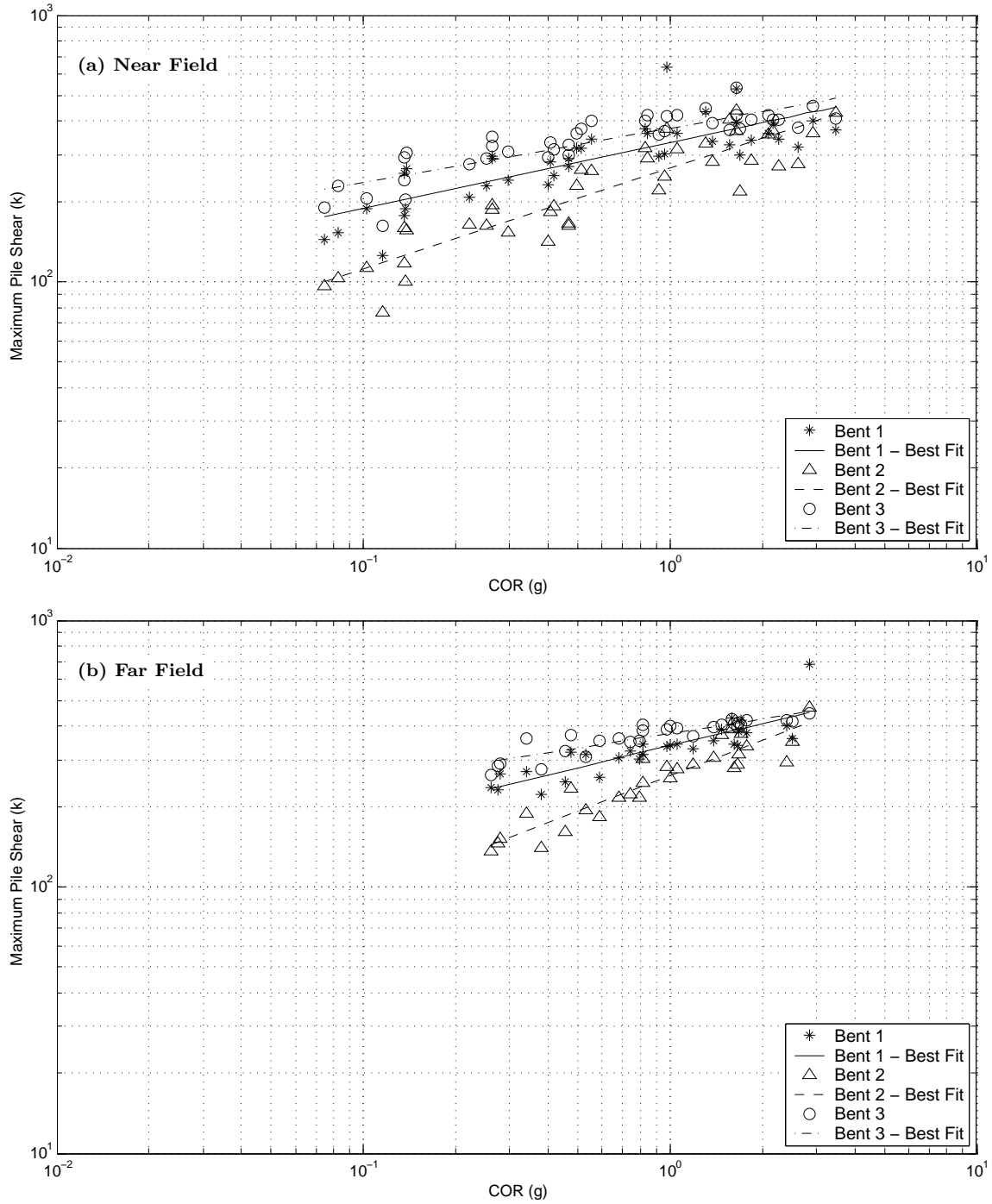
Figure 10.14: Maximum pile shear for bents 1, 2, and 3 using (a) near-field excitations and (b) far-field excitations.

10.4 Summary of Model Behavior

The prototype model was excited by a suite of 40 near-field and 30 far-field excitations. The significant conclusions from the prototype response to these excitations are listed below.

1. As expected, bents 1 (medium-height bent) and 3 (shortest bent) experienced larger drift ratios than bent 2 (longest bent). Bent 2 was the middle bent, and the clear height of its columns were at least 50% larger than the clear heights of the other bents. For low-intensity far-field excitations, the maximum drift ratios for bent 1 were generally larger than those for bent 3. For example, for the far-field excitations at a Cordova of 0.3g, the average bent 1 drift ratio was 0.88%, 13.9% higher than the average drift ratio for bent 3 (0.77%). The drift ratios of bents 1 and 3 were similar during the high-intensity excitations. At 3.0g, the average bent 1 drift ratio was only 3.6% larger than the bent 3 drift ratio.

2. During the low-intensity excitations, the depth of maximum moment in the piles ranged from 2.5 column diameters (bent 2) to 3.5 column diameters (bent 3) beneath the ground surface. During the high-intensity excitations, the depth of maximum moment for bent 3 increased from 3.5D to approximately 4D, suggesting that the ratio of the pile stiffness to the soil stiffness increased during these high-intensity excitations.

3. At a Cordova of 3g, the average drift ratios of bents 1 and 3 were approximately 8.7% and 8.4%, which could indicate significant flexural damage to the tops of the columns. For example, according the bar buckling equation developed by (Berry, 2006), the likelihood of bar buckling at drift ratios of 8.7% and 8.4% is 90% and 87%, respectively.

4. Bents 1 and 3 experienced large residual drift ratios when excited by near-field excitations. For example, at a Cordova of 3.0g for the near-field excitations, the average residual drift of bents 1 and 3 were approximately 0.9%. These high residual drifts may have important consequences on the functionality of the bridge following an earthquake.

5. The plastic curvatures at the tops of the columns were much larger than the plastic curvatures within the piles during the high-intensity excitations. For example, during a representative far-field excitation (H08L), the maximum plastic curvature within the column was approximately $27\phi_y$, nine times larger than the maximum plastic curvature in the pile $(3\phi_y)$. This difference was attributed to the gradual moment gradient within the piles, which reduced the concentration of deformations within the piles. Such large differences in the plastic deformations suggest that significant flexural damage to the system will occur at the tops of the columns rather than below the ground surface.

6. At a Cordova of 3.0g, the average plastic rotations of bents 1, 2, and 3 during the far-field excitations were 10.83%, 9.84%, and 10.66%. Similar to the large measured drift ratios, these large plastic rotations indicate that significant flexural damage could occur to the tops of the columns. For example, according to the bar buckling equation developed by Berry (2006), the likelihoods of bar buckling in bents 1, 2, and 3 are 79%, 66%, and 77% for this level of plastic rotation.

7. The shear forces within the columns were governed by the moment capacity of the column and the distance to the point of inflection. The boundary conditions in the soil are much more complicated. As a result, the shear forces within the piles were larger than the shear forces within the columns during the high-intensity excitations. For example, at a Cordova of 3.0g during the far-field excitations, the average shear force within the pile of bent 2 was 423k, 39% larger than the average shear force within the columns of bent 2 (305k). The higher shear forces in the columns signify that lightly-confined columns might fail in shear below the ground surface rather than within the visibly portion of the column.

Chapter 11

METHODOLOGY FOR EVALUATING SEISMIC MODELING STRATEGIES

This chapter describes the methodology that was used to evaluate the accuracy and precision of various seismic modeling strategies within a performance-based framework. Section 11.1 outlines the PEER performance-based framework. This chapter also describes the measures that were used to quantify the ground-motion intensity (Section 11.2), the system demands (Section 11.3), and the structural damage (Section 11.4). The methods for evaluating the accuracy and precision of the modeling strategies are described in Section 11.5.

11.1 PEER Framework

The Pacific Earthquake Engineering Research Center (PEER) has developed a probabilistic framework for implementing Performance-Based Earthquake Engineering (PBEE). This framework enables users to quantify the expected performance of bridges and other structures at multiple levels, including: structural demand, expected damage, and effects on system function and repair costs. This section reviews the methodology for using the PEER framework in a continuous domain. Mayfield (2007) describes a similar methodology for the discrete domain.

Fig. 11.1 illustrates the overall procedure for estimating the hazards at each performance level, from the intensity measure hazard to the hazard of a decision variable.

Each hazard level depends on information from previous hazard levels and models. For example, the accurate prediction of a demand hazard depends on the efficient characterization of the earthquake intensity, and accuracy and precision of demand models. The methodology for calculating the decision variable hazard from the intensity measure hazard is described in the following paragraphs.

The decision variable hazard (λ_{DV}) depends on the damage measure hazard and the
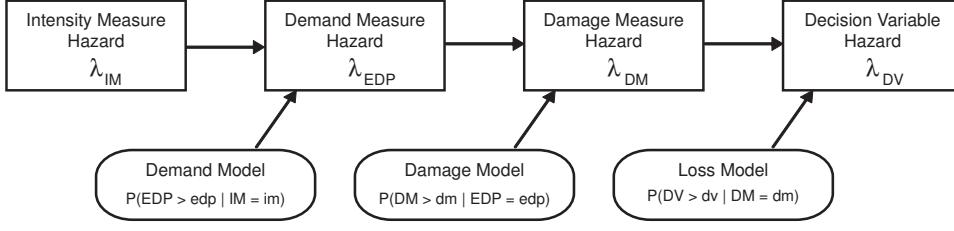
Figure 11.1: PBEE process illustration

model that describes the probability of exceeding the decision variable for a particular damage level (decision variable fragility curves). The decision variable hazard is described mathematically as

$$\lambda_{DV}(dv) = \int P[DV > dv | DM = dm] \frac{d\lambda_{DM}(dm)}{dDM} dDM \qquad (11.1)$$

where $P[\cdot]$ denotes a probability function, and $d\lambda_{DM}(dm)/dDM$ is the slope of the damage measure hazard curve at damage measure dm. In turn, the damage measure hazard (λ_{DM}) depends on the demand measure hazard (λ_{EDP}) and the damage measure fragility curves ($P[DM > dm | EDP = edp]$), defined as

$$\lambda_{DM}(dm) = \int P[DM > dm | EDP = edp] \frac{d\lambda_{EDP}(edp)}{dEDP} dEDP \qquad (11.2)$$

The demand measure hazard depends on the intensity measure hazard (λ_{IM}) and the demand measure fragility curves ($P[EDP > edp | IM = im]$), defined as

$$\lambda_{EDP}(edp) = \int P[EDP > edp | IM = im] \frac{d\lambda_{IM}(im)}{dIM} dIM \qquad (11.3)$$

The intensity measure hazard is defined by local site conditions and regional geography. By combining Eqs. 11.1 to 11.3, the hazard of the decision variable can be expressed as the following triple integral

$$\lambda_{DV}(dv) = \int \int \int P[DV > dv | DM = dm] \frac{dP[DM > dm | EDP = edp]}{dDM} \times \cdots$$
$$\frac{dP[EDP > edp | IM = im]}{dEDP} \frac{d\lambda_{IM}(im)}{dIM} dIM \cdot dEDP \cdot dDM \qquad (11.4)$$

In this equation, the hazard of the decision variable (λ_{DV}) depends on the hazard of the intensity measure (λ_{IM}), and the three fragility relationships between the various stages: IM → EDP, EDP → DM, and DM → DV. Although knowing the hazard levels at each step can yield useful information, this information is not essential for the final calculation.

The accurate estimation of the decision variable depends on the efficiency of the intensity measure, as well as the accuracy in the demand, damage, and loss models. The efficiency of over 50 intensity measures was investigated by Mackie and Stojadinovic (2005) for single and multi-span bridge systems. By assembling a database of the performance of test columns, Berry (2006) developed accurate column damage models. This thesis focuses on developing demand models for bridge systems, and evaluating the accuracy and precision of these models based on their effects on demand and damage estimates.

11.2 Motion Intensity

Mackie and Stojadinovic (2005) describe over 50 measures for quantifying earthquake intensity. This thesis concentrates on 11 intensity measures, listed in Table 11.1, chosen because of their common use and previous success in characterizing system demands.

Table 11.1: Candidate Intensity Measures

Class	IM	Intensity Measure	Definition
I	1	Peak Ground Acceleration	$PGA = max(|a(t)|)$
	2	Peak Ground Velocity	$PGV = max(|v(t)|)$
	3	Arias Intensity	$I_a = \frac{\pi}{2g} \int_0^{T_d} (a(t))^2 dt$
	4	Cumulative Absolute Velocity	$CAV = \int_0^{T_d} |a(t)| dt$
II	5	Spectral Acceleration (T_1)	$SA(T_1) = SA(T_1, \xi)$
	6	Spectral Acceleration (T_2)	$SA(T_2) = SA(T_2, \xi)$
	7	Cordova Predictor	$COR(T_1) = SA(T_1, \xi)\sqrt{\frac{SA(2T_1, \xi)}{SA(T_1, \xi)}}$
II-2	8	Square Root Sum of Squares	$SRSS = \sqrt{SA(T_1)^2 + SA(T_2)^2}$
	9	Complete Quadratic Combination	$CQC = \sqrt{\sum_{j=1}^n \sum_{k=1}^n C_{jk} SA(T_j) SA(T_k)}$
	10	SRSS(COR)	$SRSS(COR) = \sqrt{COR(T_1)^2 + COR(T_2)^2}$
	11	CQC(COR)	$CQC(COR) = \sqrt{\sum_{j=1}^n \sum_{k=1}^n C_{jk} COR(T_j) COR(T_k)}$

Class I intensity measures (peak ground acceleration, peak ground velocity, Arias intensity (Arias, 1970), and cumulative absolute velocity) only use data from the ground-motion time histories to quantify the intensity of the motion. These measures are often a maxima (e.g., PGA, PGV) or an energy (e.g., Ia, CAV).

Class II intensity measures (spectral accelerations, Cordova parameter) supplement the information from the ground motion time histories with modal information from the structure. Spectral accelerations are typically chosen at the estimated period of the structure to account for the elastic dynamic properties of the structure. The Cordova parameter (Cordova et al., 2000) accounts for both the elastic dynamic properties of the structure and the softening in the system by using the spectral accelerations at one and two times the first period of vibration of the structure.

As part of this research, Class II-2 intensity measures (square root of the sum of the squares, complete quadratic combination) were added to the list of intensity measure to investigate the effects of incorporating the modal properties from the first two frequencies of vibration of the system. The first two Class II-2 intensity measures (SRSS and CQC) combine the spectral accelerations at the first and second modes of the system, without accounting for column softening.

The CQC (DerKiureghian, 1980) combines modes, accounting for the correlation between modes j and k with the coefficient C_{jk}, defined as

$$C_{jk} = \frac{8 \left(\beta_j \beta_k \omega_j \omega_k\right)^{1/2} \left(\beta_j \omega_j + \beta_k \omega_k\right) \omega_j \omega_k}{\left(\omega_j^2 - \omega_k^2\right)^2 + 4\beta_j \beta_k \omega_j \omega_k \left(\omega_j^2 + \omega_k^2\right) + 4 \left(\beta_j^2 + \beta_k^2\right) \omega_j^2 \omega_k^2} \tag{11.5}$$

where ω_j and ω_k are the angular frequencies of modes j and k, respectively. The terms β_j and β_k are the damping ratios for modes j and k, respectively.

The SRSS and CQC methods were also applied to the Cordova parameters for the first two modes of the system to account for both column softening and the second mode of vibration.

The hazard at each level of motion intensity was modeled using a power law, defined in Eq. 11.6. The natural logarithm of this equation is defined in Eq. 11.7.

$$\lambda_{IM}(im) = k_0(im)^{-k} \tag{11.6}$$

$$\ln(\lambda_{IM}(im)) = \ln(k_0) - k \ln(im) \tag{11.7}$$

The least-squares method was used to estimate the best fit of scalars k_0 and k for these cases. Fig. 11.2 illustrates the intensity-hazard relationship in both normal and log space.
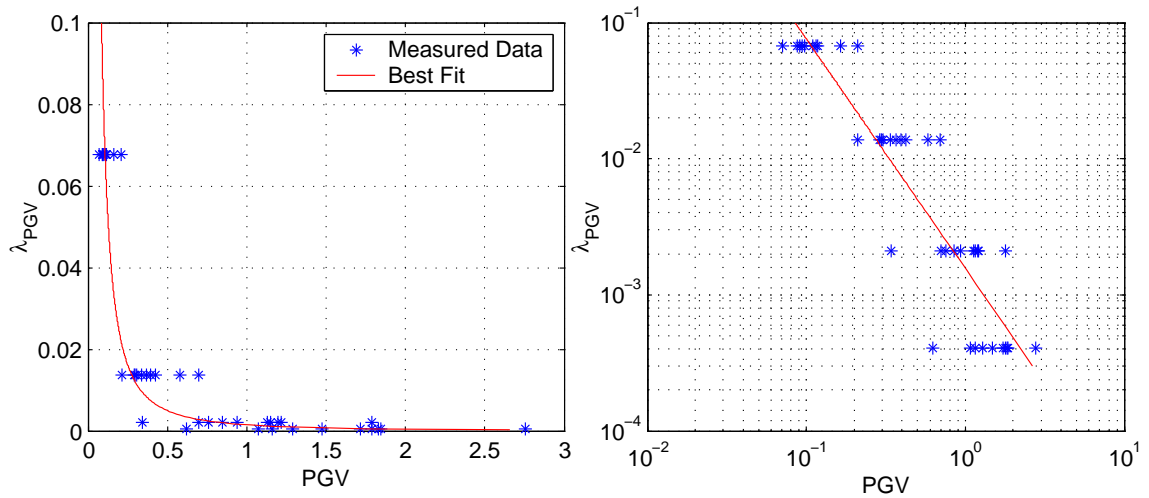
Figure 11.2: Illustration of the PGV hazard curve for the near-field excitations (Section 10.2)

11.3 Model Demand

This section describes the demand measures used in this research, the model relating the ground motion intensity to the estimated structural demand, and the methodology for calculating the estimated demand hazards.

11.3.1 Demand Measures

Four demand measures were chosen to quantify the performance of the numerical models: maximum column drift ratio, residual column drift ratio, maximum column plastic rotation, and maximum column shear. These demand measures were derived in Chapter 10 to describe the response of the prototype specimen.

Column drift ratio is useful for describing the amount of column deformation with a global parameter. Column displacements are commonly measured during experiments, which has led to substantial data relating maximum column drift ratio to subsequent damage. For example, Berry et al. (2004) assembled a database that documents the performance over 400 reinforced concrete test columns.

The residual column drift ratio is an indicator of possible differential displacement be-

tween the piers. Residual drift can affect bridge features that require alignment (e.g., railroad tracks), which would effect the post-earthquake functionality of a bridge.

The maximum column plastic rotation is a measure of local column deformation. Similar to drift ratios, the maximum plastic rotation is useful for estimating column damage in ductile columns. Berry (2006) developed a model to relate plastic rotation to various damage states within circular bridge columns.

The maximum column shear is an important demand parameter for lightly-confined or stocky columns, which might experience sudden shear failure. While researchers can easily estimate the shear forces within columns of component tests, the forces within indeterminate systems are much more difficult to approximate.

11.3.2 Demand Model

The demand model relates the intensity of a ground excitation to the demand it creates on the structure. Many researchers (Mackie and Stojadinovic, 2005; Jalayer, 2003) have found that the nonlinear relationship between the system response and the intensity of the ground motion can be accurately modeled as linear in log-space for a large range of system response. This relationship can be defined as

$$\ln(EDP) = A + B\ln(IM) \tag{11.8}$$

$$EDP = a(IM)^b \tag{11.9}$$

where $a = e^A$ and $b = B$. The constants A and B were estimated using a least-squares approach. Eq. 11.9 represents the mean IM-EDP relationship.

The uncertainty of the demand model is attributed to two sources, aleatory uncertainty and epistemic uncertainty. The aleatory uncertainty is due to the scatter of the IM-EDP relationship around the mean, quantified by the standard deviation. The standard deviation of the model error ($\sigma_{EDP|IM}$) was assumed to be constant across the entire data set, and was calculated as

$$\sigma_{EDP|IM} = \sqrt{\frac{1}{N-1}\sum_{i=1}^{N}(A + B\ln(IM_{meas}) - \ln(EDP_{meas}))^2} \tag{11.10}$$

where N is the number of data points in the data set, and IM_{meas} and EDP_{meas} are the measured IMs and EDPs, respectively, for each test. An illustration of this process is displayed in Fig. 11.3.
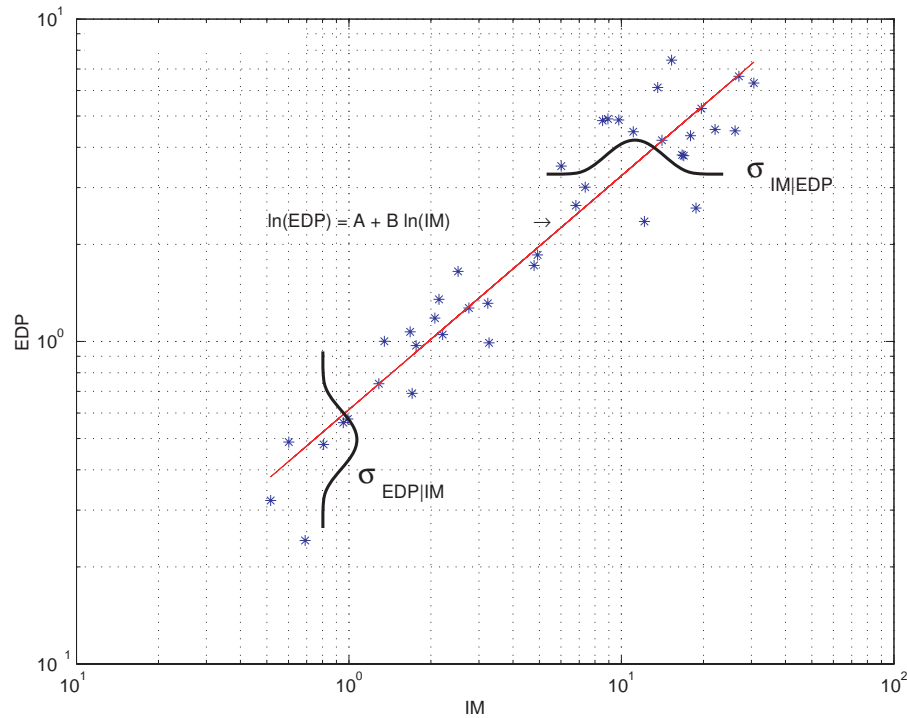
Figure 11.3: IM-EDP Illustration

Uncertainty associated with the numerical model (epistemic uncertainty) was approximated from results of the shaking table model (Chapter 8) and the centrifuge model (Shin, 2006). The uncertainty of the shaking table modal was approximated as the percent difference between the measured and simulated maximum displacements resulting from the low and high-amplitude earthquake excitations, which was approximately 10%. Assuming the epistemic uncertainty from the soil is similar to that from the structure, the total epistemic uncertainty is approximately 14%. This is close to the level of epistemic uncertainty that was proposed by Mackie and Stojadinovic (2005) for a detailed nonlinear seismic demand model (15%). Therefore, this research used an epistemic uncertainty of 15%. The total uncertainty for the seismic demand model ($\sigma_{SDM,T}$) was approximated as the square root

of the sum of the squares (SRSS) of the aleatory uncertainty ($\sigma_{EDP|IM}$) and the epistemic uncertainty ($\sigma_{U,SDM}$), defined as

$$\sigma_{SDM,T} = \sqrt{\sigma_{EDP|IM}^2 + \sigma_{U,SDM}^2} \qquad (11.11)$$

This thesis does not consider the additional uncertainty in the bridge and soil material properties.

11.3.3   Demand Hazard

Jalayer (2003) used integration by parts to develop a closed-form solution for the demand hazard (Eq. 11.3) from the intensity measure hazard and the fragility curves relating motion intensity to system demand, defined as

$$\lambda_{EDP}(edp) = k_0 \left[\left(\frac{edp}{a} \right)^{1/b} \right]^{-k} \exp \left(\frac{k^2}{2b^2} \sigma_{SDM,T}^2 \right) \qquad (11.12)$$

Mayfield (2007) illustrates the calculation of the EDP hazard curve numerically using the equation

$$\lambda_{EDP}(edp_j) = \sum_{i=1}^{N} p[EDP > edp_j | IM = im_i] \Delta\lambda_{IM}(im_i) \qquad (11.13)$$

where i and j are indices for the intensity measure and the demand parameter, respectively. The variable N is the total number of summation steps, which is defined by the discritezation size that is used.

11.4   Model Damage

Various damage measures are possible for describing the extent of damage to a bridge, including column damage measures (e.g., concrete spalling, buckling of the longitudinal reinforcement) and system damage measures (e.g., unseating, misalignment). This research focussed on the concrete spalling and bar buckling. These damage levels were chosen because: (1) each measure has an associated repair cost, (2) Berry (2006) has developed EDP/DM fragility curves for these measures, and (3) these damage states are relevant to current bridge design standards.

11.4.1 Damage Models

The UW-PEER reinforced concrete column database (Berry et al., 2004) contains performance data for over 400 columns. From this database, Berry (2006) developed empirical fragility equations relating concrete spalling and bar buckling to three measures of demand: column drift, plastic rotation, and material strains. The damage equations utilizing column drift and plastic rotation are used in this research.

Damage Estimates Based on Column Drift

According to Berry (2006), the calculated drift ratio for the mean occurrence of damage can be described by the equation

$$\frac{\delta_{dam,calc}}{L}(\%) \cong C_0 \left(1 + C_1 \frac{\rho_{eff}d_b}{D} \right) \left(1 - C_2 \frac{P}{A_g f_c'} \right) \left(1 + C_3 \frac{L}{D} \right) \qquad (11.14)$$

where P is the column axial load, A_g is the gross section area of each column, f_c' is the unconfined concrete compressive strength, D is the column diameter, d_b is the diameter of the longitudinal reinforcement, and L is the length of the column from the column fixity to the inflection point. The effective transverse reinforcement ratio (ρ_{eff}) is defined as

$$\rho_{eff} = \rho_s \frac{f_y}{f_c'} \qquad (11.15)$$

where ρ_s is the transverse reinforcement ratio and f_y is the yield stress of the reinforcement. The coefficients C_0, C_1, C_2, and C_3 were calibrated to minimize the difference between the calculated and observed damage for a subset of spiral-reinforced columns within the database (29 columns for concrete spalling and 33 columns for bar buckling). The optimal coefficients for spalling and bar buckling are listed in Table 11.2.

Table 11.2: Optimal drift coefficients for spalling and bar buckling (Berry, 2006)

damage state	C_0	C_1	C_2	C_3	$\delta_{dam,meas}/\delta_{dam,calc}$	COV
spalling	1.6	0.0	1.0	0.1	1.07	34.9
bar buckling	3.25	150	1.0	0.1	1.01	24.7

The ratios of the measured displacements at damage to those calculated using Eq. 11.14 had means of 1.07 and 1.01 for concrete spalling and bar buckling, respectively. The coefficients of variation for these ratios were 34.9% and 24.7%, respectively.

Damage Estimates Based on Column Plastic Rotation

Berry (2006) developed a similar equation to Eq. 11.14 for estimating the mean plastic rotation at which damage is expected, defined as

$$\theta_{p,dam,calc} = C_0 \left(1 + C_4 \rho_{eff}\right) \left(1 + C_1 \frac{P}{A_g f'_c}\right)^{-1} \left(1 + C_2 \frac{L}{D} + C_3 \frac{f_y d_b}{D}\right) \qquad (11.16)$$

The optimal coefficients $(C_0 - C_4)$ for both spalling and bar buckling are listed in Table 11.3. The ratio of the measured to calculated plastic rotation for the two damage states were $0.99 \pm 48.1\%$ (spalling) and $1.01 \pm 24.1\%$ (bar buckling).

Table 11.3: Optimal plastic rotation coefficients for spalling and bar buckling (Berry, 2006)

damage state	C_0	C_1	C_2	C_3	C_4	$\theta_{p,dam,meas}/\theta_{p,dam,calc}$	**COV**
spalling	0.0100	0.0010	0.0500	0.0030	0.0000	0.99	48.1
bar buckling	0.0009	0.0000	1.3000	3.0000	7.3000	1.01	24.1

11.4.2   Damage Hazard

Column damage is a series of binary observations rather than a continuous variable. For example, key column damage measures (e.g., bar yielding, concrete spalling, bar buckling, column loss of lateral load capacity) are isolated observations, with no observations of damage in between.

Because of the binary quality of column damage, the damage hazard was solved numerically. The hazard for each damage level generated a single point on the damage hazard curve. The discrete procedure for calculating the damage hazard for each level of damage is represented in Eq. 11.17, and illustrated in Fig. 11.4.

$$\lambda_{DM}(dm_j) = \sum_{i=1}^{N} p[DM > dm_j | EDP = edp_i] \Delta \lambda_{EDP}(edp_i) \qquad (11.17)$$

For a given dm, the DM hazard is the sum of the products between incremental change in the EDP hazard curve $(\Delta \lambda_{EDP}(edp_i))$ and the probability of damage $(p[DM > dm_j | EDP = edp_i])$ for each edp.
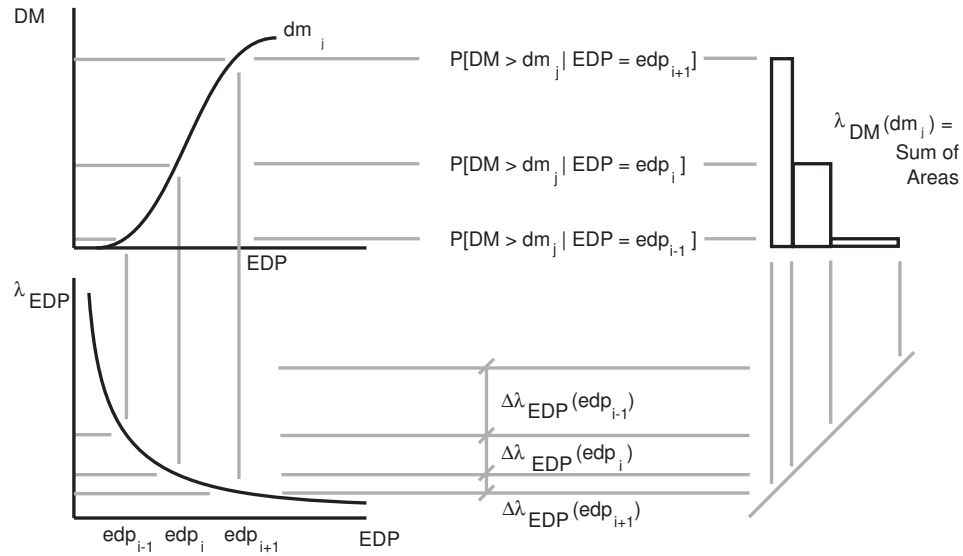
Figure 11.4: Illustration of EDP hazard curve calculation

11.5 Model Evaluation

The accuracy and precision of the seismic demand models introduced in Chapter 12 were evaluated within the performance-based framework presented in this chapter. The demand models were evaluated by comparing the response from these models to the response from the prototype model (Chapter 10) on two levels, estimated system demands and resulting damage estimates.

The system demands of the models were compared on a test-by-test basis with the prototype model for the suite near-field and far-field excitations (Section 10.2). The error of the model demands was defined as the percent difference between the demands estimated with the simpler models to the demands estimated with the prototype model. The accuracy and precision of the models was defined as the mean and standard deviation of these errors for all intensity levels.

The accuracy of the demand models was also compared on the system damage level. The damage hazards for each demand model were calculated using Eq. 11.17. These damage hazards were compared to those from the prototype model to assess the effects of each

modeling approximation on the overall damage estimates. The errors in the damage hazards were also compared to the errors in damage hazards from inefficient intensity measures to investigate the relative importance of accurately modeling the structural system.

Chapter 12

EVALUATION OF BRIDGE MODELING STRATEGIES

This chapter evaluates various foundation and structural modeling strategies for approximating the seismic behavior of a soil-foundation-structure bridge system. These strategies were evaluated within a performance-based framework (Chapter 11) by comparing their calculated performance with the calculated performance of the prototype model (Chapter 10).

Specifically, this chapter: describes the modeling strategies that were evaluated (Section 12.1); evaluates the accuracy and precision of the seismic modeling strategies by comparing the engineering demand parameters of the various models (Section 12.2); evaluates the sensitivity of the model accuracy to the estimated depth of fixity (Section 12.3); compares the efficiency of common intensity measures (Section 12.4); calculates the sensitivity of the IM efficiency to the structural parameters (Section 12.5); and estimates the damage hazard (for concrete spalling and bar buckling) for the various models and intensity measures (Section 12.6). Key conclusions from this chapter are summarized in Section 12.7.

12.1 Bridge System Modeling Strategies

This research investigated the influence of foundation and structural modeling strategies on the accuracy and precision of bridge system models. The foundation was modeled using three methodologies: two-dimensional, nonlinear soil columns; linear soil springs; and fixing the column at a depth below the ground surface. The columns and shafts were modeled with nonlinear column elements, with effective-section linear column elements, and with gross-section linear column elements. Each of the foundation and structure modeling strategies is discussed in this section.

12.1.1   Foundation Approximations

The foundation in the prototype was modeled using two-dimensional nonlinear soil columns (Chapter 10). Shin (2006) calibrated the soil elements and P-y springs in this model based on the response during centrifuge tests. To evaluate the consequences of using simpler foundation approximations, the foundations were approximated with either (1) linear soil springs or (2) fixing the column bases at a depth below the ground surface.

First, the numerical model of the prototype specimen was approximated by replacing the two-dimensional nonlinear soil columns with linear soil springs at the ground surface (Novak, 1974). In these models, flexibility and damping attributed to the soil and foundation were modeled with linear translational and rotational springs and dashpots.

The spring stiffnesses were calculated by Professor Kramer at the University of Washington with the program DYNA (Novak et al., 1993). The program used the effective elastic pile and soil properties. Stiffnesses and damping ratios were obtained for two boundary conditions at the top of the pile, pinned and fixed against rotation. The two top-of-pile constraints are illustrated in Fig. 12.1. In both cases, the bases of the shafts were assumed to be fixed. The calculated stiffness and damping values for the two boundary conditions are listed in Table 12.1. Because the structure above ground had some stiffness but was not rigid, the actual fixity conditions at the top of the pile would be expected to lie between these two extreme values. The program did not calculate spring stiffnesses for the actual boundary conditions between these two extreme cases.
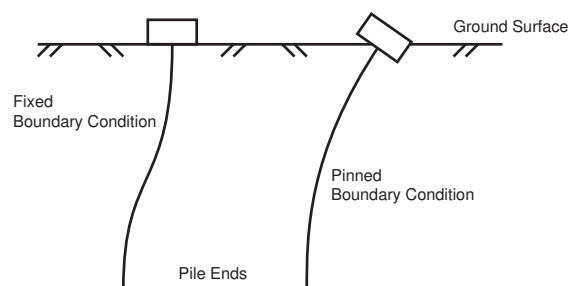
Figure 12.1: Illustration of fixed and pinned boundary conditions for spring model

Table 12.1: Stiffness and damping values for the spring models

Type	Degree of Freedom	Pinned	Fixed
Stiffness	Horizontal Translation (k/in.)	8.49E+02	1.67E+03
	Vertical Translation (k/in.)	6.25E+03	6.25E+03
	Moment Rotation (k*in./rad)	0.00E+00	6.92E+06
	Torsion Rotation (k*in./rad)	1.40E+06	1.40E+06
Damping	Horizontal Translation (k/in./s)	1.01E+01	1.81E+01
	Vertical Translation (k/in./s)	6.19E+01	6.19E+01
	Moment Rotation (k*in./rad/s)	0.00E+00	2.53E+04
	Torsion Rotation (k*in./rad/s)	3.56E+03	3.56E+03

Second, the foundation was approximated by fixing the columns below the ground surface. For this analysis, depths of zero and three times the column diameter were considered. A fixity depth at the ground surface was chosen to illustrate the effects of neglecting the influence of the soil and foundation flexibility on the structural response.

The bases of the columns were also fixed at a depth of three column diameters below the ground surface, based on the location of the maximum moment in the piles of the prototype model (Section 10.3.3). This approximation accounted for the foundation flexibility by elongating the columns. This approximation did not account for the interaction of the pile and soil between the ground surface and the assumed point of fixity, nor did it model the nonlinear behavior of the soil.

12.1.2 Structural Approximations

The nonlinear structural elements of the prototype model were calibrated based on the dynamic response from the shaking table tests (Chapter 8). To evaluate the consequences of using simpler column modeling strategies, the columns were modeled using elastic column elements with either gross-section or effective-section properties. For both approximations, the bond-slip section included in the nonlinear column model was removed, and the effective viscous damping ratio was assumed to be 5%.

The column stiffnesses were first approximated using gross-section properties ($EI = EI_g$). This assumption is the simplest to implement and may be accurate during low-intensity earthquakes, in which the columns have little cracking. However, this method was

220

expected to greatly overestimate the column stiffness during high-intensity excitations.

In practice, the most common elastic analysis methods involve approximating the column stiffness using effective-section properties. This methodology accounts for the progression of column cracking during high-intensity earthquakes. For ductile columns, Caltrans (2004) suggests using an effective modulus of rigidity ($E_c I_{eff}$) based on the secant slope to the yield point in a moment-curvature relationship.

$$E_c I_{eff} = \frac{M_y}{\phi_y} \tag{12.1}$$

where E_c is the elastic modulus of the concrete, and M_y and ϕ_y are the calculated moment and curvature at first yield of the longitudinal reinforcement. Using this effective rigidity may underestimate the column stiffness during low-intensity excitations, when columns are not typically cracked along the entire length of the member. This method neglects the flexibility due to bond slip within the anchorages at all intensity levels, and does not account for the nonlinear behavior of the columns.

12.1.3 Matrix of Bridge Modeling Strategies

The foundation and structural approximation methodologies discussed in the previous sections were combined to create the matrix of bridge modeling strategies shown in Fig. 12.2. Each row in Fig. 12.2 represent a particular foundation modeling strategy. The bottom row represents the nonlinear soil, which was calibrated based on a series of centrifuge tests (Shin et al., 2006). The other four rows represent simpler foundation approximations (Section 12.1.1). Each column in Fig. 12.2 represents the structural modeling strategies (Section 12.1.2). The right column represents the nonlinear structure that was calibrated from the shake-table tests (Chapter 8). The left column represents two linear structure approximations; gross-section and effective-section column stiffnesses.

The matrix describes a total of 13 bridge modeling strategies: 12 combinations of structure and foundation modeling approximations, and the prototype model with the calibrated soil and structure approximations. The accuracy and precision of these modeling strategies were evaluated (in comparison with the prototype model) in terms of deformation and shear demands (Section 12.2), and damage levels (Section 12.6).
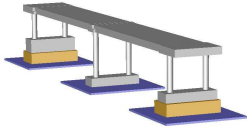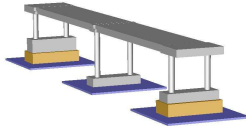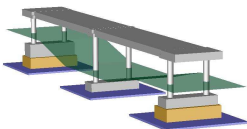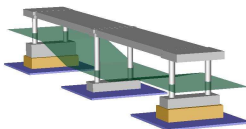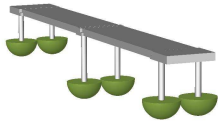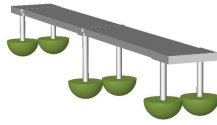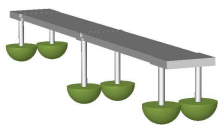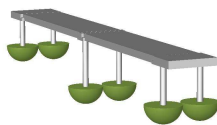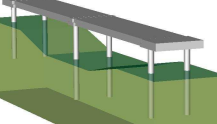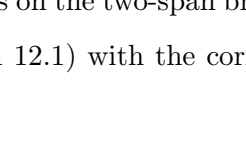
Foundation Approximation	Linear Column Properties		Nonlinear Column Properties
Fixed at Surface	$EI = E_c I_g$	$EI = E_c I_{eff}$	
Fixed at 3.0D	$EI = E_c I_g$	$EI = E_c I_{eff}$	
Soil Springs **Pinned**	$EI = E_c I_g$	$EI = E_c I_{eff}$	
Soil Springs **Fixed**	$EI = E_c I_g$	$EI = E_c I_{eff}$	
Soil Columns			*Prototype Model*
	Not Considered		

Figure 12.2: Matrix of bridge system modeling strategies

12.2   Accuracy and Precision of Bridge Modeling Strategies

This section compares the deformation and force demands on the two-span bridge estimated using the 12 simpler bridge modeling strategies (Section 12.1) with the corresponding de-

mands estimated using the prototype model.

12.2.1 Error Quantification

The errors in the structural demands for each model ($Error_{EDP}$) were quantified on a motion-by-motion basis by the relative differences between the demands from the simpler models (EDP_{model}) and the demands from the prototype model (EDP_{proto}). For each motion (i), the error in the demands of each model was defined as

$$Error_{EDP,i}(\%) = \frac{EDP_{model,i} - EDP_{proto,i}}{EDP_{proto,i}} \times 100 \tag{12.2}$$

The accuracy of the model at every bent was defined as the average error in the engineering demand parameter at each hazard level, defined as

$$Accuracy = \mu = \frac{1}{N} \sum_{i=1}^{N} Error_{EDP,i} \tag{12.3}$$

where N is the number of motions at each hazard level ($N = 10$ for this research). The precision of the modeling strategy was quantified by the standard deviation in the error of the engineering demand parameter at each hazard level, defined as

$$Precision = \sigma = \sqrt{\frac{1}{N-1} \sum_{i=1}^{N} [Error_{EDP,i} - \mu_{error}]^2} \tag{12.4}$$

The mean (accuracy, μ) and standard deviation (precision, σ) of the error of each model were calculated at all hazard levels for both near-field and far-field excitations. The overall accuracy and precision of each model was computed for each EDP using the calculated error from all motions and all bents (a total of 180 values).

The error statistics for all EDPs and modeling approximations are presented in Appendix H. The errors in the calculated drift ratios for the inelastic, effective elastic, and gross elastic models are presented in tables H.1 - H.3, and are plotted in figs. H.1 - H.3.

As an example, Table 12.2 and Fig. 12.3, repeated from the appendix, illustrates the organization of the calculated errors. The columns in Table 12.2 provide the means and standard deviations for the four foundation approximations. The rows provide the statistics for bents 1, 2, and 3, subjected to the near-field and far-field excitations for three levels of

hazard. The 97% in 50 year hazard level was not considered in these statistics because this hazard level was only developed for the near-field situation. In each plot within Fig. 12.3, the mean errors for the three hazard levels are denoted with asterisks. The standard deviations are presented using error bars centered around the mean values.

Table 12.2: Error in estimated drift ratios for the inelastic structural models

Bent	Field	Hazard	Foundation Approximations							
			Fixed @ 3D		Fixed @ 0D		Springs (Pinned)		Springs (Fixed)	
			μ	σ	μ	σ	μ	σ	μ	σ
1	NF	50%	1.0	12	34.1	43	89.7	23	53.5	42
		10%	-3.1	19	17.4	83	76.0	21	41.4	73
		2%	-6.8	11	11.6	65	85.7	28	28.2	46
	FF	50%	9.9	17	27.6	45	102.9	29	62.3	56
		10%	-1.5	8	-5.2	29	108.3	43	20.2	24
		2%	-4.7	7	-12.6	21	84.2	29	21.5	29
2	NF	50%	-3.8	8	-19.5	24	48.0	16	1.1	32
		10%	-7.9	11	-39.1	36	34.7	17	-23.5	41
		2%	-8.6	11	-40.7	29	45.5	25	-25.8	27
	FF	50%	0.9	8	-17.4	25	49.0	40	-3.3	28
		10%	-5.0	4	-41.3	20	44.9	17	-20.8	19
		2%	-8.4	7	-49.0	11	31.4	20	-31.6	14
3	NF	50%	1.4	12	-21.8	36	83.5	25	19.6	64
		10%	-10.9	13	-58.9	50	66.9	27	-29.7	65
		2%	-5.4	15	-62.1	36	87.4	36	-31.1	49
	FF	50%	6.1	15	-54.9	21	84.9	37	1.0	45
		10%	-5.9	7	-57.6	16	79.5	16	-27.0	27
		2%	-4.9	10	-68.0	14	79.2	33	-47.8	18
	Total		-3.2	12	-25.4	48	71.2	35	0.5	51

The errors in the estimated plastic rotations and column shears for the inelastic models are tabulated in Tables H.4 - H.5. These results are shown in Figs. H.4 - H.5. The statistics presented in Appendix H were used to determine the accuracy and precision of the modeling approximations on estimated drift ratios (Sections 12.2.2) and on other EDPs (Section 12.2.3).
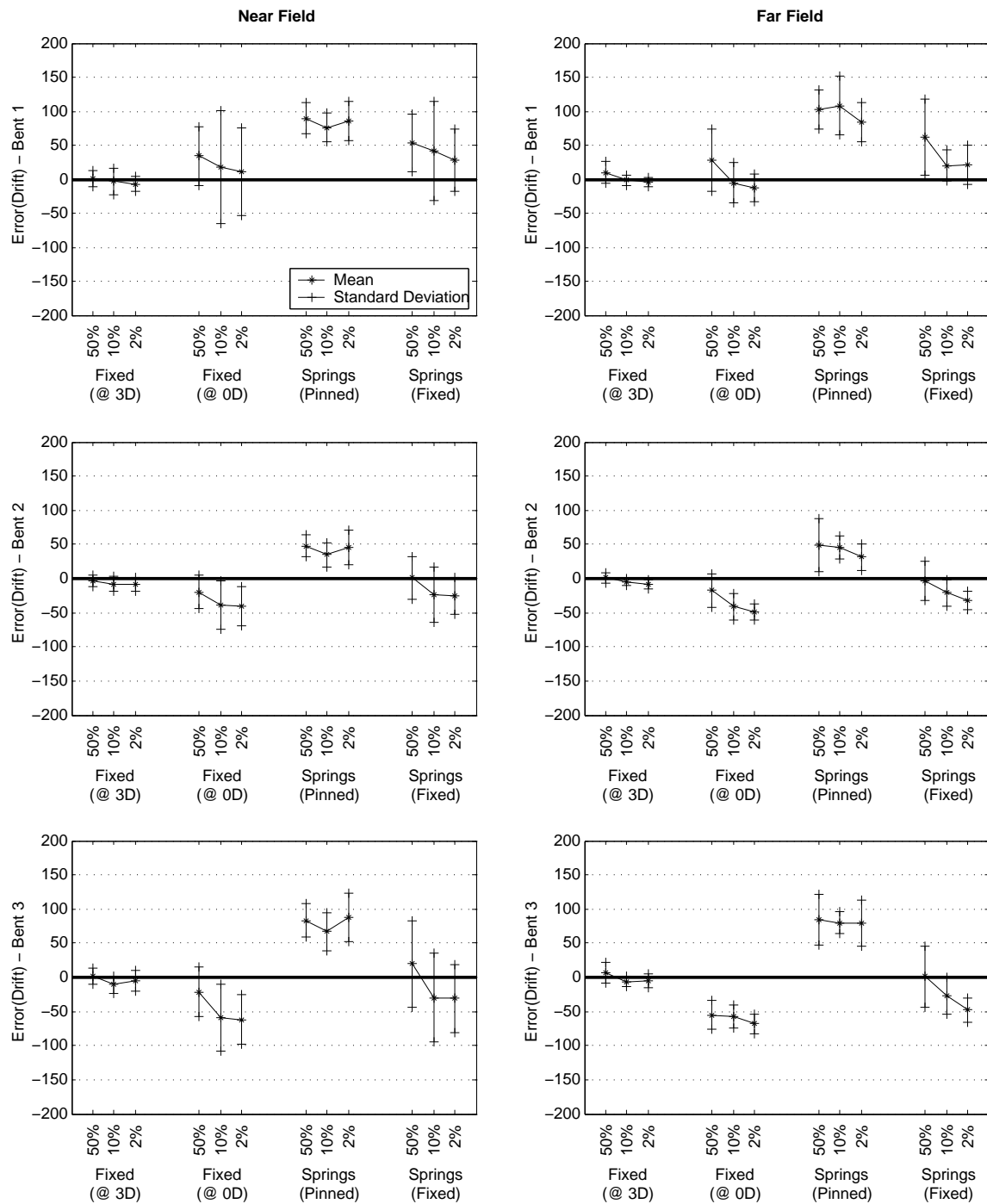
Figure 12.3: Error in estimated drift ratios for the inelastic structural models

12.2.2 Effects of Modeling Approximations on Drift Ratio

This section compares the accuracy and precision of the drift ratios estimated for the four foundation modeling approximations and three structural modeling approximations. Fig. 12.4 plots the estimated drift ratios for the 12 simpler modeling strategies versus the drift ratios estimated with the prototype model. Each row in Fig. 12.4 corresponds to a particular foundation approximation. The columns correspond to the structural approximations. For example, the top, left-hand plot in Fig. 12.4 compares the estimated drift ratios of the inelastic fixed @ 3D model with the drift ratios estimated with the prototype model.

The 1:1 ratio and 20% bounds are included in the plots to add perspective on how each model represents the prototype model. For example, the differences between the drift ratios of the inelastic fixed @ 3D model and the prototype model are nearly all less than 20%. In contrast, the differences in the drift ratios of the gross elastic springs (fixed) model and the prototype model greatly exceeded 20% for nearly all levels of drift ratio.

The correlation coefficients (R^2) for each bent are included in the plots to show the correlation between the demands estimated with the simpler models to those estimated with the prototype model. For example, the drift ratios for the inelastic fixed @ 3D model are well correlated to the drift ratios of the prototype model, with $R^2 > 0.95$ for all bents. In other words, the relationship is insensitive to the level of drift ratio.

The effects of foundation approximations were determined by comparing the rows of Fig. 12.4, and based on the statistics presented in Appendix H. As seen in Fig. 12.4, the most accurate model combined the fixed @ 3D foundation approximation with the inelastic columns. The drift ratio response of the inelastic fixed @ 3D model was almost always within 20% of the response of the prototype model. On average, this model underestimated the drift ratio by 3.2%, with a standard deviation of 12% (Table H.1). The inelastic fixed @ 3D model was also the most accurate approximation for each individual bent. Specifically, the mean percent difference in the bent 1, 2, and 3 drift ratios for the inelastic fixed @ 3D model were -0.9%, -5.5%, and -3.3%, respectively (Table H.1).

The springs (pinned) model was generally the least accurate foundation approximation
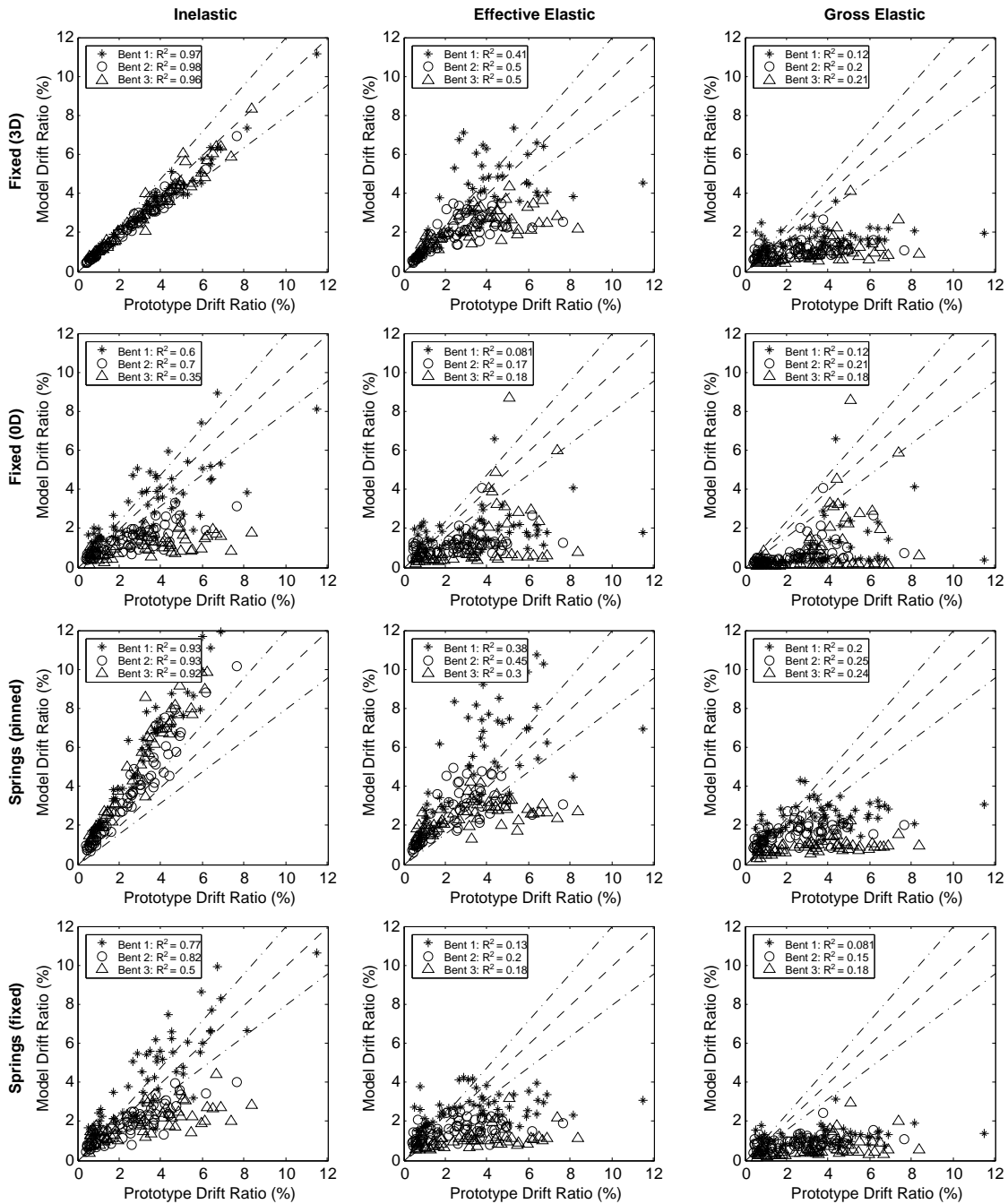
Figure 12.4: Comparison of the estimated drift ratios for the 12 simpler modeling strategies to the drift ratios estimated with the prototype model

for the inelastic models. Because the bottom of the columns were free to rotate, much of the column deformation occurred at the top of the columns. This caused the springs (pinned) model to consistently overestimate the deformation demands for each bent. The mean and standard deviation of the error with this model (considering all bents) were 71% and 35%, respectively.

The fixed @ 0D and springs (fixed) foundation approximations resulted in structures that were much stiffer and more asymmetric than the prototype model. For example, Bent 3 in the fixed @ 3D model was 1.6 times stiffer than Bent 1. In comparison, Bent 3 in the fixed @ 0D model was 2.4 times stiffer than Bent 1. This increase in the relative stiffness of bent 3 (compared to bent 1) changed the mode shapes and increased the twist response of the system. For example, for the inelastic fixed @ 0D model the average errors in the drift ratios at bents 1 and 3 were 12% and -54%, respectively.

The inelastic models were more accurate than the effective-elastic models for three of the four foundation approximations (except for the springs (pinned) model). All of the inelastic models were more precise than the effective-elastic models. For example, the mean error of the inelastic fixed @ 3D model was -3.2%. In contrast, the mean errors of the effective-elastic and gross-elastic fixed @ 3D models were -4.8% and -40%, respectively.

Although the overall mean error of the effective-elastic fixed @ 3D model (-4.8%) was only slightly larger than the overall mean error of the inelastic fixed @ 3D model (-3.2%), the errors on a bent-by-bent basis were much larger for the effective elastic model. For example, the average errors of the drift ratios at bents 1 and 3 were 13% and -16%. In contrast, the average errors of the drift ratios at bents 1 and 3 for the inelastic fixed @ 3D model were only -0.9% and -3.3%.

Regardless of the foundation approximation, all of the gross-section elastic structural models were inaccurate and imprecise. All of the gross-section elastic models underestimated the bent demands. The mean error for these models ranged from -71% to -21%.

12.2.3   Effects of Modeling Approximations on other EDPs

The estimated plastic rotation, residual drift ratio, and column shear for the inelastic column models were compared with the estimates of the prototype model in Fig. 12.5. These demand parameters were not compared for the elastic structural models.

The errors in the estimated plastic rotations at the tops of the columns were more sensitive to the foundation approximation than were the estimated drift ratios. For example, the standard deviation of the errors in the plastic rotations for the inelastic fixed @ 3D model was 26%, compared to the standard deviation of only 12% in the estimated drift ratio.

Because the calculated error in Eq. 12.2 divides the differences in the estimated EDPs by the EDP estimated with the prototype model, this error was sensitive to small values of the prototype EDP. The plastic rotation at the tops of the columns during the 50% in 50 year earthquakes was typically small. Therefore, the plastic rotation error statistics for this level of earthquake intensity should be carefully considered. For example, the mean error of the inelastic springs (fixed) model during the 50% in 50 year far field excitations was 211%. However, the mean errors for the 10% and 2% in 50 year far field excitations were only 39% and 32%, respectively.

Because the moment capacity of each column was the same for all foundation modeling approximations, the shear forces within the columns were approximately proportional to the length of the column to the inflection point. The lengths to the inflection point of the bents in the prototype column were approximately 3, 4, and 3 times the column diameter for bents 1, 2, and 3, respectively. For the fixed @ 3D model, the lengths to the inflection points were approximately 3.5D, 4.5D, and 3D, respectively. Because the lengths to the inflection points were approximately the same in the fixed @ 3D model, the estimated shear forces within the columns were similar to those in the prototype model.

The fixed @ 0D and springs (fixed) models underestimated the lengths to the inflection points of each bent. Therefore, these models overpredicted the estimated shear forces within each bent by as much as 120% in bent 3 (Table H.5). The lengths to the inflection points for the springs (pinned) model were 4D, 6D, and 3D for bents 1, 2, and 3, respectively. Fig. H.5 shows that because the length to the inflection point for bent 2 in this simpler
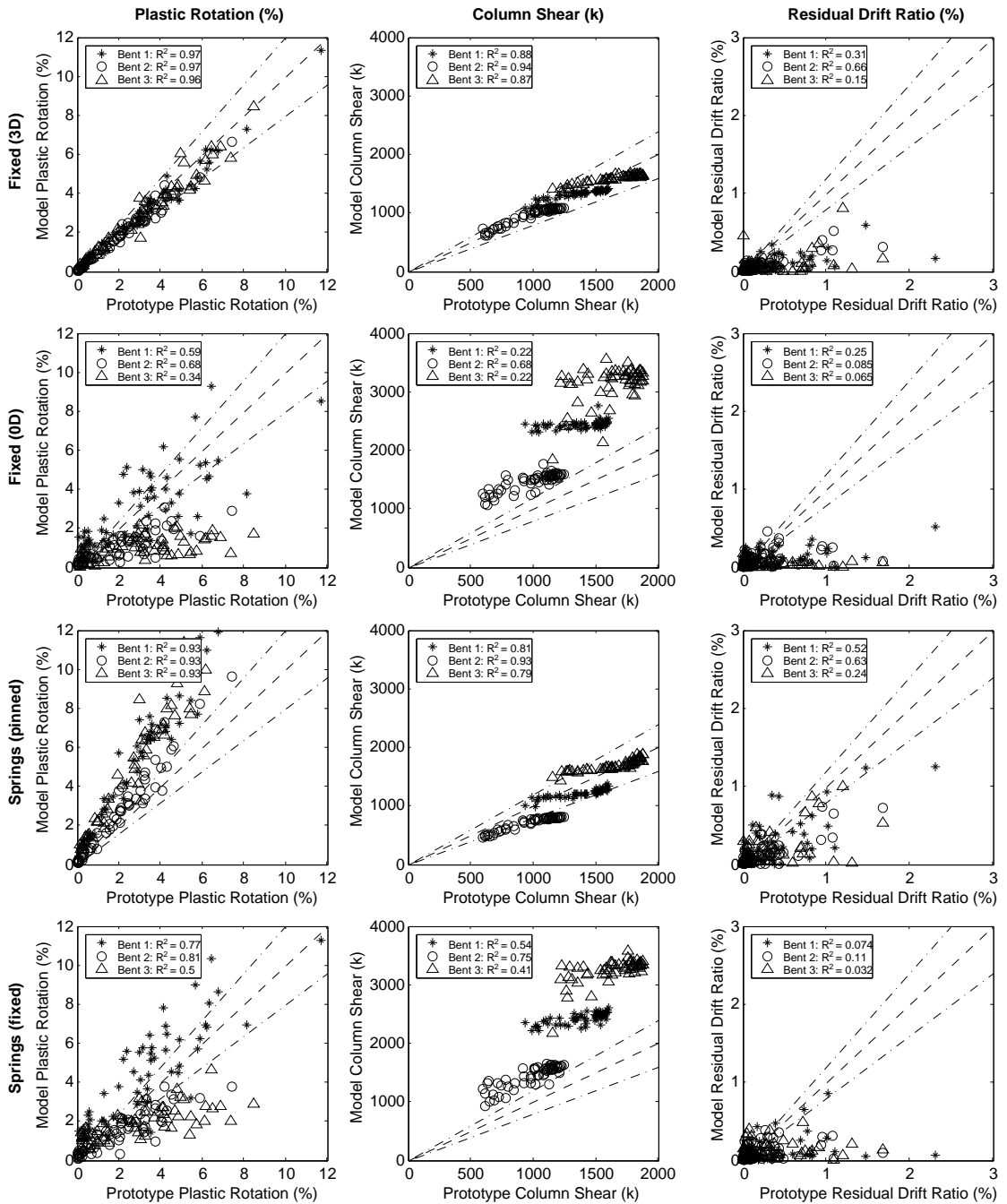
Figure 12.5: Comparison of the plastic rotation, column shear, and residual drift ratios for the four inelastic modeling strategies

model was 50% larger than the length to the inflection point of bent 2 in the prototype model, the estimated shear demands on bent 2 were always smaller. Because the lengths to the inflection points were similar to the prototype model for bents 1 and 3, the shear forces in these bents were similar to the shear forces in the prototype model.

The residual drift ratios of none of the simpler inelastic models correlated well with the residual drift ratios of the prototype. For example, the correlation coefficient (R^2) for bent 3 in the inelastic fixed @ 3D model was 15%. The correlations for the other modeling strategies were generally worse for this demand parameter. For example, the highest correlation coefficient for the inelastic springs (fixed) model was 11%. This low correlation to the prototype response was expected, since the correlation between the prototype residual drift ratios and the motion intensity was also low.

12.3   *Sensitivity of Model Accuracy to Effective Depth of Fixity*

The inelastic fixed @ 3D model was shown in Section 12.2 to be the most accurate and precise of the 12 simpler modeling strategies presented in Section 12.1. The fixity depth for this model was chosen based on the estimated location of the maximum moment within the piles of the prototype model. It is important to evaluate the sensitivity of performance estimates to this assumption, because the prototype model would not be available to designers.

According to the methodology developed by Chai (2002) for estimating the fixity depth of piles in cohesionless soils, the effective depth of fixity for bents 1, 2, and 3 was approximately 3.6 column diameters for the soil and pile properties in this research. This depth is about 20% larger than the depth that was approximated with the experimental data.

To investigate the effects of various fixity depth approximations, this section evaluates the accuracy and precision of fixed-base models for fixity depths ranging from two to four column diameters (approximately $\pm$ one column diameter from the optimal solution). The accuracy of each model was evaluated using three demand parameters: drift ratio, plastic rotation, and column shear. Fig. 12.6 compares the estimates of these three demand parameters using the fixity depth models with those of the prototype model. The effects of fixity depth on the residual column drift ratios were not investigated, because this demand parameter correlated poorly with motion intensity for all models.

The mean (accuracy) and standard deviation (precision) of the demand estimates for each bent, using the suites of near-field and far-field excitations, are tabulated in tables H.6 - H.8. These statistics are also shown in figs. H.6 - H.8.

As seen in Fig. 12.6, the considered range in fixity depth did not significantly affect the accuracy in drift ratio estimates for each model. The mean errors in the estimated drift ratios for these five fixity depths ranged from -3.2% to 0.6%. The model precision was slightly more sensitive to the fixity depth. The standard deviations of the errors for the five fixity depths ranged from 12% to 20%. Overall, the fixed @ 3D model was the most precise ($\sigma = 12\%$).

The accuracy of the plastic rotation estimates was much more sensitive to the fixity depth than the calculated drift ratios. The mean errors in the estimated plastic rotations for the five fixity depths ranged from -2.6% to 18.2%. The choice in fixity depth greatly affected the precision in the error of the estimated plastic rotation. The standard deviations of these five fixity depths ranged from 25% to 52%. In general, the fixed @ 3.5D model was the most accurate and precise for estimating the maximum plastic rotations ($\mu = -1.1\%$, $\sigma = 25\%$).

The most accurate model for representing column shear depended on the level of ground excitation. For example, for the 50% in 50 year far-field excitations, the lowest average error in the bent 1 shear occurred for the fixed at 3.5D model (-2.0%). For the 10% and 2% in 50 year motions, the lowest average errors (0.9% and -1.3%) occurred at a fixity depth of 2.5D. This illustrates that as the ground motions became more intense, the soil-to-structure stiffness ratio increased, moving the fixity depth closer to the ground surface. On average, the fixed @ 3D model was the most accurate in estimating the maximum column shears, with an average error of -3.2%. The fixed @ 3.5D model was the most precise with a standard deviation of 6.6%.
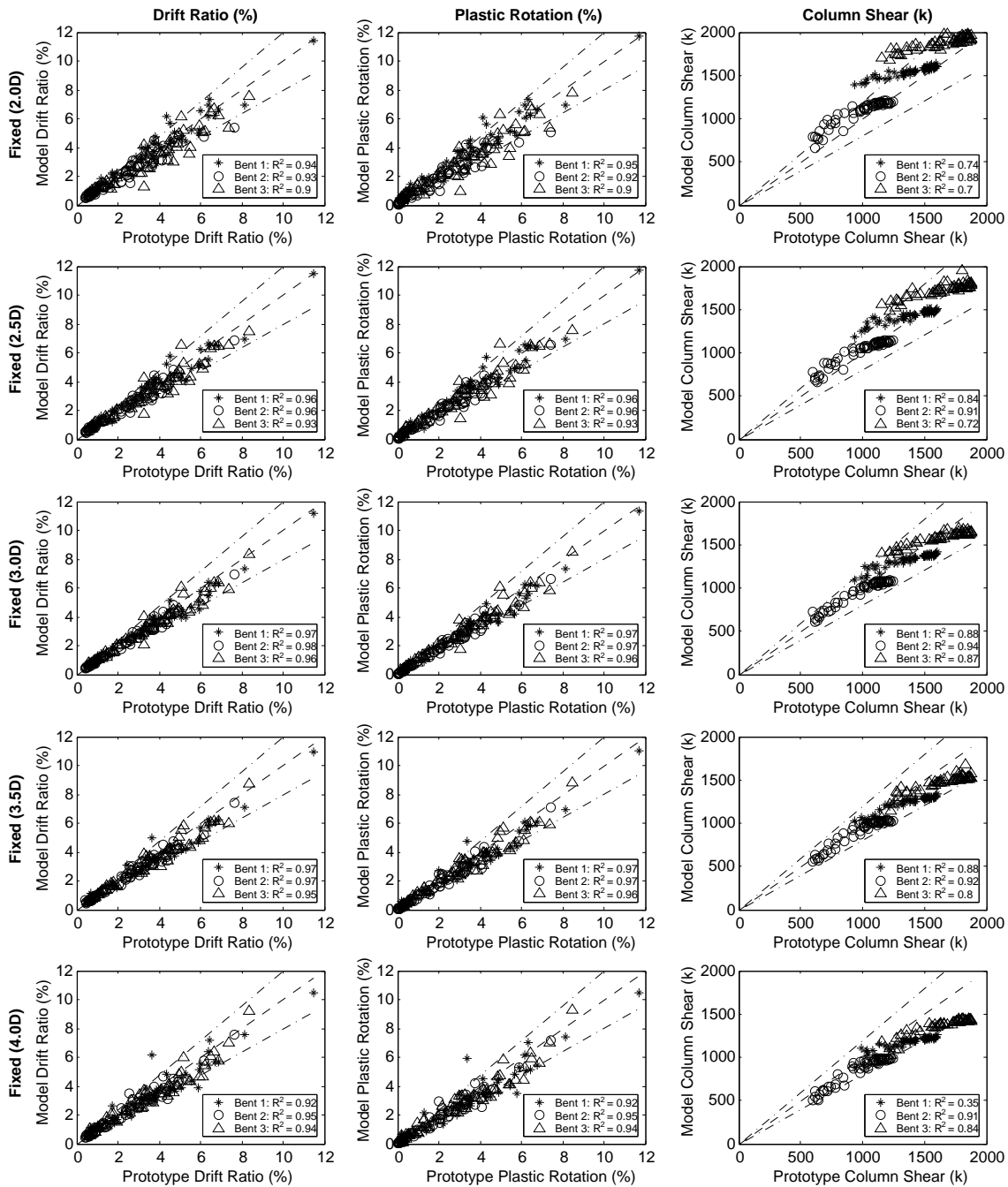
Figure 12.6: Sensitivity of estimated EDPs to fixity depth

12.4 Selection of Efficient Intensity Measures

This section compares the efficiencies of the intensity measures listed in Table 11.1 for the 40 near-field and 30 far-field excitations. The efficiency of each intensity measure was quantified

by the dispersion of the data around a best fit of the relationship between the measure of intensity and the system demands ($\sigma_{EDP|IM}$). The fixed-base models were excited by free-field motions at the point of pile fixity, whereas the prototype model was excited by soil motions along the entire pile. Each of these motions were generated from the transmission of the bedrock excitation through the soil. Therefore, to consistently compare the IM efficiencies for all models, the intensity measures were based on the bedrock excitations.

The IM efficiencies (using maximum drift ratios) are shown in Fig. 12.7 for the prototype model, inelastic fixed @ 3D model, and the effective-elastic fixed @ 3D model. For all intensity measures, the IMs for the far-field excitations were consistently more efficient than those for the near-field excitations. For example, with the prototype model, the standard deviation using the Cordova predictor for the far-field excitations was 24%, whereas the standard deviation for the near-field excitations was 40%.

Of the four Class I intensity measures (PGA, PGV, I_a, CAV), which depend only on the characteristics of the ground motions, the peak ground velocity was the most efficient for the near-field excitations for all three bridge models. For the far-field excitations, the peak ground velocity and the Arias intensity gave similar efficiency levels for the two inelastic models. For the effective-section elastic model, the peak ground acceleration was the most efficient.

Of the three Class II intensity measures (SA_1, SA_2, COR), which depend on the characteristics of the ground motion and the the dynamic properties of the bridge, the Cordova parameter was the most efficient for the two inelastic models; the spectral acceleration was the most efficient for the effective-section elastic model.

The Class II-2 intensity measures ($SRSS$, CQC, $SRSS_{COR}$, CQC_{COR}), which used dynamic properties from the first two modes of the system, generally had similar efficiencies as the Class II intensity measures. For example, for the far-field excitations, the standard deviation at bent 3 of the inelastic fixed @ 3D model using the Cordova parameter was 0.25. For this same motion set, the standard deviation using the square root of the sum of the squares of the Cordova parameters for the first two modes ($SRSS_{COR}$) was also 0.25. This similarity between the Class II and Class II-2 efficiencies was attributed to the similarity of the first two periods of vibration. For example, the second period of vibration of the
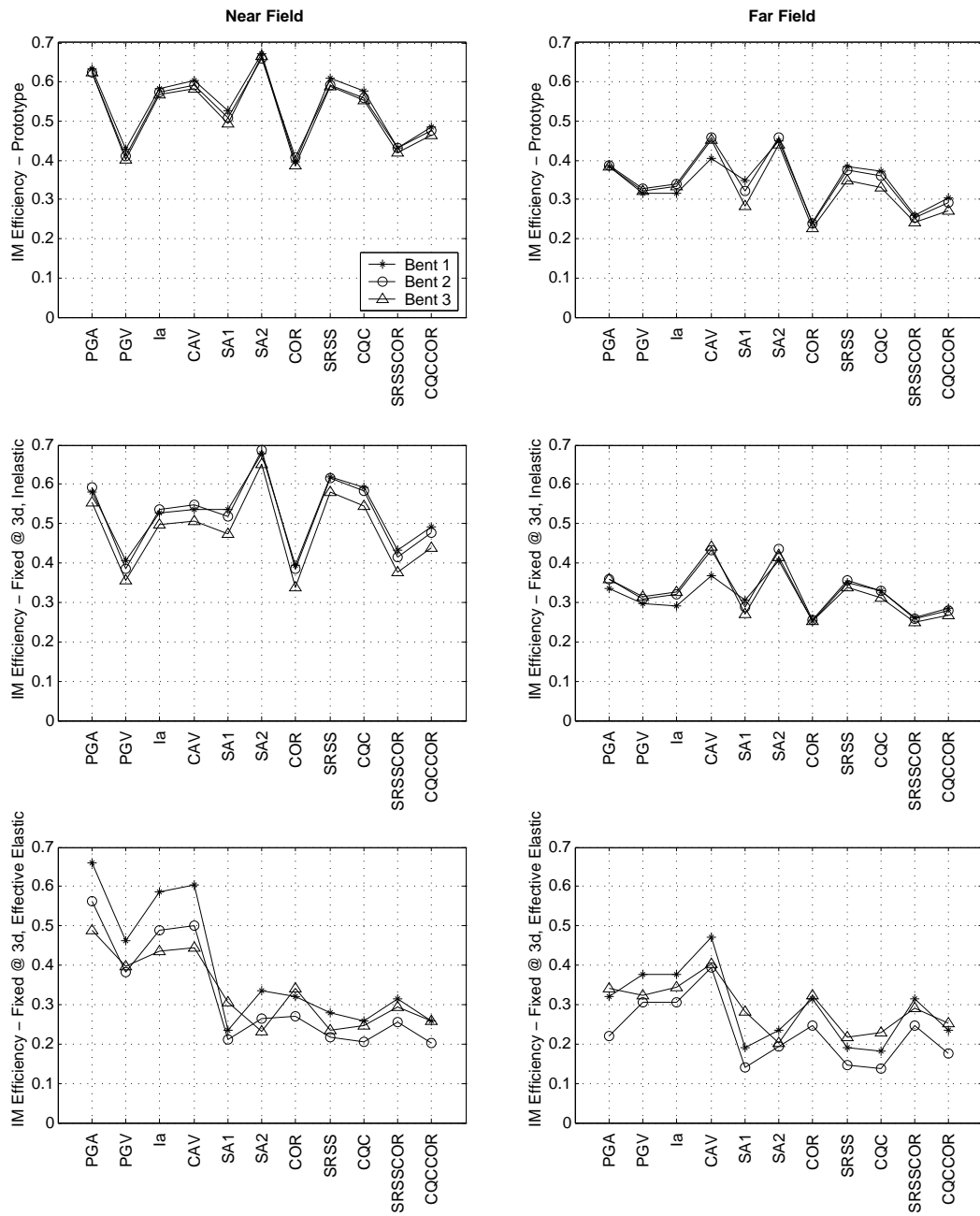
Figure 12.7: IM efficiencies (using drift) for: a) prototype model, b) inelastic fixed at 3d model, and c) effective elastic fixed at 3d model.

prototype model was 0.49s, only 20% smaller than the period of vibration of the first mode (0.61s).

12.5 Sensitivity of IM Efficiency to Cordova Parameters

This section calibrates the two coefficients of the model used by Cordova et al. (2000) to optimize the efficiency of the intensity measure for the prototype bridge system. This section also investigates the sensitivity of the efficiency of the intensity measure to slight deviations in these coefficients.

For the inelastic models, the Cordova parameter was the most efficient of the considered intensity measures (Chapter 11). The model Cordova et al. (2000) used for quantifying the intensity of a ground motion was defined as

$$SA^* = SA(T_1) \left[\frac{SA(CT_1)}{SA(T_1)} \right]^\alpha \tag{12.5}$$

where C and α are coefficients of the model determined through calibration. For four types of building frames Cordova et al. (2000) determined that the optimal coefficients for Eq. 12.5 were $C = 2.0$ and $\alpha = 0.5$. For this analysis, candidate values for the coefficients were evaluated for ranges $[1 \leq C \leq 4]$ and $[0.25 \leq \alpha \leq 1]$. The IM efficiencies using these ranges of values are shown in Fig. 12.8 for both the near-field and far-field excitations.

As seen in Fig. 12.8a, the parameters that correspond to the most efficient IM for the near-field excitations are $C = 2.5$ and $\alpha = 0.75$, resulting in an increase in efficiency of approximately 20% over the Cordova parameters. For the far-field excitations, the optimal parameters are $C = 2.5$ and $\alpha = 0.5$, only about 5% more efficient than the Cordova parameters.

As the value of the exponent α increased, the efficiency of the model was more sensitive to slight changes in the value of C. Therefore, values of $C = 2.5$ and $\alpha = 0.5$ were used for subsequent analyses, denoted as the modified Cordova parameter (MCOR).
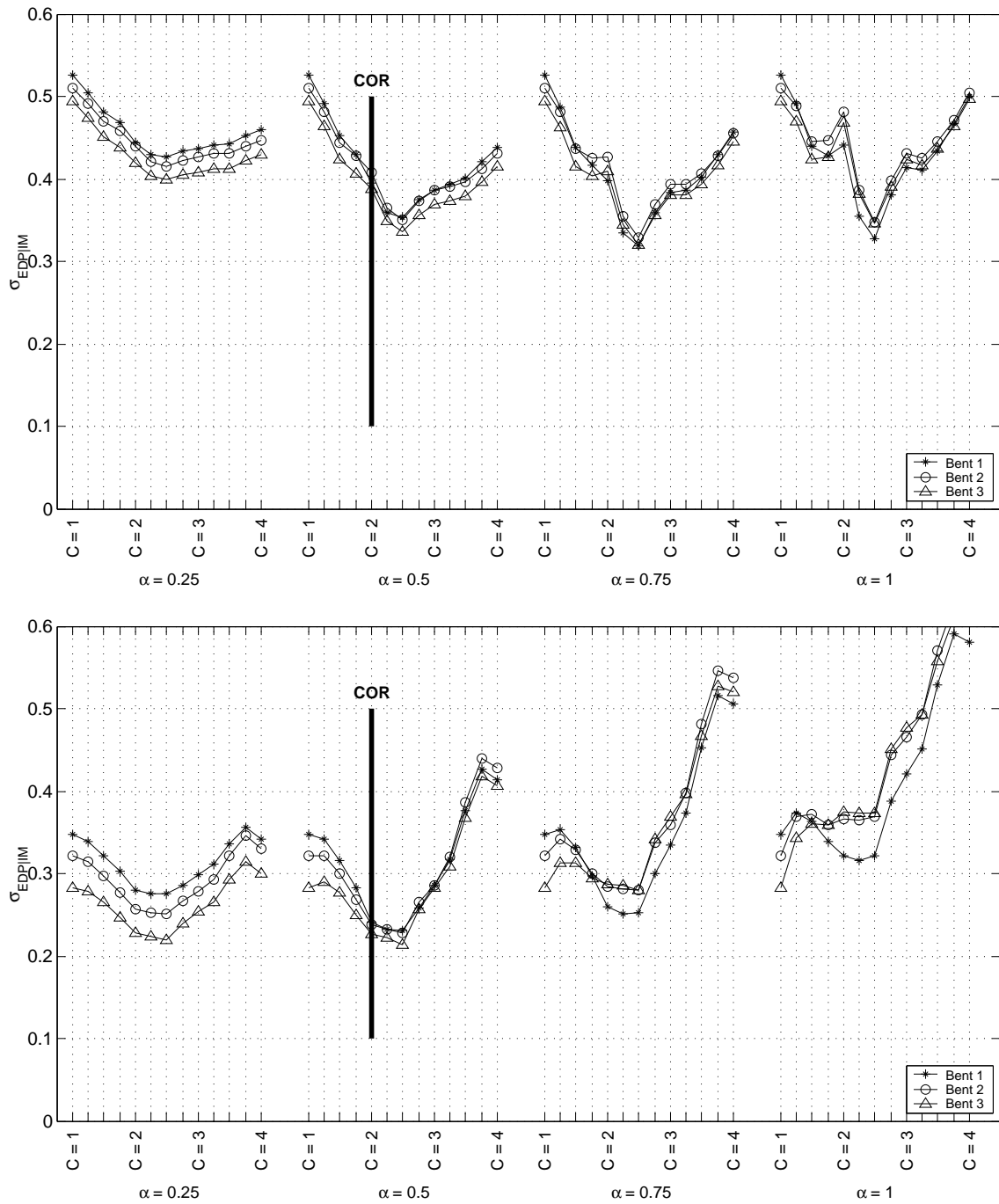
Figure 12.8: IM efficiencies sensitivity for prototype model using a) near-field and b) far-field excitations

12.6   Effects of Bridge Modeling Strategies on Estimated Damage

This section evaluates the accuracy of concrete spalling and bar buckling damage estimates for the simpler bridge models. Damage was estimated at these two damage states using the equations developed by Berry (2006), and the PBEE procedure described in Chapter 11. The error of the estimated damage was quantified by the percent difference between the estimated damage hazards from the simpler modeling strategies ($\lambda_{DM,Model}$) and the estimated damage hazard from the prototype model ($\lambda_{DM,Proto}$), defined as

$$ERROR_{DM,model}(\%) = \frac{\lambda_{DM,model} - \lambda_{DM,proto}}{\lambda_{DM,proto}} \times 100 \tag{12.6}$$

Section 12.6.1 compares the damage estimates for the 12 simpler modeling strategies outlined in Section 12.1 with the damage estimates from the prototype model. The sensitivity of the estimated column damage to the equivalent fixity depth is presented in Section 12.6.2. The sensitivity of the estimated column damage to the choice of intensity measure is presented in Section 12.6.3.

12.6.1   Effects of Foundation and Structural Modeling Strategies on Damage Estimates

This section investigates the effects of the foundation and structural modeling strategies on the levels of estimated column damage. For each model, the most efficient previously studied IM was used in the process for estimating the damage levels; the Cordova parameter for the inelastic models and the spectral acceleration for the elastic models. The errors in the damage measures for all of the models are provided in Appendix H. The error statistics for each model are presented in Tables H.9 - H.11, and are plotted in Figs. H.9 - H.11.

As an example, Fig. 12.9, repeated from the appendix, illustrates the organization of the calculated damage estimates. The columns in Fig. 12.9 represent the near-field and far-field excitations; the rows represent the bents. The errors in the spalling (SP) and bar buckling (BB) damage measures were calculated for both the estimated drift ratios and the estimated plastic rotations. For the elastic columns, only drift ratios were used to calculate the damage probabilities.
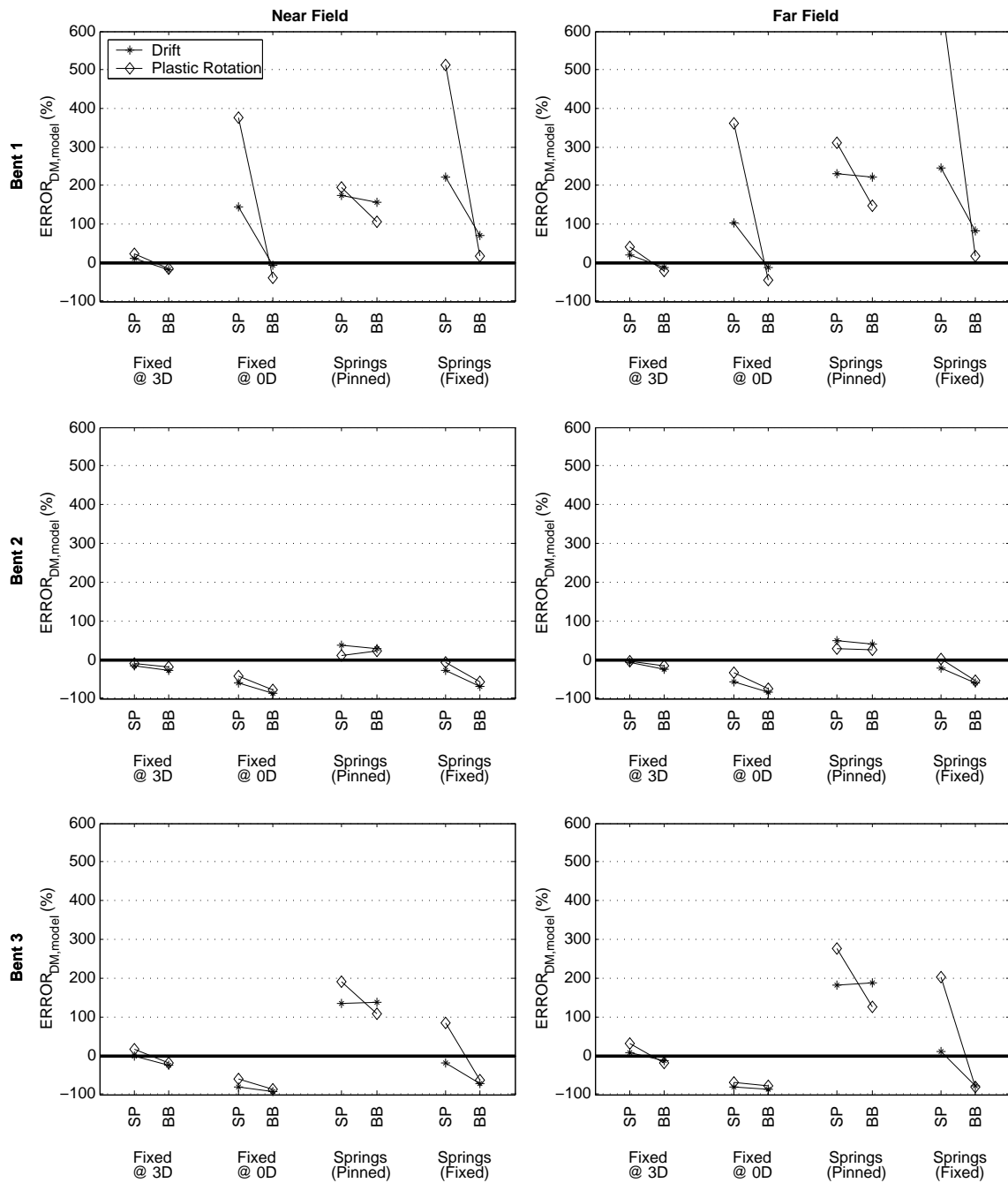
Figure 12.9: Error in the DM hazard for the inelastic structural modeling approximations

Overall, the spalling hazard was more difficult to predict than the bar buckling hazard for all the models. Of all the inelastic column modeling strategies, the plastic rotations from the

far-field excitations of the springs (fixed) model produced the largest error (700%). For this same motion set, the effective elastic springs (fixed) model overestimated spalling hazard by 2800%. This large error was attributed to the smaller demand estimates at the spalling damage level, especially for estimating damage based on plastic rotation. For example, excited by the 50% in 50 year far-field excitations, the average error in the plastic rotation estimates at Bent 1 of the inelastic springs (fixed) model was 211%. In contrast, the average error at this same location for the 10% in 50 year far-field excitations was only 39%.

The bar buckling hazard was almost always underestimated. As expected, the stiffest modeling strategies resulted in the largest underestimations for this damage state. For example, the average error of the bar buckling hazard for the four gross elastic models ranged from -99% to -89%.

The inelastic fixed @ 3D model was the most accurate and precise model for estimating the column damage hazards of all three bents. On average this model overestimated the spalling hazard by only 9.1%, with a standard deviation of 17%. The average error for the other three inelastic models ranged from 42% to 159%. The inelastic fixed @ 3D model underestimated bar buckling by only -19%, with a standard deviation of 4.3%. The average error for bar buckling of the other three inelastic models ranged from -64% to 109%.

12.6.2 Sensitivity of DM Hazard to Equivalent Fixity Depth

The inelastic fixed @ 3D model was determined to be the most accurate model for predicting the probability of spalling and bar buckling (Section 12.6.1). This section investigates the sensitivity of these damage estimates to various fixity depths. The errors in the estimated damage measure hazards were calculated for the inelastic fixed-base models, fixed at 2.0D, 2.5D, 3.0D, 3.5D, and 4.0D beneath the ground surface. For each of these models, the error in the estimated damage measure hazard was defined using Eq. 12.6. The errors in the damage measures are shown in Fig. 12.10 for all three bents using both drift ratio and plastic rotation as the engineering demand parameters. These errors are also tabulated in Table H.12.

The estimated spalling hazards for bents 1 and 3 changed significantly with fixity depth.
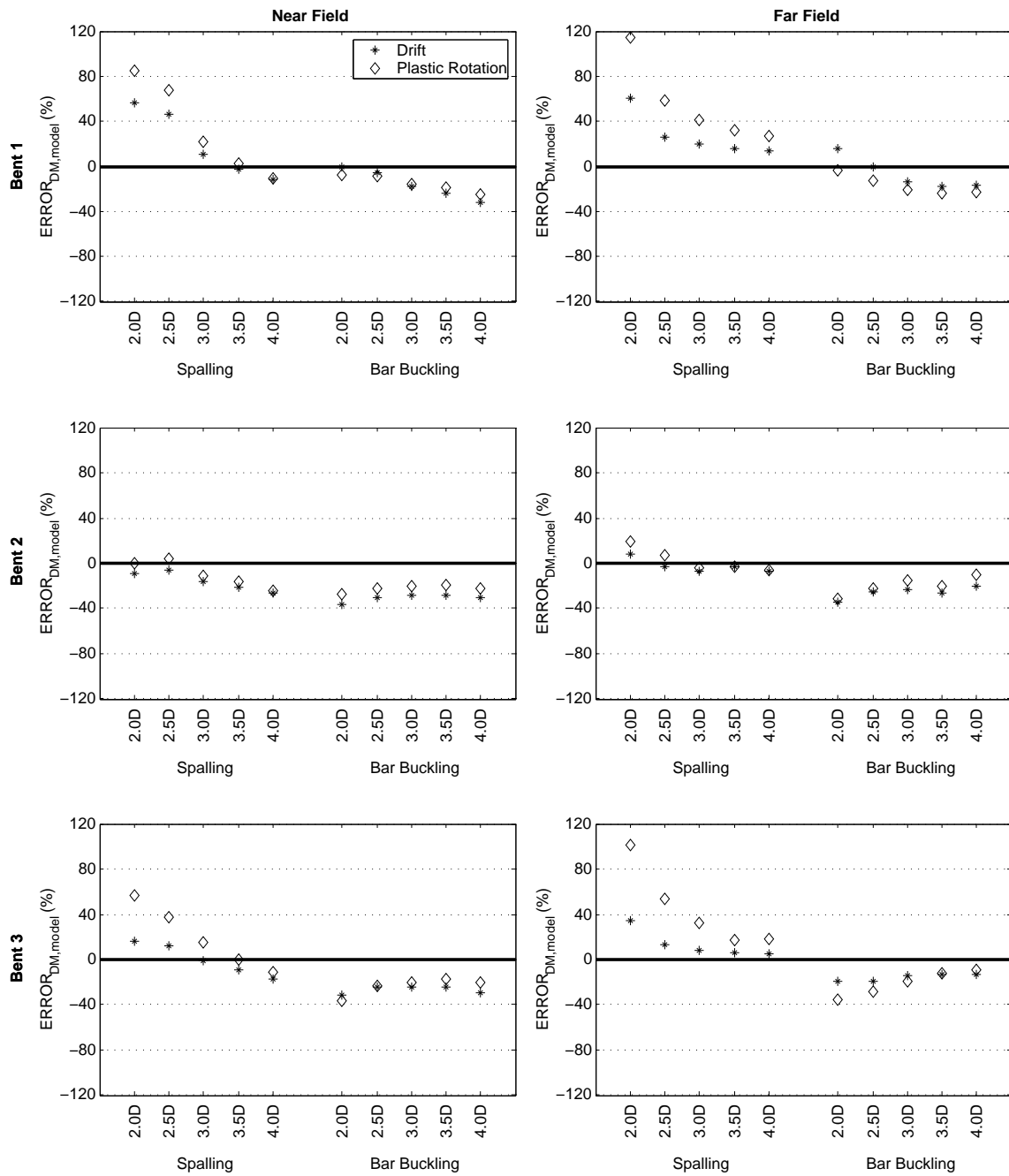
Figure 12.10: Error in the damage measure hazard for the fixity depth models for a) near-field and b) far-field excitations

For example, the percent differences in the estimated spalling hazards for bent 1 using plastic rotations excited by the far-field excitations ranged from 27% to 115%. In contrast, the probability of spalling at bent 2 was less sensitive to the fixity depth. For example, using this same motion set, the percent difference in estimated spalling using plastic rotations ranged from -6.4% to 19%. The higher sensitivity of bents 1 and 3 to the fixity depth was attributed to the increase in system asymmetry as the fixity depth decreased, which did not significantly affect the response of bent 2 (the location of the center of mass).

The fixed @ 3.5D model was the most accurate model for estimating spalling, overpredicting the spalling hazard by only 1.7% ± 14%. The fixed @ 2D model was least accurate and least precise at predicting the spalling hazard, with an average error of 47%.

The estimated bar buckling hazard was less sensitive to the fixity depth than the spalling hazard. On average, the fixity depth models underpredicted the bar buckling hazard by 18.6% to 21%. The fixed @ 2D model was the least precise, with a standard deviation of 16.6%. The fixed @ 3D model was the most precise, with a standard deviation of 4.3%. The standard deviations of the other three fixity depths ranged from 4.8% to 9.2%.

12.6.3 Sensitivity of DM Hazard to Intensity Measure

This section investigates the sensitivity of the damage hazards estimated with the prototype model to the choice of intensity measure for the 11 intensity measures described in Section 11.2, and the modified Cordova parameter (MCOR, optimized in Section 12.5). The Cordova parameter was determined to be the most efficient previously considered intensity measure for the prototype model. Therefore, the error in the demand hazard due to the choice in intensity measure ($ERROR_{DM,IM}$) was quantified by the percent difference between the damage hazard estimated with the Cordova parameter ($\lambda_{DM,COR}$) and the damage hazard estimated with an alternate IM ($\lambda_{DM,ALT}$), defined as

$$ERROR_{DM,IM}(\%) = \frac{\lambda_{DM,ALT} - \lambda_{DM,COR}}{\lambda_{DM,ALT}} \times 100 \tag{12.7}$$

The errors in the damage measure hazards for the 12 intensity measures are shown in Fig. 12.11. The statistics of these comparisons are tabulated in Table H.13 for five of the more common intensity measures.
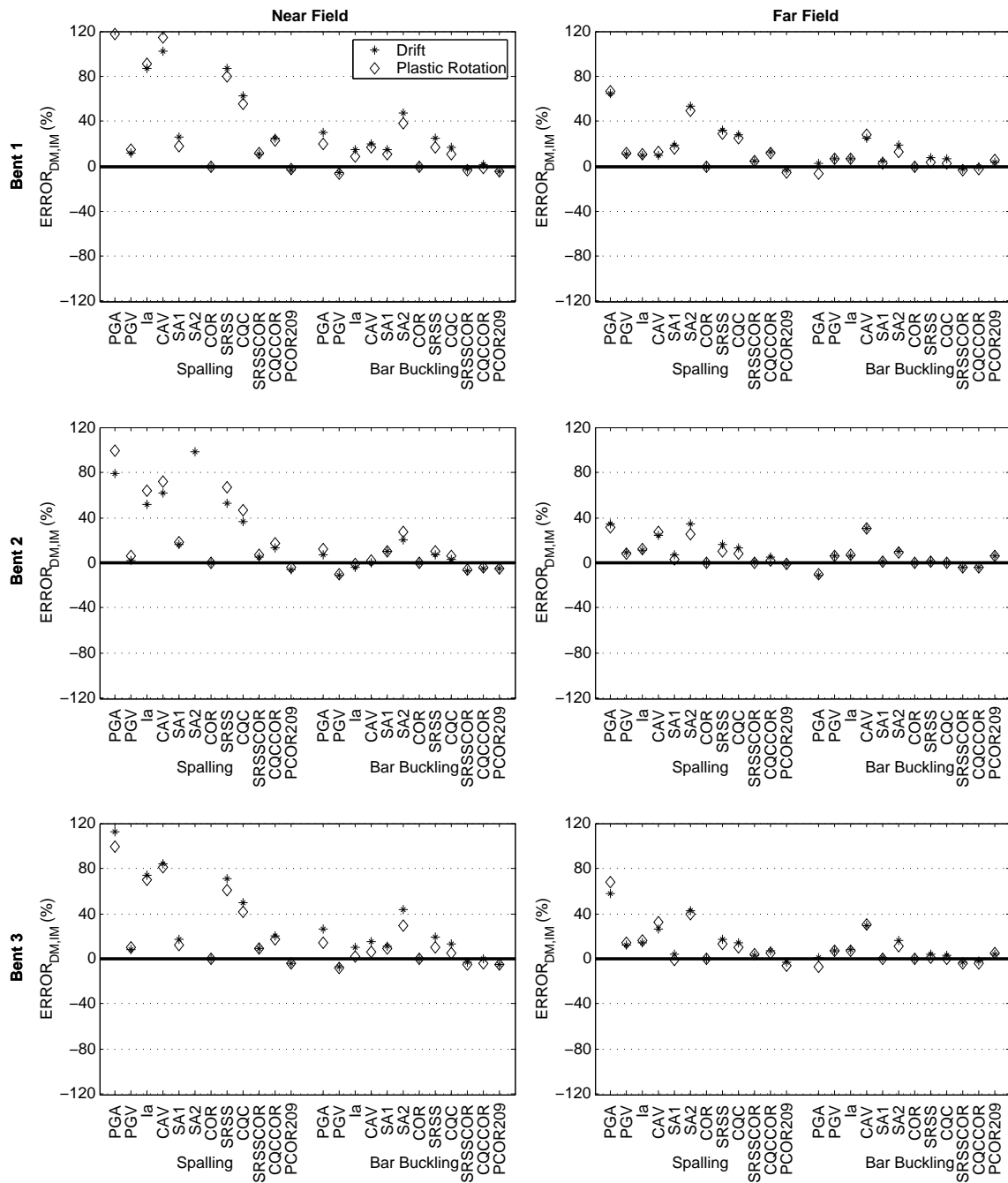
Figure 12.11: Error in the damage measure hazard for the various intensity measures for a) near-field and b) far-field excitations

For all bents, the spalling hazard was more sensitive to the choice of intensity measure than the bar-buckling hazard. For example, on average the spalling hazard calculated with the peak ground acceleration was 80% larger than the hazard estimated with the Cordova parameter. In contrast, the bar buckling hazard was overpredicted by only 12% when using peak ground acceleration as the intensity measure.

For near-field accelerations, the peak ground velocity was only slightly less efficient than the Cordova parameter. The PGV overestimated the damage hazard for spalling by 10% and underestimated the damage hazard for bar buckling by only 0.8%. Using the modified Cordova parameter, which was optimized to maximize the IM efficiency for the bridge system in this research, the spalling and bar buckling hazards were 3.9% lower and 0.2% higher, respectively, than the hazards estimated with the Cordova parameter.

Although the spectral acceleration at the first period of vibration of the structure was on average 25% less efficient than the Cordova parameter for the prototype model, the spalling and bar buckling hazards were overpredicted by only 13% and 6.4%, respectively.

For both far-field and near-field excitations, the average errors using the peak ground velocity, spectral acceleration, or the modified Cordova parameter were typically less than 10%. This observation signifies that because of the large number of earthquake excitations that were used, the damage estimates were not significantly affected by the choice in efficient intensity measure. However, one motivation for choosing an efficient intensity measure is to be able to use less motions to efficiently characterize the system response. The effects of the various intensity measures on the damage hazard levels was not investigated for a smaller number of motions, but the consequence of the choice in intensity measure is expected to become more significant.

12.7 Chapter Summary

A two-span reinforced concrete bridge on drilled shaft foundations was simulated using 13 bridge modeling strategies, which are summarized in Fig. 12.2. One of these modeling strategies (the prototype model) was a nonlinear bridge model on nonlinear soil columns. The other 12 models were assembled using combinations of simpler foundation and structural approximations.

The effects of the foundation and structural approximations were investigated by comparing component demands and damage levels estimated with the 12 simpler models with the demands and damage levels estimated with the prototype model. Key conclusions from these comparisons are listed below.

1. For the soil properties considered in this research, the inelastic fixed @ 3D model was the most accurate and precise for simulating the deformation (maximum drift ratio and maximum plastic rotation) and force (column shear) demands of the prototype model.

2. The effective elastic fixed @ 3D model was on average only slightly less accurate than the inelastic fixed @ 3D model. However, the standard deviation of the drift ratios of the effective elastic model ($\sigma = 39\%$) was three times higher than the standard deviation of the inelastic model ($\sigma = 12\%$). The use of a less precise model with the same level of accuracy means that the model would need to be excited by more ground motions to develop the same confidence in the demand estimates.

3. Twisting of the system was not effectively simulated by the gross-section or the effective-section elastic modeling strategies. These strategies typically caused the demand parameters to be overestimated for bent 1, but underestimated for bent 3. For example, on average the inelastic springs (fixed) model overestimated the maximum bent 1 drift ratio by 38%, and underestimated the maximum bent 3 drift ratio by 48%.

4. Although residual column drift ratios may have important consequences for bridge function, this EDP was difficult to predict. As a result, the correlation between ground-motion intensity and this demand parameter was low for all models.

5. For the soil and pile properties considered in this research, the accuracy and precision of the structural demands were insensitive to moderate changes in the fixity depth of the inelastic fixed base models. For example, the mean error in the estimated drift ratios ranged from -3.2% to 0.6% for fixity depths ranging from 2D to 4D. The maximum plastic rotation was more sensitive to deviations in the fixity depth. Overall, the fixed @ 3.5D model (fixity depth estimated using an empirical equation developed

by Chai (2002) for the pile and soil properties of the prototype specimen) was slightly more accurate and precise than the inelastic fixed @ 3.0D model (which was chosen based on the average point of maximum moment in the prototype model for all three bents).

6. The Cordova parameter (COR) was the most efficient considered intensity measure for the two nonlinear models. By optimizing the coefficients within the Cordova parameter ($MCOR$) for the prototype bridge system, the efficiency of this parameter was improved by as much as 20%. For the linear model, the spectral acceleration at the first period of vibration of the structure (SA_1) was the most efficient.

7. The inelastic fixed @ 3D model was the most accurate and precise at estimating the concrete spalling and bar buckling hazards for all bents. On average, spalling was overestimated by 9.1% and bar buckling was underestimated by 19%. Spalling was the most inaccurate hazard level for the other modeling strategies. The bar buckling hazard was almost always underpredicted. For example, the gross-section elastic springs (fixed) model underpredicted the bar buckling hazard by 99%.

8. Because of the number of motions used to estimate column damage levels, the estimated damage hazards were insensitive to the choice in efficient intensity measure. For example, using the peak ground velocity, spectral acceleration, or modified cordova parameter caused a difference in the estimated spalling hazard ranging from -3.9% to 13%. The choice of intensity measure is expected to have a larger impact when using less motions to characterize the system response.

Chapter 13

SUMMARY AND CONCLUSIONS

Performance Based Earthquake Engineering (PBEE) is an increasingly attractive alternative to traditional bridge design practice. PBEE attempts to explicitly predict the seismic performance of structures, such as the system force and deformation demands, expected level of damage, likely repair costs, and the extent of disruption of function. These performance predictions can be performed with numerically intensive nonlinear models of the soil, foundation and structure. However, the accuracy and precision of these numerical models have been difficult to quantify in the past because individual experiments are typically inadequate for accurately simulating the dynamic behavior of the entire nonlinear system. Even if calibrated nonlinear models were routinely available, most practitioners would prefer to use simpler models. It is important to understand the impact of using simpler models on PBEE.

The objectives of this dissertation were to develop a calibrated numerical model of a reinforced concrete bridge on drilled shafts from three experiments (shake table, centrifuge, and pseudo-static component tests), and to use this model to evaluate the accuracy of a variety of bridge modeling strategies within a performance-based framework. All analyses considered a single bridge geometry (bent heights of 5 ft, 6 ft, and 8 ft), foundation type (drilled shafts), and soil type (dense, dry sand). This research resulted in (1) the generation of experimental data from a series of shaking table tests, (2) the characterization of the shake-table specimen using response measurements and system identification methodologies, (3) the development of a calibrated numerical model of a reinforced concrete bridge on a drilled shaft foundation, and (4) the evaluation (within a performance-based framework) of the accuracy and precision of simpler foundation and structural modeling strategies.

13.1 Experimental Testing

As one in a series of four coordinated experiments, a quarter-scale, reinforced concrete bridge was dynamically tested on three shake tables at the NEES facility at the University of Nevada, Reno. The geometry of the bridge was designed to conform to the constraints of the testing facility and to represent a typical bridge in the western United States. The bridge specimen was a two-span section of a multi-span reinforced concrete box-girder bridge. The spans were supported on three bents with span-to-depth ratios of 5, 8, and 6 (Chapter 2). The reinforcement was proportioned using the NCHRP Recommended LRFD Guidelines for Seismic Design of Highway Bridges (ATC/MCEER, 2001).

The earthquake motions used to excite the shaking table specimen were derived from the 90-degree component of the Century City North (CCN090) outcrop record from the 1994 Northridge earthquake (Chapter 3). To generate the final motion for the shaking table tests, the outcrop record was deconvoluted to the bedrock level, then convoluted back to the estimated point of column fixity (2 column diameters below the ground surface) through dense, dry sand.

The experimental test schedule was composed of low and high-amplitude earthquake excitations. The low-amplitude tests were composed of coherent, incoherent, biaxial and centrifuge excitations, all designed to create bent responses smaller than the estimated bent yield displacements. The high-amplitude tests were composed of coherent excitations of increasing intensity. White-noise and square-wave excitations were dispersed throughout testing to aid in tracking the modal properties of the structure.

The achieved table accelerations differed significantly from the target values. During the low-amplitude tests, the average differences in the peak achieved and target accelerations of bents 1, 2, and 3 ranged from 17% to 76%. These differences were attributed to table friction. During the high-amplitude tests, the average differences ranged from 25% to 31%. These differences were attributed to structural feedback due to the inertial forces within the system. The differences in the spectral accelerations at the first mode of the structure were smaller, ranging from 18% to 31% during the low-amplitude tests, and from 9% to 23% during the high-amplitude tests.

The three-dimensional response of the shaking table system was captured with more than 300 instruments, including: strain gauges (160), potentiometers (111), and accelerometers (15). The longitudinal and transverse table displacement, velocity and acceleration responses were captured using 18 devices.

Each of the columns was inspected for damage intermittently throughout the low-amplitude tests, and following every high-amplitude test. The damage states that were observed include: cracking, concrete flaking, concrete spalling, exposure of the transverse and longitudinal reinforcement, buckling of the longitudinal reinforcement, fracture of the transverse and longitudinal reinforcement, and core degradation.

No damage was observed during the low-amplitude tests. Damage was first observed during the first high-amplitude test (Test 13) on bent 1 (medium-height bent), which had a maximum bent drift ratio of 0.85%. In general, bent 3 (the shortest bent) sustained the most damage throughout testing. By the end of the high-amplitude tests, in which bent 3 experienced a drift ratio of 11%, longitudinal bars had buckled at 53 of the 64 possible locations (16 at each column joint). Bars had fractured at 17 of the 64 locations.

The damage to the system was confined to the six columns until Test 20, when cracks and spalling in the cross beams were observed in circular patterns concentric to each column in bent 3. This cracking pattern was attributed to bar slip within the anchorages. No damage was observed in the footings or slab throughout testing.

Key conclusions from the experiment are listed below.

1. Despite sustaining drift ratios up to 11% in one bent, and being subjected to peak accelerations of 2.2g, the structure did not collapse. The amount of transverse reinforcement recommended by the NCHRP 12-49 commentary was adequate for preventing buckling of the longitudinal reinforcement until the bents reached large drift ratios. Bar buckling occurred in Bent 3 at a drift ratio between 5.5% and 7.9%. The detailing of the transverse reinforcement prevented the columns in the stockiest bent (shear span ratio 2.5:1) from failing in shear, even at drift ratios as large as 7.9%.

2. The maximum center-of-mass displacement of the bridge, which was dominated by the symmetric modes of the system, was independent of the motion coherency. In contrast,

motion incoherency significantly affected the twist displacements of the system, which were dominated by the asymmetric modes of the system. This experimental finding reinforces findings by Price and Eberhard (1998) based on numerical simulations of short-span bridges.

3. The maximum center of mass displacement was estimated well by the average spectral displacement for all three tables at the first mode of the structure and 5% damping.

13.2 Identified System Modal Properties

The modal properties of the shaking table specimen were determined with four system identification algorithms: a successive linear programming (SLP) algorithm, an autoregressive algorithm with exogenous excitation (ARX), a stochastic autoregressive algorithm (AR), and a subspace identification algorithm (SI).

Six modes of the shaking table specimen were identified by exciting the bridge in the transverse and longitudinal directions, including: three transverse modes, two vertical modes, and one longitudinal mode. Because the shaking table specimen was almost exclusively excited in the transverse direction, only the transverse modes were used to compare algorithms.

The periods of the first three transverse modes (identified with the ARX and SLP algorithms during the low-amplitude tests) were approximately 0.33s, 0.26s, and 0.078s. The periods of the first two transverse modes increased gradually throughout the low-amplitude tests, which was attributed to the progression of cracking within the columns. The third transverse mode did not change throughout the tests, because it depended primarily on the slab stiffness, which did not degrade during the tests.

The first three transverse mode shapes of the shaking table specimen were composed of combinations of slab translation, in-plane twisting, and slab bending. Mode 1 was primarily composed of translation (87%) and twisting (12%). Mode 2 was primarily composed of twisting (76%) and translation (24%). Mode 3 was primarily composed of slab bending (92%), and slab translation (7%).

The damping ratios from the first three transverse modes ranged from 1% to 4%. The

large scatter in the identified damping ratios was due to the relative insensitivity of the structural response to slight changes in the damping ratio, as analyzed using the SLP algorithm. For example, during the earthquake excitations, a 5% increase in the stiffness of bents 1 or 3 caused the objective function used by the SLP algorithm to increase by approximately 100% and 260%, respectively. A 5% increase in the damping ratios caused an average increase in the objective function of less than 0.5%.

The modal properties identified with each of these algorithms were compared to investigate the effects of pre-defining a structural model (parametric vs. non-parametric algorithms), accounting for the input excitation (input/output vs. stochastic algorithms), excitation type (earthquake, white noise, and square wave), and the type of response measurement (acceleration vs. displacement). Significant conclusions from these comparisons are listed below.

1. The parametric (SLP) and non-parametric (ARX) input/output algorithms had the same accuracy and precision for the identified modal properties. To implement the SLP algorithm, it was necessary to develop an adequate numerical model of the system. In addition, the SLP algorithm required a succession of linear programming steps for every variable that was optimized, making the computational demand of this algorithm computationally demanding for three-dimensional modal identification. In contrast, the non-parametric ARX algorithm did not require any a-prior knowledge of the system, and the computational demands were lower, but it required more effort to extract the properties of the individual structural components, such as bent stiffnesses.

2. For both input/output algorithms (ARX or SLP), the identified modal properties were independent of the type of excitation (white-noise, square-wave, or earthquake). In contrast, because square-wave and earthquake excitations have biased frequency content, these types of excitations affected the modal properties identified with the stochastic algorithms. For example, the identified period of mode 1 during Test 3B (earthquake excitation) was 0.41s (using the stochastic SI algorithm), 25% larger than the period of the same mode identified with the input/output SLP and ARX algorithms (0.33s).

3. The acceleration response data led to a more precise identification of modal properties than the displacement data. This difference was attributed to the existance of large accelerations in directions out of the plane of loading, and to the smaller noise-to-signal ratios in the acceleration data.

13.3 Modeling of the Shake-Table Tests

A numerical model was developed in OpenSEES to simulate the dynamic response of the 2-span, fixed-base, quarter-scale, shake-table specimen. The structural model was developed using nonlinear, distributed-plasticity elements for the columns, and elastic beam-column elements for the cross-beams and slab.

The nonlinear column elements were composed of four parts: the nonlinear material models, the zero-length sections to simulate anchorage slip, and the column integration and section discretization schemes required for the distributed plasticity elements. The nonlinear material models for the specimen were calibrated from measured concrete and steel properties. The column cross-section discretization and integration schemes were adopted from recommendations by Berry (2006), which were based on convergence tests of the moment-curvature responses for 75 circular columns from the UW-PEER column database (Berry et al., 2004). Components of the shake-table model (bond stress, effective cross-beam width, and viscous damping) were calibrated using response data recorded during the shake-table tests.

The accuracy of the numerical model was assessed by comparing the simulated response of the model with the measured response from the shaking table tests. The responses were compared for: total base shear, displacement maxima, displacement histories, and modal properties. Conclusions from the assessment of the shake-table model are listed below.

1. The calibrated OpenSEES model had a total system base shear of 391k, which differed from the measured base shear (386k) by less than 1.3%. Because the system was indeterminate, the base shear of the individual bents could not be determined experimentally.

2. The measured and simulated displacement maxima were similar at the beginning of

the low-amplitude excitations, but diverged towards the end of the low-amplitude excitations. This difference was attributed to the progression of cracking within the columns of the experimental specimen, which the numerical model did not capture.

3. During the high-amplitude tests, the calculated and measured displacement maxima were similar until Test 19, at which point significant bar buckling occurred in bent 3. The divergence in the maxima after this test was attributed to inabilities of the numerical model to adequately simulate the extent of column damage.

13.4 Model Assessment with Pseudo-Static Component Tests

Because the shaking table specimen was an indeterminate system, a primary objective of component tests conducted at Purdue University (Makido, 2007) was to directly provide the force-deformation response of the shortest bent of the shaking table specimen, and to assess the accuracy of the numerical model. Two of the five specimens tested at Purdue University (Specimens B-1 and C-1) had nominally identical properties to the columns in bent 3 (shortest bent) of the shaking table tests (Makido, 2007). For lightly-confined columns, Ranf et al. (2005) found that the amount of cycling influenced the damage progression within the columns. Therefore, a displacement history representative of the amount of cumulative plastic deformation bent 3 experienced during the shaking table tests was generated using a rainflow analysis.

The calculated response from the numerical model was similar to the measured response for various measures, including the force-displacement response, displacement-column elongation response, and displacement-rotation response.

1. The maximum base shear in the numerical model differed from the maximum base shear in the specimens by less than 4%. The strength reduction from the specimens was also simulated well by the numerical model. For example, by the end of the tests, Specimen C-1 lost 40% of it's lateral load carrying capacity, only 8% less than what the numerical model simulated.

2. The column elongation and effects of overturning were similar for the specimens and the numerical model. The experimental specimens retained larger residual column

elongations than the numerical model simulated.

3. The relationship between plastic rotation and displacement was approximately linear for the specimens and the numerical model, signifying that the proportion of the column deformation coming from the rotation within the plastic hinge zone was constant.

4. Column deformations at key damage states (yielding of the longitudinal reinforcement, spalling of the concrete cover, and fracture of the longitudinal reinforcement) were similar for both the experimental specimens and the numerical model. For example, spalling was first observed in Specimen C-1 at a drift ratio of 1.2%, which was the same as what the numerical model simulated using the strain equations for concrete spalling developed by Berry (2006).

13.5 *Predicted Prototype Behavior*

The numerical model of the prototype specimen (a reinforced concrete bridge on drilled-shaft foundations) was assembled by combining the calibrated structural components from the shaking table model and component tests, and the calibrated soil and foundation components from a centrifuge model developed by Shin (2006). All geometric properties of the full-scale prototype model resulted from scaling of the two specimens. The material properties of the prototype model were the same as those of the shaking table model, except for the compressive strength of the concrete (5000 psi).

The response of the calibrated prototype model was investigated by subjecting it to suites of 40 near-field and 30 far-field excitations. The near-field excitations were developed for the PEER I-880 Testbed Project, which modeled a bridge along I-880 in Oakland, California. The far-field excitations were developed for the PEER Van Nuys building testbed project. Each of these suites of motions contained sets of ten motions at various hazard levels: 50%, 10%, and 2% probability of exceedence in 50 years. Shin (2006) added a fourth hazard level (97% probability of exceedence in 50 years) to investigate the system response to low-level excitations.

The prototype was characterized using six demand parameters: maximum bent drift, residual bent drift, maximum plastic rotation within the column, maximum plastic rotation

within the pile, maximum column shear, and maximum pile shear. The intensity of the ground motion was quantified using the Cordova parameter (Cordova et al., 2000), which accounts for system softening by using the spectral acceleration at one and two times the first period of vibration of the structure. Significant conclusions from these tests are listed below.

1. During high-intensity excitations (Cordova parameter = 3g), the average drift ratios of bents 1 and 3 were 8.7% and 8.4%. According to the bar buckling equation developed by Berry (2006), the likelihood of bar buckling at these drift ratios would be approximately 90%.

2. The average residual drift ratios of bents 1 and 3 during high-intensity excitations (Cordova parameter = 3g) due to the near-field excitations were approximately 0.5%. These residual drift ratios might have significant consequences on the functionality of the bridge following an earthquake.

3. The top of the column in bent 3 experienced plastic curvatures that were approximately 27 times the yield curvature, and approximately 9 times the largest curvature recorded in the piles. This data suggests that for flexure-critical columns, significant damage will likely occur above ground, near the tops of the columns.

4. Until the moment capacity was reached at the tops of the columns, the maximum moment occurred above ground at the top of the columns. The moment below ground continued to increase with the motion intensity.

5. The maximum moment within the piles occurred at approximately 2.5 and 3.5 column diameters below the ground surface for the most flexible and stiffest bents, respectively. During the high-intensity excitations, the depth of maximum moment in the piles of the stiffest bent increased from 3.5D to 4D.

6. The shear forces within the columns were governed by the moment capacity of the column and the distance to the point of inflection. The boundary conditions in the soil were much more complicated. As a result, the shear forces within the piles were lower for the low level excitations. In contrast, the shear forces within the piles were larger

than the shear forces within the columns during the high-intensity excitations. For example, at a Cordova parameter of 3.0g during the far-field excitations, the average shear force within the pile of bent 2 was 423k, 39% larger than the average shear force within the columns of bent 2 (305k). The higher shear forces in the columns signify that lightly-confined or stocky columns might fail in shear below the ground surface rather than within the visible portion of the column.

13.6 *Evaluation of Seismic Modeling Strategies*

The foundation and structural components of the prototype model were approximated using various methodologies. The foundation was approximated using: two-dimensional nonlinear soil columns attached to the piles using nonlinear P-y, Q-z, and T-z springs, linear soil springs and dashpots to represent the flexibility and damping within the soil, and fixed column bases to represent the soil flexibility through equivalent column heights. The structure was approximated using: nonlinear column elements, effective-section linear column elements, and gross-section linear column elements.

The combination of the various foundation and structural approximations led to a matrix of 13 modeling strategies: one prototype model and 12 simpler models. The accuracy and precision of these models were evaluated by comparing the EDP's of the simpler models with those of the prototype model when excited by suites of 40 near-field and 30 far-field excitations. Accuracy and precision were quantified by the mean and standard deviation of the percent difference in the estimated EDPs, defined as

$$Accuracy = \mu_{error} = \frac{1}{N} \sum_{i=1}^{N} Error_{EDP,i} \tag{13.1}$$

$$Precision = \sqrt{\frac{1}{N-1} \sum_{i=1}^{N} [Error_{EDP,i} - \mu_{error}]^2} \tag{13.2}$$

The prototype model would not be available for designers to estimate the pile fixity depth. Therefore, the sensitivities of the model demands (drift ratio, plastic rotation, and column shear) to the estimated depth of pile fixity were evaluated for fixity depths raging from 2D to 4D.

The efficiencies of common intensity measures was investigated using three of the models (prototype, inelastic fixed @ 3D, and effective-elastic fixed @ 3D). The sensitivity of the IM efficiency to the modal properties of bridge were also investigated to determine whether the chosen intensity measures could be optimized for the bridge system in this research.

The effects of the modeling strategies on the estimated concrete spalling and bar buckling damage hazards ($ERROR_{DM,model}$) were investigated for the 12 simpler models. As with the demand error analysis, the sensitivity of the estimated damage levels to the effective fixity depth was also investigated. To gain perspective on the size of error for the simpler models, the errors in the damage measures due to the modeling approximations and the various fixity depths ($ERROR_{DM,model}$) were compared with the errors in the damage measures due to selecting a less efficient IM ($ERROR_{DM,IM}$).

Conclusions from the evaluation of the accuracy and precision of the bridge modeling strategies are listed below.

1. For the soil properties considered in this research, the inelastic fixed @ 3D model was the most accurate and precise of the 12 modeling strategies for estimating system demands. For example, the overall mean and standard deviation of the errors in the estimated maximum drift rations for the fixed @ 3d model was -3.2% and 12%, respectively. The mean errors from the other three nonlinear models ranged from -25.4% to 71.2%. The standard deviations of the other three models ranged from 35% to 51%.

2. Overall, the effective-elastic fixed @ 3D model was the most accurate and precise of the elastic models. This model was on average only slightly less accurate than the inelastic fixed @ 3D model. However, the standard deviation for the effective elastic fixed @ 3D model ($\sigma = 39\%$) was more than three times the standard deviation for the inelastic fixed @ 3D model ($\sigma = 12\%$).

3. System twisting was not effectively estimated with the stiff inelastic or the elastic models. This model limitation typically caused the demand parameters to be overestimated for bent 1, and underestimated for bent 3. For example, the average errors for bents 1 and 3 of the effective-elastic fixed @ 3D model were 12.7% and -16.2%,

respectively.

4. For the soil and pile properties considered in this research, the accuracy and precision of the estimated drift ratios for the inelastic fixed base models were insensitive to the assumed depth of fixity. For example, the mean errors of the estimated drift ratios for fixity depths between 2D and 4D ranged from -3.2% to 0.6%. The mean errors in the estimated plastic rotations were more sensitive to the fixity depth, with mean errors ranging from -2.6% to 18.2%. For estimating the overall drift ratios, the fixed @ 3.5D model (estimated fixity depth based on a procedure developed by Chai (2002)) was slightly more accurate, but slightly less precise, than the inelastic fixed @ 3.0D model (fixity depth based on estimated depth of maximum moment in the prototype model).

5. Of the 11 considered intensity measures that were investigated in this research, the Cordova parameter (Class II) was the most efficient for the inelastic models, followed closely by the peak ground velocity (Class I). The modified Cordova (MCOR) parameter (optimized for this bridge system) was as much as 20% more efficient than the Cordova parameter. The spectral acceleration (SA_1, Class II) was the most efficient IM for the elastic models.

6. On average, the Class II-2 intensity measures, which incorporated the frequencies of vibration for the first two modes of the structure, did not improve the IM efficiency over the Class II models for this structure. This finding was attributed to the similarity in the first two periods of vibration of the bridge (0.61s and 0.53s).

7. The inelastic fixed @ 3D model was the most accurate and precise of the 12 simpler models for estimating the concrete spalling and bar buckling hazards for all bents. On average, spalling was overestimated by 9.1% and bar buckling was underestimated by 19.4%. Spalling was very difficult to predict for all modeling strategies, and bar buckling was almost always underpredicted. For example, the gross-elastic models underpredicted bar buckling by 99% to 89%.

8. Due to the amount of motions used for estimating the damage levels for each bent, the estimated damage hazards were insensitive to the choice in an efficient intensity measure. For example, using the peak ground velocity, spectral acceleration, or modified

Cordova parameter caused a difference in the estimated spalling hazard ranging from -3.9% to 13%. The choice of intensity measure is expected to have a larger impact when using less motions to characterize the system response.

13.7 Suggestions for Model Selection

For a reinforced concrete bridge on drilled shaft foundations, founded on dense, dry sand, the most accurate and precise modeling strategy for estimating both demands and damage was achieved by modeling the columns with inelastic elements, and modeling the foundation with a fixed base, fixed at a depth below the ground surface corresponding to the location of the maximum moment within the piles. The accuracy and precision of the demand and damage estimates were not significantly affected by moderate fluctuations in the fixity depth. Therefore, the effective fixity depth can be estimated using approximate methods (e.g., Chai (2002)).

An effective-elastic, fixed-base model can be used to obtain accurate (but relatively imprecise) estimations of the overall system demands. However, the twisting of the bridge was not adequately simulated at moderate and high intensity levels with effective-elastic columns. This limitation caused damage estimates (which are based on the response of the individual bridge components) to be either overpredicted or underprecited for the bents affected by the asymmetric system modes (bents 1 and 3). More work is needed for accurately modeling the torsional response of nonlinear systems with effective-elastic systems.

Fixing the column bases at the ground surface, and modeling the foundation flexibility with elastic translational and rotational springs, did not simulate the response of the prototype system well for the two extreme spring stiffness cases. However, with the correct spring stiffnesses, this model might accurately predict the demand and damage levels. More analysis needs to be conducted to develop methods for accurately determining the values of the spring stiffnesses.

REFERENCES

AASHTO (2004). *AASHTO LRFD Bridge Design Specifications* (Third ed.). AASHTO.

ACI Committee 318 (2002). *Building Code Requirements for Structural Concrete and Commentary*. Farmington Hills, Michigan: American Concrete Institute.

Akaike, H. (1969). Fitting autoregressive models for prediction. *Annals of the Institute of Statistical Mathematics 21* (2), 243–247.

Akaike, H. (1971). Autoregressive model fitting for control. *Annals of the Institute of Statistical Mathematics 23* (2), 163–180.

Allemang, R. (1999). *Vibrations: Experimental Modal Analysis, Course Notes* (Seventh ed.). Structural Dynamics Research Laboratory, University of Cincinnati, OH. http://www.sdrl.uc.edu/courseinfo.html.

Arias, A. (1970). *Seismic Design for Nuclear Power Plants*, Chapter A measure of earthquake intensity, pp. 438–483. Cambridge: MIT Press.

Arici, Y. and K. Mosalam (2003). System identification for instrumented bridge systems. *Earthquake Engineering and Structural Dynamics 32*, 999–1020.

ATC/MCEER (2001). *Recommended LRFD Guidelines for the Seismic Design of Highway Bridges (2002) Part 1: Specifications*. MCEER/ATC joint venture, NCHRP 12-49 Project Team.

Beck, J. L. and P. C. Jennings (1980). Structural identification using linear models and earthquake records. *Earthquake Engineering and Structural Dynamics 8*, 145–160.

Berry, M. (2006). *Experimental Calibration of OpenSees Components Using the PEER Column Database*. Ph. D. thesis, Department of Civil and Environmental Engineering, University of Washington.

Berry, M., M. Parrish, and M. Eberhard (2004). *PEER Structural Performance Database User's Manual*. Pacific Earthquake Engineering Research Center, Berkely, CA.

Caltrans (2004). *Seismic Design Criteria* (1.3 ed.).

Chai, Y. (2002). Flexural strength and ductility of extended pile-shafts. i: Analytical model. *Journal of Structural Engineering 28* (5), 586–594.

Chopra, A. K. (1995). *Dynamics of Structures* (4th ed.). Prentice Hall.

Cordova, P., S. Mehanny, G. Deierlein, and C. Cornell (2000). Development of a two-parameter seismic intensity measure and probabilistic assessment procedure. In B. Pacific Earthquake Engineering Research Center, University of California (Ed.), *The Second U.S. - Japan Workshop on Performance-Based Earthquake Engineering Methodology foor Reinforced Concrete Building Structures*, Volume Report No. 2000/10.

DerKiureghian, A. (1980, June). *A REsponse Spectrum Method for Random Vibrations.* Ph. D. thesis, University of California at Berkeley.

Huang, C. and H. Lin (2001). Modal identification of structures from ambient vibration, free vibration, and seismic response data via a subspace approach. *Earthquake Engineering and Structural Dynamics 30*, 1857–1878.

Jalayer, F. (2003). *Direct Probabilistic Seismic Analysis: Implementing Non-linear Dynamic Assessments.* Ph. D. thesis, Stanford University.

Johnson, N., R. Ranf, M. Saiidi, D. Sanders, and M. Eberhard (2006, August). Shake table studies of a large scale two-span reinforced concrete bridge frame. *Eighth National Conference on Earthquake Engineering.*

Johnson, N., M. Saiidi, and D. Sanders (2006, March). Large-scale experimental and analytical seismic studies of a two-span reinforced concrete bridge system. Technical Report CCEER-06-02, University of Nevada, Reno.

Juang, J. (1994). *Applied System Identification.* Prentice Hall.

Lehman, D. (1998). *Performance-Based Seismic Design of Well-Confined Concrete Columns.* Ph. D. thesis, Department of Civil and Environmental Engineering, University of California, Berkeley.

Ljung, L. (1999). *System Identification: Theory for the User* (Second ed.). Prentice-Hall, Upper Saddle River, NJ.

Lupoi, A., P. Franchin, P. Pinto, and G. Monti (2005). Seismic design of bridges accounting for spatial variability of ground motions. *Earthquake Engineering and Structural Dynamics 34*, 327–348.

Mackie, K. and B. Stojadinovic (2005, June). Fragility basis for california highway overpass bridge seismic decision making. Technical Report 12, Pacific Earthquake Engineering Research Center.

Makido, A. (2007). *Behavior of Spirally Reinforced Concrete Columns under Load Reversals.* Ph. D. thesis, Purdue University.

Mander, J., M. Priestley, and R. Park (1988, August). Theoretical stress-strain model for confined concrete. *Journal of Structural Engineering 114*(8), 1804–1826.

Mayfield, R. (2007). *The Return Period of Soil Liquefaction.* Ph. D. thesis, University of Washington.

McVerry, G. (1980). Structural identification in the frequency domain from earthquake records. *Earthquake Engineering and Structural Dynamics 8*, 161–180.

NEES (2005). George e. brown, jr. network for earthquake engineering simulation. www.nees.org.

Neumaier, A. and T. Schneider (2001, March). Estimation of Parameters and Eigenmodes of Multivariate Autoregressive Models. *ACM Transactions on Mathematical Software 27*(1), 27–57.

Newmark, N. (1959). A method of computation for structural dynamics. *ASCE Journal of the Engineering Mechanics Division 85*(EM3).

Novak, M. (1974). Dynamic stiffness and damping of piles. *Canadian Geotechnical Journal 11*, 574–598.

Novak, M., M. Sheta, L. El-Hifnawy, H. El-Marsafawi, and O. Ramadan (1993). *DYNA4: A Computer Program for Calculation of Foundation Response to Dynamic Loads.* Report No. GEOP 93-01, Geotechnical Research Centre, The University of Western Ontario, London, Ontario, Canada.

OpenSees Development Team (2002). OpenSees: Open System for Earthquake Engineering Simulations. Version 1.5, Berkeley, CA.

PEER (2005). Peer strong motion database. http://peer.berkeley.edu/smcat.

Peeters, B. and G. De Roeck (1999). Reference-based stochastic subspace identification for output-only modal analysis. *Mechanical Systems and Signal Processing 13*(6), 855–878.

Peeters, B. and G. De Roeck (2001, December). Stochastic system identification for operational modal analysis: A review. *Journal of Dynamic Systems, Measurement, and Control 123*, 659–667.

Peeters, B. and C. Ventura (2003). Comparative study of modal analysis techniques for bridge dynamic characteristics. *Mechanical Systems and Signal Processing 17*(5), 965–988.

Petsounis, K. and S. Fassois (2001). Parametric time-domain methods for the identification of vibrating structures - a critical comparison and assessment. *Mechanical Systems and Signal Processing 15*(6), 1031–1060.

Price, T. and M. Eberhard (1998). Effects of spatially varying ground motions on short bridges. *Journal of Structural Engineering 124*(8), 948–955.

Pridham, B. and J. Wilson (2005). A reassessment of dynamic characteristics of the quincy bayview bridge using output-only identification techniques. *Earthquake Engineering and Structural Dynamics 34*, 787–805.

Ramirez, J. and A. Makido (2006). Personal communication. Purdue University.

Ranf, R., J. Nelson, Z. Price, M. Eberhard, and J. Stanton (2005). Damage accumulation in lightly confined reinforced concrete bridge columns. Pacific Earthquake Engineering Research Institute (PEER).

Ren, W., W. Zatar, and I. Harik (2004). Ambient vibration-based seismic evaluation of a continuous girder bridge. *Engineering Structures 26*, 631–640.

Shin, H. (2006). *Modeling of Soil-Pile-Structure Interaction fo Bridges and its Application for Performance Based Earthquake Engineering*. Ph. D. thesis, University of Washington.

Shin, H., M. Ilankathara, P. Arduino, B. Kutter, and S. Kramer (2006, April). Experimental and numerical analysis of seismic soil-pile-structure interaction of a two-span bridge. *Eighth National Conference on Earthquake Engineering*.

Smyth, A., J. Pei, and S. Masri (2003). System identification of the vincent thomas suspension bridge using earthquake records. *Earthquake Engineering and Structural Dynamics 32*, 339–367.

Somerville, P. and N. Collins (2002a, February). Ground motion time histories for the i880 bridge, oakland. http://www.peertestbeds.net/i880/I880BridgeReport.pdf.

Somerville, P. and N. Collins (2002b, March). Ground motion time histories for the van nuys building. http://www.peertestbeds.net/VNY/VanNuysBuildingReport.pdf.

Taucer, F., E. Spacone, and F. Filippou (1991). *A Fiber Beam-Column Element for Seismic Response Analysis of Reinforced Concrete Structures*. UCB/EERC-91/17, Earthquake Engineering Research Center, Berkeley, CA.

Van Overschee, P. and B. De Moor (1996). *Subspace Identification for Linear Systems, Theory - Implementation - Applications*. Kluwer Academic Publishers.

Wood, S., T. Anagnos, P. Arduino, M. Eberhard, G. Fenves, T. Finholt, J. Futrelle, B. Jeremic, S. Kramer, B. Kutter, A. Matamoros, K. McMullin, J. Ramirez, E. Rathje, M. Saiidi, D. Sanders, K. Stokoe, and D. Wilson (2004, August). Using nees to investigate soil-foundation-structure interaction. In *Proceedings, 13th World Conference on Earthquake Engineering, Vancouver, Canada*.

WSDOT (2000). *Washington State Bridge Inventory*. Olympia, WA: Washington State Department of Transportation.

Yang, Z. and B. Jeremic (2002). Numerical analysis of pile behaviour under lateral loads in layered elastic-plastic soils. *International Journal for Numerical and Analytical Methods in Geomechanics 26*, 1385–1406.

Zhao, Q., T. Sawada, K. Hirao, and Y. Nariyuki (1995). Localized identification of mdof structures in the frequency domain. *Earthquake Engineering and Structural Dynamics 24*, 325–338.

Appendix A

SHAKING TABLE LIMITS

The selection of the appropriate ground motion is also based on the capacity of the shaking tables, which are primarily limited by bearing capacity and oil flow capacity within the actuators. The limits are shown in Table A.1. Because the oil flow is also based on the feedback of the structure, these soft limits may deviate slightly from the ones reported. However, for choosing a final ground motion, these will be treated as hard limits to compare the ability of each motion to excite the structure while staying within the imposed limits.

Table A.1: Shaking table limits

Parameter	Dimension
Table Size	14.0 ft x 14.6 ft
Dynamic Displacement	±12 in.
Static Displacement	±14 in.
Pitch Moment (E-W direction)	1,000,000 ft-lb
Yaw Moment (torsion)	400,000 ft-lb
Roll Moment (N-S direction)	400,000 ft-lb
Velocity	±40 in./s
Force	165,000 lb
Acceleration	±1.4 g

The acceleration limit is based on an allowable actuator force of 165,000 lb for each shaking table. Using the allowable actuator force (F_a), the bent shear capacities, V_u, shaking table mass (M_T), spacer block mass (M_S) and footing mass (M_F), the shaking table acceleration limit can be calculated as

$$a_{max} = \frac{F_a - V_u}{M_T + M_S + M_F} \tag{A.1}$$

Bent 3 has the largest ultimate shear capacity $(V_u = 45\ k)$ and the most massive footing and spacer block $(M_S + M_F = 21.8\ lbm)$. The mass of the tables is $M_T = 64\ lbm$. Therefore,

the table acceleration limit is controlled by Bent 3, with an allowable acceleration of 1.4g.

The moment demand on the shaking tables were checked by using the estimated column plastic moment capacities as an estimate of the maximum table demand. The largest pitch moment (the moment in the transverse bridge direction) occurs on bent 3, which has the largest shear and moment capacity. Table A.2 outlines the largest moments that would be demanded on the tables.

Table A.2: Shaking table moment demand in the transverse bridge direction

Unit Description	Unit Moment
Bent End Moment (675 $k-in.$ per column)	1,350
Bent Base Shear (45 k)	4,860
Footing @ a = 1.4g ($M_F = 10125$ lbm)	553
Spacer Block @ a = 1.4g ($M_S = 11700$ lbm)	197
Axial Load Unbalance ($2[0.082f_c'A_g]$)	3,478
Total Moment Demand ($k-in.$)	10,437
Total Moment Demand ($lb-ft$)	869,761
Total Moment Capacity ($lb-ft$)	1,000,000

As seen in Table A.2, the most conservative estimate of the shaking table moment demand in the transverse direction is less than the allowable capacity. The moment limits in the other two directions were investigated using the preliminary numerical model subjected to high-amplitude earthquake excitations.

Appendix B

DESIGN DOCUMENTS

The design documents were created by Johnson et al. (2006) at the University of Nevada, Reno.

98in [2.49m]

30in [0.76m]
30in [0.76m]
30in [0.76m]

1in [25.4mm]
1in [25.4mm]
1in [25.4mm]

See Duct Details (Sheets 16-17)

Top View

See Bents (Sheet 2)

See Footing Blocks (Sheet 12)

360in [9.14m]

43.5in [1.1m]

Bent 1

NOTES:

- Concrete is $\frac{3}{8}$in agg.; 28-day comp strength = 5000psi
- Reinforcement is ASTM A706 Grade 60

15in [0.38m]

114in [2.9m]

See Bents (Sheet 2)

See Footing Blocks (Sheet 12)

Bent 3

14in [0.36m]

See Beam Plans (Sheet 13)

See Bents (Sheet 2)

360in [9.14m]

Bent 2

See Beam Plans (Sheet 13)

Elevation View

Bridge Specimen Proposed Plans

Span

Drawn by: N. Johnson

University of Nevada, Reno

Sheet: 1 of 24

Date: 9-1-04

268

Bent 1

63in [1.6m]

See Bent 1&3
Cap Beam Sections
(Sheet 3)

37.5in [0.95m]

20.5in [0.52m]

72in [1.83m]

12in [305mm]

18in [457mm]

See Bent 1&2 Footings
(Sheet 10)

36in [0.91m]

Side View

98in [2.49m]

15in [381mm]

5.5in [140mm]

12in [305mm]

63in [1.6m]

12in [305mm]

5.5in [140mm]

108in [2.74m]

Elevation View

Bent 2

15in [381mm]

See Bent 2
Cap Beam Section
Dimensions (Sheet 3)

8.5in [216mm]

8.5in [216mm]

96in [2.44m]

12in [305mm]

18in [457mm]

See Bent 1&2 Footings
(Sheet 10)

36in [0.91m]

Side View

98in [2.49m]

15in [381mm]

5.5in [140mm]

12in [305mm]

63in [1.6m]

12in [305mm]

5.5in [140mm]

108in [2.74m]

Elevation View

Bent 3

63in [1.6m]

See Bent 1&3
Cap Beam Sections
(Sheet 3)

37.5in [0.95m]

20.5in [0.52m]

60in [1.52m]

12in [305mm]

30in [0.76m]

See Bent 3 Footing
(Sheet 11)

36in [0.91m]

Side View

98in [2.49m]

15in [381mm]

5.5in [140mm]

12in [305mm]

63in [1.6m]

12in [305mm]

5.5in [140mm]

108in [2.74m]

Elevation View

Bridge Specimen Proposed Plans	Bents	Sheet: 2 of 24
	Drawn by: N. Johnson	Date: 9-1-04
	University of Nevada, Reno	

See Bent 1&3 Ledge (Sheet 6)

4in [102mm]

See Bent 1&3 Joint Reinf. (Sheet 5)

cc = 0.5in (12.7mm)

See Column Reinf. (Sheet 4)

20.5in [521mm]

Bent 1 & 3 Cap Beam
Section Dimensions

See Cantilever Bolt Details (Sheet 18)

See Bent 1&3 Cantilevers (Sheet 7)

63in [1600mm]

37.5in [952mm]

15in [381mm]

See Bent 2 Joint Reinf. (Sheet 8)

See Bent 2 Ledges (Sheet 9)

4in [102mm]

See Column Reinf. (Sheet 4)

8.5in [216mm]

8.5in [216mm]

15in [381mm]

7in [178mm]

8in [203mm]

15in [381mm]

Bent 2 Cap Beam
Section Dimensions

Bridge Specimen Proposed Plans

Bent Sections

Sheet: 3 of 24

Drawn by: N. Johnson

Date: 9-1-04

University of Nevada, Reno

NOTES:
- Hbent1 and Hbent3 = 101.5 in
- Hbent2 = 125.5 in
- Spiral Reinforcement:
  W2.9 (0.192 in Wire) @ 1.25 in
  Grade 60 Steel
- Welds:
  made after cap cage placement
  E80-xx

Column Section
(all columns)

12in [305mm]

16-#3
(C-23) for bent 1&3
(C-24) for bent 2

Spiral Reinf.

cc =0.75in [19mm]

Top Weld Plan

C-25 (#3)

1.89in [48mm]

3in [76mm]

Spiral Reinf

See Weld
Details (This Sheet)

Plan View

Anchor Bar (C-25)

db

lw = 3/4*db

tw = db/2

tw = db/2

Elevation View
Weld Details

0.125in [3mm]

tw = db/2

db = 0.375 in (9.5 mm)

tw = db/2

Col. Long. Steel

lw = 3/4*db

Elevation View

See Top Weld Plan (This Sheet)

H (varies by bent)

Bridge Specimen Proposed Plans

Column Reinf.	Sheet:4 of 24
Drawn by: N. Johnson	Date: 9-1-04
University of Nevada, Reno	

271

Beam Section Ties

Side View

Beam Section Ties at Column Joint

#3 (C-4)
(4-per column joint)

Top View

Beam Section Ties

Beam Section Ties at Column Joint

#4@4.5in ((C-3)

2-#4@4.5in (C-2)

Beam Section Ties
at Column Joint

#3 (C-4)
(4-per column joint)

6-#6 (C-10) equally spaced

3-#3 (C-12) @ equal spaces

#4@4.5in (C-1)

4-#6 (C-11) (in pairs)

Beam Section Ties

Bridge Specimen Proposed Plans
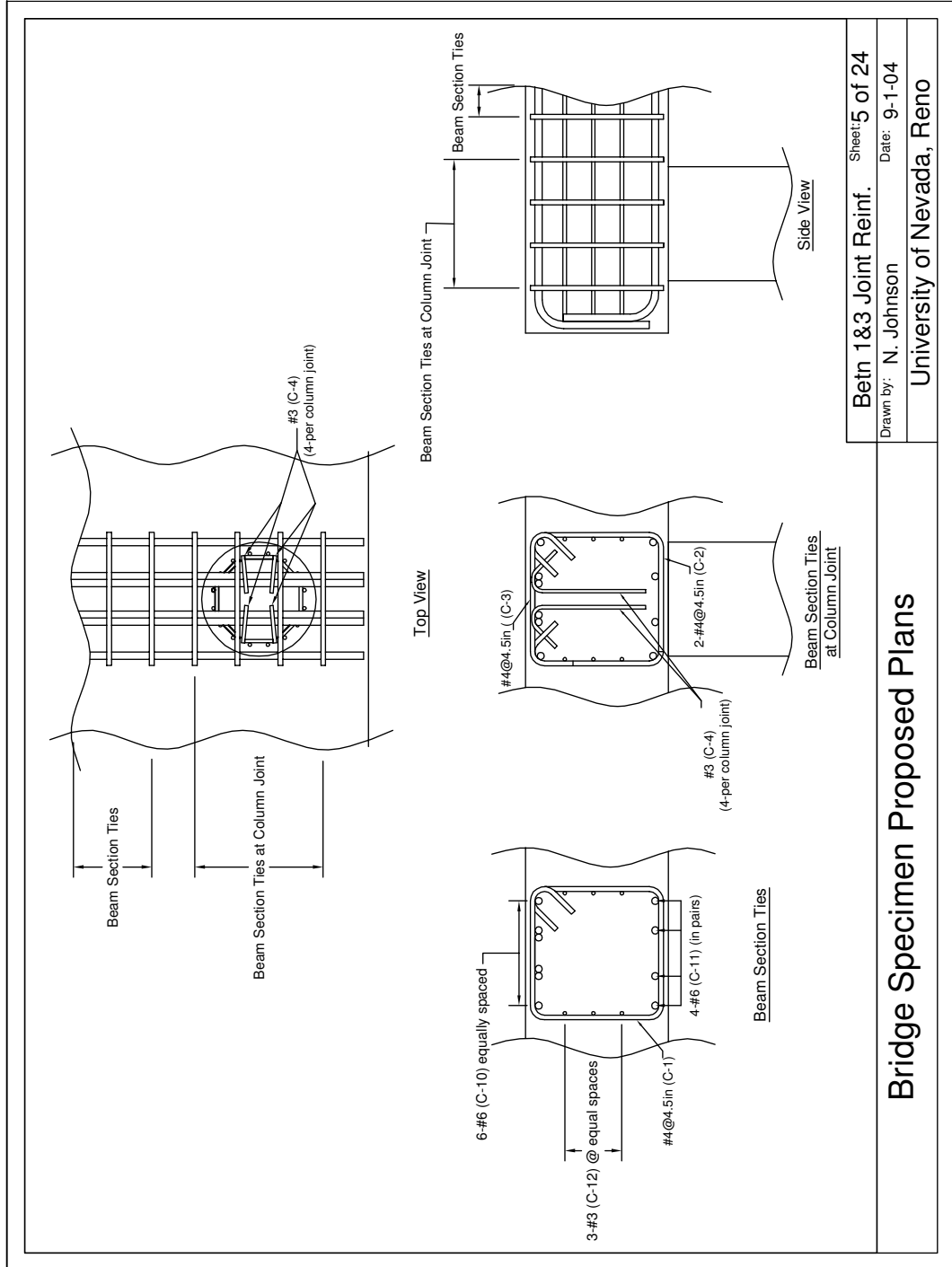
Betn 1&3 Joint Reinf.   Sheet:5 of 24
Drawn by: N. Johnson   Date: 9-1-04
University of Nevada, Reno

272

Ledge Steel Elevation View (Level 1)

#6 (C-14) @ 5in (127mm)

1.5in [38mm]

Ledge Steel Elevation View (Level 2)

8 #3 (C-15) @ 10in (254mm)

30in [762mm]

19in [483mm]

#6 (C-14)
(127mm)
(Level 1)
@ 5in (127mm)

#3 (C-16)
(Level 2)

Bearing Plates (Supplied by UNR)

Post-Tension Ducts

#3 (C-16)
(Level 2)

1.13in [29mm]

2.5in [63mm]

#3 (C-15) @ 10in (254mm) (Level 2)

#3 (C-15) @ 10in (254mm) (Level 2)

Ledge Steel Elevation View

#4 (C-13)

#3 (C-17)

Bridge Specimen Proposed Plans

A   B

24in [610mm]

24in [610mm]

#4 (C-20)

#4 (C-21)

#4 (C-22)

#4 (C-21)

#4 (C-20)

A   B

Top View

Sec. A-A

Sec. B-B

3-#4 (C-26) @ 1in

3-#4 (C-26) @ 1in

3-#4 (C-26) @ 1in

3-#4 (C-26) @ 1in

3-#4 (C-26) @ 1in

3-#4 (C-26) @ 1in

4in [102mm]

5 @ 6in

21in [533mm]

6in [152mm]

3in [76mm]

3.5in [89mm]

cc = 0.5in (13mm)

Lifting Hooks
(See Detail Sheet 12)

Elevation View

#6 (C-18) @ 5in

#6 (C-19) @ 5in
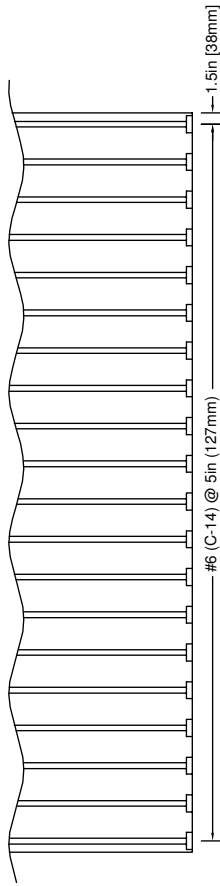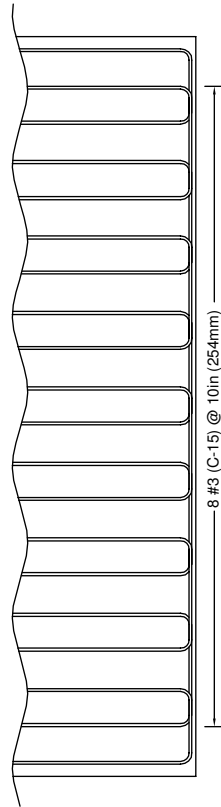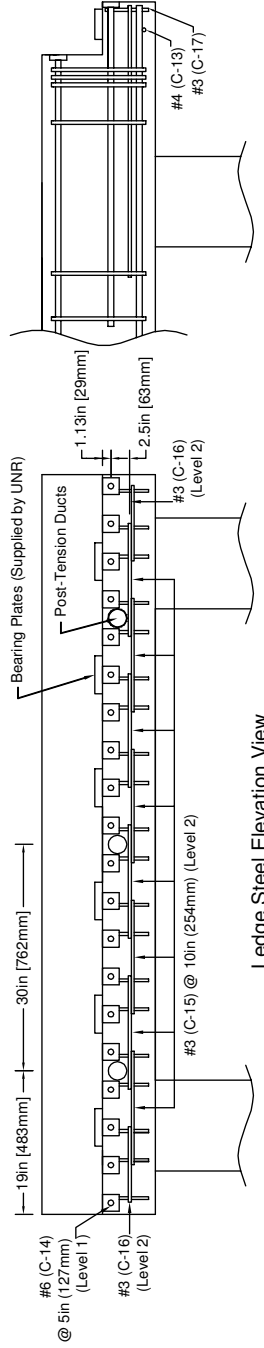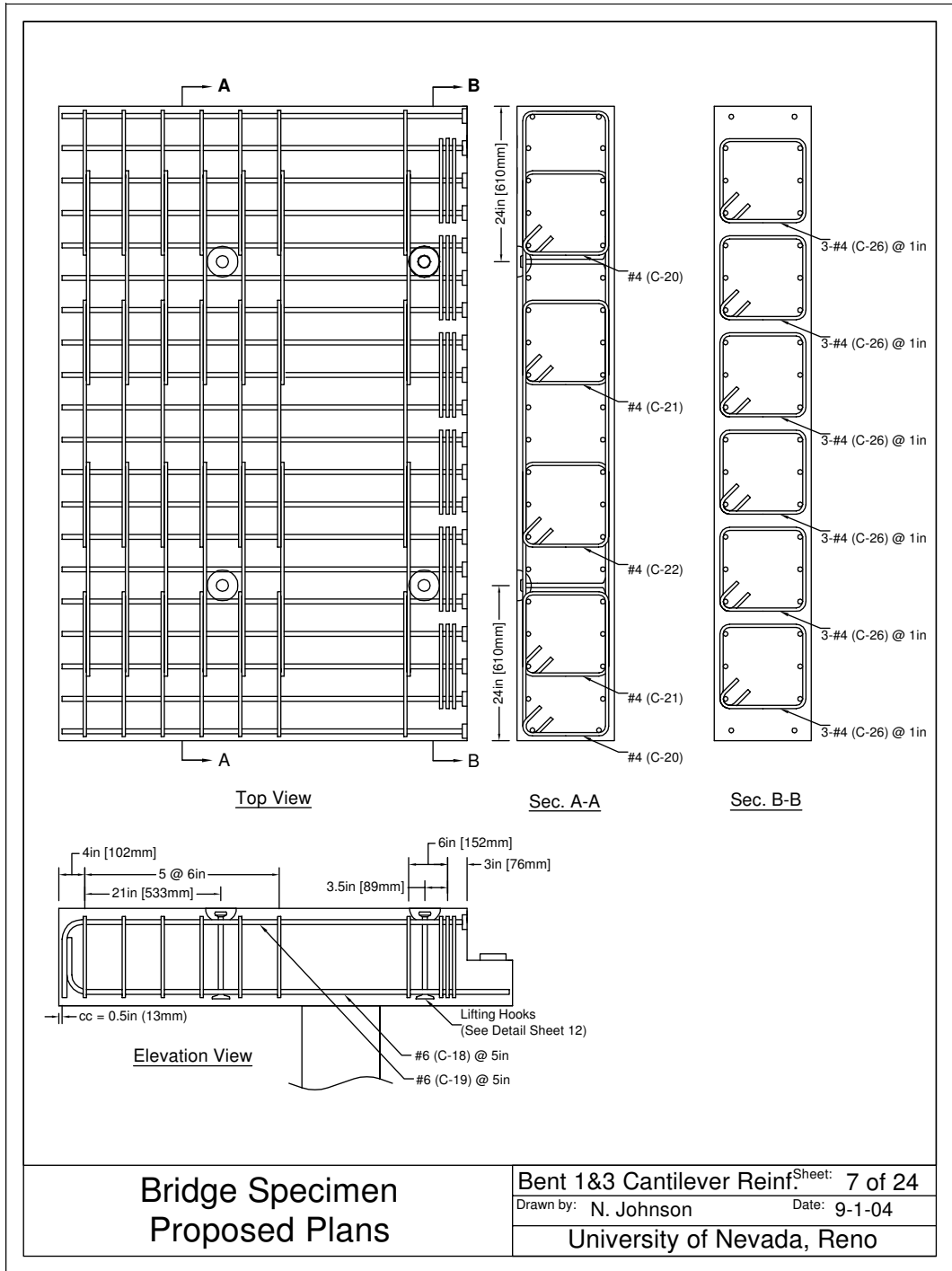
Bridge Specimen Proposed Plans	Bent 1&3 Cantilever Reinf.	Sheet: 7 of 24
	Drawn by: N. Johnson	Date: 9-1-04
	University of Nevada, Reno	
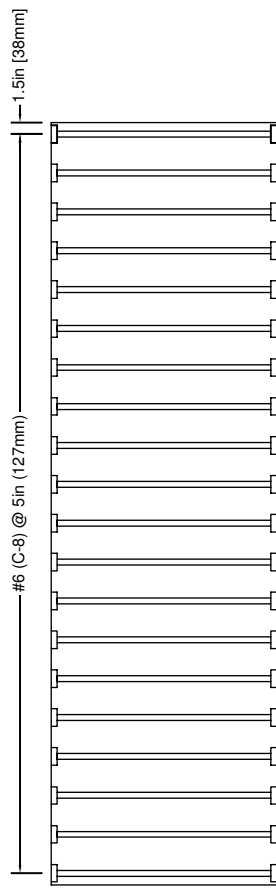
Bridge Specimen Proposed Plans

Bent 2 Joint Reinf. Sheet: 8 of 24
Drawn by: N. Johnson Date: 9-1-04
University of Nevada, Reno

#6 (C-8) @ 5in (127mm)

1.5in [38mm]

Ledge Steel Elevation View (Level 1)

8 sets #3 (C-7) @ 10in (254mm)

Ledge Steel Elevation View (Level 2)

30in [762mm]

19in [483mm]

Post-Tension Ducts

Bearing Plates (Supplied by UNR)

#6 (C-8) @ 5in (127mm) (Level 1)

#3 (C-6) (Level 2)

#3 (C-7) @ 10in (254mm) (Level 2)

Ledge Steel Elevation View

1.13in [29mm]

2in [51mm]

#3 (C-6) (Level 2)

#3 (C-9)
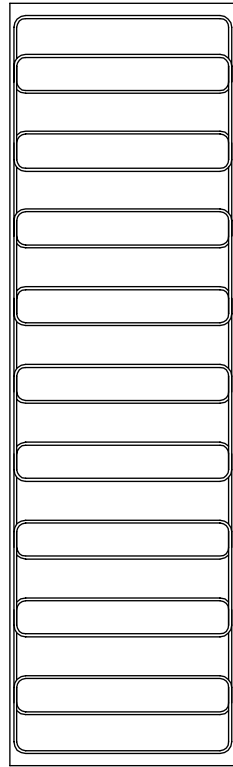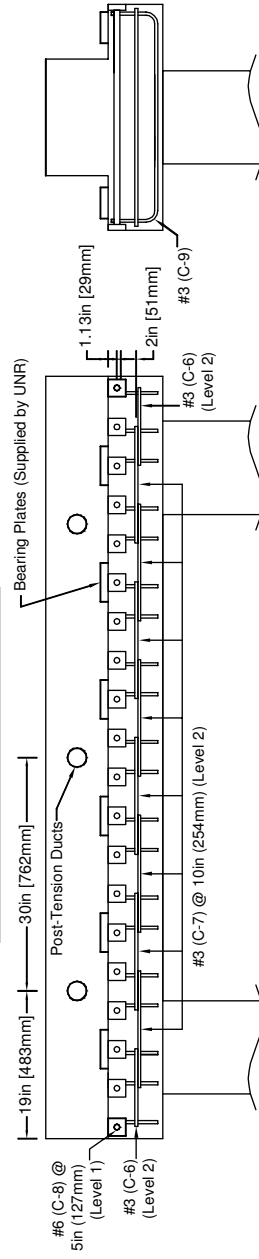
Bridge Specimen Proposed Plans

Bent 2 Ledge Reinf.	Sheet: 9 of 24
Drawn by: N. Johnson	Date: 9-1-04
University of Nevada, Reno	

276

NOTE:
Axial Ducts 3" (76mm) F (PVC Sleeve)

5in [133mm]
5in [133mm]
26in [668mm]
26in [668mm]

Top View
#8 (F-3) & (F-4)
#8 (F-1) & (F-2)
#8 (F-9) at each face

2in [51mm]
8in [203mm]
8in [203mm]
8in [203mm]
5.5in [140mm]
14in [356mm]
2.5in [63mm]
6in [152mm]

4in [102mm]
2in [51mm]
2in [51mm]
4in [108mm]
6in [146mm]

36in [914mm]
Side View
18in [457mm]
10in [254mm]

cc = 1in (25mm)
#10 (LB-1)
#3 Stirrup (F-5)
108in [2743mm]
Elevation View

Bridge Specimen Proposed Plans
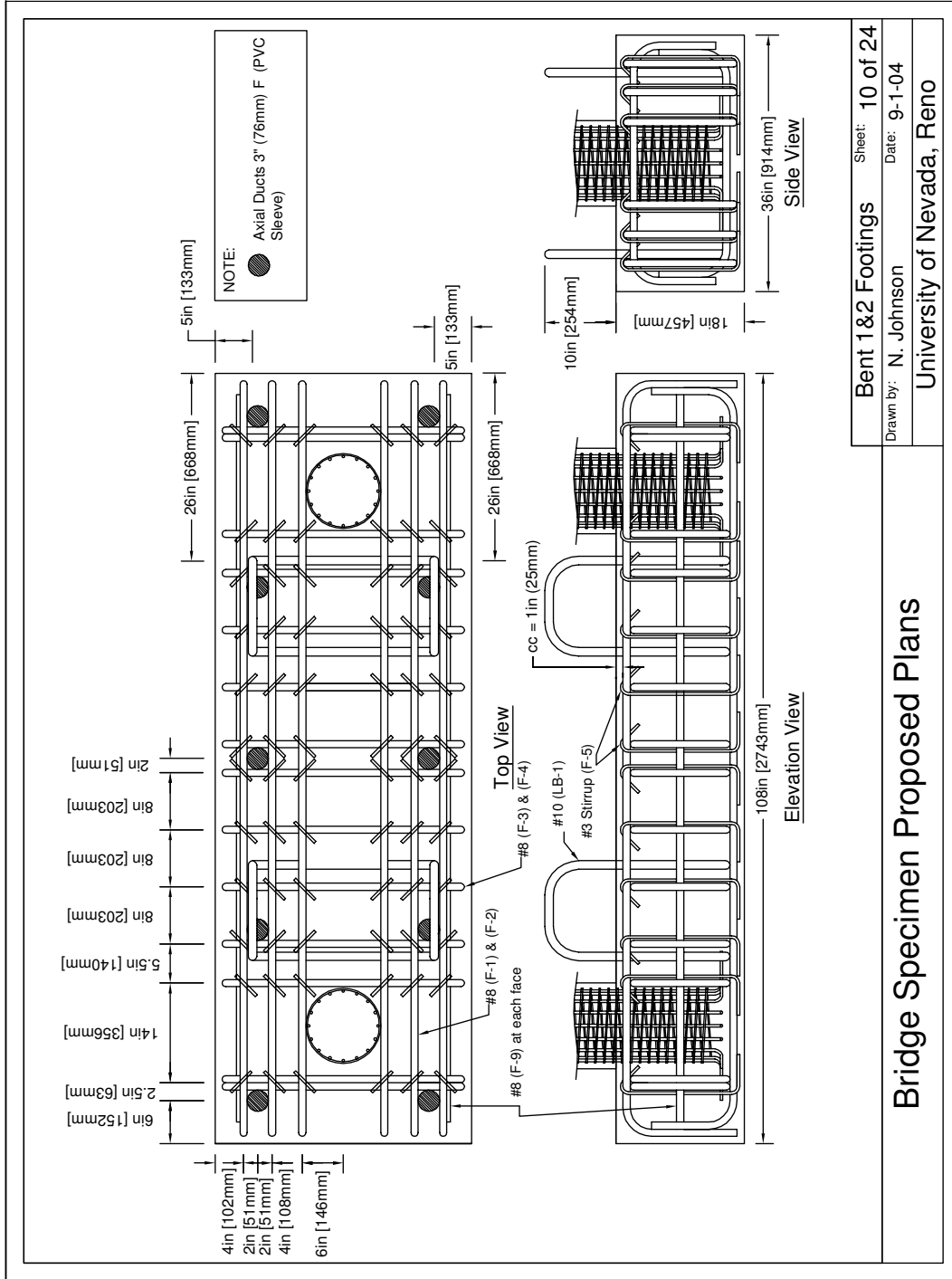
Bent 1&2 Footings	Sheet: 10 of 24
Drawn by: N. Johnson	Date: 9-1-04
University of Nevada, Reno	
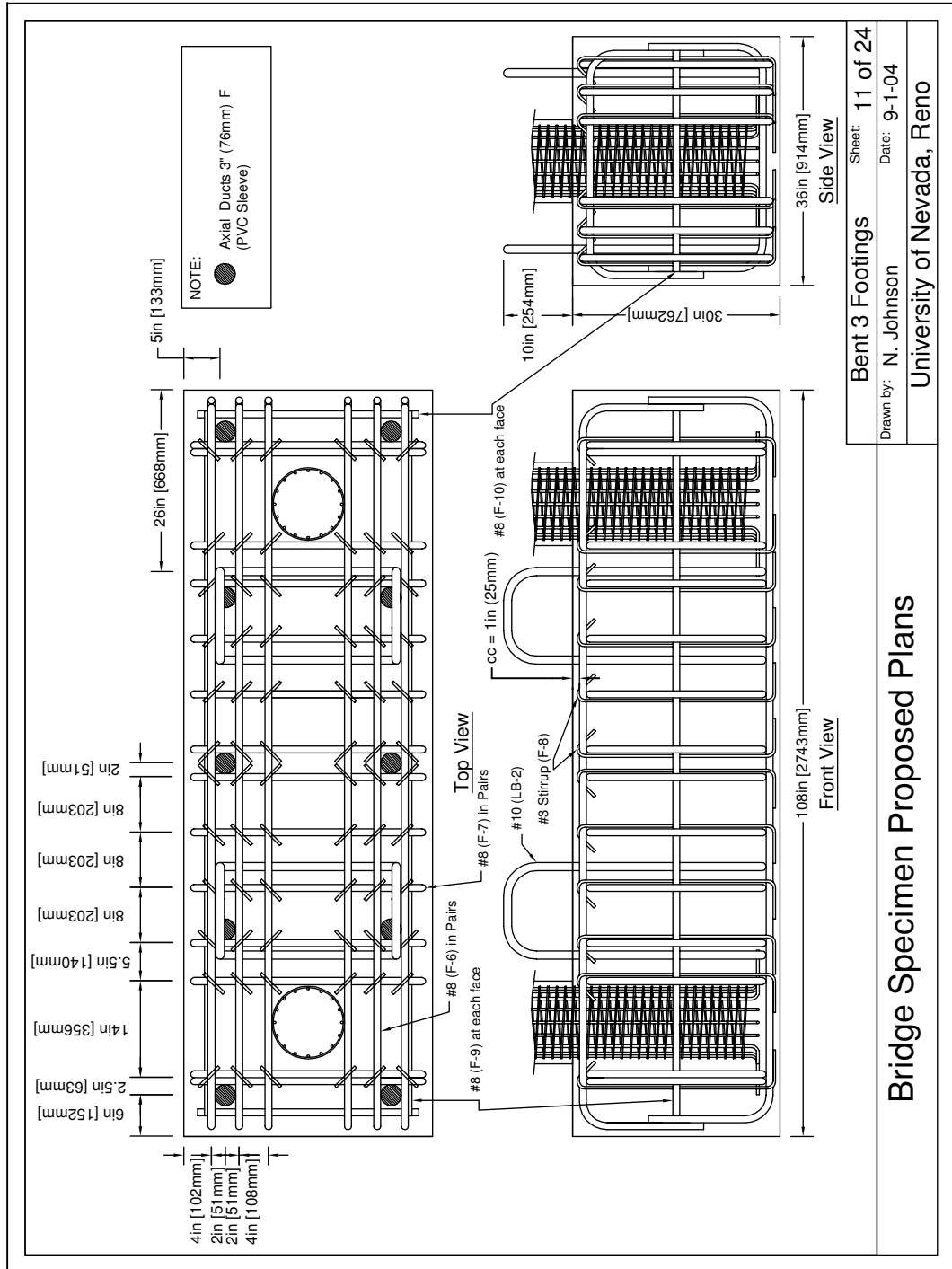
Bridge Specimen Proposed Plans

Bent 3 Footings — Sheet: 11 of 24
Drawn by: N. Johnson — Date: 9-1-04
University of Nevada, Reno

Bridge Specimen Proposed Plans

331in [8.41m]

7.5in [0.19m]

7.5in [0.19m]

Top View

Lifting Hooks
(See Detail Sheet 12)

146in [3.71m]

50.5in [1.28m]

7in [0.18m]

7in [0.18m]

317in [8.05m]

Elevation View

See Beam Bolt
Details (Sheet 18)

7in [0.18m]

See Beam Long.
Steel (Sheet 15)

Elevation View

See Duct Details
(Sheet 16)

See Beam End and
Stirrups (Sheet 15)

30in [0.76m]
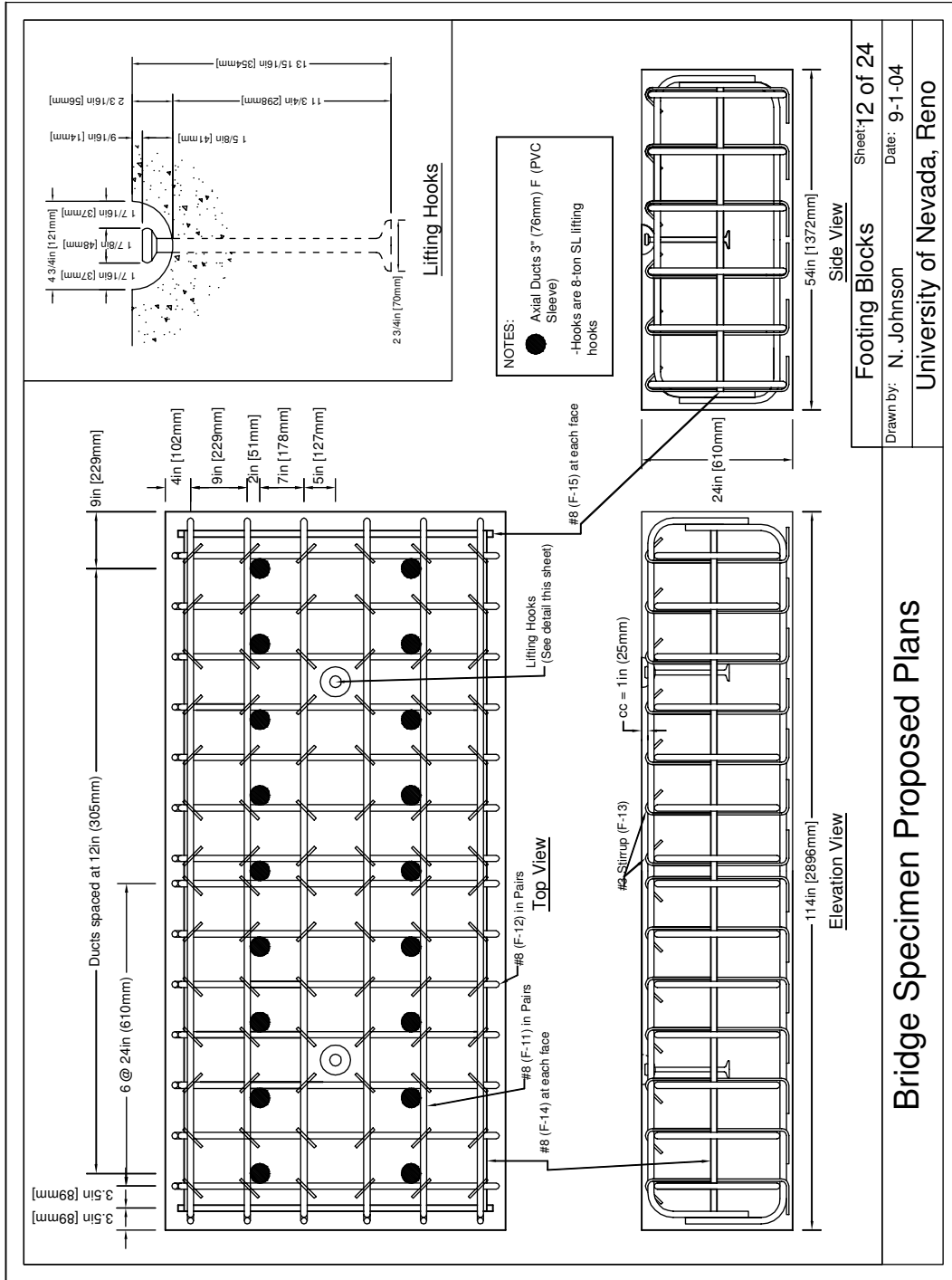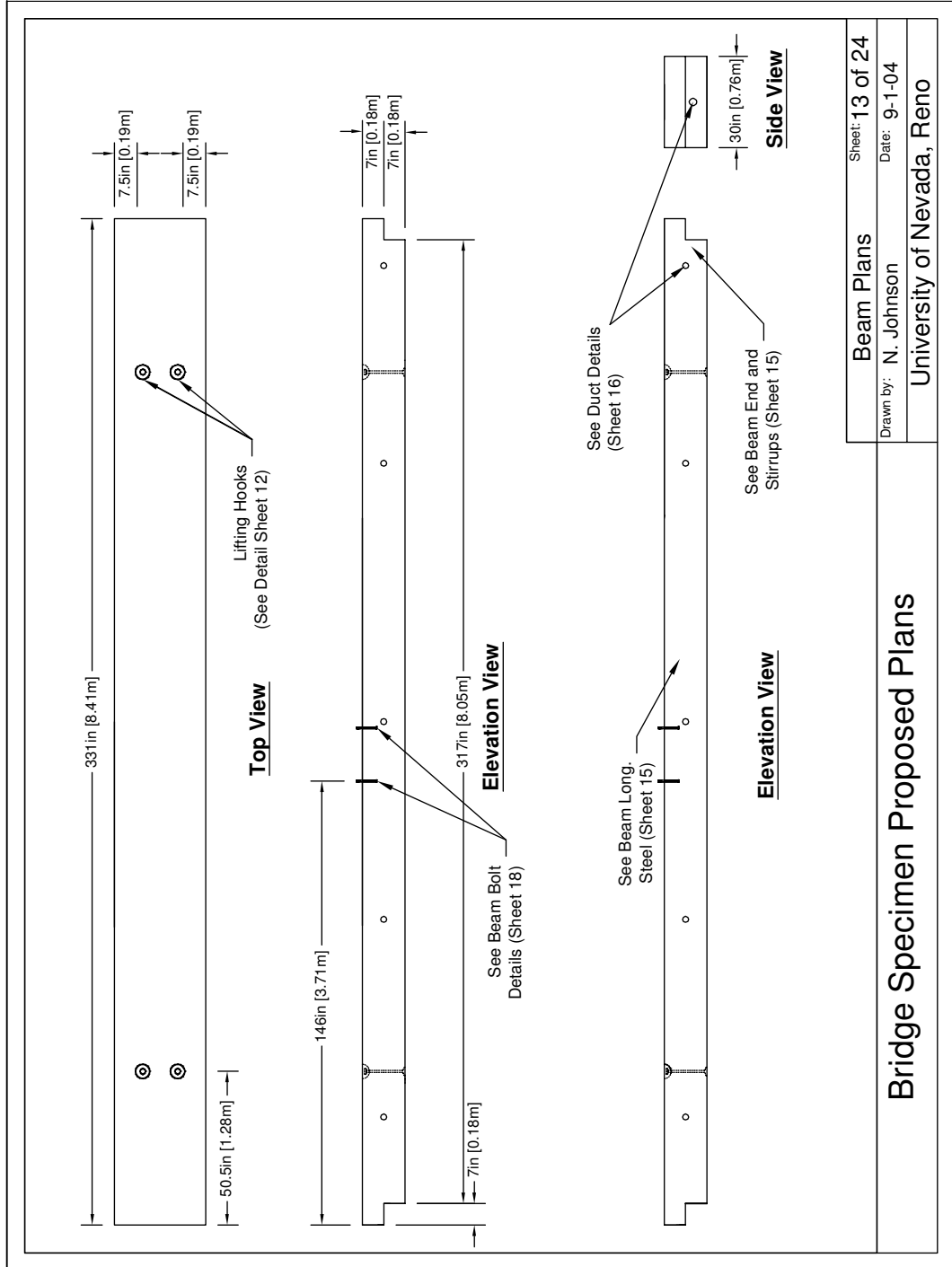
Side View

Bridge Specimen Proposed Plans

Beam Plans

Sheet: 13 of 24

Drawn by: N. Johnson

Date: 9-1-04

University of Nevada, Reno

280

Beam Top Reinforcement (Plan)

Beam Bottom Reinforcement (Plan)

Beam Reinforcement (Elevation)

331in [8m]

151in [4m]

317in [8m]

47in [1m]

36in [1m]

Beam Top Reinf

Beam Bottom Reinf.

Sec. E-E

Sec. D-D

Sec. C-C

6-#6 (B-4)

6-#6 (B-1)

9-#6 (B-2)

#6 (B-2)

6-#6 (B-3)

7.25in [184mm]

Bridge Specimen Proposed Plans
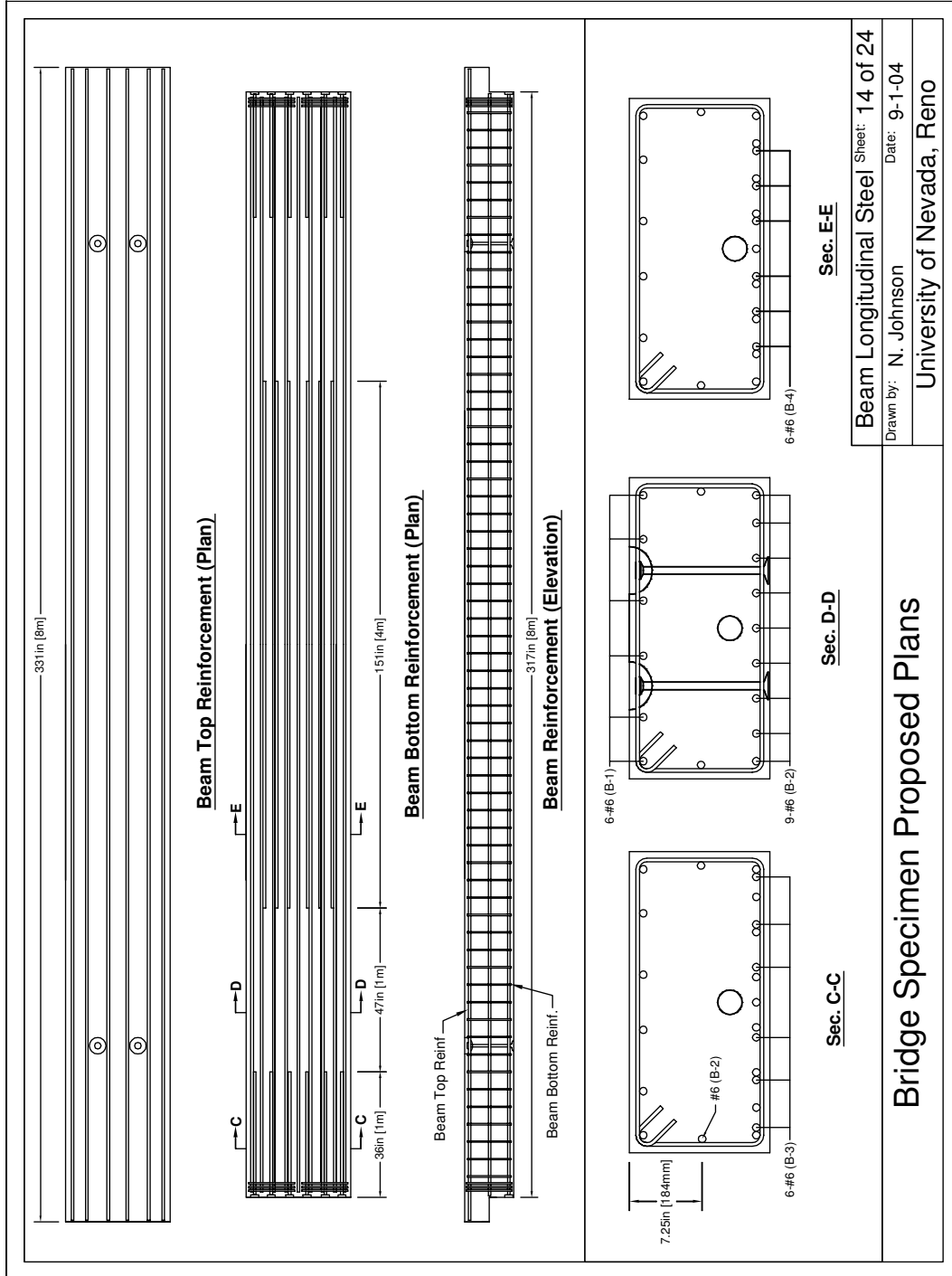
Beam Longitudinal Steel

Sheet: 14 of 24

Drawn by: N. Johnson

Date: 9-1-04

University of Nevada, Reno

#3 (B-8)

#3 (B-9)

Elevation View

#6 (B-7) @ 5in

Elevation View

#3 (B-5) @ 5in

Beam Stirrups

3-#4 (B-6) @ 1.5in

3-#4 (B-6) @ 1.5in

Beam End Stirrups

#3 (B-10)

F-F Side View

Beam End Stirrups

F

Beam Stirrups

F

3in [76mm]
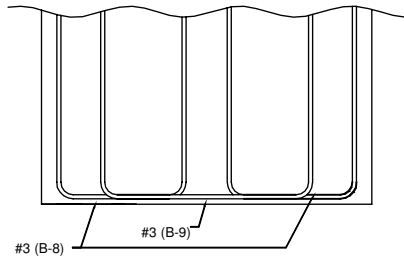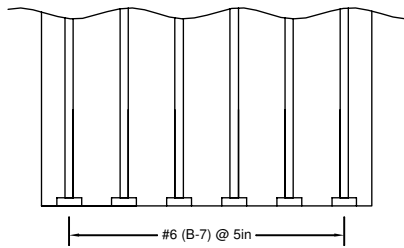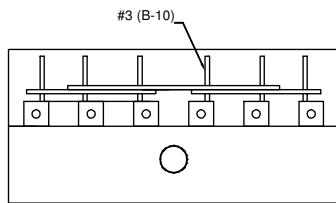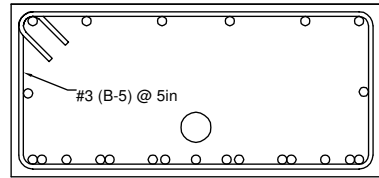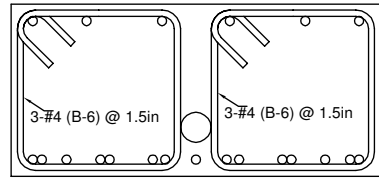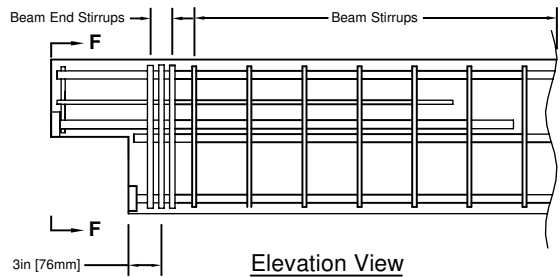
Elevation View

Bridge Specimen Proposed Plans	Beam end & Stirrups	Sheet: 15 of 24
	Drawn by: N. Johnson	Date: 9-1-04
	University of Nevada, Reno	

Plan View

Type 1 Beam

Type 2 Beam

Type 3 Beam

See Cantilever Duct
Details (Sheet 17)

See Beam Duct Details

See Bent 2 Cap Duct
Details (Sheet 17)

Elevation View

Symmetric

2⅟₁₆ in dia.
Post-Tension Ducts

2in dia. PVC Ducts

35.5in [902mm]

65in [1651mm]

65in [1651mm]

65in [1651mm]

These Ducts for
Type 1 Beam Only

These Ducts for Type 3 Beam Only

Beam Duct Details

35.5in [902mm]

15in [381mm]

65in [1651mm]

11in [279mm]

10in [254mm]

28in [711mm]

7.5in [191mm]

36in [914mm]

4.5in [114mm]

36in [914mm]

4in [102mm]

36in [914mm]

7in [178mm]

188in [4775mm]

32in [813mm]

25.5in [648mm] 24in [610mm] 25.5in [648mm] 24in [610mm]

6in [152mm]

6in [152mm]

4in [102mm]

Bridge Specimen Proposed Plans

Duct Details

Sheet:16 of 24

Drawn by: N. Johnson

Date: 9-1-04

University of Nevada, Reno

283

Post Tension NOTES:

-Strand Post-Tensioning System w/ 6-0.6" 270 ksi tendons
-Each Duct Effective Post Tension Force = 230 kip
-Post-Tension Duct Diameter $2\frac{7}{16}$ "
-Anchors Located in Cantilevers

19in [483mm]

30in [762mm]

30in [762mm]

19in [483mm]

Plan View

19in [483mm]

30in [762mm]

30in [762mm]

19in [483mm]

Plan View

8.5in [216mm]

Additional steel to be provided
for anchorage zones

10in [254mm]

10in [254mm]
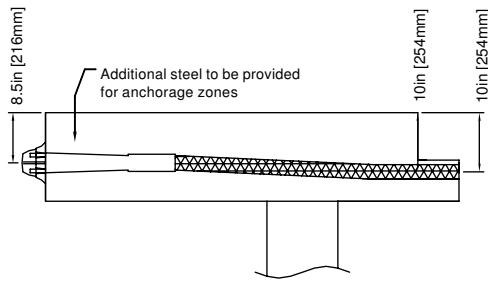
Elevation View

Cantilever Duct Details

3in [76mm]

Elevation View

Bent 2 Cap Duct Details

Bridge Specimen Proposed Plans	Duct Details	Sheet: 17 of 24
	Drawn by: N. Johnson	Date: 9-1-04
	University of Nevada, Reno	

284

NOTES:
- Bolts are A325
- Bolt Length = 6.5 in (203 mm)

2in [51mm]

4.5in [114mm]

Typ. Bolts (Elev.)

Plan View

#3 (C-27)

2in [51mm]

1.375in [35mm]

Elevation View

Bolts w/ Anchor

19in [483mm]

Type 1 Beam Plan View

6.75in [171mm]

16.5in [419mm]

6.75in [171mm]

Type 2 Beam Plan View

11in [279mm]

Type 3 Beam Plan View

17.5in [444mm]

Beam Elevation View

Beam Bolt Details

5.75in [146mm]

54.5in [1384mm]

Plan View

Elevation View

Cantilever Bolt Details

2.75in [70mm]

2.25in [57mm]
10.5in [267mm]
10.5in [267mm]
10.5in [267mm]
10.5in [267mm]
9.5in [241mm]
10.5in [267mm]
10.5in [267mm]
10.5in [267mm]
10.5in [267mm]
2.25in [57mm]

Bridge Specimen Proposed Plans

Bolt Details

Sheet: 18 of 24

Drawn by: N. Johnson

Date: 9-1-04

University of Nevada, Reno

C-8 (#6 bar) Headed Reinforcement

29in [737mm]

C-3 (#4 bar)
14in [356mm]
3in [76mm]
4.5in [114mm]

C-4 (#3 bar)
0.5in [13mm]
3in [76mm]
12in [305mm]

C-5 (#3 bar)
13.75in [349mm]
7.75in [197mm]
3in [76mm]

C-2 (#4 bar)
3in [76mm]
14in [356mm]
12.5in [318mm]

C-7 (#3 bar)
15in [381mm]
20in [508mm]

C-9 (#3 bar)
27in [686mm]
6in [152mm]

C-1 (#4 bar)
3in [76mm]
14in [356mm]
14in [356mm]

C-6 (#3 bar)
10in [254mm]
20in [508mm]

Bridge Specimen Proposed Plans

Steel Details 1	Sheet: 19 of 24
Drawn by: N. Johnson	Date: 9-1-04
University of Nevada, Reno	

286

C-14 (#6 bar) Headed Reinf. — 43in [1092mm]

C-15 (#3 bar) — 36in [914mm], 15in [381mm]

C-16 (#3 bar) — 36in [914mm], 10in [254mm]

C-17 (#3 bar) — 5.75in [146mm]

C-19 (#6 bar) — 12in [305mm], 62.5in [1588mm]

C-10 (#6 bar) — 97in [2464mm], 12in [305mm]

C-11 (#6 bar) — 79.75in [2026mm], 10.02in [254mm]

C-12 (#3 bar) — 97in [2464mm]

C-13 (#4 bar) — 97in [2464mm]

C-18 (#6 bar) — 68.25in [1734mm], 8.75in [222mm]

Bridge Specimen Proposed Plans

Steel Details 2

Drawn by: N. Johnson

Sheet: 20 of 24

Date: 9-1-04

University of Nevada, Reno

C-23 (#3 bar)

5.75in [146mm]

101.5in [2578mm]

13in [330mm]

13.25in [337mm]

3in [76mm]

C-26 (#4 bar)

7.25in [184mm]

2.25in [57mm]

C-27 (#3 bar)

22.5in [571mm]

13.25in [337mm]

3in [76mm]

C-20 (#4 bar)

125.5in [3188mm]

C-24 (#3 bar)

33in [838mm]

13.25in [337mm]

3in [76mm]

C-21 (#4 bar)

3in [76mm]

C-25 (#3 bar)

38in [965mm]

13.25in [337mm]

3in [76mm]

C-22 (#4 bar)

5.75in [146mm]

Bridge Specimen Proposed Plans
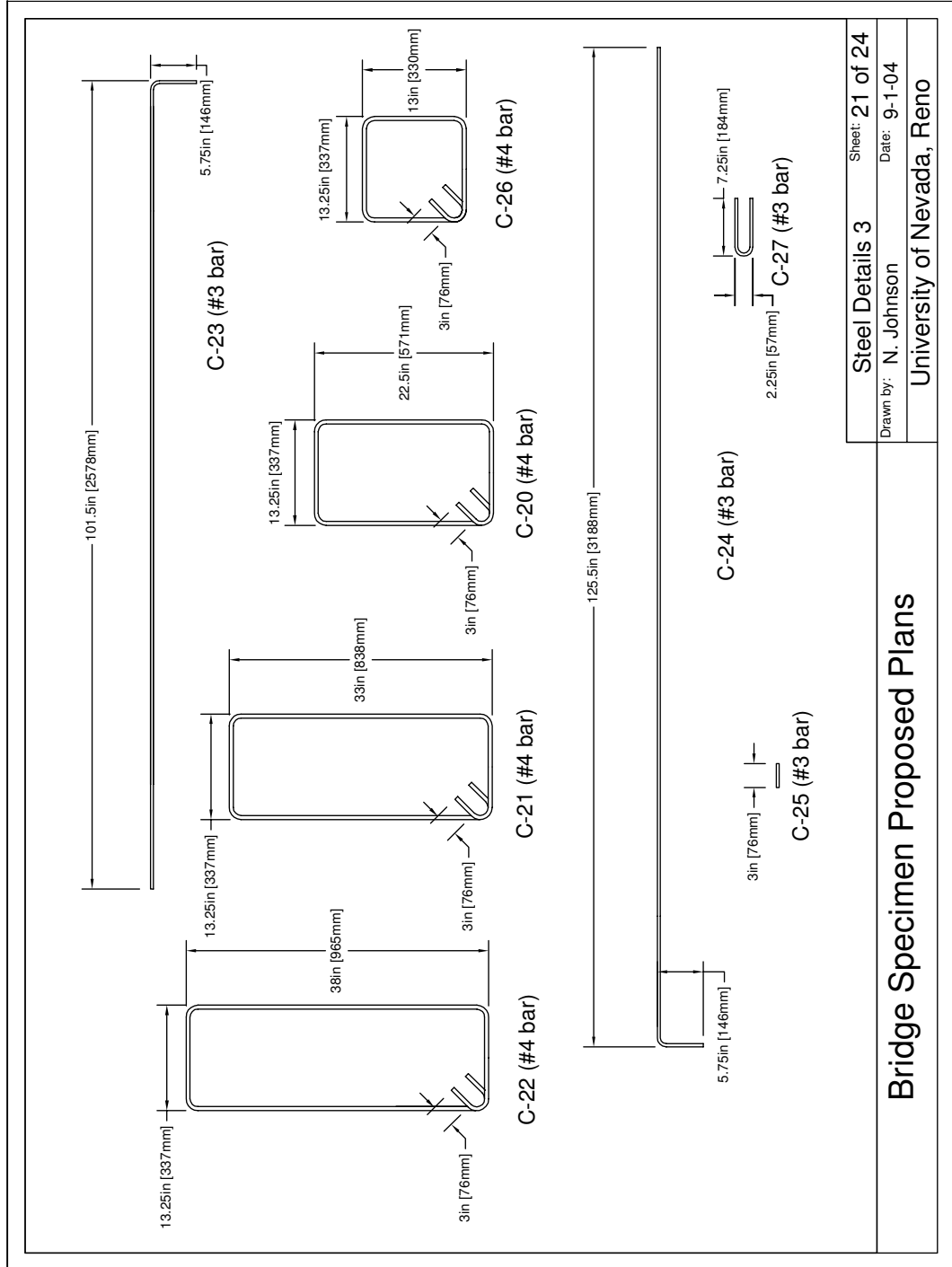
Steel Details 3

Sheet: 21 of 24

Drawn by: N. Johnson   Date: 9-1-04

University of Nevada, Reno

288

Bridge Specimen Proposed Plans

Steel Details 4

Drawn by: N. Johnson

University of Nevada, Reno

Sheet: 22 of 24

Date: 9-1-04

Bridge Specimen Proposed Plans

Steel Details 5

Drawn by: N. Johnson

University of Nevada, Reno

Sheet: 23 of 24

Date: 9-1-04

F-4 (#8 bar)

32in [813mm]

10in [254mm]

F-3 (#8 bar)

34in [864mm]

12in [305mm]

F-5 (#3 bar)

3in [76mm]

16.75in [425mm]

4.25in [108mm]

LB-2 (#10 bar)

Side

20in [508mm]

Front

14in [356mm]

38in [965mm]

LB-1 (#10 bar)

Front

Side

20in [508mm]

14in [356mm]

26in [660mm]

F-1 (#8 bar)

106in [2692mm]

16in [406mm]

F-2 (#8 bar)

104in [2642mm]

12in [305mm]

F-6 (#8 bar)

105in [2667mm]

16in [406mm]

F-8 (#3 bar)

3in [76mm]

28.75in [730mm]

4.25in [108mm]

F-7 (#8 bar)

33in [838mm]

17in [432mm]

290

F-10 (#8 bar)
32in [813mm]

F-9 (#8 bar)
102in [2591mm]

F-11 (#8 bar)
111in [2819mm]
16in [406mm]

F-13 (#3 bar)
3in [76mm]
22.75in [578mm]
4.25in [108mm]

F-12 (#8 bar)
51in [1295mm]
16in [406mm]

F-15 (#8 bar)
48.25in [1226mm]

F-14 (#8 bar)
108in [2743mm]
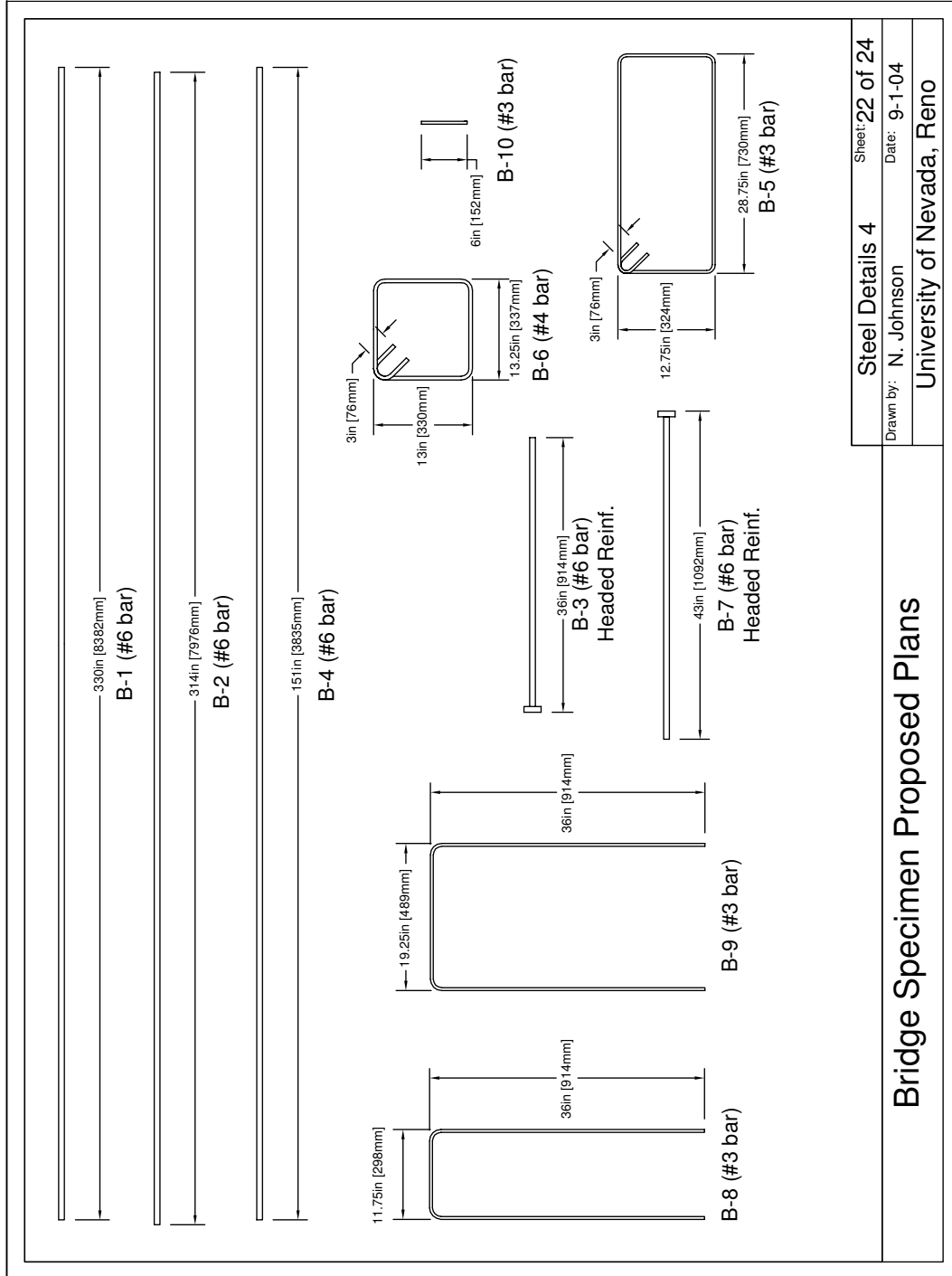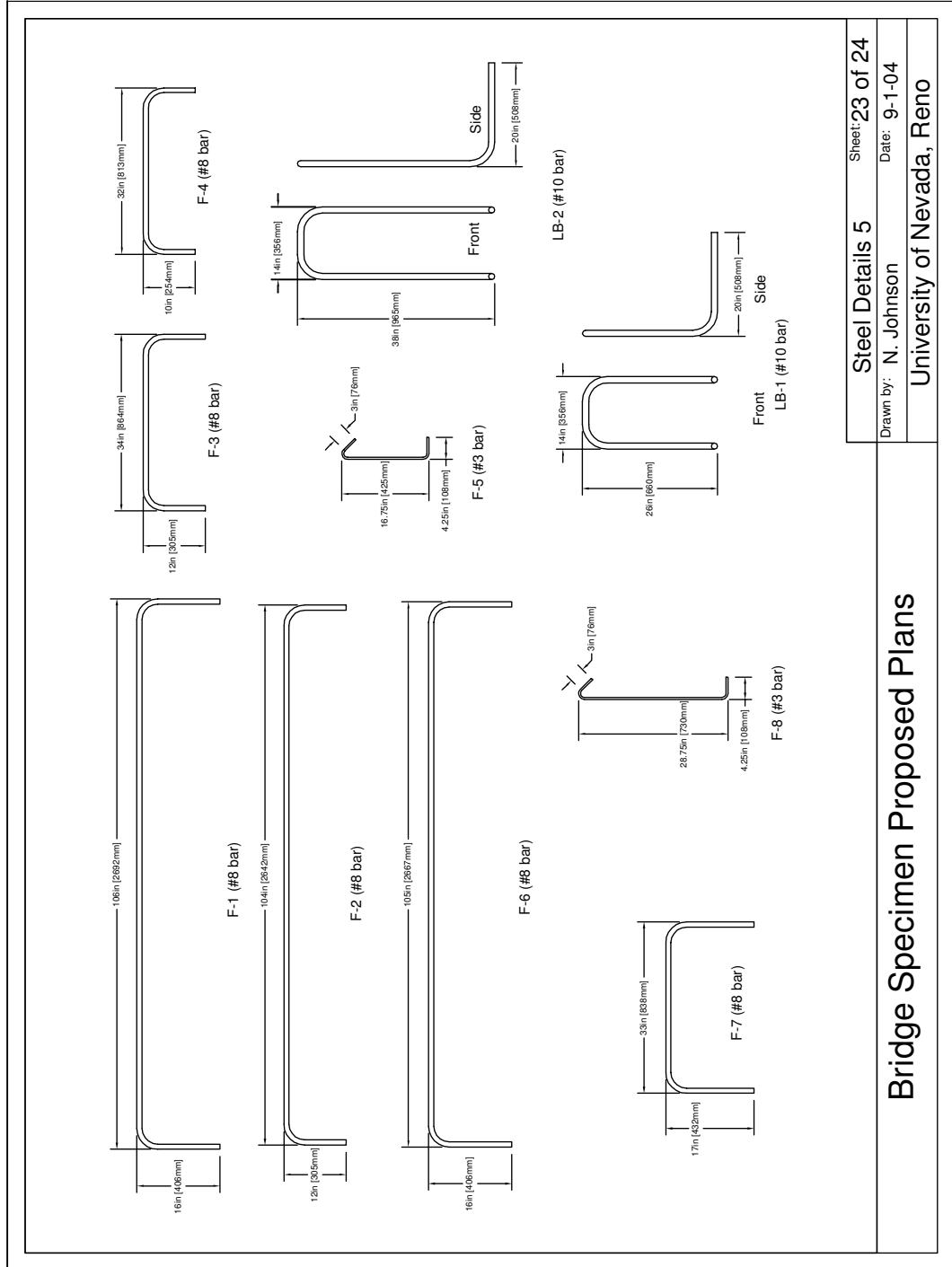
Bridge Specimen Proposed Plans
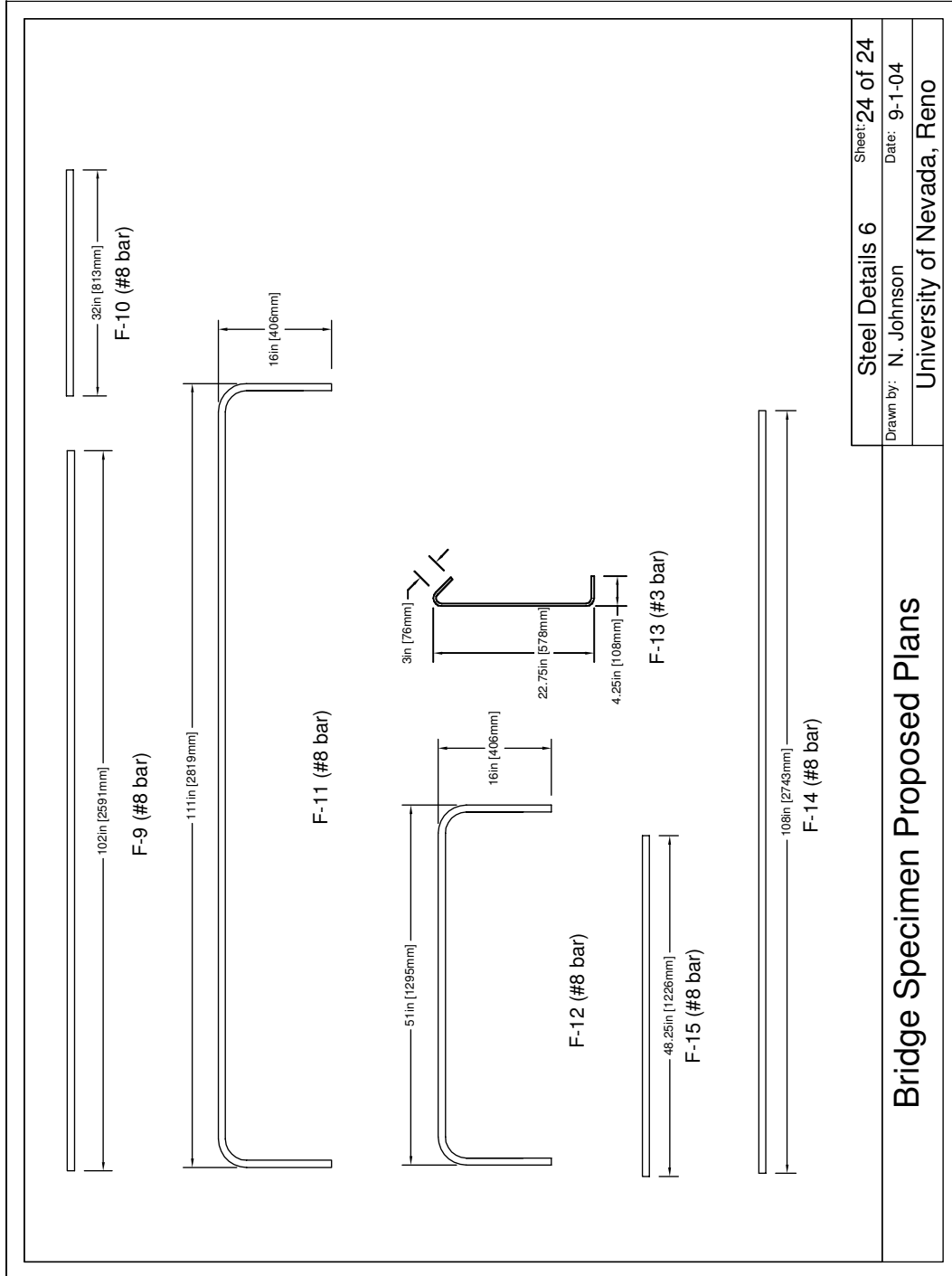
Steel Details 6   Sheet: 24 of 24
Drawn by: N. Johnson   Date: 9-1-04
University of Nevada, Reno

Appendix C

INSTRUMENTATION PLANS

The instrumentation plans were created by Johnson et al. (2006) at the University of Nevada, Reno.

292

Bent 1

Side View

W◄──►E

Elevation View

East: 1ETR1 — 1ETR2
West: 1WTR1 — 1WTR2

1WTR3 — 1WTR4 1ETR3 — 1ETR4
1WTR5 — 1WTR6 1ETR5 — 1ETR6

East: 1EBR1 — 1EBR2
West: 1WBR1 — 1WBR2

1WBR3 — 1WBR4 1EBR3 — 1EBR4
1WBR5 — 1WBR6 1EBR5 — 1EBR6

Bent 2

Side View

W◄──►E

Elevation View

East: 2ETR1 — 2ETR2

2WTR1 — 2WTR2 2ETR3 — 2ETR4
2WTR3 — 2WTR4 2ETR5 — 2ETR6

East: 2EBR1 — 2EBR2

2WBR1 — 2WBR2 2EBR3 — 2EBR4
2WBR3 — 2WBR4 2EBR5 — 2EBR6

Bent 3

Side View

W◄──►E

Elevation View

East: 3ETR1 — 3ETR2
West: 3WTR1 — 3WTR2

3WTR3 — 3WTR4 3ETR3 — 3ETR4
3WTR5 — 3WTR6 3ETR5 — 3ETR6

East: 3EBR1 — 3EBR2
West: 3WBR1 — 3WBR2

3WBR3 — 3WBR4 3EBR3 — 3EBR4
3WBR5 — 3WBR6 3EBR5 — 3EBR6

DT6 — DT7

DT8 — DT9

Top of Column Dimensions (Typ.)

5in [127mm]   5in [127mm]
7in [178mm]   7in [178mm]
3.5in [89mm] 3.5in [89mm]

Bottom of Column Dimensions (Typ.)

3.5in [89mm] 3.5in [89mm]
7in [178mm]   7in [178mm]
5in [127mm]   5in [127mm]

NOTES:

✕ = out of plane measurement location

Notation Examples:

1 (Bent 1)
W (West Column)
T (Top of Column)
R (Rotation Measurement)
1 (Gauge 1)

D (Displacement)
T (Transverse)
1 (Gauge 1)

Bridge Specimen Instrumentation Plans	Column Curvature	Sheet: 1 of 8
	Drawn by: N. Johnson	Date: 2-28-05
	University of Nevada, Reno	

Bent 1 Elevation View

W ←→ E

6in [152mm]
6in [152mm]
6in [152mm]
6in [152mm]
6in [152mm]
6in [152mm]
6in [152mm]
6in [152mm]

Notation
Example:

1 (Bent 1)
W (West Column)
T (Top of Column)
S (Strain Measurement)
L (Longitudinal Bar)
1 (Gauge Number)

Bridge Specimen Instrumentation Plans

Bent 1 Long. Strain	Sheet: 2 of 8
Drawn by: N. Johnson	Date: 2-28-05
University of Nevada, Reno	

294

Bent 2 Long. Strain

Drawn by: N. Johnson   Date: 2-28-05

University of Nevada, Reno

Bent 2 Elevation View

Bridge Specimen Instrumentation Plans

W ← → E
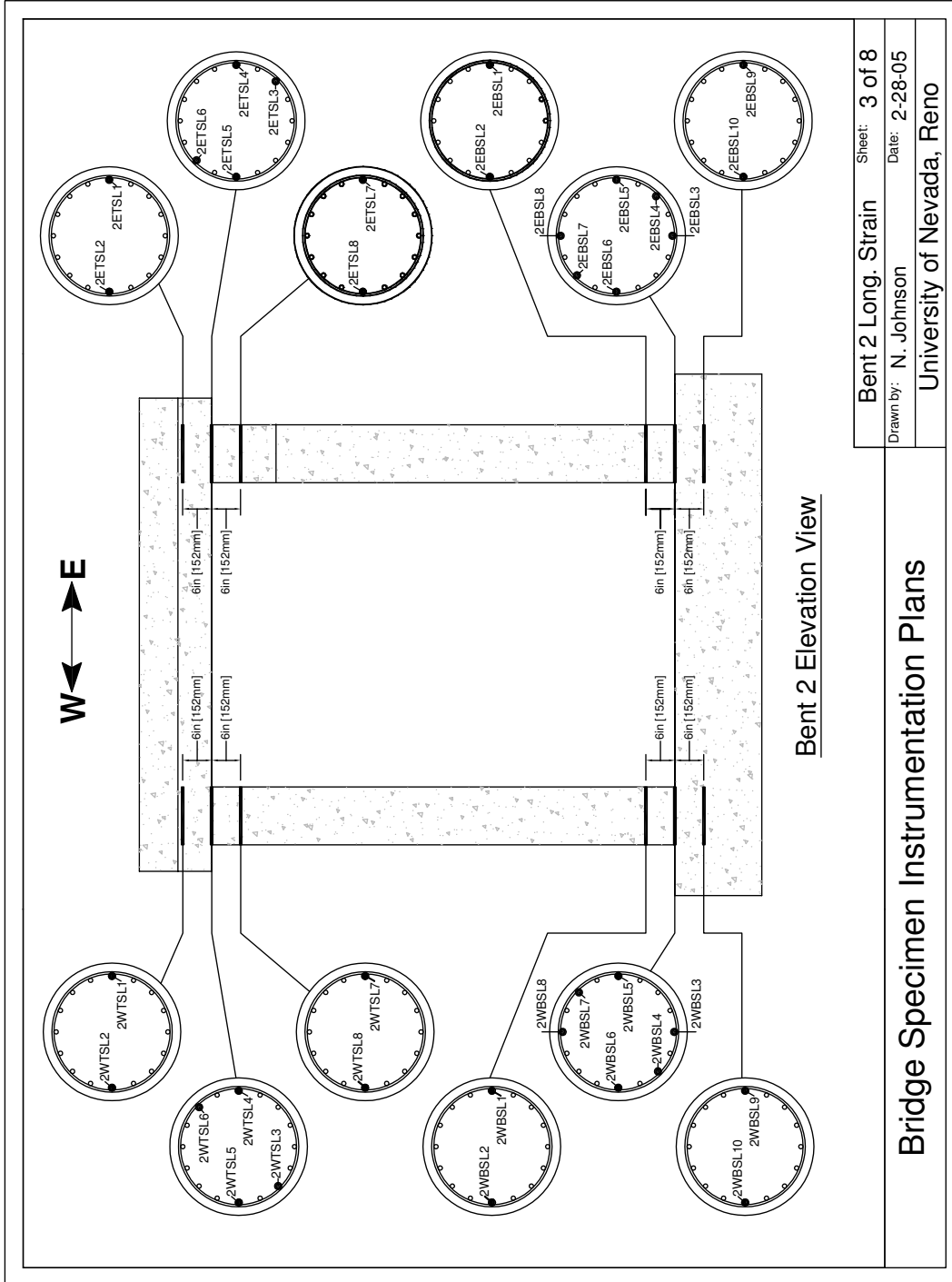
Bent 3 Elevation View

Bridge Specimen Instrumentation Plans
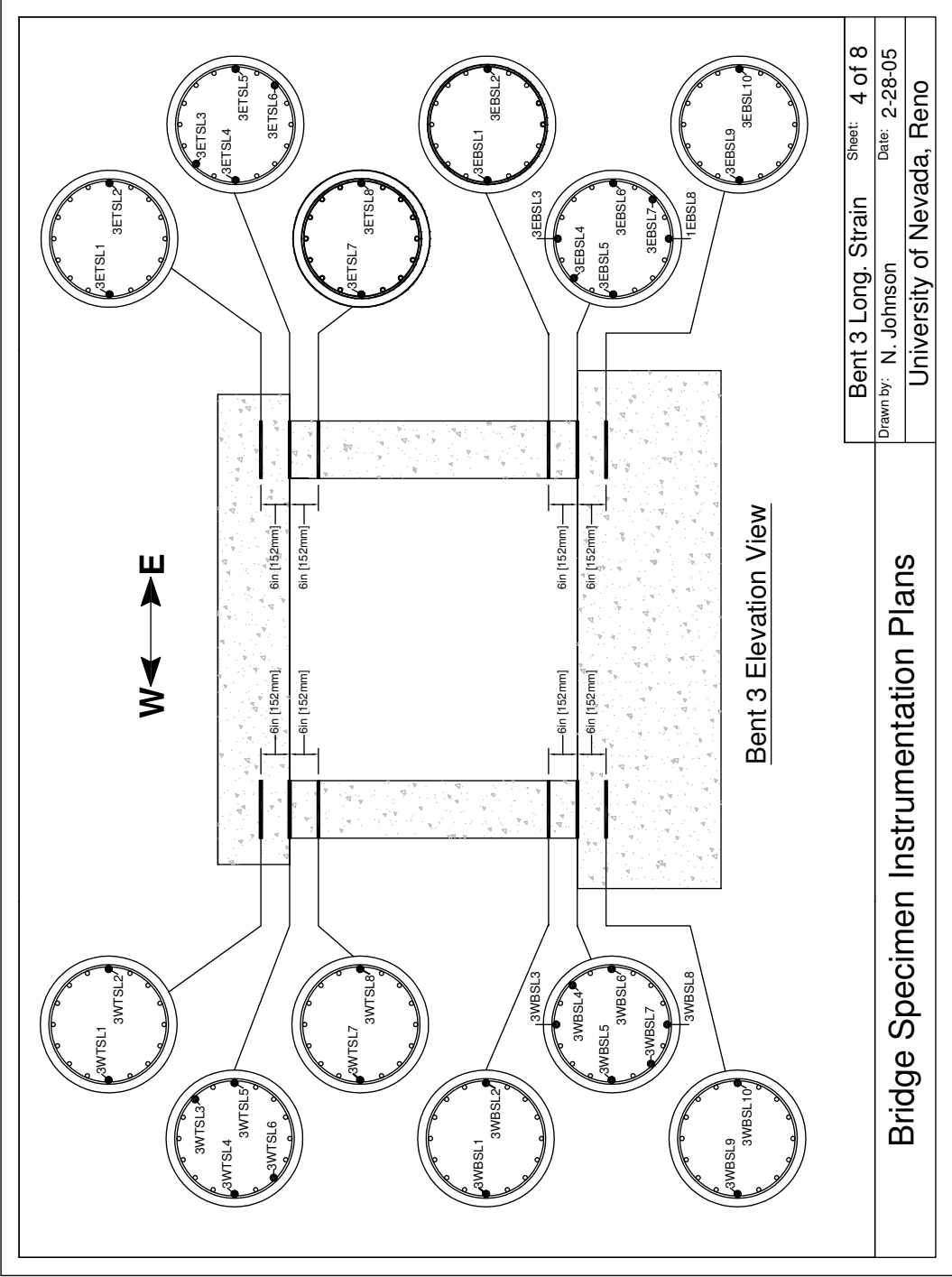
Bent 3 Long. Strain	Sheet: 4 of 8
Drawn by: N. Johnson	Date: 2-28-05
University of Nevada, Reno	

296

Bent 1 Elevation View

Bent 2 Elevation View

Bridge Specimen Instrumentation Plans	Bents 1&2 Trans. Strain	Sheet: 5 of 8
	Drawn by: N. Johnson	Date: 2-28-05
	University of Nevada, Reno	

W◄──►E

3WTSH1

3WTSH4
3WTSH2

3WTSH3

3WTSH5

3WTSH6

3WTSH7

3ETSH1

3ETSH3 3ETSH2

3ETSH4

3ETSH5

3ETSH6

3ETSH7

4in [102mm]
4in [102mm]
4in [102mm]

4in [102mm]
4in [102mm]
4in [102mm]

Bent 3 Elevation View

3WBSH1

3WBSH2

3WBSH4

3WBSH7
3WBSH5

3WBSH3

3WBSH6

3EBSH4

3EBSH2

3EBSH5
3EBSH7

3EBSH6

3EBSH3

3EBSH1

E◄──►W

Notation
Example:

1 (Bent 3)
E (East Column)
T (Top of Column)
V (Shear Measurement)
1 (Gauge 1)

15in [381mm]

15in [381mm]

15in [381mm]

15in [381mm]

3ETV1
3ETV2
3ETV3
3ETV4
3ETV5
3ETV6
3ETV7
3ETV8
3EBV1
3EBV2
3EBV3
3EBV4
3EBV5
3EBV6
3EBV7

Bent 3 Elevation View

Bridge Specimen Instrumentation Plans

Bent 3 Trans. Strain & Shear	Sheet: 6 of 8
Drawn by: N. Johnson	Date: 2-28-05
University of Nevada, Reno	

298

Bridge Specimen Instrumentation Plans

Top View

Elevation View

DL3 (N-S)
DL4 (N-S)
DT5 (E-W)
DT4 (E-W)
DT3 (E-W)
DT2 (E-W)
DT1 (E-W)
DL1 (N-S)
DL2 (N-S)

N
E W
S

DV13 (U-D) (east side)
DV14 (U-D)
DV15 (U-D)
DV16 (U-D) (west side)
DL3 (N-S)
DL4 (N-S)
Bent 3

DV11 (U-D) (east side)
DV12 (U-D) (west side)

DV7 (U-D) (east side)
DV8 (U-D)
DV9 (U-D)
DV10 (U-D) (west side)
Bent 2

DV5 (U-D) (east side)
DV6 (U-D) (west side)

DV1 (U-D) (east side)
DV2 (U-D)
DV3 (U-D)
DV4 (U-D) (west side)
DL1 (N-S)
DL2 (N-S)
Bent 1

U
D

Notation
Example:

D (Displacement)
L (Longitudinal)
1 (Gauge 1)

NOTES:

= Out of Plane Measurement (not labeled)

= Displacement Transducer Measurement
  Direction (labeled)

Displacement	Sheet: 7 of 8
Drawn by: N. Johnson	Date: 2-28-05
University of Nevada, Reno	

Bridge Specimen Instrumentation Plans

Appendix D

MEASURED RESPONSE FIGURES

This appendix presents auxiliary figures from Chapter 4 of characteristics of the measured response of the shaking table specimen.
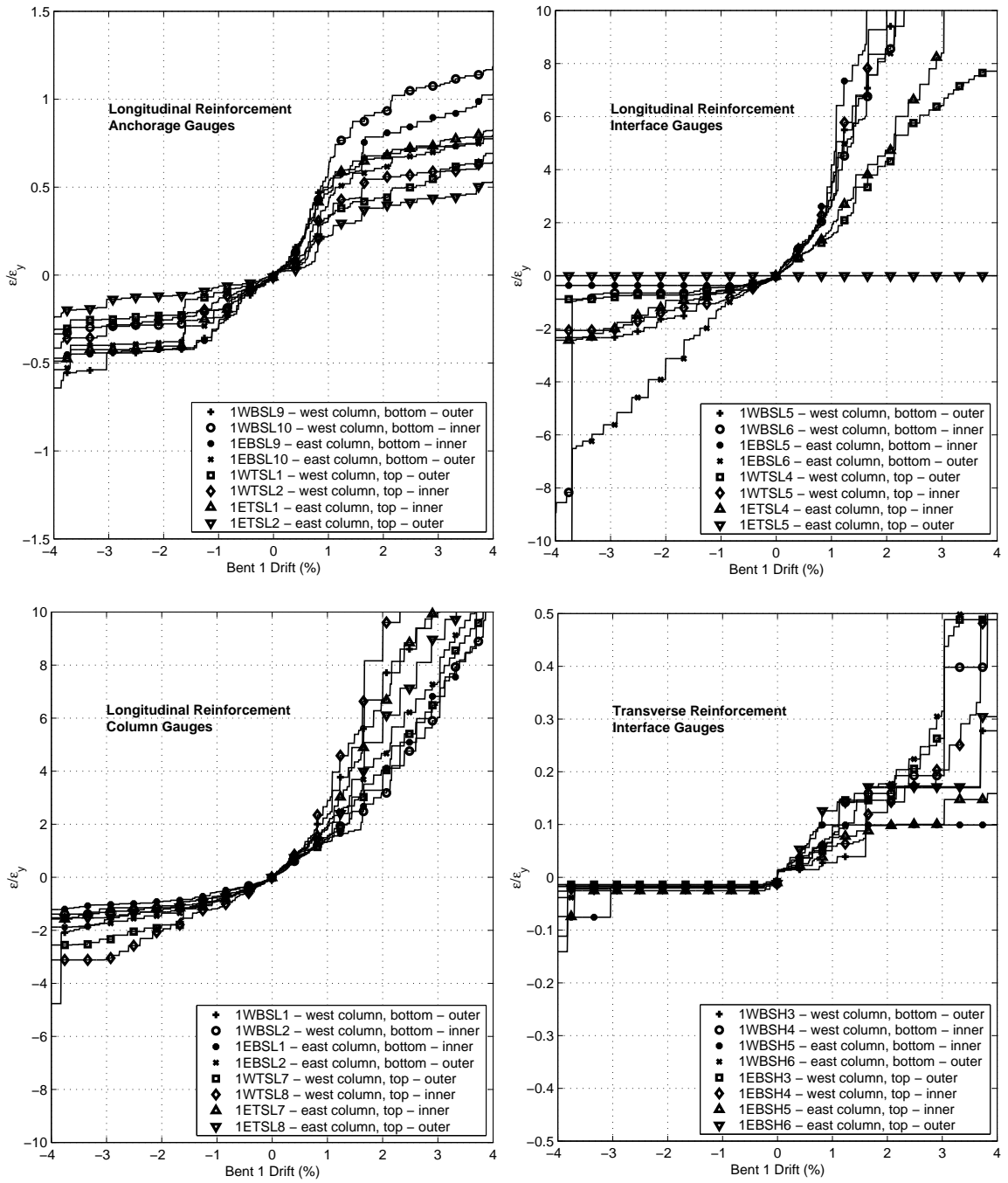
Figure D.1: Displacement-strain envelopes for bent 1: (a) longitudinal anchorage gauges, (b) longitudinal interface gauges, (c) longitudinal column gauges, and (d) transverse anchorage gauges
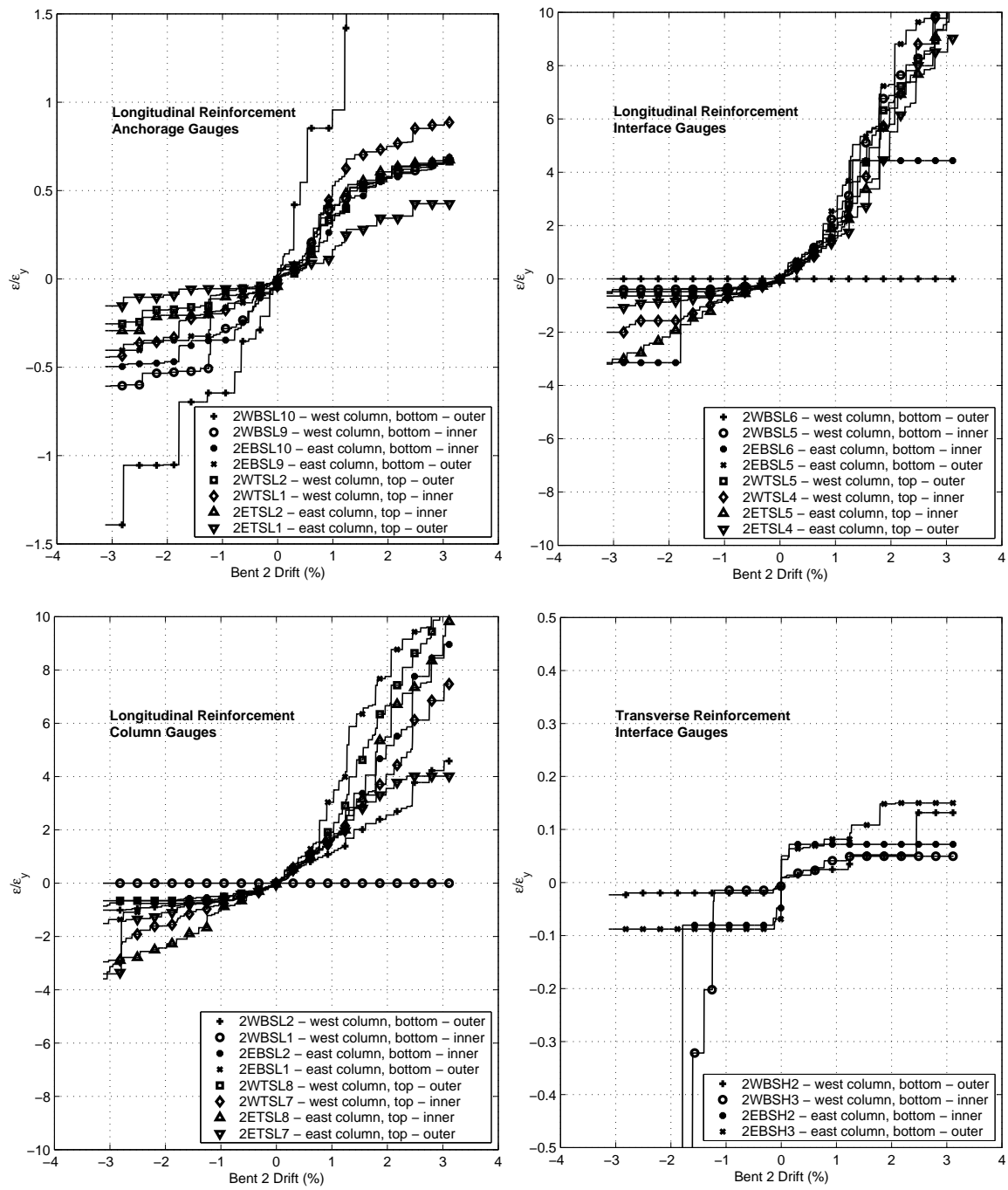
Figure D.2: Displacement-strain envelopes for bent 2: (a) longitudinal anchorage gauges, (b) longitudinal interface gauges, (c) longitudinal column gauges, and (d) transverse anchorage gauges
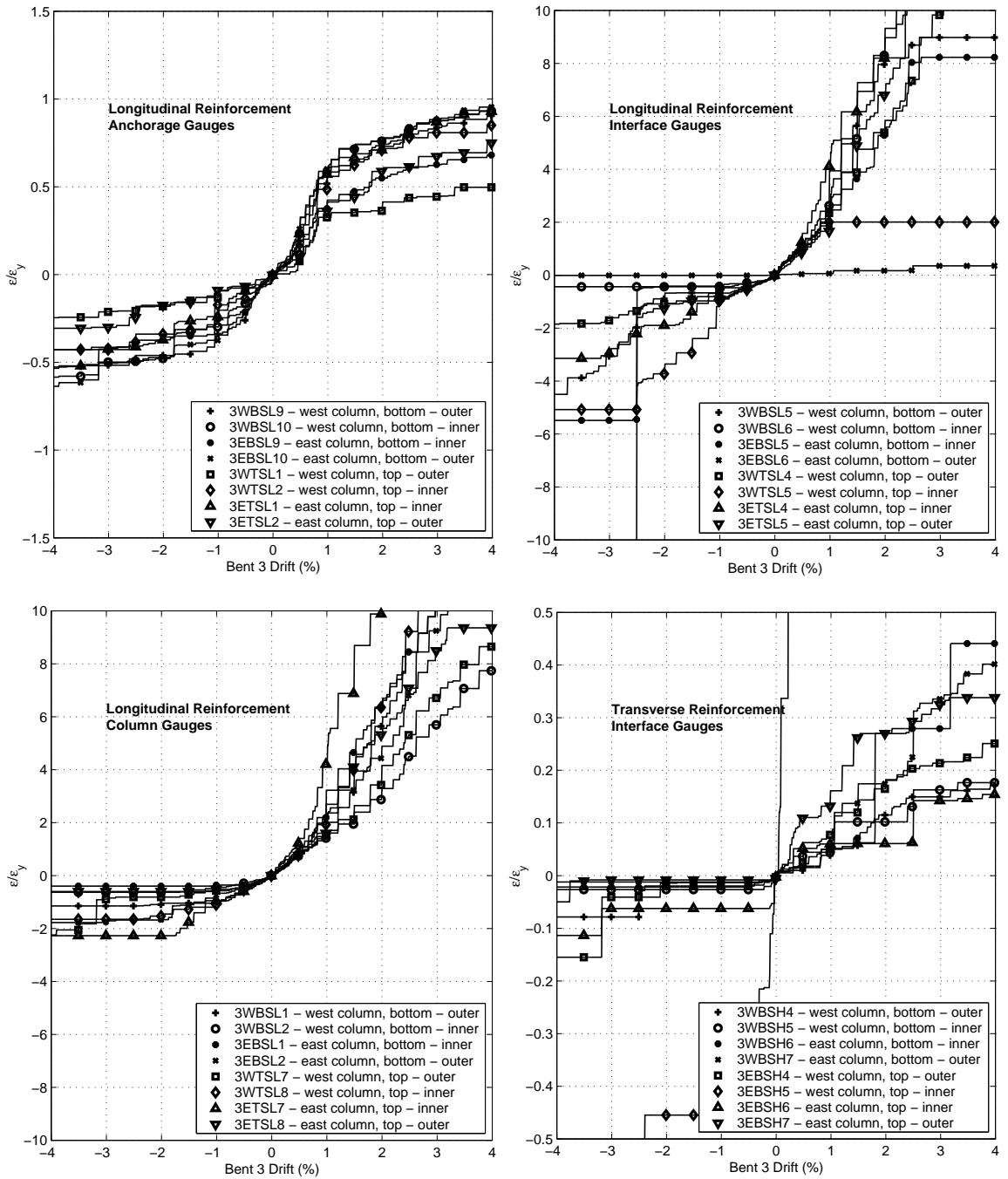
Figure D.3: Displacement-strain envelopes for bent 3: (a) longitudinal anchorage gauges, (b) longitudinal interface gauges, (c) longitudinal column gauges, and (d) transverse anchorage gauges
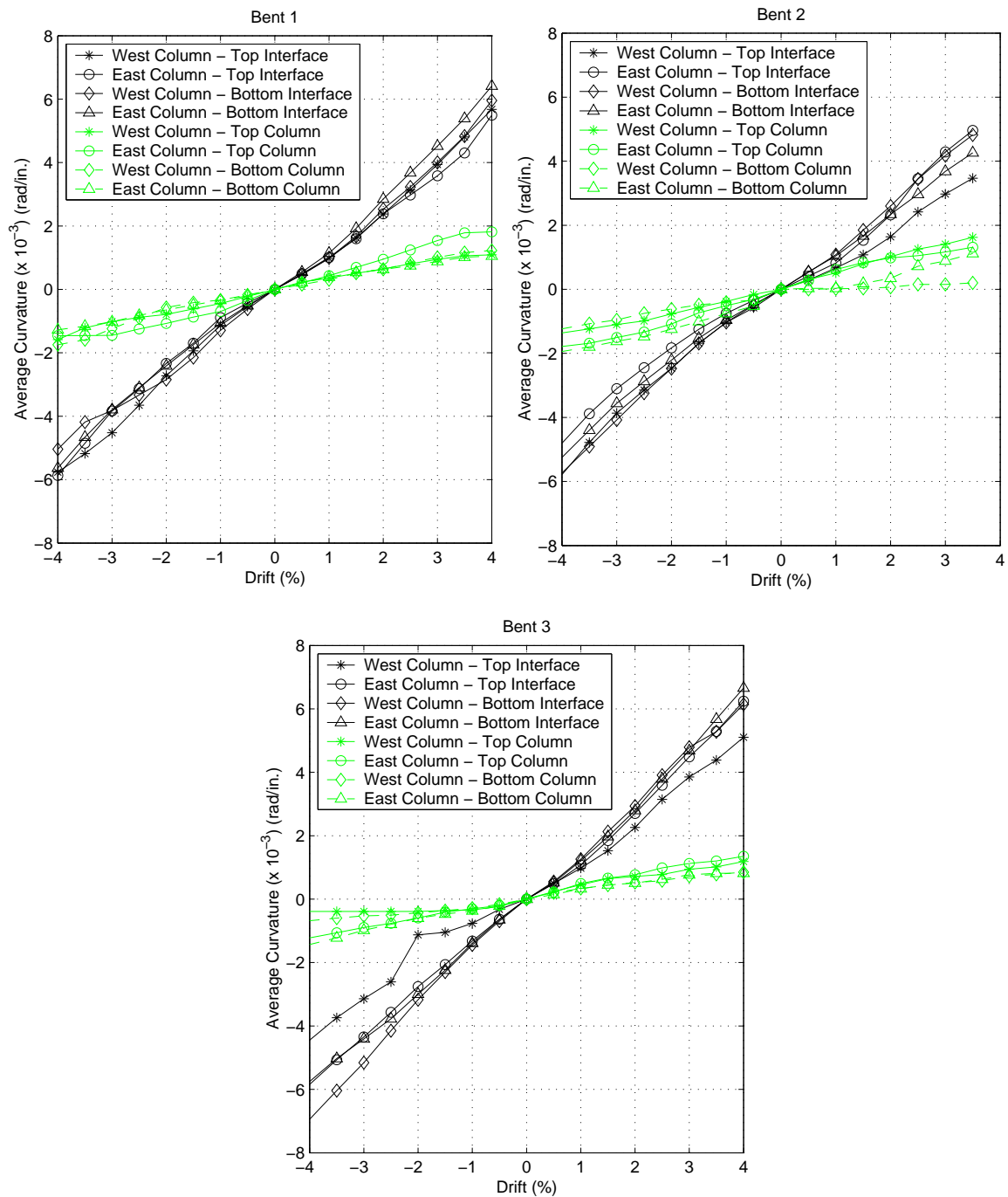
Figure D.4: Displacement-rotation envelopes for the first 7 inches and the next 5 inches of column for bents 1, 2, and 3

Appendix E

DAMAGE OBSERVATIONS

The columns were inspected for damage after each test. Because the columns were essentially fixed-fixed, each column had four main locations to inspect for damage; the east and west faces at the top and bottom of each column. The tables below present the damage that was found at each of these locations for each of the high-amplitude tests.

Table E.1: Recorded damage observation abbreviations

Damage Abbrev.	Description
CR(#, size)	Column residual cracking (the crack number refers to the nth crack from the column-anchorage interface, which may be due to the spalling of previous cracks, size = maximum crack width in mm)
FL	Flaking of cover concrete
SP(height)	Column spalling at the column-anchorage interface (height of spalling in mm)
TE(#)	Exposure of the transverse reinforcement (number of bars)
LE(#)	Exposure of the longitudinal reinforcement (number of bars)
iLB(#)	Incipient buckling of the longitudinal reinforcement (This accounts for bars that are separated from the concrete, but do not appear buckled at the end of the test. These bars may have buckled during the tests)
LB(#)	Buckling of longitudinal reinforcement (number of bars)
TF(#)	Fracture of transverse reinforcement (number of bars)
LF(#)	Fracture of longitudinal reinforcement (number of bars)
CD	Core degradation

Table E.2: Observed damage for the east column on bent 1

Test	East		West	
	Top	**Bottom**	**Top**	**Bottom**
12	—	—	—	—
13	CR(1,neg)	—	—	—
14	CR(1,0.08)	CR(1,neg)	CR(1,neg)	CR(1,neg)
15	CR(1,0.17), FL	CR(1,0.17)	CR(1,0.25), FL	CR(1,0.17)
16	CR(1,0.25), SP(75)	CR(1,0.33), FL	CR(1,0.33), SP(125)	CR(1,0.33), FL
17	CR(1,0.25), SP(90)	CR(1,0.33), SP(63)	CR(1,0.33), SP(150), TE(2)	CR(1,0.33), SP(50)
18	CR(1,0.25), SP(90)	CR(1,0.33), SP(114), TE(2)	CR(1,0.33), SP(150), TE(2)	CR(1,0.33), SP(90)
19	CR(2,0.75), SP(90)	CR(2,0.33), SP(140), TE(3)	CR(1,0.33), SP(150), TE(3), LE(1)	CR(1,0.33), SP(90)
20	CR(2,0.75), SP(90)	CR(2,0.33), SP(140), TE(3)	CR(1,0.33), SP(150), TE(3), LE(1)	CR(1,0.33), SP(90)
21	CR(2,0.75), SP(90)	CR(2,0.33), SP(140), TE(3)	CR(1,0.33), SP(150), TE(3), LE(1)	CR(1,0.33), SP(90)
22	CR(2,0.75), SP(90)	CR(2,0.33), SP(140), TE(3), LE(2)	CR(1,0.33), SP(150), TE(3), LE(2), iLB(1)	CR(1,0.33), SP(90)

Table E.3: Observed damage for the west column on bent 1

Test	East		West	
	Top	**Bottom**	**Top**	**Bottom**
12	—	—	—	—
13	—	—	CR(1,neg)	—
14	—	—	CR(1,neg)	—
15	CR(1,0.17), FL	CR(1,0.17)	CR(1,0.25)	CR(1,0.17)
16	CR(1,0.50), SP(100)	CR(1,0.33), FL	CR(1,0.25), SP(75)	CR(1,0.50), FL
17	CR(1,0.50), SP(100)	CR(1,0.50), FL	CR(1,0.33), SP(75)	CR(1,0.50), FL
18	CR(1,0.50), SP(100)	CR(2,0.17), SP(65)	CR(1,0.50), SP(75)	CR(1,0.50), SP(100), TE(1)
19	CR(2,0.50), SP(130), TE(2)	CR(2,0.75), SP(90)	CR(2,0.50), SP(115)	CR(2,0.50), SP(100), TE(1)
20	CR(2,0.50), SP(130), TE(2)	CR(2,0.75), SP(100)	CR(2,0.50), SP(115)	CR(2,0.50), SP(100), TE(1)
21	CR(2,0.50), SP(130), TE(2)	CR(2,0.75), SP(100)	CR(2,0.50), SP(115)	CR(2,0.50), SP(100), TE(1), LE(2)
22	CR(2,0.50), SP(130), TE(2)	CR(2,0.75), SP(130)	CR(2,0.50), SP(115)	CR(2,0.50), SP(100), TE(2), LE(2), iLB(1)

Table E.4: Observed damage for the east column on bent 2

Test	East		West	
	Top	Bottom	Top	Bottom
12	—	—	—	—
13	—	—	—	—
14	—	—	—	—
15	CR(1,0.08)	CR(1,0.08)	CR(1,0.08)	—
16	CR(1,0.17)	CR(1,0.08), FL	CR(1,0.17), FL	CR(1,0.08)
17	CR(1,0.17)	CR(1,0.17), FL	CR(1,0.25), FL	CR(1,0.17)
18	CR(1,0.33), FL	CR(1,0.50), FL	CR(1,0.33), SP(100)	CR(1,0.17)
19	CR(1,1.00), SP(95)	CR(2,0.50), SP(90)	CR(1,1.00), SP(115)	CR(1,0.33), SP(115)
20	CR(1,1.00), SP(100)	CR(2,0.50), SP(100)	CR(1,2.00), SP(115)	CR(1,0.33), SP(115)
21	CR(1,1.00), SP(100)	CR(2,0.50), SP(100)	CR(1,2.00), SP(115)	CR(1,0.33), SP(115)
22	CR(1,1.00), SP(140)	CR(2,0.50), SP(100)	CR(1,2.00), SP(200), TE(1)	CR(1,0.33), SP(115)

Table E.5: Observed damage for the west column on bent 2

Test	East		West	
	Top	Bottom	Top	Bottom
12	—	—	—	—
13	—	—	—	—
14	—	—	—	CR(1,neg)
15	CR(1,0.08)	CR(1,0.08)	—	CR(1,0.08)
16	CR(1,0.17), FL	CR(1,0.08)	CR(1,0.08)	CR(1,0.17)
17	CR(1,0.17), FL	CR(1,0.08)	CR(1,0.17)	CR(1,0.17)
18	CR(1,0.50), SP(100)	CR(2,0.17), SP(100), TE(1)	CR(1,0.25), FL	CR(1,2.00), SP(40)
19	CR(1,2.00), SP(130)	CR(2,0.33), SP(120), TE(1)	CR(1,2.00), SP(25)	CR(2,0.33), SP(125)
20	CR(1,2.00), SP(130)	CR(2,0.33), SP(120), TE(1)	CR(1,2.00), SP(25)	CR(2,0.33), SP(125)
21	CR(1,2.00), SP(130)	CR(2,0.33), SP(120), TE(1)	CR(1,2.00), SP(25)	CR(2,0.33), SP(125)
22	CR(1,2.00), SP(140), TE(2), LE(2), LB(1)	CR(2,0.33), SP(120), TE(1)	CR(1,2.00), SP(125)	CR(2,0.33), SP(125), TE(1)

Table E.6: Observed damage for the east column on bent 3

Test	East		West	
	Top	Bottom	Top	Bottom
12	—	—	—	—
13	—	—	—	—
14	CR(1,neg)	—	CR(1,neg)	—
15	CR(1,0.17), FL	CR(1,0.17), FL	CR(1,0.25), FL	CR(1,0.08)
16	CR(1,0.25), SP(40)	CR(1,0.25), SP(60)	CR(1,0.25), SP(90)	CR(1,0.17), FL
17	CR(2,0.17), SP(100)	CR(1,0.33), SP(65)	CR(1,0.50), SP(90), TE(1)	CR(1,0.25), SP(100)
18	CR(2,0.50), SP(100), TE(1)	CR(2,0.33), SP(90), TE(2)	CR(2,0.17), SP(140), TE(3), LE(2)	CR(1,0.75), SP(127)
19	CR(2,2.00), SP(115), TE(3), LE(2), LB(3)	CR(2,0.33), SP(150), TE(4), LE(8), LB(6), TF(2)	SP(140), TE(3), LE(5), LB(2)	SP(180), TE(4), LE(6), LB(4)
20	CR(3,0.75), SP(140), TE(4), LE(5), LB(3)	CR(2,0.33), SP(150), TE(4), LE(8), LB(8), TF(2)	SP(140), TE(3), LE(6), LB(4), LF(4)	SP(180), TE(4), LE(6), LB(8)
21	CR(3,0.75), SP(140), TE(4), LE(5), LB(5), LF(2)	CR(2,0.33), SP(150), TE(4), LE(8), LB(8), TF(2), LF(5)	SP(140), TE(4), LE(6), LB(4), LF(4)	SP(180), TE(4), LE(6), LB(8)

Table E.7: Observed damage for the west column on bent 3

Test	East		West	
	Top	Bottom	Top	Bottom
12	—	—	—	—
13	—	—	—	—
14	—	—	CR(1,neg)	CR(1,neg)
15	CR(1,0.25), SP(65)	CR(1,0.17)	CR(1,0.17)	CR(1,0.17), SP(100)
16	CR(1,0.33), SP(90)	CR(1,0.25)	CR(1,0.25), FL	CR(1,0.25), SP(100), TE(1)
17	CR(2,0.33), SP(115)	CR(1,0.25)	CR(1,0.33), FL	CR(2,0.25), SP(100), TE(1)
18	CR(3,0.17), SP(140), TE(3), LE(2)	CR(1,0.33), SP(65)	CR(2,2.00), SP(25)	CR(2,0.25), SP(100), TE(2), LE(2), iLB
19	CR(3,0.33), SP(190), TE(6), LE(7), LB(6), TF(1)	CR(3,0.33), SP(115), TE(3), LE(6), LB(6)	CR(3,2.00), SP(165), TE(4), LB(6)	CR(3,0.33), SP(205), TE(4), LE(7), LB(3), TF(1)
20	CR(3,0.33), SP(190), TE(6), LE(7), LB(6), TF(1), LF(2)	SP(115), TE(3), LE(6), LB(6)	CR(3,2.00), SP(165), TE(4), LB(6)	SP(205), TE(4), LE(7), LB(3), TF(1), LF(1)
21	SP(190), TE(6), LE(8), LB(8), TF(1), LF(2)	SP(150), TE(3), LE(8), LB(6), LF(2)	SP(165), TE(5), LE(8), LB(6)	SP(205), TE(4), LE(8), LB(8), TF(1), LF(2)

Appendix F

SYSTEM IDENTIFICATION RESULTS USING DISPLACEMENT DATA

This appendix presents the identified modal properties (periods, damping ratios and mode shapes) of the shaking table specimen using displacement measurements. These properties were used with the identified modal properties using acceleration data (Section 6.1) to investigate the influence of noise corrupted data on the identified properties. Discussions of the results documented in this appendix are provided in Section 6.6.

Table F.1: Period comparison for earthquake excitations (disp. data)

Test	Mode 1			Mode 2			Mode 3		
	ARX	SLP	Ratio	ARX	SLP	Ratio	ARX	SLP	Ratio
$1A$	0.33	0.32	1.0	0.24	0.23	1.1	0.18	0.09	2.1
$1B$	0.33	0.32	1.0	0.25	0.24	1.0	0.15	0.09	1.7
$2A$	0.33	0.32	1.0	0.25	0.24	1.0	0.02	0.09	0.2
$2B$	0.34	0.31	1.1	0.26	0.24	1.1	0.03	0.09	0.4
$3A$	0.33	0.32	1.0	0.26	0.28	0.9	0.15	0.09	1.8
$3B$	0.34	0.33	1.0	0.26	0.24	1.1	0.16	0.09	1.9
4	0.34	0.33	1.0	0.27	0.26	1.0	0.03	0.09	0.3
5	0.34	0.33	1.0	0.26	0.26	1.0	0.08	0.09	0.9
6	0.34	0.33	1.0	0.26	0.25	1.0	0.16	0.09	1.8
7	0.34	0.33	1.0	0.26	0.26	1.0	0.03	0.09	0.3
$9A$	0.34	0.34	1.0	0.27	0.24	1.1	0.13	0.09	1.6
$9B$	0.35	0.34	1.0	0.27	0.26	1.0	0.11	0.09	1.2
10	0.35	0.34	1.0	0.27	0.26	1.0	0.27	0.09	3.1
11	0.35	0.34	1.0	0.27	0.27	1.0	0.26	0.09	3.0
12	0.36	0.35	1.0	0.27	0.27	1.0	0.24	0.09	2.8
μ	0.34	0.33	1.0	0.26	0.25	1.0	0.13	0.09	1.5
σ	0.01	0.01	0.0	0.01	0.01	0.0	0.08	0.00	1.0
δ	0.03	0.03	0.0	0.03	0.05	0.0	0.63	0.00	0.6

Table F.2: Period comparison for white-noise excitations (disp. data)

Test	Mode 1			Mode 2			Mode 3		
	ARX	SLP	Ratio	ARX	SLP	Ratio	ARX	SLP	Ratio
$WN0001T$	0.32	0.31	1.0	0.24	0.24	1.0	0.07	0.08	0.8
$WN0304TA$	0.32	0.32	1.0	0.25	0.24	1.1	0.04	0.09	0.5
$WN0304TB$	0.34	0.33	1.0	0.25	0.25	1.0	0.07	0.09	0.8
$WN0709TA$	0.34	0.33	1.0	0.26	0.25	1.0	0.07	0.09	0.8
$WN0709TB$	0.34	0.34	1.0	0.26	0.26	1.0	0.08	0.09	0.9
$WN1112TA$	0.35	0.34	1.0	0.26	0.26	1.0	0.08	0.09	0.9
$WN1112TB$	0.35	0.34	1.0	0.27	0.26	1.1	0.08	0.09	0.9
μ	0.34	0.33	1.0	0.26	0.25	1.0	0.07	0.09	0.8
σ	0.01	0.01	0.0	0.01	0.01	0.0	0.01	0.00	0.2
δ	0.03	0.03	0.0	0.04	0.03	0.0	0.20	0.01	0.2

Table F.3: Period comparison for square-wave excitations (disp. data)

Test	Mode 1			Mode 2			Mode 3		
	ARX	SLP	Ratio	ARX	SLP	Ratio	ARX	SLP	Ratio
$SQ0709$	0.33	0.33	1.0	0.27	0.26	1.0	0.02	0.09	0.3
$SQ1112A$	0.34	0.34	1.0	0.27	0.26	1.1	0.06	0.09	0.7
$SQ1112B$	0.34	0.34	1.0	0.29	0.26	1.1	0.26	0.09	3.0
μ	0.34	0.34	1.0	0.27	0.26	1.1	0.11	0.09	1.3
σ	0.01	0.00	0.0	0.01	0.00	0.0	0.12	0.00	1.4
δ	0.02	0.01	0.0	0.04	0.00	0.0	1.08	0.00	1.1
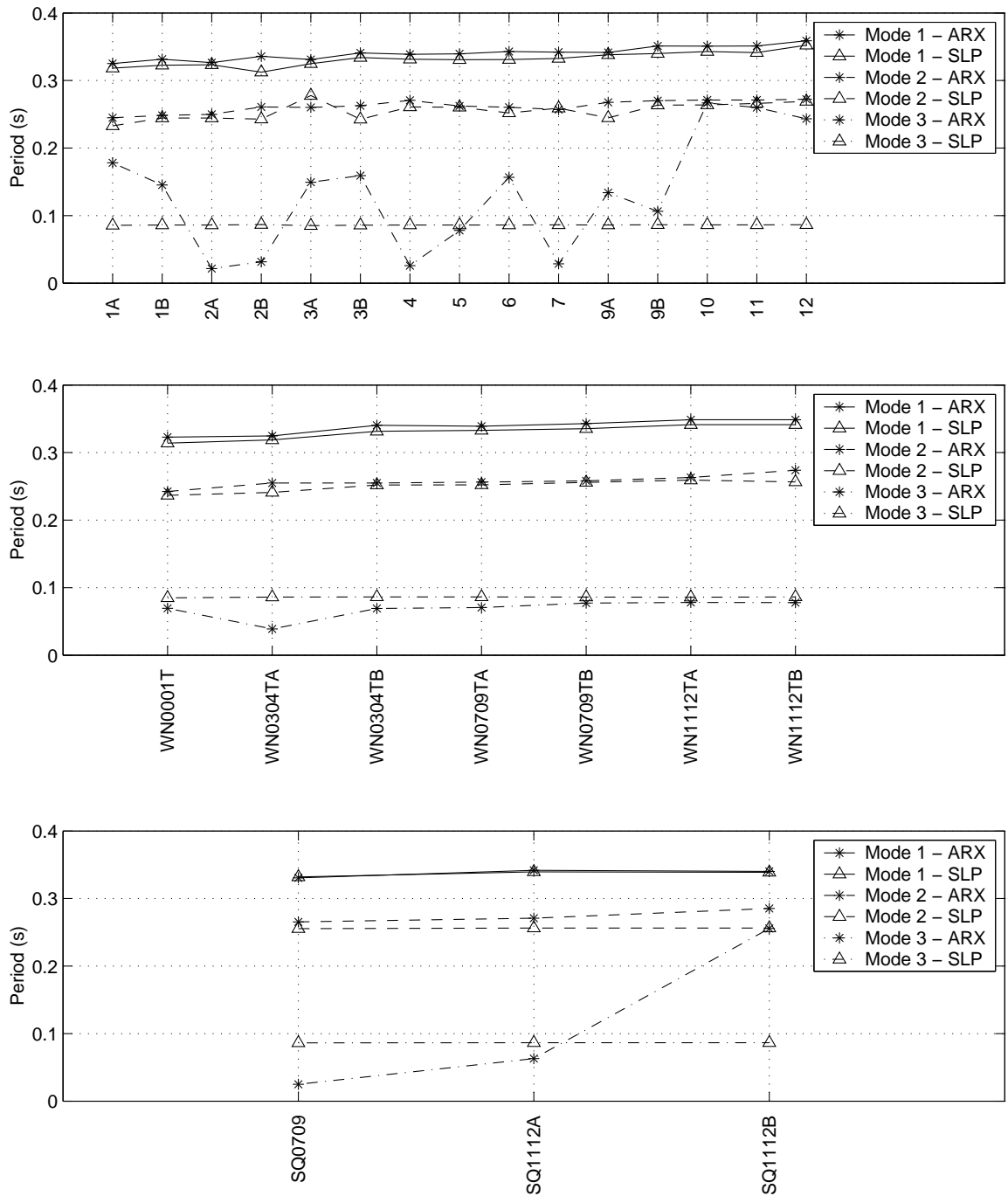
Figure F.1: Estimated periods using displacement data for (a) low-amplitude, (b) white noise, and (c) square wave excitations

Table F.4: Damping comparison for earthquake excitations (disp. data)

Test	Mode 1			Mode 2			Mode 3		
	ARX	SLP	Ratio	ARX	SLP	Ratio	ARX	SLP	Ratio
1A	1.3	1.9	0.7	4.0	5.0	0.8	24.4	13.3	1.8
1B	1.4	2.0	0.7	4.0	1.9	2.1	15.6	11.0	1.4
2A	3.0	2.0	1.5	4.5	2.5	1.8	4.6	34.1	0.1
2B	1.6	10.9	0.1	3.9	25.0	0.2	6.6	11.1	0.6
3A	2.7	2.2	1.2	17.1	50.0	0.3	22.8	1.6	14.2
3B	2.3	2.0	1.1	11.3	8.3	1.4	16.0	50.0	0.3
4	1.9	1.8	1.1	6.5	3.7	1.7	4.4	11.4	0.4
5	1.4	1.8	0.8	7.1	3.4	2.1	10.4	9.2	1.1
6	2.0	2.0	1.0	3.5	2.4	1.5	16.0	26.7	0.6
7	1.4	1.5	1.0	6.2	4.1	1.5	9.6	19.7	0.5
9A	2.9	4.3	0.7	15.4	25.8	0.6	27.7	9.8	2.8
9B	1.8	1.9	1.0	6.0	2.5	2.4	15.9	19.7	0.8
10	1.7	1.4	1.1	4.0	3.1	1.3	62.3	3.5	17.8
11	2.0	1.7	1.2	2.7	2.1	1.3	41.2	1.7	24.2
12	1.9	1.8	1.1	3.6	2.4	1.5	47.9	17.2	2.8
μ	2.0	2.6	0.9	6.6	9.5	1.4	21.7	16.0	4.6
σ	0.5	2.4	0.3	4.4	13.7	0.6	16.9	13.0	7.6
δ	0.3	0.9	0.3	0.7	1.4	0.5	0.8	0.8	1.6

Table F.5: Damping comparison for white-noise excitations (disp. data)

Test	Mode 1			Mode 2			Mode 3		
	ARX	SLP	Ratio	ARX	SLP	Ratio	ARX	SLP	Ratio
$WN0001T$	2.3	1.5	1.5	7.6	4.1	1.9	23.8	19.7	1.2
$WN0304TA$	4.3	2.5	1.7	21.6	3.0	7.1	13.5	20.7	0.7
$WN0304TB$	2.5	2.5	1.0	5.3	2.0	2.6	19.1	22.2	0.9
$WN0709TA$	2.6	2.0	1.3	5.8	2.5	2.3	17.3	21.7	0.8
$WN0709TB$	2.0	2.0	1.0	5.1	3.6	1.4	10.3	19.2	0.5
$WN1112TA$	2.1	1.5	1.4	6.8	4.6	1.5	9.9	16.7	0.6
$WN1112TB$	1.7	2.0	0.8	70.3	3.0	23.0	9.5	19.7	0.5
μ	2.5	2.0	1.2	17.5	3.3	5.7	14.8	20.0	0.7
σ	0.9	0.4	0.3	24.0	0.9	7.9	5.5	1.8	0.2
δ	0.3	0.2	0.2	1.4	0.3	1.4	0.4	0.1	0.3

Table F.6: Damping comparison for square-wave excitations (disp. data)

Test	Mode 1			Mode 2			Mode 3		
	ARX	SLP	Ratio	ARX	SLP	Ratio	ARX	SLP	Ratio
$SQ0709$	2.7	2.5	1.1	25.2	2.0	12.4	8.6	25.8	0.3
$SQ1112A$	2.0	2.0	1.0	25.0	1.0	24.3	18.5	24.8	0.7
$SQ1112B$	3.7	2.0	1.8	7.6	1.5	5.0	30.5	26.3	1.2
μ	2.8	2.2	1.3	19.3	1.5	13.9	19.2	25.6	0.7
σ	0.9	0.3	0.5	10.1	0.5	9.7	11.0	0.8	0.4
δ	0.3	0.1	0.4	0.5	0.3	0.7	0.6	0.0	0.6
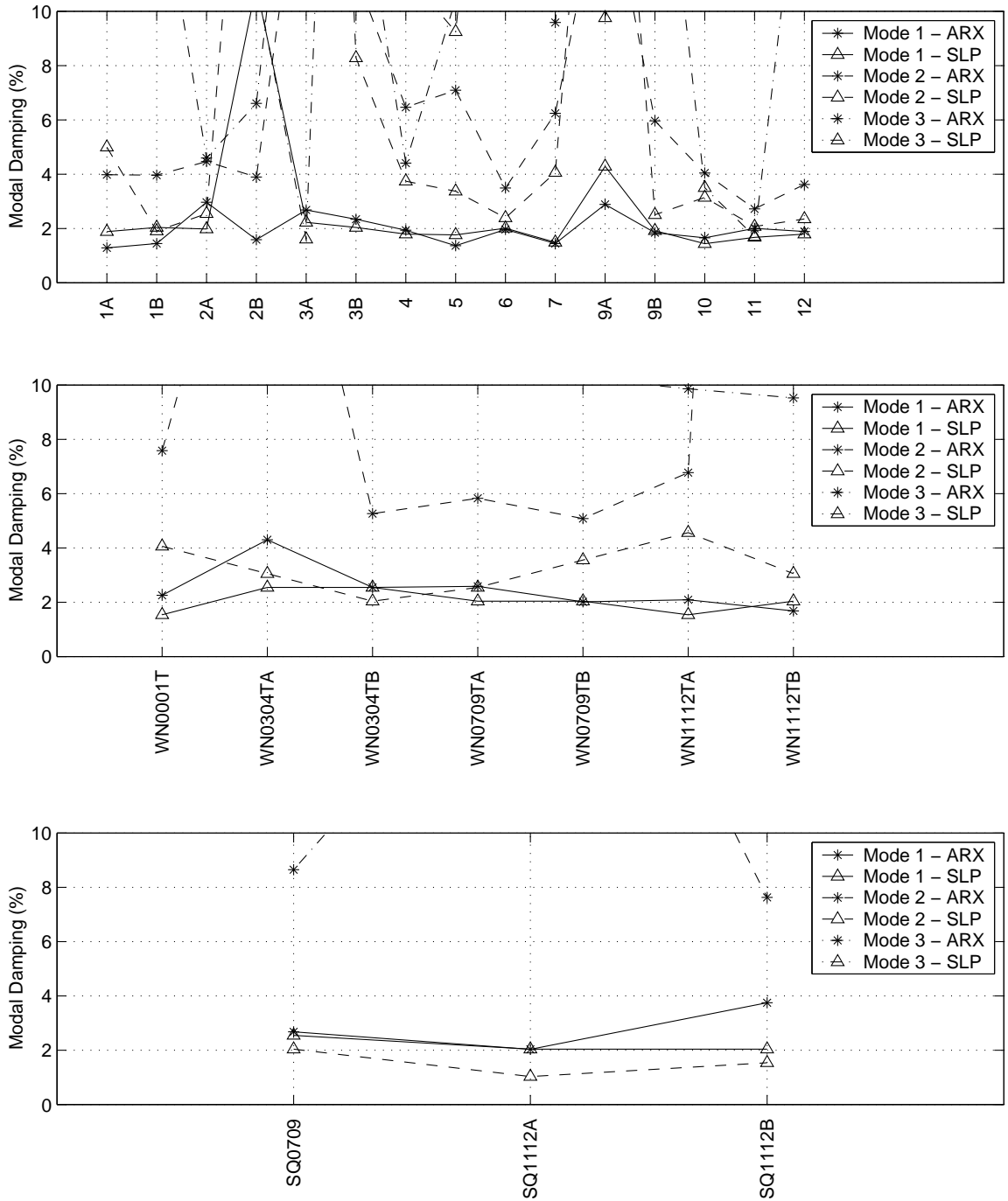
Figure F.2: Estimated damping ratios using displacement data for (a) low-amplitude, (b) white noise, and (c) square wave excitations

Table F.7: Mode 1 basis vector contributions for earthquake excitations (disp. data)

Test	basis vector 1			basis vector 2			basis vector 3		
	ARX	SLP	Ratio	ARX	SLP	Ratio	ARX	SLP	Ratio
1A	0.833	0.899	0.9	-0.489	-0.528	0.9	0.419	-0.227	-1.8
1B	0.941	0.925	1.0	-0.455	-0.464	1.0	-0.402	-0.228	1.8
2A	0.793	0.931	0.9	-0.449	-0.446	1.0	-0.498	-0.226	2.2
2B	0.971	0.997	1.0	-0.465	0.008	-59.1	-0.332	-0.209	1.6
3A	0.798	0.813	1.0	-0.380	-0.663	0.6	0.748	-0.268	-2.8
3B	0.824	0.894	0.9	-0.529	-0.537	1.0	0.073	-0.232	-0.3
4	0.916	0.910	1.0	-0.504	-0.498	1.0	-0.413	-0.242	1.7
5	0.931	0.909	1.0	-0.505	-0.502	1.0	-0.201	-0.242	0.8
6	0.912	0.918	1.0	-0.481	-0.480	1.0	0.450	-0.233	-1.9
7	0.943	0.917	1.0	-0.575	-0.482	1.2	0.816	-0.238	-3.4
9A	0.821	0.897	0.9	-0.341	-0.532	0.6	0.217	-0.231	-0.9
9B	0.947	0.921	1.0	-0.438	-0.472	0.9	0.519	-0.238	-2.2
10	0.943	0.897	1.1	-0.466	-0.529	0.9	0.476	-0.243	-2.0
11	0.960	0.905	1.1	-0.460	-0.511	0.9	0.405	-0.243	-1.7
12	0.923	0.903	1.0	-0.556	-0.514	1.1	-0.386	-0.242	1.6
μ	0.897	0.909	1.0	-0.473	-0.477	-3.1	0.126	-0.236	-0.5
σ	0.063	0.037	0.1	0.060	0.143	15.5	0.460	0.013	1.9
δ	0.071	0.040	0.1	0.128	0.300	5.1	3.647	0.053	3.9

Table F.8: Mode 1 basis vector contributions for white-noise excitations (disp. data)

Test	basis vector 1			basis vector 2			basis vector 3		
	ARX	SLP	Ratio	ARX	SLP	Ratio	ARX	SLP	Ratio
$WN0001T$	0.862	0.868	1.0	-0.466	-0.586	0.8	0.889	-0.242	-3.7
$WN0304TA$	0.839	0.930	0.9	-0.420	-0.448	0.9	0.394	-0.225	-1.8
$WN0304TB$	0.897	0.919	1.0	-0.484	-0.478	1.0	0.378	-0.233	-1.6
$WN0709TA$	0.891	0.921	1.0	-0.546	-0.473	1.2	0.124	-0.232	-0.5
$WN0709TB$	0.897	0.904	1.0	-0.448	-0.514	0.9	-0.500	-0.238	2.1
$WN1112TA$	0.879	0.871	1.0	-0.481	-0.578	0.8	-0.061	-0.247	0.2
$WN1112TB$	0.895	0.914	1.0	0.556	-0.491	-1.1	-0.139	-0.234	0.6
μ	0.880	0.904	1.0	-0.327	-0.510	0.6	0.155	-0.236	-0.7
σ	0.022	0.025	0.0	0.391	0.053	0.8	0.449	0.007	1.9
δ	0.025	0.027	0.0	1.197	0.105	1.2	2.898	0.031	2.8

Table F.9: Mode 1 basis vector contributions for square-wave excitations (disp. data)

Test	basis vector 1			basis vector 2			basis vector 3		
	ARX	SLP	Ratio	ARX	SLP	Ratio	ARX	SLP	Ratio
$SQ0709$	0.935	0.924	1.0	-0.723	-0.465	1.6	0.457	-0.234	-2.0
$SQ1112A$	0.947	0.923	1.0	-0.640	-0.467	1.4	-0.094	-0.232	0.4
$SQ1112B$	0.828	0.922	0.9	-0.508	-0.470	1.1	0.447	-0.233	-1.9
μ	0.903	0.923	1.0	-0.624	-0.467	1.3	0.270	-0.233	-1.2
σ	0.066	0.001	0.1	0.108	0.002	0.2	0.315	0.001	1.4
δ	0.073	0.001	0.1	0.173	0.005	0.2	1.167	0.004	1.2

Figure F.3: Estimated mode shape envelopes using displacement data for mode 1 using the low-amplitude (a) earthquake, (b) white noise, and (c) square wave excitations

Table F.10: Mode 2 basis vector contributions for earthquake excitations (disp. data)

Test	basis vector 1			basis vector 2			basis vector 3		
	ARX	SLP	Ratio	ARX	SLP	Ratio	ARX	SLP	Ratio
$1A$	0.546	0.437	1.2	0.862	0.847	1.0	-0.597	-0.027	22.4
$1B$	0.330	0.378	0.9	0.884	0.884	1.0	0.398	-0.020	-19.9
$2A$	0.588	0.362	1.6	0.883	0.894	1.0	0.644	-0.020	-32.8
$2B$	0.223	-0.006	-37.0	0.882	1.000	0.9	0.673	0.000	1836.9
$3A$	0.600	0.583	1.0	0.829	0.748	1.1	-0.430	-0.011	40.0
$3B$	0.565	0.446	1.3	0.835	0.842	1.0	0.412	-0.025	-16.5
4	0.391	0.413	0.9	0.852	0.866	1.0	0.633	-0.016	-39.9
5	0.357	0.417	0.9	0.847	0.864	1.0	0.306	-0.016	-19.1
6	0.409	0.394	1.0	0.859	0.876	1.0	0.076	-0.019	-4.0
7	0.332	0.397	0.8	0.786	0.875	0.9	-0.438	-0.016	26.6
$9A$	0.546	0.442	1.2	0.877	0.845	1.0	-0.531	-0.025	21.5
$9B$	0.317	0.388	0.8	0.893	0.881	1.0	0.442	-0.016	-27.9
10	0.327	0.442	0.7	0.881	0.848	1.0	-0.562	-0.017	32.4
11	0.263	0.426	0.6	0.883	0.859	1.0	-0.617	-0.016	38.5
12	0.384	0.428	0.9	0.827	0.857	1.0	0.760	-0.017	-45.2
μ	0.412	0.396	-1.5	0.859	0.866	1.0	0.078	-0.017	120.9
σ	0.125	0.122	9.8	0.030	0.050	0.1	0.540	0.006	475.6
δ	0.302	0.308	6.4	0.034	0.058	0.1	6.951	0.371	3.9

Table F.11: Mode 2 basis vector contributions for white-noise excitations (disp. data)

Test	basis vector 1			basis vector 2			basis vector 3		
	ARX	SLP	Ratio	ARX	SLP	Ratio	ARX	SLP	Ratio
$WN0001T$	0.506	0.496	1.0	0.816	0.809	1.0	-0.258	-0.024	10.6
$WN0304TA$	0.539	0.364	1.5	0.643	0.893	0.7	0.561	-0.020	-27.6
$WN0304TB$	0.441	0.393	1.1	0.811	0.877	0.9	0.636	-0.019	-33.6
$WN0709TA$	0.454	0.387	1.2	0.787	0.880	0.9	0.281	-0.019	-14.8
$WN0709TB$	0.440	0.427	1.0	0.873	0.856	1.0	0.354	-0.019	-18.7
$WN1112TA$	0.476	0.490	1.0	0.857	0.815	1.1	-0.067	-0.020	3.4
$WN1112TB$	0.444	0.405	1.1	-0.633	0.870	-0.7	0.019	-0.019	-1.0
μ	0.471	0.423	1.1	0.593	0.857	0.7	0.218	-0.020	-11.7
σ	0.038	0.052	0.2	0.546	0.033	0.6	0.332	0.002	16.5
δ	0.081	0.122	0.2	0.920	0.038	0.9	1.525	0.098	1.4

Table F.12: Mode 2 basis vector contributions for square-wave excitations (disp. data)

Test	basis vector 1			basis vector 2			basis vector 3		
	ARX	SLP	Ratio	ARX	SLP	Ratio	ARX	SLP	Ratio
$SQ0709$	0.353	0.381	0.9	0.611	0.884	0.7	-0.609	-0.017	35.2
$SQ1112A$	0.318	0.382	0.8	0.702	0.883	0.8	0.432	-0.018	-23.6
$SQ1112B$	0.557	0.385	1.4	0.801	0.882	0.9	-0.648	-0.018	35.4
μ	0.409	0.383	1.1	0.704	0.883	0.8	-0.275	-0.018	15.7
σ	0.129	0.002	0.3	0.095	0.001	0.1	0.613	0.001	34.0
δ	0.316	0.005	0.3	0.135	0.002	0.1	2.230	0.032	2.2
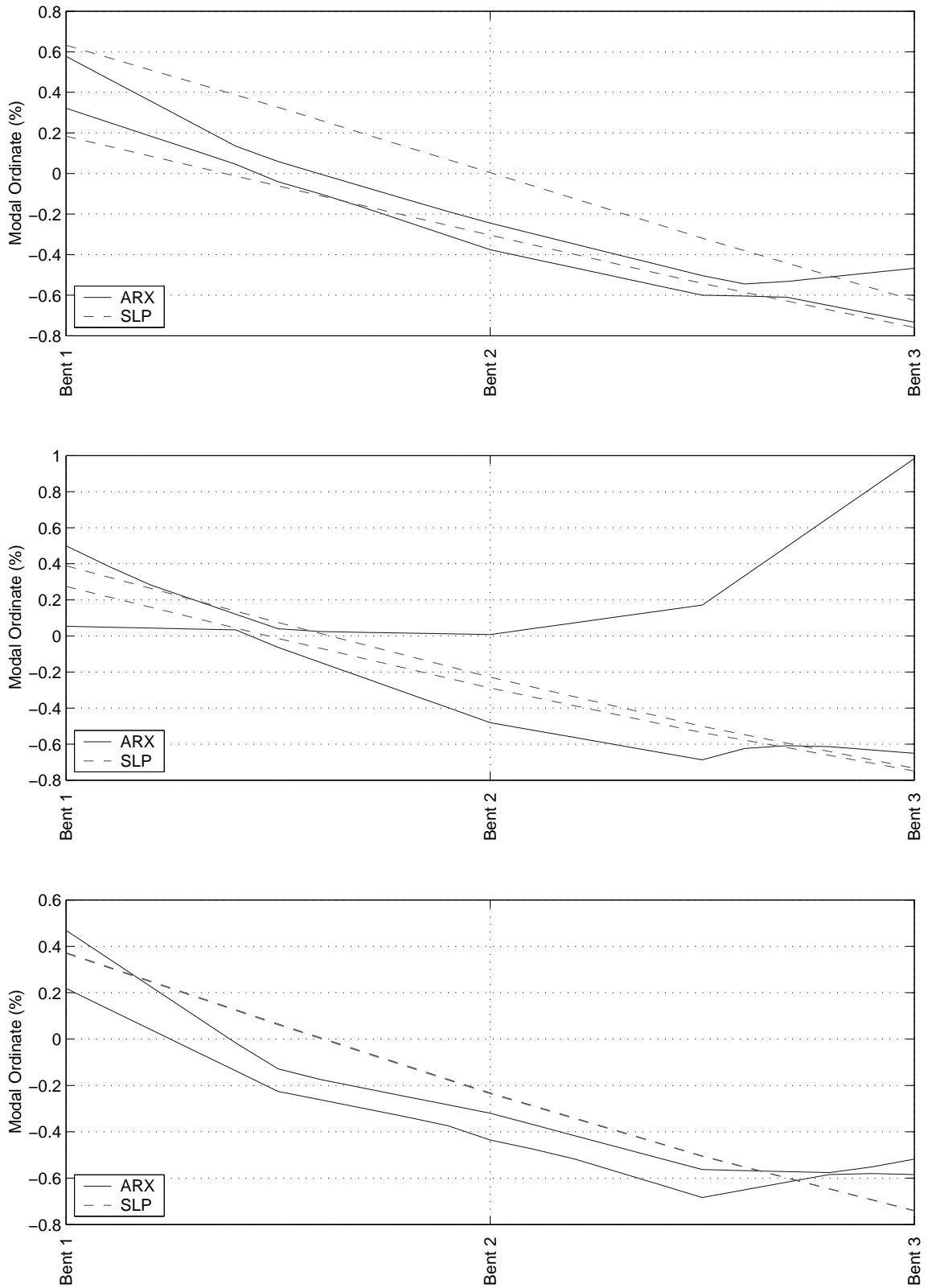
Figure F.4: Estimated mode shape envelopes using displacement data for mode 2 using the low-amplitude (a) earthquake, (b) white noise, and (c) square wave excitations

Table F.13: Mode 3 basis vector contributions for earthquake excitations (disp. data)

Test	basis vector 1			basis vector 2			basis vector 3		
	ARX	SLP	Ratio	ARX	SLP	Ratio	ARX	SLP	Ratio
1A	-0.023	-0.035	0.7	0.129	0.061	2.1	0.645	0.973	0.7
1B	0.049	-0.041	-1.2	0.106	0.051	2.1	-0.372	0.973	-0.4
2A	0.086	-0.045	-1.9	0.131	0.051	2.6	-0.477	0.974	-0.5
2B	0.074	-0.078	-0.9	0.074	-0.001	-65.9	-0.574	0.978	-0.6
3A	0.023	0.003	6.7	0.403	0.016	25.2	0.473	0.963	0.5
3B	-0.016	-0.030	0.5	0.148	0.057	2.6	-0.698	0.972	-0.7
4	0.081	-0.027	-3.0	0.137	0.039	3.5	-0.547	0.970	-0.6
5	0.047	-0.026	-1.8	0.166	0.039	4.2	0.834	0.970	0.9
6	-0.017	-0.036	0.5	0.167	0.047	3.5	0.820	0.972	0.8
7	0.011	-0.031	-0.4	0.218	0.041	5.3	0.340	0.971	0.4
9A	0.127	-0.031	-4.0	0.328	0.057	5.8	0.634	0.973	0.7
9B	0.039	-0.032	-1.2	0.100	0.040	2.5	-0.665	0.971	-0.7
10	0.065	-0.023	-2.8	0.082	0.041	2.0	0.633	0.970	0.7
11	0.094	-0.025	-3.8	0.095	0.039	2.5	0.611	0.970	0.6
12	-0.009	-0.025	0.3	0.077	0.041	1.9	-0.522	0.970	-0.5
μ	0.042	-0.032	-0.8	0.157	0.041	-0.0	0.076	0.971	0.1
σ	0.046	0.017	2.6	0.094	0.016	19.1	0.622	0.003	0.6
δ	1.098	0.520	3.1	0.598	0.387	2471.6	8.209	0.003	8.1

Table F.14: Mode 3 basis vector contributions for white-noise excitations (disp. data)

Test	basis vector 1			basis vector 2			basis vector 3		
	ARX	SLP	Ratio	ARX	SLP	Ratio	ARX	SLP	Ratio
$WN0001T$	-0.020	-0.017	1.2	0.321	0.051	6.4	-0.329	0.970	-0.3
$WN0304TA$	0.044	-0.045	-1.0	0.613	0.052	11.7	0.724	0.974	0.7
$WN0304TB$	-0.012	-0.036	0.3	0.309	0.047	6.5	0.666	0.972	0.7
$WN0709TA$	-0.010	-0.037	0.3	0.267	0.048	5.6	0.932	0.973	1.0
$WN0709TB$	0.020	-0.028	-0.7	0.190	0.045	4.2	0.710	0.971	0.7
$WN1112TA$	0.015	-0.015	-1.0	0.179	0.042	4.3	0.985	0.969	1.0
$WN1112TB$	0.013	-0.034	-0.4	0.495	0.047	10.5	0.980	0.972	1.0
μ	0.007	-0.030	-0.2	0.339	0.047	7.0	0.667	0.972	0.7
σ	0.022	0.011	0.8	0.160	0.003	3.0	0.459	0.002	0.5
δ	3.134	0.364	4.4	0.472	0.073	0.4	0.689	0.002	0.7

Table F.15: Mode 3 basis vector contributions for square-wave excitations (disp. data)

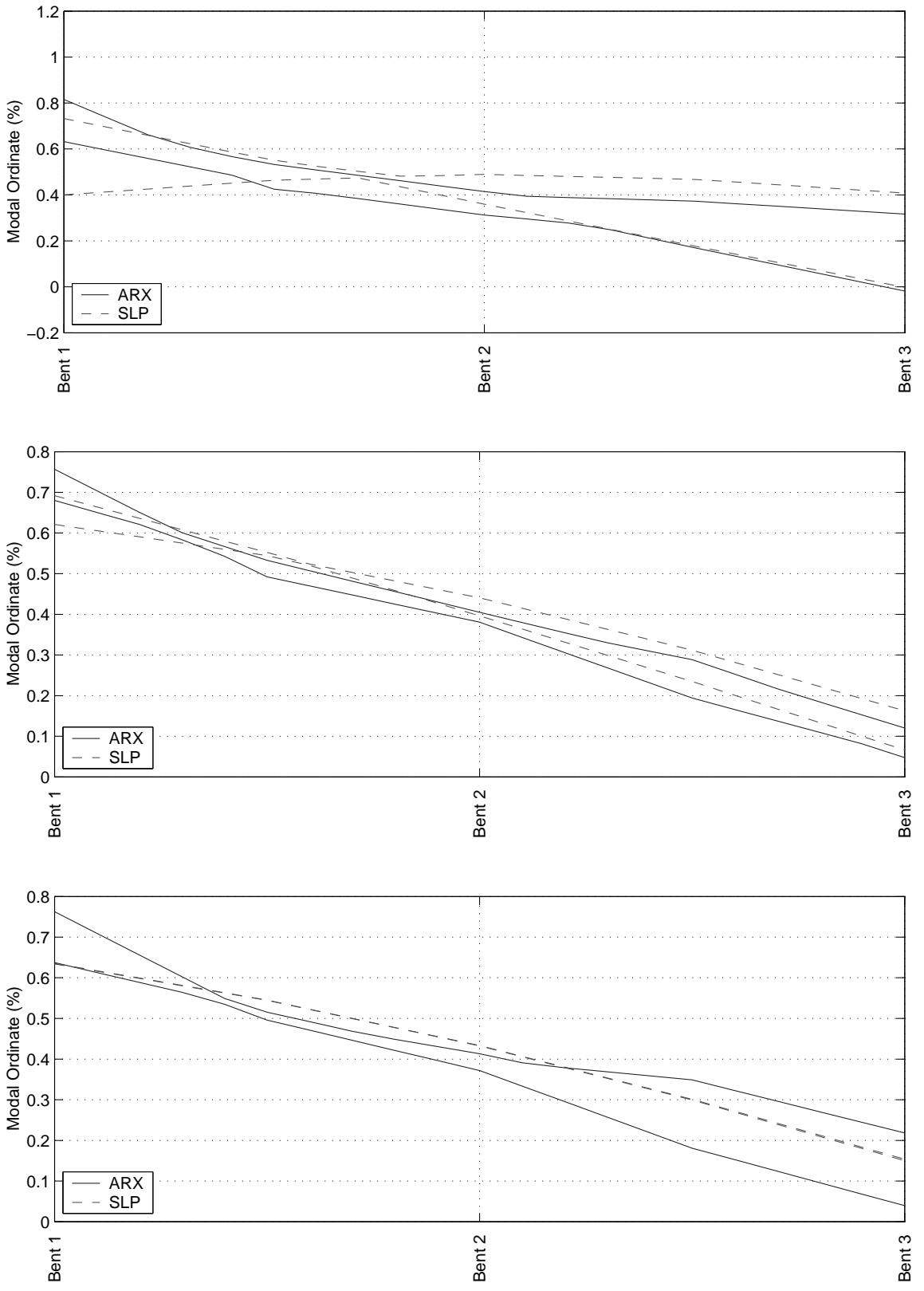| Test	basis vector 1			basis vector 2			basis vector 3		
	ARX	SLP	Ratio	ARX	SLP	Ratio	ARX	SLP	Ratio
$SQ0709$	0.031	-0.036	-0.9	0.296	0.044	6.7	0.547	0.972	0.6
$SQ1112A$	0.014	-0.038	-0.4	0.307	0.047	6.6	0.891	0.973	0.9
$SQ1112B$	0.047	-0.037	-1.3	0.293	0.046	6.3	0.567	0.972	0.6
μ	0.031	-0.037	-0.8	0.299	0.046	6.5	0.668	0.972	0.7
σ	0.017	0.001	0.5	0.008	0.001	0.2	0.193	0.000	0.2
δ	0.537	0.022	0.5	0.025	0.029	0.0	0.289	0.000	0.3
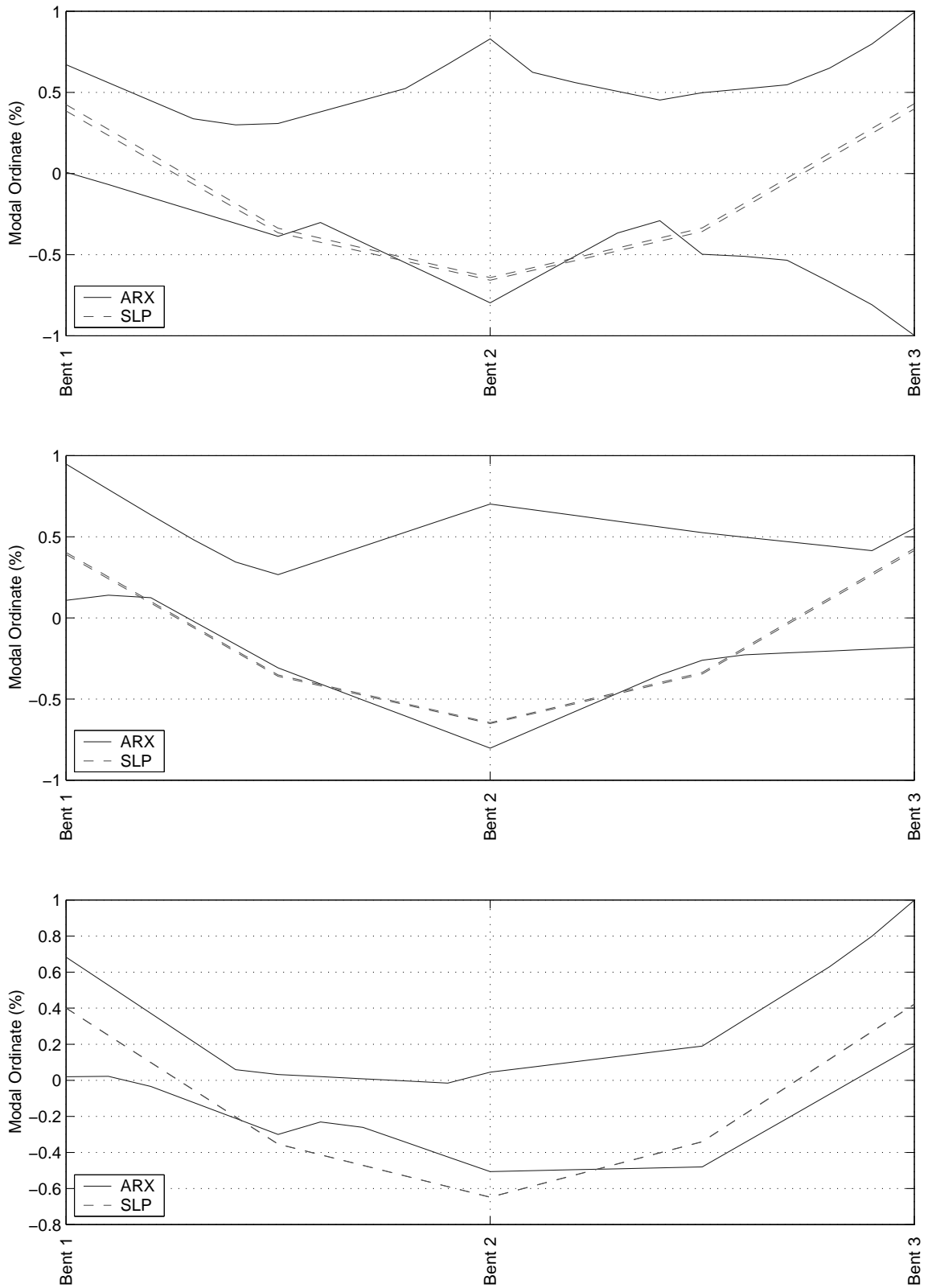
Figure F.5: Estimated mode shape envelopes using displacement data for mode 3 using the low-amplitude (a) earthquake, (b) white noise, and (c) square wave excitations

Appendix G

ACCELERATION RESPONSE SPECTRA FOR NEAR-FIELD AND FAR-FIELD MOTIONS

This chapter presents the acceleration response spectra (2% damping) of the near-field and far-field bedrock motions that were described in Chapter 10.
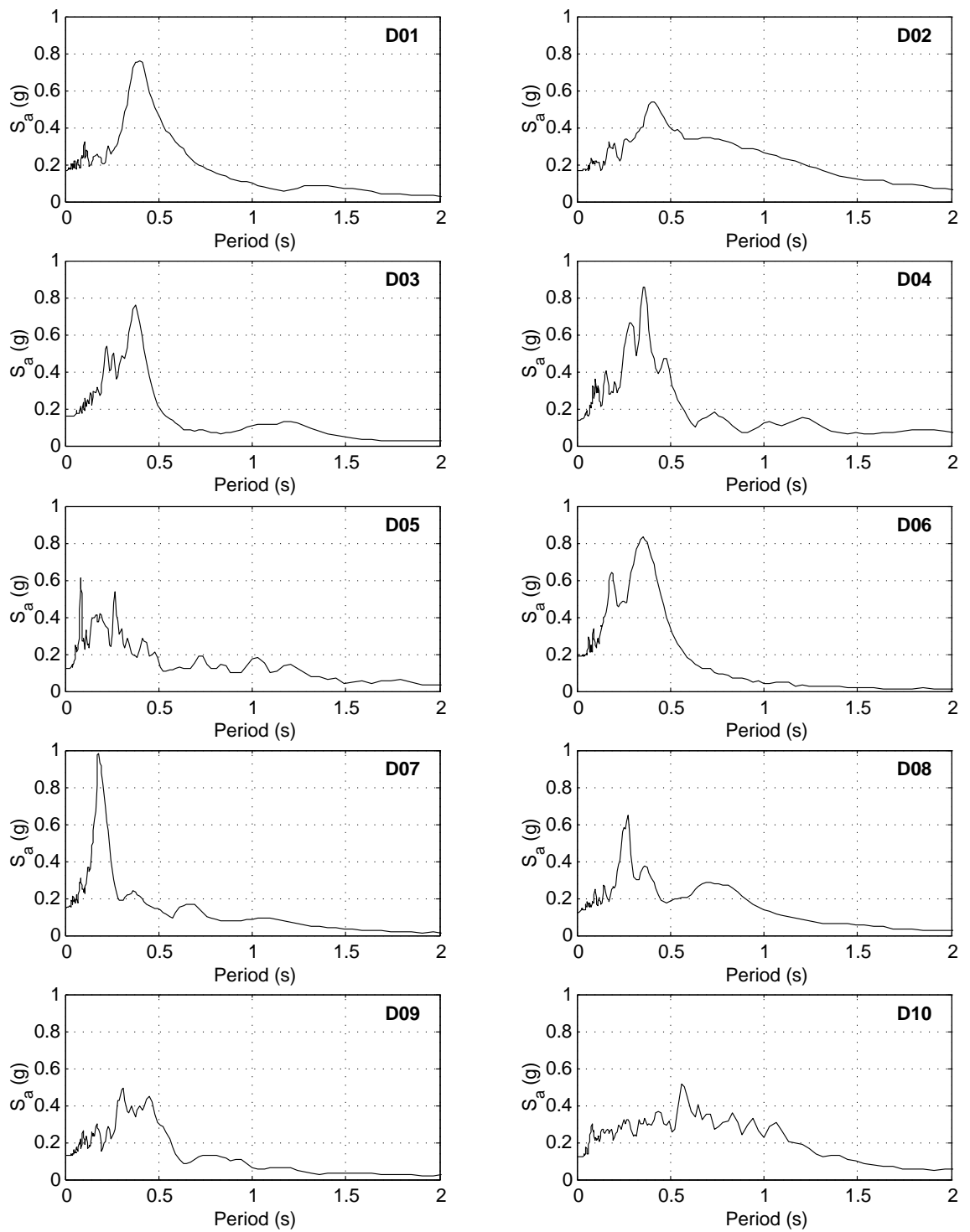
Figure G.1: Response spectra for near-field motion set D
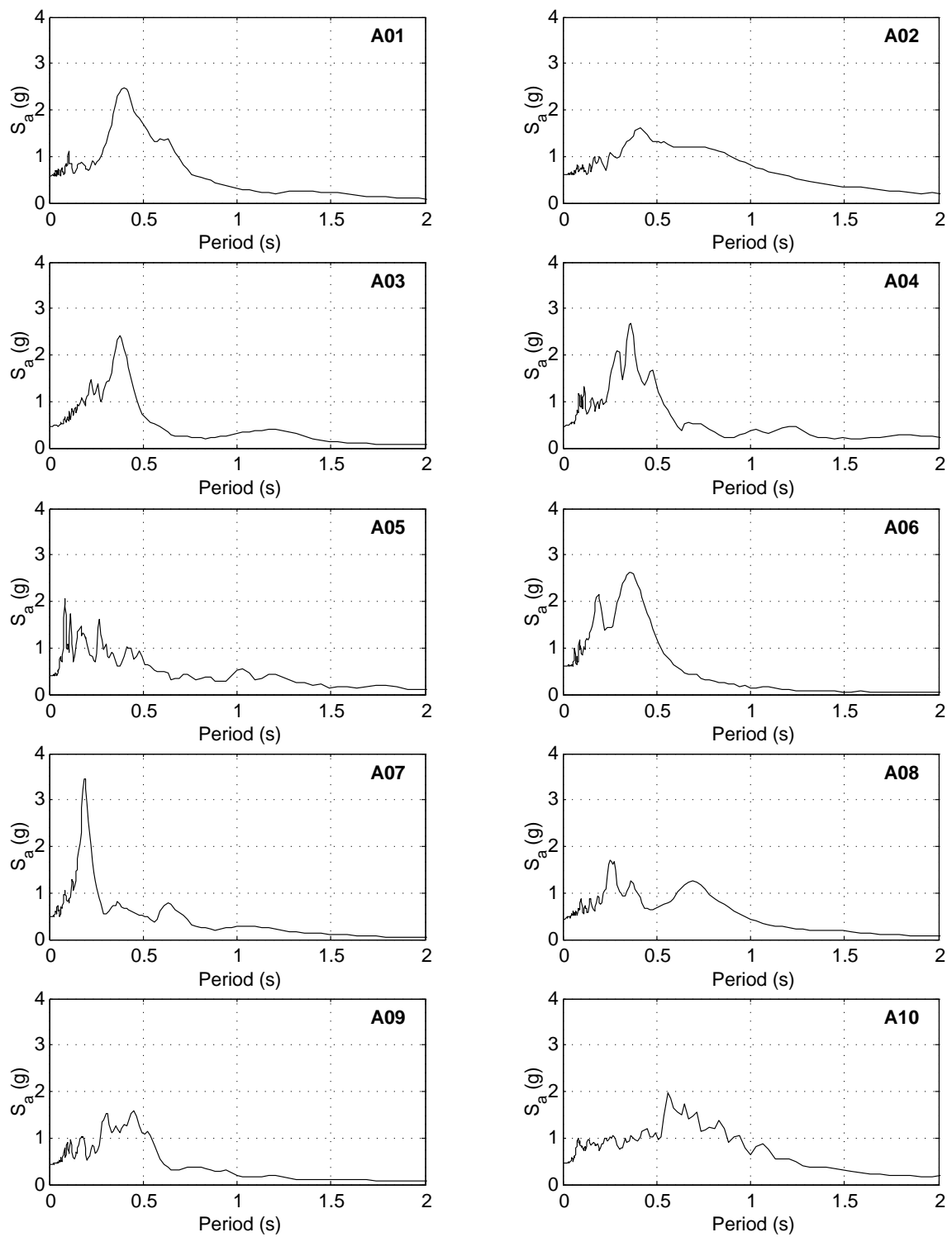
Figure G.2: Response spectra for near-field motion set A
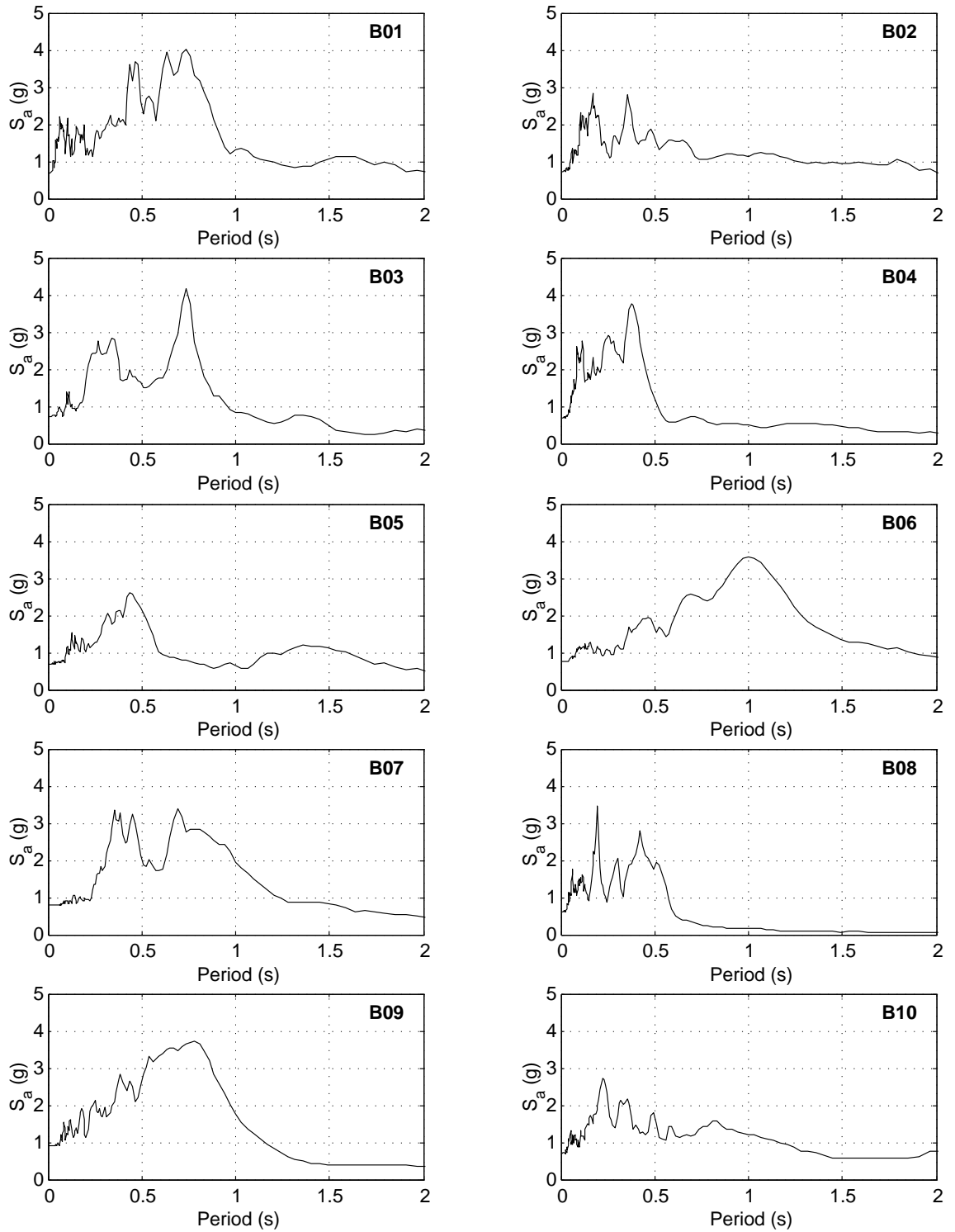
Figure G.3: Response spectra for near-field motion set B
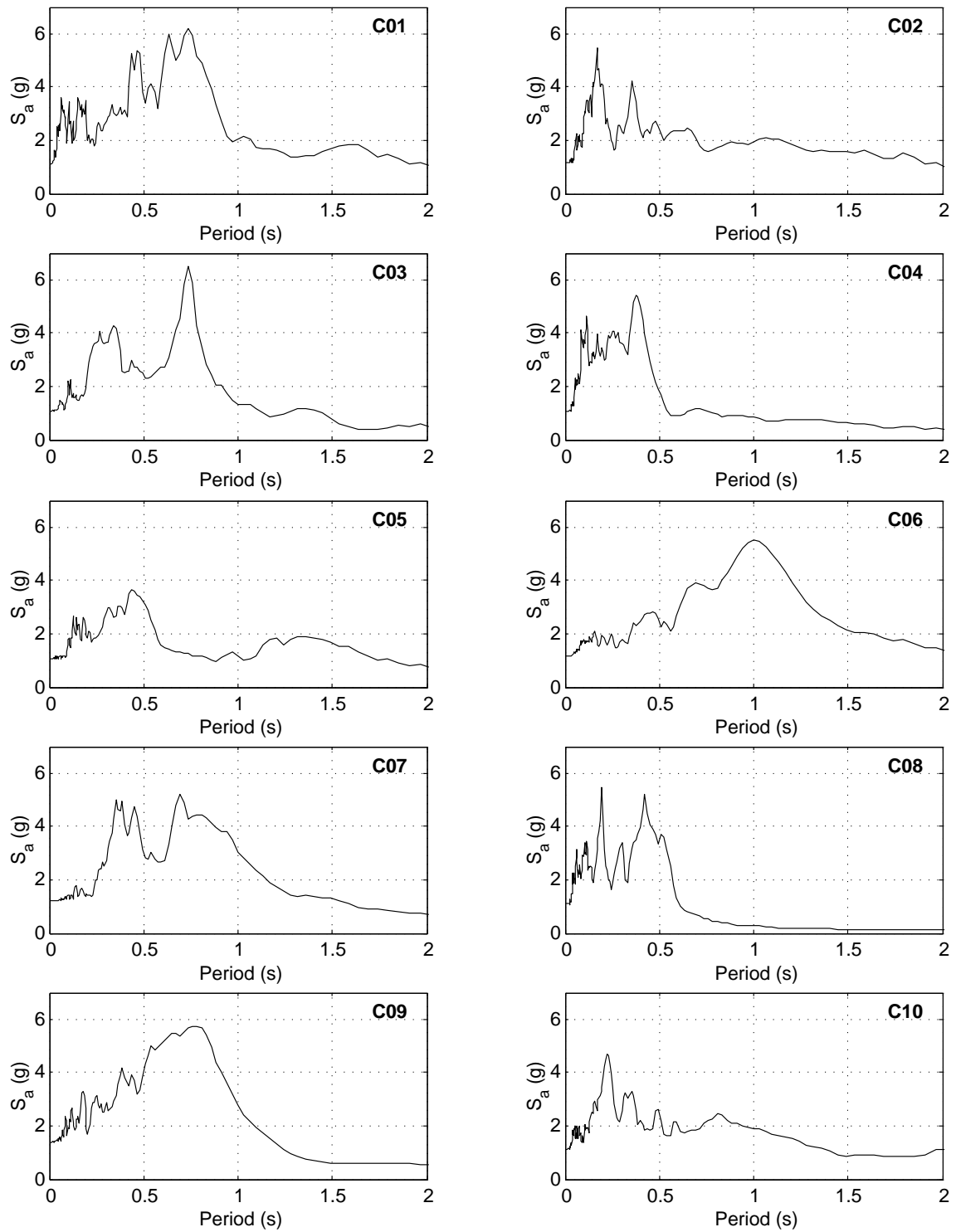
Figure G.4: Response spectra for near-field motion set C
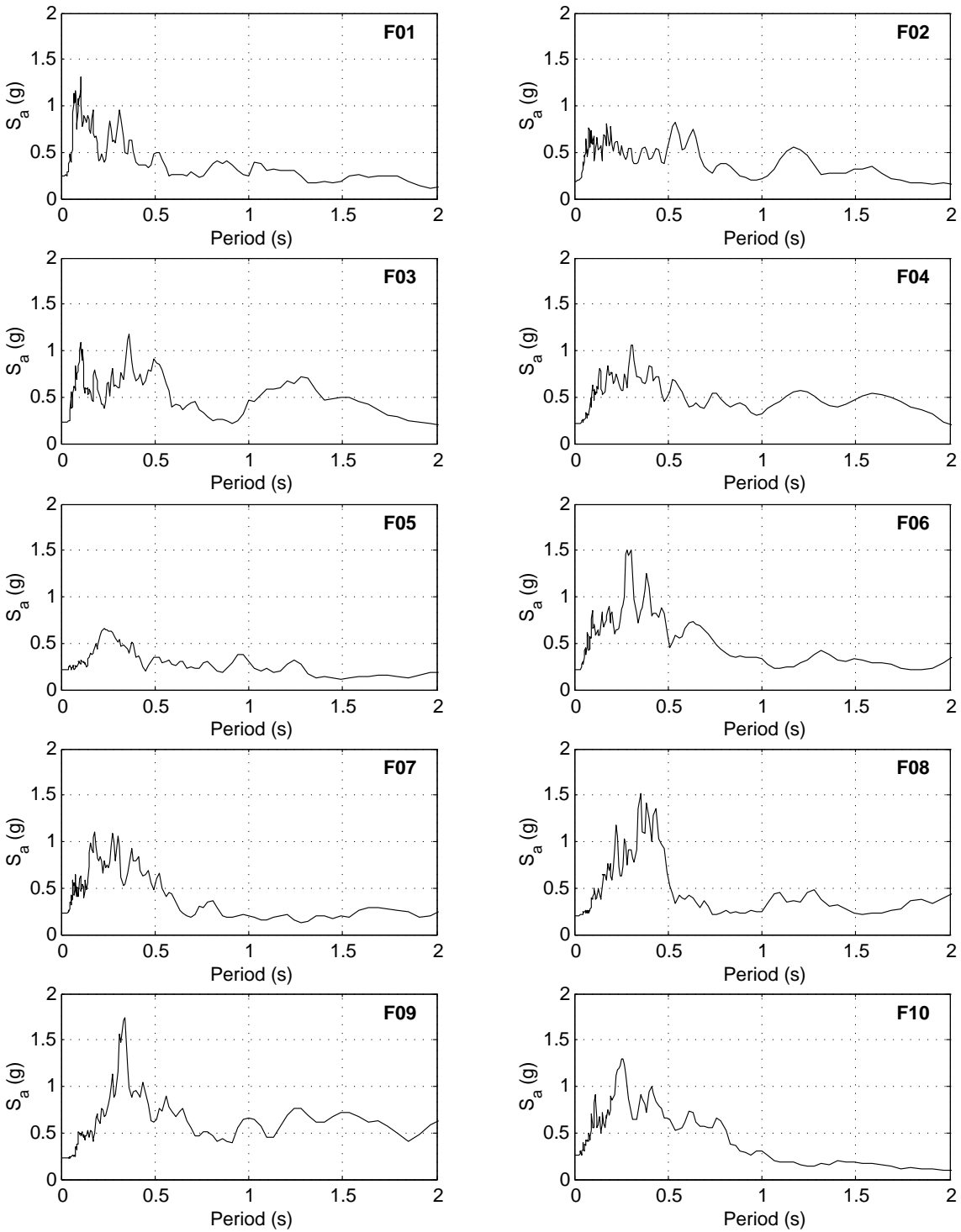
Figure G.5: Response spectra for far-field motion set F
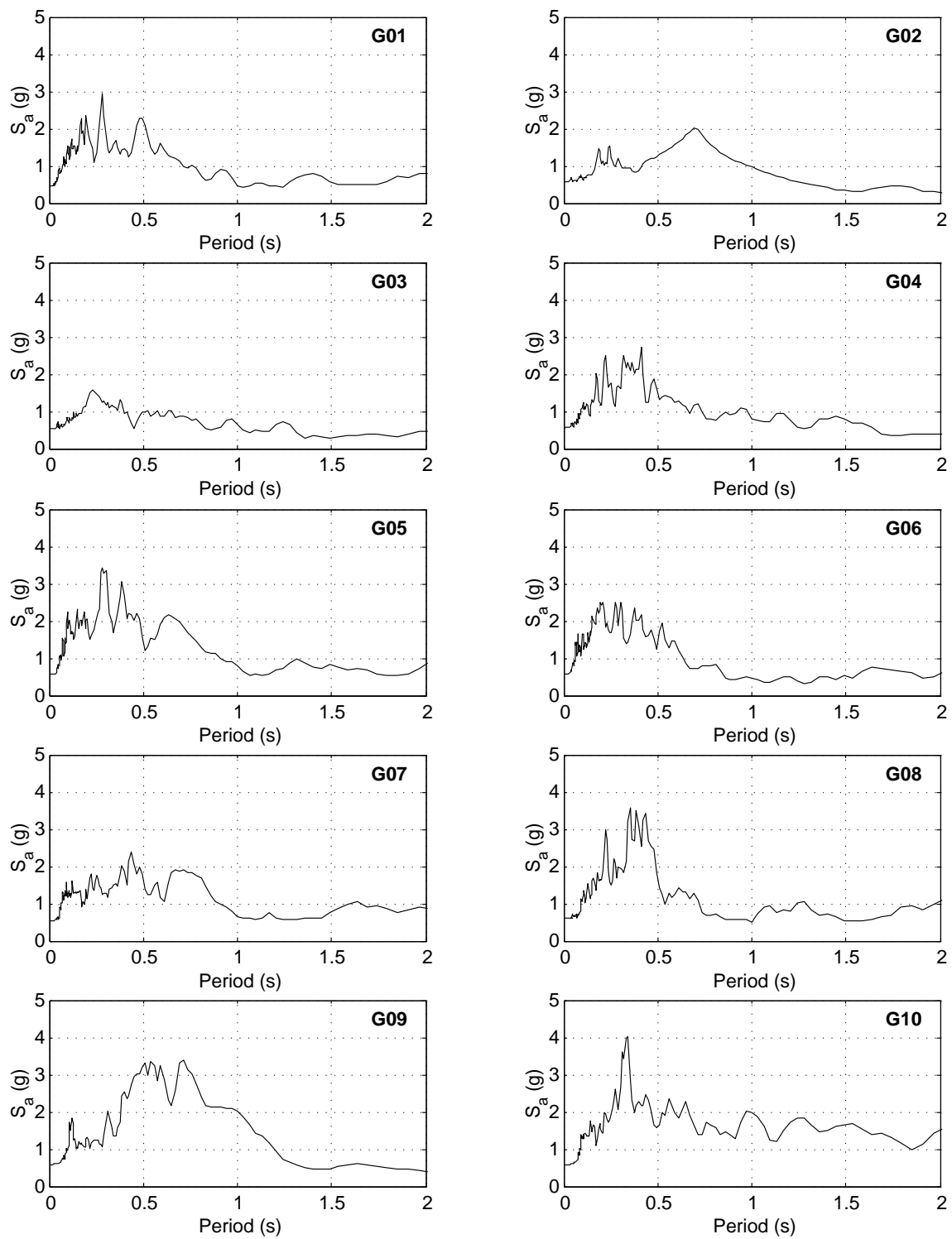
Figure G.6: Response spectra for far-field motion set G
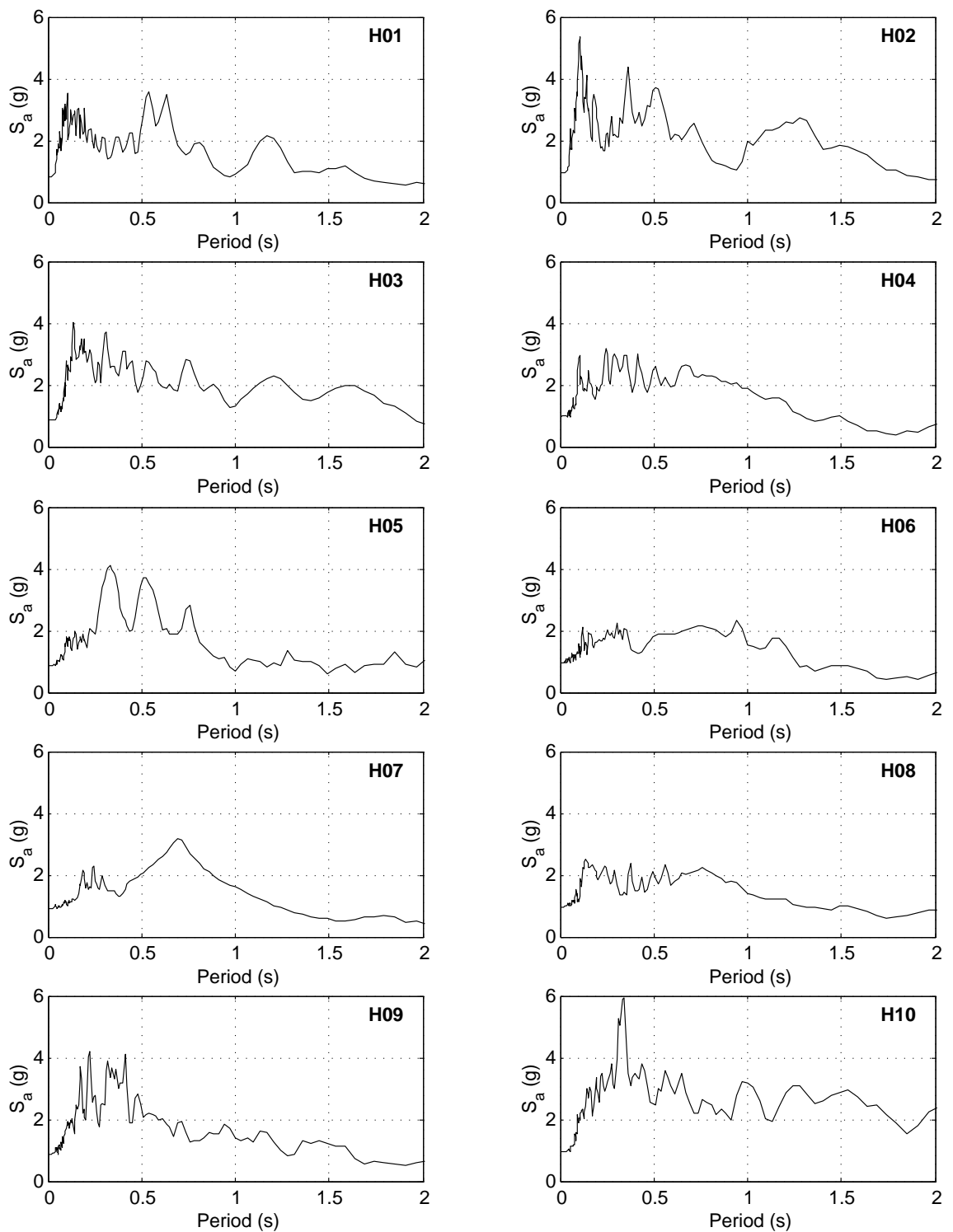
Figure G.7: Response spectra for far-field motion set H

Appendix H

SUPPLEMENT TO THE EVALUATION OF BRIDGE MODELING STRATEGIES

This appendix presents tables and figures referred to in Chapter 12 for evaluating the bridge modeling strategies in a performance-based framework.

Table H.1: Error in estimated drift ratios for the inelastic structural models

Bent	Field	Hazard	Foundation Approximations							
			Fixed @ 3D		Fixed @ 0D		Springs (Pinned)		Springs (Fixed)	
			μ	σ	μ	σ	μ	σ	μ	σ
1	NF	50%	1.0	12	34.1	43	89.7	23	53.5	42
		10%	-3.1	19	17.4	83	76.0	21	41.4	73
		2%	-6.8	11	11.6	65	85.7	28	28.2	46
	FF	50%	9.9	17	27.6	45	102.9	29	62.3	56
		10%	-1.5	8	-5.2	29	108.3	43	20.2	24
		2%	-4.7	7	-12.6	21	84.2	29	21.5	29
2	NF	50%	-3.8	8	-19.5	24	48.0	16	1.1	32
		10%	-7.9	11	-39.1	36	34.7	17	-23.5	41
		2%	-8.6	11	-40.7	29	45.5	25	-25.8	27
	FF	50%	0.9	8	-17.4	25	49.0	40	-3.3	28
		10%	-5.0	4	-41.3	20	44.9	17	-20.8	19
		2%	-8.4	7	-49.0	11	31.4	20	-31.6	14
3	NF	50%	1.4	12	-21.8	36	83.5	25	19.6	64
		10%	-10.9	13	-58.9	50	66.9	27	-29.7	65
		2%	-5.4	15	-62.1	36	87.4	36	-31.1	49
	FF	50%	6.1	15	-54.9	21	84.9	37	1.0	45
		10%	-5.9	7	-57.6	16	79.5	16	-27.0	27
		2%	-4.9	10	-68.0	14	79.2	33	-47.8	18
		Total	-3.2	12	-25.4	48	71.2	35	0.5	51

Table H.2: Error in estimated drift ratios for the effective elastic structural models

Bent	Field	Hazard	Foundation Approximations							
			Fixed @ 3D		Fixed @ 0D		Springs (Pinned)		Springs (Fixed)	
			μ	σ	μ	σ	μ	σ	μ	σ
1	NF	50%	19.0	38	24.0	79	107.0	64	54.0	72
		10%	19.6	60	-26.0	105	81.1	94	14.4	148
		2%	8.2	56	-28.0	75	64.6	85	2.2	132
	FF	50%	20.4	37	3.3	61	100.0	66	71.6	46
		10%	13.4	48	-43.1	28	73.0	75	-6.3	35
		2%	-4.0	33	-54.8	25	38.9	42	-37.3	27
2	NF	50%	3.9	19	15.6	81	47.7	26	30.5	51
		10%	-13.3	39	-42.8	69	22.0	60	-18.3	88
		2%	-21.5	32	-43.4	55	8.5	51	-24.7	83
	FF	50%	8.7	21	-7.6	45	52.0	34	51.2	44
		10%	-11.5	31	-48.9	24	26.4	52	-18.3	33
		2%	-32.5	23	-59.4	21	-10.0	28	-51.4	19
3	NF	50%	16.9	35	-45.4	24	53.7	58	-23.0	45
		10%	-32.0	33	-63.0	28	-9.6	80	-62.3	41
		2%	-33.0	31	-44.1	54	-16.2	78	-60.6	39
	FF	50%	8.8	19	-64.4	15	55.3	48	-30.9	26
		10%	-14.6	26	-76.2	10	-4.9	35	-60.8	17
		2%	-43.6	14	-54.1	42	-40.7	21	-69.6	15
		Total	-4.8	39	-36.6	58	36.0	70	-13.3	75

Table H.3: Error in estimated drift ratios for the gross elastic structural models

Bent	Field	Hazard	Foundation Approximations							
			Fixed @ 3D		Fixed @ 0D		Springs (Pinned)		Springs (Fixed)	
			μ	σ	μ	σ	μ	σ	μ	σ
1	NF	50%	2.8	61	-68.2	10	38.3	62	-20.2	46
		10%	-25.8	109	-76.9	15	-6.4	98	-46.0	86
		2%	-33.0	87	-58.1	46	-16.4	88	-52.2	63
	FF	50%	7.3	38	-78.2	9	41.1	42	-27.4	43
		10%	-41.5	28	-84.8	8	-11.3	36	-61.1	18
		2%	-58.2	19	-68.2	30	-44.3	22	-73.6	11
2	NF	50%	-2.7	54	-52.6	21	39.7	46	-9.4	55
		10%	-44.4	70	-73.3	16	-17.9	80	-49.9	70
		2%	-47.1	58	-63.8	31	-25.9	73	-54.1	52
	FF	50%	0.9	38	-63.5	13	48.9	41	-19.1	42
		10%	-48.4	26	-78.0	8	-12.4	37	-57.6	20
		2%	-66.2	13	-67.3	26	-49.0	18	-71.3	13
3	NF	50%	-41.4	38	-76.7	16	-34.8	34	-63.0	21
		10%	-67.9	33	-75.8	20	-66.9	37	-79.6	23
		2%	-62.4	32	-49.1	55	-67.7	32	-75.8	23
	FF	50%	-44.7	22	-89.1	4	-45.1	21	-71.5	13
		10%	-70.1	14	-87.9	10	-66.4	12	-84.2	6
		2%	-72.4	15	-63.6	38	-76.8	10	-79.9	14
		Total	-39.7	53	-70.8	26	-20.7	62	-55.3	45
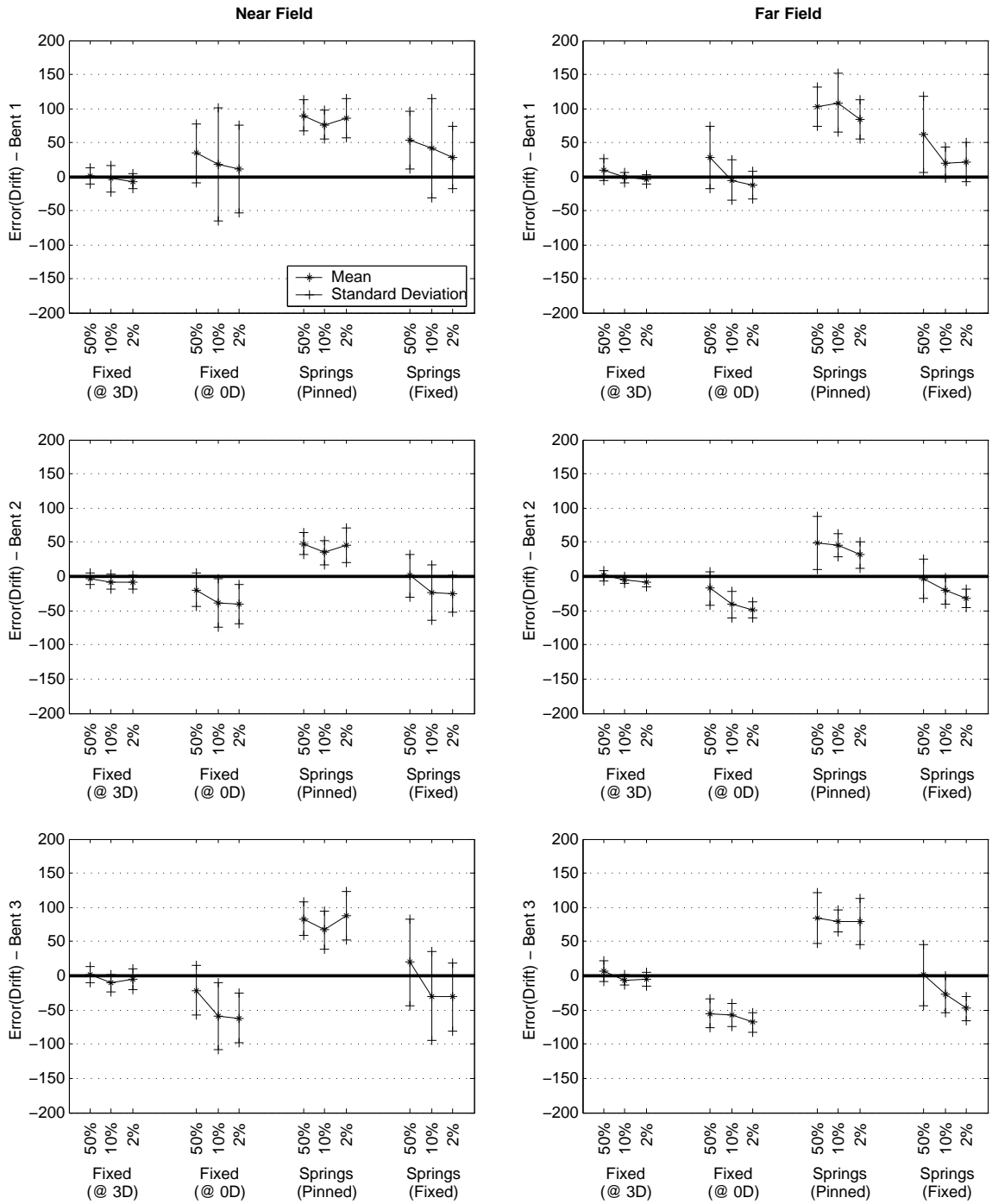
Figure H.1: Error in estimated drift ratios for the inelastic structural models
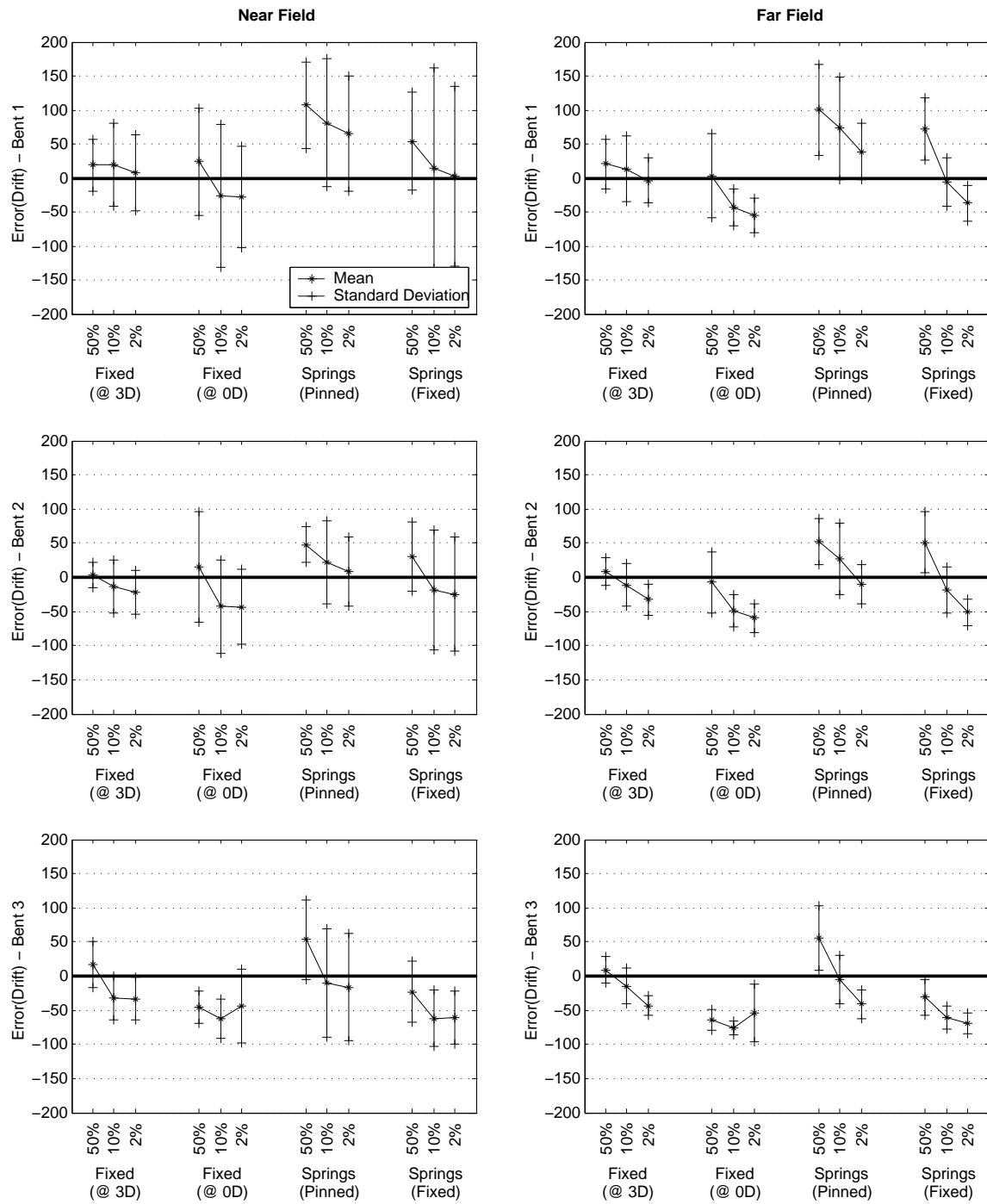
Figure H.2: Error in estimated drift ratios for the effective elastic structural models
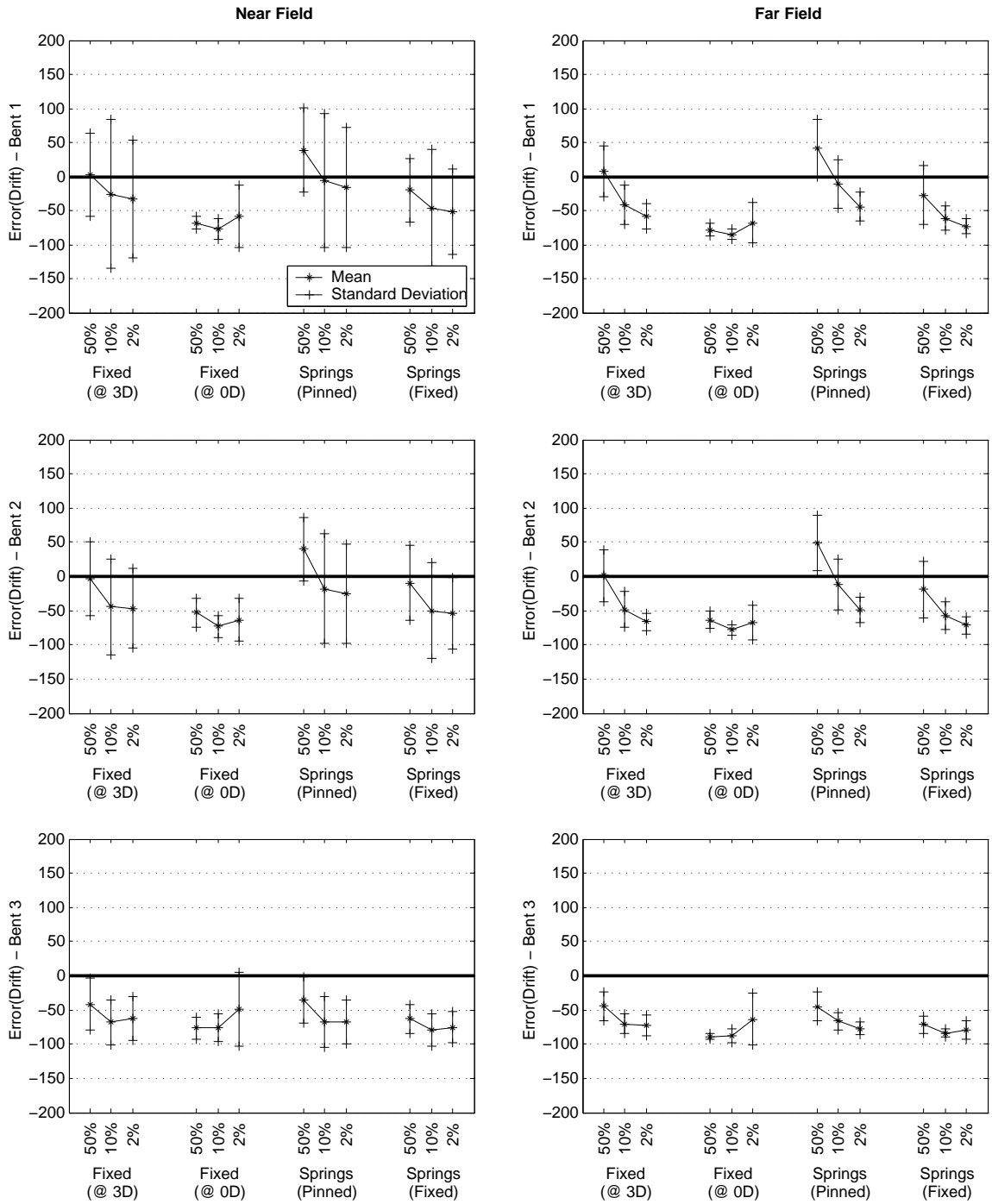
Figure H.3: Error in estimated drift ratios for the gross elastic structural models

Table H.4: Error in estimated plastic rotation for the inelastic structural models

Bent	Field	Hazard	Foundation Approximations							
			Fixed @ 3D		Fixed @ 0D		Springs (Pinned)		Springs (Fixed)	
			μ	σ	μ	σ	μ	σ	μ	σ
1	NF	50%	7.6	24	120.1	119	141.1	63	150.4	117
		10%	9.8	59	150.1	465	105.5	90	175.6	445
		2%	-5.1	15	48.7	145	99.4	42	60.0	96
	FF	50%	29.8	37	139.4	148	194.4	112	211.3	163
		10%	0.0	12	7.8	41	122.0	49	38.7	33
		2%	-5.9	8	-6.8	25	87.0	32	32.2	36
2	NF	50%	-2.0	20	39.2	99	60.9	44	109.6	158
		10%	-9.0	18	-9.4	136	26.1	18	29.1	203
		2%	-9.3	13	-12.8	117	47.4	35	5.7	116
	FF	50%	0.6	21	35.1	84	69.0	103	69.2	115
		10%	-6.4	7	-39.4	32	39.8	22	-9.2	38
		2%	-10.8	8	-51.7	13	25.4	22	-30.3	18
3	NF	50%	16.0	24	28.4	98	165.1	90	129.1	185
		10%	-9.3	17	-33.1	135	90.6	66	14.9	195
		2%	-2.1	21	-50.3	75	105.4	60	-8.1	109
	FF	50%	28.4	40	-43.1	48	186.6	135	79.9	140
		10%	-3.8	10	-54.8	23	96.4	24	-13.3	42
		2%	-4.9	12	-68.4	17	85.9	37	-45.2	21
		Total	1.3	26	11.1	150	97.1	80	55.5	167

Table H.5: Error in estimated column shear for the inelastic structural models

Bent	Field	Hazard	Foundation Approximations							
			Fixed @ 3D		Fixed @ 0D		Springs (Pinned)		Springs (Fixed)	
			μ	σ	μ	σ	μ	σ	μ	σ
1	NF	50%	3.8	10	98.4	25	-8.1	9	90.3	24
		10%	-5.7	9	74.5	33	-13.9	8	75.2	29
		2%	-7.5	8	67.0	19	-14.2	7	68.2	16
	FF	50%	5.0	8	102.7	24	-1.2	10	98.3	23
		10%	-7.2	3	67.4	10	-15.4	3	67.0	9
		2%	-10.6	2	58.7	3	-17.5	1	61.5	4
2	NF	50%	1.6	8	68.2	21	-24.8	3	57.5	27
		10%	-4.7	5	47.2	24	-27.4	6	46.7	26
		2%	-6.3	5	44.9	22	-29.6	4	43.1	15
	FF	50%	2.8	3	68.3	22	-22.5	4	55.6	18
		10%	-4.1	5	38.9	12	-28.4	3	40.8	9
		2%	-7.5	3	36.3	4	-31.3	2	36.9	3
3	NF	50%	4.2	7	116.6	29	10.8	10	119.7	23
		10%	-6.2	7	90.7	30	1.4	11	97.3	28
		2%	-7.4	6	86.7	22	0.8	6	91.1	19
	FF	50%	7.3	9	96.0	33	13.8	10	112.4	21
		10%	-5.7	4	89.2	11	-0.7	4	93.2	11
		2%	-9.2	2	80.4	8	-2.5	1	83.6	6
		Total	-3.2	8	74.0	30	-11.7	15	74.4	31

Figure H.4: Error in estimated maximum plastic rotations for the inelastic structural models

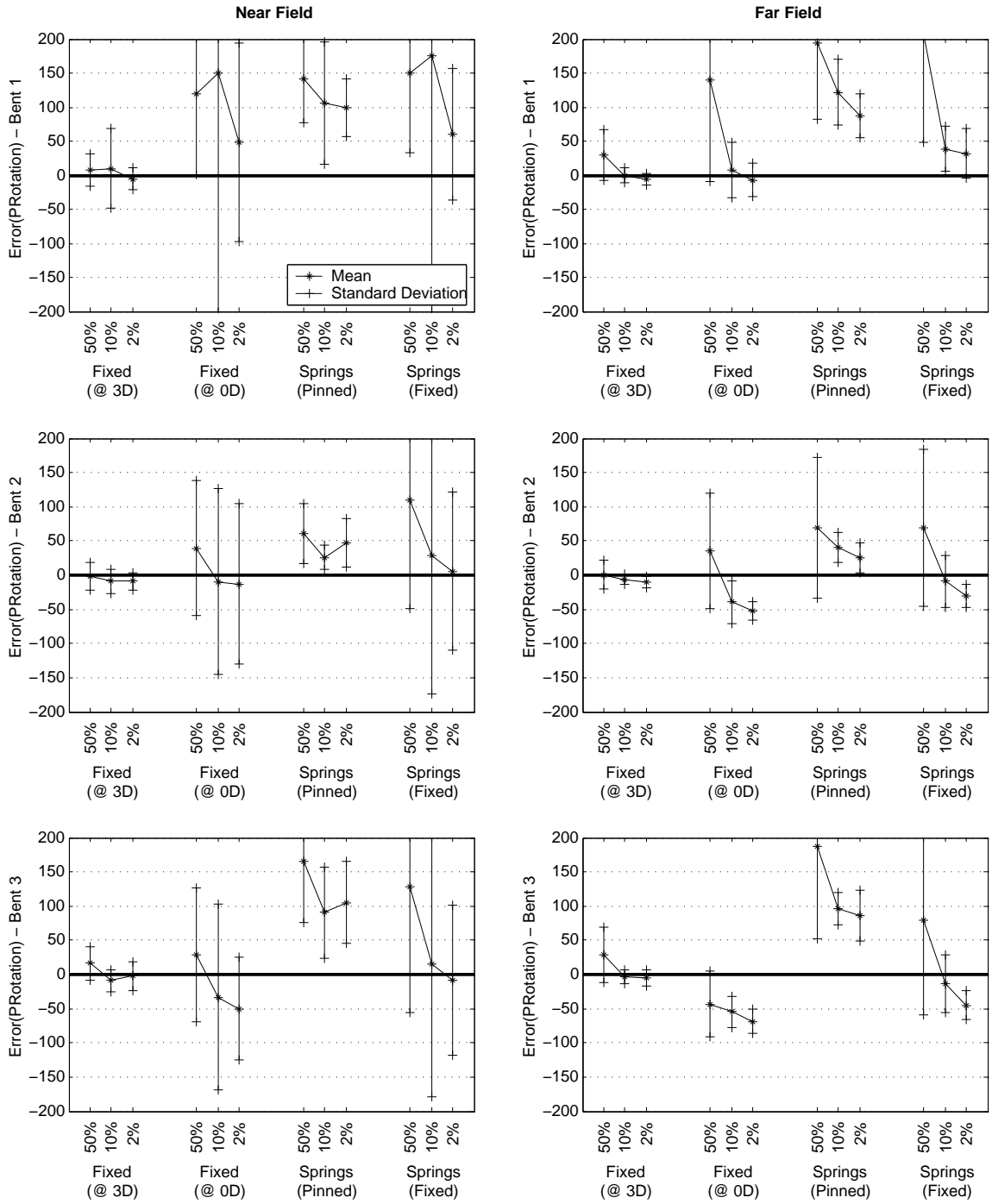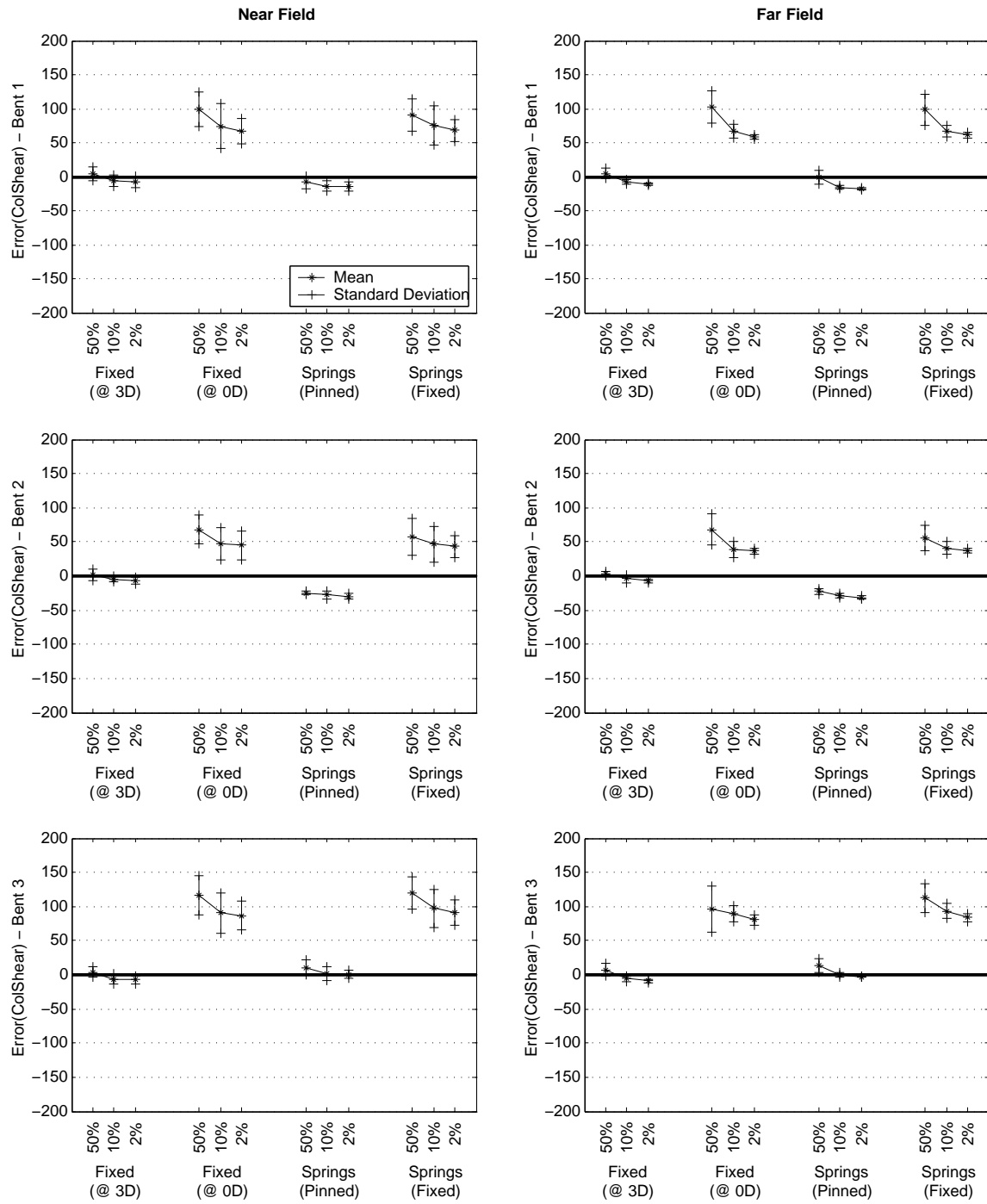Figure H.5: Error in estimated column shear for the inelastic structural models

Table H.6: Error in the estimated drift ratios for the inelastic fixed base models

Bent	Field	Hazard	Fixity Depth									
			2.0D		2.5D		3.0D		3.5D		4.0D	
			μ	σ	μ	σ	μ	σ	μ	σ	μ	σ
1	NF	50%	9.0	10	5.8	14	1.0	12	2.9	13	3.3	17
		10%	7.2	26	5.1	24	-3.1	19	-7.9	12	-12.9	14
		2%	4.3	19	-3.4	13	-6.8	11	-8.7	9	-6.9	13
	FF	50%	13.9	25	11.4	22	9.9	17	9.3	24	22.0	30
		10%	9.1	16	4.8	9	-1.5	8	3.0	16	4.0	23
		2%	5.4	10	0.3	8	-4.7	7	-8.4	8	-11.4	11
2	NF	50%	2.8	15	2.4	15	-3.8	8	-3.7	8	-2.8	13
		10%	-6.8	24	-6.3	17	-7.9	11	-9.5	9	-11.9	8
		2%	-7.2	14	-7.6	13	-8.6	11	-8.8	10	-7.4	10
	FF	50%	6.2	19	5.6	14	0.9	8	8.8	20	8.1	16
		10%	-6.5	14	-4.2	7	-5.0	4	0.1	11	2.2	16
		2%	-11.6	11	-9.1	8	-8.4	7	-8.1	8	-9.7	10
3	NF	50%	7.9	22	7.5	18	1.4	12	-1.4	12	-3.6	15
		10%	-10.0	29	-10.7	20	-10.9	13	-9.8	12	-10.7	14
		2%	-5.1	22	-1.8	20	-5.4	15	-7.9	12	-9.0	12
	FF	50%	9.6	23	7.8	17	6.1	15	7.4	10	10.0	25
		10%	-8.1	15	-7.1	9	-5.9	7	1.8	7	1.7	14
		2%	-8.5	16	-8.6	15	-4.9	10	-6.0	12	-7.6	11
	Total		0.6	20.0	-0.5	16.2	-3.2	12.1	-2.6	13.6	-2.4	17.9

Table H.7: Error in the estimated plastic rotation for the inelastic fixed base models

Bent	Field	Hazard	Fixity Depth									
			2.0D		2.5D		3.0D		3.5D		4.0D	
			μ	σ	μ	σ	μ	σ	μ	σ	μ	σ
1	NF	50%	29.7	23	21.8	33	7.6	24	8.2	22	6.7	30
		10%	42.1	125	32.1	102	9.8	59	-5.2	27	-15.0	20
		2%	13.1	32	-0.1	16	-5.1	15	-9.6	11	-8.3	16
	FF	50%	53.4	59	42.4	55	29.8	37	26.8	58	48.0	74
		10%	16.0	23	8.9	13	0.0	12	3.6	20	2.7	27
		2%	7.4	11	0.7	8	-5.9	8	-10.9	9	-14.7	12
2	NF	50%	35.3	51	25.0	49	-2.0	20	-9.7	12	-12.9	25
		10%	3.2	55	-2.1	34	-9.0	18	-14.1	11	-18.1	10
		2%	-1.5	25	-5.9	16	-9.3	13	-11.8	12	-11.5	13
	FF	50%	41.6	55	25.4	34	0.6	21	13.9	43	6.3	39
		10%	-2.3	26	-2.5	14	-6.4	7	-0.8	15	0.0	22
		2%	-12.1	14	-10.6	10	-10.8	8	-11.7	10	-14.6	12
3	NF	50%	44.8	55	36.6	43	16.0	24	4.0	23	-5.8	26
		10%	3.7	62	-3.3	37	-9.3	17	-11.5	12	-12.7	14
		2%	4.1	41	6.7	40	-2.1	21	-7.6	14	-11.1	13
	FF	50%	57.1	64	41.1	45	28.4	40	18.6	23	21.5	58
		10%	-1.0	23	-3.0	13	-3.8	10	4.6	10	3.6	20
		2%	-6.7	18	-7.7	17	-4.9	12	-7.4	13	-9.9	12
	Total		18.2	52.3	11.4	41.3	1.3	25.9	-1.1	24.6	-2.6	32.4

Table H.8: Error in the estimated column shear for the inelastic fixed base models

Bent	Field	Hazard	Fixity Depth									
			2.0D		2.5D		3.0D		3.5D		4.0D	
			μ	σ	μ	σ	μ	σ	μ	σ	μ	σ
1	NF	50%	21.3	13	11.8	12	3.8	10	-5.6	6	-10.6	8
		10%	9.4	15	0.9	11	-5.7	9	-11.4	8	-17.5	6
		2%	6.4	9	-1.3	9	-7.5	8	-14.5	5	-13.6	17
	FF	50%	24.2	13	15.1	11	5.0	8	-2.0	6	-5.0	9
		10%	7.1	4	-0.6	4	-7.2	3	-12.9	3	-17.7	3
		2%	3.2	3	-4.0	2	-10.6	2	-16.0	2	-20.7	2
2	NF	50%	18.9	11	11.0	11	1.6	8	-6.4	5	-13.2	3
		10%	7.6	8	1.8	7	-4.7	5	-9.8	4	-14.4	5
		2%	5.3	9	-1.5	6	-6.3	5	-11.0	6	-15.4	5
	FF	50%	19.2	12	11.1	8	2.8	3	-2.5	5	-8.5	7
		10%	5.4	5	0.5	5	-4.1	5	-9.0	5	-12.6	5
		2%	2.1	3	-3.2	3	-7.5	3	-11.3	3	-15.7	3
3	NF	50%	24.2	11	13.8	9	4.2	7	-3.3	7	-12.0	5
		10%	12.5	14	2.8	11	-6.2	7	-13.7	4	-19.8	3
		2%	10.2	9	1.6	10	-7.4	6	-14.3	5	-20.2	5
	FF	50%	28.6	13	16.6	10	7.3	9	-3.5	6	-9.8	6
		10%	10.8	5	1.8	4	-5.7	4	-12.5	4	-18.1	4
		2%	7.2	4	-1.4	4	-9.2	2	-14.6	3	-21.2	2
		Total	12.4	12.2	4.3	10.3	-3.2	8.2	-9.7	6.6	-14.8	7.5

Figure H.6: Sensitivity of drift accuracy to equivalent fixity depth

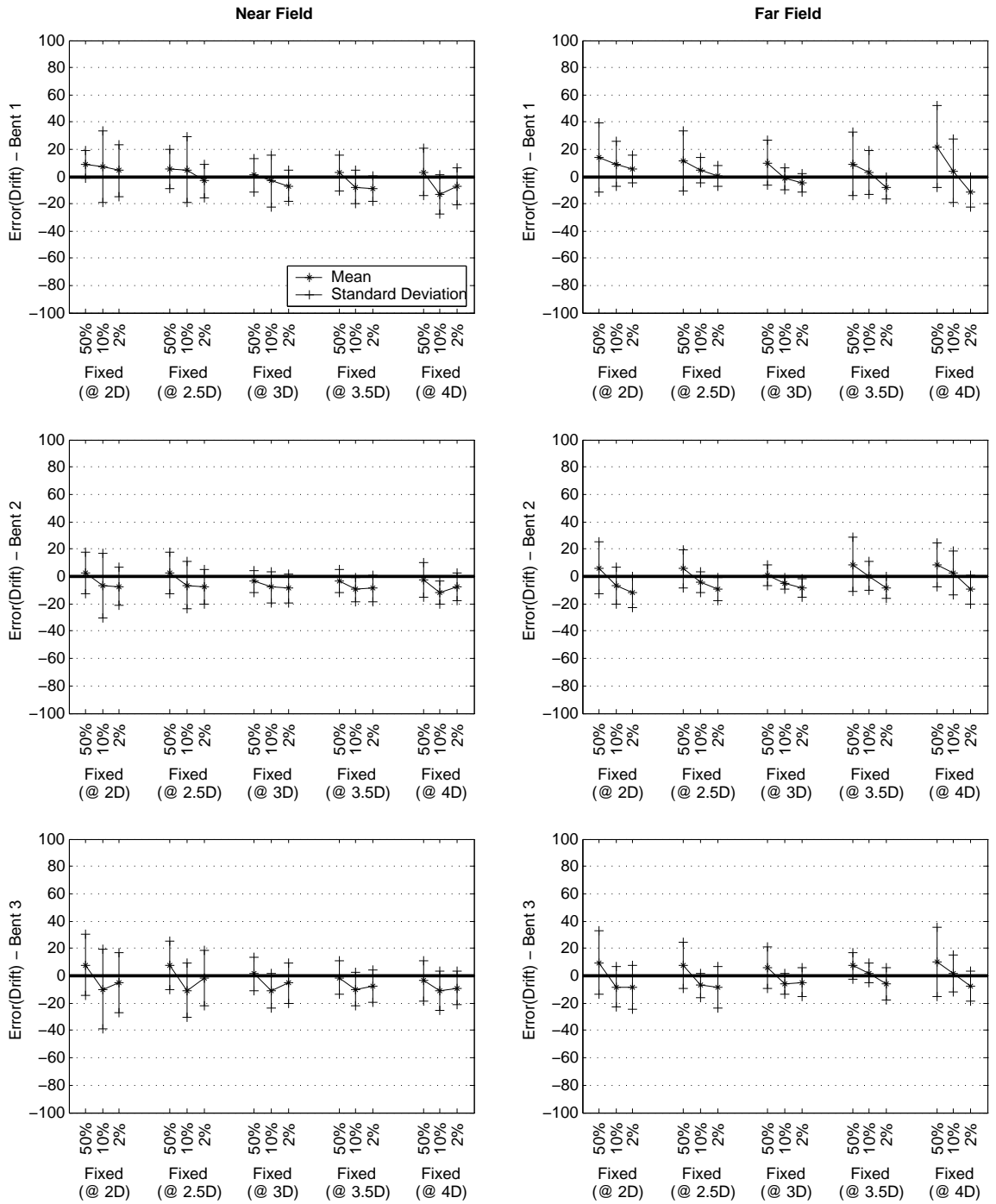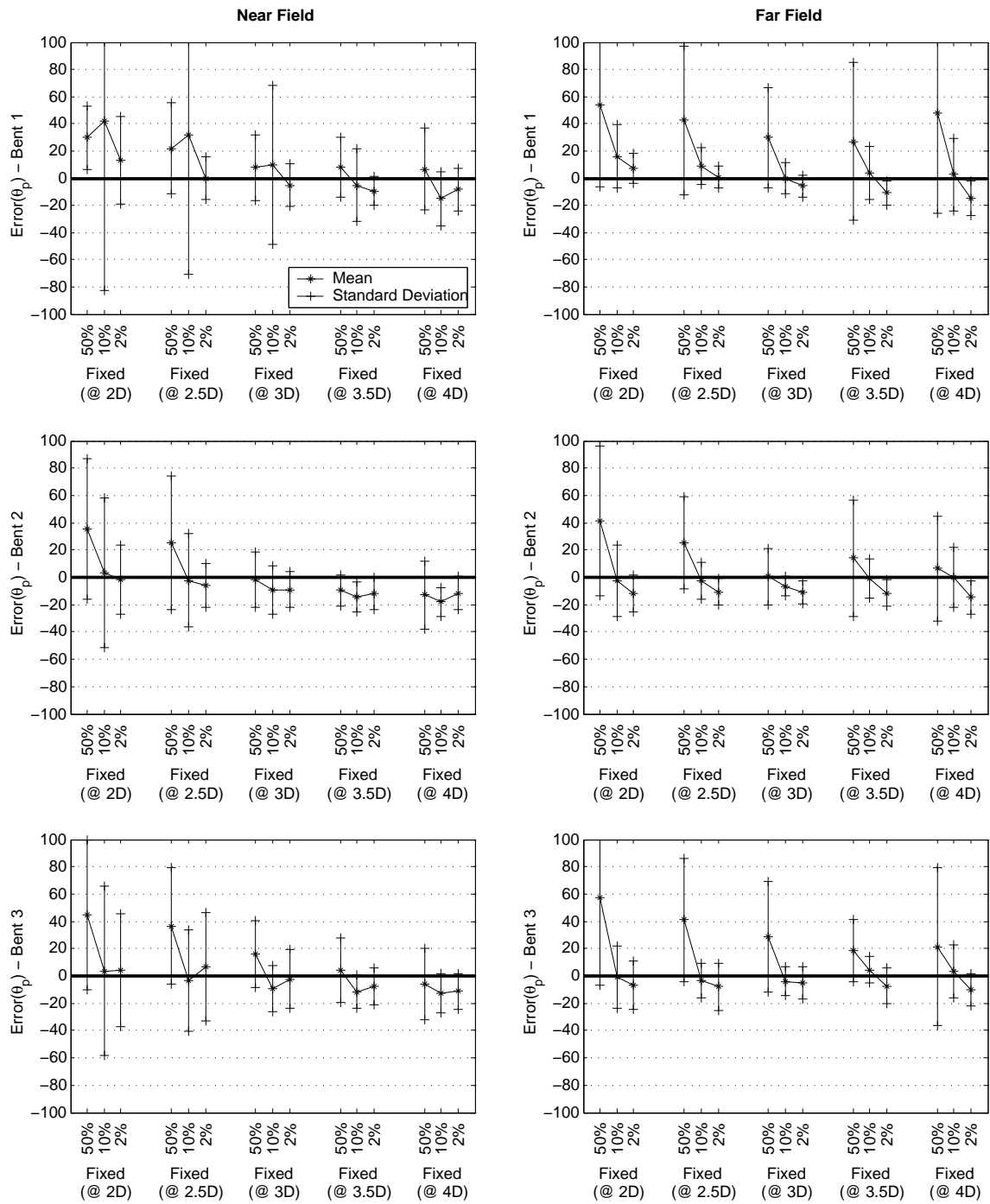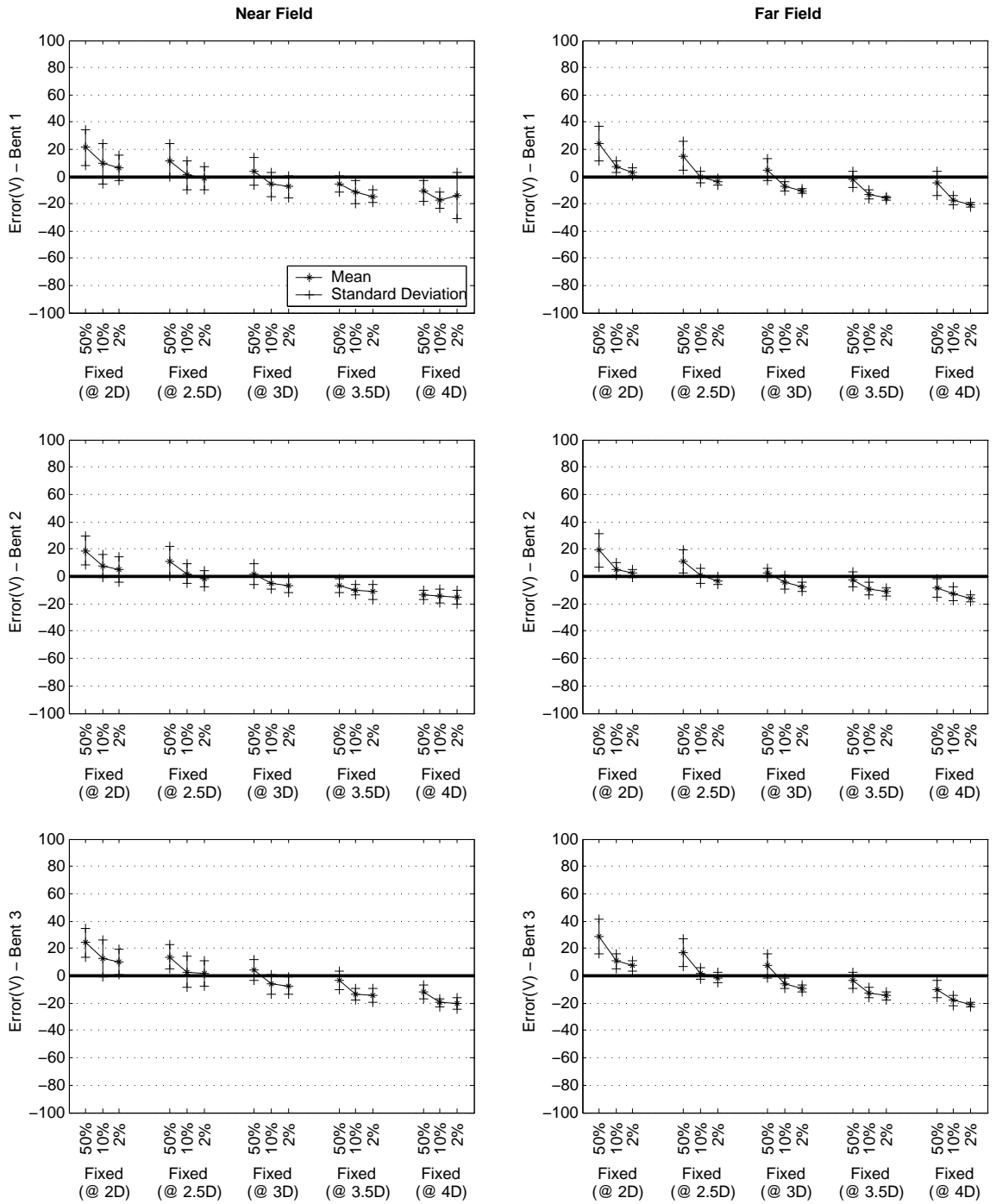Figure H.7: Sensitivity of plastic rotation accuracy to equivalent fixity depth

Figure H.8: Sensitivity of shear accuracy to equivalent fixity depth
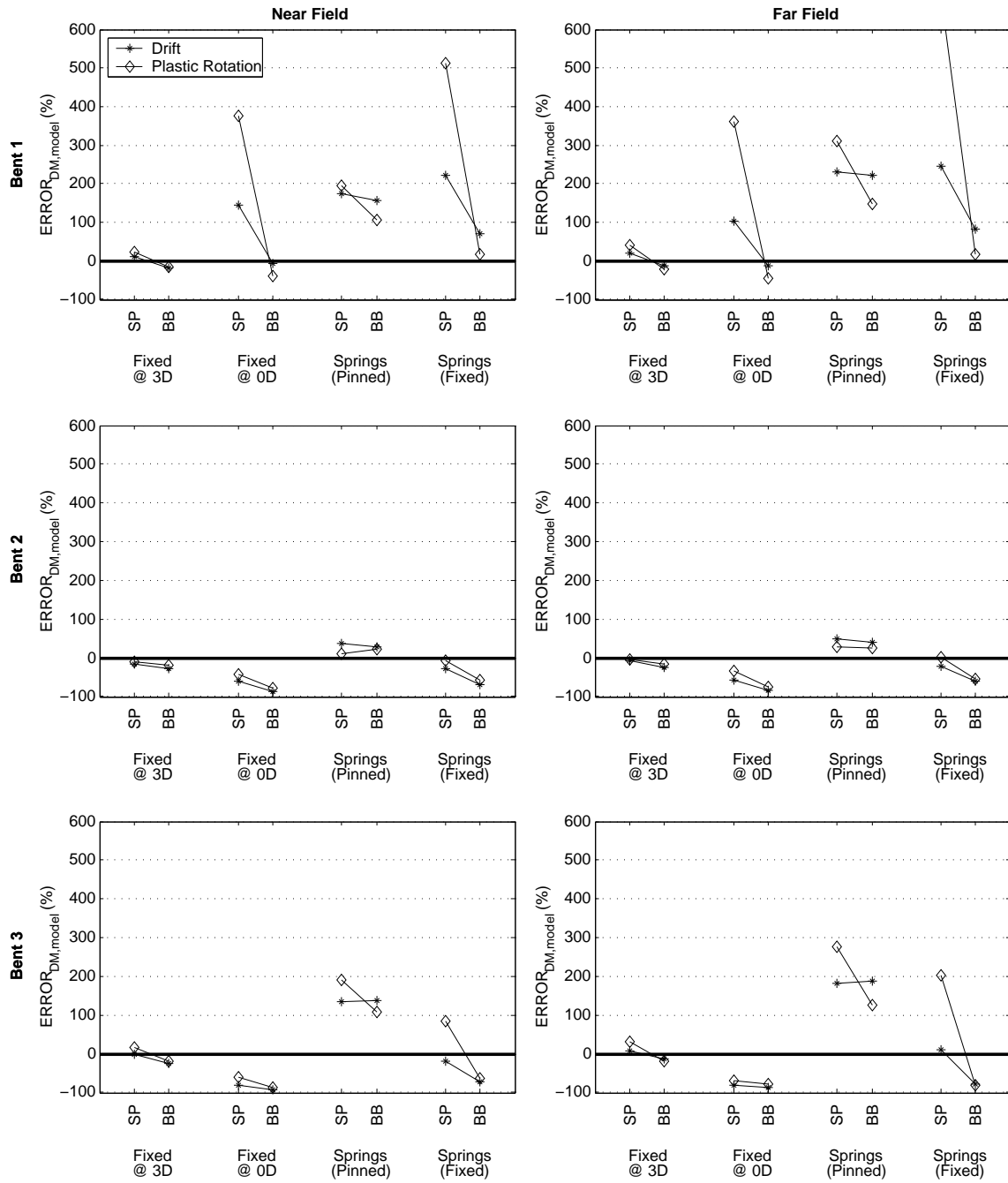
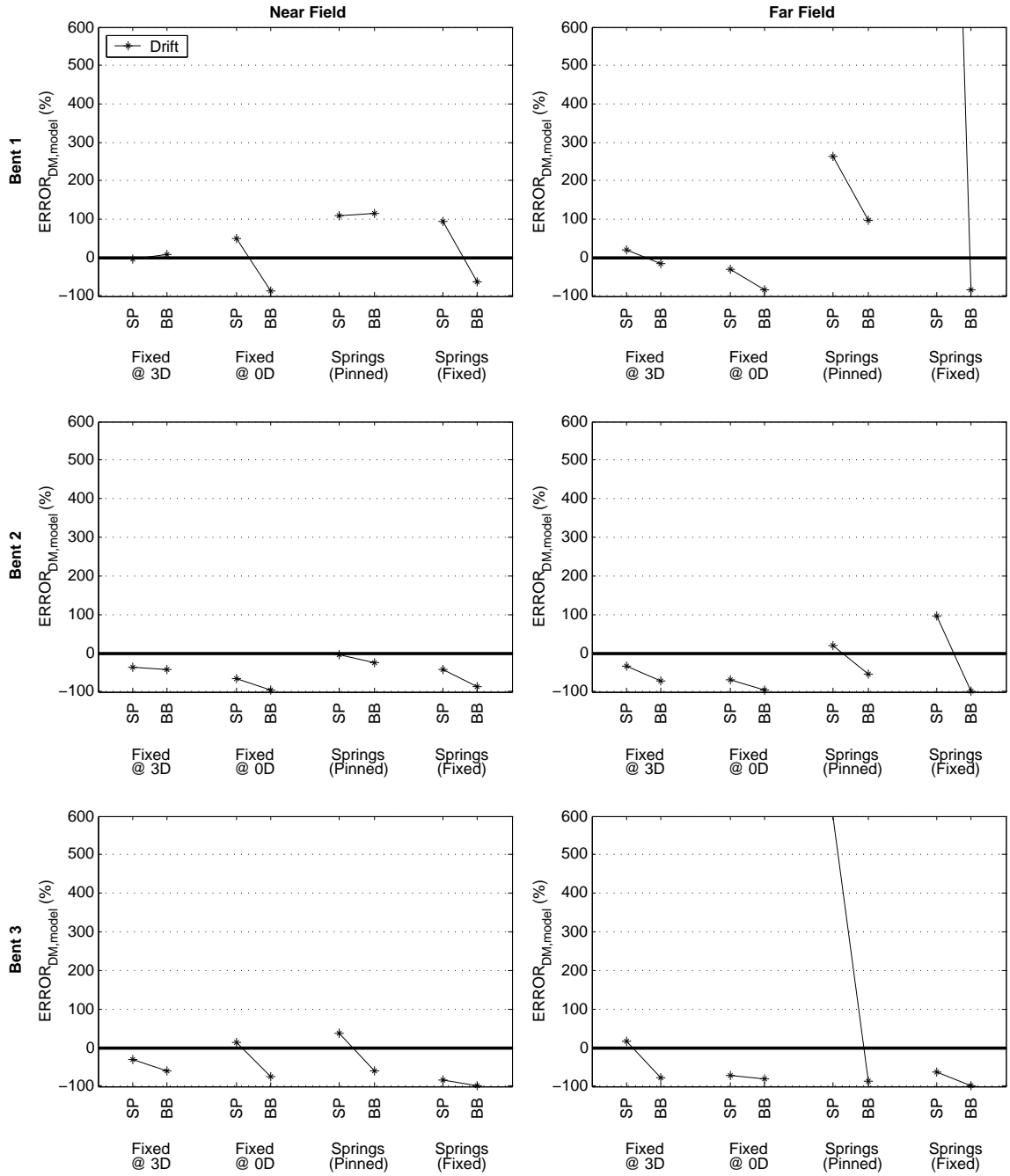Figure H.9: DM hazard error for inelastic structural modeling approximations

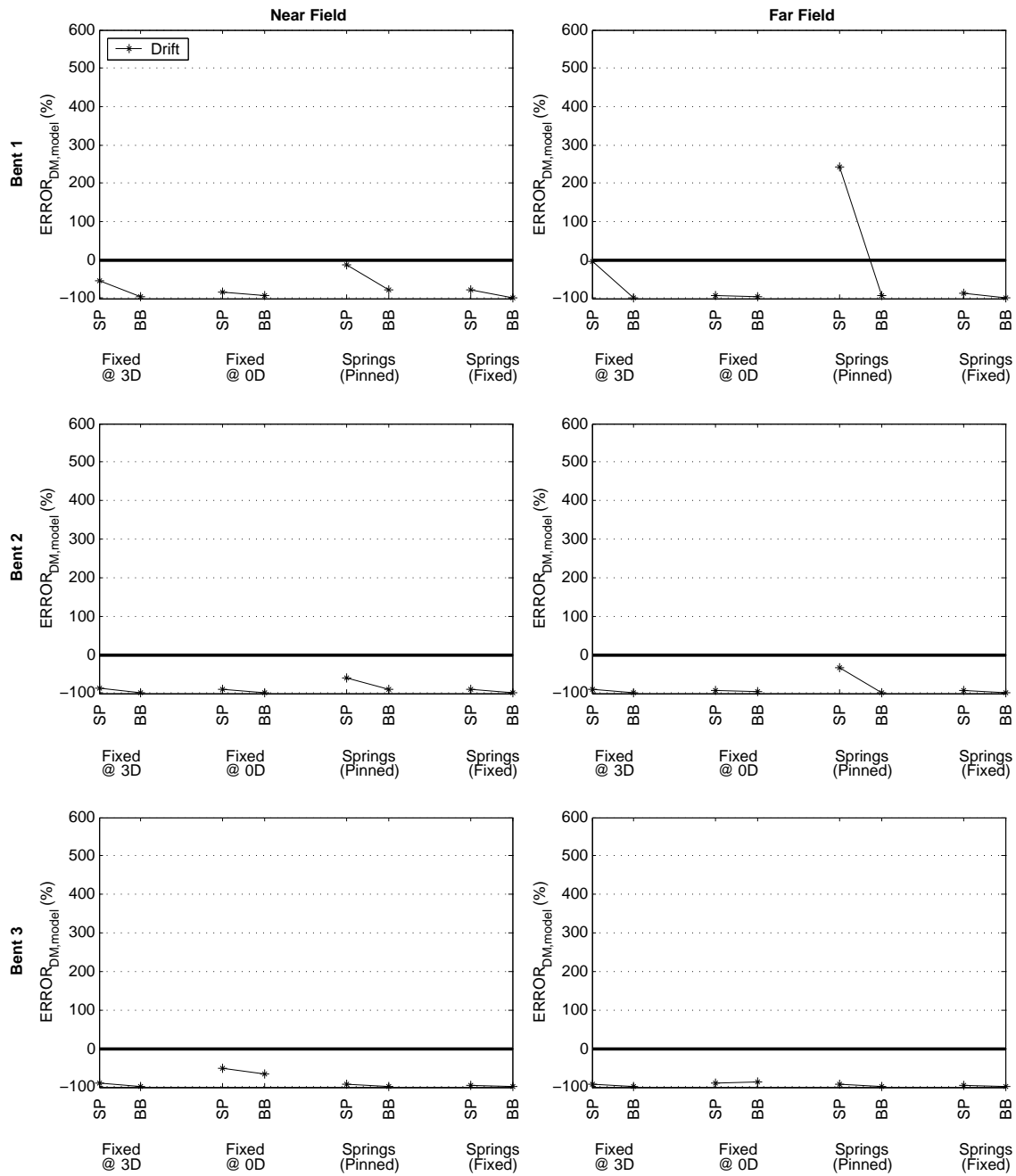Figure H.10: DM hazard error for effective elastic structural modeling approximations

Figure H.11: DM hazard error for gross elastic structural modeling approximations

Table H.9: Error in the estimated damage for the inelastic models

Bent	Field	EDP	Foundation Approximations							
			Fixed @ 3D		Fixed @ 0D		Springs (Pinned)		Springs (Fixed)	
			SP	BB	SP	BB	SP	BB	SP	BB
1	NF	Drift Ratio	11.0	-17.8	143.5	-5.4	173.3	155.8	223.1	69.6
		Plastic Rotation	21.8	-15.4	377.0	-38.2	194.7	106.8	511.5	17.3
	FF	Drift Ratio	19.5	-13.6	102.3	-13.6	230.1	221.1	244.8	83.8
		Plastic Rotation	41.6	-21.0	360.7	-45.1	309.5	148.1	700.3	16.7
2	NF	Drift Ratio	-16.7	-28.2	-61.0	-85.5	36.3	28.6	-28.4	-69.5
		Plastic Rotation	-11.0	-20.2	-42.0	-76.7	11.1	22.6	-5.5	-57.7
	FF	Drift Ratio	-7.4	-23.2	-56.6	-84.0	48.4	39.0	-22.3	-59.1
		Plastic Rotation	-4.0	-14.9	-34.3	-76.3	29.1	25.1	3.4	-53.0
3	NF	Drift Ratio	-1.4	-24.7	-82.3	-92.3	134.3	138.4	-18.9	-72.2
		Plastic Rotation	15.2	-20.1	-60.2	-85.5	190.0	107.0	85.4	-64.2
	FF	Drift Ratio	8.6	-13.9	-80.6	-86.5	182.7	188.2	10.6	-77.4
		Plastic Rotation	31.9	-19.6	-68.3	-78.7	275.4	126.0	203.1	-81.1
		μ	9.1	-19.4	41.5	-64.0	151.2	108.9	158.9	-28.9
		σ	17.1	4.3	161.8	29.1	95.8	64.3	225.3	56.8

Table H.10: Error in the estimated damage for the effective elastic models

Bent	Field	EDP	Foundation Approximations							
			Fixed @ 3D		Fixed @ 0D		Springs (Pinned)		Springs (Fixed)	
			SP	BB	SP	BB	SP	BB	SP	BB
1	NF	Drift Ratio	-4.1	7.0	50.1	-86.6	110.3	114.2	95.1	-61.8
	FF	Drift Ratio	19.1	-15.5	-30.5	-84.3	263.3	96.4	2838.0	-82.6
2	NF	Drift Ratio	-36.9	-43.0	-65.2	-97.0	-4.5	-25.4	-43.6	-86.9
	FF	Drift Ratio	-32.3	-71.9	-68.7	-94.6	19.0	-55.6	95.9	-98.8
3	NF	Drift Ratio	-32.0	-61.1	14.3	-75.0	38.0	-60.9	-82.6	-98.2
	FF	Drift Ratio	16.4	-78.0	-71.3	-80.2	605.0	-88.1	-62.7	-99.5
		μ	-11.7	-43.8	-28.5	-86.3	171.8	-3.2	473.4	-88.0
		σ	25.6	33.6	50.6	8.4	233.3	86.6	1161.1	14.6

Table H.11: Error in the estimated damage for the gross elastic models

Bent	Field	EDP	Foundation Approximations							
			Fixed @ 3D		Fixed @ 0D		Springs (Pinned)		Springs (Fixed)	
			SP	BB	SP	BB	SP	BB	SP	BB
1	NF	Drift Ratio	-54.0	-95.6	-83.1	-92.9	-13.0	-76.4	-78.9	-98.9
	FF	Drift Ratio	-2.6	-99.0	-92.2	-95.1	242.9	-92.9	-85.8	-98.6
2	NF	Drift Ratio	-86.6	-98.5	-89.1	-97.5	-61.6	-90.6	-90.8	-99.4
	FF	Drift Ratio	-89.1	-99.9	-92.0	-96.8	-32.3	-98.8	-91.2	-99.3
3	NF	Drift Ratio	-90.3	-98.3	-51.6	-66.1	-93.3	-99.3	-95.9	-99.5
	FF	Drift Ratio	-91.7	-99.6	-90.5	-86.4	-94.0	-99.7	-96.5	-99.0
		μ	-69.0	-98.5	-83.1	-89.2	-8.6	-93.0	-89.8	-99.1
		σ	35.5	1.5	15.8	12.0	127.4	9.0	6.6	0.4

Table H.12: Error in damage measure hazard for inelastic fixed base models

Bent	Field	EDP	Fixity Depth									
			2.0D		2.5D		3.0D		3.5D		4.0D	
			SP	BB	SP	BB	SP	BB	SP	BB	SP	BB
1	NF	Drift Ratio	56.0	-0.6	45.9	-5.4	11.0	-17.8	-2.1	-23.5	-11.9	-32.0
		Plastic Rotation	85.2	-7.9	67.9	-8.7	21.8	-15.4	3.0	-18.7	-10.2	-25.2
	FF	Drift Ratio	60.5	15.3	26.1	-0.4	19.5	-13.6	16.0	-17.8	13.7	-16.7
		Plastic Rotation	114.5	-3.9	58.4	-12.7	41.6	-21.0	32.2	-23.5	27.3	-22.6
2	NF	Drift Ratio	-9.5	-36.7	-5.8	-30.8	-16.7	-28.2	-20.9	-28.0	-26.8	-30.7
		Plastic Rotation	0.4	-27.2	3.9	-21.9	-11.0	-20.2	-16.4	-19.6	-24.7	-22.6
	FF	Drift Ratio	7.7	-34.8	-3.0	-25.7	-7.4	-23.2	-2.7	-26.6	-7.3	-20.6
		Plastic Rotation	18.8	-31.1	7.0	-21.9	-4.0	-14.9	-3.0	-19.9	-6.4	-10.2
3	NF	Drift Ratio	16.7	-31.6	12.6	-24.8	-1.4	-24.7	-9.3	-24.1	-17.1	-28.9
		Plastic Rotation	57.0	-36.0	37.8	-23.2	15.2	-20.1	0.1	-17.4	-10.6	-20.0
	FF	Drift Ratio	34.8	-19.5	12.7	-19.1	8.6	-13.9	5.6	-12.7	4.7	-13.1
		Plastic Rotation	101.1	-35.0	54.2	-28.3	31.9	-19.6	17.7	-12.3	18.5	-9.3
		μ	45.3	-20.8	26.5	-18.6	9.1	-19.4	1.7	-20.4	-4.2	-21.0
		σ	38.8	16.6	24.5	9.2	17.1	4.3	14.2	4.8	16.2	7.3

Table H.13: Error in damage measure hazard for intensity measures

Bent	Field	EDP	Fixity Depth									
			PGA		PGV		SA_1		Ia		MCOR	
			SP	BB	SP	BB	SP	BB	SP	BB	SP	BB
1	NF	Drift Ratio	117.1	19.9	14.6	-6.3	17.9	11.0	91.4	9.1	-2.9	-4.2
		Plastic Rotation	125.9	30.2	12.0	-5.5	25.9	15.1	87.4	14.3	-3.6	-4.4
	FF	Drift Ratio	66.9	-6.9	11.3	6.4	16.2	2.1	10.9	6.6	-6.0	5.3
		Plastic Rotation	65.0	2.6	10.3	7.0	19.1	5.1	9.2	6.9	-4.0	3.8
2	NF	Drift Ratio	99.1	11.9	5.7	-10.5	18.5	10.6	63.3	-1.4	-4.4	-4.9
		Plastic Rotation	78.6	7.4	1.7	-11.6	16.4	10.0	51.5	-3.9	-5.8	-5.3
	FF	Drift Ratio	31.1	-10.4	8.4	6.1	2.6	0.6	11.8	6.6	-1.4	5.9
		Plastic Rotation	34.5	-11.3	9.5	6.0	7.0	0.8	11.0	6.3	-0.6	6.3
3	NF	Drift Ratio	99.7	13.7	10.4	-8.1	12.3	8.8	70.1	1.9	-4.2	-4.7
		Plastic Rotation	112.1	26.7	8.2	-6.8	17.6	11.6	74.0	10.5	-4.6	-4.8
	FF	Drift Ratio	67.7	-7.3	13.7	6.6	-1.2	0.2	16.7	7.1	-5.6	5.4
		Plastic Rotation	58.2	0.7	12.6	7.5	4.2	1.3	13.9	7.9	-3.2	4.2
		μ	79.7	6.4	9.9	-0.8	13.0	6.4	42.6	6.0	-3.9	0.2
		σ	31.3	14.3	3.6	7.9	8.1	5.3	33.3	5.0	1.7	5.2

CURRICULUM VITAE

Richard Tyler Ranf

EDUCATION -

Ph.D.	**Structural Engineering**	University of Washington	'07
M.S.	**Structural Engineering**	University of Washington	'03
B.S.	**Civil Engineering**	Washington U. in St. Louis	'02
B.A.	**Physics**	University of Puget Sound	'02

PROFESSIONAL EXPERIENCE -

Magnusson Klemencic Associates   Seattle, Washington   '02
- Analyzed loading conditions, including seismic, wind and snow.
- Designed gravity and lateral systems
- Designed steel, concrete and cmu systems

RESEARCH EXPERIENCE -

NSF Graduate Research Fellow   University of Washington   '02-'07
- Identified effects of cycling on damage progression in concrete columns
- Dynamically tested an asymmetric quarter-scale two-span reinforced concrete bridge
- Performed system identification and structural health monitoring techniques to investigate the state of the two-span bridge during testing
- Investigated the effects of soil-structure interaction on bridge response
- Investigated the effects of motion incoherency on bridge response

Earthquake Engineering and   Washington U. in St. Louis   '00-'02
Structural Control Laboratory
- Reproduced historic earthquakes on an instructional shake table
- Interpreted earthquake signals using Laplace and Fourier Transforms
- Constructed small scale structure to test joint damping

PEER Undergraduate Research   University of Washington   '01
Assistant
- Compiled database bridges damaged from the Nisqually earthquake
- Analyzed data to estimate bridge damage for similar occurrences

AWARDS & HONORS -

National Science Foundation Graduate Research Fellowship - Currently a fellow at the University of Washington while investigating the response of a two-span reinforced concrete bridge to seismic loading.

Brown Fellowship - Received from Washington University in St. Louis for two years of undergraduate study in engineering.

EERI Undergraduate Student Paper Competition - Presented by the Earthquake Engineering Research Institute for a paper investigating *The Possibility of Damage to the Melvin Price Lock due to Soil Liquefaction*

PUBLICATIONS -

Ranf, R. T., M. Eberhard, and S. Malone (2007). Post-Earthquake Prioritization of Bridge Inspections. Earthquake Spectra, Earthquake Engineering Research Institute, February 2007.

Ranf, R., M. Eberhard, and J. Stanton (2006). Effect of cyclic loading on shear strength of reinforced concrete columns. ACI Special Publication, ACI-236.

Ranf, R. T., H. Shin, M. Eberhard, P. Arduino, and S. Kramer (2006). Experimentally Based Evaluation of Soil-Foundation-Structure Interaction for a Reinforced Concrete Bridge. Eighth National Conference on Earthquake Engineering, Paper # 504.

Johnson, N., R. T. Ranf, M. S. Saiidi, D. Sanders, and M. Eberhard (2006). Shaketable Studies of a two-span reinforced concrete bridge. Eighth National Conference on Earthquake Engineering, Paper # 1437.

Ranf, R., J. Nelson, Z. Price, M. Eberhard, and J. Stanton (2005). Damage accumulation in lightly confined reinforced concrete bridge columns. Pacific Earthquake Engineering Research Center 2005/08.

Ranf, R., M. O. Eberhard, and M. Berry (2001). Damage to bridges during the 2001 nisqually earthquake. Technical Report 2001/15, Pacific Earthquake Engineering Research Center.

Ranf, R. (2001). The possibility of damage to the melvin price lock due to soil liquefaction. Proceedings of the EERI Annual Consortium on Risk Assessment.

CONFERENCE PRESENTATIONS -

Ranf, R., H. Shin, M. Eberhard, P. Arduino, and S. Kramer (2006). Experimentally based evaluation of soil-foundation-structure interaction for a reinforced concrete bridge. Eighth National Conference on Earthquake Engineering.

Ranf, R. and M. Eberhard (2003). Bridge damage during the 2001 nisqually earthquake. ASCE Structures Congress.

Ranf, R. and M. Eberhard (2003). Prioritizing post-earthquake bridge inspections using shakemaps. 7th US/Japan Workshop on Earthquake Hazard Mitigation.